UNIVERSIDADE FEDERAL DE SÃO CARLOS
CENTRO DE CIÊNCIAS EXATAS E TECNOLOGIA
DEPARTAMENTO DE ENGENHARIA CIVIL
PROGRAMA DE PÓS-GRADUAÇÃO EM ENGENHARIA CIVIL

FELIPE PIANA VENDRAMELL FERREIRA

CAPACIDADE RESISTENTE DE VIGAS CELULARES MISTAS À INSTABILIDADE NO MONTANTE DE ALMA

São Carlos
2021

UNIVERSIDADE FEDERAL DE SÃO CARLOS
CENTRO DE CIÊNCIAS EXATAS E TECNOLOGIA
DEPARTAMENTO DE ENGENHARIA CIVIL
PROGRAMA DE PÓS-GRADUAÇÃO EM ENGENHARIA CIVIL

FELIPE PIANA VENDRAMELL FERREIRA

CAPACIDADE RESISTENTE DE VIGAS CELULARES MISTAS À INSTABILIDADE NO MONTANTE DE ALMA

Tese apresentada ao Programa de Pós-Graduação em Engenharia Civil da Universidade Federal de São Carlos, para obtenção do título de doutor em Engenharia Civil.
Área de concentração: Estruturas e Geotecnia.

Orientador: Prof. Dra. Silvana de Nardin
Coorientador: Prof. Dr. Carlos Humberto Martins

São Carlos
2021

UNIVERSIDADE FEDERAL DE SÃO CARLOS

Centro de Ciências Exatas e de Tecnologia
Programa de Pós-Graduação em Engenharia Civil

Folha de Aprovação

Defesa de Tese de Doutorado do candidato Felipe Piana Vendramell Ferreira, realizada em 07/06/2021.

Comissão Julgadora:

Profa. Dra. Silvana de Nardin (UFSCar)

Prof. Dr. Ana Lúcia Homce de Cresce El Debs (EESC/USP)

Prof. Dr. Gerson Moacyr Sisniegas Alva (UFU)

Prof. Dr. Pedro Colmar Gonçalves da Silva Vellasco (UERJ)

Prof. Dr. Daniel de Lima Araújo (UFG)

O presente trabalho foi realizado com apoio da Coordenação de Aperfeiçoamento de Pessoal de Nível Superior - Brasil (CAPES) - Código de Financiamento 001.
O Relatório de Defesa assinado pelos membros da Comissão Julgadora encontra-se arquivado junto ao Programa de Pós-Graduação em Engenharia Civil.

Ao meu Amor, Flavianne.

AGRADECIMENTOS

Ao Professor Dr. Konstantinos Daniel Tsavdaridis, da Universidade de Leeds, pelo incentivo e colaboração técnico-científica que foram fundamentais para o desenvolvimento do presente trabalho, bem como na escrita dos artigos.

Ao meu coorientador, Professor Dr. Carlos Humberto Martins, da Universidade Estadual de Maringá, que me deu a oportunidade de conhecer a pesquisa pela iniciação científica, meus agradecimentos pela amizade e ânimo.

À minha orientadora, Professora Dra. Silvana De Nardin, por acreditar no desenvolvimento do trabalho, e principalmente, pela orientação e contribuição nas tomadas de decisões.

À Gerdau Brasil, Eng. Henrique José Ferreira da Silva, por tornar disponível o relatório técnico COPPETEC/PEC-18541/2016.

Ao grupo de pesquisa Construções Metálicas e Mistas (CMM), do Departamento de Engenharia Civil (DECIv), da Universidade Federal de São Carlos.

Ao Programa de Pós Graduação em Engenharia Civil da Universidade Federal de São Carlos (PPGECiv-UFSCar).

À Coordenação de Aperfeiçoamento de Pessoal de Nível Superior (CAPES).

À Fundação de Amparo à Pesquisa do Estado de São Paulo (FAPESP), processo nº 2018/22803-1, pela bolsa concedida.

"– Sam:[...] isso não é justo. Na verdade, nem devíamos estar aqui. Mas estamos. É como nas grandes histórias, Sr. Frodo. As que tinham mesmo importância. Eram repletas de escuridão e perigo. E, às vezes, você não queria saber o fim, porque como podiam ter um final feliz? Como podia o mundo voltar a ser o que era depois de tanto mal? Mas, no fim, é só uma coisa passageira essa sombra. Até a escuridão tem de passar. Um novo dia virá. E, quando o sol brilhar, brilhará ainda mais forte. Eram essas as histórias que ficavam na lembrança, que significavam algo. Mesmo que você fosse pequeno demais para entender o por quê. Mas eu acho, Sr. Frodo, que eu entendo, sim. Agora eu sei. As pessoas dessas histórias tinham várias oportunidades de voltar atrás, mas não voltavam. Elas seguiam em frente porque tinham no que se agarrar.

– Frodo: E em que nós nos agarramos, Sam?

– Sam: No bem que existe nesse mundo, Sr. Frodo, pelo qual vale a pena lutar."

O Senhor dos Anéis: As Duas Torres (Peter Jackson, 2002)

RESUMO

FERREIRA, F. P. V. **Capacidade resistente de vigas celulares mistas à instabilidade no montante de alma**. 2021. Tese (Doutorado em Engenharia Civil) – Universidade Federal de São Carlos, São Carlos, 2021.

O presente trabalho tem como objetivo investigar a capacidade resistente à instabilidade no montante de alma de vigas celulares mistas. Para isso, análises não lineares físicas e geométricas foram desenvolvidas no software ABAQUS®. O modelo computacional foi calibrado considerando modelos físicos de vigas celulares mistas com lajes mistas e vigas mistas com lajes alveolares pré-fabricadas. Posteriormente, os modelos numéricos foram unificados para representar as vigas celulares mistas associadas às lajes alveolares pré-fabricadas de concreto. Dois estudos paramétricos foram então realizados variando parâmetros relevantes para vigas celulares como o comprimento do montante de alma e o diâmetro das aberturas. No primeiro estudo foi avaliada a influência do tipo de laje e nele foram consideradas lajes mistas e alveolares pré-fabricadas de concreto. O segundo estudo investiga a ação mista, variando o espaçamento, com uma e duas linhas de conexão, entre os conectores de cisalhamento tipo pino com cabeça. No primeiro estudo, considerando a seção com dupla simetria e laje alveolar, o modo de falha predominante foi a instabilidade no montante de alma. Para a seção com assimetria, o modo de falha predominante foi a combinação do mecanismo plástico com a instabilidade no montante de alma acompanhada (ou não) pela ruptura do conector de cisalhamento tipo pino com cabeça. Na análise da influência do tipo de laje foi constatado que as vigas mistas com lajes pré-fabricadas apresentaram maior capacidade resistente. Os resultados do primeiro estudo paramétrico mostraram que a capacidade resistente das vigas celulares mistas não é limitada apenas pela resistência do perfil celular de aço, mas também pelas características da laje, sobretudo sua resistência ao cisalhamento. Por outro lado, no segundo estudo paramétrico foi observado queda da capacidade resistente à força cortante global devido à ausência de conectores de cisalhamento tipo pino com cabeça acima da segunda abertura, próxima ao apoio. Os modelos numéricos de viga celular mista, com laje alveolar e capa de concreto, apresentaram maior capacidade resistente à força cortante global, do que os modelos sem capa. Entretanto, para esses modelos, houve um número maior de observações em que ocorreu a ruptura dos conectores de cisalhamento. Finalmente, os resultados do segundo estudo foram comparados com uma equação proposta que leva em consideração a capacidade resistente à força cortante global devido à instabilidade no montante de alma, mecanismo Vierendeel e ação mista. O modelo analítico proposto mostrou excelente correlação com os resultados da análise numérica sobretudo para os modelos em que foi identificada a combinação da instabilidade no montante de alma com o mecanismo plástico.

Palavras-chave: Viga celular mista. Laje alveolar pré-fabricada. Conectores de cisalhamento.

Instabilidade no montante de alma. Modelagem numérica.

ABSTRACT

FERREIRA, F. P. V. **Web post buckling resistance of composite cellular beams**. 2021. Thesis (Ph.D. in Civil Engineering) –Federal University of São Carlos, São Carlos, 2021.

The present work aims to investigate the web post buckling resistance of composite cellular beams. For this task, geometrical and physical non-linear analyses are developed in the ABAQUS® software. The computational model was calibrated considering physical models of composite cellular beams, with steel-concrete composite slabs, and steel-concrete composite beams with precast hollow-core slabs. Subsequently, the numerical models were unified to represent the composite cellular beams associated with precast hollow-core slabs. Two parametric studies were carried out, varying the cellular beams key parameters, such as the web-post width and the opening diameter. The first study evaluated the floor systems, considering steel-concrete composite and precast hollow core slabs. The second study investigated the composite action, varying the spacing, with one and two connecting lines, between the shear studs. In the first study, considering the section with double symmetry and precast hollow core slab, the predominant failure mode was web post buckling. For the section with asymmetry, the predominant failure mode was the combination of the plastic mechanism with the web post buckling accompanied (or not) by the shear stud rupture. In the analysis of the type of slab it was found that the composite cellular beams with precast hollow-core slabs presented greater resistance. The results of the first parametric study showed that the resistance of the composite cellular beams was not limited only by the resistance of the cellular profile, but also, of the slab, due to the shear resistance. On the other hand, in the second parametric study, a drop in global shear resistance was observed due to the absence of shear studs above the second opening, close to the support. The numerical models of composite cellular beams with hollow-core slab and concrete topping presented greater global shear resistance than the models without concrete topping. However, for those models with concrete topping, there were a greater number of observations in which the shear studs rupture occurred. Finally, the results of the second study were compared with a proposed equation, which takes into account the global shear resistance due to web post buckling, Vierendeel mechanism and composite action. The proposed analytical model showed an excellent correlation with the results of the numerical analyses, especially for the models in which the combination of the web post buckling with the plastic mechanism was identified.

Keywords: Composite Cellular beams. Precast hollow-core slabs. Shear Connectors. Web post buckling. Numerical modeling.

LISTA DE PUBLICAÇÕES

As análises realizadas nessa tese geraram resultados que foram publicados nos artigos a seguir:

1. FERREIRA, F. P. V.; MARTINS, C. H.; DE NARDIN, S. Advances in composite beams with web openings and composite cellular beams. **Journal of Constructional Steel Research**, v. 172, p. 106182, 1 set. 2020. https://doi.org/10.1016/j.jcsr.2020.106182
(FERREIRA; MARTINS; DE NARDIN, 2020a);

2. FERREIRA, F. P. V.; MARTINS, C. H.; DE NARDIN, S. A parametric study of steel-concrete composite beams with hollow core slabs and concrete topping. **Structures**, v. 28, p. 276–296, dez. 2020. https://doi.org/10.1016/j.istruc.2020.08.045
(FERREIRA; MARTINS; DE NARDIN, 2020b);

3. FERREIRA, F. P. V.; TSAVDARIDIS, K. D.; MARTINS, C. H.; DE NARDIN, S. Steel–Concrete-Composite Beams with Precast Hollow-Core Slabs: A Sustainable Solution. **Sustainability**, v. 13, n. 8, p. 4230, 10 abr. 2021. https://doi.org/10.3390/su13084230
(FERREIRA et al., 2021b);

4. FERREIRA, F. P. V.; MARTINS, C. H.; DE NARDIN, S. Sensitivity Analysis of Composite Cellular Beams to Constitutive Material Models and Concrete Fracture. **International Journal of Structural Stability and Dynamics**, v. 21, n. 01, p. 2150008, 29 jan. 2021. https://doi.org/10.1142/S0219455421500085
(FERREIRA; MARTINS; DE NARDIN, 2021b);

5. FERREIRA, F. P. V.; MARTINS, C. H.; DE NARDIN, S. Assessment of web post buckling resistance in steel-concrete composite cellular beams. **Thin-Walled Structures**, v. 158, p. 106969, jan. 2021. https://doi.org/10.1016/j.tws.2020.106969
(FERREIRA; MARTINS; DE NARDIN, 2021a);

6. FERREIRA, F. P. V.; TSAVDARIDIS, K. D.; MARTINS, C. H.; DE NARDIN, S. Buckling and post-buckling analyses of composite cellular beams. **Composite Structures**, v. 262, p. 113616, 2021. https://doi.org/10.1016/j.compstruct.2021.113616
(FERREIRA et al., 2021a);

7. FERREIRA, F. P. V.; TSAVDARIDIS, K. D.; MARTINS, C. H.; DE NARDIN, S. Ultimate strength prediction of steel-concrete composite cellular beams with PCHCS. **Engineering Structures**, v. 236, p. 112082, 2021. https://doi.org/10.1016/j.engstruct.2021.112082
(FERREIRA et al., 2021c);

8. FERREIRA, F. P. V.; TSAVDARIDIS, K. D.; MARTINS, C. H.; DE NARDIN, S. Composite action on web post buckling shear resistance of composite cellular beams with PCHCS and PCHCSCT. **Engineering Structures**. (Em revisão, R1)

SUMÁRIO

PARTE I:

INTRODUÇÃO

E

ESTADO DA ARTE

1.

INTRODUÇÃO

A utilização de elementos mistos de aço e concreto em edifícios de múltiplos pavimentos vem ganhando mercado em vários países da Europa, nos Estados Unidos, Canadá e Austrália. As principais vantagens da utilização de elementos mistos são: possibilidade de redução na altura da edificação, no peso próprio da estrutura, rapidez de execução, redução ou dispensa de fôrmas e escoramentos, aumento da precisão dimensional dos elementos estruturais, redução considerável do consumo de aço estrutural e aumento da rigidez da estrutura (QUEIROZ; VELLASCO; NETHERCOT, 2007).

Os elementos mistos de aço e concreto são aqueles cuja seção transversal é formada de concreto estrutural e aço na forma de perfil, ambos trabalhando em conjunto para resistir aos esforços aplicados. No caso das vigas mistas, a principal vantagem dessa associação é que o concreto e o aço trabalham de maneira solidária: o concreto resiste fundamentalmente à compressão, enquanto que o aço resiste à tração. Isso resulta em economia de aço e na mobilização de uma largura útil de laje de concreto que contribuirá na resistência aos esforços de flexão a que a viga está submetida.

Em uma estrutura mista, o perfil de aço e a laje concreto, pré-fabricada[1] ou não, são unidos por meio de conectores de cisalhamento, que são dispositivos mecânicos que conectam os elementos de aço e de concreto de forma a promover o comportamento conjunto. A ligação promovida pelos conectores de cisalhamento é essencial para resistir aos esforços cortantes longitudinais na interface de conexão. Os conectores tipo pino com cabeça são os dispositivos mecânicos mais comumente empregados, embora existam outros tipos de conectores de cisalhamento, como por exemplo, em perfil U.

Em edifícios de múltiplos pavimentos executados com vigas mistas formadas por perfis de aço, compondo pisos aqui denominados pisos convencionais, a laje de concreto é disposta na mesa superior do perfil de aço. Nesse contexto, a laje de concreto pode ser executada *in loco* – maciça ou mista, ou ainda de unidades pré-fabricadas de concreto. A solução que vem sendo cada vez mais utilizada é o uso de perfis I, laminados ou soldados, associados a lajes alveolares pré-fabricadas de concreto. Esses elementos apresentam qualidade superior à dos elementos estruturais moldados in loco, pois são produzidos em ambientes específicos com acompanhamento e rigoroso controle tecnológico. O uso de lajes alveolares pré-fabricadas de concreto oferece vantagens como a possibilidade de vencer grandes vãos, velocidade e redução no custo da construção (DE NARDIN; DEBS, 2013; LAM, 2007; IBRAHIM *et al*., 2016).

No início da década de 1990, devido ao desenvolvimento do corte automatizado e da solda, as vigas alveolares passaram a ser fabricadas a baixos custos, ocorrendo assim, a expansão do produto no mercado da construção civil. Esse avanço possibilitou o uso dessas vigas em pisos. São consideradas vigas alveolares aquelas com aberturas sequenciais ao longo da alma, fabricadas a partir do corte térmico e solda, objetivando a expansão da seção transversal, e consequentemente, maior rigidez à flexão. As vigas alveolares, que apresentam as aberturas no formato de circunferência, são denominadas de vigas celulares (**Figura 1.1**).

Este trabalho apresenta o estudo da capacidade resistente à instabilidade no montante de alma de vigas celulares mistas, compostas por perfis celulares de aço e lajes alveolares pré-fabricadas de concreto.

[1] Denomina-se elemento pré-moldado de fábrica àquele executado em instalações permanentes distantes da obra. Esse tipo de elemento pré-moldado pode ou não atingir o nível de pré-fabricado, segundo os critérios da norma ABNT NBR 9062:2017.

Figura 1.1 – Vigas celulares de aço

Fonte: https://www.kloecknermetalsuk.com

1.1 JUSTIFICATIVA

A construção civil brasileira, tradicionalmente, emprega o concreto armado como material para os elementos estruturais das edificações. No setor industrial é comum o uso de soluções estruturais em aço. Entretanto, nas últimas duas décadas, outros segmentos da construção civil têm utilizado elementos de aço para compor o arcabouço estrutural, por exemplo, de edifícios de múltiplos pavimentos. Dentre outros fatores, o aço possui resistência bastante superior à do concreto armado, resultando em estruturas mais leves com maior precisão dimensional e de execução mais rápida, característica importantíssima dos sistemas industrializados. Outro aspecto importante é a necessidade de utilizar processos construtivos que resultam na rápida entrega do empreendimento. A utilização de elementos industrializados alia a velocidade de execução com a segurança de trabalhar com elementos estruturais que passam por rigoroso controle de qualidade, além de evitar o desperdício de materiais e atender aos requisitos de sustentabilidade. Inseridos nesse âmbito estão os perfis de aço e as lajes alveolares pré-fabricadas de concreto.

Do ponto de vista estrutural são inquestionáveis as boas características das vigas mistas de aço e concreto, merecendo destaque a redução do consumo de aço, com consequente redução do peso próprio, e a possibilidade de vencer grandes vãos. Trata-se de um elemento estrutural

com uso difundido mundialmente e com procedimentos de cálculo consolidados. No sentido de reduzir ainda mais o consumo de aço surgem os perfis celulares, resultando do corte do perfil I e posterior soldagem de forma a obter uma seção transversal de maior altura, maior rigidez e sem aumentar o consumo de aço. Quanto às vigas celulares mistas, o fato de a laje trabalhar em conjunto com o perfil celular de aço aumenta consideravelmente sua capacidade resistente, podendo vencer vãos entre 12m e 20m. Outro aspecto importante é a facilidade de passar as tubulações de serviços através das aberturas na alma, solução que pode reduzir a altura total do pavimento (LAWSON et al., 2006; LAWSON; SAVERIRAJAN, 2011). No caso de elementos Offshore, as vigas celulares de aço reduzem o peso próprio da estrutura e solucionam problemas de passagem de tubulações para integração dos serviços (**Figura 1.2**).

Figura 1.2 – Passagem de tubulações para integração dos serviços

Fonte: https://www.kloecknermetalsuk.com

As vigas celulares são ideais para estruturas com requisitos de espaço aberto tais como garagens de estacionamento, indústrias e armazéns, fábricas, edifícios de escritórios, escolas e hospitais, e também, para reforma e modernização de edifícios antigos. Um exemplo é a reforma da Royal Vale Church, construída em 1873 em Londres, Inglaterra (**Figura 1.3a**). Além disso, as vigas celulares são uma boa solução para vencer grandes vãos e reduzir o peso próprio da estrutura. Nesse contexto, um bom exemplo é a construção do Ballymore's Three Snowhill, o maior empreendimento de escritórios construído fora de Londres (**Figura 1.3b**) e o 1ST Manchester Street (**Figura 1.3c**), no mesmo segmento.

Figura 1.3 – Exemplos de aplicações de vigas celulares

(a) Reforma da *Royal Vale Church*, construída em 1873 em Londres, Inglaterra

(b) *Snowhill Development*

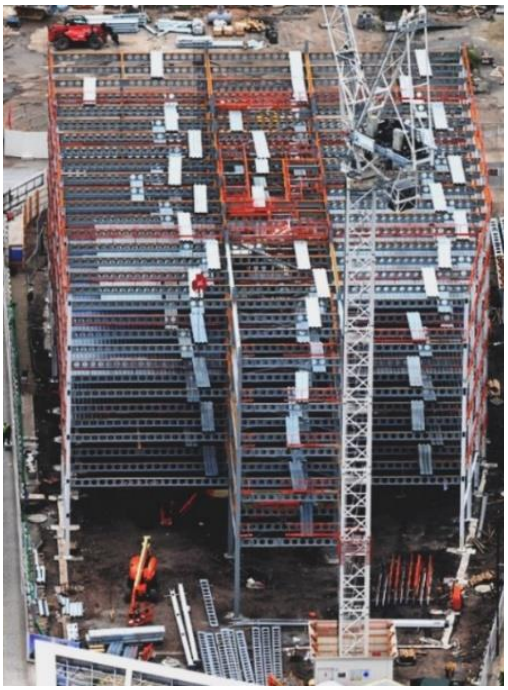

(c) *1ST Manchester Street*

Fonte: https://www.kloecknermetalsuk.com

Os edifícios-garagem também são excelentes exemplos da utilização de vigas celulares, e as principais razões são a capacidade de vencer maiores vãos, redução do número de pilares, facilidade de drenagem e fluxo de ar e aspecto estético da estrutura. Como exemplo, cita-se o estacionamento do *Altnagelvin Hospital*, em *Londonderry* na Irlanda do Norte (**Figura 1.4**).

Figura 1.4 – Estacionamento do *Altnagelvin Hospital*

Fonte: https://www.kloecknermetalsuk.com

Assim, se vigas mistas de aço e concreto, lajes alveolares pré-fabricadas e perfis de aço são elementos estruturais com aspectos bastante interessantes para uso em edifícios de múltiplos pavimentos, a combinação perfil celular trabalhando em conjunto com a laje alveolar pré-fabricada de concreto parece bastante interessante e promissora. Contudo, não é uma associação que vem sendo investigada pela comunidade científica. Além disso, em comparação com outros elementos mistos, a utilização de vigas celulares mistas é limitada pela falta de recomendações de projeto e de procedimentos para análise (CHEN; LIMAZIE; TAN, 2015). No Brasil, as duas causas principais para o reduzido emprego de vigas celulares mistas são o desconhecimento por parte dos engenheiros de estruturas e arquitetos e a não inclusão dos perfis celulares e de vigas celulares mistas nas normas técnicas nacionais e estrangeiras. Esse panorama deixa transparecer a necessidade de estudos nacionais nessa linha, podendo ampliar, no Brasil, o uso das lajes alveolares pré-fabricadas e das vigas mistas de aço e concreto. Assim, se do ponto de vista do meio acadêmico há muito a investigar, do ponto de vista da iniciativa privada, a inserção de uma opção ainda pouco difundida nacionalmente pode ampliar o potencial de utilização das lajes pré-fabricadas de concreto.

Corroboram e justificam o desenvolvimento do presente estudo o fato de, em nível internacional, embora as vigas celulares mistas venham sendo mais amplamente estudadas, não

há registro de estudos envolvendo esse tipo de viga mista, ou seja, composta de lajes alveolares pré-fabricadas de concreto sobre a mesa superior do perfil celular.

Finalmente, quer seja do ponto de vista da modernização da construção civil brasileira e da redução do consumo de materiais e mão de obra, quer seja do ponto de vista estrutural, acredita-se que a presente tese reúne as características de inovação e de avanço da fronteira do conhecimento, além de poder gerar frutos profícuos para a construção civil brasileira.

1.2 OBJETIVOS

O objetivo geral da presente tese foi avaliar a capacidade resistente à instabilidade no montante de alma de vigas celulares mistas, biapoiadas e formadas por lajes alveolares pré-fabricadas de concreto. A partir desse objetivo geral foram definidos os seguintes objetivos específicos:

i. Identificar os modos de falha que governam o comportamento de vigas celulares mistas de aço e concreto biapoiadas e submetidas a forças estáticas;
ii. Avaliar a influência de parâmetros como taxa de armadura transversal imersa na laje alveolar, capa de concreto, resistência do concreto moldado in loco, perfil de aço e espaçamento entre os conectores de cisalhamento, na capacidade resistente e modo de falha de vigas mistas formadas por lajes alveolares;
iii. Avaliar a influência do tipo de laje no comportamento último de vigas celulares mistas, considerando lajes mistas e lajes alveolares com e sem capa de concreto;
iv. Avaliar os efeitos produzidos pela variação do diâmetro das aberturas na alma no comportamento global da viga celular mista com laje alveolar, nos modos de falha, e no grau de interação aço-concreto, considerando o espaçamento entre os conectores de cisalhamento.
v. Propor um modelo analítico simplificado em função da máxima força cortante resistente.

1.3 METODOLOGIA

Para analisar o comportamento de vigas mistas com lajes pré-fabricadas de concreto foi utilizada a modelagem numérica no pacote computacional ABAQUS®. Havia uma previsão

inicial de realizar um conjunto de ensaios experimentais, mas este foi inviabilizado pela necessidade de isolamento imposta pela pandemia de covid-19, decretada em março de 2020 pela OMS (Organização Mundial de Saúde), ainda em vigor em 2021.

Assim, a modelagem numérica consistiu na metodologia utilizada para realizar todas as análises contidas nessa tese. Devido à ausência de resultados experimentais de vigas celulares mistas com lajes pré-fabricadas, a validação do modelo numérico foi dividida em duas etapas: validação do modelo do perfil celular e validação da laje pré-fabricada de concreto. A etapa de validação será denominada de análises prévias. Nas análises prévias foram utilizados resultados experimentais de vigas celulares mistas com lajes mistas (validação do modelo do perfil celular) e vigas mistas com laje alveolar (validação do modelo de laje alveolar) disponíveis na literatura. As análises prévias, bem como os parâmetros avaliados, são apresentadas em função dos artigos publicados (**Tabela 1.1**).

Tabela 1.1 – Análises prévias

Artigo	**Análise**
Sensitivity Analysis of Composite Cellular Beams to Constitutive Material Models and Concrete Fracture	Modelos constitutivos dos materiais aço e concreto.
Assessment of web post buckling resistance in steel-concrete composite cellular beams *Buckling and post-buckling analyses of composite cellular beams*	Relação diâmetro e altura da seção transversal original em vigas celulares mistas formadas por lajes mistas; Relação do diâmetro e passo em vigas celulares mistas formadas por lajes mistas; Modelos de cálculo resistente de vigas celulares mistas formadas por lajes mistas;
A parametric study of steel-concrete composite beams with hollow core slabs and concrete topping *Steel–Concrete-Composite Beams with Precast Hollow-Core Slabs: A Sustainable Solution*	Influência da capa concreto, altura da laje alveolar, taxa de armadura, resistência do concreto moldado in loco e grau de interação em vigas mistas de aço e concreto com laje alveolar pré-fabricada de concreto.

Nas análises definitivas (**Tabela 1.2**), os modelos desenvolvidos de vigas celulares mistas, com lajes mistas, e vigas mistas de aço e concreto, com laje alveolares, foram unificados para representar o modelo numérico de vigas celulares mistas com lajes alveolares.

Tabela 1.2 – Análises definitivas

Artigo	Análise
Ultimate strength prediction of steel-concrete composite cellular beams with PCHCS	Capacidade resistente de vigas celulares mistas com lajes alveolares pré-fabricadas de concreto, considerando a influência da capa de concreto.
Composite action on web post buckling shear resistance of composite cellular beams with PCHCS and PCHCSCT	Influência do espaçamento entre conectores de cisalhamento, considerando uma e duas linhas de conexão, no comportamento último de vigas celulares mistas com lajes alveolares pré-fabricadas de concreto.

As análises numéricas de vigas celulares mistas foram divididas em duas etapas: análise de estabilidade elástica e análise de pós flambagem. A primeira foi realizada com o objetivo de estimar a carga crítica de flambagem elástica. Para isso, foi utilizado o método de perturbação linear "*Buckle*" com o qual foi possível estimar, por meio dos autovalores e seus respectivos autovetores, a carga de flambagem elástica. Na etapa seguinte foram inseridas a não linearidade geométrica, como as imperfeições iniciais. A configuração da estrutura na primeira etapa (análise de estabilidade elástica), normalizada para o valor de imperfeição inicial no perfil é adotada como sendo a configuração inicial dessa nova análise (*Post-buckling*).

1.4 ORIGINALIDADE

Os seguintes resultados, que foram obtidos por meio de modelagens numéricas, constituem aspectos inovadores:

i. Análises de sensibilidade em vigas celulares mistas, formadas por lajes mistas, para a verificação do comportamento pós pico, considerando a variação dos modelos constitutivos dos materiais aço e concreto;
ii. Análises elásticas (ou *buckling*) para avaliar os modos de deformação em vigas celulares mistas, formadas por lajes mistas. Parâmetros analisados: seções simétricas e assimétricas, diâmetro de abertura e passo;
iii. Análises inelásticas (ou *post-buckling*) para investigar o comportamento último em vigas celulares mistas, formadas por lajes mistas. Parâmetros analisados: seções simétricas e assimétricas, diâmetro de abertura e passo;
iv. Análises em vigas mistas de aço e concreto, formadas por lajes alveolares pré-fabricadas com capa de concreto, para investigar o comportamento à flexão. Parâmetros analisados: altura da laje alveolar, capa de concreto, resistência do concreto moldado in loco, diâmetro da armadura transversal e do espaçamento entre conectores de cisalhamento;
v. Desenvolvimento de um modelo numérico capaz de estimar a capacidade resistente de vigas celulares mistas formadas por lajes alveolares pré-fabricadas de concreto;
vi. Análises inelásticas (ou *post-buckling*) em vigas celulares mistas, formadas por lajes alveolares pré-fabricadas de concreto, para investigar o comportamento último. Parâmetros analisados: seções simétricas e assimétricas, diâmetro de abertura e passo;
vii. Estudo paramétrico de vigas celulares mistas, formadas por lajes alveolares pré-fabricadas de concreto, considerando análises inelásticas ou (*post-buckling*). Parâmetros analisados: diâmetro de abertura, passo e espaçamento entre os conectores de cisalhamento com uma ou duas linhas de conectores;

1.5 ESTRUTURA DA TESE

O presente trabalho foi estruturado em três partes:

Parte I contêm os capítulos 1 e 2. No **Capítulo 1** foi introduzido o objeto de estudo, justificativas para o desenvolvimento do trabalho bem como objetivos e metodologia. O **Capítulo 2**, que é fundamentado no artigo de revisão sistemática "*Advances in composite beams with web openings and composite cellular beams*", já publicado no periódico *Journal of Constructional Steel Research*, consiste na apresentação do estado da arte que justifica o desenvolvimento do presente trabalho.

Parte II é formada pelos capítulos 3 e 4. O **Capítulo 3** apresenta as análises prévias referentes a vigas celulares mistas com lajes mistas com fôrma de aço incorporada. Tal capítulo é fundamentado nos artigos "*Sensitivity analysis of composite cellular beams to constitutive material models and concrete fracture*", "*Assessment of web post buckling resistance in steel-concrete composite cellular beams*" e "*Buckling and post-buckling analyses of composite cellular beams*" já publicados nos periódicos *International Journal of Structural Stability and Dynamics*, *Thin-Walled Structures* e *Composite Structures*, respectivamente.

No **Capítulo 4** são apresentadas as análises prévias de vigas mistas com lajes alveolares pré-fabricadas. Tal capítulo é baseado nos artigos "*A parametric study of steel-concrete composite beams with hollow core slabs and concrete topping*" e "*Steel-Concrete Composite Beams with Precast Hollow Core Slabs: A Sustainable Solution*", publicados nos periódicos *Structures* e *Sustainability*, respectivamente.

E, para finalizar, a **Parte III** é composta pelos capítulos 5, 6 e 7. O **Capítulos 5** apresenta o modelo numérico referente a vigas celulares mistas com lajes alveolares pré-fabricadas de concreto. Um conjunto completo de informações sobre a modelagem foi publicado no artigo "*Ultimate strength prediction of steel-concrete composite cellular beams with PCHCS*" no periódico *Engineering Structures*. No **Capítulo 6** é apresentado o estudo paramétrico no qual foi avaliada a influência da variação do espaçamento entre os conectores de cisalhamento. Maiores informações podem ser vistas no artigo "*Composite action on web post buckling shear resistance of composite cellular beams with PCHCS and PCHCSCT*".

O **Capítulo 7** traz as principais conclusões do estudo bem como sugestões para trabalhos futuros.

2.

O ESTADO DA ARTE

O Capítulo 1 é fundamentado no artigo de revisão sistemática "***Advances in composite beams with web openings and composite cellular beams***" (FERREIRA; MARTINS; DE NARDIN, 2020a). Nesse contexto, o processo de fabricação e o comportamento estrutural das vigas celulares de aço são apresentados. Em seguida, é mostrado um dos principais dispositivos mecânicos que é utilizado em sistemas mistos de aço e concreto. Finalmente, os estados da arte de viga mistas com aberturas na alma e vigas mistas formadas por lajes alveolares são descritos. No presente texto, o estado da arte é escrito de maneira resumida. Para maiores informações e detalhes, o artigo publicado pode ser consultado no Apêndice do presente trabalho.

A utilização de elementos mistos na construção civil aumentou devido a uma utilização mais eficiente dos materiais de construção, podendo alcançar economias de 20% a 30% do aço na forma de perfis. Alguns benefícios da utilização dessa composição são a redução da altura dos elementos, maior rigidez dos sistemas de piso e aumento da capacidade resistente (CLAWSON; DARWIN, 1982a). O uso de aberturas na alma no perfil de aço em vigas mistas é uma ferramenta vantajosa que pode ser usada, também, para reduzir a altura do pavimento solucionando problemas de passagens de tubulações. A demanda por estruturas econômicas e eficientes, como é o caso das vigas mistas com aberturas na alma, tem aumentado na construção civil, principalmente na Europa e nos Estados Unidos (DONAHEY; DARWIN, 1988).

2.1 VIGAS CELULARES DE AÇO

As vigas de aço de seção expandida com aberturas sequenciais foram bastante utilizadas no passado em países como EUA, Japão, Alemanha, no Reino Unido, entre outros, para a construção de edifícios, pontes, estruturas para a indústria e construção naval. Essa ideia de corte e expansão com o objetivo de aumentar a rigidez da seção transversal, foi utilizada primeiramente em 1910 pela empresa *Chicago Bridge and Iron Works*[1], fundada em 1889 (DAS; SRIMANI, 1984).

Em 1935 na Argentina, Geoffrey Murray Boyd utilizou essa ideia como uma alternativa interessante para vencer vãos maiores sem aumentar o consumo de aço. Embora a ideia tenha sido patenteada no Reino Unido, nesse primeiro momento a produção dessas vigas esbarrou na limitação de técnicas de corte e soldagem disponíveis na época.

Na década de 1940, o uso de vigas com aberturas sequenciais na alma e seção expandida aumentou substancialmente devido ao número limitado de perfis estruturais que as siderúrgicas podiam fabricar na Europa. Com baixos custos de mão-de-obra, as usinas siderúrgicas produziam perfis de diversas alturas com a expansão da seção transversal e a presença de aberturas. Entretanto, não foram utilizadas frequentemente na América do Norte devido aos altos custos de produção (MEGHARIEF, 1997).

No início da década de 1990, com o desenvolvimento do corte automatizado, ocorreu a redução nos custos do processo de fabricação e as com aberturas sequenciais na alma passaram a ser produzidas nos Estados Unidos. Esse avanço tecnológico permitiu o uso dessas vigas como vigas de pisos em elementos mistos, com menor custo de produção. Também, nessa mesma década, a patente das vigas celulares de aço foi efetivada, em nome de Peter A. Walker[2] (GRILO, 2018; OLIVEIRA, 2012).

2.1.1 Processo de Fabricação

O processo de fabricação das vigas celulares e os parâmetros geométricos são ilustrados na **Figura 2.1**. As vigas celulares de aço são produzidas por meio de duas linhas de corte

[1] Atualmente conhecida como *Chicago Bridge and Iron Company (CBI®)*.

[2] PETER A. WALKER. Method of making Castellated beams, 1990.

térmico, no formato de semicircunferências, em todo o comprimento longitudinal da alma. Posteriormente à etapa de corte térmico, faz-se a separação dos módulos, processo denominado defasagem e, em seguida, a soldagem. O resultado desse processo é uma viga com seção transversal cuja altura varia entre 130% a 160% da altura do perfil original, com maior rigidez à flexão.

Figura 2.1 – Processo de fabricação das vigas celulares

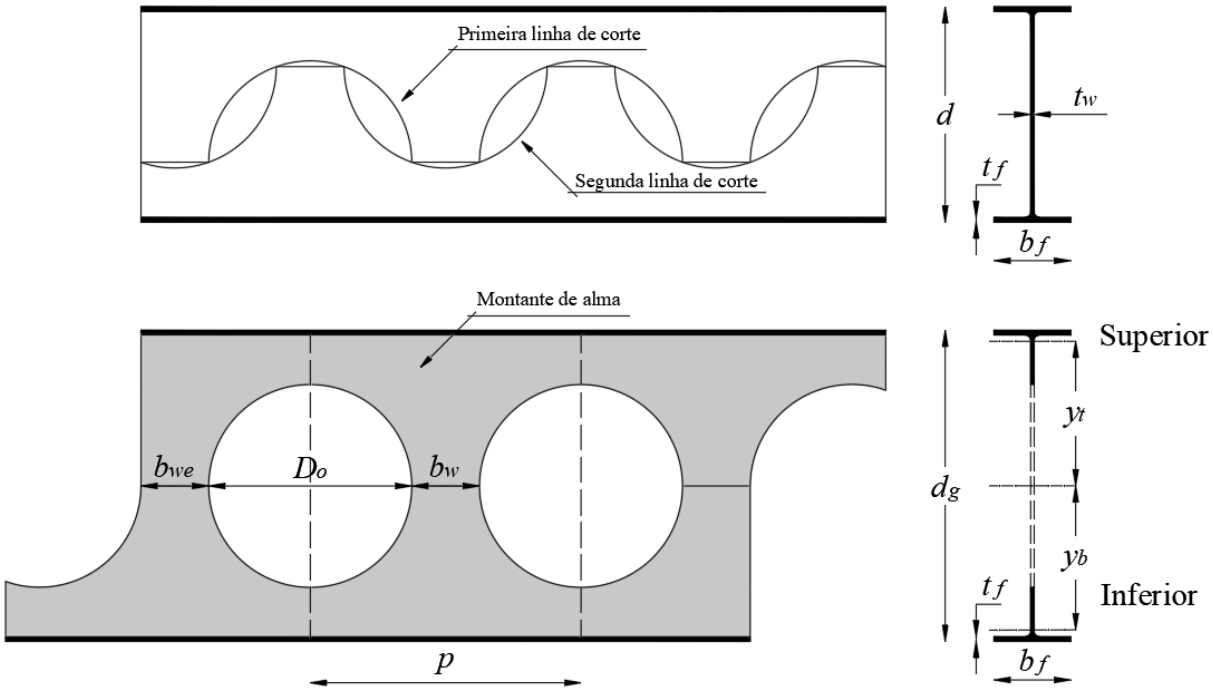

Fonte: Autor (2020)

No presente trabalho é utilizada a simbologia dos parâmetros geométricos das vigas celulares, padronizada no Brasil por diversos pesquisadores, em que p é o passo, D_0 é o diâmetro das aberturas, d é a altura da seção transversal do perfil original, d_g é a altura da seção transversal do perfil celular, b_w é a largura do montante de alma intermediário, b_{we} é a largura do montante de extremidade, b_f é a largura das mesas, t_f é a espessura das mesas, t_w é a espessura da alma, y_t e y_b são as distâncias verticais dos centroides dos tês superior e inferior ao eixo da viga e h_t é altura total do tê (ABREU, 2011; SILVEIRA, 2011; OLIVEIRA, 2012; FERRARI, 2013; VIEIRA, 2014; GONÇALVES, 2015; GRILO, 2018; FERREIRA, 2019).

2.1.2 Comportamento Estrutural

Embora a expansão da seção transversal aumente a rigidez à flexão, a presença das aberturas torna as vigas celulares mais susceptíveis à instabilidade lateral com torção (FLT), à distorção da alma (DA), à instabilidade no montante da alma (FMA), à instabilidade local da alma, à formação do mecanismo Vierendeel (MV), à ruptura do montante de alma, à flexão do montante de alma, ou até mesmo à combinação dos modos de instabilidade (EL-SAWY; SWEEDAN; MARTINI, 2014; ELLOBODY, 2012; PANEDPOJAMAN; SAE-LONG; CHUB-UPPAKARN, 2016)

A FLT é um comportamento típico de perfis de aço, que são fletidos em torno do eixo de maior inércia e que não possuem restrição lateral. Devido à expansão da seção transversal e à presença de aberturas, as vigas celulares de aço estão mais vulneráveis à FLT (**Figura 2.2**). Em vigas celulares esse fenômeno ocorre pelo fato do "tê" comprimido ser insuficientemente suportado lateralmente (BOISSONNADE *et al*., 2013; PANEDPOJAMAN; SAE-LONG; CHUB-UPPAKARN, 2016; SONCK; BELIS, 2015). Nesse contexto, destacam-se os trabalhos de Abreu (2011), Sweedan (2011), Ellobody (2012), Boissonnade *et al*. (2013), El-sawy, Sweedan e Martini (2014), Sonck e Belis (2015) e Ferreira, Rossi e Martins (2019).

Figura 2.2 – Instabilidade lateral com torção (FLT) em vigas celulares de aço

Fonte: Sonck e Belis (2015)

A distorção da alma, fenômeno que leva a mesa a se curvar lateralmente com torção, reduz efetivamente a resistência à torção do perfil de aço. Nesse caso, a clássica consideração de que as seções planas permanecem planas após a deformação não é válida em razão da natureza das condições de contorno que podem potencializar esse fenômeno (BRADFORD, 1985, 1986, 1988, 1992; HASSAN; MOHAREB, 2015). É importante ressaltar que esse fenômeno, também, ocorre nas vigas mistas sujeitas a momento fletor negativo. Assim, quando

a laje está tracionada e a mesa inferior comprimida, em regiões de momento negativo, pode ocorrer instabilidade lateral por distorção (FLD), pois a rigidez da laje de concreto é relativamente maior que a da viga de aço (CHEN; JIA, 2010; ZHOU; YAN, 2017). O fenômeno de FLD é caracterizado pelo deslocamento lateral da mesa inferior comprimida, acompanhado pela distorção da alma fora do plano de flexão. Nesse contexto destacam-se os trabalhos de Zirakian e Showkati (2006), El-sawy, Sweedan e Martini (2014), Panedpojaman, Sae-long e Chub-uppakarn, (2016) e Ferreira, Rossi e Martins (2019).

Outro fenômeno, a instabilidade no montante da alma (FMA), pode ser subdividida em dois modos: por cisalhamento e por compressão. A instabilidade no montante da alma por cisalhamento (FMAV, **Figura 2.3**) se torna crítica quando a largura do montante de alma é pequena (PANEDPOJAMAN; THEPCHATRI; LIMKATANYU, 2014). De acordo com a ilustração, uma força V_h age ao longo das juntas soldadas. Na **Figura 2.3**, y_0 é a distância do centro geométrico da seção "tê" até a solda, V é o esforço cortante global e V_h é a força horizontal originada pelo momento Vierendeel. Observa-se na ilustração que a borda AB é solicitada por tensões de tração, enquanto que a borda CD é solicitada por tensões de compressão. Em consequência, surgirão tensões de flexão no montante de alma. Esse fenômeno é caracterizado por um deslocamento lateral no montante da alma com torção, como ilustra a linha diagonal xx' na **Figura 2.3**.

Figura 2.3 – Instabilidade no montante da alma por cisalhamento

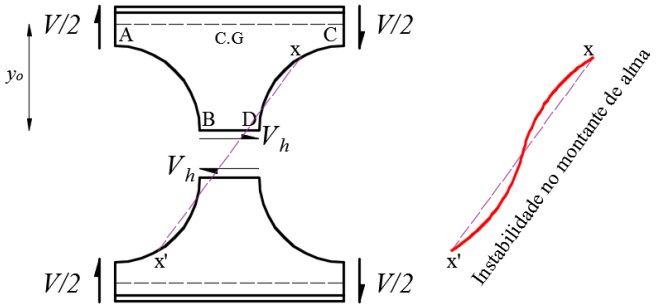

Fonte: adaptado de Kerdal e Nethercot (1984)

Para melhor visualização, na **Figura 2.4** tem-se a caracterização desse modo de instabilidade. A capacidade resistente à FMAV depende de características geométricas do perfil celular de aço, como o diâmetro da abertura, o espaçamento entre as aberturas e a espessura da alma. Sobre os trabalhos relacionados a FMAV em vigas celulares destacam-se Tsavdaridis e

D'mello (2011), Erdal e Saka (2013), Panedpojaman, Thepchatri e Limkatanyu (2014) e Grilo *et al*. (2018).

Figura 2.4 – Instabilidade no montante de alma por cisalhamento em viga celular

Fonte: Grilo (2018)

Por outro lado, a instabilidade no montante da alma por compressão pode ocorrer em vigas alveolares sujeitas a força concentrada na região do montante de alma com a ausência de enrijecedores. Esse fenômeno, diferentemente da FMAV, é caracterizado apenas pelo enrugamento do montante de alma.

A instabilidade local da alma (FLA) pode ocorrer em seções transversais esbeltas. A transferência de forças pela abertura faz com que a alma seja solicitada à compressão, o que pode causar a FLA se a esbeltez da alma (altura/espessura da alma) for relativamente alta. Esse tipo de instabilidade tem pouca influência na capacidade resistente das vigas mistas com aberturas (CHUNG; LAWSON, 2001; REDWOOD; CHO, 1993).

O mecanismo Vierendeel é dependente da presença do esforço cortante de alta magnitude, e trata-se de um fenômeno caracterizado pela distorção e formação de rótulas plásticas em regiões próximas à abertura (**Figura 2.5**). Fisicamente, o mecanismo Vierendeel ocorre quando o aço nas extremidades dos tês atinge a resistência ao escoamento devido à combinação de tensões normais e de cisalhamento. Ainda, essa deformação pode ocorrer com a presença ou não de reforços em regiões próximas às aberturas. Os principais parâmetros que afetam este comportamento estrutural são a espessura da alma e o diâmetro da abertura (KERDAL; NETHERCOT, 1984; REDWOOD; CHO, 1993; TSAVDARIDIS; D'MELLO, 2012). Os principais trabalhos que tratam desse fenômeno em vigas celulares de aço são Chung, Liu e Ko (2001), Warren (2001), Tsavdaridis e D'Mello (2012), Erdal e Saka (2013) e Panedpojaman, Rongram (2014).

Figura 2.5 – Mecanismo Vierendeel

Fonte: adaptado de Erdal e Saka (2013)

Na maioria dos casos, a soldagem no montante de alma entre as seções tês não influencia no comportamento local e global das vigas celulares. Isso porque a espessura requerida da alma é determinada de tal forma que a força de cisalhamento horizontal pode ser transmitida. Entretanto, quando não se atende aos requisitos mínimos de projeto, pode ocorrer a ruptura da solda (**Figura 2.6**), principalmente quando o montante de alma tem largura reduzida (VERWEIJ, 2010).

Figura 2.6 – Ruptura da solda no montante de alma

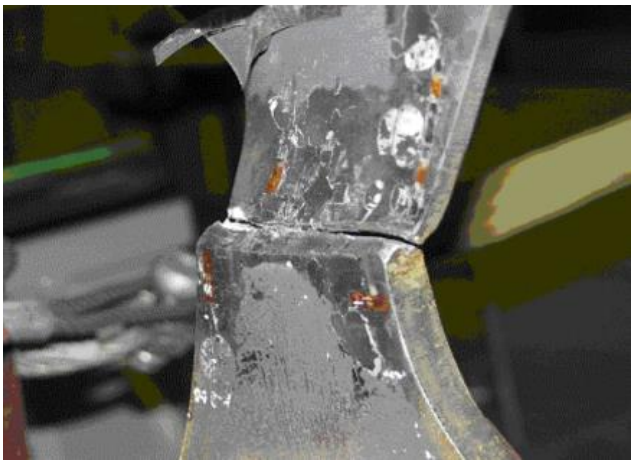

Fonte: Verweij (2010)

Considerando o comportamento misto, primeiramente serão apresentados os conectores de cisalhamento, que são os dispositivos mecânicos fundamentais para que os materiais aço e concreto trabalhem de forma solidária.

2.2 CONECTORES DE CISALHAMENTO

O primeiro estudo experimental foi reportado por Mackay, Gilespie e Leluau (1923)[1]. Até o final da década de 1930, foram realizadas investigações para avaliar a interação entre a laje de concreto e o perfil de aço, de forma a constituir a viga mista. Nesse contexto destacaram-se Batho, Lash e Kirkham (1939)[2], os quais verificaram os altos valores de deslizamento na interface aço-concreto, constatando a ineficiência da ligação natural, uma vez que até então não eram utilizados dispositivos mecânicos. A sugestão foi a utilização de conectores mecânicos para aumentar a resistência da interface aço-concreto ao deslizamento. A partir da década de 1940, todos os estudos realizados em vigas mistas de aço e concreto consideraram conectores mecânicos. Como exemplo, em 1943, na Universidade de *Lehigh* foi realizada uma série de ensaios experimentais (LAM, 1998).

Os estudos dos conectores tipo pino tiveram início com Viest (1956)[3], o qual realizou ensaios de cisalhamento direto e verificou que esse tipo de conexão é adequado para a resistência ao cisalhamento devido ao comportamento flexível. Além disso, o autor descreveu que a capacidade resistente ao cisalhamento foi dependente do diâmetro e da altura do pino, e também, da resistência do concreto.

Chapman e Balakrishnan (1964) realizaram um dos primeiros estudos para investigar o comportamento do conector tipo pino com cabeça. Ensaios de cisalhamento direto foram realizados de modo que os resultados pudessem ser relacionados com os resultados de ensaios de flexão de vigas mistas, objetivando avaliar o efeito do comprimento e do diâmetro dos pinos, e também, de um dispositivo alternativo para ancoragem vertical. Nos ensaios, os autores descreveram o comportamento flexível do conector tipo pino com cabeça, com base no diagrama Força *vs*. Deslizamento. Embora esse tipo de conector estivesse sendo amplamente

[1] MACKAY, H. M.; GILLESPIE, P.; LELUAU, C. Report on the strength of steel I-beams haunched with concrete. **Engineering Journal, Eng. Inst. of Canada**. v. 6, n. 8, p. 365-369, 1923.

[2] BATHO, C.; LASH, S. D.; KIRKHAM, R. H. H. The properties of composite beams, consisting of steel joists encased in concrete, under direct and sustained loading. **Journal Institution of Civil Engineering**, v. 11, n. 4, p. 6l-114, 1939.

[3] VIEST, I. M. Investigation of stud shear connectors for composite concrete and steel T-beams. **Journal of American Concrete Institute**, v. 27, n. 8, p. 875-891, 1956.

utilizado e estudado nos Estados Unidos[1,2,3], não havia resultados experimentais disponíveis sobre o comportamento de vigas mistas com esses elementos de conexão. A resistência ao cisalhamento ainda era desconhecida e só foi investigada posteriormente (MENZIES, 1971; OLLGAARD; SLUTTER; FISHER, 1971).

Com a justificativa que as investigações anteriores apresentaram resultados limitados e não tornaram possível a elaboração de recomendações de projeto, Ollgaard, Slutter e Fisher (1971) determinaram a resistência e o comportamento de conectores tipo pino com cabeça imersos em concretos de densidade normal e leve. Para a avaliação foram realizados ensaios de cisalhamento direto. Os autores concluíram que a resistência ao cisalhamento dos conectores tipo pino com cabeça, tanto no concreto de densidade normal quanto de densidade leve, foi influenciada, principalmente, pela resistência à compressão e pelo módulo de elasticidade do concreto. Outras propriedades do concreto, incluindo a resistência à tração e a densidade do concreto, não influenciaram significativamente e a resistência ao cisalhamento foi aproximadamente proporcional à área da seção transversal do corpo dos conectores.

Em Menzies (1971) foram comparadas as resistências teóricas de conectores de cisalhamento considerando *Codes of Practice* , CP 117 *Part* 1[4] e *Part* 2[5], com resultados experimentais de ensaios de cisalhamento direto realizados na *Building Research Station*. Embora as recomendações da CP 117 *Part* 1 e *Part* 2 tenham apresentado resultados satisfatórios, foi sugerido a distinção entre conectores embutidos em concretos de densidade normal e leves.

As primeiras investigações relacionadas a vigas mistas formadas por lajes pré-fabricadas de concreto tiveram ênfase nos conectores de cisalhamento (HAMILTON, 1989; MOY; TAYLER, 1996). Hamilton (1989) avaliou o comportamento de vigas mistas com lajes

[1] BALDWIN, J. W.; HENRY, J. R.; SWEENEY, C. M. **Study of composite bridge stringers - Phase II**. University of Missouri, May, 1965.

[2] BUTTRY, K. E. **Behavior of stud shear connectors in lightweight and normal-weight concrete**. 1965. M.Sc. thesis. University of Missouri, August, 1965, Unpublished.

[3] CHINN, J. **The use of Nelson studs with idealite lightweight-aggregate concrete in composite construction - Part 1.** Engineering Experiment Station, University of Colorado, Boulder, Colorado, April, 1961 (Summarized in AISC Engineering Journal, Vol. 2, No.4, October, 1965).

[4] BRITISH STANDARDS INSTITUTION. CP117: Part 1 – Composite construction in structural steel and concrete: simply-supported beams in building, London, 1965.

[5] BRITISH STANDARDS INSTITUTION. CP117: Part 2 – Composite construction in structural steel and concrete: beams for bridges, London, 1967.

pré-fabricadas de concreto com 150mm de altura e conectores tipo pino com cabeça de 19mm de diâmetro. Os resultados mostraram aumento de 70% na capacidade resistente da viga mista quando comparada à viga de aço (LAM, 1998). Em Moy e Tayler (1996) foi avaliado a resistência dos conectores tipo pino com cabeça de 19mm de diâmetro em vigas mistas com lajes de concreto pré-fabricadas e utilizaram uma série de ensaios de cisalhamento direto. Os autores apontaram que os principais fatores que afetam a capacidade resistente dos conectores são o diâmetro da cabeça do pino, a espessura da laje de concreto e a quantidade e localização das armaduras transversais. Na **Figura 2.7** é apresentado o comportamento típico dos conectores de cisalhamento tipo pino com cabeça. Diferentemente desse comportamento, como apresentado em Lam e El-Lobody (2005), em lajes sólidas não é observado o patamar da perda de ligação entre os estágios 1 e 2.

Figura 2.7– Curva típica da relação força por deslizamento para o conector tipo pino com cabeça

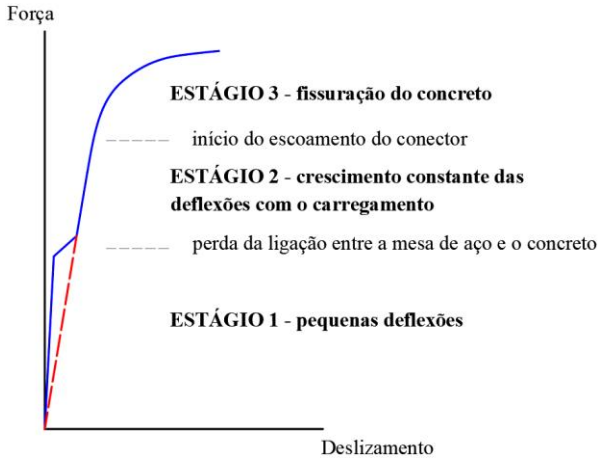

Fonte: adaptado de Moy e Tayler (1996)

Os estudos de Hamilton (1989) e Moy e Tayler (1996) foram os precursores de vigas mistas formadas por lajes pré-fabricadas, pois validaram o aumento da resistência e a eficiência do conector tipo pino com cabeça nessa composição. Entretanto, a avalição do comportamento de vigas mistas considerando as lajes alveolares pré-fabricadas ainda era relativamente novo e desconhecido.

Nesse cenário, Lam (2007a) realizou 72 ensaios de cisalhamento direto para a determinação da resistência ao cisalhamento de vigas mistas formadas por lajes alveolares pré-fabricadas. Nesse estudo foi investigado a influência de parâmetros como o ângulo de corte da laje (corte reto ou inclinado), taxa de armadura, diâmetro do conector e contribuição das

armaduras transversais (**Figura 2.8**). Tais armaduras auxiliam na transferência de forças do perfil para a laje, confinam o concreto reduzindo o fendilhamento.

Figura 2.8 – Disposição das armaduras transversais

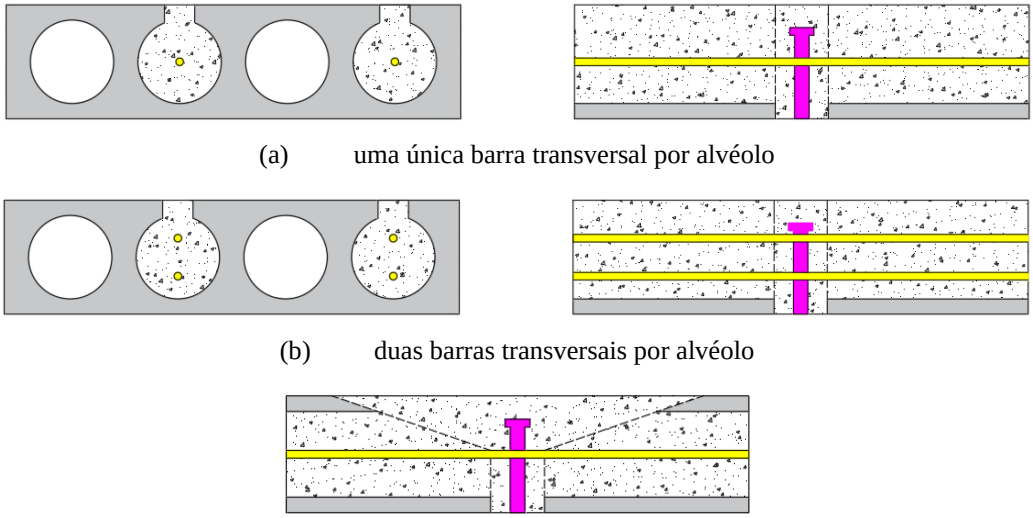

(a) uma única barra transversal por alvéolo

(b) duas barras transversais por alvéolo

(c) acabamento chanfrado com uma única barra transversal por alvéolo

Fonte: adaptado de Lam (2007a)

No Brasil, Araújo *et al*. (2016) investigaram o comportamento de conectores de cisalhamento tipo pino com cabeça em vigas mistas com lajes alveolares pré-fabricadas de concreto, por meio de ensaios de cisalhamento direto. Diferentemente dos estudos de Lam (2007a), os autores consideraram a presença da capa de concreto sobre as unidades pré-fabricadas de laje, objetivando avaliar a influência da resistência do concreto *in loco* e da taxa de armadura transversal na transferência de forças aço-concreto. Segundo os autores, podem haver mudanças na capacidade resistente de cada conector em função da presença da capa de concreto moldada no local e de outros fatores característicos desse tipo de laje de concreto. Nesse estudo foi concluído que a resistência à compressão do concreto executado *in loco* é o parâmetro mais importante para a capacidade resistente dos conectores. No exemplar com concreto mais resistente (40 MPa) ocorreu falha do conector por cisalhamento ao passo que para concreto com 30 MPa, a falha foi caracterizada pelo esmagamento do concreto que circunda o conector. Além disso, os autores modificaram a equação de previsão de capacidade resistente proposta por Lam (2007a), acrescentando um parâmetro que leva em conta a altura da capa da laje de concreto moldada *in loco*.

O comportamento dos conectores de cisalhamento é classificado em função da capacidade resistente ao fluxo de cisalhamento que ocorre na interface aço-concreto, relação

entre força e deslizamento, em flexível ou rígido. Um conector flexível próximo a atingir sua capacidade resistente continua a se deformar sem que ocorra ruptura, permitindo que conectores vizinhos absorvam cada vez mais o fluxo de cisalhamento. O comportamento flexível dos conectores tipo pino com cabeça, que permite o escorregamento entre a laje de concreto e o perfil de aço antes de atingir o estado limite último, é uma das razões da grande utilização desse tipo de conector em vigas mistas. Diferentemente do conector flexível, o conector rígido não apresenta essa capacidade de se deformar após a força máxima ser atingida. Entretanto, a resistência ao esforço cortante e a rigidez da conexão aço-concreto não dependem somente da resistência do conector de cisalhamento, mas também da resistência da laje de concreto contra a fissuração causada pela alta concentração da tensão de cisalhamento em cada conector (ARAÚJO et al., 2016; ELLOBODY; LAM, 2002; LAM, 2007a).

A interação dos conectores na interface aço-concreto pode ser classificada como *total* ou *parcial*. O termo *interação total* se refere ao caso em que a conexão entre os elementos é capaz de resistir totalmente às forças aplicadas. No entanto, nas últimas duas décadas, o uso de vigas mistas levou a muitos casos em que a conexão não pôde resistir à totalidade da força aplicada. Nesse caso, a conexão pode falhar por cisalhamento antes de qualquer um dos outros elementos atingir sua capacidade resistente (QUEIROZ; VELLASCO; NETHERCOT, 2007). Assim, as vigas mistas são geralmente projetadas por *interação parcial*. Nesse caso, a conexão pode se deformar resultando em deslocamento relativo ao longo da interface aço-concreto, causando a perda de rigidez do elemento misto. Diferentemente da *interação total*, a *interação parcial* favorece a ductilidade no sistema estrutural como um todo (AGGELOPOULOS; HANUS; LAWSON, 2018).

Na **Tabela 2.1** são apresentados modelos de cálculo, da capacidade resistente de conectores tipo pino com cabeça, consolidados na literatura. Vale ressaltar que o presente trabalho tem foco em vigas celulares mistas formadas por lajes alveolares pré-fabricadas de concreto. Para maiores informações sobre os estudos desenvolvidos em conectores tipo pino com cabeça, em Bonilla et al. (2018) foi apresentado o estado da arte, considerando lajes maciças e lajes mistas de aço e concreto (com fôrma de aço incorporada).

Tabela 2.1 – Modelos para o cálculo da capacidade resistente de conectores tipo pino com cabeça

Perfil	Laje	Referência	Fundamentação	Esmagamento do concreto	Ruptura do aço
Sólido	Alveolar	Lam (2007a)	EN 1994-1-1 (2004)	$0,29\alpha_{sc}\beta_{sc}\varepsilon_{sc}{d_{sc}}^2\sqrt{f_cE_c}$ $\alpha_{sc}=0,2\left(h_{sc}/d_{sc}+1\right)\le 1,0$ $\beta_{sc}=0,5\left(g/71+1\right)\le 1,0 \quad e \quad g\ge 30mm$ $\varepsilon_{sc}=0,5\left(\phi/20+1\right)\le 1,0 \quad e \quad \phi\ge 8mm$	$0,8f_{u,sc}A_{sc}$
Sólido	Alveolar	Gouchman (2014)	EN 1994-1-1 (2004)	$0.29k\alpha_{sc}{d_{sc}}^2\sqrt{f_cE_c}$	$0,8f_{u,sc}A_{sc}$
Sólido	Alveolar	Araújo *et al*. (2016)	EN 1994-1-1 (2004)	$0,29\alpha_{sc}\beta_{sc}\varepsilon_{sc}\lambda_{sc}{d_{sc}}^2\sqrt{f_cE_c}$ $\alpha_{sc}=0,2\left(h_{sc}/d_{sc}+1\right)\le 1,0$ $\beta_{sc}=0,5\left(g/71+1\right)\le 1,0 \quad e \quad g\ge 30mm$ $\varepsilon_{sc}=0,5\left(\phi/23+1\right)\le 1,0 \quad e \quad 8\le\phi\le 16mm$ $\lambda_{sc}=0,43\left[\left(H+c\right)/150+1\right] \quad e \quad \left(H+c\right)mm$	$0,75f_{u,sc}A_{sc}$
Celular	Mista	Lawson e Hicks (2011)	EN 1994-1-1 (2004)	$0,29\alpha_{sc}{d_{sc}}^2\sqrt{f_cE_c}$	$0,8f_{u,sc}A_{sc}$
Celular	Mista	Fares, Coulson e Dinehart (2016)	ANSI/AISC 360-16	$0,5A_{sc}\sqrt{f_cE_c}$	$f_{u,sc}A_{sc}$

d_{sc} é o diâmetro do conector, h_{sc} é a altura do corpo do conector de cisalhamento, A_{sc} é a área da seção transversal do conector de cisalhamento, f_c é a resistência à compressão do concreto, E_c é o módulo de elasticidade do concreto, f_u é a resistência última do conector, g é o espaçamento entre as lajes alveolares, c é a altura da capa de concreto, α é o fator que leva em consideração a altura do conector de cisalhamento, β é o fator que leva em consideração o espaçamento entre as lajes alveolares, ε é o fator que leva em consideração o diâmetro da armadura transversal, λ_{sc} fator que leva em consideração a altura da laje alveolar e a altura da capa de concreto moldada in loco, φ é o diâmetro da armadura transversal, k=0,9. De acordo com a SCI P401 (GOUCHMAN, 2014), este fator leva em consideração a influência do confinamento dos conectores de cisalhamento devido a armadura transversal, e a geometria dos conectores em relação às unidades alveolares.

2.3 VIGAS MISTAS COM ABERTURAS NA ALMA

Os estudos iniciais envolvendo as vigas mistas com aberturas na alma contemplaram as vigas casteladas mistas e aquelas com uma única abertura retangular, formadas por lajes maciças de concreto ou lajes mistas. Embora existam estudos de vigas mistas casteladas na literatura, o presente trabalho considera apenas os estudos de vigas mistas com apenas uma abertura na alma e vigas celulares mistas. Este último é o foco do presente trabalho.

O primeiro estudo a ser citado foi fundamental para o desenvolvimento de modelos analíticos para cálculo da capacidade resistente. Trata-se do trabalho de Granade (1968), que apresentou resultados de dois ensaios experimentais para prever as tensões com base na teoria do mecanismo Vierendeel. As tensões teóricas se mostraram imprecisas em comparação com os valores experimentais. Apesar disso, o estudo de Granade (1968) foi de suma importância para o desenvolvimento do modelo analítico de Todd e Cooper (1980), o qual apresentou uma metodologia de cálculo que considerou diagramas de interação momento-cortante, para estimar a capacidade resistente de vigas mistas. No modelo, a posição da abertura retangular é variável no comprimento de vão. O modelo de cálculo foi fundamentado em hipóteses como:

i. interação total aço-concreto;
ii. a resistência à compressão do concreto na flexão assumida como sendo $0{,}85f_c$;
iii. a resistência à tração do concreto foi desconsiderada;
iv. o cisalhamento que causa momento secundário foi distribuído uniformemente na alma;
v. apenas a alma da seção de aço resiste ao cisalhamento;
vi. a capacidade resistente decorre da formação do mecanismo Vierendeel (formação de quatro rótulas plásticas);
vii. não ocorrerá a perda de estabilidade;
viii. o escoamento na seção de aço devido à combinação das tensões normais e de cisalhamento segue o critério de von Mises, aplicando a redução da espessura da alma e comprimento da mesa de tal modo que todas as fibras da seção transversal atinjam o escoamento;
ix. linha neutra plástica se encontra na laje de concreto.

O modelo de cálculo foi comparado aos resultados experimentais de Granade (1968), conforme ilustrado na **Figura 2.9.**

Figura 2.9 – Comparação do modelo de Todd e Cooper (1980) com os resultados de Granade (1968)

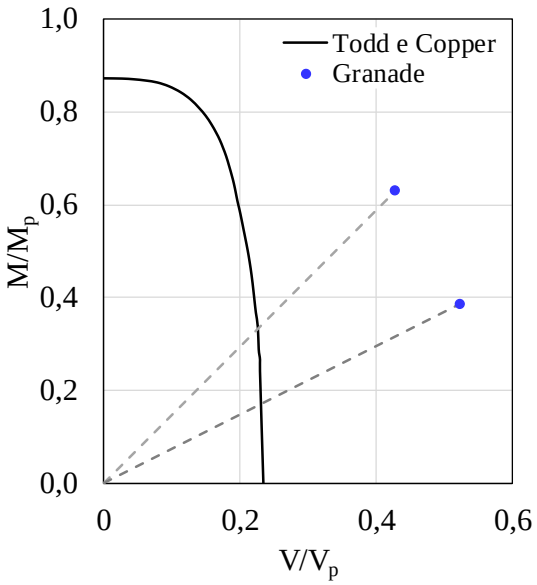

Fonte: adaptado de Todd e Cooper (1980)

O modelo subestima a capacidade resistente de vigas mistas com apenas uma abertura na alma, pois os autores não consideraram a contribuição da laje de concreto na resistência ao cisalhamento. Outra forma de investigar a interação momento-cortante foi por meio de estudo paramétrico e variação de parâmetros como espessura da laje, comprimento da abertura, altura e excentricidade da abertura. Nesse contexto, os resultados teóricos foram conservadores quanto à previsão da capacidade resistente, a variação da espessura da laje não afetou a interação entre o momento fletor e o esforço cortante e a capacidade resistente diminui com o aumento da abertura (TODD; COOPER, 1980).

Quanto à desconsideração da contribuição da laje de concreto na resistência ao cisalhamento, Donoghue (1982) propôs o reforço da abertura na alma com o objetivo de aumentar a resistência ao cisalhamento. Entretanto, diferentemente de Todd e Cooper (1980), Donoghue (1982) considerou interação parcial entre os elementos de aço e de concreto. Contudo, a contribuição da capacidade resistente à flexão da laje de concreto foi negligenciada por ela ser relativamente pequena se comparada à capacidade resistente à flexão do perfil de aço. A partir do modelo de Donoghue (1982) foi verificado que a adição de reforço próximo à região de abertura na alma aumenta consideravelmente a capacidade resistente ao cisalhamento do perfil de aço.

Notavelmente era necessário um número maior de investigações quanto à capacidade resistente ao cisalhamento, visto que até então sua consideração estava relacionada unicamente

com a alma do perfil de aço, desconsiderando a contribuição da laje de concreto da viga mista. Nesse âmbito se destaca o trabalho de Clawson e Darwin (1982a). Os autores ensaiaram seis vigas mistas com apenas uma abertura na alma e duas vigas de aço, de mesma seção, para avaliar a capacidade resistente do perfil de aço, isolado, ao cisalhamento. Com os ensaios foi possível avaliar a contribuição da laje de concreto para a resistência ao cisalhamento, o que é fundamental para a adequação modelos de cálculo. Nesse estudo foi possível concluir que a presença da abertura reduz significativamente a capacidade resistente das vigas mistas; na região da abertura, as deformações por compressão no concreto permaneceram baixas, mesmo depois do aço ter iniciado o escoamento; o modo de falha das vigas mistas com aberturas é dúctil (falha do concreto ocorre posteriormente ao escoamento do aço na região de abertura); a capacidade resistente das vigas mistas com aberturas foi governada pela falha do concreto; ocorreu deslizamento aço-concreto antes da falha na abertura da alma; a razão momento-cortante na abertura tem efeito pronunciado no comportamento último. As vigas que apresentaram altos valores dessa razão falharam por plastificação do aço e esmagamento do concreto. Por outro lado, vigas que apresentaram valores intermediários da razão momento-cortante falharam por formação de rótula plástica acompanhada de falha por tração no concreto.

Como na teoria do concreto armado, a capacidade resistente última a flexão em seções mistas pode decorrer do escoamento do aço à tração ou do esmagamento do concreto à compressão. Para vigas mistas com ruptura dúctil, a capacidade resistente a flexão é dada pelo momento de plastificação do perfil de aço. No entanto, para perfis de aço que apresentam altos valores de resistência ao escoamento, o esmagamento do concreto da laje pode ocorrer antes do perfil de aço atingir sua capacidade resistente. Isso ocorre porque a linha neutra se encontra na região da alma do perfil, o que causa esforço excessivo de compressão em lajes de concreto e valores baixos de tensão de tração na mesa inferior do perfil de aço.

Diante das observações anteriores, Clawson e Darwin (1982b) propuseram um método para estimar a capacidade resistente sem a utilização de reforço, considerando a contribuição da laje de concreto na resistência ao cisalhamento. O modelo proposto estimou a capacidade resistente na região da abertura por meio de diagramas de interação momento-cortante, como apresentado anteriormente por Todd e Cooper (1980). Para verificar a acurácia do modelo, Clawson e Darwin (1982b) compararam os resultados experimentais de Clawson e Darwin (1982a) e Granade (1968). Entretanto, nesse último caso, os autores também

compararam os resultados com o modelo analítico anteriormente proposto por Todd e Cooper (1980).

Sobre a comparação do modelo analítico com os ensaios de Clawson e Darwin (1982a), o modelo em questão se apresentou conservador, conforme ilustrado nas **Figura 2.10a** e **Figura 2.10b**. Por outro lado, quando comparado com os ensaios de Granade (1968), (**Figura 2.10c**), o modelo se mostrou mais próximo dos valores experimentais, diferentemente do modelo de Todd e Cooper (1980), que subestimam a capacidade resistente desses elementos estruturais por negligenciarem a contribuição da laje para a resistência ao cisalhamento.

Figura 2.10 – Comparações do modelo de Clawson e Darwin (1982b)

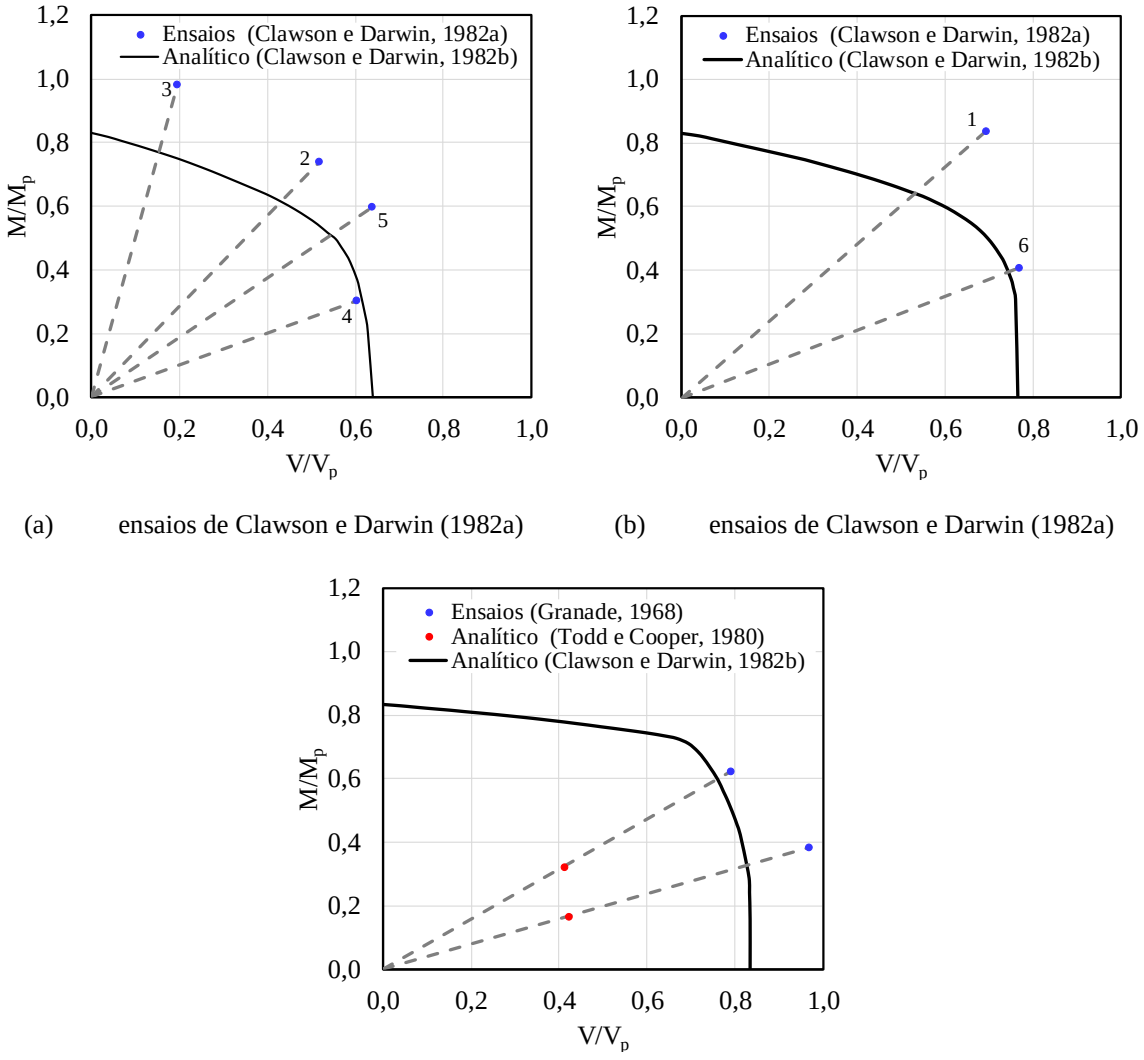

(a) ensaios de Clawson e Darwin (1982a) (b) ensaios de Clawson e Darwin (1982a)

(c) ensaios de Granade (1968) e modelo de Todd e Cooper (1980)

Fonte: adaptado de Clawson e Darwin (1982b)

O modelo de cálculo proposto por Clawson e Darwin (1982b), posteriormente, foi sustentado pelos resultados experimentais de Cho (1982, *apud* CHO, 1990). Nesse estudo, os modos de falha foram classificados em função dos esforços momento e cortante. A comparação do modelo analítico com os resultados experimentais, incluindo aqueles de Granade (1968), indicou que a previsão melhorou bastante quando comparada a Todd e Cooper (1980), mas ainda foi conservador, particularmente para os resultados de Granade (1968).

Em Narayanan, Al-amery e Roberts (1989) e Roberts e Al-amery (1991) foi investigada experimentalmente a capacidade resistente ao cisalhamento em longarinas mistas com aberturas na alma. O primeiro estudo considerou o conector tipo pino com cabeça na interface aço-concreto. Já o segundo, utilizou conectores parafusados e protendidos, projetados para oferecerem resistência aos esforços horizontais na interface aço-concreto. Os resultados mostraram que se houver conexão adequada na interface aço-concreto, a resistência ao cisalhamento da longarina mista com abertura na alma seria significativamente maior do que a da longarina, sozinha. Ambos os resultados foram utilizados para o desenvolvimento de um modelo analítico de previsão da capacidade resistente ao cisalhamento das longarinas mistas com abertura na alma.

A seguir, na **Tabela 2.2** são apresentados, de modo resumido, os trabalhos desenvolvidos com vigas mistas com apenas uma abertura na alma e confeccionadas com lajes maciças. Na **Figura 2.11** é mostrado uma linha do tempo em relação aos trabalhos desenvolvidos para a identificar quais autores se destacaram no período descrito.

Tabela 2.2 – Vigas mistas com apenas uma abertura e lajes maciças

Modelo	Referência	Observações
Experimental	Granade (1968)	Verificou as tensões em função do mecanismo Vierendeel.
	Clawson e Darwin (1982a)	Observaram a influência da laje na resistência ao cisalhamento.
	Cho (1982)	Sustentou a contribuição da laje na resistência ao cisalhamento.
	Narayanan, Al-Amery e Roberts (1989)	Observaram a eficiência dos conectores tipo pino com cabeça na interface aço-concreto.
	Roberts e Al-Amery (1991)	Observaram a eficiência de parafusos protendidos na interface aço-concreto.
Analítico	Todd e Cooper (1980)	Negligenciaram a contribuição da laje na resistência ao cisalhamento.
	Donoghue (1982)	Sugeriu a utilização de reforços para contribuírem na resistência ao cisalhamento.
	Clawson e Darwin (1982b)	Consideraram a contribuição da laje na resistência ao cisalhamento.

Figura 2.11 – Linha do tempo em função dos trabalhos desenvolvidos pelos autores, considerando vigas mistas com aberturas na alma com laje maciça

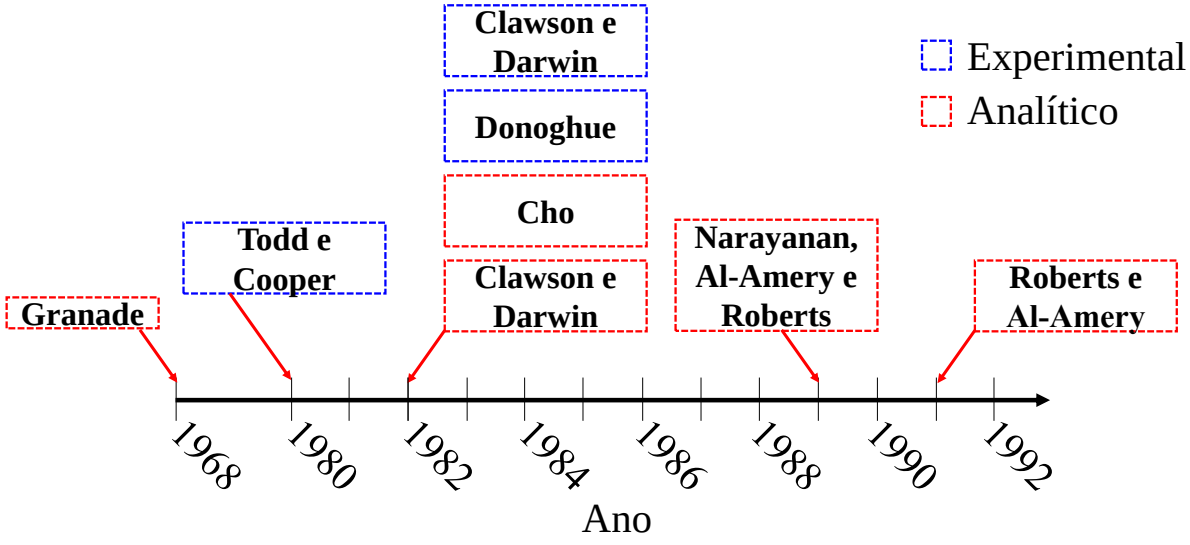

Considerando agora as vigas mistas com abertura na alma formadas por lajes mistas, em Redwood e Wong (1982) foram apresentados resultados experimentais com a fôrma de aço disposta transversalmente ao eixo longitudinal do perfil de aço, para avaliar o efeito da relação momento-cortante na região da abertura. Os autores observaram que para altos valores da razão momento-cortante, os modos de falha foram governados pela flexão. A flexão local, tanto do tê superior quanto do tê inferior, causou a formação do mecanismo Vierendeel, e tornou-se cada vez mais evidente à medida que a relação momento-cortante diminuiu. Já para baixos valores dessa relação, o mecanismo Vierendeel governou o modo de falha e resultou em fissuras de flexão na laje de concreto. Além disso, a separação da fôrma ocorreu em todos os ensaios, levando à falha por compressão na porção maciça da laje de concreto, acima da fôrma, em função dos médios e altos valores da razão momento-cortante e a quase completa separação na interface aço-concreto acima da abertura para baixos valores da razão momento-cortante.

A fissuração do concreto ocorre em função das deflexões através da abertura, com a progressão do carregamento. Além disso, próximo à capacidade resistente, o concreto pode desenvolver trincas transversais, longitudinais e diagonais próximas à região da abertura (DONAHEY; DARWIN, 1988). Em lajes maciças, geralmente são observadas fissuras transversais nas extremidades da abertura, tanto na parte superior quanto inferior da laje (**Figura 2.12a**). Já em lajes mistas, a fissuração se inicia próximo ao canto superior da nervura

e avança diagonalmente até o topo, conforme ilustrado na **Figura 2.12b** (REDWOOD; CHO, 1993).

Figura 2.12 – Fissuração no concreto

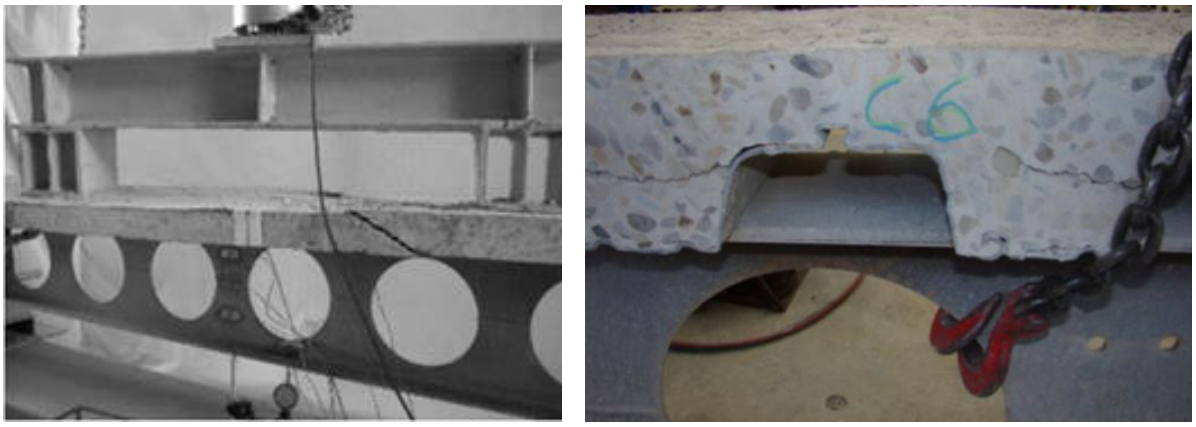

(a) Laje maciça (b) Laje mista

Fonte: adaptado de Sheehan *et al*. (2016)

Em contraponto a Clawson e Darwin (1982b), Redwood e Wong (1982) forneceram um método analítico simplificado que levava em conta a falha por mecanismo Vierendeel com a formação de quatro rótulas plásticas, que representa um modo típico de deformação de vigas com abertura na alma submetidas a elevados valores de esforço cortante (CLAWSON; DARWIN, 1982b, 1982c; DONOGHUE, 1982; TODD; COOPER, 1980). Importante ressaltar que Clawson e Darwin (1982b) utilizaram como critério de falha para o concreto as tensões normais e de cisalhamento, enquanto que Redwood e Wong (1982) consideraram a falha da laje de concreto por compressão. A justificativa para isso é que quando o esforço cortante é intenso, a tensão de compressão média na laje de concreto é limitada a um valor baixo de tensão, devido à conexão de cisalhamento entre laje de concreto e perfil de aço próximo à região de abertura. Além disso, a tensão de cisalhamento resistida pela viga mista é limitada à capacidade resistente ao cisalhamento da viga de aço com abertura, isolada.

Em Redwood e Poumbouras (1983) foram ensaiados dois modelos: o primeiro para avaliar a necessidade de conectores de cisalhamento na interface laje de concreto e perfil de aço, alocados no comprimento da abertura; o segundo para avaliar o efeito da construção não escorada, pois essa situação poderia produzir condições severas na viga de aço com abertura, antes que a ação mista seja desenvolvida. Os autores verificaram que a ausência de conectores de cisalhamento no comprimento de abertura reduz significativamente a capacidade resistente

da viga mista com abertura na alma. O efeito das cargas variáveis na construção não-escorada não exerceu influência para as situações em que não excederam 60% da capacidade resistente prevista da viga de aço com abertura na alma.

Posteriormente, Redwood e Poumbouras (1984) apresentaram um modelo para o cálculo da capacidade resistente, considerando o aumento das tensões de compressão devido ao deslizamento causado pela deformação dos conectores de cisalhamento. Nesse modelo foram consideradas a contribuição da laje de concreto na resistência ao esforço cortante e a interação parcial. Tal metodologia se mostrou conservadora quando comparada aos resultados experimentais anteriores (REDWOOD; POUMBOURAS, 1983).

Donahey e Darwin (1988) realizaram ensaios de vigas mistas com as fôrmas de aço situadas tanto na direção perpendicular quanto na direção paralela ao eixo longitudinal do perfil de aço. Os objetivos dos experimentos foram investigar os efeitos da relação momento-cortante, quantidade e posição dos conectores de cisalhamento, orientação e posição da fôrma de aço. Os resultados experimentais mostraram que o concreto contribuiu significativamente para a capacidade resistente à flexão e ao cisalhamento; à medida que a relação momento-cortante diminui em uma abertura, a deflexão através da abertura aumenta acompanhada de fissuração transversal; o comportamento das vigas mistas formadas por lajes mistas é dúctil e a falha é precedida por fissurações na laje, escoamento do aço e grandes deflexões; há considerável deslizamento aço-concreto antes da falha; a capacidade resistente é governada pela falha da laje de concreto e; à medida que aumenta número de conectores de cisalhamento acima da abertura e entre a abertura e o apoio, a resistência na abertura aumenta.

No mesmo ano, Darwin e Donahey (1988) apresentaram modelo de cálculo sem a utilização do reforço. O modelo levava em conta a interação momento-cortante, abordando a capacidade resistente na abertura submetida à flexão, ao cisalhamento puro e as combinações de flexão e cisalhamento. Nesse método, as capacidades resistentes de flexão e cisalhamento puros são calculadas separadamente. Também, os autores discutiram o valor apropriado do *Load Resistance Factor Design* (AISC/LRFD). A comparação é justificada pelo fato de que a especificação AISC/LRFD (1986)[1] define a capacidade resistente à flexão de projeto como $\Phi_b M_n$, em que Φ_b é o fator de resistência para flexão. Para seções mistas compactas, Φ_b é igual

[1] **Load and resistance factor design manual of steel construction**. (1986). 1st Ed., American Institute of Steel Construction, Inc., Chicago, 1986.

a 0,85. Por outro lado, a resistência ao cisalhamento de projeto é definida como $\Phi_v V_n$, em que Φ_v é o fator de resistência para o cisalhamento. Para o projeto de seções mistas, tem-se o valor Φ_v igual a 0,90. Esse valor é fundamentado no pressuposto de que o cisalhamento é resistido apenas pela alma do perfil de aço. O método de cálculo dos autores foi comparado com os resultados experimentais, considerando lajes sólidas (CLAWSON; DARWIN, 1982a; CHO, 1982; GRANADE, 1968) e lajes nervuradas (DONAHEY; DARWIN, 1988; REDWOOD; POUMBOURAS, 1983; REDWOOD; WONG, 1982). Os resultados se apresentaram com acurácia. Além disso, os autores sugeriram a utilização do valor do fator de resistência igual 0,85, tanto para o cisalhamento quanto para a flexão.

Observa-se que até a década de 1980 foram desenvolvidos procedimentos de cálculos com a utilização ou não de reforço, pois os autores já consideraram a contribuição da laje de concreto na resistência ao cisalhamento. Embora tenham sido apresentadas metodologias de cálculo para situações distintas de utilização ou não de reforço na abertura, não havia até então uma abordagem unificada para tais considerações.

Nesse contexto, Darwin e Lucas (1990) modificaram o método originalmente desenvolvido por Darwin e Donahey (1988), unificando tais considerações. O procedimento fornece uma única equação para estimar a resistência ao cisalhamento na abertura da alma. O método foi comparado aos resultados experimentais, considerando lajes mistas (DONAHEY; DARWIN, 1988; REDWOOD; POUMBOURAS, 1983; REDWOOD; WONG, 1982) e lajes maciças (CHO, 1982; CLAWSON; DARWIN, 1982a; GRANADE, 1968). A acurácia do método foi superior aos modelos de cálculo anteriores como, por exemplo, o método de Redwood e Poumbouras (1984). Além disso, os autores sugeriram fatores de resistência iguais a 0,90 e 0,85 para a flexão e o cisalhamento, respectivamente, diferentemente de Darwin e Donahey (1988), que sugeriram o valor igual a 0,85 para ambas as situações.

Assim como Darwin e Lucas (1990), Benitez, Darwin e Donahey (1998) deram continuidade aos trabalhos desenvolvidos por Darwin e Donahey (1988) e Donahey e Darwin (1988), e descreveram procedimentos matriciais para a determinação da flecha. Os resultados foram comparados com análises experimentais (CLAWSON; DARWIN, 1982a; DONAHEY; DARWIN, 1988; GRANADE, 1968; REDWOOD; WONG, 1982). A aplicação do método dos deslocamentos, na forma matricial, fornece uma estimativa razoável da flecha total e da deflexão na abertura, quando comparada com os valores experimentais. Os autores concluíram que, na maioria dos casos, uma única abertura na alma tem pouco efeito na flecha

total, os efeitos de uma abertura e de deflexões de cisalhamento são da mesma ordem de grandeza e ignorar a abertura na alma e a deformação por cisalhamento pode levar a um erro significativo.

Em Chung e Lawson (2001) foi apresentado procedimentos de projeto de vigas mistas com abertura retangular e circular na alma para a aplicação no EN 1994-1-1 (2004). Tais procedimentos apresentaram informações gerais sobre o dimensionamento de aberturas em função da resistência ao cisalhamento e flexão, e o efeito dessas aberturas nas deflexões. Embora já existissem metodologias de projeto para vigas mistas com aberturas na alma, como o de Lawson (1987)[1], a principal justificativa para a publicação é de que o EN 1994-1-1 (2004) não estava concluído. Assim, não havia métodos para o projeto de vigas mistas com aberturas de várias formas e dimensões.

Em Lawson, Chung e Price (1992) foram realizados ensaios experimentais. Tais ensaios tiveram como objetivo avaliar a influência de enrijecedores longitudinais na ação global e local, flambagem local da alma por compressão, transferência de cisalhamento por meio da laje de concreto, capacidade resistente à formação do mecanismo Vierendeel e o aumento de deflexões decorrentes das aberturas. Os modelos apresentaram comportamento dúctil, sem a ocorrência da fissuração, esmagamento do concreto e perda de estabilidade. A formação do mecanismo Vierendeel governou a capacidade resistente. Os resultados foram comparados com a publicação de Lawson (1987). O método foi fundamentado nos ensaios experimentais realizados anteriormente (DONAHEY; DARWIN, 1988; REDWOOD; POUMBOURAS, 1983). Importante ressaltar que o método aborda a posição da abertura no comprimento de vão e na seção transversal, e faz considerações a respeito dos reforços na abertura. Além disso, a resistência ao cisalhamento leva em consideração a contribuição da laje de concreto. Os autores concluíram que o método de cálculo é conservador, quando comparado com os resultados experimentais. Além disso, o conservadorismo é maior no caso de aberturas localizadas na região de cisalhamento intenso. Os ensaios também demonstraram que a soldagem de enrijecedores somente em um lado da abertura não afeta o desempenho da alma e isso pode trazer economia considerável na execução de aberturas enrijecidas.

[1] LAWSON, R. M. **Design for openings in the webs of composite beams**, SCI/CIRIA publication, SCI-P-068, 1987.

Em Cho e Redwood (1992a) foi apresentado uma metodologia capaz de estimar a capacidade resistente de vigas mistas com abertura na alma, considerando os conectores de cisalhamento na região da abertura como elementos tracionados. Tal metodologia foi fundamentada no conceito de treliça (bielas e tirantes). Segundo os autores, o conceito básico dessa analogia é que após a fissuração, o concreto carrega um conjunto de tensões de compressão em diagonais (escoras) e a armadura tensões de tração (tirantes). Essa abordagem relaciona a resistência ao cisalhamento à localização dos conectores de cisalhamento. As soluções propostas pelos autores preveem a resistência e fornecem informações úteis sobre a posição dos conectores na região das aberturas. Uma observação importante é que foi constatada a contribuição da laje de concreto na resistência ao cisalhamento (CHO e REDWOOD, 1992a). Tal observação relaciona uma gama de ensaios experimentais de vigas mistas com aberturas retangulares, conforme ilustrado na **Figura 2.13**, em que n_h é o número de conectores de cisalhamento no comprimento de abertura, n é o número total de conectores e cisalhamento, t_s é a altura da laje de concreto e d é a altura do perfil de aço.

Figura 2.13 – Contribuição da laje de concreto para a resistência ao cisalhamento de vigas mistas com aberturas na alma

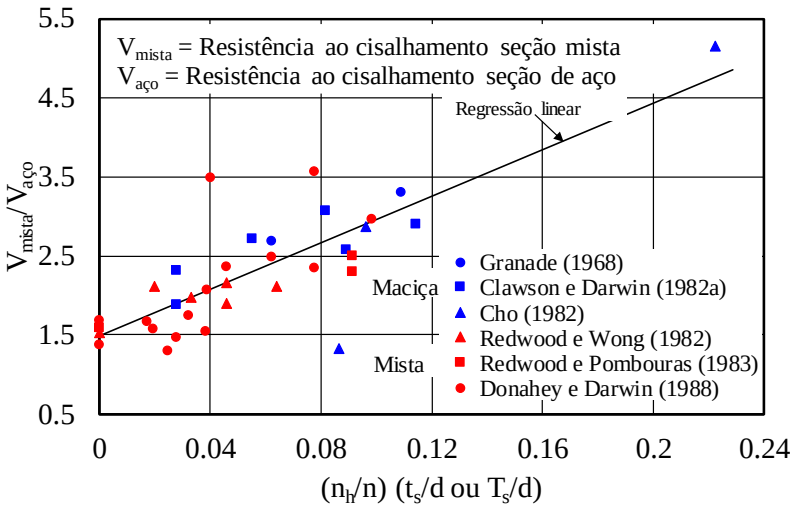

Fonte: adaptado de Cho e Redwood (1992a)

Os ensaios indicaram que a contribuição da laje de concreto na capacidade resistente ao cisalhamento na região de abertura pode atingir a ordem de 40%-420% para as lajes maciças (CLAWSON; DARWIN, 1982a; CHO, 1982; GRANADE, 1968) e 30%-260% para lajes mistas (DONAHEY; DARWIN, 1988; GRANADE, 1968; REDWOOD; POUMBOURAS, 1983; REDWOOD; WONG, 1982), quando comparadas ao perfil de aço isolado, mantendo a

geometria das aberturas (CHO; REDWOOD, 1992a). Assim, ao considerar a laje de concreto no cálculo da resistência ao cisalhamento, é possível desconsiderar a utilização de reforços no perfil de aço com abertura.

Posteriormente, para verificar o modelo de cálculo fundamentado na analogia de treliça em que os conectores de cisalhamento são os elementos tracionados e o concreto constitui as diagonais comprimidas, Cho e Redwood (1992b) realizaram ensaios em modelos físicos. Além de seus resultados experimentais, os autores também consideraram alguns resultados experimentais disponíveis na literatura (CHO, 1982; CLAWSON; DARWIN, 1982a; DONAHEY; DARWIN, 1988; GRANADE, 1968; REDWOOD; POUMBOURAS, 1983; REDWOOD; WONG, 1982). Embora as resistências estimadas considerando o modelo de treliça sejam satisfatórias, em particular para lajes mistas, o modelo de treliça fornece previsões ligeiramente mais conservadoras em relação aos resultados experimentais. Por outro lado, para vigas mistas com aberturas na alma formadas por lajes maciças, o modelo não apresentou acurácia. Assim, o modelo de treliça é mais apropriado para lajes mistas (CHO; REDWOOD, 1992b). Em relação aos resultados experimentais, os autores verificaram que os conectores de cisalhamento posicionados no comprimento da abertura são os principais responsáveis pela contribuição da laje de concreto na resistência ao cisalhamento. A largura da laje de concreto não é um fator que afeta a capacidade resistente da laje ao cisalhamento. Em lajes maciças, as evidências indicaram que a falha, na parte inferior da laje próxima à abertura, iniciou com uma fissura em função da diagonal tracionada através da espessura da laje.

Em Redwood e Cho (1993) foi apresentado um método de cálculo simplificado, considerando, como o caso geral, vigas mistas com abertura reforçada na alma. A análise foi fundamentada nas tensões próximas aos quatro cantos da abertura que estão em equilíbrio com as cargas externas e que satisfazem o critério de escoamento de von Mises. O método foi validado considerando resultados de vigas mistas com abertura na alma, mas sem reforço (CHO, 1982; CLAWSON; DARWIN, 1982a; DONAHEY; DARWIN, 1988; LAWSON; CHUNG; PRICE, 1992; REDWOOD; POUMBOURAS, 1983; REDWOOD; WONG, 1982). Nesse estudo, o valor médio da razão entre os resultados experimentais e do modelo analítico foi de 1,064, com coeficiente de variação de 0,146.

Ainda visando o desenvolvimento de modelos analíticos, Fahmy (1996) propôs um método que levava em conta as curvas de interação momento-cortante. Embora o autor tenha partido das hipóteses de Todd e Cooper (1980), o procedimento proposto levou em conta a

contribuição da laje de concreto na capacidade resistente ao cisalhamento e interação completa. Os resultados teóricos apresentaram boa correlação com resultados experimentais disponíveis na literatura, como Granade (1968), Clawson e Darwin (1982a) e Lawson, Chung e Price (1992).

Park, Kim e Yang (2003) ensaiaram vigas mistas com lajes mistas. Os parâmetros avaliados foram a largura da laje e a relação momento-cortante. Os autores verificaram que os modos de falha, como a diagonal tracionada (**Figura 2.14a**) e o arrancamento (**Figura 2.14b**) dependem da largura da laje. Os resultados experimentais fomentaram o desenvolvimento de um modelo analítico para avaliar a capacidade resistente considerando a combinação da flexão e do cisalhamento. Park, Kim e Yang (2003) justificam que o modelo de treliça desenvolvido por Cho e Redwood (1992a) não considera o efeito da largura efetiva das lajes mistas, assumindo que a fissura da diagonal tracionada não ocorre antes da falha por arrancamento dos conectores. A combinação da flexão e do cisalhamento resultou em um modelo analítico com boa correlação com os ensaios experimentais e com o modelo de Cho e Redwood (1992a).

Figura 2.14 – Comportamento último dos modelos físicos de Park, Kim e Yang (2003)

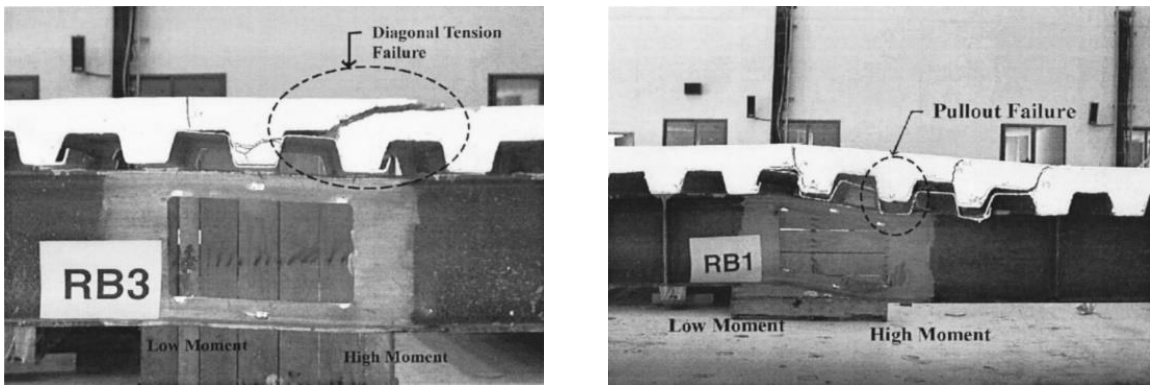

(a) Diagonal tracionada (b) Arrancamento

Fonte: Park, Kim e Yang (2003)

O trabalho mais recente em vigas mistas com aberturas na alma foi publicado por Du et al. (2021). O estudo apresentado pelos autores objetivou a investigação do tipo e área dos enrijecedores longitudinais e transversais para o reforço da abertura na alma, bem como a proposição de equações para estimar a capacidade resistente, considerando enrijecedores. Como constatado por autores anteriormente (DONOGHUE, 1982; LAWSON; CHUNG; PRICE, 1992), os enrijecedores longitudinais melhoraram, consideravelmente a capacidade resistente das vigas com abertura na alma. Em contrapartida, a utilização de enrijecedores

transversais não apresentaram contribuição significativa na capacidade resistente desse sistema estrutural. O modelo de cálculo dos autores apresentaram resultados coerentes, quando comparados com os modelos experimentais (DONAHEY; DARWIN, 1988; LAWSON; CHUNG; PRICE, 1992; PARK; KIM; YANG, 2003; REDWOOD; POUMBOURAS, 1983).

A seguir nas **Tabela 2.3** e **Figura 2.15** são apresentados, de forma resumida, os estudos experimentais em vigas mistas com lajes mistas e almas com apenas uma abertura. Nas **Tabela 2.4** e **Figura 2.16** são apresentados os estudos analíticos.

Tabela 2.3 – Estudos experimentais de vigas mistas com lajes mistas e almas com aberturas

Referência	Observações
Redwood e Wong (1982)	Avaliaram a relação momento-cortante na região da abertura.
Redwood e Poumbouras (1983)	Investigaram a necessidade de conectores no comprimento de abertura e os efeitos da construção não escorada.
Donahey e Darwin (1988)	Observaram o comportamento em função da disposição da laje (nervuras da fôrma de aço), situadas tanto na direção perpendicular quanto na direção paralela ao eixo longitudinal do perfil de aço.
Lawson, Chung e Price (1992)	Observaram a influência de enrijecedores longitudinais na ação de flexão global e local, instabilidade local da alma por compressão e flexão, transferência de cisalhamento por meio da laje de concreto, resistência à formação do mecanismo Vierendeel e o aumento de deflexões decorrentes das aberturas.
Cho e Redwood (1992b)	Verificaram o modelo de cálculo com analogia de treliça em que os conectores de cisalhamento são considerados elementos tracionados.
Park, Kim e Yang (2003)	Observaram os efeitos da largura da laje e da relação momento-cortante.
Du et al. (2021)	Avaliaram a resistência das aberturas na alma considerando enrijecedores.

Figura 2.15 –Experimentos desenvolvidos pelos autores, considerando vigas mistas com aberturas na alma com laje mistas de aço e concreto

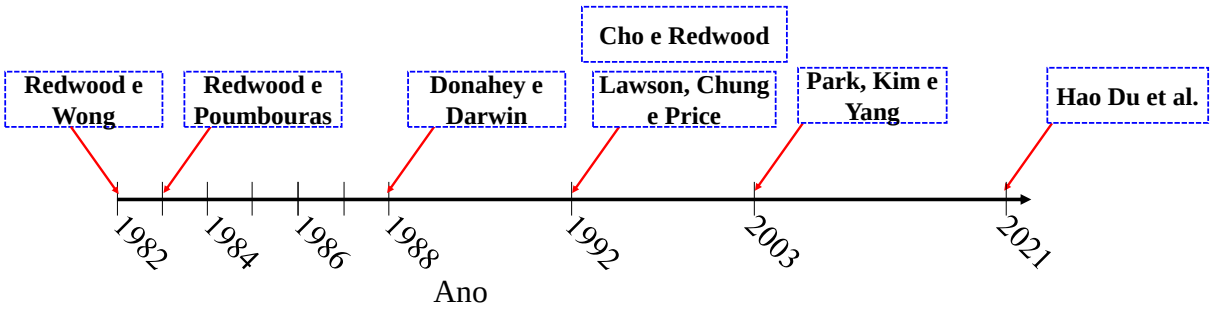

Tabela 2.4 – Modelos analíticos para vigas mistas com lajes mistas e almas com aberturas

Referência	Observações
Redwood e Wong (1982)	Consideraram a falha da laje de concreto por compressão
Redwood e Poumbouras (1984)	Consideraram o aumento das tensões de compressão devido ao deslizamento aço-concreto causado pela deformação dos conectores de cisalhamento
Darwin e Donahey (1988)	Determinaram a capacidade resistente sem a utilização do reforço
Cho e Redwood (1992)	Fundamentaram o conceito de analogia à treliça (bielas e tirantes) e apresentaram uma metodologia para estimar a capacidade resistente de vigas mistas com abertura na alma, considerando os conectores de cisalhamento na região da abertura como elementos tracionados
Redwood e Cho (1993)	Apresentaram um modelo de cálculo simplificado, considerando vigas mistas com abertura na alma reforçada como o caso geral
Fahmy (1996)	Propôs um modelo para cálculo da capacidade resistente considerando interação completa aço-concreto
Benitez, Darwin e Donahey (1998)	Descreveram procedimentos matriciais para a determinação da máxima deflexão em vigas mistas com aberturas na alma
Chung e Lawson (2001)	Apresentaram procedimentos de projeto de vigas mistas com aberturas retangulares e circulares na alma para a aplicação no EN 1994-1-1 (2004)
Du et al. (2021)	Propuseram um modelo analítico capaz de estimar a resistência de vigas mistas com aberturas na alma considerando enrijecedores.

Figura 2.16 – Modelos analíticos desenvolvidos pelos autores, considerando vigas mistas com aberturas na alma com laje mistas de aço e concreto

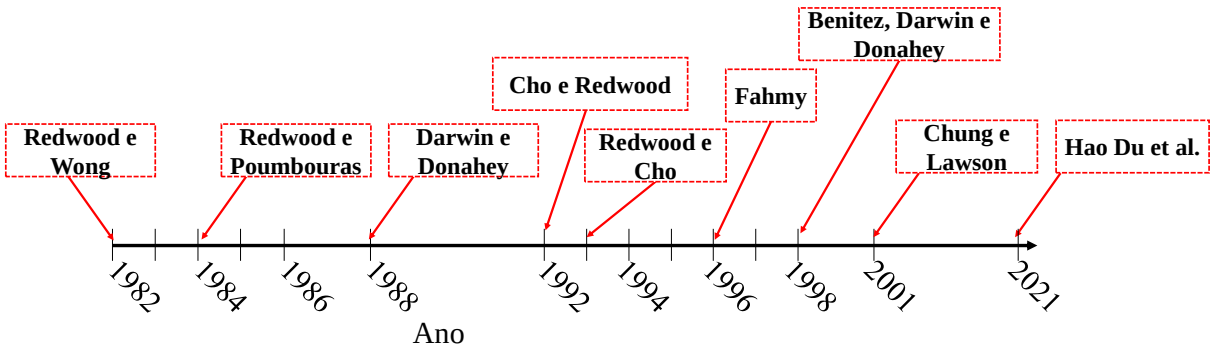

2.4 VIGAS CELULARES MISTAS

Os estudos apresentados até aqui abordaram vigas mistas com lajes maciças e mistas com uma única abertura na alma, ou seja, não foram consideradas vigas com aberturas sequenciais ao longo do vão, como é o caso das vigas celulares mistas. Nesse cenário, destacam-se Gizejowski e Khalil (2010), que realizaram um conjunto de ensaios. Em todas as situações avaliadas, os autores observaram modos de falha associados à distorção da alma (**Figura 2.17**), isso porque as condições de contorno potencializarem esse fenômeno, como o momento fletor negativo.

Figura 2.17– Distorção da alma em vigas celulares mistas

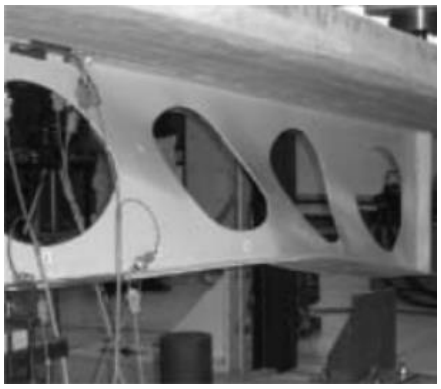

Fonte: Gizejowski e Khalil (2010)

Em relação aos estudos de vigas celulares mistas com lajes mistas, nos últimos anos, a viga celular mista assimétrica tem sido amplamente utilizada na construção. Como a mesa superior age em conjunto com a laje, a parte inferior da viga é formada por uma seção mais rígida do que a parte superior, para aumentar a capacidade resistente à flexão e ao cisalhamento (**Figura 2.18**).

Figura 2.18 – Viga celular assimétrica

Fonte: Lawson, Hanus e Sonck (2017)

A proporção entre as áreas das mesas inferior e superior varia entre 1,5 e 2,5 (SHEEHAN *et al*., 2016). Nesse contexto, vários são os trabalhos que avaliaram o comportamento de vigas celulares mistas com perfis assimétricos (HECHLER; MÜLLER; SEDLACEK, 2006; MÜLLER *et al*., 2006; NADJAI, 2005; SHEEHAN *et al*., 2016). Por exemplo, o estudo de Müller *et al*. (2006) apresentou resultados experimentais de dois modelos: vigas mistas celular com seção simétrica e assimétrica. Ambos os exemplares foram projetados de tal forma que em uma extremidade fosse possível investigar a ação conjunta nos elementos mistos e, na outra extremidade, apenas o perfil celular. O comportamento último dos ensaios

foi semelhante. De acordo com os autores, foi observada a formação do mecanismo Vierendeel para baixos valores de carregamento na extremidade correspondente à viga mista (com ação conjunta aço-concreto). Em contrapartida, na extremidade em que havia apenas o perfil celular de aço, a capacidade resistente foi atingida por instabilidade no montante de alma.

Posteriormente, em Nadjai et al. (2007) e Nadjai (2005) foram apresentados resultados de dois modelos físicos considerando vigas celulares mistas simétricas e assimétricas. Ambos os modelos tiveram a capacidade resistente governada pela instabilidade no montante da alma, situação análoga aos modelos de Müller *et al*. (2006).

Sheehan *et al*. (2016) ensaiaram vigas celulares mistas de grandes vãos formadas por seções assimétricas. O grau de conexão de cisalhamento foi de 36%, valor bem inferior ao recomendado no EN 1994-1-1 (2004) que foi de 88%. As vigas celulares mistas foram submetidas a carregamento uniformemente distribuído e a cargas concentradas aplicadas a 5/16 e 7/16 do comprimento do vão. O deslizamento na interface aço-concreto, a flecha, a distribuição de tensões e o efeito da construção não escorada foram avaliados no estudo. Os observaram que a viga celular mista solicitada por carregamento uniformemente distribuído resistiu a 3,4 vezes o carregamento estimado de projeto, apesar do grau de interação consideravelmente menor que o mínimo exigido pelo EN 1994-1-1 (2004).

Djebli, Kerdal e Abidelah (2019) propuseram um modelo analítico para o cálculo da deflexão total de vigas celulares mistas submetidas a cargas transversais concentradas ou uniformemente distribuídas. Esse modelo inclui situações em que a abertura se encontra ou não no centro do vão. A máxima deflexão é composta por duas parcelas: a de flexão em função do momento fletor global e a de cisalhamento devido ao mecanismo Vierendeel. De acordo com os autores, o modelo analítico fornece diretamente a deflexão adicional a partir do efeito do cisalhamento vertical na abertura. A contribuição da deflexão adicional é mais significativa no caso de vigas com vãos curtos.

No panorama nacional Veríssimo (1996) e Veríssimo e Fakury (1998) divulgam o primeiro estudo de vigas mistas com abertura na alma. Nesse trabalho são descritos os estados limites últimos para vigas mistas com uma ou mais aberturas na alma e um código computacional para a verificação desses estados limites. Posteriormente, uma série de estudos voltados para a modelagem numérica vem sendo conduzida por pesquisadores brasileiros. Ferrari (2013) e Gonçalves (2015) propõem modelos numéricos para representar o

comportamento estrutural de vigas celulares e casteladas mistas. Badke-Neto, Calenzani e Ferreira (2015), Brinkhus (2015) e Piassi et al. (2018) apresentaram sínteses de modelos de cálculo para verificação dos modos de falha em vigas de aço e mistas com perfis celulares. Em Piassi et al. (2018) foi dado destaque à instabilidade lateral com distorção e apresentado uma formulação para estimar a rigidez rotacional de vigas mistas com perfil celular e laje maciça de concreto. A seguir na **Tabela 2.5** o resumo dos trabalhos publicados em vigas celulares mistas.

Tabela 2.5 – Vigas celulares mistas

Modelo	Referência	Observações
Experimental	Gizejowski e Khalil (2010)	Verificaram a influência da distorção da alma
	Müller *et al.* (2006)	Realizaram ensaios de vigas celulares mistas com seção duplamente simétrica e com um eixo de simetria. A capacidade resistente foi atingida com formação de mecanismo Vierendeel e instabilidade no montante da alma
	Nadjai (2005)	Observou que a capacidade resistente foi definida pela instabilidade no montante da alma
	Sheehan *et al.* (2016)	Investigaram o efeito da construção não escorada em vigas celulares mistas de grandes vãos
Analítico	Djebli, Kerdal e Abidelah (2019)	Propuseram modelo analítico para cálculo da flecha de vigas celulares mistas com dupla simetria submetidas a cargas concentradas ou uniformemente distribuídas.

Na **Figura 2.19** é mostrado uma linha do tempo em relação aos trabalhos desenvolvidos para a identificar quais autores se destacaram no período descrito.

Figura 2.19 –Trabalhos desenvolvidos pelos autores, considerando vigas celulares mistas

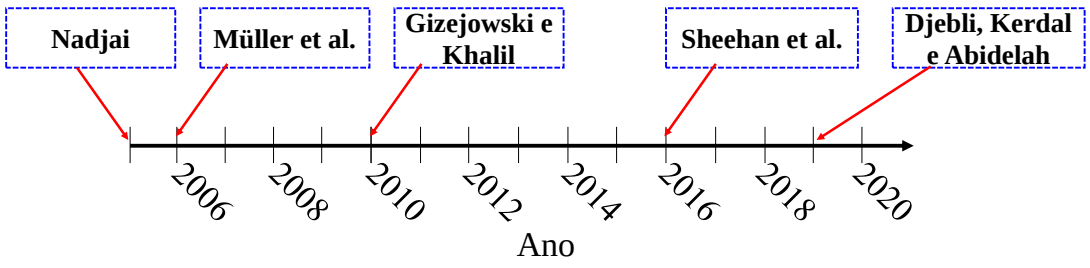

2.5 VIGAS MISTAS COM LAJES ALVEOLARES

As vigas mistas formadas por lajes maciças ou mistas apresentam desvantagens em relação ao alto custo operacional da soldagem do conector de cisalhamento, o tempo de cura do concreto úmido em climas frios e vãos curtos em relação à altura do piso. Assim, para reduzir algumas dessas limitações, as vigas mistas com a utilização de lajes alveolares pré-fabricadas

de concreto se apresentam como uma alternativa a investigar (AHMED; TSAVDARIDIS, 2019).

Os tipos de lajes de concreto pré-moldado associadas a perfis de aço para formar as vigas mistas são alveolares, com altura entre 150 e 260mm, aberturas circulares ou alongadas contínuas ao longo do comprimento; também podem ser utilizadas lajes sólidas, com 75 a 100mm de altura, para uso com capa de concreto moldado *in loco* (**Figura 2.20**) (HICKS; LAWSON, 2003).

Figura 2.20 – Lajes alveolares

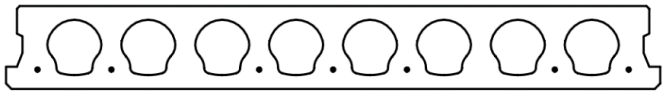

(a) alvéolo não circular

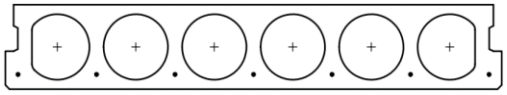

(b) alvéolo circular

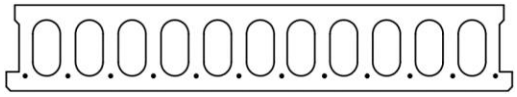

(c) alvéolo alongado

Fonte: Hicks e Lawson (2003)

Um dos usos comuns das lajes alveolares pré-fabricadas é em sistemas de piso, em composição com os perfis de aço. Nesse contexto, as lajes podem ser dispostas em apoios rígidos (**Figura 2.21a**) ou flexíveis (**Figura 2.21b**).

Figura 2.21 – Lajes alveolares

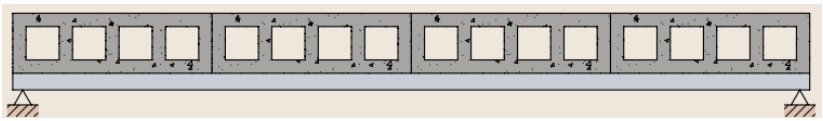

(a)

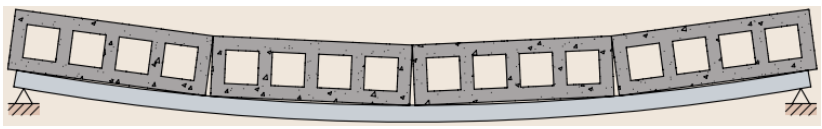

(b)

Fonte: SCI P401 (GOUCHMAN, 2014)

Um elemento estrutural, como os perfis de aço que suportam as lajes alveolares, é considerado flexível se a resistência ao cisalhamento das lajes for reduzida devido à deflexão do membro (PAJARI; KOUKKARI, 1998). Essas deflexões fazem com que ocorra escorregamento relativo entre as unidades alveolares e o perfil de aço. Dessa forma, a conexão e o atrito entre as extremidades da laje e a viga tendem a impedir o deslizamento. Como resultado, tensões transversais e deformações surgem na laje (PAJARI, 1998). Tal efeito é conhecido como interação de cisalhamento entre lajes e vigas.

A publicação SCI P401 (GOUCHMAN, 2014) descreve que a capacidade resistente das unidades alveolares em apoios flexíveis pode ser melhorada pelo preenchimento dos alvéolos com o concreto moldado in loco, ou com a execução de um capa de concreto sobre as unidades alveolares. A capa de concreto moldada no local fornece resistência às ações e acabamento liso e uniforme. Usualmente, a capa de concreto moldada no local tem de 40 a 100mm de espessura, faixas de resistência de 25 a 40 MPa e uma pequena quantidade de armadura para controlar a retração. Ao usar lajes alveolares com capa de concreto moldada *in loco* não são utilizados dispositivos mecânicos para promover o comportamento conjunto entre o elemento pré-fabricado e a capa. Nesse caso, a resistência ao cisalhamento longitudinal da interface depende da aderência entre o concreto pré-fabricado e o moldado no local. O comportamento conjunto entre esses componentes da laje é desejado pois leva ao aumento da resistência e da rigidez sob cargas verticais, além de resistir e transmitir forças resultantes da ação da laje como diafragma sob forças laterais (BARAN, 2015; IBRAHIM et al., 2016).

Devido à presença dos alvéolos e à baixa resistência à tração do concreto, as lajes alveolares pré-fabricadas são naturalmente mais suscetíveis aos colapsos por cisalhamento. Este fator é ainda mais crítico em lajes com alvéolos não circulares e alturas superiores a 300mm (NGUYEN; TAN; KANDA, 2019). De forma geral, podem ser destacados os seguintes mecanismos de ruptura nas lajes alveolares pré-fabricadas de concreto: perda da ancoragem por escorregamento da armadura, cisalhamento com tensão no ponto crítico da nervura superior à resistência do concreto à tração (**Figura 2.22**), cisalhamento em região fissurada, cisalhamento combinado com torção, flexão (com grande possibilidade, próximo à ruptura, do escorregamento da armadura ativa junto ao apoio), interação dos mecanismos de flexão e cisalhamento que pode ocorrer em peças com vãos pequenos e/ou carregamentos elevados e escorregamento da armadura ativa (CATOIA, 2011).

Figura 2.22 – Combinação de fissuras de cisalhamento com efeito da flexão e fendilhamento por falha de ancoragem

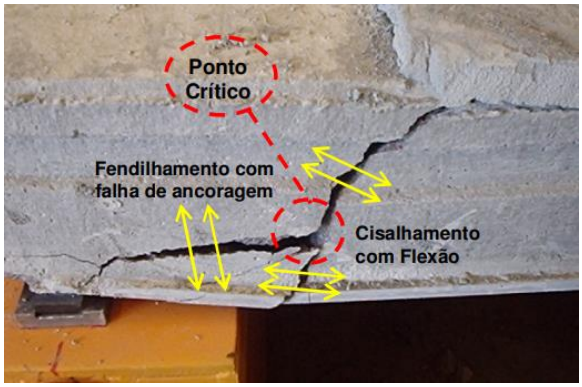

Fonte: Catoia (2011)

Lam (1998), pioneiro no estudo de vigas mistas formadas por lajes alveolares pré-fabricadas, investigou a interação entre o perfil de aço e laje pré-fabricada, a capacidade resistente à flexão e a rigidez das lajes (**Figura 2.23)**, além da capacidade resistente ao esforço cortante horizontal. Nesse estudo, dois modos de falha foram observados: falha repentina devido à ruptura dos conectores de cisalhamento associada à alta porcentagem de armadura transversal e a fissuração do concreto devido ao escoamento da armadura transversal, que resulta em perda de rigidez e de capacidade resistente.

Figura 2.23 – Viga mista formada por laje alveolar pré-fabricada

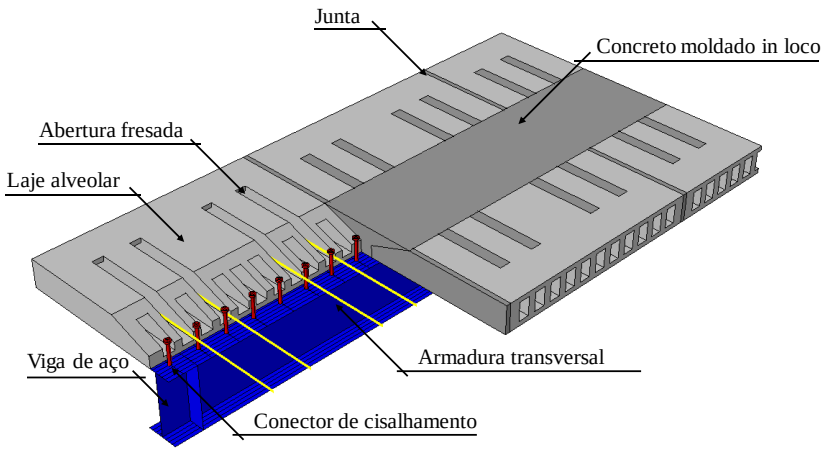

Fonte: adaptado de Lam, Elliott e Nethercot (2000a)

Posteriormente a esse pioneirismo, diversas foram as publicações envolvendo o autor (ELLOBODY; LAM, 2002; LAM, 2007a, 2007b; LAM; ELLIOTT; NETHERCOT, 2000a, 2000b). Em Lam, Elliott e Nethercot (2000a) foram apresentados resultados de ensaios de

flexão em quatro pontos de vigas mistas com lajes alveolares pré-fabricadas. Os modelos ensaiados tinham, vão de 6m, conectores tipo pino com cabeça com 19mm de diâmetro e lajes alveolares de 150mm de altura, sem capa moldada *in loco*. Os autores verificaram que a viga mista apresentou capacidade resistente três vezes maior que da viga de aço, isolada; foi observada falha dúctil e que pode ser controlada pelo uso adequado de armadura transversal e de concreto moldado in loco.

Lam, Elliott e Nethercot (2000b) complementaram o estudo anterior utilizando modelos numéricos e análises paramétricas para avaliar o comportamento à flexão. Um dos principais objetivos dos autores foi determinar como a capacidade resistente da viga mista com laje alveolar pré-fabricada variava em função de parâmetros geométricos. Os autores concluíram que o aumento na armadura transversal aumenta significativamente a capacidade resistente a flexão mas, reduz a ductilidade levando a ruptura frágil devido ao esmagamento da laje de concreto; aumentar a espessura da laje leva a aumento do momento resistente embora possa ocorrer falha na laje devido à tração e; e quando a razão entre a altura da viga de aço e a altura da laje de concreto é superior a 3, as vigas mistas não são eficazes, podendo ocorrer falha por esmagamento do concreto.

Ellobody e Lam (2002) investigaram parâmetros como a altura da laje, altura do perfil e taxa de armadura transversal por meio de modelagens numéricas que foram fundamentados em ensaios de cisalhamento direto. Quanto aos resultados obtidos, a capacidade resistente do conector de cisalhamento aumentou com o aumento da garganta com armadura transversal inferior a 16mm. Este aumento foi observado para larguras de garganta de até 80mm. Para larguras de garganta maiores ou iguais a 80mm, não foi observado efeito sobre a capacidade resistente ao cisalhamento. Além disso, ambos os aumentos, quer seja no diâmetro das barras ou na largura entre as lajes alveolares não tiveram efeito significativo na capacidade resistente ao cisalhamento do pino, mas afetaram a resposta Força *vs*. deslizamento. A resistência do concreto moldado in loco tem um efeito considerável na capacidade do conector de cisalhamento (ELLOBODY; LAM, 2002).

Em 2003, o *Steel Construction Institute* (SCI) publicou um manual contendo critérios de projeto para vigas mistas com lajes pré-fabricadas de concreto (HICKS; LAWSON, 2003). Posteriormente, Gouchman (2014) atualizou tal publicação. O documento atualizado reúne recomendações de dimensões mínimas, arranjo dos conectores tipo pino com cabeça, armadura

transversal e recomendações para estados limites últimos e de serviço na fase construtiva para os casos de interação total e parcial.

Posteriormente, como o projeto de vigas mistas com lajes alveolares pré-fabricadas estava fora das disposições do EN 1994-1-1 (2004), Lam (2007b) apresentou alguns fatores específicos das vigas mistas com lajes pré-fabricadas. Um dos principais pontos abordados estava relacionado com a resistência dos conectores de cisalhamento e fundamentado em ensaios anteriores (LAM, 2007a). Além disso, recomendações a respeito da largura efetiva das lajes alveolares pré-fabricadas, bem como a capacidade resistente à flexão de vigas mistas foram explanadas, com base no EN 1994-1-1 (2004).

Baran (2015) investigou o comportamento à flexão de lajes alveolares pré-fabricadas com capa de concreto moldada no local. Os resultados mostraram que a presença da capa de concreto resultou em melhorias no momento de fissuração e na rigidez inicial das lajes alveolares. Nesse mesmo cenário, em Ibrahim et al. (2016) foi apresentado um estudo experimental da capacidade resistente cisalhamento-flexão de lajes alveolares pré-fabricadas com capa de concreto. Os resultados mostraram que a condição da superfície da laje alveolar e a junta longitudinal são fatores que afetam a rigidez e a capacidade resistente à flexão e ao cisalhamento desses elementos estruturais.

No Brasil, Batista e Landesmann (2016) ensaiaram três vigas mistas com lajes alveolares e capa de concreto submetidas a flexão em quatro pontos (**Figura 2.24**).

Figura 2.24 – Ensaios de Batista e Landesmann (2016)

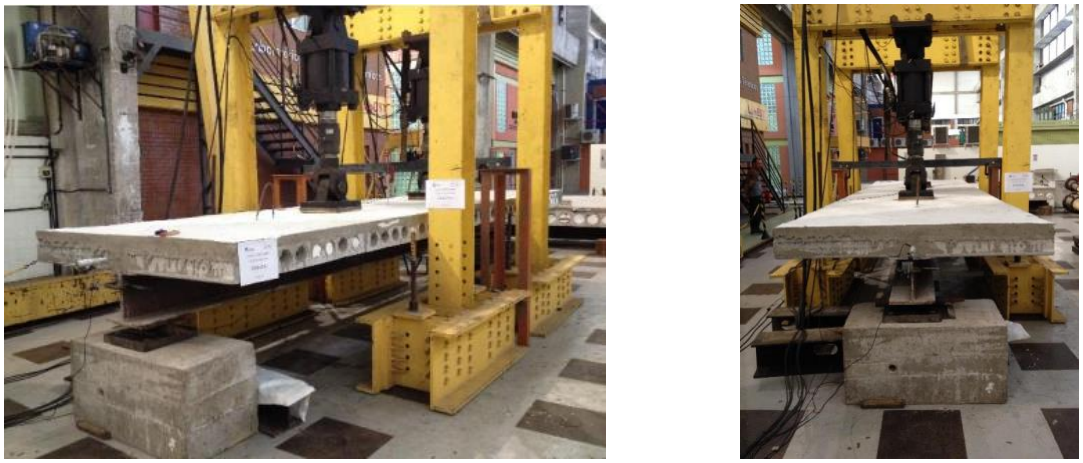

(a) (b)

Fonte: adaptado de Batista e Landesmann (2016)

Os autores investigaram os efeitos da altura da laje alveolar (150mm e 265mm), e também, os efeitos da armadura longitudinal na região da garganta. Os três ensaios apresentaram modos de colapso semelhantes, com o desenvolvimento de trincas iniciadas na face inferior dos painéis de laje e na região central entre os pontos de aplicação de carga.

Do panorama exposto até aqui, verifica-se que os estudos sobre vigas mistas com lajes pré-fabricadas são bastante recentes e se concentram na Europa e no Oriente. É possível observar que poucos pesquisadores têm se dedicado a esse tema e, quando lançamos o olhar para os estudos brasileiros, esses são ainda mais escassos, quase inexistentes.

2.6 SÍNTESE E CONCLUSÕES

Os pontos mais importantes apresentados nesse capítulo são:

- As vigas mistas com aberturas se apresentam como uma solução interessante devido à economia de materiais e à possibilidade de facilitar a passagem de tubulações;
- Os principais modos de falha apresentados pelas vigas mistas com aberturas são a instabilidade no montante da alma por cisalhamento e a formação do mecanismo Vierendeel no perfil de aço;
- A laje de concreto contribui efetivamente para a capacidade resistente ao cisalhamento da viga mista com perfil celular;
- A falha da laje de concreto ocorre após o perfil de aço ter atingido a resistência ao escoamento;
- O dimensionamento dos conectores de cisalhamento pode ser de grau de interação parcial ou total, fatores que influenciam na ductilidade da estrutura com um todo;
- Os estudos envolvendo aberturas em almas de vigas mistas se dividem em duas situações: vigas com uma única abertura e vigas com aberturas sequenciais;
- No cenário nacional, os estudos que contemplaram as vigas mistas com abertura única e sequenciais (vigas alveolares mistas) se restringiram à modelagem numérica;
- Não há estudo que descreva o comportamento estrutural de vigas celulares mistas formadas por perfis simétricos e lajes alveolares pré-fabricadas de concreto;
- As vigas mistas formadas por lajes alveolares pré-fabricadas de concreto são uma alternativa para substituir o sistema de vigas mistas formadas por lajes com fôrmas de aço incorporadas;
- Os modos de falhas das vigas mistas formadas por lajes alveolares pré-fabricadas são: a falha repentina devido à ruptura dos conectores de cisalhamento, associada à alta porcentagem de armadura transversal e à fissuração do concreto devido ao escoamento da armadura transversal que resulta em perda de rigidez e de capacidade resistente;
- Os estudos que envolvem as lajes alveolares pré-fabricadas em vigas mistas são relativamente recentes e deram ênfase aos conectores de cisalhamento;
- No Brasil se destaca o estudo de Araújo et al. (2016), com resultados de ensaios de cisalhamento direto de conectores de cisalhamento tipo pino com cabeça em vigas mistas com lajes de concreto alveolares pré-fabricadas.

PARTE II:

ESTUDOS TEÓRICOS

E

NUMÉRICOS PRÉVIOS

3.

VIGAS CELULARES MISTAS COM LAJES MISTAS

Na literatura são encontrados alguns modelos analíticos para estimar a capacidade resistente à instabilidade no montante de alma de vigas celulares (GRILO et al., 2018; LAWSON; HICKS, 2011; LAWSON et al., 2006; PANEDPOJAMAN; THEPCHATRI; LIMKATANYU, 2014; WARD, 1990). O primeiro método foi desenvolvido por Ward (1990). O procedimento apresentado considera apenas vigas celulares de aço com a seção transversal duplamente simétrica. O método é utilizado no *AISC Steel Design Guide 31* (SAMEER S. FARES; COULSON; DAVID W. DINEHART, 2016), que recomenda, para seções assimétricas, a verificação da situação mais crítica entre os tês superior e inferior. O modelo é fundamentado em uma série de ensaios realizados no *Steel Construction Institute* do Reino Unido e em estudos paramétricos de simulações numéricas. Tais estudos permitiram a investigação de análises de regressão para a aplicação do modelo analítico.

O segundo modelo analítico é encontrado no *Steel Construction Institute* SCI P355 (LAWSON; HICKS, 2011; LAWSON et al., 2006). Tal modelo leva em consideração a teoria de barras comprimidas, considerando um comprimento efetivo do montante de alma que está submetido à compressão. O método não menciona a contribuição da laje de concreto na capacidade resistente à instabilidade no montante de alma. Em Abambres et al. (2018) foi desenvolvida uma rede neural artificial para estimar a carga crítica em vigas celulares de aço. O estudo dos autores mostrou que a instabilidade no montante de alma governou no comportamento último para montantes de alma esbeltos, e as recomendações do SCI P355 subestimou a capacidade resistente à instabilidade no montante de alma, quando comparado com os resultados numéricos.

Em Panedpojaman et al. (2014) foi apresentado uma adaptação no comprimento efetivo do montante de alma proposto no SCI P355 (LAWSON; HICKS, 2011; LAWSON et al., 2006). O procedimento foi desenvolvido para seções com dupla simetria, via estudo paramétrico e análises não linear físicas e geométricas. No entanto, o modelo pode ser aplicado a seções assimétricas desde que seja identificada a seção mais crítica entre as seções tês superior e inferior.

Posteriormente, Grilo et al. (2018) desenvolveu um procedimento, que é fundamentado em um modelo numérico de montante de alma, considerando apenas as seções duplamente simétricas. Tal recomendação é sustentada em resultados paramétricos e calibrada por curvas de regressão não linear de resistência.

Iniciando a apresentação das análises prévias, o Capítulo 3 tem como objetivo investigar o comportamento de vigas celulares mistas levando em conta a instabilidade no montante de alma. Para isto, são realizadas análises elásticas e inelásticas. O modelo numérico foi calibrado por meio de ensaios consolidados, que estão disponíveis na literatura, considerando a imperfeição geométrica inicial. Elementos finitos sólidos foram utilizados na modelagem da laje e dos conectores de cisalhamento, e elementos de casca para a viga celular de aço. Em todas as análises foram consideradas vigas biapoiadas sujeitas à aplicação de duas forças espaçadas simetricamente em relação aos apoios. Seções assimétricas e simétricas foram investigadas. Além da variação na simetria, foi avaliada a influência dos seguintes parâmetros: relação entre a largura do montante de alma e o diâmetro da abertura (p/D_o), relação entre o diâmetro da abertura e a altura da seção original (D_o/d). Os resultados foram comparados com os modelos analíticos, que são apresentados no item 3.1.

O presente Capítulo é fundamentado nos resultados publicados em "***Sensitivity analysis of composite cellular beams to constitutive material models and concrete fracture***" (FERREIRA; MARTINS; DE NARDIN, 2021b), "***Assessment of web post buckling resistance in steel-concrete composite cellular beams***" (FERREIRA; MARTINS; DE NARDIN, 2021a) e "***Buckling and post-buckling analyses of composite cellular beams***" (FERREIRA et al., 2021a). Portanto, o Capítulo foi redigido de maneira resumida, com o objetivo de apresentar ao leitor a metodologia de análise numérica desenvolvida e validada. O Capítulo foi organizado em cinco seções. Primeiramente, os modelos de resistência de cálculo analítico, considerando a instabilidade no montante de alma são abordados. Em seguida, é mostrada a metodologia que foi utilizada para os estudos de validação. Posteriormente a etapa de validação numérica, as considerações gerais do estudo paramétrico são descritas. Finalmente, o Capítulo 3 se encerra com a apresentação dos principais resultados e a síntese das conclusões, que foram obtidas nos estudos publicados (FERREIRA et al., 2021a; FERREIRA; MARTINS; DE NARDIN, 2021a, 2021b). Maiores informações e detalhes podem ser encontradas nos artigos publicados que se encontram no Apêndice do presente trabalho.

Os seguintes símbolos são usados neste Capítulo:

b_c	largura da laje de concreto;	t_f	espessura da mesa;
b_f	largura da mesa;	t_w	espessura da alma;
b_p	largura da linha de plastificação;	T_i	força axial no tê inferior;
b_w	largura do montante de alma;	V_b	força cortante no tê inferior;
b_{we}	largura do montante de extremidade;	V_h	força cortante horizontal;
C_i	força axial no concreto;	$V_{h,eff}$	força cortante horizontal efetiva;
C_1	constante adimensional na Eq. (3.3);	$V_{h,p}$	força cortante horizontal plástica resistente;
C_2	constante adimensional na Eq. (3.3);	$V_{Gh,Rk}$	força cortante horizontal resistente conforme o modelo de Grilo;
C_3	constante adimensional na Eq. (3.3);		
D_o	diâmetro de abertura;	$V_{Wv,Rk}$	resistência à força cortante vertical conforme modelo SCI P355;
d	altura da seção original de aço;		
$d_{ef,comp}$	altura efetiva da viga celular mista;	V_t	força cortante no tê superior;
d_g	altura da viga celular;	$V_{Wh,Rk}$	força cortante horizontal resistente conforme o modelo de Ward;
h_F	altura da fôrma de aço incorporada;		
l_{eff}	comprimento efetivo do montante de alma;	$y_{o,inf}$	distância do centro geométrico do tê inferior até a borda inferior;
$l_{eff,P}$	comprimento efetivo do montante de alma de acordo com o modelo de Panedpojaman et al.;		
M_i	momento fletor na abertura i;	y_p	altura da linha de plastificação;
M_{vh}	momento fletor gerado pela força cortante horizontal;	β_G	constante adimensional na Eq. (3.27);
		$\bar{\lambda}$	fator de esbeltez reduzida;
$M_{W,e}$	momento fletor elástico no montante de alma	λ_w	esbeltez da alma;
$M_{W,Rk}$	momento fletor resistente conforme o modelo de Ward;	σ_{max}	a tensão de compressão máxima, em relação à tensão de cisalhamento horizontal a meia altura do montante de alma;
p	passo;	χ	fator de redução.
t_c	espessura de concreto acima da fôrma de aço;		

3.1 MODELOS ANALÍTICOS PARA A DETERMINAÇÃO DA RESISTÊNCIA À INSTABILIDADE NO MONTANTE DE ALMA

Esta seção apresenta procedimentos de cálculo, considerando a instabilidade no montante de alma.

3.1.1 Ward (1990)

Neste método, três parâmetros são considerados C_1, C_2 e C_3 (**Eqs. 3.5-3.7**), que são funções das propriedades geométricas do montante de alma. O método tem algumas restrições geométricas. Como exemplo, o procedimento é aplicável para os intervalos $1{,}08 \leq p/D_o \leq 1{,}50$ e $1{,}25 \leq d_g/D_o \leq 1{,}75$. A força cortante horizontal entre as aberturas i e i+1 (**Figura 3.1**) é calculada utilizando a **Eq. (3.1)**:

Figura 3.1 – Modelo de Ward

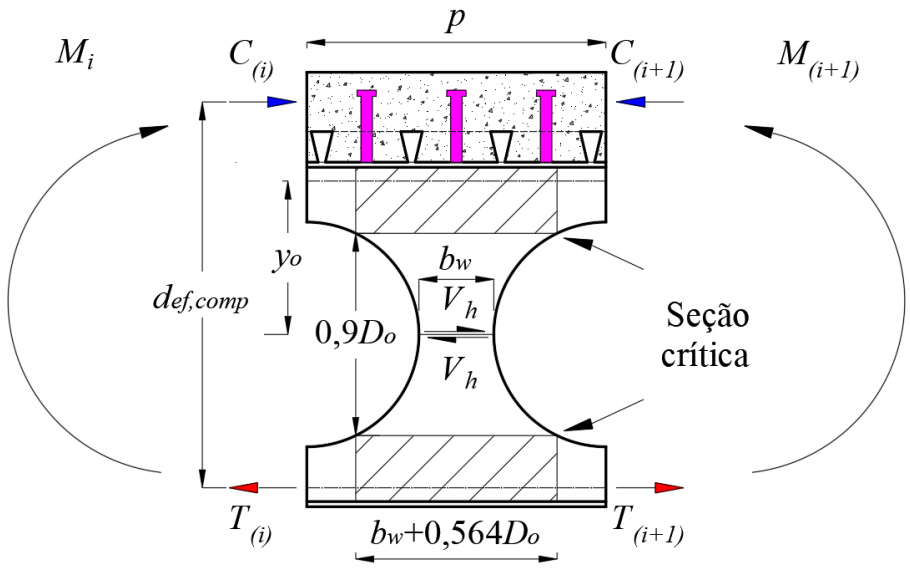

Fonte: adaptado de Sameer S. Fares et al. (2016)

$$V_h = \left| \frac{M_{(i+1)} - M_{(i)}}{d_{ef,comp}} \right| \qquad \text{Eq. (3.1)}$$

O momento fletor, que corresponde ao escoamento na seção crítica (**Eq. 3.2**), gerado pela força cortante horizontal é igual a:

$$M_{vh} = 0.9\left(\frac{D_o}{2}\right)V_h \qquad \text{Eq. (3.2)}$$

Então, a resistência à instabilidade no montante de alma é calculada (**Eqs 3.3-3.7**):

$$M_{W,\mathrm{Rk}} = M_{W,e}\left[C1\left(\frac{p}{D_o}\right) - C2\left(\frac{p}{D_o}\right)^2 - C3\right] \qquad \text{Eq. (3.3)}$$

$$M_{W,e} = \frac{t_w\left(p - D_o + 0.564D_o\right)^2}{6} f_y \qquad \text{Eq. (3.4)}$$

$$C1 = 5.097 + 0.1464\left(\frac{D_o}{t_w}\right) - 0.00174\left(\frac{D_o}{t_w}\right)^2 \qquad \text{Eq. (3.5)}$$

$$C2 = 1.441 + 0.0625\left(\frac{D_o}{t_w}\right) - 0.000683\left(\frac{D_o}{t_w}\right)^2 \qquad \text{Eq. (3.6)}$$

$$C3 = 3.645 + 0.0853\left(\frac{D_o}{t_w}\right) - 0.00108\left(\frac{D_o}{t_w}\right)^2 \qquad \text{Eq. (3.7)}$$

Dessa forma, a resistência à força cortante horizontal é calculada (**Eq. 3.8**):

$$V_{Wh,\mathrm{Rk}} = \frac{M_{W,e}}{0.45D_o}\left[C1\left(\frac{p}{D_o}\right) - C2\left(\frac{p}{D_o}\right)^2 - C3\right] \qquad \text{Eq. (3.8)}$$

3.1.2 Lawson et al. (2011) (SCI P355)

De acordo com este método, a ação da força cortante horizontal na metade da altura da alma causa tensões de tração e de compressão devido à flexão entre os têes superior e inferior. Essas tensões variam em torno da abertura (**Figura 3.2**). O comprimento efetivo l_{eff} leva em consideração a variação das tensões ao redor da abertura, conforme a **Eq. (3.9)**.

$$l_{eff} = 0,5\sqrt{b_w^2 + D_o^2} \le 0,7D_o \qquad \text{Eq. (3.9)}$$

Uma vez determinado o comprimento efetivo, é aplicada a teoria das barras submetidas à compressão, fundamentada no EN 1993-1-1:2005, considerando a esbeltez da alma e utilizando a curva *c* de resistência (**Eqs. 3.10-3.15**):

$$\sigma_{Rk} = \chi f_y \qquad \text{Eq. (3.10)}$$

$$\chi = \frac{1}{\phi + \sqrt{\phi^2 - \bar{\lambda}^2}} \leq 1{,}0 \qquad \text{Eq. (3.11)}$$

$$\phi = 0{,}5\left[1 + 0{,}49\left(\bar{\lambda} - 0{,}2\right) + \bar{\lambda}^2\right] \qquad \text{Eq. (3.12)}$$

$$\bar{\lambda} = \sqrt{\frac{f_y}{f_{cr,w}}} \qquad \text{Eq. (3.13)}$$

$$f_{cr,w} = \frac{\pi^2 E}{\lambda_w^2} \qquad \text{Eq. (3.14)}$$

$$\lambda_w = \frac{l_{eff}\sqrt{12}}{t_w} \qquad \text{Eq. (3.15)}$$

Figura 3.2 – Modelo de treliça

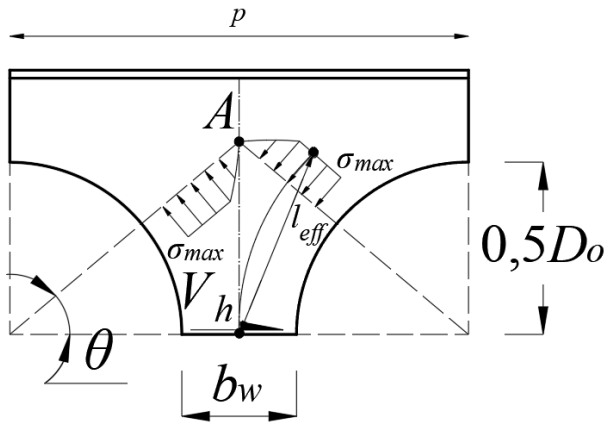

Fonte: adaptado de Lawson et al. (2006)

Assim, a resistência à cortante pode ser calculada (**Eq. 3.16**):

$$V_{Lv,Rk} = \sigma_{Rk} t_w b_w \qquad \text{Eq. (3.16)}$$

Observa-se até aqui que o modelo apresentado da SCI P355 (LAWSON; HICKS, 2011) é fundamentado na teoria de barras submetidas à compressão, enquanto que o modelo de Ward (1990) foi desenvolvido por meio de análises de regressão não linear.

3.1.3 Panedpojaman et al. (2014)

Neste modelo, o comprimento efetivo do montante de alma é multiplicado por um fator *k* que considera a restrição parcial do montante de alma em relação ao fenômeno de

instabilidade (**Figura 3.3**). De acordo com o estudo, o coeficiente apresentado nas **Eqs. (17-18)** considera o efeito da variação da altura dos tês com os valores das relações D_o/d e p/D_o.

$$l_{eff,P} = k\left(0,5\sqrt{p^2 - D_o^2}\right) \quad \text{Eq. (3.17)}$$

$$k = 0,9\left(\frac{p}{D_o}\right)\left(\frac{D_o}{d}\right)^2 \leq \min\left(1,15\frac{D_o}{d};1,15\right) \quad \text{Eq. (3.18)}$$

Figura 3.3 – Modelo de Panedpojaman et al. (2014)

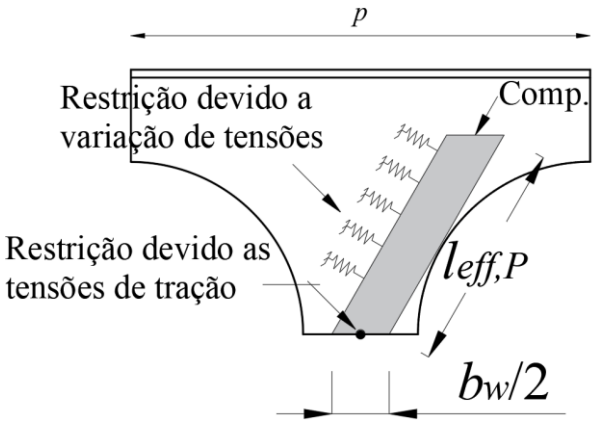

Fonte: adaptado de Panedpojaman et al. (2014)

3.1.4 Grilo et al. (2018)

A formulação proposta (**Eqs. 3.19-3.27**) é baseada na determinação de uma força cortante de plastificação e um fator de redução (GRILO, 2018). A força cortante de plastificação e o fator de redução são estimados por meio das modelagens numéricas e análises de regressão.

$$V_{Gh,Rk} = V_{h,p}\chi \quad \text{Eq. (3.19)}$$

$$V_{h,p} = \beta_G f_y \frac{t_w b_p^{\,2}}{\sqrt{3b_p^{\,2} + 16y_p^{\,2}}} \quad \text{Eq. (3.20)}$$

$$\beta_G = 1,198 - 0,42\left(\frac{D_o}{d_g}\right) - \left(\frac{p}{5D_o}\right) \quad para\ (p/Do) < 1,2 \quad \text{Eq. (3.21)}$$

$$\beta_G = 1,838 - 0,42\left(\frac{D_o}{d_g}\right) - \left(\frac{p}{3D_o}\right) \quad para\ (p/Do) \geq 1,2 \quad \text{Eq. (3.22)}$$

$$y_p = \frac{D_o}{2}\left[0,445\left(\frac{p}{D_o}\right)^3 - 2,578\left(\frac{p}{D_o}\right)^2 + 4,770\left(\frac{p}{D_o}\right) - 2,475\right] \quad \text{Eq. (3.23)}$$

$$b_p = b_w\sqrt{1-\frac{4{y_p}^2}{{D_o}^2}} \quad \text{Eq. (3.24)}$$

$$\lambda_{ma,0} = \sqrt{\frac{3\left(p^2 - D_o^2\right) f_y}{\pi^2 t_w^2 E}} \quad \text{Eq. (3.25)}$$

Para $\lambda_{ma,0} \geq 1,0$:

$$\chi = \frac{m}{{\lambda_{ma,0}}^n} \leq 1,0 \quad \text{Eq. (3.26)}$$

Para $\lambda_{ma,0} < 1,0$:

$$\chi = op^{\left(\lambda_{ma,0}{}^q\right)} \leq 1,0 \quad \text{Eq. (3.27)}$$

Os coeficientes m, n, o, p e q (**Eqs. 3.26-3.27**) são apresentados na **Tabela 3.1**.

Tabela 3.1: Valores de *m* e *n* para o modelo de Grilo et al. (2018)

D_o/d_q	p/D_o	*m*	*n*	*o*	*p*	*q*
0,5	1,1	0,759	1,35	1,15	0,660	3,5
	1,2	0,730	1,39	1,42	0,514	2,1
	1,3	0,780	1,40	1,16	0,672	3,5
	1,4	0,840	1,42	1,26	0,667	2,7
	1,5	0,916	1,40	1,09	0,840	5,0
0,6	1,1	0,798	1,42	1,14	0,700	3,5
	1,2	0,791	1,42	1,13	0,700	3,8
	1,3	0,836	1,40	1,10	0,760	4,5
	1,4	0,909	1,36	1,15	0,790	3,3
	1,5	0,970	1,31	1,09	0,890	4,5
0,7	1,1	0,849	1,47	1,08	0,786	4,5
	1,2	0,844	1,44	1,11	0,760	3,9
	1,3	0,903	1,39	1,15	0,785	4,0
	1,4	0,980	1,34	1,12	0,870	3,0
	1,5	1,130	1,33	-	-	-
0,8	1,1	0,888	1,46	1,09	0,815	4,0
	1,2	0,901	1,42	1,14	0,790	3,5
	1,3	1,020	1,42	-	-	-
	1,4	1,175	1,42	-	-	-
	1,5	1,285	1,36	-	-	-

Segundo os autores, algumas ramificações das curvas não foram determinadas, devido à falha ocorrida por um mecanismo diferente da instabilidade no montante de alma, como por exemplo algum mecanismo plástico.

Conforme apresentado, todos os procedimentos citados não consideram a contribuição da laje de concreto na resistência a instabilidade no montante de alma em vigas celulares mistas. Essa é a motivação para o desenvolvimento do estudo que é apresentado no presente Capítulo.

3.2 MODELAGEM NUMÉRICA: ESTUDO DE VALIDAÇÃO

Esta seção apresenta a metodologia utilizada na validação da modelagem numérica. Aqui cabe lembrar que o objetivo principal dessa etapa foi a validação do modelo numérico correspondente à viga celular mista. A validação do modelo numérico em etapas foi necessária dada a ausência de resultados experimentais de vigas celulares mistas com lajes pré-fabricadas.

3.2.1 Análises

Conforme citado anteriormente no subitem de metodologia, as modelagens são realizadas em dois passos: análise elástica (*buckling*) e análise inelástica (*post-buckling*). Maiores informações sobre essas análises podem ser encontradas nos artigos publicados (FERREIRA et al., 2021a; FERREIRA; MARTINS; DE NARDIN, 2021a, 2021b).

3.2.2 Ensaios

Nessa etapa foram utilizados quatro ensaios experimentais para a validação numérica (HECHLER; MÜLLER; SEDLACEK, 2006; MÜLLER et al., 2006; NADJAI, 2005; NADJAI et al., 2007), conforme **Figura 3.4**. Para a validação foram consideradas duas vigas celulares com seção duplamente simétrica e duas vigas celulares com seção assimétrica (**Tabela 3.2**). Maiores informações podem ser encontradas nos artigos publicados (FERREIRA et al., 2021a; FERREIRA; MARTINS; DE NARDIN, 2021a, 2021b).

Figura 3.4 – Modelos físicos

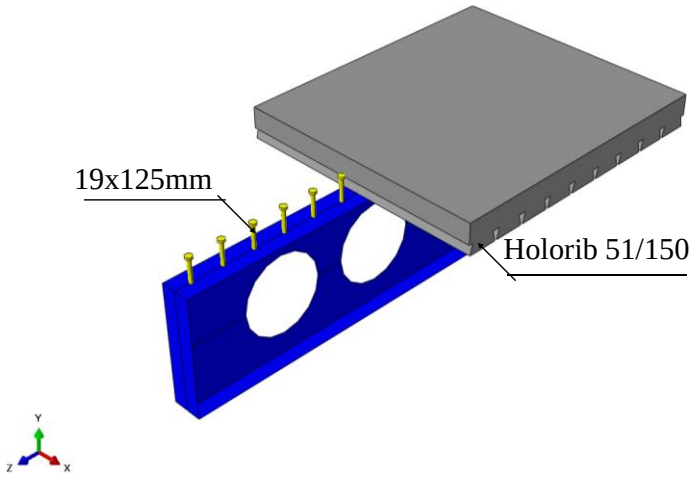

(a) CCB1

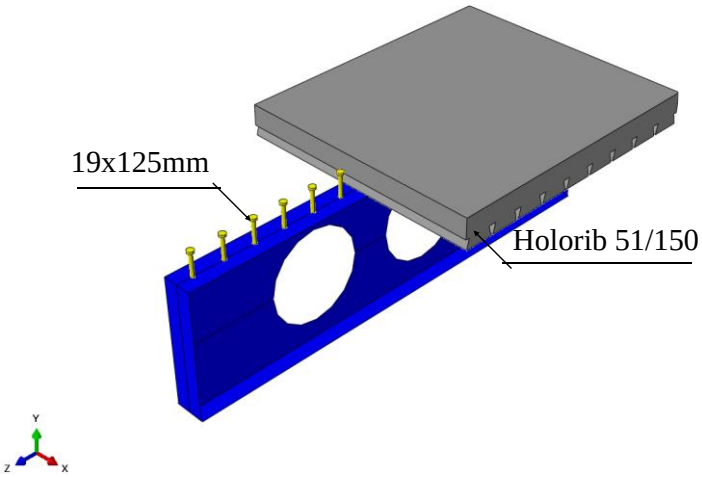

(b) CCB2

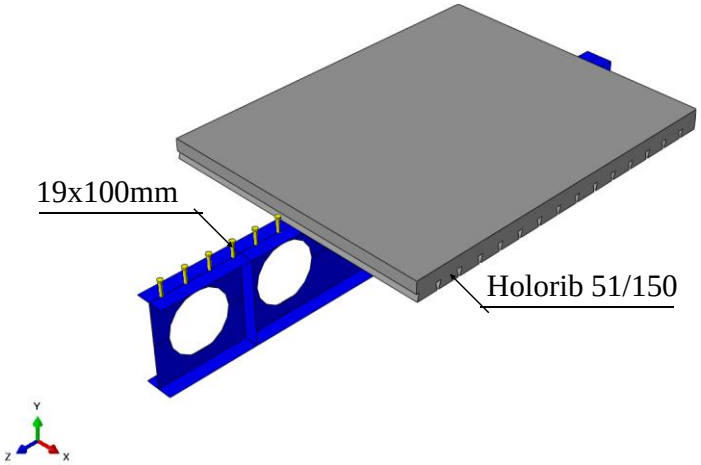

(c) CCB3

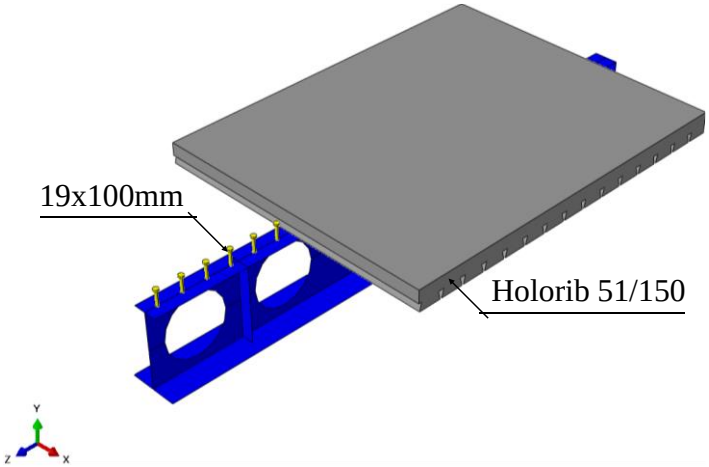

(d) CCB4

Tabela 3.2 – Modelos (em mm, MPa e GPa)

Modelo	d_g	D_o	p	Tê superior				
				b_f	t_f	t_w	f_y (mesa/alma)	f_u (mesa/alma)
CCB1	575	375	500	141,8	8,6	6,4	312	438,5
CCB2	630	450	630	141,8	8,6	6,4	312	438,5
CCB3	555	380	570	180	13,5	8,6	451/489	541/587
CCB4	485	380	570	150	10,7	7,1	407/467	524/588
Modelo	d_g	D_o	p	Tê inferior				
				b_f	t_f	t_w	f_y (mesa/alma)	f_u (mesa/alma)
CCB1	575	375	500	141,8	8,6	6,4	312	438,5
CCB2	630	450	630	152,4	10,9	7,6	312	438,5
CCB3	555	380	570	180	13,5	8,6	451/489	541/587
CCB4	485	380	570	300	21,5	12	453/488	519/582

Modelo	E	Laje		L_b	L_p
		f_c	b		
CCB1	200	28,6	1200	4500	1750
CCB2	200	28,6	1200	4500	2250
CCB3	195	33,6	1800	6840[a]	1140/2850
CCB4	195	24,0	1800	6840[a]	1140/2850

[a]Laje cortada em 285 mm no final da viga celular

3.2.3 Materiais

Como escrito anteriormente, esse Capítulo foi fundamentado em três artigos. No artigo "***Sensitivity analysis of composite cellular beams to constitutive material models and concrete fracture***" (FERREIRA; MARTINS; DE NARDIN, 2021b) foi avaliada a sensibilidade do modelo numérico de vigas celulares mistas frente às variações de parâmetros dos modelos constitutivos dos materiais aço e concreto. Variações nos parâmetros que constituem o modelo de Dano Plástico (CDP), o ângulo de dilatação e a viscosidade, foram realizadas no estudo. Alguns problemas de convergência nas respostas numéricas foram identificados e discutidos. Nesse primeiro momento, dois modelos constitutivos do concreto foram investigados (CARREIRA; CHU, 1985, 1986; GUO, 2014), bem como a variação do ângulo de dilatação e viscosidade. Os modelos de Carreira e Chu (1985, 1986) e Guo (2014) são apresentados nas **Equações (3.28-3.30)** e **Equações (3.31-3.33)**, respectivamente. Ambos os modelos

apresentam os ramos ascendente e descendente dos diagramas tensão por deformação do concreto.

$$\frac{\sigma}{f_{cm}} = \frac{\beta_c \left(\varepsilon / \varepsilon_c\right)}{\beta_c - 1 + \left(\varepsilon / \varepsilon_c\right)^{\beta_c}} \qquad \text{Eq. (3.28)}$$

$$\frac{\sigma}{f_t} = \frac{\beta_c \left(\varepsilon / \varepsilon_t\right)}{\beta_c - 1 + \left(\varepsilon / \varepsilon_t\right)^{\beta_c}} \qquad \text{Eq. (3.29)}$$

$$\beta = \left(\frac{f_{cm}}{32,4}\right)^3 + 1,55 \ \ (MPa) \qquad \text{Eq. (3.30)}$$

$$\frac{\sigma}{f_{cm}} = \begin{cases} \alpha_a \left(\varepsilon / \varepsilon_c\right) + \left(3 - 2\alpha_a\right)\left(\varepsilon / \varepsilon_c\right)^2 + \left(\alpha_a - 2\right)\left(\varepsilon / \varepsilon_c\right)^3, \ \varepsilon / \varepsilon_c \le 1 \\ \dfrac{\varepsilon / \varepsilon_c}{\alpha_d \left[\left(\varepsilon / \varepsilon_c\right) - 1\right]^2 + \left(\varepsilon / \varepsilon_c\right)}, \ \varepsilon / \varepsilon_c > 1 \end{cases} \qquad \text{Eq. (3.31)}$$

$$\frac{\sigma}{f_t} = \begin{cases} 1.2\left(\varepsilon / \varepsilon_t\right) - 0.2\left(\varepsilon / \varepsilon_t\right)^6, \ \varepsilon / \varepsilon_t \le 1 \\ \dfrac{\varepsilon / \varepsilon_t}{\alpha_t \left[\left(\varepsilon / \varepsilon_t\right) - 1\right]^{1,7} + \varepsilon / \varepsilon_t}, \ \varepsilon / \varepsilon_t > 1 \end{cases} \qquad \text{Eq. (3.32)}$$

$$\alpha_t = 0,312\, f_t^{\,2} \qquad \text{Eq. (3.33)}$$

Para o aço (**Figura 3.5a-e**), além do modelo elasto-plástico perfeito, mais quatro modelos foram analisados (BYFIELD; DAVIES; DHANALAKSHMI, 2005; EARLS, 1999; EUROPEAN COMMITTEE FOR STANDARDIZATION, 2006; YUN; GARDNER, 2017). Os resultados das modelagens numéricas permitiram concluir que o modelo de Guo (2014) para o concreto e o modelo de Yun and Gardner (2017) resultaram nas melhores opções tanto para a convergência quanto na pós-flambagem. Além disso, comportamento à flexão não foi sensível ao estudo da variação dos ângulos de dilatação, ao contrário das estruturas em que a resistência última é governada pelo cisalhamento. O melhor comportamento pós-pico foi verificado pela relação carga-deslocamento para o ângulo de dilatação igual a 40º. Com a variação da viscosidade (ou do tempo de relaxamento), o comportamento da relação carga-deslocamento permaneceu inalterado, e foi verificado que quanto menor o valor da viscosidade, maior a área de dano do elemento finito e maior o custo computacional. Em relação aos conectores de pinos

com cabeça, foi utilizado o modelo bilinear (ARAÚJO et al., 2016), ou seja, a resistência ao escoamento e a tensão de ruptura foram de 460 MPa e 559 MPa, respectivamente. O alongamento na ruptura foi de 18,8%. Maiores informações podem ser obtidas no artigo publicado (FERREIRA; MARTINS; DE NARDIN, 2021b).

Figura 3.5 – Modelos constitutivos do aço

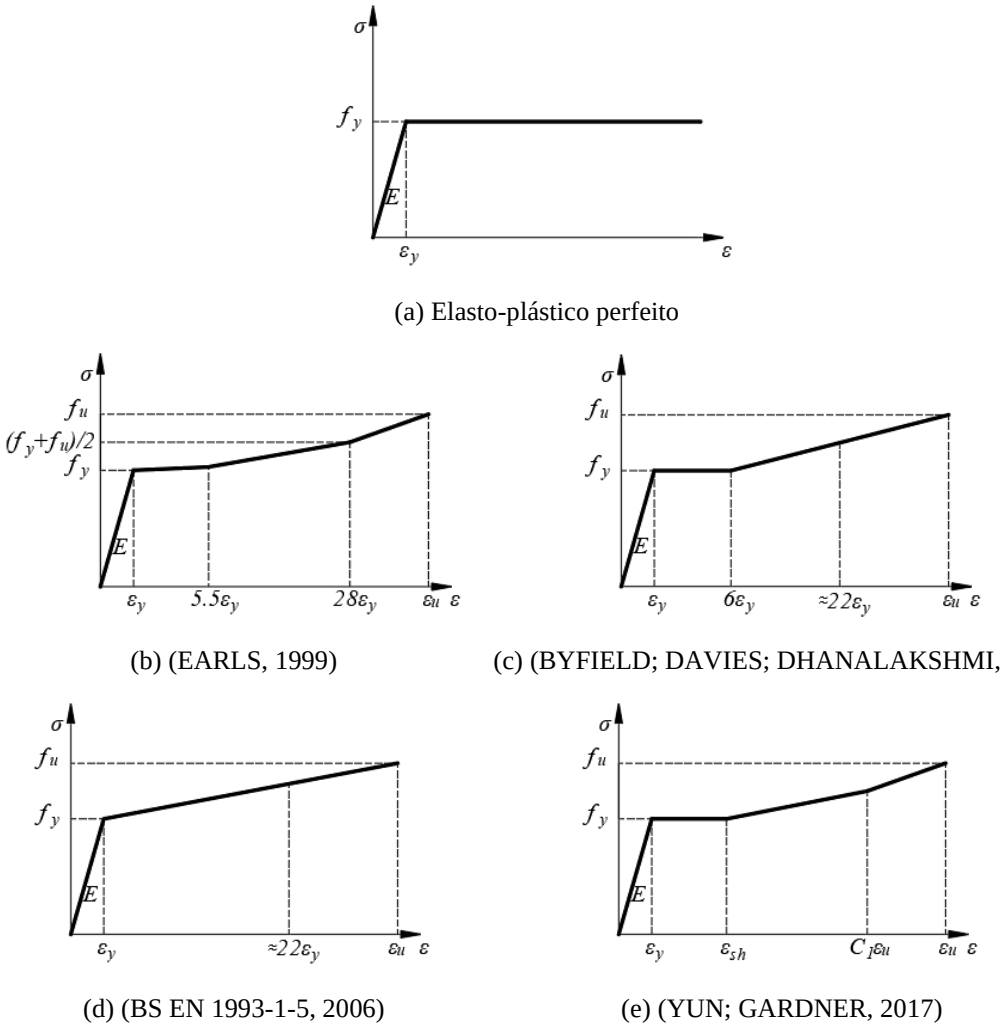

(a) Elasto-plástico perfeito

(b) (EARLS, 1999)

(c) (BYFIELD; DAVIES; DHANALAKSHMI, 2005)

(d) (BS EN 1993-1-5, 2006)

(e) (YUN; GARDNER, 2017)

Fonte: (FERREIRA; MARTINS; DE NARDIN, 2021b)

3.2.4 Superfícies de Contato

Dois tipos de interação foram utilizados nas modelagens (**Figura 3.6**). A primeira foi a *tie constraint*, que permitiu modelar a aderência perfeita entre o conector de cisalhamento tipo pino com cabeça e o perfil de aço. Na segunda, foi utilizado o comportamento tangencial/normal entre as seguintes superfícies de contato: laje-conector e laje-perfil de aço.

Tal modelagem considera o coeficiente de atrito de Coulomb. A utilização dessa técnica de modelagem da superfície de contato entre a laje o conector vem sendo amplamente utilizada (GUEZOULI; LACHAL, 2012; KATWAL et al., 2020; LIU et al., 2016; SJAARDA et al., 2017). Para maiores informações sobre todo o processo de modelagem, faz-se necessário consultar os artigos (FERREIRA et al., 2021a; FERREIRA; MARTINS; DE NARDIN, 2021a, 2021b)

Figura 3.6 – Superfícies de contato

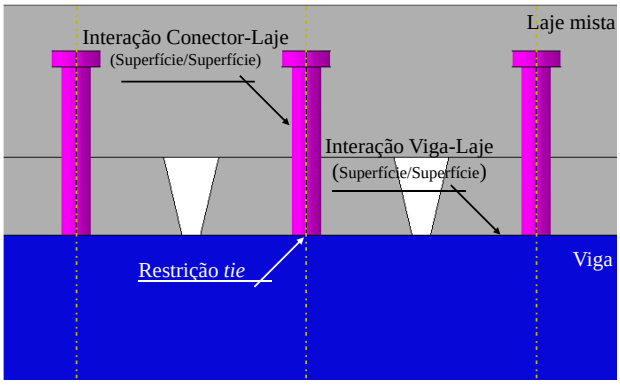

3.2.5 Condições de Contorno e Discretização

Em todas as análises as vigas celulares mistas foram consideradas biapoiadas e foi representada apenas metade da viga; foi considerada a simetria longitudinal (**Figura 3.7**). Na **Figura 3.8** é apresentada a discretização do conector tipo pino com cabeça e uma vista longitudinal da viga discretizada.

Figura 3.7 – Condições de contorno

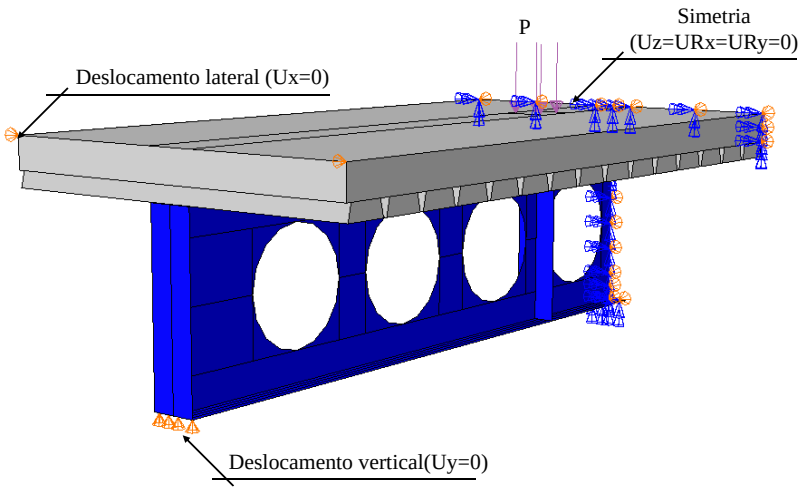

Figura 3.8 – Discretização

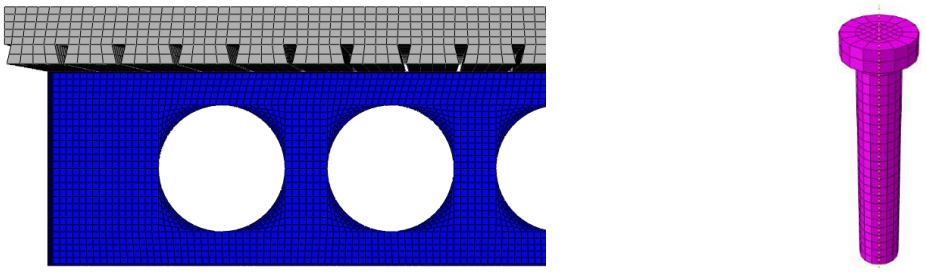

(a) Vigas celulares mistas (b) Conector

Conforme a **Figura 3.8**, foram utilizados elementos de casca e elementos sólidos. Os elementos de casca (S4R) foram implementados nas vigas celulares. O elemento S4R é um elemento quadrilateral com quatro nós e integração reduzida. Por outro lado, no conector de cisalhamento e na laje de concreto, foi implantado o elemento sólido C3D8R, que possui oito nós, integração reduzida e suporta análises plásticas.

3.2.6 Resultados de Validação

Os resultados de validação são apresentados por meio da trajetória de equilíbrio (**Figura 3.9**) e configuração deformada final (**Figura 3.10**).

Figura 3.9 – Resultados de validação

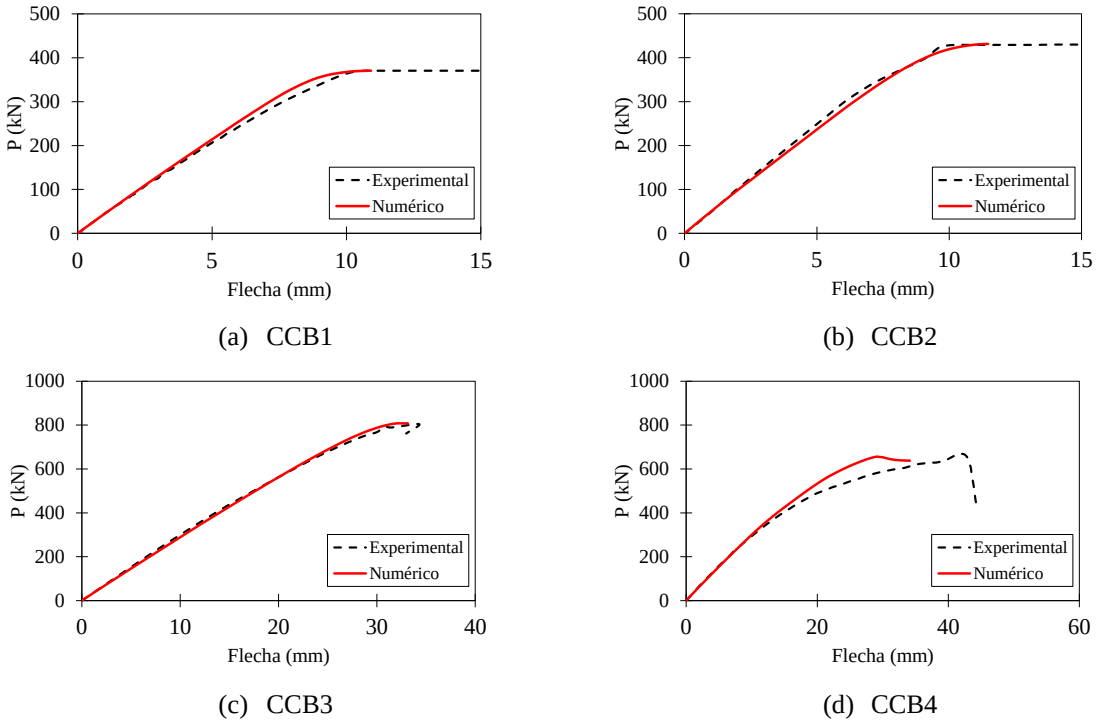

(a) CCB1 (b) CCB2

(c) CCB3 (d) CCB4

De acordo com Nadjai et al. (2007), ambos os testes CCB1 e CCB2 apresentaram a capacidade resistente definida por instabilidade no montante de alma. Além disso, foi verificado o desenvolvimento de tensões de tração acima das aberturas, indicando que a linha neutra plástica estava próxima ou na laje de concreto e, após a instabilidade no montante de alma, surgiram rótulas plásticas ao redor das aberturas. A deflexão máxima de ambos os testes imediatamente antes da falha foi de aproximadamente 10 mm. Considerando os modelos CCB3 e CCB4, os modos de falha foram semelhantes aos ensaios (HECHLER; MÜLLER; SEDLACEK, 2006; MÜLLER et al., 2006). Segundo os autores, a resistência ao escoamento foi atingida para baixos níveis de carregamento nas aberturas, e o comportamento final foi governado pela instabilidade no montante de alma.

Figura 3.10 – Configuração final dos modelos

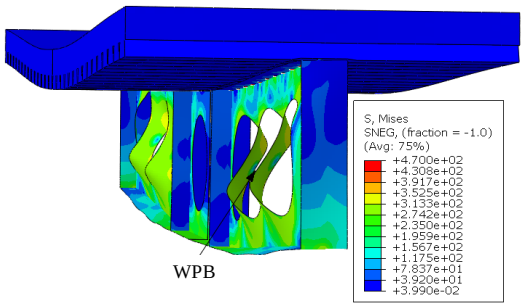

(a) CCB1

(b) CCB1 (NADJAI, 2005)

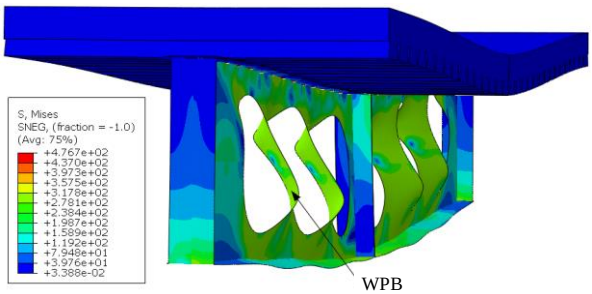

(c) CCB2

(d) CCB2 (NADJAI, 2005)

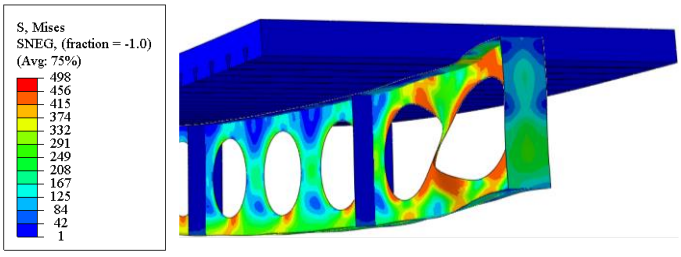

(e) CCB3

3.3 MODELAGEM NUMÉRICA: ESTUDO PARAMÉTRICO

Uma vez que o modelo numérico de viga celular mista com laje mista foi validado, a etapa seguinte foi o desenvolvimento de estudo paramétrico no qual foram avaliados os efeitos dos seguintes parâmetros geométricos:

1. O comprimento da viga celular mista é igual a 6m e a largura efetiva da laje é $L/4$;
2. As razões p/D_o e D_o/d variam em 1,2-1,5 e 0,8-1,2, respectivamente;
3. A do montante de extremidade (b_{we}) não deve ser menor do que a largura dos demais montantes de alma (b_w);
4. São consideradas seis seções transversais (**Tabela 3.3**)
5. A altura da laje é igual a 150mm, com geometria *Holorib HR* 51/150;
6. A dimensão do conector tipo pino com cabeça é 19x120mm;

Tabela 3.3: Seções analisadas

Modelo	d_g	Tê superior			Tê inferior		
		b_f	t_f	t_w	b_f	t_f	t_w
CCB1	575	141,8	8,6	6,4	141,8	8,6	6,4
CCB2	630	141,8	8,6	6,4	152,4	10,9	7,6
CCB3	555	180	13,5	8,6	180	13,5	8,6
CCB4	485	150	10,7	7,1	300	21,5	12
CCB5	580	180	13,5	8,6	180	13,5	8,6
CCB6	580	180	13,5	8,6	300	21,5	12

7. O aço ASTM A572 Grau 50 é adotado (f_y=345 MPa e f_u=450 MPa). O módulo elasticidade longitudinal é igual a 200 GPa;
8. A resistência do concreto é de 35 MPa para as seções CCB1-4 e de 30 MPa para as seções CCB5-6;
9. As vigas celulares mistas são biapoiadas e submetidas a dois pontos de cargas, espaçados simetricamente em 2m dos apoios. Os apoios bem como os pontos de aplicação de carga foram providos com enrijecedores.

A seguir, nos itens 3.4 e 3.5, são apresentadas os principais resultados e conclusões extraídas da análise paramétrica (**Figura 3.11**), respectivamente.

Figura 3.11 – Síntese do estudo paramétrico em vigas celulares mistas

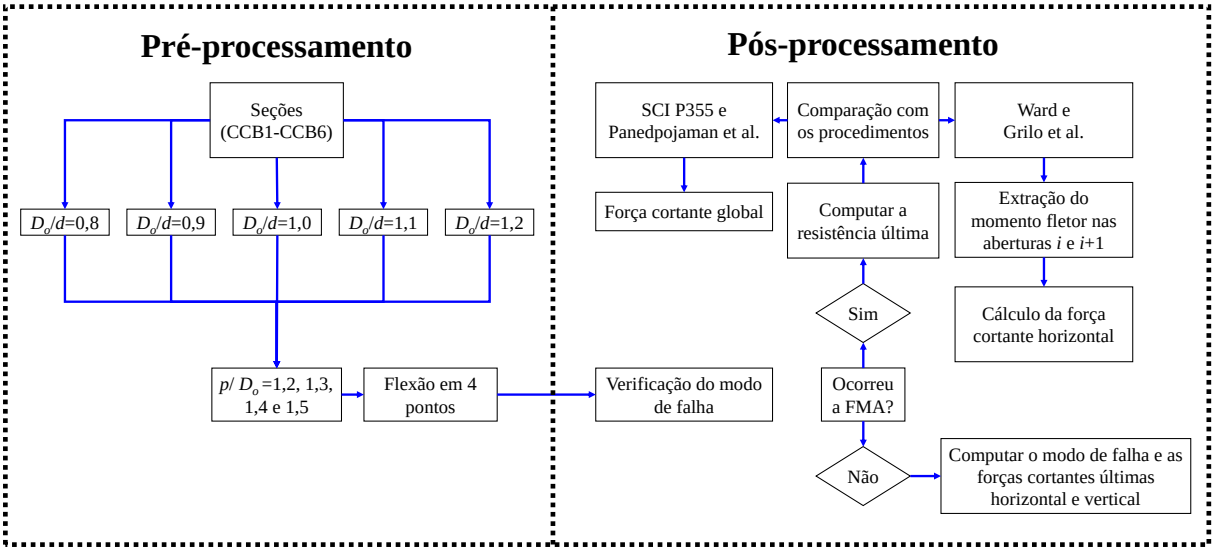

3.4 PRINCIPAIS RESULTADOS DO ESTUDO PARAMÉTRICO

Essa seção tem como objetivo apresentar alguns dos principais resultados do estudo paramétrico, considerando análises elásticas e inelásticas. Os resultados e discussões detalhadas podem ser encontrados nos artigos publicados (FERREIRA et al., 2021a; FERREIRA; MARTINS; DE NARDIN, 2021a) que se encontram no Apêndice do presente trabalho.

3.4.1 Análises Elásticas

Em geral, os modos de deformação apresentados pela seção CCB1 foram caracterizados pela FMA. A **Figura 3.12** ilustra alguns exemplos. Uma observação importante a ser notada na **Figura 3.12** a foi a instabilidade local do montante de extremidade de alma. Este fenômeno foi observado para os modelos em que a largura do montante de extremidade foi muito maior que a largura dos demais montantes. Em relação a seção CCB2, para alguns modelos, o primeiro modo de deformação não foi caracterizado pela FMA (**Figura 3.13**). Conforme observado, o primeiro modo de flambagem foi caracterizado pela instabilidade local da alma, especificamente no tê superior. Isso ocorreu pelo fato do tê inferior ser mais rígido do que o tê superior.

Figura 3.12 – Modos de deformação para o modelo CCB1

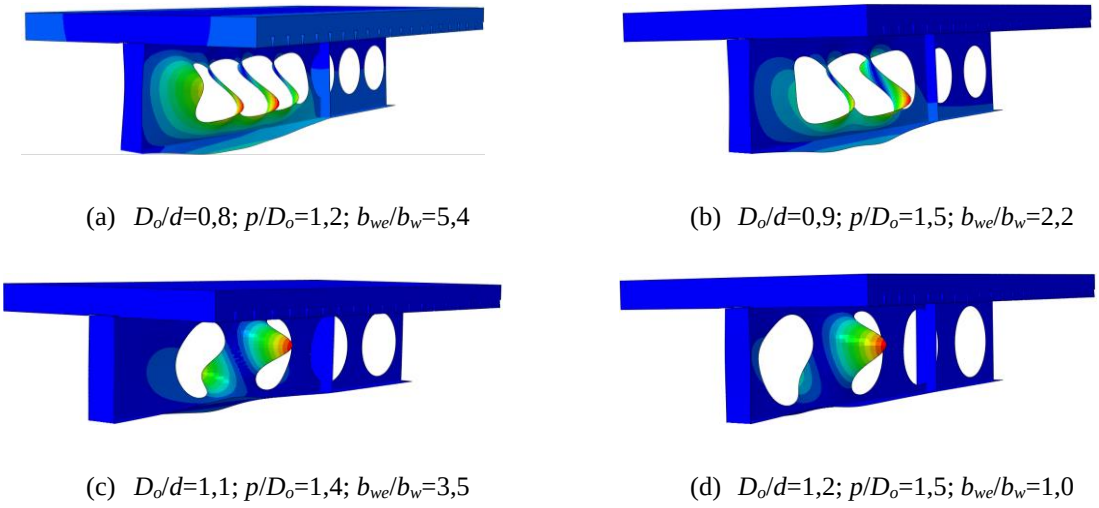

(a) D_o/d=0,8; p/D_o=1,2; b_{we}/b_w=5,4

(b) D_o/d=0,9; p/D_o=1,5; b_{we}/b_w=2,2

(c) D_o/d=1,1; p/D_o=1,4; b_{we}/b_w=3,5

(d) D_o/d=1,2; p/D_o=1,5; b_{we}/b_w=1,0

Fonte: (FERREIRA et al., 2021a)

Figura 3.13 – Modos de deformação para o modelo CCB2 (FERREIRA et al., 2021a)

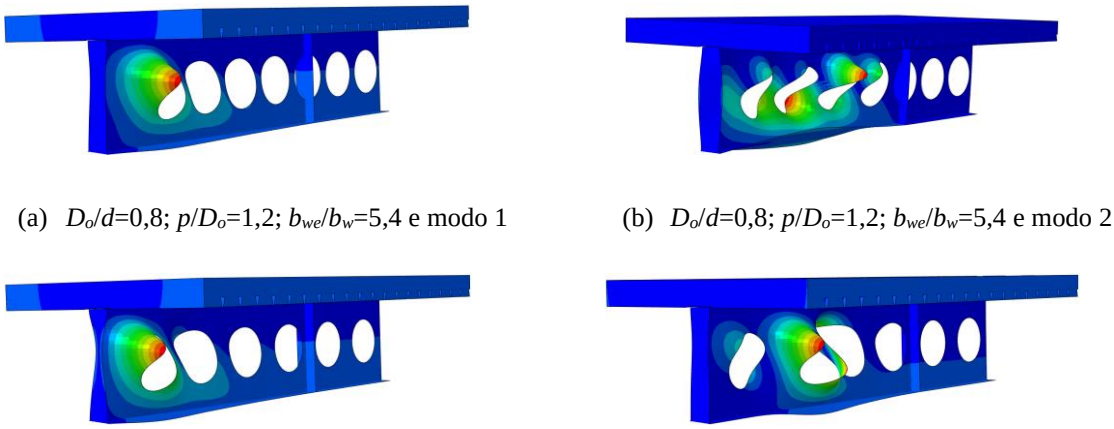

(a) D_o/d=0,8; p/D_o=1,2; b_{we}/b_w=5,4 e modo 1

(b) D_o/d=0,8; p/D_o=1,2; b_{we}/b_w=5,4 e modo 2

(c) D_o/d=0,8; p/D_o=1,5; b_{we}/b_w=1,3 e modo 1

(d) D_o/d=0,8; p/D_o=1,5; b_{we}/b_w=1,3 e modo 2

Fonte: (FERREIRA et al., 2021a)

Os modos de deformação para as seções CCB4 e CCB6, considerando a FMA, são ilustrados a seguir (**Figura 3.14**). As seções CCB4 e CCB6 possuem os tees superior e inferior formados pelas seções IPE 300 e HEB 340, respectivamente. Conforme mostrado na **Figura 3.14a**, **Figura 3.14c** e **Figura 3.14d**, o modo de deformação para a seção CCB4 foi caracterizado pela formação de uma curvatura em forma de “C” no tê superior, devido ao tê inferior ser mais rígido. Notavelmente, para a seção CCB6 (**Figura 3.14b**, **Figura 3.14d** e **Figura 3.14f**), a FMA foi caracterizado por uma curvatura em forma de "S". O que difere a

seção CCB4 e CCB6 é uma variação na altura total do perfil celular em aproximadamente 100 mm, ou seja, a seção CCB6 é mais esbelta que a seção CCB4.

Figura 3.14 – Modos de deformação para os modelos CCB4 e CCB6

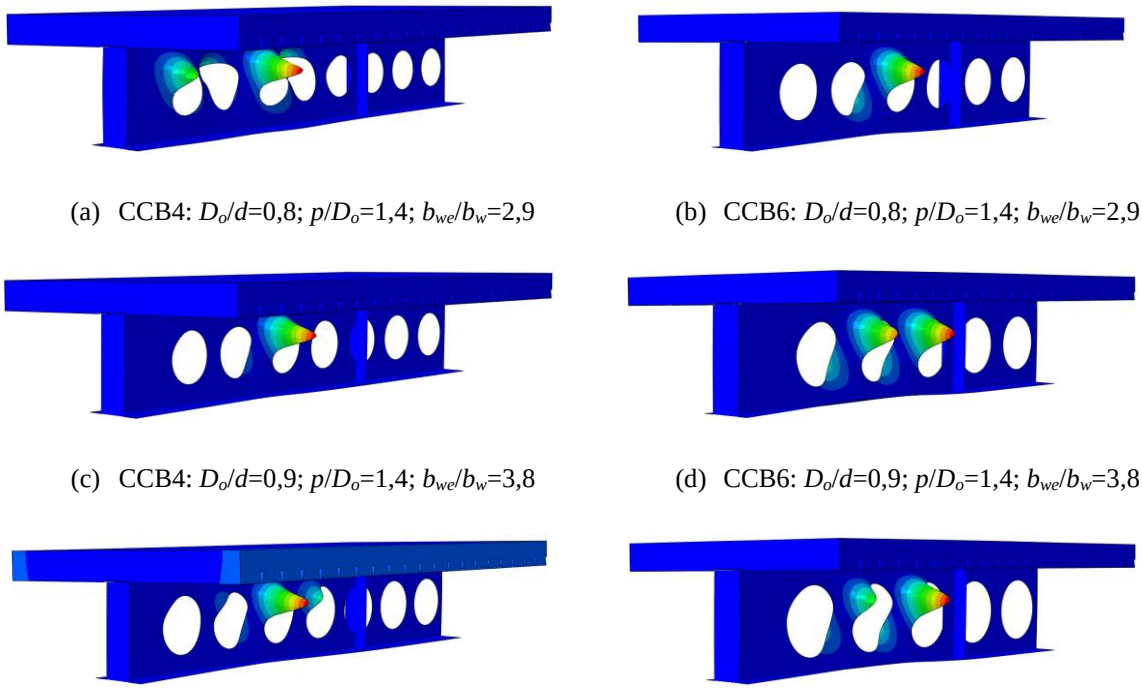

(a) CCB4: D_o/d=0,8; p/D_o=1,4; b_{we}/b_w=2,9

(b) CCB6: D_o/d=0,8; p/D_o=1,4; b_{we}/b_w=2,9

(c) CCB4: D_o/d=0,9; p/D_o=1,4; b_{we}/b_w=3,8

(d) CCB6: D_o/d=0,9; p/D_o=1,4; b_{we}/b_w=3,8

(e) CCB4: D_o/d=1,0; p/D_o=1,3; b_{we}/b_w=3,8

(f) CCB6: D_o/d=1,0; p/D_o=1,3; b_{we}/b_w=3,8

Fonte: (FERREIRA et al., 2021a)

3.4.2 Análises Inelásticas

Para a seção simétrica CCB1, a FMA foi caracterizada para as vigas celulares mistas que apresentaram p/D_o=1,3, 1,4 e 1,5, embora existissem regiões que iniciaram a formação do mecanismo plástico, conforme modelo p/D_o=1,2 (**Figura 3.15**). O comprimento do montante de extremidade mostrou influenciar consideravelmente a capacidade resistente de vigas celulares mistas. Os resultados que são apresentados na **Figura 3.16** mostraram comportamento diferente dos apresentados anteriormente em Panedpojaman, Thepchatri e Limkatanyu (2014). Por exemplo, segundo os resultados dos autores, a capacidade resistente à instabilidade no montante de alma aumentou com o menor valor da razão D_o/d, e com o maior valor da razão p/D_o. Diferentemente dos modelos dos autores, que consideraram apenas a modelagem do montante de alma em vigas celulares de aço, os modelos numéricos desenvolvidos no presente trabalho foram formados pela laje de concreto, conectores de cisalhamento, e principalmente montante de alma de extremidade.

Figura 3.15 –Mecanismo plástico para o modelo CCB1

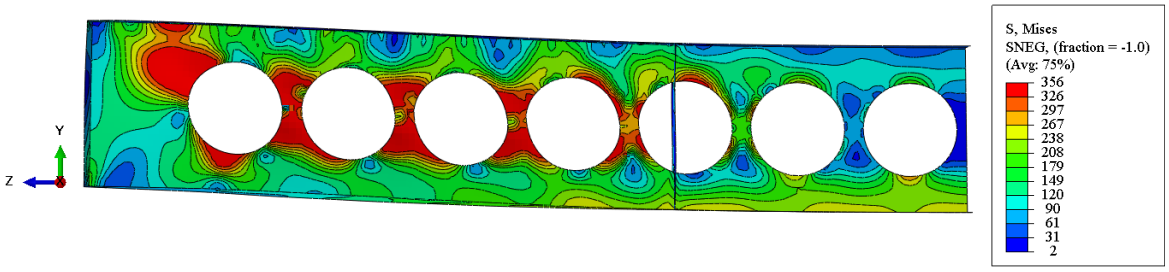

Fonte: (FERREIRA; MARTINS; DE NARDIN, 2021a)

Figura 3.16 – Capacidade resistente dos modelos CCB1

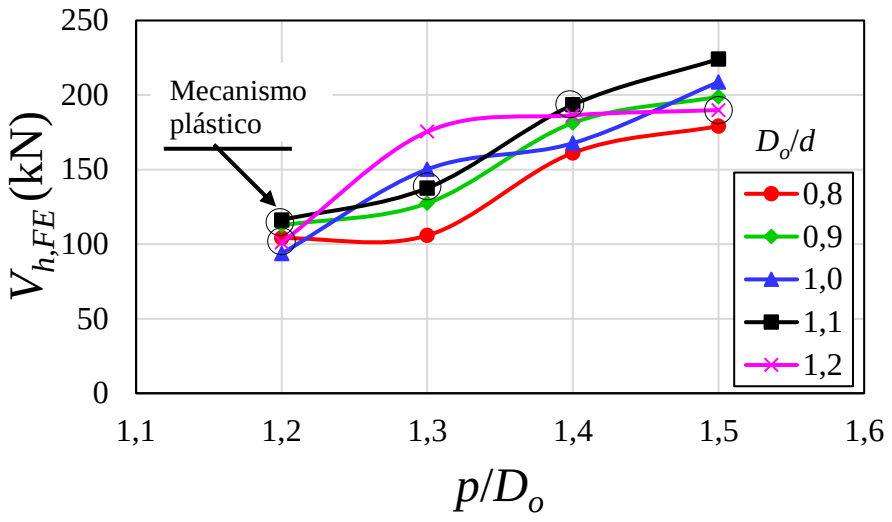

Fonte: (FERREIRA; MARTINS; DE NARDIN, 2021a)

Para melhor verificar o efeito da largura do montante de extremidade, parâmetro que influencia diretamente na formação do mecanismo plástico, a **Figura 3.17** apresenta a capacidade resistente de alguns modelos. Conforme mostrado nas ilustrações, a FMA é um fenômeno local caracterizado por um deslocamento lateral com torção. Além disso, quanto maior o comprimento do montante de extremidade, maior será o dano na laje de concreto, em função da transferência das tensões de cisalhamento.

Figura 3.17 – Influência do montante de extremidade para o modelo CCB1

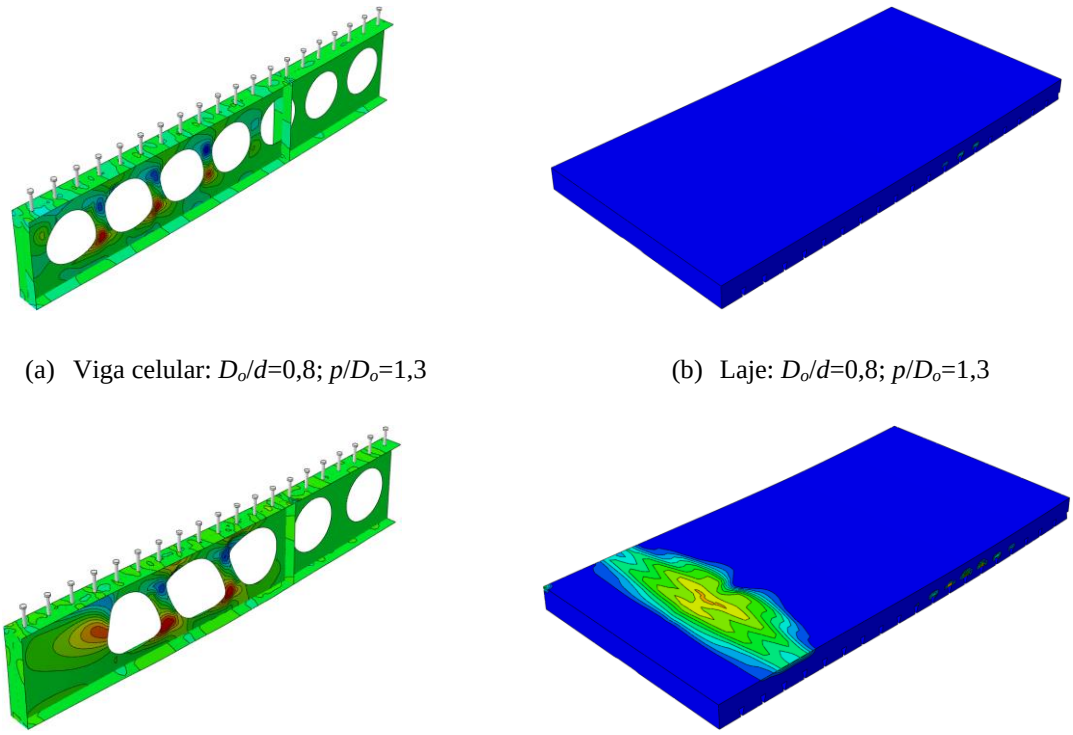

(a) Viga celular: D_o/d=0,8; p/D_o=1,3

(b) Laje: D_o/d=0,8; p/D_o=1,3

(c) Viga celular: D_o/d=0,9; p/D_o=1,4

(d) Laje: D_o/d=0,8; p/D_o=1,3

Fonte: (FERREIRA; MARTINS; DE NARDIN, 2021a)

Para a seção assimétrica CCB4, o mecanismo de Vierendeel ocorreu em todas as análises. A **Figura 3.18** ilustra o comportamento das vigas celulares mistas com razões D_o/d=1.2 e p/D_o=1.5. Uma observação importante apresentada na ilustração é a distribuição de tensões no montante de alma. Nesse contexto, a distribuição das tensões ocorre de forma descontínua, visto que a seção celular é assimétrica, formada pelos perfis IPE 300 e HEB 340. No modelo analisado, a seção assimétrica mostra a razão da área do tê inferior para a área do tê superior, aproximadamente, igual a 3,0. Isso significa que quando o comportamento final é definido por um mecanismo de plástico, para cada incremento de carga, o nível de tensão no tê inferior será muito menor que o nível de tensão no tê superior.

Figura 3.18 – Formação do mecanismo Vierendeel (em MPa)

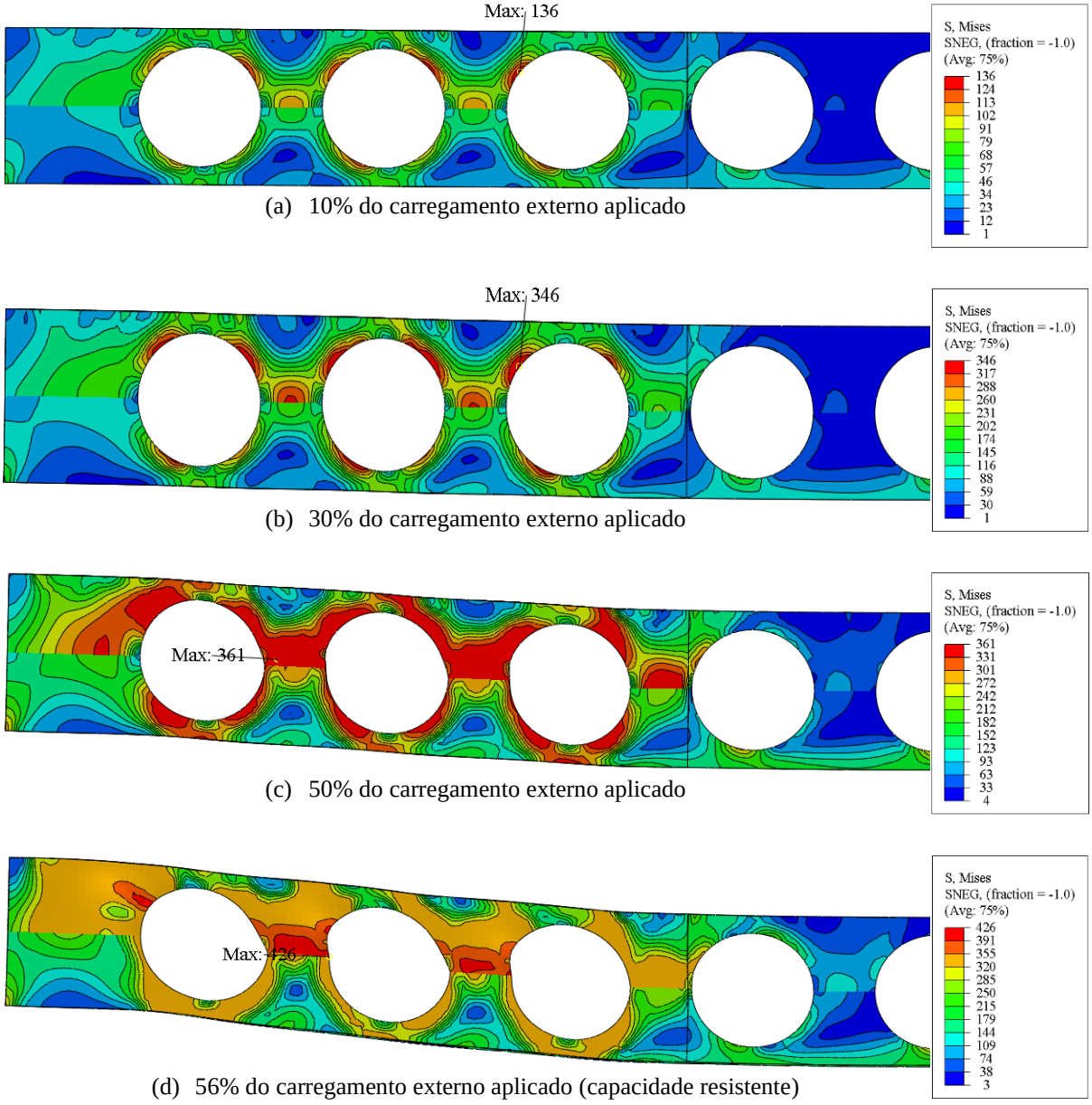

(a) 10% do carregamento externo aplicado

(b) 30% do carregamento externo aplicado

(c) 50% do carregamento externo aplicado

(d) 56% do carregamento externo aplicado (capacidade resistente)

Fonte: (FERREIRA; MARTINS; DE NARDIN, 2021a)

Conforme apresentado no item 3.3, todos as vigas celulares mistas que foram analisadas estão dentro dos intervalos $1{,}1 \leq p/D_o \leq 1{,}5$, $0{,}8 \leq D_o/d \leq 1{,}2$, e $0{,}5 \leq D_o/d_g \leq 0{,}86$. Nesse contexto, os resultados da modelagem numérica, que atingiu a capacidade resistente pela FMA, são comparados com os procedimentos de cálculo pela razão analítica/numérica (**Figura 3.19)**. Como mostrado, todos os procedimentos mencionados subestimam a capacidade resistente à FMA das vigas celulares mistas. Pelas análises realizadas, foi possível concluir que tanto a presença da laje de concreto quanto o montante de extremidade contribuíram para a capacidade

resistente à FMA. Os modelos de cálculo apresentados não consideram a contribuição desses dois fatores. Conforme observado nas análises realizadas no presente trabalho.

Figura 3.19 – Comparação entre os modelos analíticos com os modelos numéricos

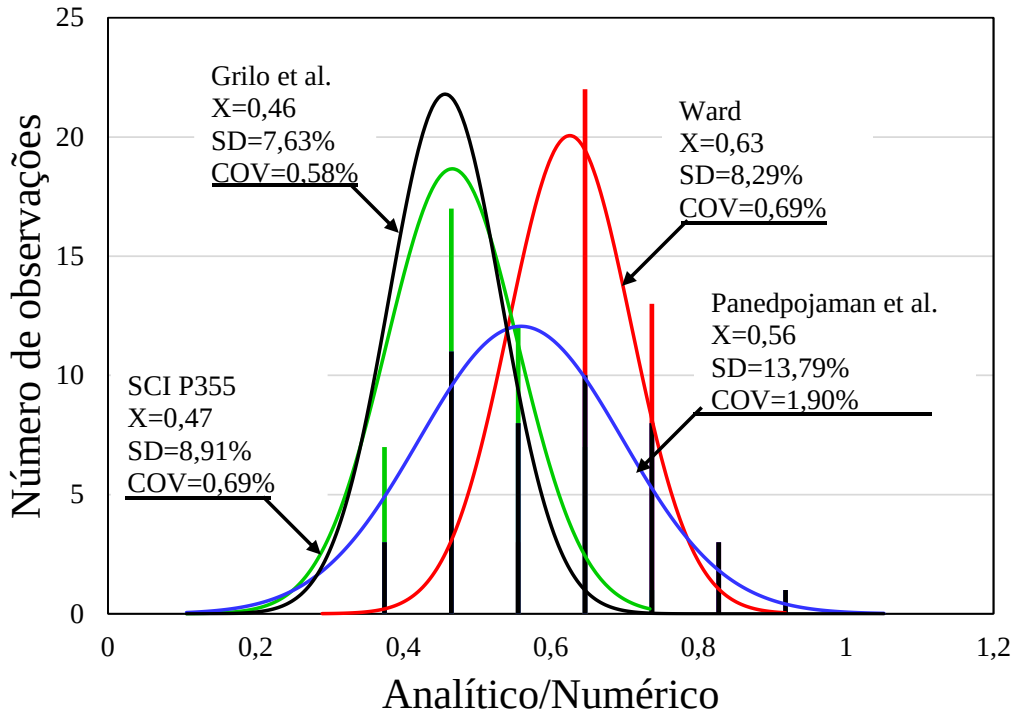

Fonte: (FERREIRA; MARTINS; DE NARDIN, 2021a)

3.5 SÍNTESE E CONCLUSÕES

Os pontos mais importantes apresentados nesse capítulo são:

- O modelo constitutivo quadrilinear do aço apresentou o melhor comportamento pós-pico quando comparado aos resultados experimentais e, por isso, foi adotado em todas as análises posteriores;
- Em vigas celulares mistas com alma menos esbelta foi observada a instabilidade local da alma na seção do tê superior, próximo ao apoio;
- Aumentando a esbeltez da alma, houve mudança no modo de falha que passou de instabilidade local da alma para instabilidade no montante da alma. Este efeito gerou aumento na força cortante global crítica, pois na primeira situação apenas o tê superior foi solicitado, enquanto que na segunda situação ambos os tês superior e inferior foram solicitados;
- As diferenças entre as forças cortantes das análises elástica e inelástica mostraram valores médios de 36% e 39%, respectivamente para as seções simétricas e assimétricas.
- O procedimento de cálculo recomendado pelo SCI P355 (LAWSON; HICKS, 2011) superestima as capacidade resistentes obtidas nas análises elásticas, enquanto que o procedimento que apresenta a modificação do comprimento efetivo é uma boa aproximação para a estimativa da capacidade resistente na análise elástica.
- Para seções simétricas, o mecanismo Vierendeel foi caracterizado para as razões p/D_o=1,2 e D_o/d=0,8, p/D_o=1,2 e D_o/d=0,9, p/D_o=1,4; 1.5 e D_o/d=1,0, p/D_o=1,2-1,5 e D_o/d=1,1, e p/D_o=1,2-1.5 e D_o/d=1,2. Para as outras razões, ocorreu instabilidade no montante de alma;
- Para a seção com menor grau de assimetria, para todas as situações (p/D_o=1,2-1,5; D_o/d=0,8-1,2), o comportamento último foi caracterizado pela instabilidade no montante de alma;
- Para a seção com maior grau de assimetria, para todas as situações (p/D_o=1,2-1,5; D_o/d=0,8-1,2), o comportamento último foi caracterizado pelo mecanismo Vierendeel. Além disso, quando a capacidade resistente é governada pelo mecanismo plástico, a ruptura do conector de cisalhamento pode ocorrer;
- A largura do montante de extremidade e a presença da laje de concreto contribuíram, significativamente, para a capacidade resistente das vigas celulares mistas. Quanto maior

o comprimento do montante de extremidade, maior a região danificada na laje de concreto, considerando a tração;

- De modo geral, os deslizamentos relativos entre a laje e o perfil celular foram nulos;
- Os procedimentos analíticos subestimaram a capacidade resistente à instabilidade no montante de alma, uma vez que eles não consideram a contribuição da laje de concreto no cálculo resistente.

4.

VIGAS MISTAS COM LAJES ALVEOLARES

O presente Capítulo, também contêm análises prévias, e é fundamentado nos artigos publicados "***A parametric study of steel-concrete composite beams with hollow core slabs and concrete topping***" (FERREIRA; MARTINS; DE NARDIN, 2020b) e "***Steel-Concrete Composite Beams with Precast Hollow Core Slabs: A Sustainable Solution"*** (FERREIRA et al., 2021b). Dessa forma, o presente Capítulo foi redigido de maneira resumida com o objetivo de apresentar a metodologia empregada na validação do modelo numérico correspondente à laje alveolar pré-fabricada de concreto. Portanto, o conteúdo desse capítulo é complementado pelas informações e detalhes contidos em Ferreira, Martins e De Nardin (2020b) e Ferreira et al. (2021c) que se encontram no Apêndice do presente trabalho. Com a validação numérica dos modelos ensaiados por Lam[1] e por Batista e Landesmann (2016) a pedido da Gerdau[2] foi

[1] LAM, D. **Composite steel beams using precast concrete hollow core floor slabs**. [s.l.] 1998. Ph.D. thesis. University of Nottingham, 1998.

[2] BATISTA, E. M.; LANDESMANN, A. **Análise experimental de vigas mistas de aço e concreto compostas por lajes alveolares e perfis laminados. COPPETEC, PEC-18541.** Rio de Janeiro, 2016.

possível desenvolver um estudo paramétrico para avaliar a influência da altura da laje alveolar e da capa de concreto no comportamento das vigas mistas de aço e concreto.

Conforme apresentado no Capítulo 2, os estudos em vigas mistas de aço e concreto formadas por lajes alveolares são recentes, e poucos pesquisadores têm se dedicado a este tema. Além disso, de acordo com a apresentação do estado da arte no item 2.5, não há estudos paramétricos que considerem o comportamento à flexão de vigas mistas associadas às lajes alveolares com capa de concreto. Assim, o estudo publicado "***A parametric study of steel-concrete composite beams with hollow core slabs and concrete topping****"* teve como objetivo investigar o comportamento de vigas mistas formadas por unidades alveolares de 150mm de altura e com capa de concreto. Para isso, foi realizado um estudo paramétrico, considerando análises geométricas não lineares. O modelo numérico foi calibrado, considerando modelos físicos. Para esta tarefa, a simetria no eixo longitudinal e controle de deslocamento foram utilizados. As vigas mistas foram consideradas biapoiadas e submetidas à flexão em quatro pontos. A influência da capa de concreto (50mm de espessura), a resistência do concreto moldado in loco (25MPa, 30MPa e 40MPa), o diâmetro da armadura transversal (10mm, 12,5mm e 16mm), o grau de interação (conectores de cisalhamento espaçados em 120mm, 175mm e 225mm), e a seção transversal do aço (W360x51, W460x74 e W530x72) foram os parâmetros investigados. Os resultados são discutidos e comparados com procedimentos de cálculo de resistência, que são descritos na seção 4.1.

O segundo estudo, "***Steel-Concrete Composite Beams with Precast Hollow Core Slabs: A Sustainable Solution"***, fez uma abordagem voltada para a sustentabilidade. A industrialização da construção torna os processos de execução de edifícios mais ecologicamente correta e sustentável. Essa mudança se faz necessária por se tratar de uma indústria que demanda grande consumo de água e energia, além de ser responsável pelo descarte de grande volume de resíduos. De modo geral, a transformação do setor da construção é um grande desafio mundial. O maior volume de material concreto, que é usado na execução de edifícios de múltiplos andares, é atribuído às lajes. Essa utilização em grandes volumes aumenta a quantidade de emissão de CO_2. As vigas mistas de aço-concreto formadas por lajes alveolares pré-fabricadas são desenvolvidas devido aos seus benefícios técnicos e econômicos, sobretudo à sua alta resistência e redução do peso próprio do concreto, tornando esse sistema econômico e com menor impacto ambiental, reduzindo assim as emissões de carbono. Pesquisas significativas foram realizadas com foco em lajes alveolares de grandes alturas devido à

necessidade de superar vãos cada vez maiores (AHMED K. EL-SAYED AND ABDULRAHMAN M. ALHOZAIMY, [s.d.]; BRUNESI; BOLOGNINI; NASCIMBENE, 2015; JOO et al., 2020; MICHELINI et al., 2020; NGUYEN; TAN; KANDA, 2019; PALMER; SCHULTZ, 2011; TAWADROUS; MORCOUS, 2018; WALRAVEN; MERCX, 1983). A publicação *do Steel Construction Institute* SCI P401 (GOUCHMAN, 2014), que é fundamentada no EN 1994-1-1 (2004), limita-se a lajes alveolares com alturas de 150 a 250mm, com ou sem cobertura de concreto. Dessa forma, o presente estudo teve como objetivo investigar lajes alveolares com 265mm de altura e com cobertura de concreto para entender seu efeito no comportamento à flexão de vigas mistas de aço-concreto, considerando que essa altura final da laje alveolar é maior do que a recomendação SCI P401. Para esse estudo, unidades alveolares de 150mm e 265mm com cobertura de concreto foram consideradas para avaliar se o aumento da altura da unidade alveolar (ou consumo de concreto pré-fabricado) proporciona maior resistência ao sistema estrutural.

O presente Capítulo foi organizado em cinco seções. Primeiramente é apresentado modelos de resistência à flexão de vigas mistas de aço e concreto formadas por lajes alveolares pré-fabricadas. Em seguida, é apresentado a metodologia que foi utilizada para os estudos de validação. Posteriormente a etapa, as considerações gerais do estudo paramétrico são descritas. Finalmente, o Capítulo 4 se encerra com a apresentação dos principais resultados e a síntese das conclusões, que foram obtidas nos estudos publicados (FERREIRA et al., 2021b; FERREIRA; MARTINS; DE NARDIN, 2020b).

Os seguintes símbolos são usados neste Capítulo:

A_a	área da seção transversal da seção de aço;	$M_{pl,FULL}$	momento de plastificação da seção mista considerando interação total
A_s	área total da armadura transversal;	n	número de conectores de cisalhamento;
A_{sc}	área da seção transversal do pino com cabeça;	s	espaçamento entre os conectores de cisalhamento;
A_s	área da seção transversal da armadura transversal;	t_c	altura da laje de concreto (incluindo a capa de concreto);
b	largura efetiva da laje;	t_f	espessura da mesa;
b_f	largura da mesa;	t_w	espessura da alma;
C_c	resistência axial do concreto;	T_a	resistência axial da seção de aço tracionada;
C_s	resistência axial da seção de aço à compressão;	$T_{a,mesa}$	resistência axial da mesa tracionada;
c	espessura da capa de concreto;	$T_{a,alma}$	resistência axial da alma tracionada;
d	altura da seção de aço;	Z_x	módulo resistente plástico da seção de aço;
g	garganta;	η	relação entre a soma das resistências dos conectores de cisalhamento fornecidos e a soma das resistências dos conectores de cisalhamento necessárias para à interação total;
h_c	altura da laje alveolar;		
h_w	altura da alma da seção de aço;		
L	vão;		
L_φ	comprimento da armadura transversal;		
M_{pl}	momento de plastificação da seção mista;	φ	diâmetro da armadura transversal.
$M_{pl,a}$	momento de plastificação da seção de aço;		

4.1 CAPACIDADE RESISTENTE DE VIGAS MISTAS À FLEXÃO

O cálculo da resistência de vigas mistas com laje alveolar pré-fabricada é fundamentado nas prescrições do *Steel Construction Institute: Design of composite beams using precast concrete slabs in accordance with Eurocode 4* , SCI P401 (GOUCHMAN, 2014), considerando interação total (**Figura 4.1a**) e parcial (**Figura 4.1b**). A resistência à flexão é calculada de acordo com a posição da linha neutra plástica (L.N.P).

Figura 4.1 – Blocos de tensões normais

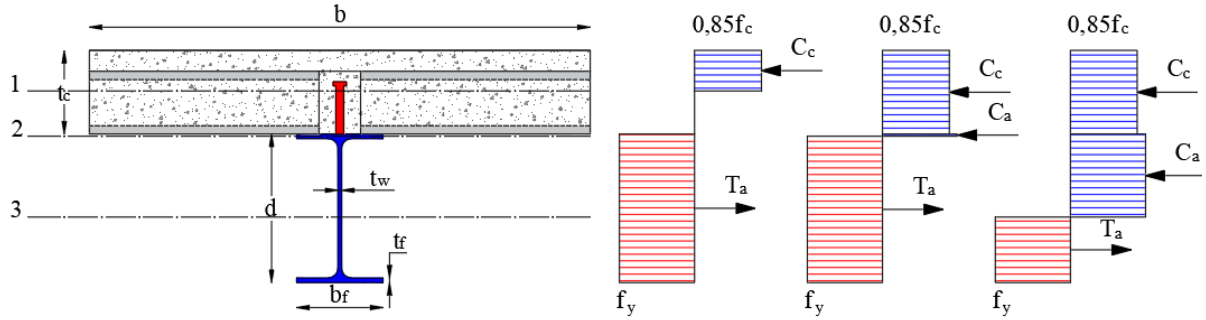

(a) Interação total

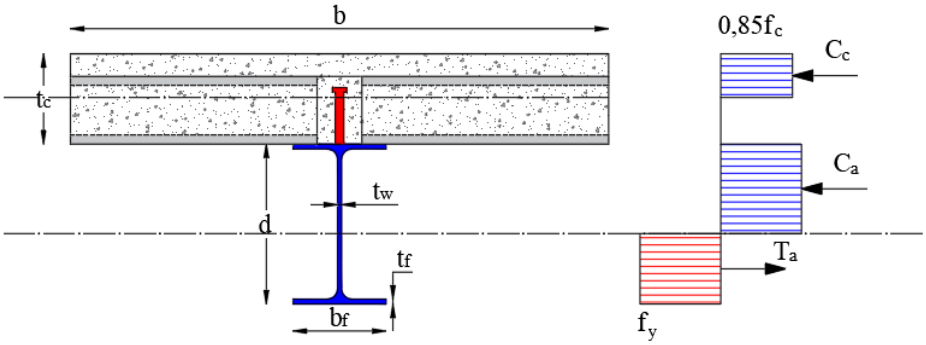

(b) Interação parcial

A SCI P401 menciona que para o caso de vigas mistas com lajes alveolares, a L.N.P não pode estar localizada na laje, pois tais elementos estruturais apresentam baixa resistência à tração. Quando isso ocorrer, é necessário aumentar a altura do perfil de aço. Caso contrário, de acordo com a recomendação, a solução alternativa seria considerar a interação parcial. Entretanto, para os casos de interação parcial, a seção mista terá duas linhas L.N.P: uma na laje e outra no perfil de aço. Tal situação implica que ambos o perfil de aço e a laje alveolar estarão submetidos à tração e compressão.

Considerando interação total, quando a L.N.P. se encontra na mesa superior ($C_c \geq T_{a,alma}$ e $T_a > C_c$), a resistência à flexão é calculada de acordo com as **Eqs. (4.1-4.8)**:

$$\sum Q_R \geq 0{,}85 f_c b t_c \qquad \text{Eq. (4.1)}$$

$$M_{pl} = T_a \left(\frac{d}{2}\right) + C_c \left(\frac{t_c}{2}\right) - \left[\frac{\left(T_a - C_c\right)^2}{T_{a,mesa}}\right]\left(\frac{t_f}{4}\right) \qquad \text{Eq. (4.2)}$$

$$C_c = 0{,}85 f_c b t_c \qquad \text{Eq. (4.3)}$$

$$b \leq \begin{cases} L/4 \\ 2L_\phi + g \end{cases} \qquad \text{Eq. (4.4)}$$

$$T_{a,mesa} = b_f t_f f_y \qquad \text{Eq. (4.5)}$$

$$T_{a,alma} = h_w t_w f_y \qquad \text{Eq. (4.6)}$$

$$h_w = d - 2t_f \qquad \text{Eq. (4.7)}$$

$$T_a = A_a f_y \qquad \text{Eq. (4.8)}$$

Considerando interação total, quando o L.N.P se encontra na alma do perfil de aço ($T_{a,alma} > C_c$), a resistência à flexão é calculada (**Eqs. 4.9-4.10**):

$$M_{pl} = M_{pl,a} + C_c \left(\frac{d + t_c}{2}\right) - \frac{C_c^{\,2}}{T_{a,alma}}\left(\frac{h_w}{4}\right) \qquad \text{Eq. (4.9)}$$

$$M_{pl,a} = Z_x f_y \qquad \text{Eq. (4.10)}$$

Por outro lado, sobre a interação parcial, o método mais simples de determinar a resistência à flexão é a abordagem de "interação linear" (**Eq. 4.11**), abrangida pelo EN 1994 1-1 (2004):

$$M_{pl} = M_{pl,a} + \left(M_{pl,FULL} - M_{pl,a}\right)\eta \qquad \text{Eq. (4.11)}$$

De acordo com as recomendações da SCI P401 (GOUCHMAN, 2014), o método apresentado na **Eq. (4.11)** é conservador em relação ao método dos blocos de tensão (**Figura 4.2**).

Figura 4.2 – Interação entre o momento resistente e grau de conexão em vigas mistas, adaptado de (GOUCHMAN, 2014)

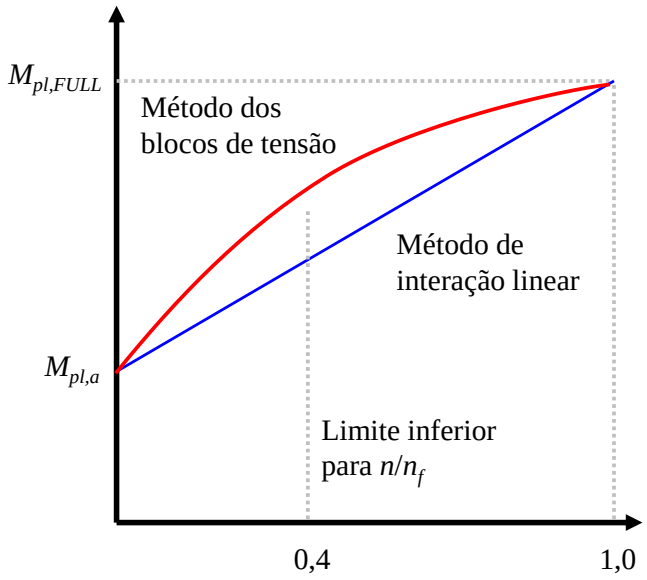

Os métodos de cálculo resistente, que nesta seção foram apresentados, serão utilizados para a comparação dos modelos desenvolvidos no estudo paramétrico (seção 4.3).

4.2 MODELAGEM NUMÉRICA: ESTUDO DE VALIDAÇÃO

Esta seção apresenta a metodologia desenvolvida na modelagem numérico para o estudo de validação.

4.2.1 Tipo de Análise

Para as vigas mistas com lajes alveolares, as análises não-lineares são realizadas em apenas uma etapa, uma vez que tais sistemas estruturais estão suscetíveis apenas aos mecanismos de plastificação. Para resolver o problema de não linearidade geométrica, é utilizado o método *Static Riks*. Este método, também é conhecido como algoritmo de Riks modificado. Outras referências também utilizaram esse mesmo procedimento para a

modelagem de vigas mistas de aço e concreto (EL-LOBODY; LAM, 2003; LAM, 1998; LAM; ELLIOTT; NETHERCOT, 2000b).

4.2.2 Modelos Experimentais Utilizados na Validação

Para o estudo de validação, quatro ensaios são considerados: dois ensaios do estudo de Lam (1998) (CB1 e CB2), e dois ensaios (CB3 e CB4) realizado na COPPE (BATISTA; LANDESMANN, 2016). As dimensões dos conectores tipo pino com cabeça são 19x125mm (CB1 e CB2) e 19x135mm (CB3 e CB4). O espaçamento entre os conectores dos modelos CB1 e CB2 é de 150 mm. Para os modelos CB3 e CB4, o espaçamento entre os conectores é de 200mm. Maiores informações a respeito desses ensaios são apresentadas na **Tabela 4.1** e **Figuras 4.3-4.4**.

Tabela 4.1 – Características dos ensaios

Model	d	b_f	t_f	t_w	b	g	h_c	c	L_e	L_p	L_b	φ
CB1	355	171,5	11,5	7,4	1665	65	150	-	150	1500	5700	16
CB2	355	171,5	11,5	7,4	1665	65	150	-	150	1500	5700	8
CB3	299	306	11	11	1756	156	150	50	185	1915	5830	12,5
CB4	299	306	11	11	1756	106	265	50	185	1915	5830	12,5

Model	$f_{y,f}$	$f_{y,w}$	$f_{y,s}$	$f_{c,HCU}$	$f_{c,in}$
CB1	310	355	585	50[a]	32[a]
CB2	310	355	473	50[a]	26[a]
CB3	345	345	500	45[b]	30[b]
CB4	345	345	500	45[b]	30[b]

[a]Resistência cúbica;
[b]Resistência cilíndrica.

Figura 4.3 – Detalhes geométricos dos ensaios

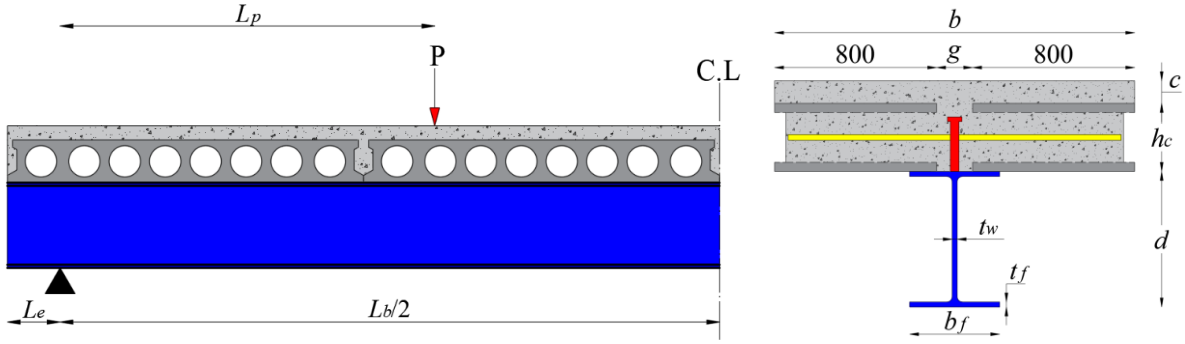

(a) Vista lateral (b) Seção transversal

Fonte: (FERREIRA et al., 2021b)

Figura 4.4 – Modelos numéricos

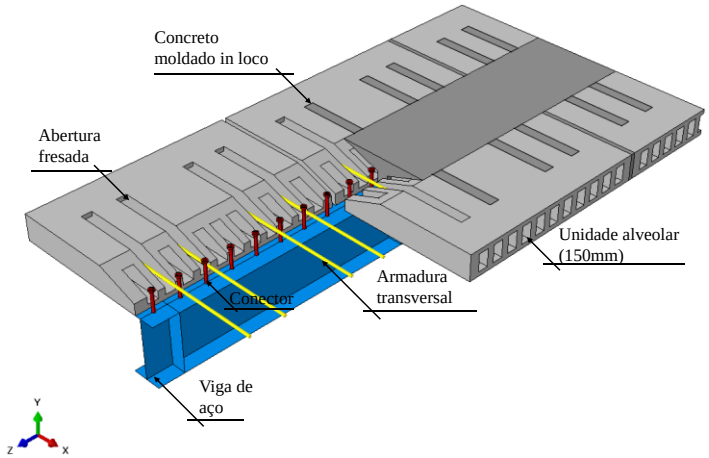

(a) Modelos CB1 e CB2

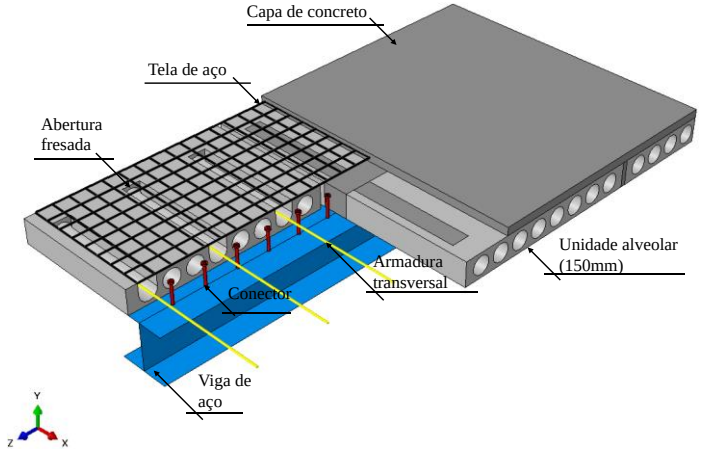

(b) Modelo CB3

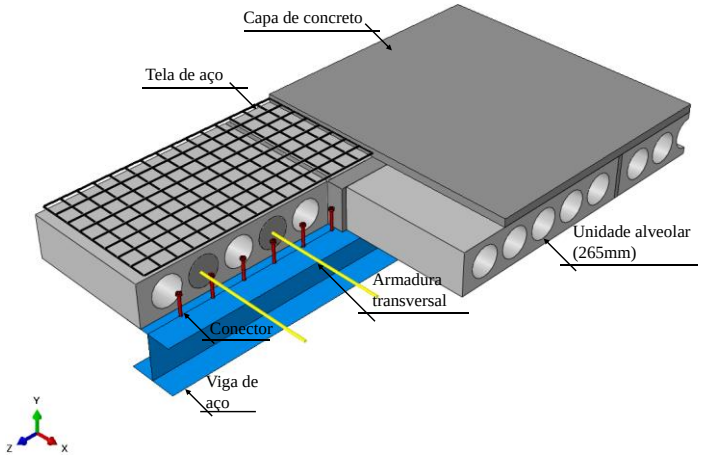

(c) Modelo CB4

Fonte: (FERREIRA et al., 2021b)

4.2.3 Materiais

Para a seção de aço foi considerado o modelo elasto-plástico perfeito (**Figura 4.5a**), e para os conectores tipo pino com cabeça o modelo bilinear, conforme apresentado no Capítulo 3, seção (**Figura 4.5b**).

Figura 4.5 – Modelos constitutivos para o aço

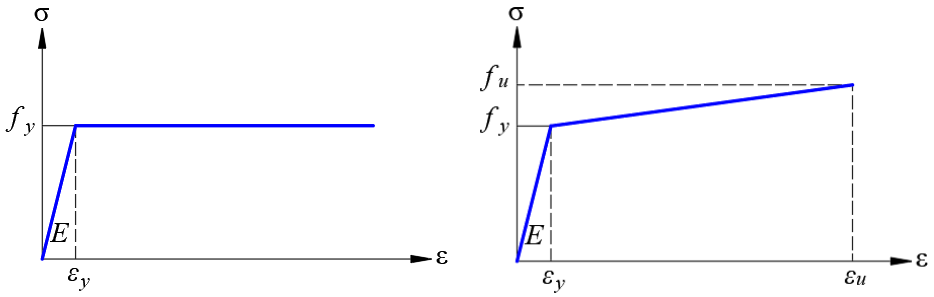

(a) Elasto-plástico perfeito (a) Bilinear

Para o concreto, os modelos do concreto à tração e compressão de Carreira e Chu (1985, 1986) **(Figura 4.6**) foram adotados (**Eqs. 4.1-4.3**).

Figura 4.6– Modelo de Carreira e Chu (1985, 1986)

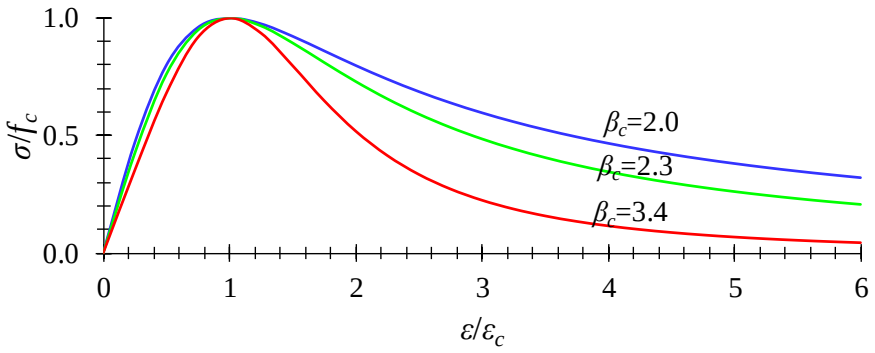

$$\frac{\sigma}{f_c} = \frac{\beta_c \left(\varepsilon / \varepsilon_c\right)}{\beta_c - 1 + \left(\varepsilon / \varepsilon_c\right)^{\beta_c}} \qquad \text{Eq. (4.1)}$$

$$\frac{\sigma}{f_t} = \frac{\beta_c \left(\varepsilon / \varepsilon_t\right)}{\beta_c - 1 + \left(\varepsilon / \varepsilon_t\right)^{\beta_c}} \qquad \text{Eq. (4.2)}$$

$$\beta_c = \left(\frac{f_c}{32.4}\right)^3 + 1.55 \ \ (MPa) \qquad \text{Eq. (4.3)}$$

Conforme descrito no Capítulo 3, o modelo de dano Concrete Damage Plasticity (CDP) (HILLERBORG; MODÉER; PETERSSON, 1976; LEE; FENVES, 1998; LUBLINER et al., 1989) foi adotado. A seguir na **Tabela 4.2** são apresentados os parâmetros de entrada.

Tabela 4.2 – Parâmetros de entrada CDP

Parâmetro	Valor	Referência
Ψ (º) (In-loco concrete)	40	(BEHNAM; KUANG; SAMALI, 2018; FERREIRA et al., 2021b, 2021c; FERREIRA; MARTINS; DE NARDIN, 2020b, 2021b; GENIKOMSOU; POLAK, 2015)
Ψ (º) (HCU concrete)	28	(NGUYEN; TAN; KANDA, 2019)
ξ	0.1 (*default*)	(BEHNAM; KUANG; SAMALI, 2018; DASSAULT SYSTÈMES SIMULIA, 2016; GENIKOMSOU; POLAK, 2015; NGUYEN; TAN; KANDA, 2019)
σ_{b0}/σ_{c0}	1.16 (*default*)	(BEHNAM; KUANG; SAMALI, 2018; DASSAULT SYSTÈMES SIMULIA, 2016; GENIKOMSOU; POLAK, 2015; NGUYEN; TAN; KANDA, 2019)
K_c	2/3 (*default*)	(BEHNAM; KUANG; SAMALI, 2018; DASSAULT SYSTÈMES SIMULIA, 2016; GENIKOMSOU; POLAK, 2015; NGUYEN; TAN; KANDA, 2019)
μ (s^{-1})	0.001	(BEHNAM; KUANG; SAMALI, 2018; GENIKOMSOU; POLAK, 2015)

4.2.4 Superfícies de Contato

Sobre a interação entre as superfícies de contato, o processo de aplicação foi semelhante ao descrito no Capítulo 3 (**Figura 4.7**). Além disso, entre as superfícies do concreto moldado in loco e o concreto pré-fabricado foi considerado a aderência perfeita por meio da *Tie constraint*. Maiores informações podem ser consultadas nos artigos publicados (FERREIRA et al., 2021b; FERREIRA; MARTINS; DE NARDIN, 2020b). Na **Tabela 4.3** são apresentados os pares de interação.

Figura 4.7– Superfícies de contato

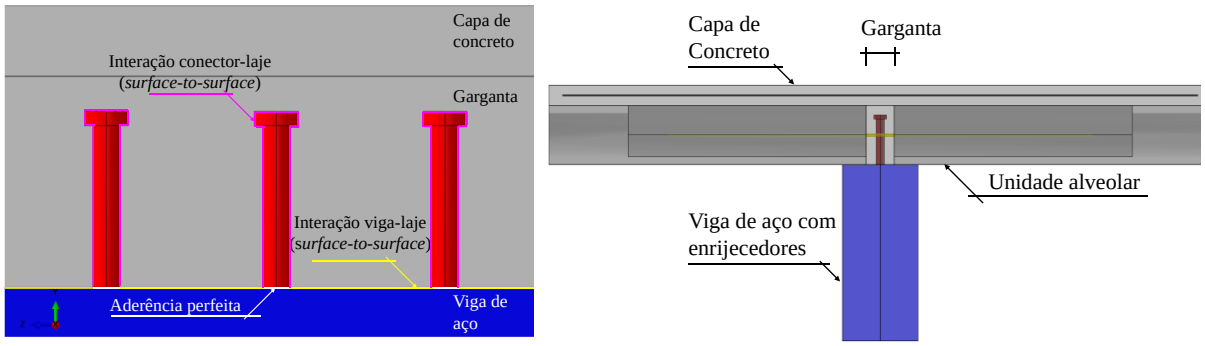

(a) Vista lateral (b) Seção

4.2.5 Condições de Contorno e Discretização

Sobre as condições de contorno, a aplicação foi semelhante ao apresentado no Capítulo 3. Entretanto, foi considerado controle de carregamento por deslocamento (FERREIRA; MARTINS; DE NARDIN, 2020b). A discretização é apresentada na **Figura 4.8**. A dimensão dos elementos finitos foi adotada conforme estudos anteriores (LIU et al., 2016; NGUYEN; TAN; KANDA, 2019; SJAARDA et al., 2017).

Figura 4.8 – Discretização

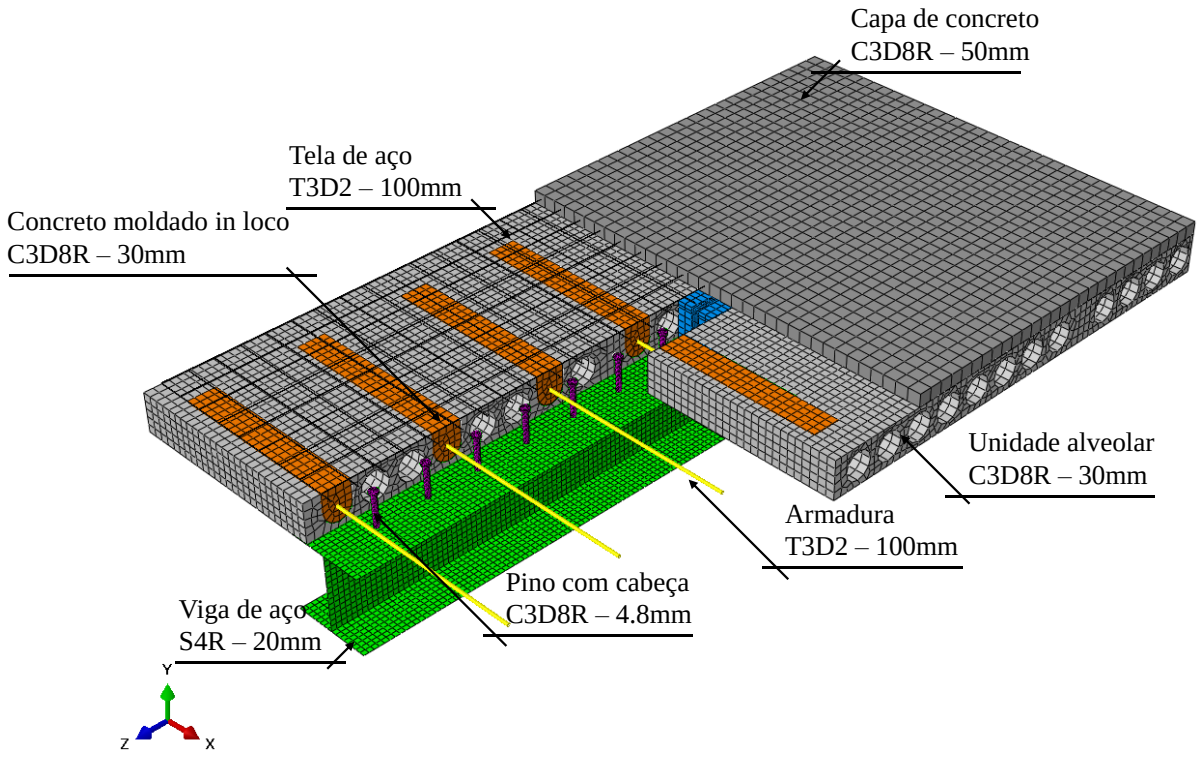

4.2.6 Resultados de Validação

Uma vez que as desvantagens no controle de deslocamento estão relacionadas à seleção da variável de deslocamento adequada, o que pode resultar em custo computacional ou divergência do procedimento de solução iterativa (CRISFIELD, 1981, 1986; MAEWAL; NACHBAR, 1977), o critério de parada adotado foi por controle de deslocamento no meio do vão, em comparação com os modelos experimentais.

Os modos de falha dos modelos CB1 e CB2 foram semelhantes (**Figura 4.9a**). Os resultados de validação (**Figura 4.9**) são apresentados por meio da trajetória de equilíbrio.

Conforme descrito por Lam (1998), nos modelos CB1 e CB2 foi possível observar a plastificação da mesa inferior e o excesso de fissuração na parte inferior da laje alveolar. Por outro lado, o modelo CB3 (**Figura 4.9b**) apresentou fissuração excessiva, principalmente no ponto de aplicação do carregamento. Tais fissuras se estenderam para as laterais da laje, conforme descrito por Batista e Landesmann (2016). As configurações finais dos modelos são apresentadas na **Figura 4.10**.

Figura 4.9– Resultados de Validação

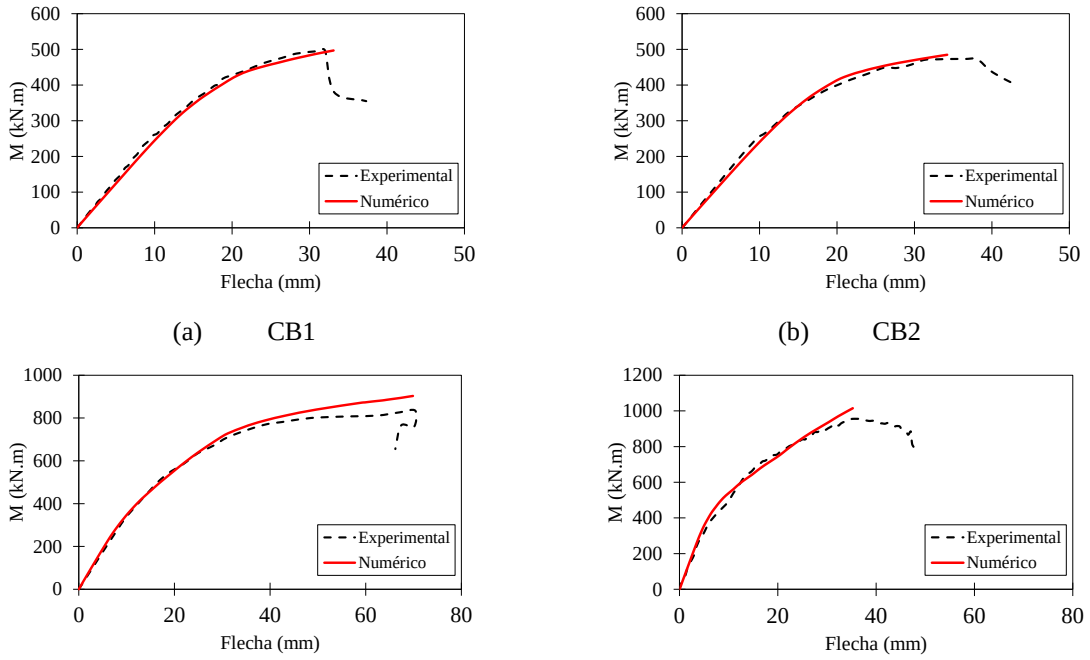

(a) CB1 (b) CB2

(c) CB3 (d) CB4

Figura 4.10– Resultados de Validação

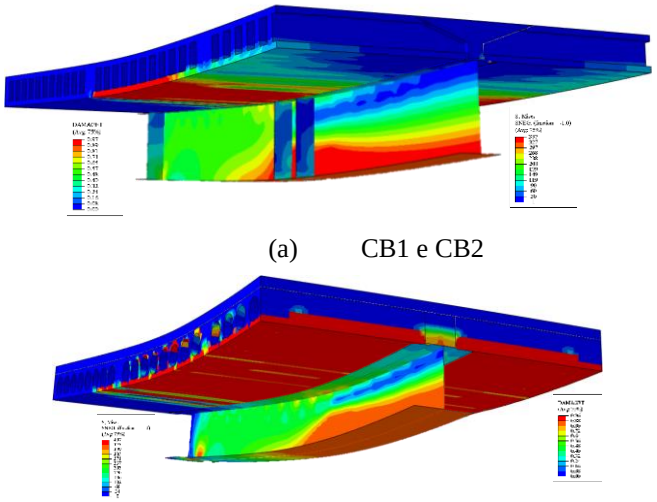

(a) CB1 e CB2

(b) CB3

De acordo com os resultados ilustrados, é possível aferir que os modelos de vigas mistas de aço e concreto formados por lajes alveolares pré-fabricadas foram calibrados. Tal calibração é fundamental para a realização do estudo paramétrico que é descrito a seguir.

4.3 MODELAGEM NUMÉRICA: ESTUDO PARAMÉTRICO

A seguir estão as considerações gerais para o estudo paramétrico:

1. O grau de interação foi variado em função do espaçamento dos conectores de cisalhamento (**Figura 4.11a-b e Tabela 4.3**), cujas dimensões são 19x125mm;
2. Foram consideradas as unidades LP15 e LP26 (**Figura 4.11c-d**), resistência à compressão igual a 40 MPa, sem chanfro e gap (*g*) igual a 70mm;

Figura 4.11 – Seção, espaçamento e unidades alveolares

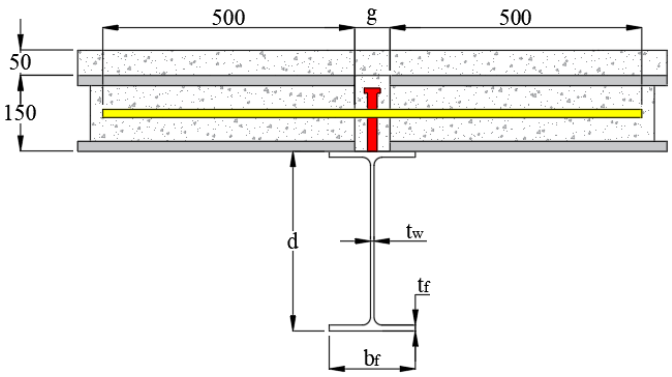

(a) Seção, considerando o modelo com laje LP15 (em milímetros)

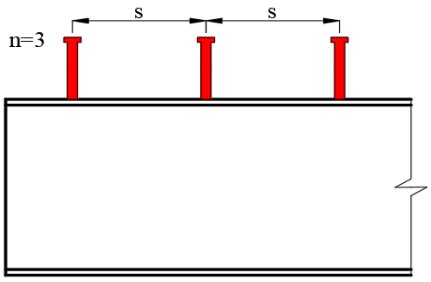

(b) Espaçamento

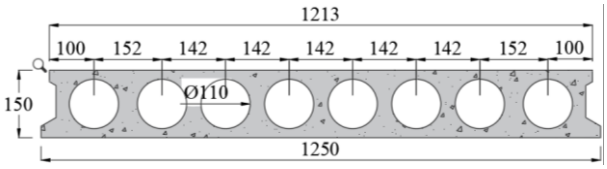

(c) LP15 (em milímetros)

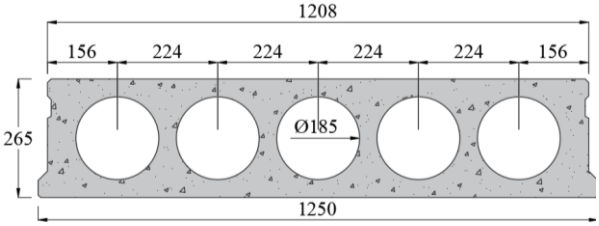

(d) LP26 (em milímetros

Tabela 4.3 – Características geométricas dos modelos para o estudo paramétrico

Seção	d (mm)	b_f (mm)	t_f (mm)	t_w (mm)	L (mm)	s (mm)	$n/2$
W360x51	355	171	11,6	7,2	6000	120	24
						175	17
						225	13
W460x74	457	190	14,5	9,0	6000	120	24
						175	17
						225	13
W530x72	524	207	10,9	9,0	6000	120	24
						175	17
						225	13

*De acordo com a SCI P401 (GOUCHMAN, 2014), os conectores de cisalhamento são frequentemente alocados com o espaçamento de 120 a 225mm ao longo da viga.

3. Para o perfil foi adotado o aço ASTM A572 Gr.50, cuja resistência ao escoamento é de 345MPa. O módulo de elasticidade e o coeficiente de Poisson foram iguais a 200 GPa e 0,3, respectivamente;
4. Foram consideradas três seções transversais de perfis de aço da série W: W360x51, W460x74 e W530x72;
5. Para cada modelo, as resistências do concreto moldado in loco variaram de 25, 30 e 40 MPa;
6. A espessura da capa de concreto foi de 50mm, sendo os modelos de referência aqueles que não possuem cobertura de concreto;
7. Foi considerada tela de aço soldada com 4,2mm de diâmetro e espaçamento de 100 mm na capa de concreto;
8. Para cada modelo, os diâmetros da armadura transversal foram variados em 10mm, 12,5mm e 16mm. O comprimento da armadura transversal foi de 1000+g, em mm;
9. Foi considerado o preenchimento do 1º, 3º, 5º e 7º alvéolos;
10. As vigas foram consideradas biapoiadas e submetidas a dois pontos de carregamento espaçados L/4 de cada apoio.
11. O critério de parada adotado foi o deslocamento vertical no meio do vão em L/100.

A seguir, nos itens 4.4 e 4.5 são apresentados os principais resultados e as conclusões extraídas da análise paramétrica (**Figura 4.12**), respectivamente. Os resultados e discussões detalhadas podem ser encontrados nos artigos publicados (FERREIRA et al., 2021b; FERREIRA; MARTINS; DE NARDIN, 2020b), que se encontram no Apêndice do presente trabalho.

Figura 4.12 –Síntese do estudo paramétrico em vigas mistas com lajes alveolares

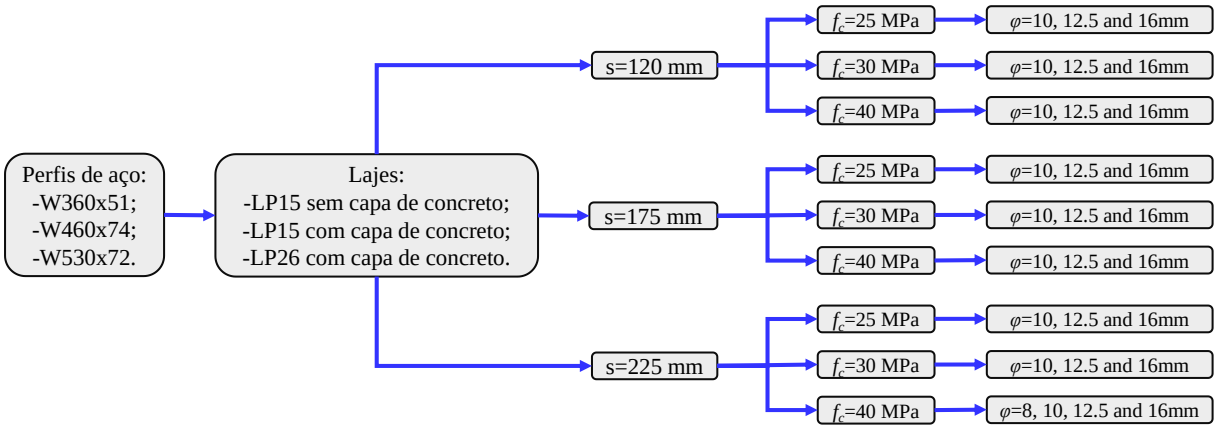

4.4 PRINCIPAIS RESULTADOS DO ESTUDO PARAMÉTRICO

Essa seção tem como objetivo apresentar alguns dos principais resultados do estudo paramétrico desenvolvido em vigas mistas formadas por lajes alveolares, conforme descrito na seção anterior. Os resultados e discussões detalhadas podem ser encontrados nos artigos publicados (FERREIRA et al., 2021b; FERREIRA; MARTINS; DE NARDIN, 2020b) que se encontram no Apêndice do presente trabalho.

4.4.1 Laje Alveolar LP15

Para avaliar a influência da capa de concreto, a razão do modelo numérico com e sem cobertura do concreto ($M_{FE,50}/M_{FE,0}$) foi calculada, conforme **Figura 4.13**.

Figura 4.13 –Influência da capa de concreto na capacidade resistente

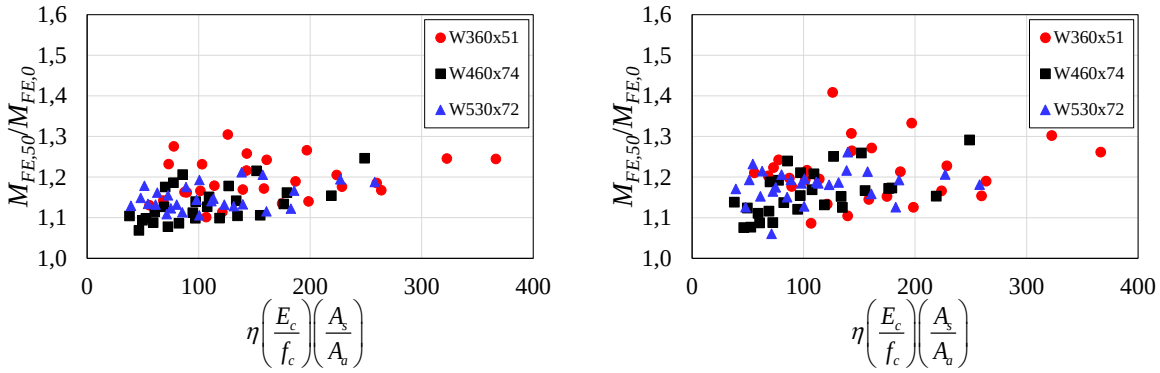

(a) $L/200$ (b) $L/100$

Dois pontos de deslocamentos foram monitorados, considerando o deslocamento vertical máximo no meio do vão ($L/200$) (GOUCHMAN, 2014), bem como o deslocamento

para o último incremento de carregamento, aproximadamente $L/100$. Nessas análises, foi observado um aumento de pelo menos 7% na capacidade resistente das vigas mistas devido a presença da capa de concreto. Além disso, a presença da capa de concreto resultou em melhorias na rigidez inicial do sistema estrutural. Tal aumento de capacidade resistente foi avaliado anteriormente por Baran (2015), considerando apenas a laje alveolar com capa de concreto. Alguns exemplos estão ilustrados na **Figura 4.14**. Além disso, foi possível observar que com o aumento do espaçamento entre os conectores, houve uma redução na capacidade resistente das vigas mistas.

Figura 4.14 – Aumento na rigidez inicial das vigas mistas

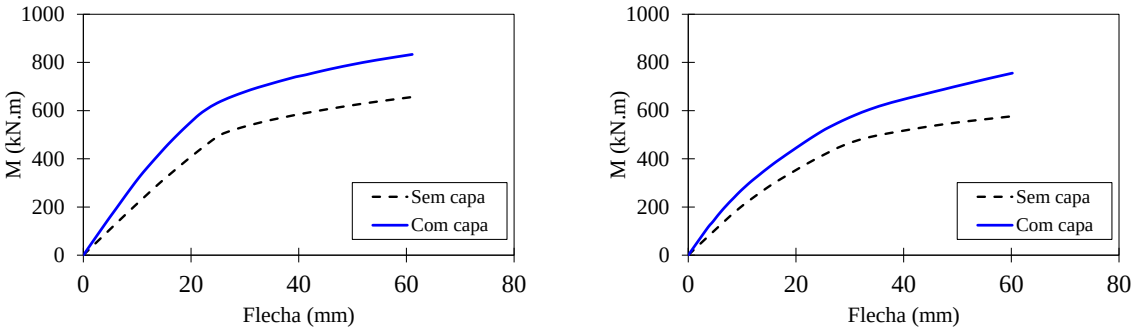

(a) W360: (n/2)=24, f_c=25 MPa and φ=16 mm (b) W360: (n/2)=13, f_c=25 MPa and φ=16 mm

Em relação a variação da resistência do concreto moldado in loco, foi verificado que quanto maior foi a resistência à compressão do concreto, maior foi o valor das tensões de von Mises nos conectores de cisalhamento. A **Figura 4.15** mostra alguns exemplos.

Figura 4.15 – Influência da resistência do concreto moldado in loco no conector de cisalhamento

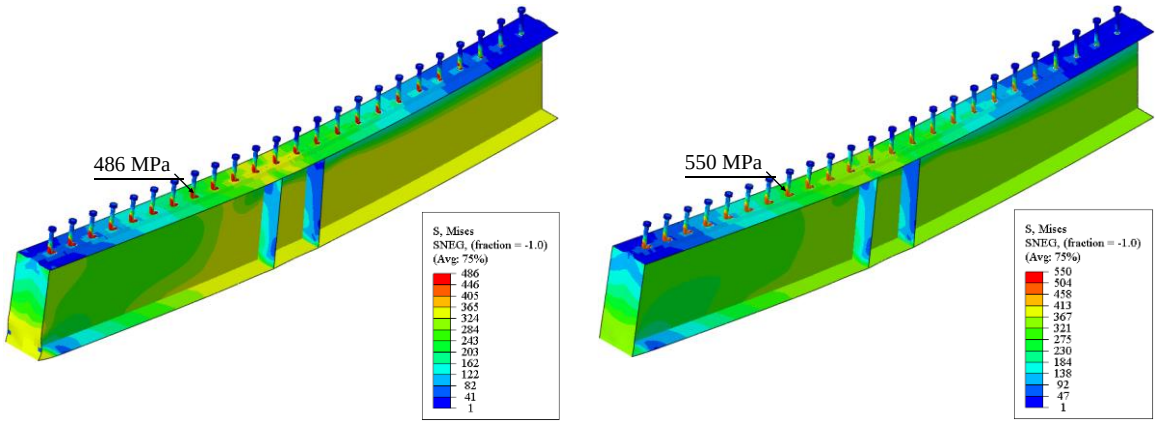

(a) f_c =30MPa e φ=10 mm (b) f_c =40MPa e φ =10 mm

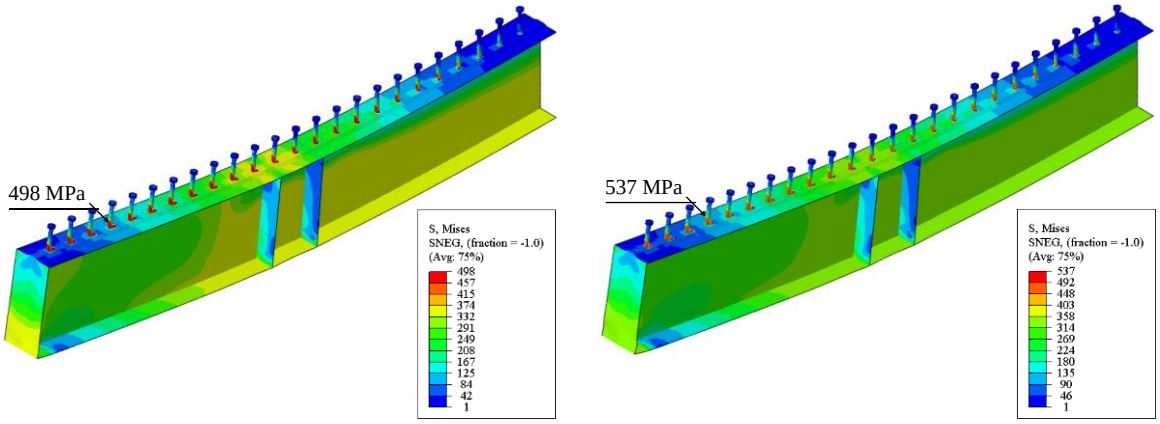

(c) f_c =30MPa e φ =16mm (d) f_c =40MPa e φ =16mm

Fonte: (FERREIRA; MARTINS; DE NARDIN, 2020b)

De acordo com ARAÚJO et al. (2016), quando a resistência média à compressão do concreto foi maior que 40MPa, a falha pode ocorrer na ruptura do conector tipo pino com cabeça, e quando a resistência média à compressão do concreto foi reduzida para menos de 30 MPa, a falha foi governada pelo esmagamento do concreto moldado in loco. No modelo numérico foi possível observar a fissuração do concreto causada pelas altas tensões nos conectores, e também pelo ponto de aplicação do carregamento (BATISTA; LANDESMANN, 2016).

Considerando a variação da taxa de armadura, a relação cortante por deslizamento foi afetada nos modelos que apresentaram (n/2)=24 e menor resistência à compressão do concreto moldado in loco. A taxa de armadura transversal, considerando o diâmetro de 16mm, proporcionou maior capacidade resistente nas vigas mistas com capa de concreto, para os modelos (n/2)=24. Por outro lado, com o aumento do espaçamento entre os conectores de cisalhamento, o diâmetro de 10 mm proporcionou maior capacidade resistente. Além disso, foi possível avaliar o comportamento dúctil com a variação da taxa de armadura, considerando o espaçamento entre os conectores (**Figura 4.16**). O parâmetro adotado para essa classificação foi 6mm de escorregamento, conforme o ensaio de cisalhamento direto apresentado no EN 1994-1-1 (2004). Vale ressaltar que é um tipo de ensaio diferente do que foi modelado. Conforme a ilustração, o comportamento dúctil foi observado, nos modelos (n/2)=24, para os perfis W460x74 e W530x72. Para o perfil W460x74, esse comportamento foi avaliado a partir dos modelos em que as vigas mistas apresentavam resistência à compressão do concreto moldado in loco de 30MPa e diâmetro da armadura transversal de 12,5mm. Em relação ao perfil W530x72, foi aferido apenas um modelo com o comportamento dúctil, conforme mostrado na **Figura 4.16c**.

Figura 4.16 – Valores do escorregamento na interface aço e concreto

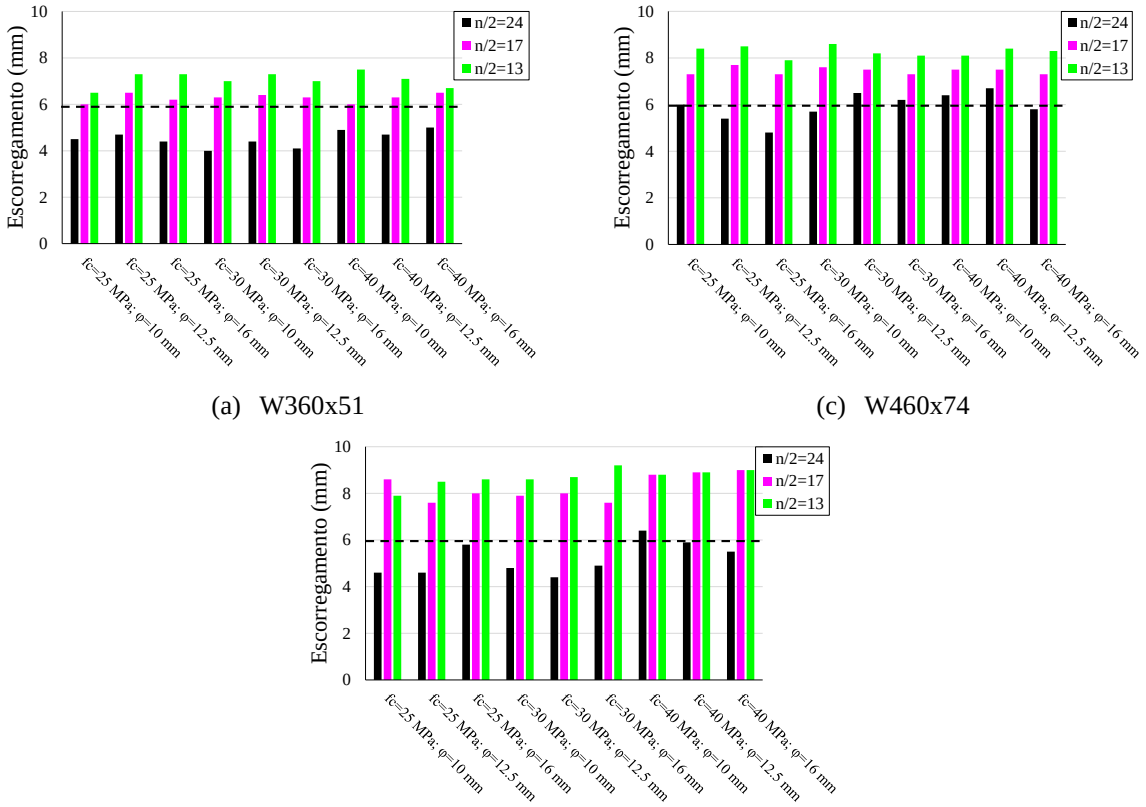

(a) W360x51 (c) W460x74

(d) W530x72

Fonte: (FERREIRA; MARTINS; DE NARDIN, 2020b)

Os resultados do estudo paramétrico foram comparados com as equações de cálculo resistente apresentados no item 4.1 (**Figura 4.17**), considerando os modelos de resistência dos conectores de cisalhamento apresentados na **Tabela 2.1** (ARAÚJO et al., 2016; GOUCHMAN, 2014).

Figura 4.17 – Comparação entre os modelos de resistência com os modelos numéricos

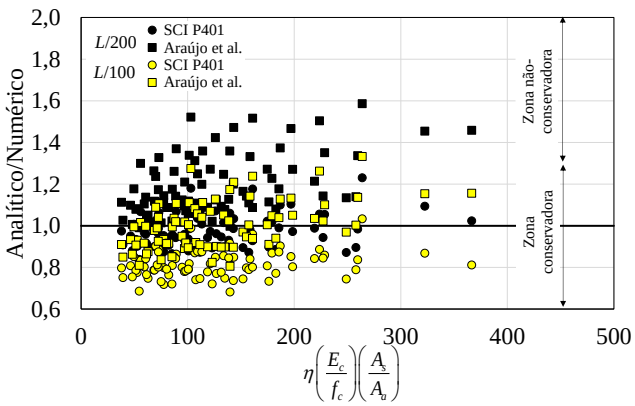

Fonte: (FERREIRA; MARTINS; DE NARDIN, 2020b)

Conforme a ilustração, considerando o limite de deslocamento igual a *L*/200, algumas situações foram encontradas na zona não conservadora. Por outro lado, considerando o deslocamento prescrito em aproximadamente *L*/100, grande parte dos modelos analisados se apresentaram na zona conservadora. Isso significa que os valores dos momentos fletores dos modelos numéricos foram superiores às recomendações.

4.4.2 Laje Alveolar LP26

Para as seções formadas pelo perfil W360x51, com a variação da taxa de armadura transversal e da resistência do concreto moldado in loco, não houve diferenças nas relações cortante por escorregamento e momento por flecha. A **Figura 4.18** ilustra alguns exemplos desses comportamentos, considerando as resistências do concreto moldado in loco igual a 25MPa e 40 MPa.

Figura 4.18 – Influência da taxa de armadura transversal para o perfil W360x51

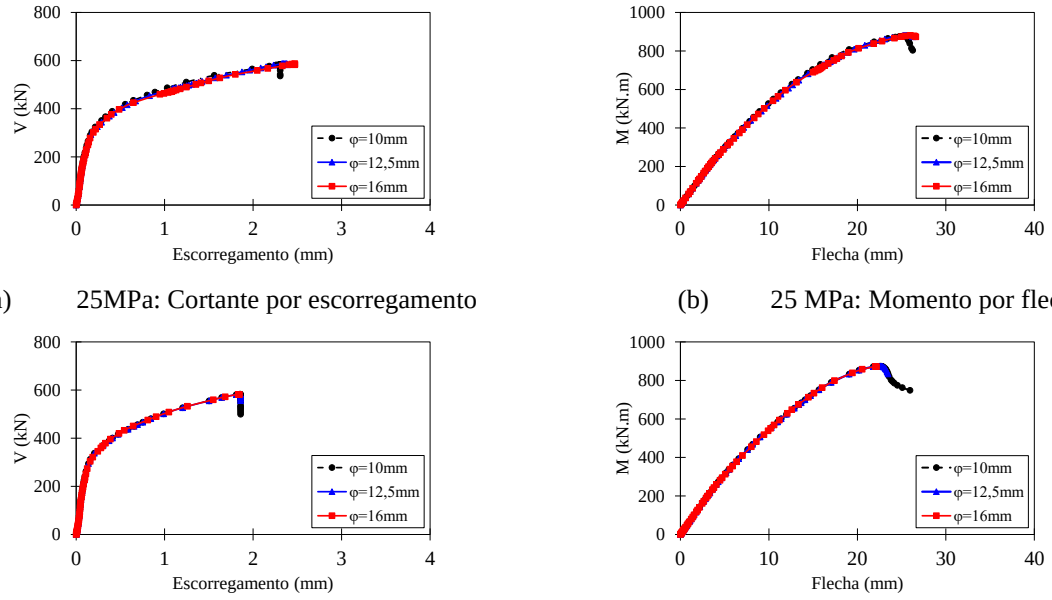

(a) 25MPa: Cortante por escorregamento (b) 25 MPa: Momento por flecha

(c) 40MPa: Cortante por escorregamento (d) 40 MPa: Momento por flecha

Fonte: (FERREIRA et al., 2021b)

Conforme as ilustrações acima, esse comportamento semelhante pode ser explicado em função das resistências axiais do perfil de aço e da laje alveolar. Nesse contexto, quando a linha neutra plástica se situa na laje alveolar, pode ocorrer fissuração excessiva devido as tensões de tração (**Figura 4.19**). Esta observação pode ser concluída, pois na configuração final, a parte superior da laje alveolar, que se encontrava na região de flexão pura, foi danificada.

Figura 4.19 – Configuração final para o modelo W360x51

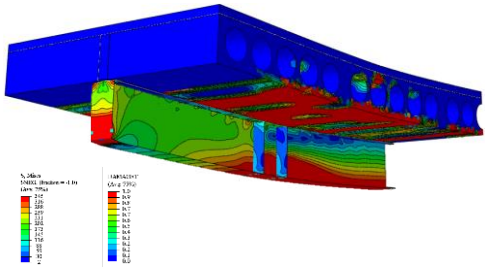

Fonte: (FERREIRA et al., 2021b)

Outra observação importante foi o comportamento frágil das vigas mistas (**Figura 4.18a e Figura 4.18c**), uma vez que os valores de escorregamento na interface aço-concreto foram menores que 6mm, parâmetro de referência para o ensaio de cisalhamento direto, conforme EN 1994-1-1 (2004). Devido a este comportamento frágil, como a fissuração excessiva da laje alveolar, bem como valores baixos de escorregamentos na interface aço-concreto, com a variação de parâmetros, como taxa de armadura transversal e resistência do concreto moldado in loco, não houve diferenças significativas na capacidade resistente dos modelos analisados.

Em relação a variação do espaçamento entre os conectores de cisalhamento, embora houve maiores escorregamentos na interface aço-concreto, a capacidade resistente foi governada pela fissuração excessiva na parte inferior da laje alveolar. Com o aumento da área de seção transversal de aço, isto é, considerando os modelos formados pelas seções W460x74 (**Figura 4.20a**) e W530x72 (**Figura 4.20b**), a capacidade resistente foi governada, também, pela fissuração excessiva da laje alveolar. A seguir, no item 4.4.3, é feito uma comparação entre as capacidades resistente entre os modelos LP15 e LP26.

Figura 4.20 – Configuração final para os modelos formados pelas seções W460x74 e W530x72

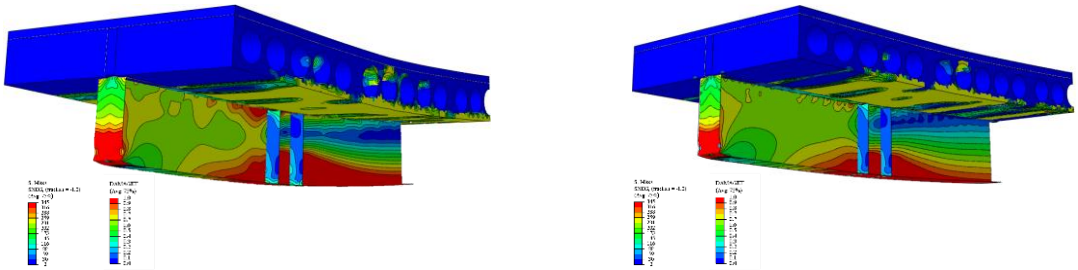

(a) W460x74 (b) W530x72

Fonte: (FERREIRA et al., 2021b)

4.4.3 Comparação Numérica

Nessa seção, uma comparação entre as capacidades resistentes dos modelos LP15 e LP26 é realizada (**Figura 4.21)**. Conforme a ilustração, em alguns modelos, os modelos LP26 mais proporcionaram uma maior capacidade resistente. Essa diferença atingiu um máximo de 30%, considerando a razão entre as capacidades resistentes dos modelos analisados. Esses valores foram aferidos considerando a seção W360x51. Com o aumento da seção transversal do perfil de aço (seções W460x74 e W530x72), essa diferença não foi tão significativa. Isso demonstrou que, para os modelos estudados, não foi vantajoso aumentar a altura da laje alveolar, uma vez que a capacidade resistente foi determinada pela fissuração excessiva da laje.

Figura 4.21 – Comparação da capacidade resistente entre os modelos LP15 e LP26, considerando a capa de concreto

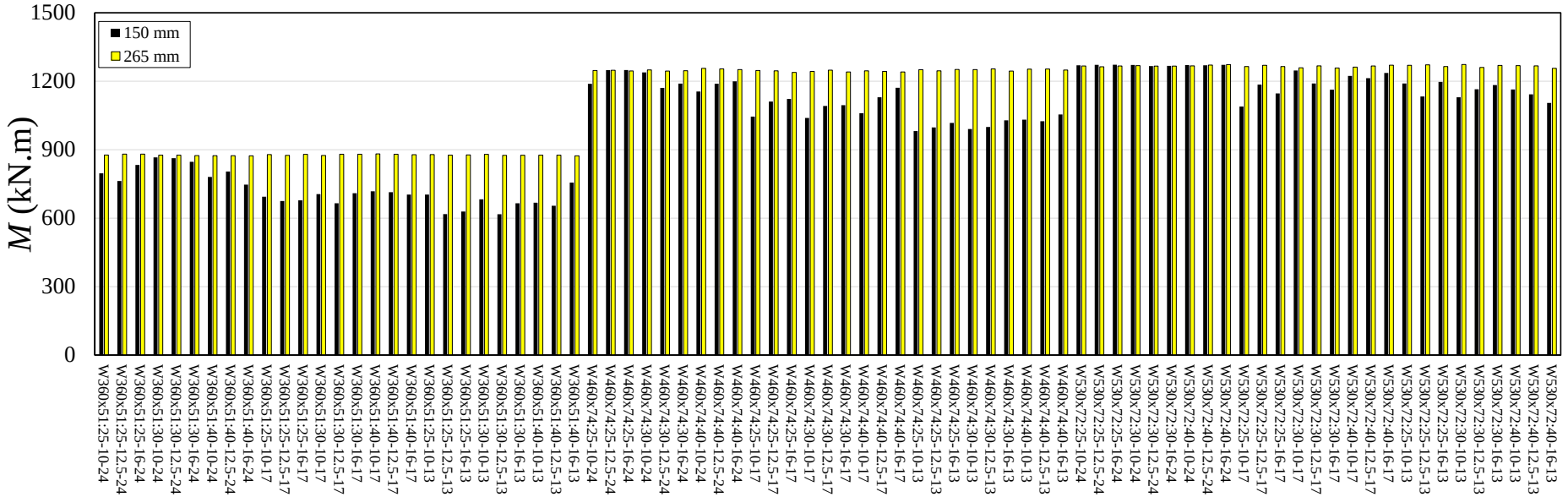

"Seção":"Resistência do concreto"-"Diâmetro"-"*n*/2"

Fonte: (FERREIRA et al., 2021b)

4.5 SÍNTESE E CONCLUSÕES

Os pontos mais importantes apresentados nesse capítulo são,

Considerando unidades alveolares LP15:

- A capa de concreto aumentou a capacidade resistente das vigas mistas com lajes alveolares pré-fabricadas em pelo menos 7%;
- Quanto maior a resistência à compressão do concreto moldado in loco, maior será o valor das tensões de von Mises nos conectores de cisalhamento;
- A área da seção transversal do aço influenciou a magnitude das tensões de von Mises na armadura transversal;
- Em relação ao espaçamento dos conectores de cisalhamento, para interação total ($n/2=24$):

1. As vigas mistas aço-concreto com laje alveolar e capa de concreto apresentaram maior capacidade resistente quando comparadas aos demais graus de interação;

2. Os valores de escorregamento na interface aço-concreto foram menores que 6mm;

3. A taxa de armadura transversal, considerando o diâmetro de 16mm, proporcionou maior capacidade resistente nas vigas mistas com capa de concreto;

- Interação parcial ($n/2=17$ e 13):

1. Com a redução do grau de interação, houve redução na capacidade resistente das vigas mistas com lajes alveolares pré-fabricadas;

2. Não houve diferenças significativas na capacidade resistente das vigas mistas com e sem capa de concreto, considerando a variação da resistência à compressão do concreto moldado in loco;

3. Com o aumento do espaçamento entre os conectores de cisalhamento, o diâmetro de 10mm proporcionou maior capacidade resistente.

Considerando unidades alveolares LP26:

1. Em todos os modelos, a capacidade resistente do sistema estrutural foi atingida pela fissuração excessiva da laje alveolar. Isso ocorreu porque a linha neutra plástica se encontra dentro da laje alveolar, fator que gera tensões de tração. Assim, o dimensionamento de vigas mistas de aço-concreto com lajes alveolares de maior altura não foi vantajoso, de acordo com

os modelos analisados. Isso porque a capacidade resistente foi governada pela laje de concreto, fator que não aproveita a seção de aço.

2. Quanto maior for a área da seção transversal de aço, maior será o aproveitamento da seção transversal de aço. Quando há uma seção transversal de aço maior área, há um aumento na resistência axial no perfil de aço. Este aumento faz com que a linha neutra plástica desça em direção ao perfil de aço, causando apenas tensões de compressão na laje alveolar.

3. Quanto maior o espaçamento entre os conectores de cisalhamento, maior será o aproveitamento da seção de aço. Ao considerar a hipótese de interação parcial, apresentada para os modelos de espaçamento de 175mm e 225mm, o sistema estrutural pode atingir comportamento dúctil, fator que favorece a capacidade dos elementos estruturais de se deformarem sem atingir a capacidade resistente. O uso de um número menor de conectores de cisalhamento (modelos de 175mm e 225mm) proporcionou capacidade resistente equivalente aos modelos de 120mm.

4. A taxa de armadura transversal teve pouca influência na capacidade resistente dos modelos analisados.

5. Com a variação da resistência do concreto moldado in loco, não houve diferenças significativas na capacidade resistente. Portanto, a utilização de menor resistência no concreto moldado in loco pode ser vantajosa, ou seja, quanto menor a resistência do concreto, menor será a resistência axial da laje, fator que faz com que a linha neutra plástica se desloque em direção ao perfil de aço.

6. O comportamento dúctil foi observado para os modelos com espaçamento de 225mm, considerando as seções W460x74 e W530x72. Também foi verificado que quanto menor o grau de interação, maior o deslocamento vertical do meio vão, podendo ultrapassar o limite de $L/200$.

7. Em relação à verificação da capacidade resistente com o procedimento de cálculo, alguns modelos considerando interação total mostraram-se contra a segurança ($M_{FE} \leq M_{Rk}$). Por outro lado, todas as observações considerando interação parcial mostraram-se seguras ($M_{FE} > M_{Rk}$).

8. Os modelos numéricos com unidades alveolares de 265mm apresentaram capacidade resistente maior do que os modelos com unidades alveolares de 150mm, considerando a seção W360x51. No entanto, para as seções W460x74 e W530x72, não houve diferenças significativas entre as comparações.

PARTE III:

VIGAS CELULARES MISTAS COM LAJES ALVEOLARES

5.

CAPACIDADE RESISTENTE DE VIGAS CELULARES MISTAS COM LAJES ALVEOLARES

As lajes alveolares pré-fabricadas de concreto e os perfis celulares de aço são elementos estruturais com aspectos muito interessantes para uso em edificações de vários andares. No entanto, não é uma associação que tem sido investigada pela comunidade científica e, embora as recomendações publicadas no SCI P355 (LAWSON; HICKS, 2011) e no *Steel Design Guide 31* (FARES; COULSON; DINEHART, 2016) sejam direcionadas ao comportamento de vigas mistas com aberturas na alma, tais recomendações se limitam a vigas mistas associadas às lajes mistas de aço e concreto.

O presente Capítulo tem como objetivo apresentar a avaliação da capacidade resistente de vigas celulares mistas com lajes alveolares pré-fabricadas de concreto. Três tipos de lajes foram estudados: laje alveolar (LP15), laje alveolar (LP15) com capa de concreto e laje mista. A unificação dos modelos numéricos desenvolvidos em vigas celulares mistas e vigas mistas formadas por lajes alveolares, que foram apresentadas nos Capítulos 3 e 4, respectivamente,

permitiu o desenvolvimento de um modelo numérico de vigas celulares mistas com lajes alveolares pré-fabricadas de concreto. Com o desenvolvimento desse modelo, foi realizado um estudo paramétrico, considerando as vigas celulares mistas biapoiadas, com vão de 6m. Seções simétricas (IPE 400) e assimétricas (IPE 400/HEB 340) foram consideradas. Para cada seção, a influência do tipo de laje foi estudada e os principais parâmetros, como a largura do montante de alma e o diâmetro da abertura, foram variados. No total 120 análises foram realizadas. Os resultados foram discutidos de acordo com os parâmetros apresentados e comparados com as recomendações técnicas (FARES; COULSON; DINEHART, 2016; LAWSON; HICKS, 2011).

O presente Capítulo inicia o estudo das análises definitivas em vigas celulares mistas com lajes alveolares pré-fabricadas de concreto. Estruturado em quatro seções, o Capítulo 5 apresenta a nova metodologia de validação numérica, bem como os seus respectivos resultados. Em seguida é mostrado as considerações gerais do estudo paramétrico. Finalmente, o presente Capítulo se encerra com a apresentação dos principais resultados e síntese das conclusões. O Capítulo 5 é fundamentado no artigo publicado "***Ultimate strength prediction of steel-concrete composite cellular beams with PCHCS***" (FERREIRA et al., 2021c). Dessa forma o texto é escrito de maneira resumida, com o objetivo de apenas apresentar ao leitor a metodologia que já foi desenvolvida e validada. Maiores informações e detalhes podem ser encontradas no Apêndice do presente trabalho.

Os seguintes símbolos são usados neste Capítulo:

b_c	largura da laje de concreto;	D_o	diâmetro de abertura;
b_f	largura da mesa;	d	altura da seção original de aço;
b_w	largura do montante de alma;	d_g	altura da viga celular;
b_{we}	largura do montante de extremidade;		

5.1 MODELAGEM DE VIGAS CELULARES MISTAS COM LAJES ALVEOLARES

Conforme apresentado anteriormente, nos Capítulos 3 e 4 foram desenvolvidos e validado um modelo numérico capaz de representar o comportamento de vigas celulares mistas com lajes mistas e vigas mistas com lajes alveolares pré-fabricadas, respectivamente. No presente Capítulo, tais modelos numéricos foram combinados de forma a elaborar o modelo numérico de vigas celulares mistas com lajes alveolares pré-fabricadas (**Figura 5.1**). Para isso, os modelos constitutivos dos materiais foram unificados. Vale ressaltar que no Capítulo 3 foram considerados os modelos de Guo (2014) e Yun e Gardner (2017) para o concreto e o aço, respectivamente, enquanto que no Capítulo 4 foram considerados os modelos de Carreira e Chu (1985, 1986) e elasto-plástico perfeito para o concreto e o aço, respectivamente. Dessa forma, foi necessário fazer uma nova etapa de validação, considerando os modelos experimentais que foram apresentados nas **Tabela 3.2** e **Tabela 4.1**, que será descrita a seguir.

Figura 5.1 – Modelo de viga celular mista com laje alveolar pré-fabricada de concreto

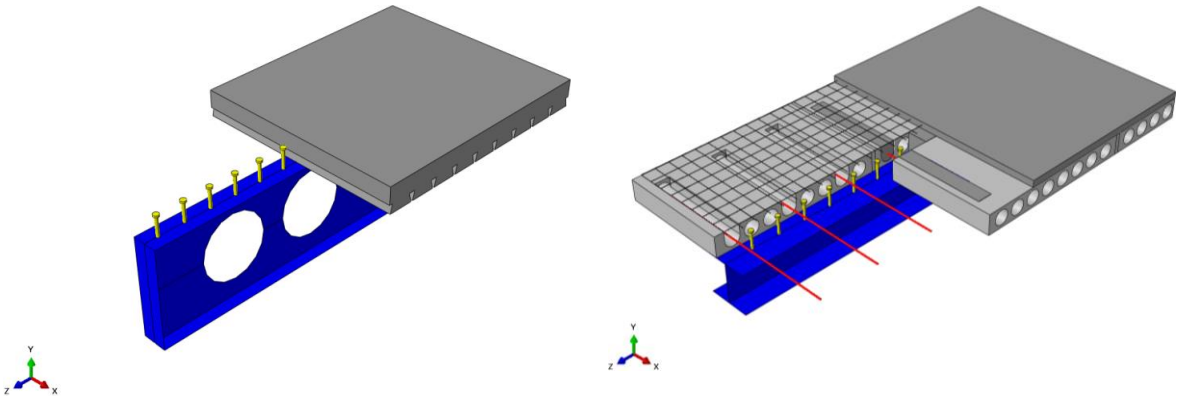

(a) Viga celular mista com laje mista

(b) Viga mista com laje alveolar

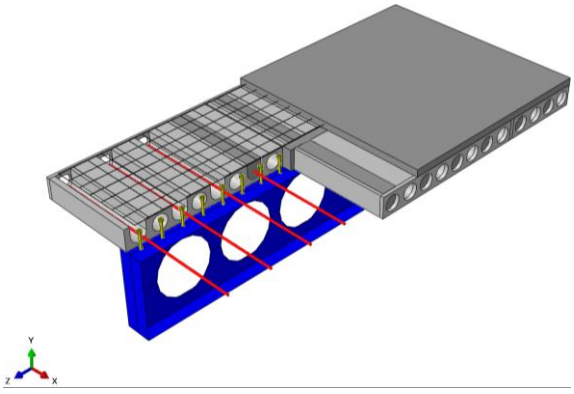

(c) Viga celular mista com laje alveolar

5.1.1 Análises

Como a viga celular mista é suscetível ao fenômeno de instabilidade no montante de alma, as análises foram realizadas em duas etapas: elástica (*buckling*) e inelástica (*post-buckling*) – conforme apresentado no Capítulo 3. Para recordar, a análise elástica é realizada para estimar a carga crítica de flambagem por meio de autovalores e seus respectivos autovetores. Na análise inelástica são consideradas a não-linearidade física e geométrica, incluindo as imperfeições geométricas iniciais. A configuração deformada na análise elástica, normalizada para a amplitude de imperfeição inicial, é adotada como a deformação inicial dessa nova análise.

5.1.2 Materiais

Com o objetivo de unificar os modelos numéricos, em uma nova etapa de validação, foram utilizados os mesmos modelos constitutivos dos materiais. Nesse contexto, para o concreto foi utilizado os modelos de Carreira e Chu (1985, 1986), conforme apresentado no Capítulo 4. A armadura transversal e a tela de aço foram modeladas com o modelo elasto-plástico perfeito (**Figura 5.2a**); para os conectores tipo pino com cabeça, o modelo bilinear (**Figura 5.2b**) foi adotado; e por fim, para as vigas celulares, o modelo quadrilinear (YUN; GARDNER, 2017) foi utilizado (**Figura 5.2c**), conforme apresentado no Capítulo 3.

Figura 5.2 – Modelos constitutivos para o aço

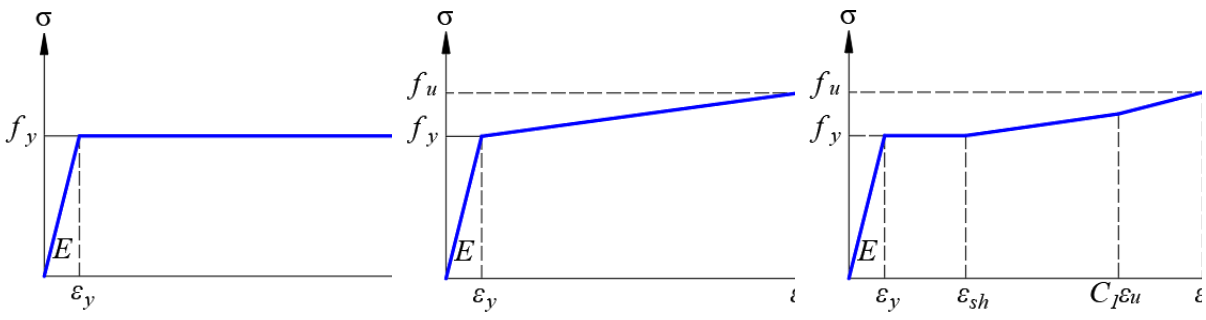

(b) Elasto-plástico perfeito (c) Bilinear (d) Quadrilinear

5.1.3 Superfícies de Contato

As superfícies de contato (**Figura 5.3**) foram aplicadas conforme descrito anteriormente nos Capítulos 3 e 4.

Figura 5.3 – Superfícies de contato

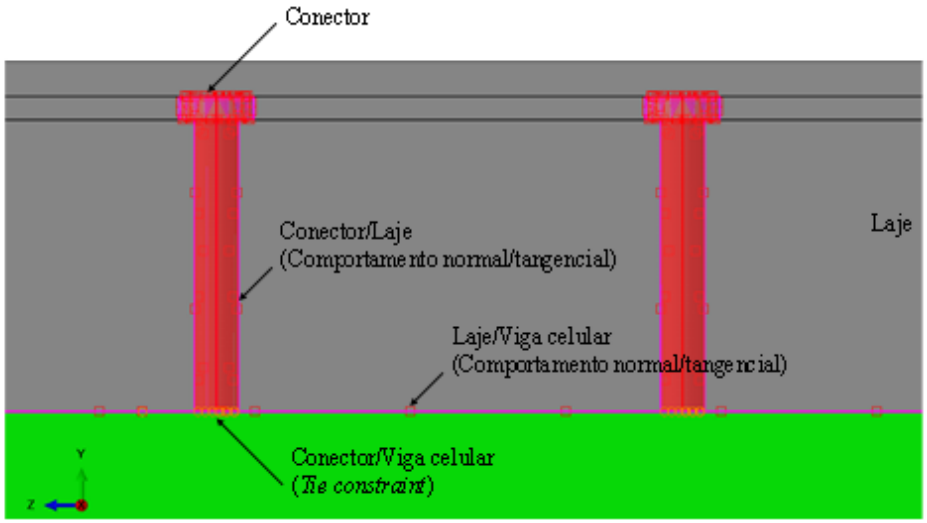

Conforme a ilustração, a aderência perfeita (*tie constraint*) foi aplicada entre as superfícies inferiores dos conectores de cisalhamento e a mesa superior da viga celular, e entre o concreto pré-fabricado e o concreto moldado in loco (FERREIRA; MARTINS; DE NARDIN, 2020b). Os contatos entre o concreto e a armadura transversal, bem como o concreto e a tela de aço, foram feitos através do *embedded region*. Os conectores de cisalhamento foram representados na modelagem e alocados no volume de concreto da laje. Nessa metodologia, o mesmo volume do conector de cisalhamento é cortado da laje (KATWAL et al., 2020; WIJESIRI PATHIRANA et al., 2016). Objetivo dessa remoção de volume é tal que ocorra a interação entre as superfícies de contato da laje e o conector de cisalhamento. O comportamento tangencial é baseado no modelo de atrito de Coulomb. Os valores dos coeficientes de atrito foram tomados iguais a 0,2 e 0,3 para as interfaces entre a laje-conector e o perfil de aço e laje de concreto, respectivamente (GUEZOULI; LACHAL, 2012).

5.1.4 Condições de Contorno e Discretização

Os tipos de elementos, as dimensões, discretização e condições de contorno, estão de acordo com o descrito nos Capítulos 3 e 4. A **Figura 5.4** traz a discretização e condições de contorno de vigas celulares com lajes alveolares pré-fabricadas de concreto.

Figura 5.4 – Discretização e condições de contorno

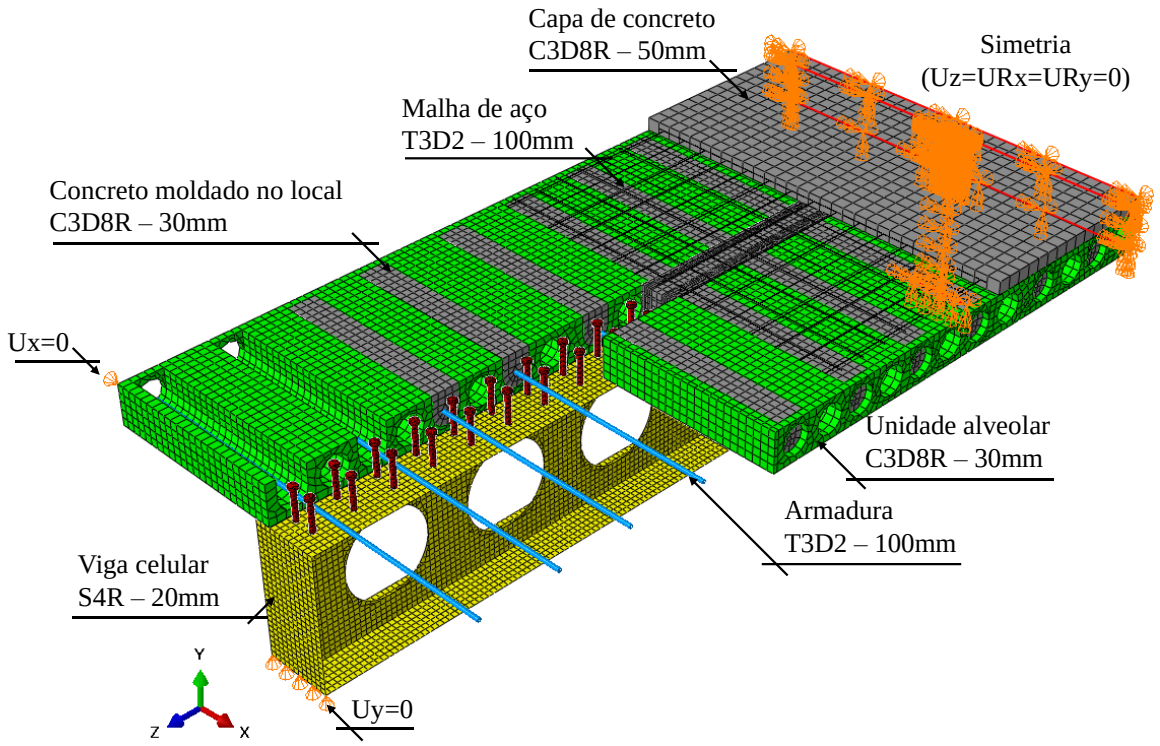

5.1.5 Resultados de Validação

Os resultados de validação são apresentados na **Tabela 5.1** e **Figura 5.5**. Maiores informações sobre a etapa de validação podem ser consultadas no artigo publicado (FERREIRA et al., 2021c), que se encontra no Apêndice do presente trabalho.

Tabela 5.1 – Resultados de validação

Modelo	Sistema Estrutural	P_{Exp} (kN)	P_{FE} (kN)	P_{FE}/P_{Exp}
CCB1	Viga celular mista	370	373	1,01
CCB2	Viga celular mista	430	425	0,99
CCB3	Viga celular mista	806	808	1,00
CCB4	Viga celular mista	658	655	1,00
CB1	Viga mista com laje alveolar	331	331	1,00
CB2	Viga mista com laje alveolar	316	323	1,02
CB3	Viga mista com laje alveolar	442	469	1.06
			Média	1,01
			Desvio padrão	2,17%
			Variância	0,05%

Figura 5.5 – Resultados de validação

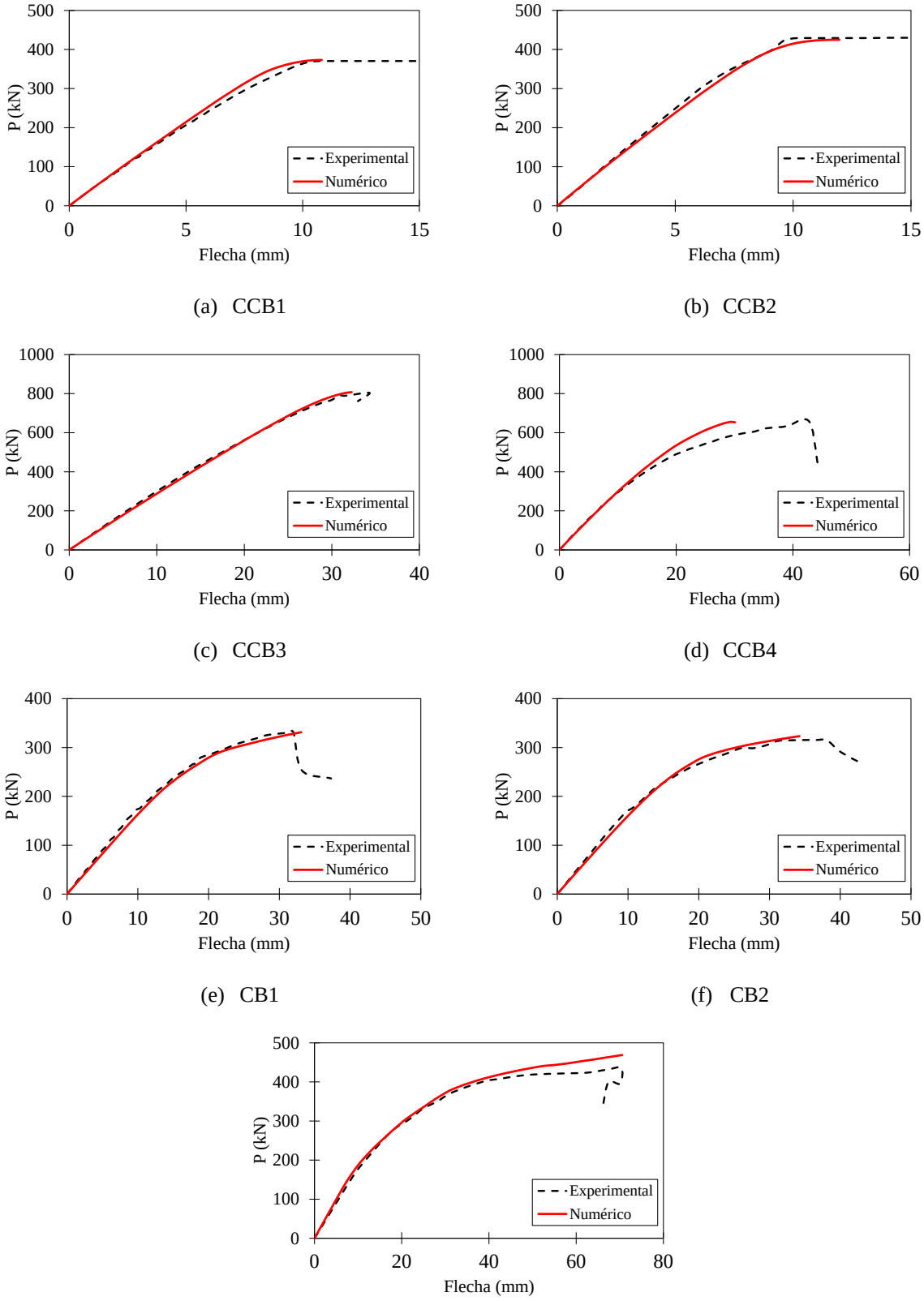

(a) CCB1 (b) CCB2

(c) CCB3 (d) CCB4

(e) CB1 (f) CB2

(g) CB3

De acordo com os resultados ilustrados, é possível aferir que os modelos de vigas mistas de aço e concreto formados por lajes alveolares pré-fabricadas foram calibrados. Tal calibração é fundamental para a realização do estudo paramétrico que é descrito a seguir.

5.2 MODELAGEM NUMÉRICA: ESTUDO PARAMÉTRICO

A seguir são apresentadas as considerações gerais para o desenvolvimento do estudo paramétrico:

1. São consideradas duas seções, conforme **Tabela 5.2**;

Tabela 5.2: Seções analisadas

Seções (Tê superior/ Tê inferior)	d_g	D_o/d	p/D_o	D_o	p	$i/2$
IPE 400 e IPE 400/HEB 340	580	0,8	1,2	320	384	7
		0,8	1,3	320	416	7
		0,8	1,4	320	448	6
		0,8	1,5	320	480	6
		0,9	1,2	360	432	6
		0,9	1,3	360	468	6
		0,9	1,4	360	504	5
		0,9	1,5	360	540	5
		1,0	1,2	400	480	6
		1,0	1,3	400	520	5
		1,0	1,4	400	560	5
		1,0	1,5	400	600	4
		1,1	1,2	440	528	5
		1,1	1,3	440	572	5
		1,1	1,4	440	616	4
		1,1	1,5	440	660	4
		1,2	1,2	480	576	5
		1,2	1,3	480	624	4
		1,2	1,4	480	672	4
		1,2	1,5	480	720	4

2. Para cada seção, três tipos de lajes são estudados: vigas mistas com lajes mistas e unidades LP15 (**Figura 4.3c**) com e sem capa de concreto;

3. Para o perfil celular, considera-se o aço ASTM Gr.50. O módulo de elasticidade e o coeficiente de Poisson são iguais a 200 GPa e 0,3, respectivamente;
4. A resistência à compressão do concreto moldado no local é de 30 MPa, e a resistência à compressão da laje alveolar é de 40 MPa;
5. Para a unidade LP15, foi considerado o preenchimento do 1º, 3º, 5º e 7º alvéolos, sendo colocada uma armadura transversal com 16mm de diâmetro;
6. Para a laje alveolar, é considerado 70mm de garganta;
7. A espessura da capa concreto é de 50mm;
8. A tela de aço tem 4,2mm com espaçamento de 100mm;
9. A dimensão dos pinos com cabeça é 19x120mm, espaçados em 150mm;
10. As vigas mistas são biapoiadas, conforme condições de contorno apresentadas na seção 5.1 (**Figura 5.6**), com vão de 6 m;
11. A largura da laje é igual a ¼ do vão;
12. É considerada a flexão de quatro pontos e as cargas são aplicadas a 2m dos apoios. Enrijecedores foram alocados nos pontos de aplicação de carga e apoios (**Figura 5.6**).

Figura 5.6 – Flexão em quatro pontos

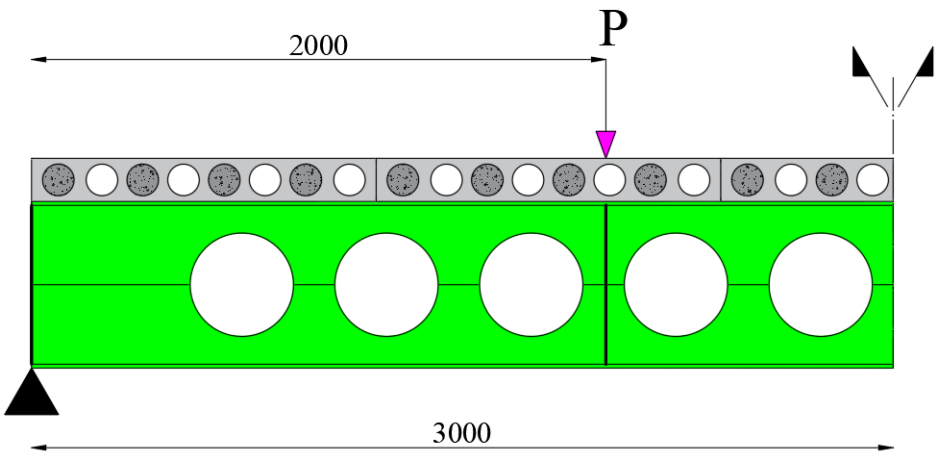

A seguir, nos itens 5.3 e 5.4, são apresentados os principais resultados do estudo paramétrico e conclusões extraídas da análise paramétrica (**Figura 5.7**), respectivamente.

Figura 5.7 – Síntese do estudo paramétrico em vigas celulares mistas com lajes alveolares

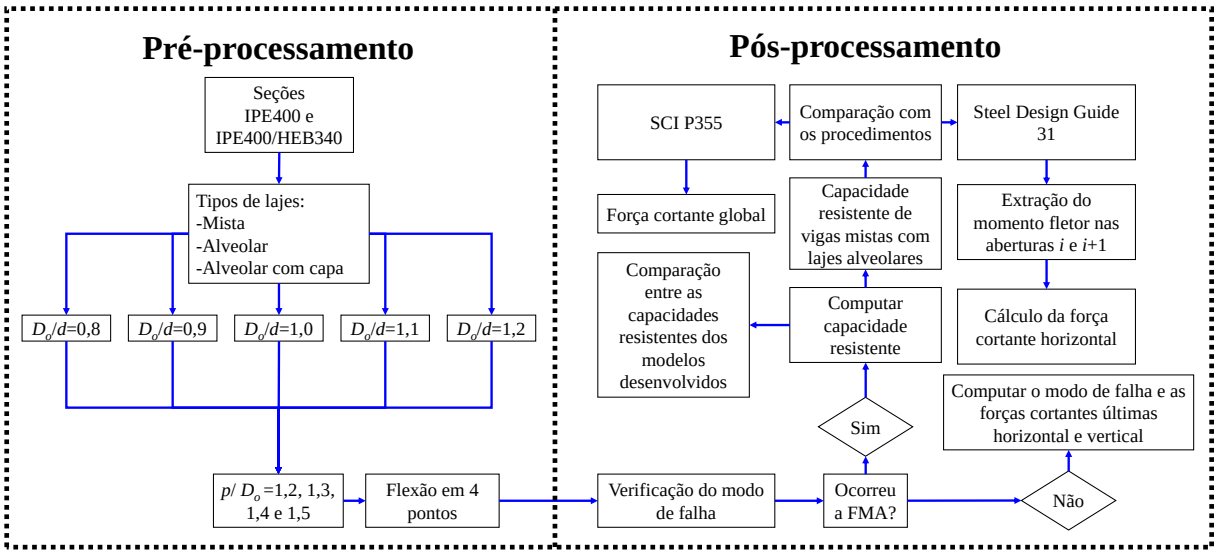

5.3 PRINCIPAIS RESULTADOS DO ESTUDO PARAMÉTRICO

Essa seção tem como objetivo apresentar alguns dos principais resultados do estudo paramétrico desenvolvido em vigas celulares mistas formadas por lajes alveolares, conforme descrito na seção anterior. Os resultados e discussões detalhadas podem ser encontrados no artigo publicado(FERREIRA et al., 2021c), que se encontra no Apêndice do presente trabalho.

5.3.1 Seções Simétricas

Os principais resultados dos modelos com seções simétricas são apresentados na **Figura 5.8**. Conforme mostrado na **Figura 5.8a**, para os modelos D_o/d=0,8, os quais apresentam maior altura das seções têm em relação as demais séries D_o/d, as diferenças máximas entre as capacidades resistentes dos modelos com laje alveolar e laje mista ($V_{Alveolar}$-V_{mista}), laje alveolar com capa e laje mista ($V_{Alveolar,c}$-V_{mista}), e laje alveolar com capa e laje alveolar ($V_{Alveolar,c}$-$V_{Alveolar}$) foram 22kN, 62kN e 54kN, respectivamente. Esses valores foram aferidos para os modelos p/D_o=1,4-1,5 e b_{we}/b_w=1,3-2,9. Nestes casos, os modelos com laje alveolar obtiveram maior capacidade resistente quando comparados aos modelos de laje mista. Isso significa que a laje contribuiu significativamente para o aumento da capacidade resistente das vigas celulares mistas. Para os modelos D_o/d=0,9 (**Figura 5.8b**), as diferenças máximas entre os valores de capacidade resistente foram $V_{Alveolar}$-V_{mista}=29kN (p/D_o=1,4 e b_{we}/b_w=3,8),

$V_{Alveolar,c}$-V_{mista}=86kN (p/D_o=1,4 e b_{we}/b_w=3,8), e $V_{Alveolar,c}$-$V_{Alveolar}$=64kN (p/D_o=1,5 e b_{we}/b_w=2,2). Embora nos presentes modelos as alturas das seções tês diminuíram com o aumento do diâmetro, a largura do montante de extremidade aumentou. Assim, quando as capacidades resistentes foram comparadas ao modelo anterior (D_o/d=0,8), as diferenças entre os tipos de laje aumentaram, evidenciando a influência da largura do montante de extremidade na capacidade resistente.

Figura 5.8 – Capacidade resistente os modelos de seção simétrica

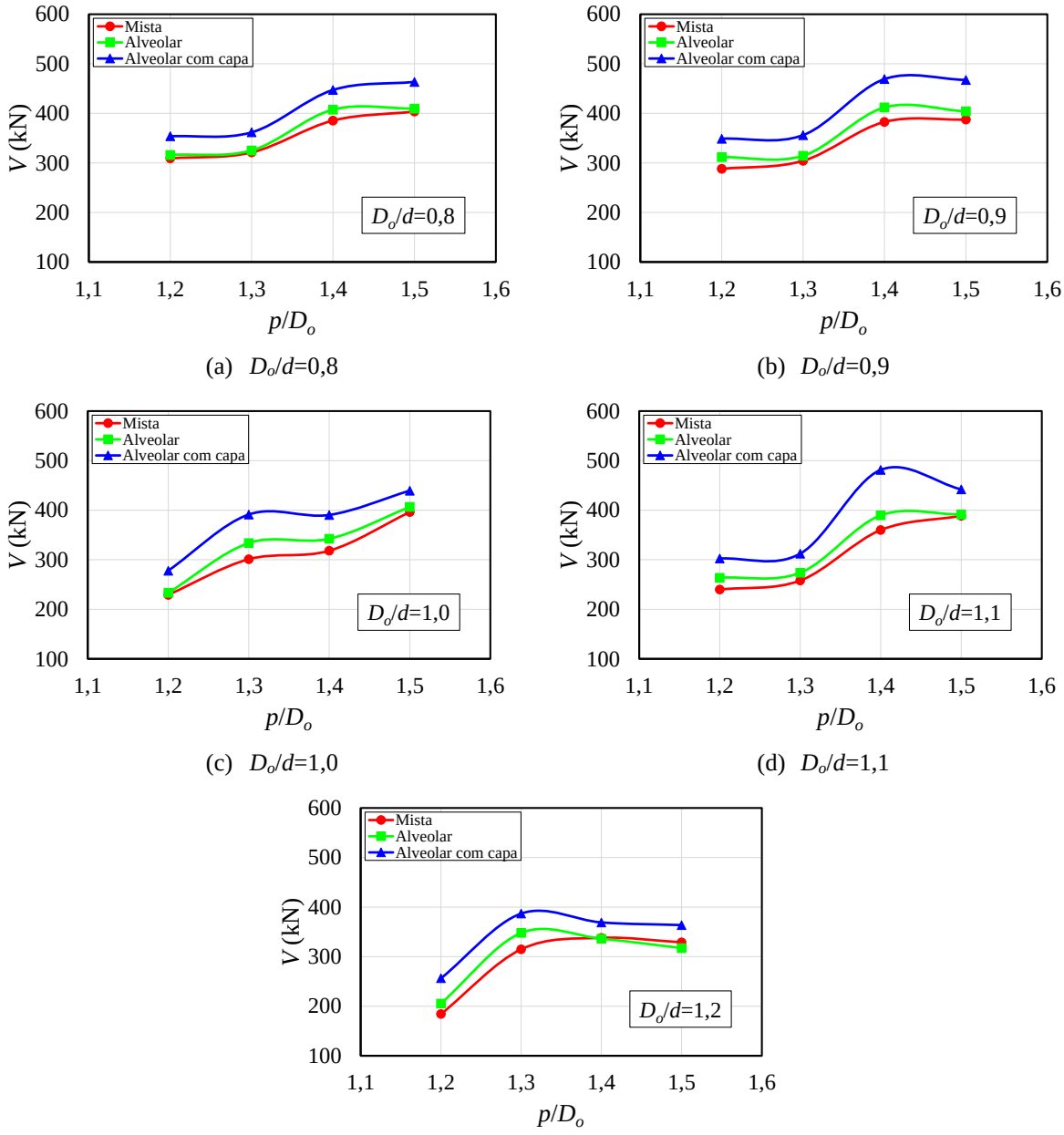

(a) D_o/d=0,8 (b) D_o/d=0,9

(c) D_o/d=1,0 (d) D_o/d=1,1

(e) D_o/d=1,2

Fonte: (FERREIRA et al., 2021c)

Para os modelos D_o/d=1,0 (**Figura 5.8c**), as diferenças máximas entre as capacidades resistentes foram medidas para p/D_o=1,3. Os valores obtidos foram $V_{Alveolar}$-V_{mista}=33kN, $V_{Alveolar,c}$-V_{mista}=90kN e $V_{Alveolar,c}$-$V_{Alveolar}$=57kN. Para essas situações, foi observado a FMA. Considerando os modelos D_o/d=1,1 (**Figura 5.8d**), as diferenças máximas $V_{Alveolar}$-V_{mista}, $V_{Alveolar,c}$-V_{mista}, e $V_{Alveolar,c}$-$V_{Alveolar}$ foram 29kN, 121kN e 92kN, respectivamente. Esses valores foram aferidos para os modelos p/D_o=1,4 e b_{we}/b_w=3,5. Nesses casos, à medida que o diâmetro de abertura foi aumentado, a diferença entre as capacidades resistentes dos modelos com laje alveolar e laje mistas diminuía. Entretanto, as diferenças entre as capacidades resistentes desses dois tipos de laje, quando comparadas às PCHCS com cobertura de concreto, aumentaram. Finalmente, considerando os modelos D_o/d=1,2, (**Figura 5.8e**), para as análises em que a FMA foi observadas (p/D_o=1,2), as diferenças foram $V_{Alveolar}$-V_{mista}=21kN, $V_{Alveolar,c}$-V_{mista}=72kN e $V_{Alveolar,c}$-$V_{Alveolar}$=51kN. A seguir na **Tabela 5.3**, são apresentados os valores da razão entre $V_{PCHCSCT}/V_{PCHCS}$ para a avaliação do ganho de capacidade resistente em função da presença da capa de concreto.

Tabela 5.3: Influência da capa de concreto no sistema misto com laje alveolar para a seção simétrica

D_o/d	p/D_o	b_{we}/b_w	$V_{PCHCSCT}/V_{PCHCS}$	D_o/d	p/D_o	b_{we}/b_w	$V_{PCHCSCT}/V_{PCHCS}$
0,8	1,2	5,4	1,12	1,1	1,2	4,6	1,15
	1,3	1,4	1,11		1,3	1,6	1,14
	1,4	2,9	1,10		1,4	3,5	1,24
	1,5	1,3	1,13		1,5	2,1	1,13
0,9	1,2	6,2	1,12	1,2	1,2	1,8	1,25
	1,3	2,3	1,13		1,3	4,0	1,11
	1,4	3,8	1,14		1,4	2,1	1,10
	1,5	2,2	1,16		1,5	1,0	1,15
1,0	1,2	2,0	1,19				
	1,3	3,8	1,17				
	1,4	1,8	1,14				
	1,5	3,5	1,08				

Para os demais modelos, os quais apresentaram algum mecanismo plástico, as diferenças entre as capacidades resistentes diminuíram, uma vez que esse modo de falha é

limitado pela capacidade resistente dos têes. Alguns exemplos dessas diferenças discutidas são ilustrados na **Figura 5.9**.

Figura 5.9 – Trajetórias de equilíbrio: seções simétricas

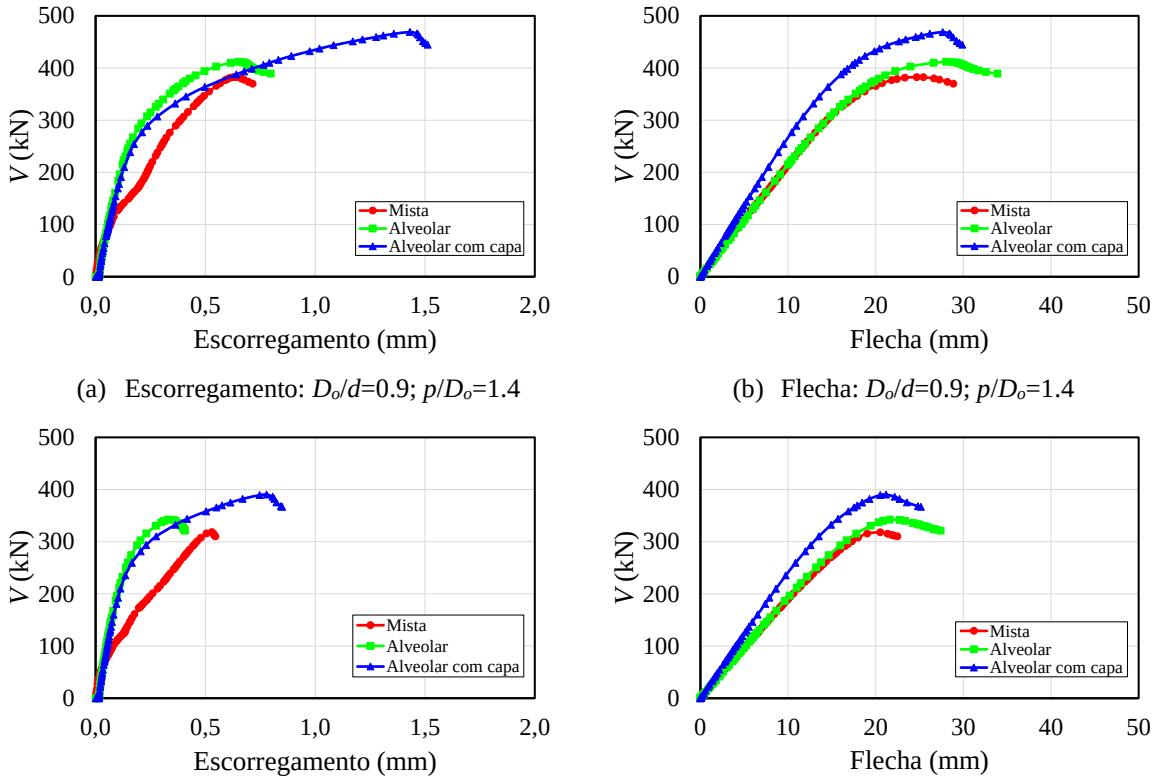

(a) Escorregamento: D_o/d=0.9; p/D_o=1.4

(b) Flecha: D_o/d=0.9; p/D_o=1.4

(c) Escorregamento: D_o/d=1.0; p/D_o=1.4

(d) Flecha D_o/d=1.0; p/D_o=1.4

Fonte: (FERREIRA et al., 2021c)

5.3.2 Seções Assimétricas

A **Figura 5.10** ilustra os principais resultados para a seção assimétrica. Considerando os modelos D_o/d=0,8 (**Figura 5.10a**), as diferenças máximas entre as capacidades resistentes foram $V_{Alveolar}$-V_{mista}=25kN, $V_{Alveolar,c}$-V_{mista}=74kN e $V_{Alveolar,c}$-$V_{Alveolar}$=64kN. Esses valores foram aferidos para os modelos p/D_o=1,3-1,4 e b_{we}/b_w=1,3-2,9. Para os modelos D_o/d=0,9 (**Figura 5.10b**), as diferenças máximas entre os valores de capacidade resistente foram $V_{Alveolar}$-V_{mista}=46kN (p/D_o=1,2 e b_{we}/b_w=6,2), $V_{Alveolar,c}$-V_{mista}=90kN (p/D_o=1,3 e b_{we}/b_w=2,3), e $V_{Alveolar,c}$-$V_{Alveolar}$=76 kN (p/D_o=1,3 e b_{we}/b_w=2,3). Considerando os modelos D_o/d=1,0 (**Figura 5.10c**), as diferenças máximas entre as capacidades resistentes foram analisadas para os modelos p/D_o=1,2; 1,4. Os valores obtidos foram $V_{Alveolar}$-V_{mista}=49kN (p/D_o=1,2), $V_{Alveolar,c}$-V_{mista}=91kN (p/D_o=1,4) e $V_{Alveolar,c}$-$V_{Alveolar}$=77kN (p/D_o=1,4). Durante essas análises foi observado a combinação da FMA com algum mecanismo plástico seguido da ruptura do conector de

cisalhamento. Para os modelos D_o/d=1,1 (**Figura 5.10d**), as diferenças máximas entre as capacidades resistentes foram $V_{Alveolar}$-V_{mista}=65kN, $V_{Alveolar,c}$-V_{mista}=88kN e $V_{Alveolar,c}$-$V_{Alveolar}$=68kN. Esses valores foram observados para os modelos p/D_o=1,2-1,3 e b_{we}/b_w=1,6-4,6. Finalmente, considerando os modelos D_o/d=1,2, (**Figura 5.10e**), as diferenças entre as capacidades resistentes foram $V_{Alveolar}$-V_{mista}=81kN (p/D_o=1,5), $V_{Alveolar,c}$-V_{mista}=103kN (p/D_o=1,5) e $V_{Alveolar,c}$-$V_{Alveolar}$=56kN (p/D_o=1,4). Na **Figura 5.11**, alguns exemplos dessas diferenças são ilustrados.

Figura 5.10 – Capacidade resistente os modelos de seção assimétrica

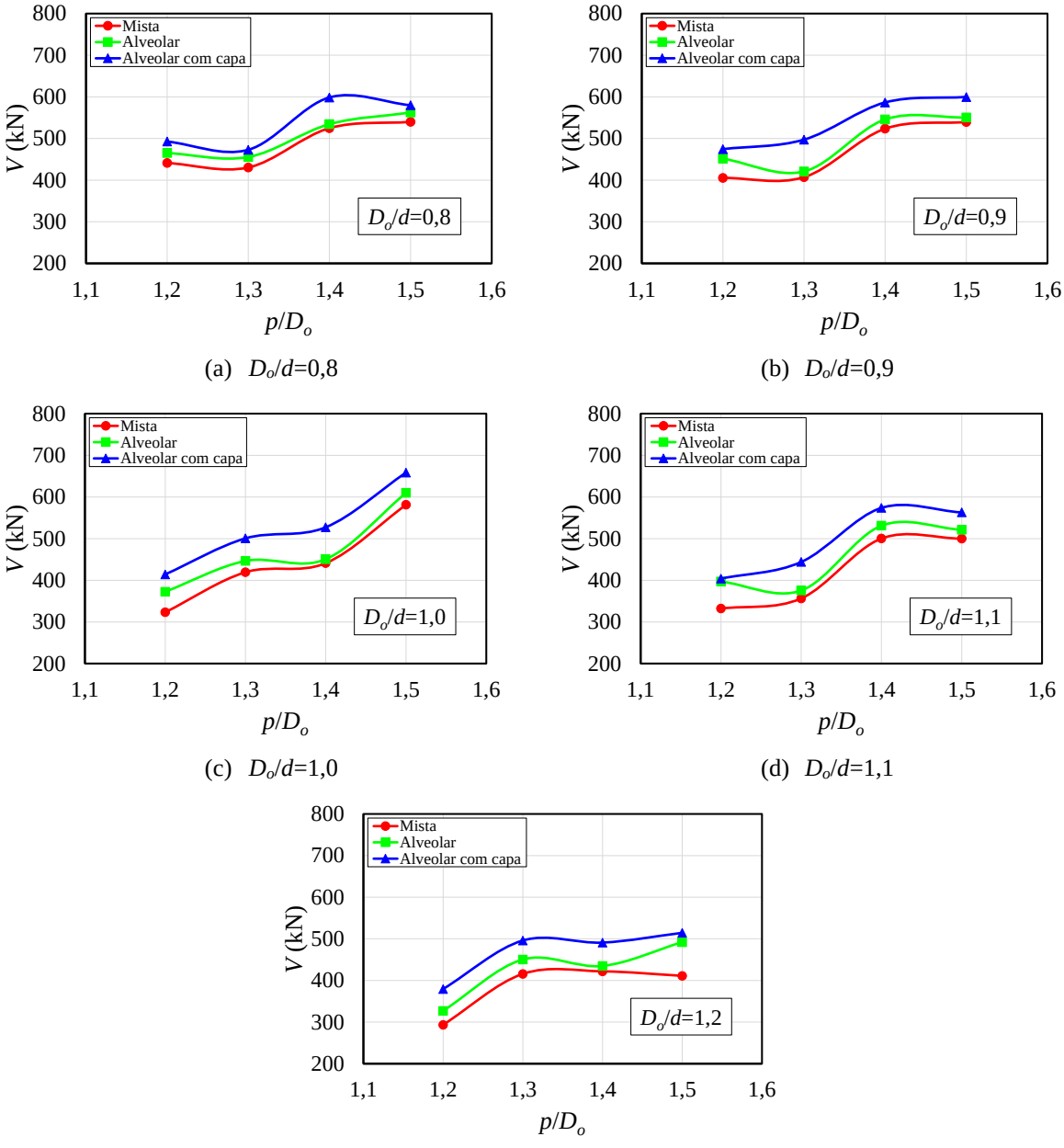

(a) D_o/d=0,8 (b) D_o/d=0,9

(c) D_o/d=1,0 (d) D_o/d=1,1

(e) D_o/d=1,2

Fonte: (FERREIRA et al., 2021c)

Figura 5.11 – Trajetórias de equilíbrio: seções assimétricas

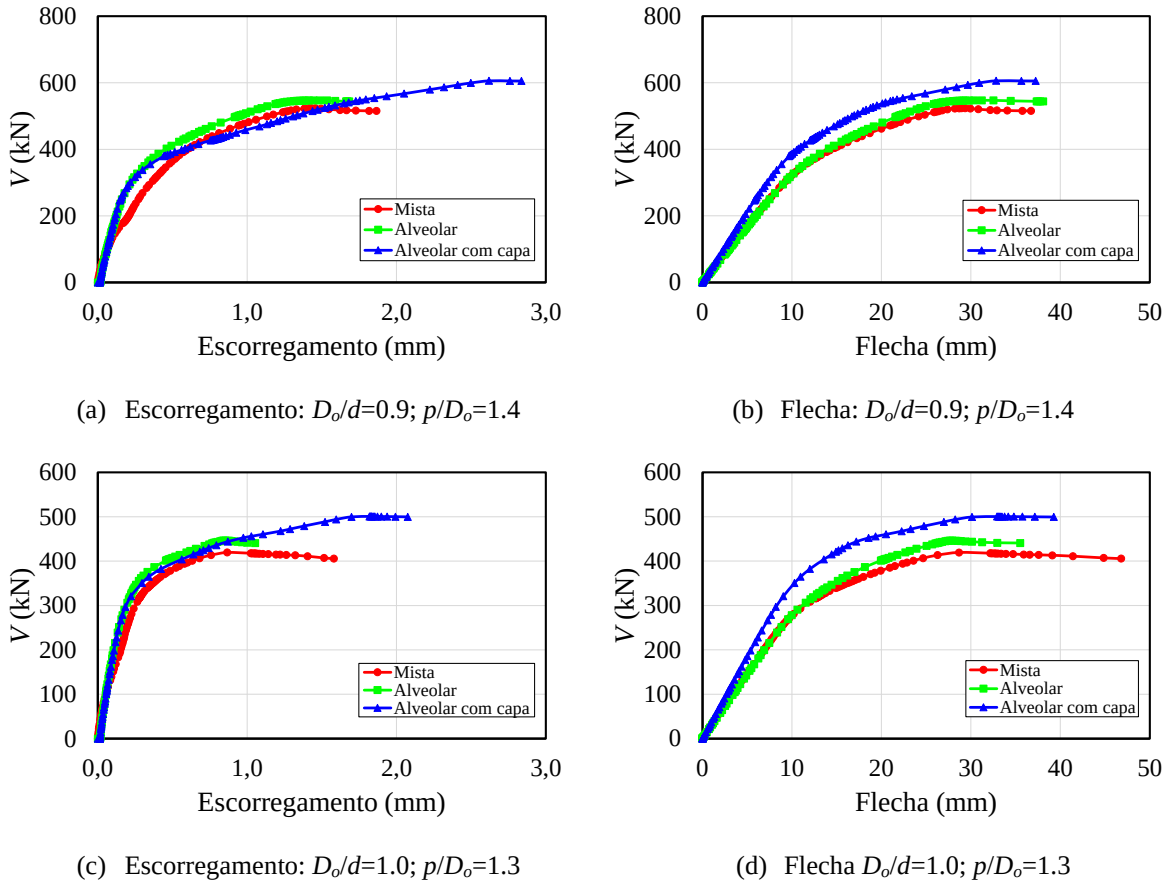

(a) Escorregamento: D_o/d=0.9; p/D_o=1.4

(b) Flecha: D_o/d=0.9; p/D_o=1.4

(c) Escorregamento: D_o/d=1.0; p/D_o=1.3

(d) Flecha D_o/d=1.0; p/D_o=1.3

Fonte: (FERREIRA et al., 2021c)

A seguir na **Tabela 5.4**, são apresentados os valores da razão entre $V_{PCHCSCT}/V_{PCHCS}$ para a avaliação do ganho de capacidade resistente em função da presença da capa de concreto.

Em geral, na comparação dos modelos com laje mistas e lajes alveolares, a seção assimétrica apresentou maior capacidade resistente. Por outro lado, considerando os modelos de laje alveolar com capa de concreto, as seções simétricas apresentaram maior capacidade resistente. Isso se deve ao fato de que os modelos analisados de seções assimétricas obtiveram um maior número de observações em que ocorreu a ruptura do conector de cisalhamento.

Tabela 5.4: Influência da capa de concreto no sistema misto com laje alveolar para a seção assimétrica

D_o/d	p/D_o	b_{we}/b_w	$V_{PCHCSCT}/V_{PCHCS}$	D_o/d	p/D_o	b_{we}/b_w	$V_{PCHCSCT}/V_{PCHCS}$
0,8	1,2	5,4	1,06	1,1	1,2	4,6	1,02
	1,3	1,4	1,04		1,3	1,6	1,18
	1,4	2,9	1,12		1,4	3,5	1,08
	1,5	1,3	1,03		1,5	2,1	1,08
0,9	1,2	6,2	1,05	1,2	1,2	1,8	1,16
	1,3	2,3	1,18		1,3	4,0	1,10
	1,4	3,8	1,07		1,4	2,1	1,13
	1,5	2,2	1,09		1,5	1,0	1,05
1,0	1,2	2,0	1,11				
	1,3	3,8	1,12				
	1,4	1,8	1,17				
	1,5	3,5	1,08				

5.4 SÍNTESE E CONCLUSÕES

Os pontos mais importantes apresentados nesse capítulo são:

- As capacidades resistentes de vigas celulares mistas com lajes alveolares pré-fabricadas e capa de concreto apresentaram diferença significativa e superior quando comparados às capacidades resistentes de vigas celulares mistas associadas às lajes mistas;
- Os resultados mostraram que a capacidade resistente das vigas celulares mistas não é limitada apenas pelo perfil celular de aço;
- Os modos de falha observados foram instabilidade no montante de alma, instabilidade no montante de alma acompanhada de mecanismo plástico, mecanismo de plástico e mecanismo de Vierendeel;
- Em algumas situações foi observada a ruptura do conector de cisalhamento. Isso mostrou que a variação da largura do montante de alma contribuiu para a mudança no grau de interação;
- Na maioria das observações, a capacidade resistente das vigas celulares mistas com lajes alveolares pré-fabricadas apresentou capacidade resistente igual ou superior aos modelos de vigas celulares mistas com lajes mistas. Isso significa que modelos de cálculo existentes, como SCI-P355 e *Steel Design Guide 31*, podem ser usados para projetar tais sistemas estruturais;
- O uso de modelos de cálculo atuais pode subestimar a capacidade resistente de vigas celulares mistas com lajes alveolares pré-fabricadas e capa de concreto. Isso se deve ao fato de a laje alveolar com capa de concreto apresentar maior capacidade resistente aos demais modelos.

6.

AÇÃO MISTA NA CAPACIDADE RESISTENTE À INSTABILIDADE DO MONTANTE DE ALMA

Com o desenvolvimento do modelo numérico de vigas celulares mistas compostas por lajes alveolares pré-fabricas de concreto, apresentado no Capítulo 5, foi possível investigar a capacidade resistente desse sistema estrutural.

Conforme apresentado no Capítulo 2, a capacidade resistente de vigas celulares mistas é governada pela instabilidade do montante de alma ou pela formação do mecanismo Vierendeel, acompanhada pelos mecanismos relacionados à laje de concreto. No estudo paramétrico apresentado no Capítulo 5 foi verificado, em alguns modelos, a ocorrência simultânea da instabilidade no montante de alma e do mecanismo plástico, acompanhado ou não da falha do conector de cisalhamento. A formação de algum mecanismo plástico como o mecanismo Vierendeel é afetada por parâmetros como a espessura da alma, o diâmetro da abertura e o número conectores de cisalhamento acima do comprimento crítico da abertura. O número de conectores acima da abertura promove a ação mista local entre o tê superior e a laje

de concreto (**Figura 6.1**) (KERDAL; NETHERCOT, 1984; LAWSON et al., 2006; REDWOOD; CHO, 1993). Nas vigas celulares, o comprimento crítico (l_o) é tomado igual a 0,45D_o (LAWSON; HICKS, 2011; LAWSON *et al*., 2006). Esse valor é equivalente a largura de uma abertura retangular.

Figura 6.1 – Ação mista entre o tê superior e a laje de concreto

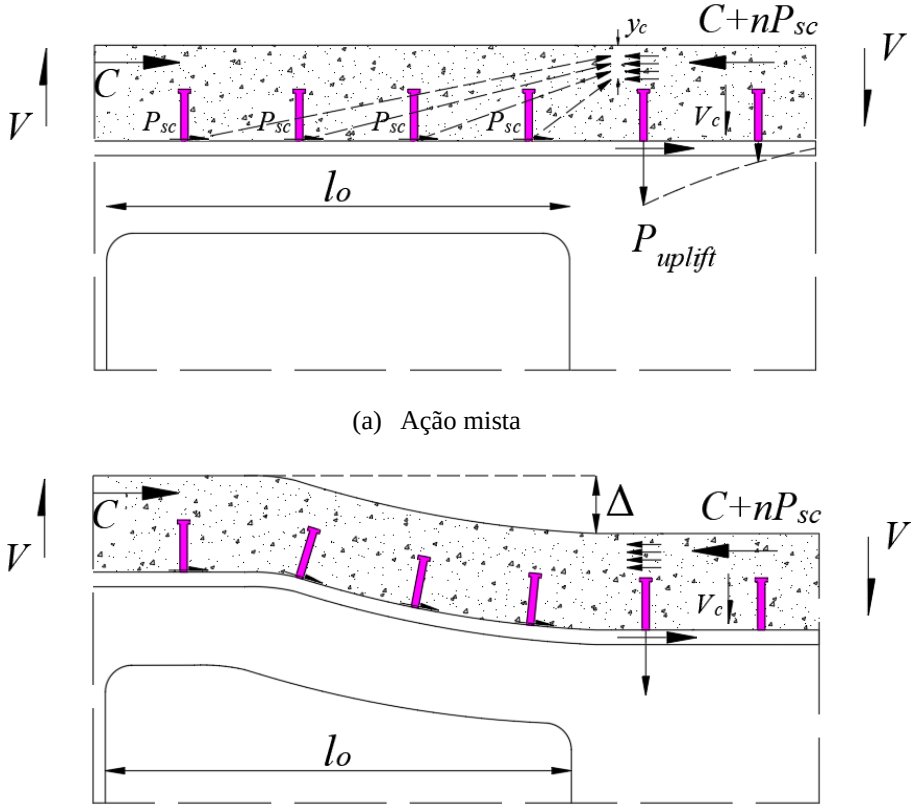

(a) Ação mista

(b) Efeito da flexão ao longo da abertura

Fonte: adaptado de (LAWSON et al., 2006)

Conforme mostrado na **Figura 6.1**, a SCI P355 (LAWSON; HICKS, 2011) descreve que a magnitude da resistência da ação mista local é dependente da flexibilidade da viga na abertura, a qual causa deflexões relativas entre o perfil celular e a laje, podendo causar o arrancamento do conector de cisalhamento, devido às tensões de tração verticais desenvolvidas próximas a borda superior da abertura. Vale ressaltar que essa flexibilidade tende aumentar com o aumento do comprimento do vão, bem como o aumento do diâmetro de abertura (LAWSON; LIM; POPO-OLA, 2013).

Para verificação de vigas celulares mistas existem, atualmente, duas recomendações: SCI P355 (LAWSON; HICKS, 2011) e a *Steel Design Guide 31* (FARES; COULSON;

DINEHART, 2016), que são fundamentadas no EN 1992-1-1 (2004) e ANSI/AISC 360-16, respectivamente. Ambas as publicações se referem às vigas celulares mistas formadas por lajes mistas de aço e concreto, condição em que a posição dos conectores de cisalhamento é limitada pela fôrma de aço. As recomendações do SCI P355 levam em conta a influência dos conectores de cisalhamento tanto na verificação da flexão (interação total ou parcial) quanto na resistência ao mecanismo Vierendeel. Por outro lado, o *Steel Design Guide 31* considera a resistência dos conectores de cisalhamento apenas na verificação da flexão.

Na literatura são encontrados diversos estudos que investigaram a influência dos conectores de cisalhamento localizados acima do comprimento da abertura em vigas mistas com abertura na alma (CHO; REDWOOD, 1992a, 1992b; DONAHEY; DARWIN, 1988; REDWOOD; POUMBOURAS, 1983, 1984). No entanto, tais estudos se concentraram em vigas mistas com uma única abertura retangular na alma, situação diferente daquela em que há aberturas sequenciais na alma, como é o caso das vigas celulares mistas.

No presente Capítulo é investigada a influência do espaçamento dos conectores de cisalhamento na capacidade resistente à força cortante global de vigas celulares mistas. É realizado um estudo paramétrico no qual são avaliados parâmetros como a largura do montante de alma e o diâmetro da abertura bem como o espaçamento entre os conectores de cisalhamento (150mm, 300mm e 450mm), dispostos em uma ou duas linhas de conexão. Para isso, foram analisados 240 modelos considerando análises não-lineares geométrica e física. A capacidade resistente à força cortante global que causa a instabilidade no montante de alma é investigada em função do espaçamento e do número de conectores de cisalhamento. Os resultados permitiram propor uma equação simplificada para estimar a capacidade resistente à instabilidade no montante de alma que leva em consideração a força cortante resistente global à instabilidade no montante da alma, a ação mista e mecanismo Vierendeel. Tal equação pode prever o valor limite da força cortante global na capacidade resistente de vigas celulares mistas formadas por lajes alveolares pré-fabricadas de concreto.

O presente Capítulo é fundamentado no artigo "***Composite action on web post buckling shear resistance of composite cellular beams with PCHCS and PCHCSCT***" que se encontra no Apêndice. Nesse contexto, o Capítulo foi dividido em quatro itens: estudo paramétrico; principais resultados e discussão; modelo analítico para a previsão da capacidade resistente; síntese e conclusões.

Os seguintes símbolos são usados neste Capítulo:

A_T	área da seção tê	P_{sc}	resistência do conector de cisalhamento
A_{wT}	área da alma do tê	p	comprimento do montante de alma
b_f	largura da mesa	s	espaçamento
b_w	diferença entre o comprimento do montante de alma pelo diâmetro de abertura (p-D_o)	t_f	espessura da mesa
D_o	diâmetro de abertura	t_w	espessura da alma
d	altura da seção original	V	força cortante global
d_{sc}	diâmetro do conector de cisalhamento	$V_{pl,T}$	cortante resistente plástica do tê
d_g	altura da viga celular	V_{VC}	resistência à cortante devido à ação mista
$f_{cr,w}$	tensão crítica no montante de alma	V_{WPB}	cortante resistente devido à instabilidade no montante de alma
g	garganta	z_{pl}	altura do eixo plástico neutro do tê à face externa da mesa
h_c	altura de concreto acima da fôrma de aço	y_t	altura do centro geométrico do tê à face externa da mesa
h_{eff}	altura efetiva da viga celular	λ_0	fator de esbeltez reduzida
h_s	altura total da laje	λ_w	esbeltez da alma
k	número de linhas de conectores	χ	fator de redução
L	comprimento da viga celular mista		
l_o	comprimento da abertura		
l_{eff}	comprimento efetivo do montante de alma		
n	número de conectores para L/2		

6.1 MODELAGEM NUMÉRICA: ESTUDO PARAMÉTRICO

No presente estudo é utilizado o mesmo modelo numérico que foi desenvolvido e validado no Capítulo 5.

As seguintes considerações gerais se aplicam ao estudo paramétrico aqui apresentado:

1. A dimensão do conector de cisalhamento foi mantida constante na análise. O conector tem diâmetro de 19mm e altura de 125mm, arranjado em uma ou duas fileiras, e com espaçamento longitudinal de 150mm, 300mm ou 450mm (**Figura 6.2**). O espaçamento transversal entre os conectores é constante e igual a $4d_{sc}$;

Figura 6.2 – Espaçamento dos conectores de cisalhamento para estudo paramétrico

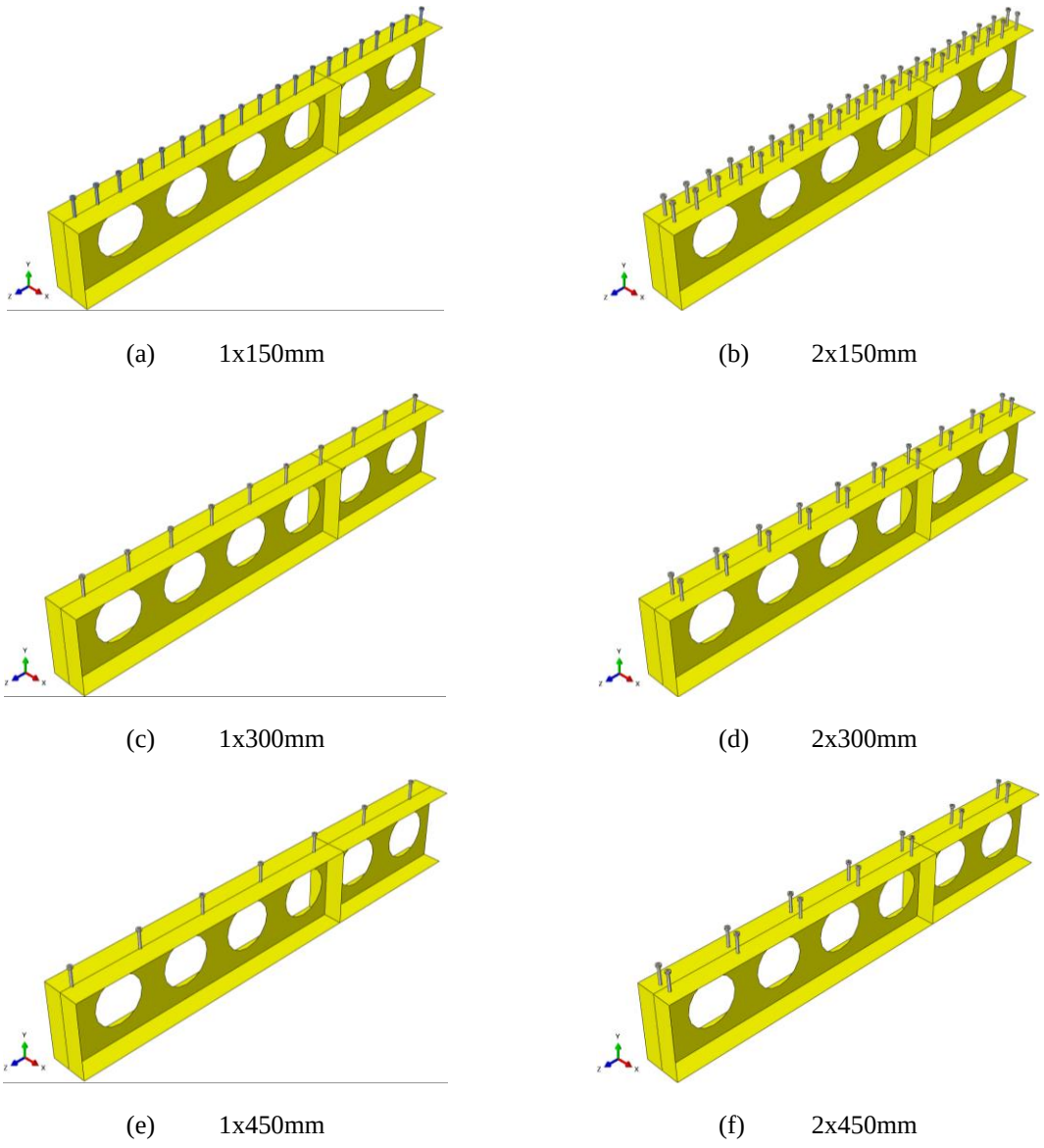

(a) 1x150mm (b) 2x150mm

(c) 1x300mm (d) 2x300mm

(e) 1x450mm (f) 2x450mm

2. Tomando como referência as especificações do EN 1994-1-1 (2004) e SCI P355 (LAWSON; HICKS, 2011), a **Tabela 6.1** apresenta os valores mínimo e máximo dos graus de interação (n/n_f) para cada série analisada, sendo n o número de conectores de cisalhamento entre os pontos de momento nulo e máximo. No caso das vigas biapoiadas, foi tomado o número de conectores entre o apoio e o meio vão. O número de conectores de cisalhamento necessários para interação total (n_f) foi definido pelo menor valor entre a resistência à compressão da laje de concreto e a resistência à tração do perfil celular.

Tabela 6.1 – Grau de interação dos modelos

Modelo	1x150mm	2x150mm	1x300mm	2x300mm	1x450mm	2x450mm
n	20	40	10	20	7	14
n/n_f	0,40-0,47	0,81-0,93	0,20-0,23	0,40-0,47	0,14-0,16	0,28-0,33

3. O perfil W360x91 é considerado como seção original e a partir dele se deu a expansão. A altura total da seção celular (d_g) é de 530 mm;
4. Perfis em aço ASTM A572 Grau 50 (f_y=345 MPa e f_u=450 MPa) e módulo de elasticidade igual a 200 GPa;
5. As razões p/D_o e D_o/d variam entre 1,2-1,5 e 0,8-1,2, respectivamente;
6. Garganta com largura de 130mm;
7. Unidades alveolares LP15 foram consideradas (conforme apresentadas nos Capítulos 4 e Capítulo 5). Os 1º, 3º, 5º e 7º alvéolos foram preenchidos e armadura transversal com 16mm de diâmetro foi considerada
8. Capa de concreto com 50mm de espessura;
9. Concreto de preenchimento com 30 MPa de resistência à compressão e laje alveolar confeccionada com concreto com resistência à compressão igual a 40 MPa;
10. Viga celular mista com 6m de vão e laje com largura igual a $L/4$ sendo L o vão da viga;
11. As vigas celulares mistas são biapoiadas e submetidas a flexão em quatro pontos, com as cargas espaçadas simetricamente de 2m em relação aos apoios. Enrijecedores foram inseridos no ponto de aplicação de carga e no apoio.

A seguir, nos itens 6.2, 6.3 e e 6.4, são apresentados os principais resultados do estudo paramétrico, proposta de previsão da capacidade resistente e síntese conclusões extraídas da análise paramétrica (**Figura 6.3**), respectivamente.

Figura 6.3 – Síntese do estudo paramétrico para a análise da ação mista

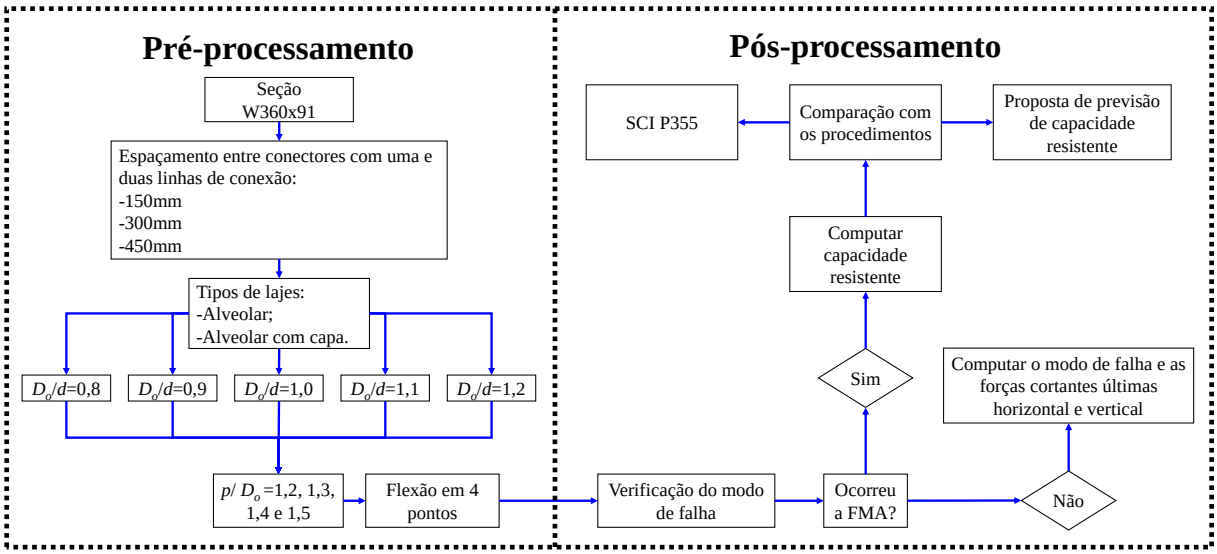

6.2 PRINCIPAIS RESULTADOS DO ESTUDO PARAMÉTRICO

Esta seção reúne os principais resultados do estudo paramétrico realizado para investigar a ação mista em vigas celulares mistas. Mais informações sobre os resultados e discussões podem ser encontrados no Apêndice do presente trabalho. Ao todo foram desenvolvidos 240 modelos numéricos e alguns exemplos dos modos de falha identificados são ilustrados na **Figura 6.4**.

Figura 6.4 – Modos de falha

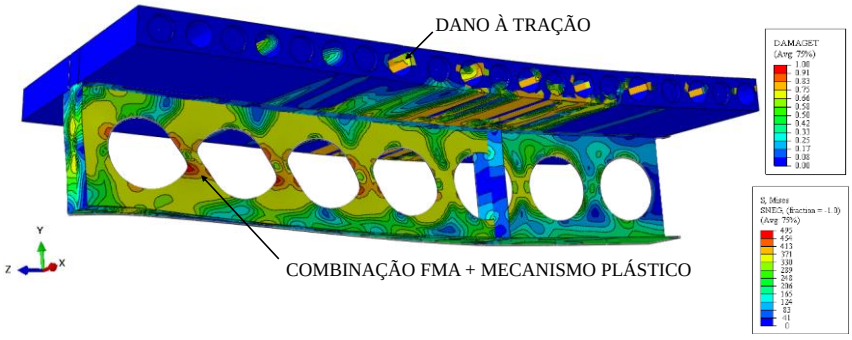

(a) Modelo: D_o/d=0,9; p/D_o=1,3 com 2x150mm

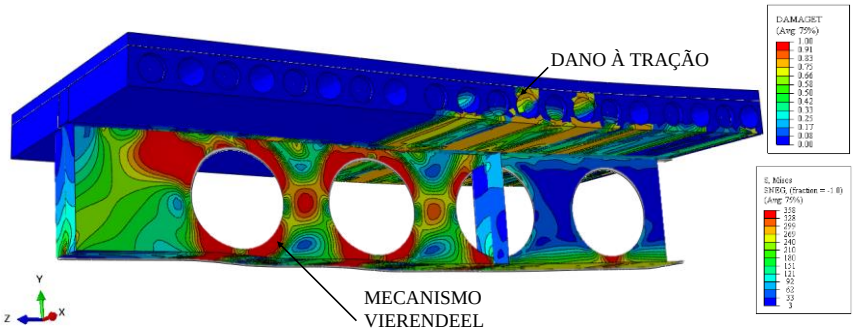

(b) Modelo: D_o/d=1,5; p/D_o=1,5 com 1x300mm

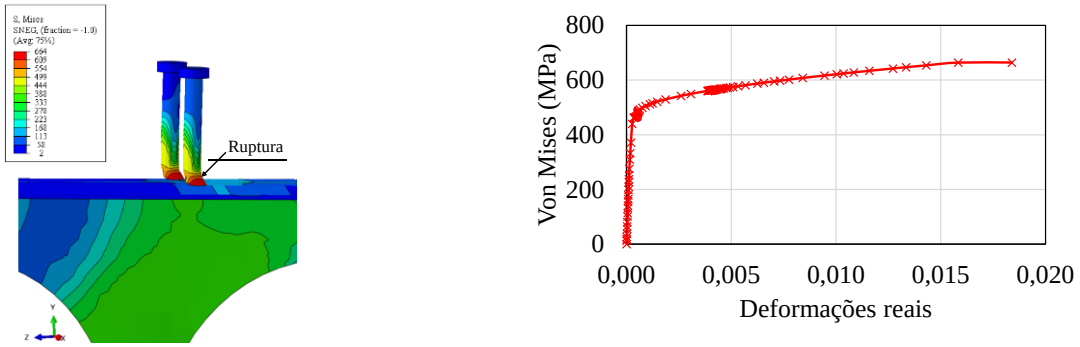

(c) Ruptura do conector

Os modos de falha observados foram a instabilidade do montante de alma (FMA) combinada com o mecanismo plástico (**Figura 6.4a**) e a formação do mecanismo Vierendeel (**Figura 6.4b**). Esses modos de falha também foram observados em combinação com a ruptura do conector de cisalhamento (**Figura 6.4c**). Os principais resultados são apresentados, considerando espaçamentos de 150mm, 300mm e 450mm.

6.2.1 Modelos com Conectores Espaçados em 150mm

A **Figura 6.5a-e** ilustra a capacidade resistente dos modelos analisados em função das variações nos parâmetros-chave D_o/d e p/D_o que representam as relações entre o diâmetro de abertura pela altura da seção original e largura do montante de alma pelo diâmetro de abertura, respectivamente. Observa-se a influência direta entre o número de conectores e a capacidade resistente; os modelos com dois conectores (2x150mm) apresentaram capacidade resistente maior ou igual aos modelos com um conector (1x150mm). Outro aspecto importante é que os resultados mostram que a capacidade resistente à instabilidade no montante de alma é influenciada pela ação mista aqui representada pelo número de conectores acima da abertura. Além disso, uma redução na capacidade resistente é observada para os modelos com D_o/d=1,0;

p/D_o=1,2 (**Figura 6.5c**) e D_o/d=1,2; p/D_o=1,2 (**Figura 6.5e**) em comparação com os modelos com p/D_o=1,4. Vale ressaltar que para cada série D_o/d, com a variação da relação p/D_o, isto é, aumento da largura do montante de alma, há uma tendência no aumento da capacidade resistente. Entretanto, a queda na capacidade resistente ocorreu porque a largura do montante de extremidade dos modelos p/D_o=1,4 é maior que nos modelos com p/D_o=1,5. Isso foi relatado em Ferreira, Martins e De Nardin (2021a).

Figura 6.5 – Influência do número de conectores - modelos com conectores espaçados de 150mm

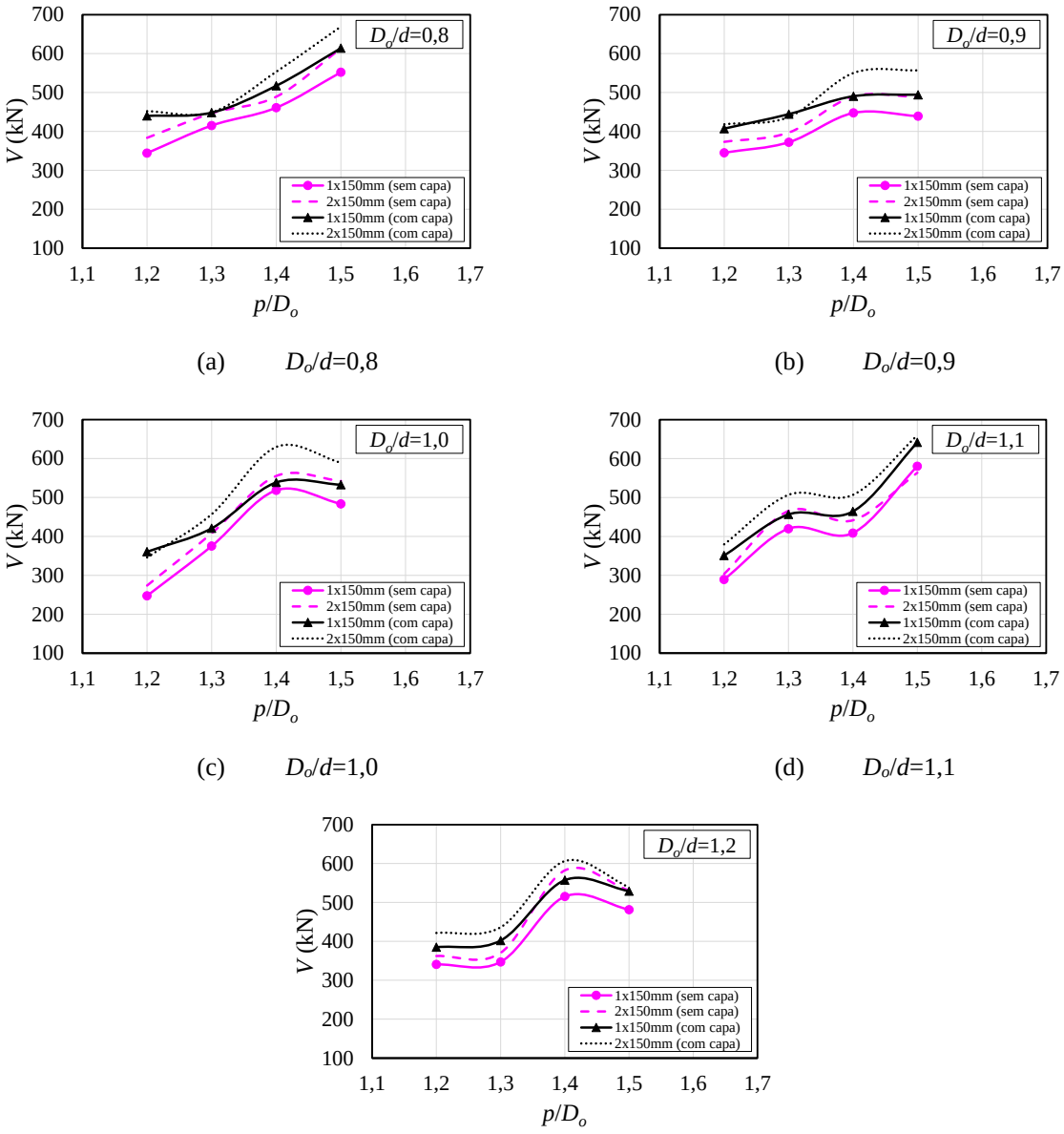

(a) D_o/d=0,8 (b) D_o/d=0,9

(c) D_o/d=1,0 (d) D_o/d=1,1

(e) D_o/d=1,2

Na **Tabela 6.2** são apresentados os modos de falhas dos modelos analisados em função dos parâmetros-chaves D_o/d e p/D_o que representam as relações entre o diâmetro de abertura

pela altura da seção original e largura do montante de alma pelo diâmetro de abertura, respectivamente.

Tabela 6.2 – Modos de falha dos modelos com conectores espaçados de 150mm

D_o/d	p/D_o	1x150mm		2x150mm	
		Com capa	Sem capa	Com capa	Sem capa
0,8	1,2	WPB+PM*	VM	WPB+PM	VM
	1,3	WPB+PM*	WPB+PM	VM	WPB+PM
	1,4	WPB+PM	WPB+PM	WPB+PM	WPB+PM
	1,5	WPB+PM*	WPB+PM	WPB+PM	WPB+PM
0,9	1,2	WPB+PM*	WPB+PM	WPB+PM	WPB+PM
	1,3	WPB+PM*	WPB+PM	WPB+PM	WPB+PM
	1,4	WPB+PM	WPB+PM	WPB+PM	WPB+PM
	1,5	WPB+PM	WPB+PM	WPB+PM	WPB+PM
1,0	1,2	WPB+PM*	WPB+PM	WPB+PM	WPB+PM
	1,3	WPB+PM*	WPB+PM	WPB+PM	WPB+PM
	1,4	WPB+PM	WPB+PM	VM	WPB+PM
	1,5	WPB+PM	WPB+PM	VM	WPB+PM
1,1	1,2	WPB+PM*	WPB+PM	WPB+PM	WPB+PM
	1,3	WPB+PM	WPB+PM	WPB+PM	WPB+PM
	1,4	VM	WPB+PM	WPB+PM	WPB+PM
	1,5	VM*	WPB+PM	VM	VM
1,2	1,2	WPB+PM*	VM	WPB+PM	VM
	1,3	VM	VM	VM	VM
	1,4	VM*	VM	VM	VM
	1,5	VM*	VM	VM	VM

WPB+PM: instabilidade no montante de alma combinada com mecanismo plástico;
WPB+PM*: instabilidade no montante de alma combinada com mecanismo plástico e ruptura do conector;
VM: mecanismo Vierendeel;
VM*:mecanismo Vierendeel acompanhado com a ruptura do conector.

De acordo com os modos de falha apresentados na **Tabela 6.2**, quanto maior for a relação D_o/d, a capacidade resistente tende a ser governada pelo mecanismo Vierendeel. Vale ressaltar que quanto maior o diâmetro de abertura, menor serão as alturas das seções tês, fator que reduz a capacidade resistente ao mecanismo Vierendeel.

6.2.2 Modelos com Conectores Espaçados em 300mm

No geral, os modelos desenvolvidos para os conectores espaçados em 300mm, apresentaram valores menores de capacidade resistente que a situação anterior. A **Figura 6.6**

ilustra a capacidade resistente dos modelos analisados em função das razões dos parâmetros chaves D_o/d e p/D_o. Observam-se que os modelos com 2 conectores em paralelo e espaçados de 300mm apresentaram maior capacidade resistente que aqueles com um único conector (1x300mm). Além disso, de forma semelhante ao que foi apresentado e discutido nas **Figura 6.5c** e **Figura 6.5e**, houve queda na capacidade resistente em função da largura do montante de extremidade (**Figura 6.6c** e **Figura 6.6**e).

Figura 6.6 – Influência do número de conectores - modelos com conectores espaçados de 300mm

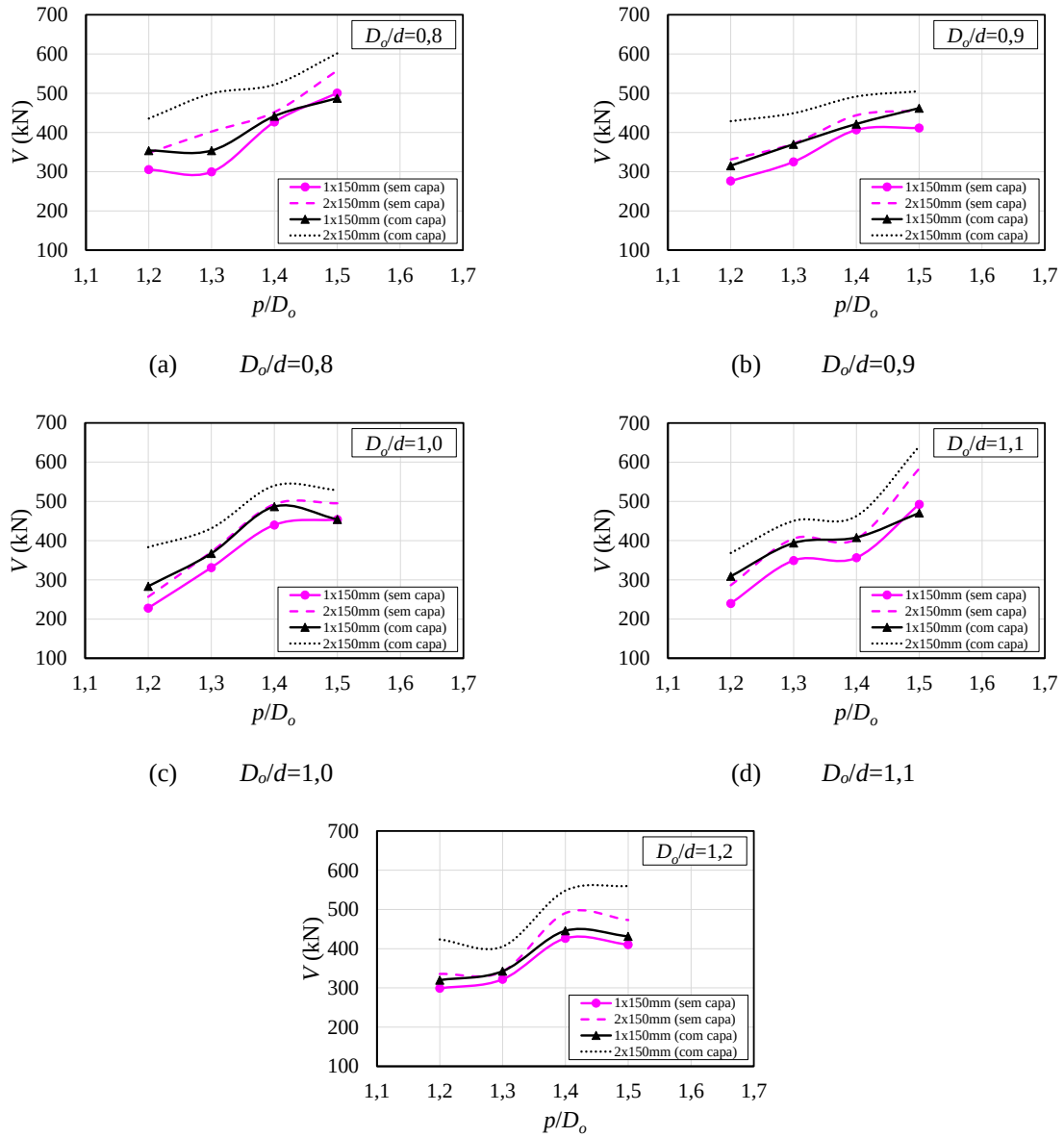

(a) D_o/d=0,8 (b) D_o/d=0,9

(c) D_o/d=1,0 (d) D_o/d=1,1

(e) D_o/d=1,2

Na **Tabela 6.3** são apresentados os modos de falhas dos modelos analisados em função dos parâmetros-chaves D_o/d e p/D_o. Diferentemente dos modelos desenvolvidos com 150mm

de espaçamento entre os conectores, para a presente situação, maior foi o número de observações em que foi verificado a formação do mecanismo Vierendeel combinada com a ruptura do conector de cisalhamento. Isso deve-se a mudança na capacidade resistente das vigas celulares mistas em função do espaçamento entre os conectores.

Tabela 6.3 – Modos de falha dos modelos com conectores espaçados de 300mm

D_o/d	p/D_o	1x300mm		2x300mm	
		Com capa	Sem capa	Com capa	Sem capa
0,8	1,2	VM*	VM	WPB+PM*	VM
	1,3	VM*	VM*	WPB+PM*	WPB+PM
	1,4	WPB+PM*	WPB+PM	WPB+PM*	WPB+PM
	1,5	VM	WPB+PM*	WPB+PM	WPB+PM
0,9	1,2	VM*	VM	WPB+PM*	VM
	1,3	WPB+PM*	WPB+PM	WPB+PM*	WPB+PM
	1,4	VM*	WPB+PM	WPB+PM	WPB+PM
	1,5	VM*	WPB+PM	WPB+PM	WPB+PM
1,0	1,2	WPB+PM*	WPB+PM	WPB+PM*	WPB+PM
	1,3	WPB+PM*	WPB+PM	WPB+PM	WPB+PM
	1,4	VM*	WPB+PM	VM	WPB+PM
	1,5	VM*	WPB+PM	VM	WPB+PM
1,1	1,2	VM*	WPB+PM	WPB+PM*	WPB+PM
	1,3	VM*	WPB+PM	WPB+PM	WPB+PM
	1,4	VM*	WPB+PM	VM	WPB+PM
	1,5	VM*	WPB+PM*	VM*	WPB+PM
1,2	1,2	VM*	VM	WPB+PM*	WPB+PM
	1,3	VM*	VM	VM	VM
	1,4	VM*	VM*	VM	VM
	1,5	VM*	VM*	VM*	VM

WPB+PM: instabilidade no montante de alma combinada com mecanismo plástico;
WPB+PM*: instabilidade no montante de alma combinada com mecanismo plástico e ruptura do conector;
VM: mecanismo Vierendeel;
VM*:mecanismo Vierendeel acompanhado com a ruptura do conector.

6.2.3 Modelos com Conectores Espaçados em 450mm

De todos os modelos analisados, os modelos com conectores espaçados em 450mm apresentaram os menores valores de capacidade resistente. A **Figura 6.7** ilustra os valores da capacidade resistente dos modelos analisados em função da razão dos parâmetros-chave D_o/d e p/D_o. De acordo com a ilustração, é observado que os modelos com 2x450mm apresentaram maior capacidade resistente que os modelos com 1x450mm. Também, houve uma queda na capacidade resistente dos modelos D_o/d=1.0; p/D_o=1.2 (**Figura 6.7c**), e D_o/d=1.2; p/D_o=1.2

(**Figura 6.7e**), como apresentado anteriormente (**Figura 6.5c**, **Figura 6.5e**, **Figura 6.6c** e **Figura 6.6e)**. Portanto, até o momento, é possível afirmar que, para todos os modelos analisados, duas linhas de conectores proporcionaram maior capacidade resistente.

Figura 6.7 – Influência do número de conectores - modelos com conectores espaçados de 450mm

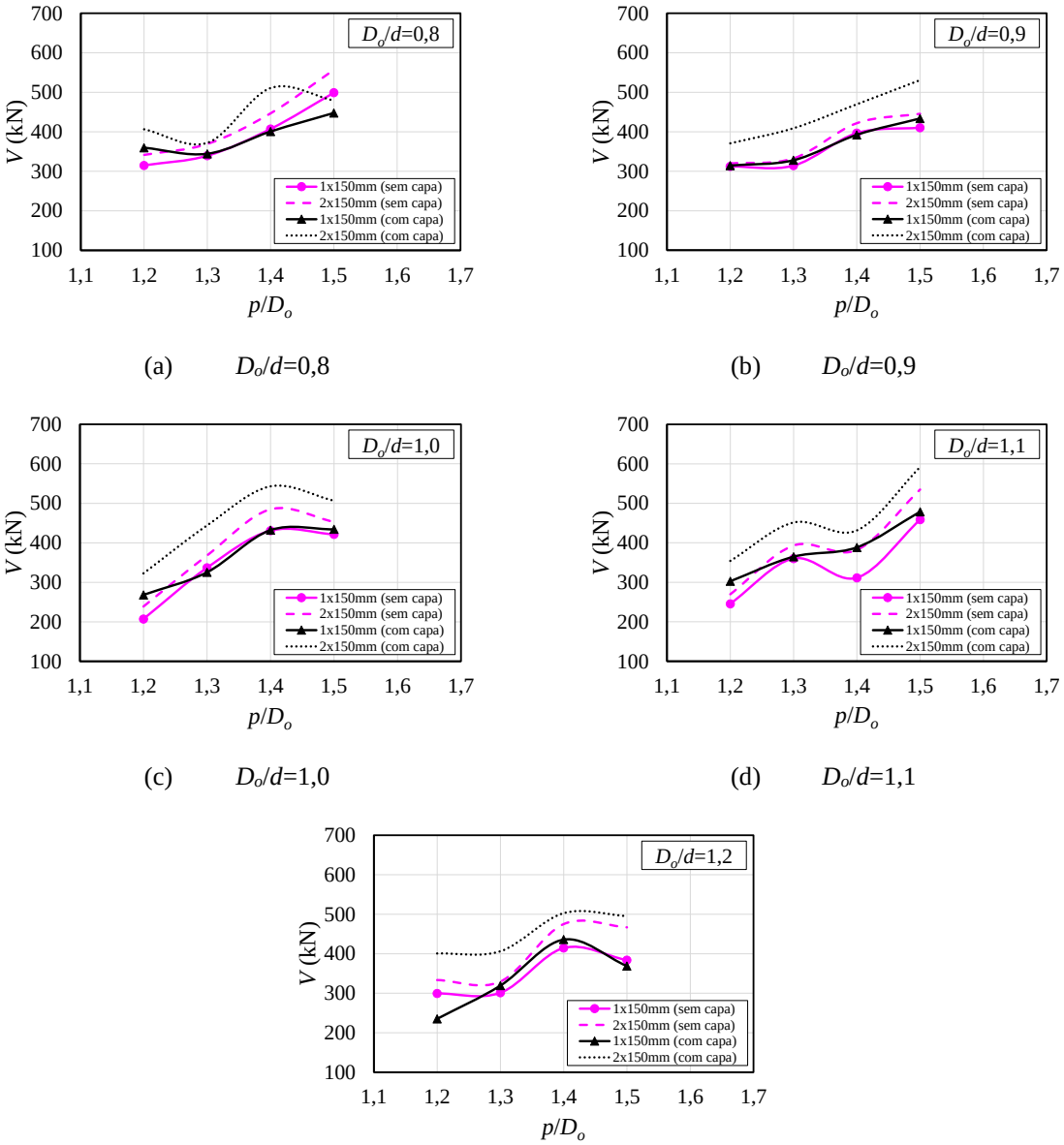

(a) D_o/d=0,8 (b) D_o/d=0,9

(c) D_o/d=1,0 (d) D_o/d=1,1

(e) D_o/d=1,2

Na **Tabela 6.4** são apresentados os modos de falhas dos modelos analisados em função dos parâmetros-chaves D_o/d e p/D_o.

Tabela 6.4 – Modos de falha dos modelos com conectores espaçados de 450mm

D_o/d	p/D_o	1x300mm		2x300mm	
		Com capa	Sem capa	Com capa	Sem capa
0,8	1,2	VM*	VM*	WPB+PM*	VM*
	1,3	VM*	WPB+PM*	VM*	WPB+PM*
	1,4	VM*	WPB+PM*	WPB+PM*	WPB+PM
	1,5	VM*	PM*	VM*	WPB+PM
0,9	1,2	VM*	WPB+PM*	WPB+PM*	VM
	1,3	WPB+PM*	WPB+PM*	WPB+PM*	WPB+PM*
	1,4	VM*	WPB+PM*	WPB+PM*	WPB+PM*
	1,5	VM*	WPB+PM	WPB+PM*	WPB+PM
1,0	1,2	WPB+PM*	VM*	WPB+PM*	VM
	1,3	VM*	WPB+PM	WPB+PM*	WPB+PM
	1,4	VM*	WPB+PM*	VM	WPB+PM
	1,5	VM*	WPB+PM*	VM	WPB+PM*
1,1	1,2	VM*	WPB+PM	WPB+PM*	WPB+PM
	1,3	VM *	WPB+PM*	WPB+PM	WPB+PM*
	1,4	VM *	PM*	VM	WPB+PM
	1,5	VM*	VM*	VM*	VM
1,2	1,2	VM*	WPB+PM*	WPB+PM*	WPB+PM
	1,3	VM*	VM	WPB+PM*	VM
	1,4	VM*	VM*	VM*	WPB+PM
	1,5	VM*	VM*	VM*	VM

WPB+PM: instabilidade no montante de alma combinada com mecanismo plástico;
WPB+PM*: instabilidade no montante de alma combinada com mecanismo plástico e ruptura do conector;
VM: mecanismo Vierendeel;
VM*:mecanismo Vierendeel acompanhado com a ruptura do conector.

6.2.4 Influência do Espaçamento entre os Conectores

Uma observação importante a ser destacada refere-se à comparação entre as capacidades resistentes dos modelos com 150mm e 300mm de espaçamento entre os conectores. A **Figura 6.8** mostra um exemplo, considerando o modelo com D_o/d=0,9 e p/D_o=1,5 sem capa de concreto. Todos os modelos que são apresentados na ilustração tiveram a capacidade resistente definida pela instabilidade no montante de alma combinada com o mecanismo plástico. Conforme apresentado, nota-se que quanto maior o número de conectores, maior será a capacidade resistente. Na **Figura 6.8a** é observada a capacidade resistente semelhante entre os modelos 1x150mm e 2x300mm. Embora os modelos tenham espaçamentos diferentes entre os conectores de cisalhamento, o número de conectores alocados no comprimento entre o apoio e o meio do vão é o mesmo em ambas as situações. Em relação ao escorregamento na interface

aço-concreto (**Figura 6.8b)**, nota-se que quanto menor o número de conectores, maior será o escorregamento.

Figura 6.8 – Influência do espaçamento dos conectores (150mm e 300mm), modelos sem capa de concreto

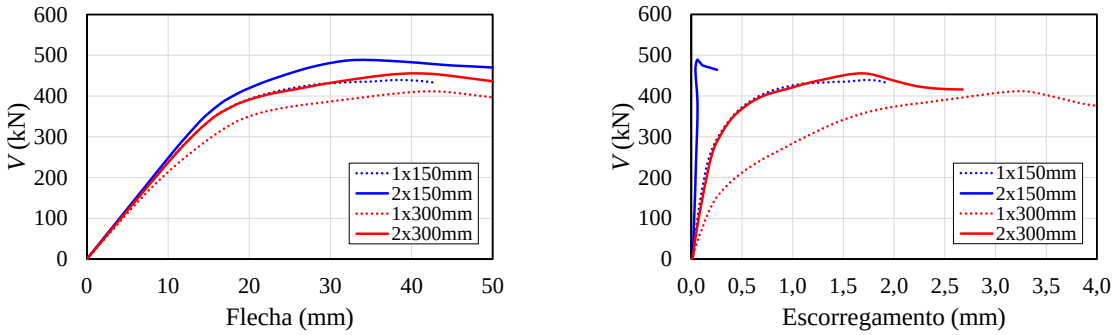

(a) Cortante por flecha (b) Cortante por escorregamento

Por outro lado, nas **Figuras 6.9a-b**, tais comparações são realizadas considerando os modelos D_o/d=0.8 e p/D_o=1.4 e capa de concreto.

Figura 6.9 – Influência do espaçamento dos conectores (150mm e 300mm), modelos com capa de concreto

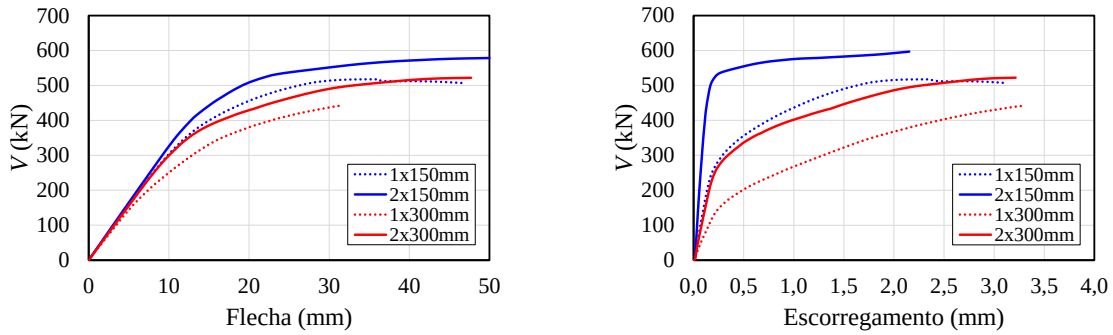

(a) Cortante por flecha (b) Cortante por escorregamento

Conforme a ilustração, os modos de falha observados foram a combinação da instabilidade do montante de alma com o mecanismo plástico para os modelos de 150mm. Já para os modelos de 300mm, foi verificado esses modos de falha acompanhados pela ruptura do conector de cisalhamento. Nota-se, também, nas figuras acima, uma observação semelhante ao apresentado na **Figura 6.8**, isto é, a capacidade resistente equivalente entre os modelos 1x150mm e 2x300mm, que apresentam o mesmo número de conectores alocados no comprimento entre o apoio e o meio do vão.

A **Figura 6.10a-b** mostra um exemplo de comparação das capacidades resistentes entre os modelos com 300mm e 450mm sem capa de concreto. Tal comparação é feita pelos modelos com os parâmetros D_o/d=0,9 e p/D_o=1,5.

Figura 6.10 – Comparação entre os modelos de 300mm com os modelos de 450mm, sem capa de concreto

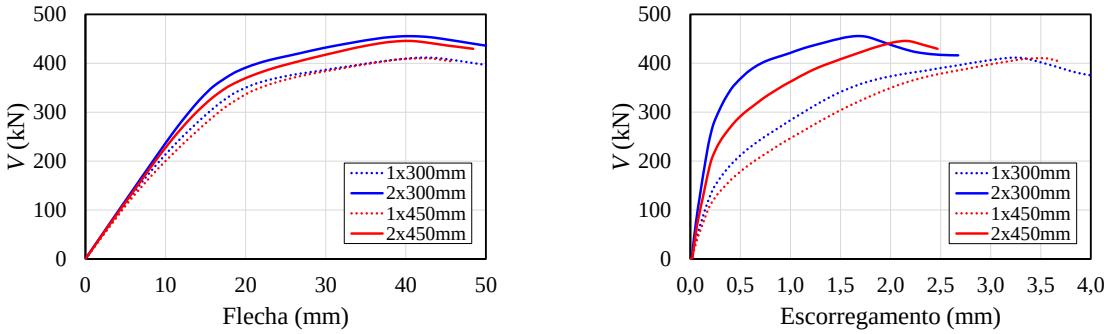

(a) Cortante por flecha (b) Cortante por escorregamento

De acordo com a ilustração, ambos os modelos tiveram a capacidade resistente definida pela instabilidade do montante de alma combinada com o mecanismo plástico. Embora os modelos com 300mm apresentaram capacidade resistente maior que os modelos com 450mm, a diferença não foi significativa. Uma observação importante a ser destacada na **Figura 6.10b** foi o comportamento frágil na interface aço-concreto, isto é, os valores de escorregamento não atingiram o valor de referência de 6mm, conforme ensaio de cisalhamento direto descrito no EN 1994-1-1 (2004).

Na **Figura 6.11a-b**, também, é feita a comparação entre os modelos de 300mm com os modelos de 450mm, considerando a capa de concreto. O exemplo é mostrado considerando o modelo com as razões D_o/d=1.2 e p/D_o=1.5.

Figura 6.11 – Comparação entre os modelos de 300mm com os modelos de 450mm, com capa de concreto

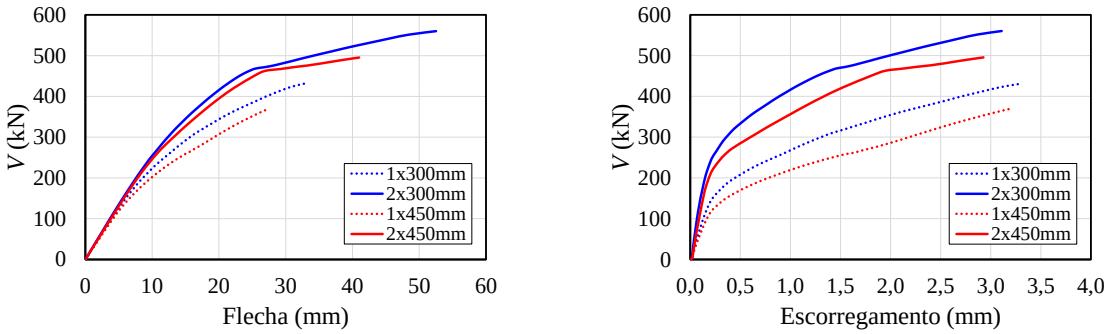

(a) Cortante por flecha (b) Cortante por escorregamento

Nesse contexto, a capacidade resistente foi atingida pelo início da formação do mecanismo Vierendeel combinada com a ruptura do conector de cisalhamento. Analogamente ao discutido anteriormente, os modelos com 1x300mm apresentaram capacidade resistente maior que os modelos com 450mm. Embora houve a ruptura em ambos os modelos

apresentados, essa diferença na capacidade resistente se deu em função da ação mista, uma vez que os modelos de 300mm apresentam um número maior de conectores de cisalhamento.

Na maioria dos modelos analisados, foi observado que quanto maior o número de conectores, maior será a capacidade resistente. Em contraste, quanto menor o número de conectores, menor será a capacidade resistente. Esses valores de capacidade resistente tendem a convergirem, uma vez que o modo de falha é limitado pela ruptura do conector de cisalhamento. Outro fator importante em relação ao número de conectores de cisalhamento foi a capacidade resistente equivalente. Por exemplo, a capacidade resistente dos modelos 1x150mm foi semelhante à capacidade resistente dos modelos 2x300mm. Em ambos os modelos, o número de conectores de cisalhamento foi o mesmo. Tal observação foi avaliada para os modelos com capa e sem capa de concreto. Este apontamento também é válido para os modelos 1x300mm e 2x450mm. Porém, neste contexto, houve uma pequena diferença entre as capacidades resistentes, devido à diferença entre o número de conectores, uma vez que os modelos 1x300mm e 2x450 possuem 10 e 14 conectores (do apoio ao meio vão), respectivamente.

6.2.5 Influência da Posição do Conector e da Largura do Montante de Extremidade

Nesta seção é apresentada uma síntese dos principais resultados do estudo paramétrico. Nos gráficos é possível avaliar a relação entre a capacidade resistente e os parâmetros-chave D_o/d e p/D_o. Nas figuras a seguir são apresentados os valores de força cortante resistente em vigas celulares mistas com lajes alveolares sem capa (**Figura 6.12**) e com capa (**Figura 6.13**). As ilustrações são acompanhadas da vista lateral dos modelos (para o trecho $L/4$ do apoio) para mostrar a posição dos conectores de cisalhamento em relação à abertura mais crítica, ou seja, aquela mais próxima ao apoio.

Em relação à **Figura 6.12a**, na série D_o/d=0,8; p/D_o=1,3, houve queda da capacidade resistente nos modelos com uma linha de conectores espaçados de 300mm (1x300mm) em relação aqueles espaçados de 450 mm (1x450mm). Essa redução também foi observada nas séries D_o/d=0,9; p/D_o= 1,2 (**Figura 6.12b**). Tal comportamento é atribuído ao fato dos modelos espaçados em 300mm não possuírem conectores de cisalhamento no comprimento correspondente à segunda abertura em relação ao apoio. Isso indica que a influência da posição do conector em relação à abertura se estende para além da primeira abertura.

Figura 6.12 – Variação da força cortante resistente em função da relação D_o/d, espaçamento dos conectores, número de conectores por linha e relação p/D_o em modelos sem capa de concreto

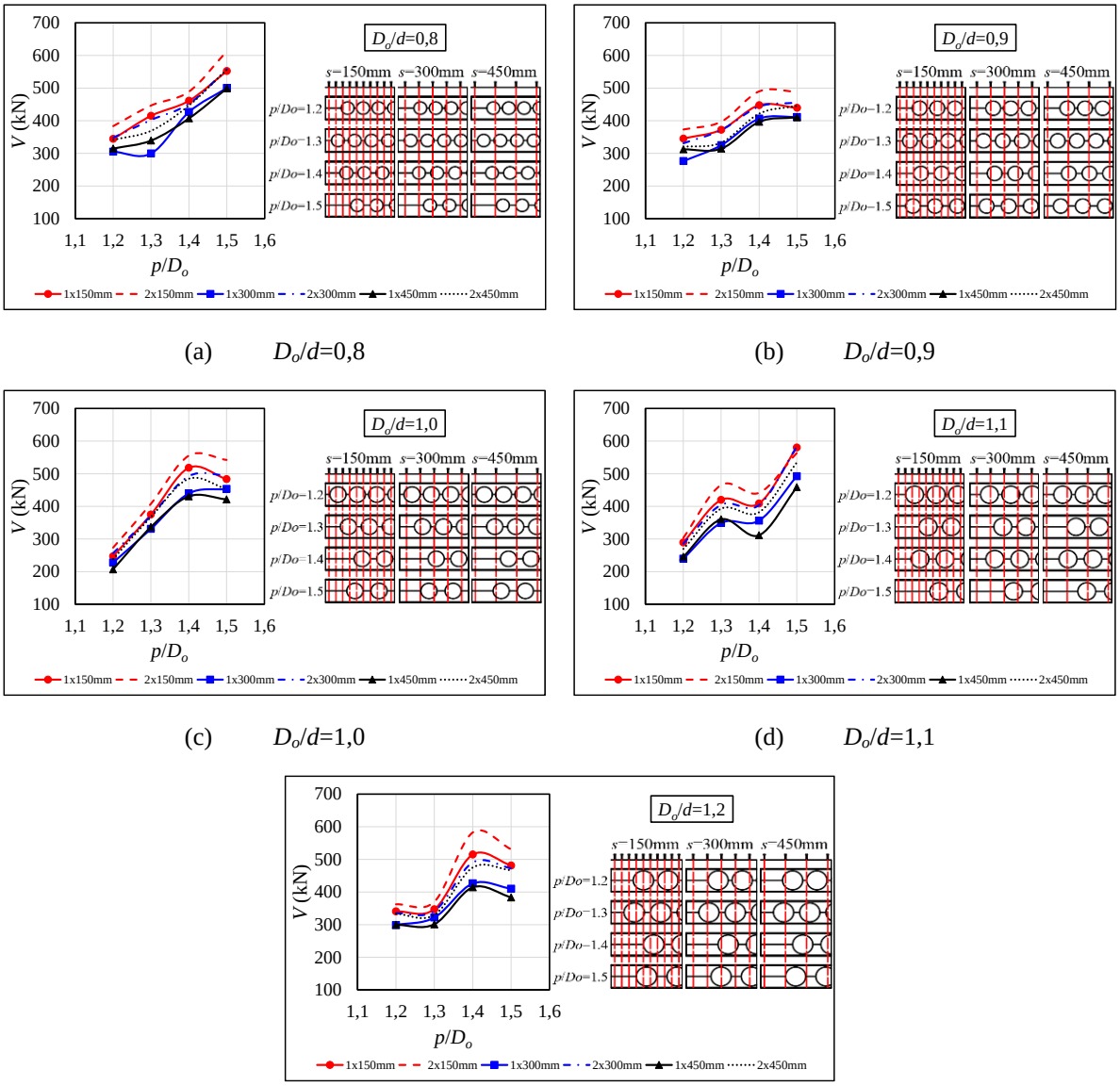

(a) D_o/d=0,8 (b) D_o/d=0,9

(c) D_o/d=1,0 (d) D_o/d=1,1

(e) D_o/d=1,2

Uma observação interessante é apresentada na **Figura 6.13a**: na série D_o/d=0,8; p/D_o=1,2-1,5 e 2x450mm ocorreu mudança na capacidade resistente devido ao posicionamento do conector de cisalhamento nas aberturas. Nos modelos das séries D_o/d=0,8; p/D_o=1,2; 1,4 foi observado instabilidade no montante de alma combinada com mecanismo plástico e ruptura do conector de cisalhamento. Por outro lado, nos modelos D_o/d=0,8; p/D_o=1,3;1,5, houve formação do mecanismo Vierendeel acompanhada da ruptura do conector de cisalhamento. Isso ocorreu porque os modelos D_o/d=0,8; p/D_o=1,2; 1,4 tinham conectores de cisalhamento alocados acima

da primeira abertura em relação ao apoio, ao contrário dos modelos D_o/d=0,8; p/D_o=1,3;1,5, que não tinham conectores posicionados na região correspondente à primeira abertura.

Figura 6.13 – Variação da força cortante resistente em função das relações D_o/d, espaçamento dos conectores, número de conectores por linha e relação p/D_o em modelos com capa de concreto

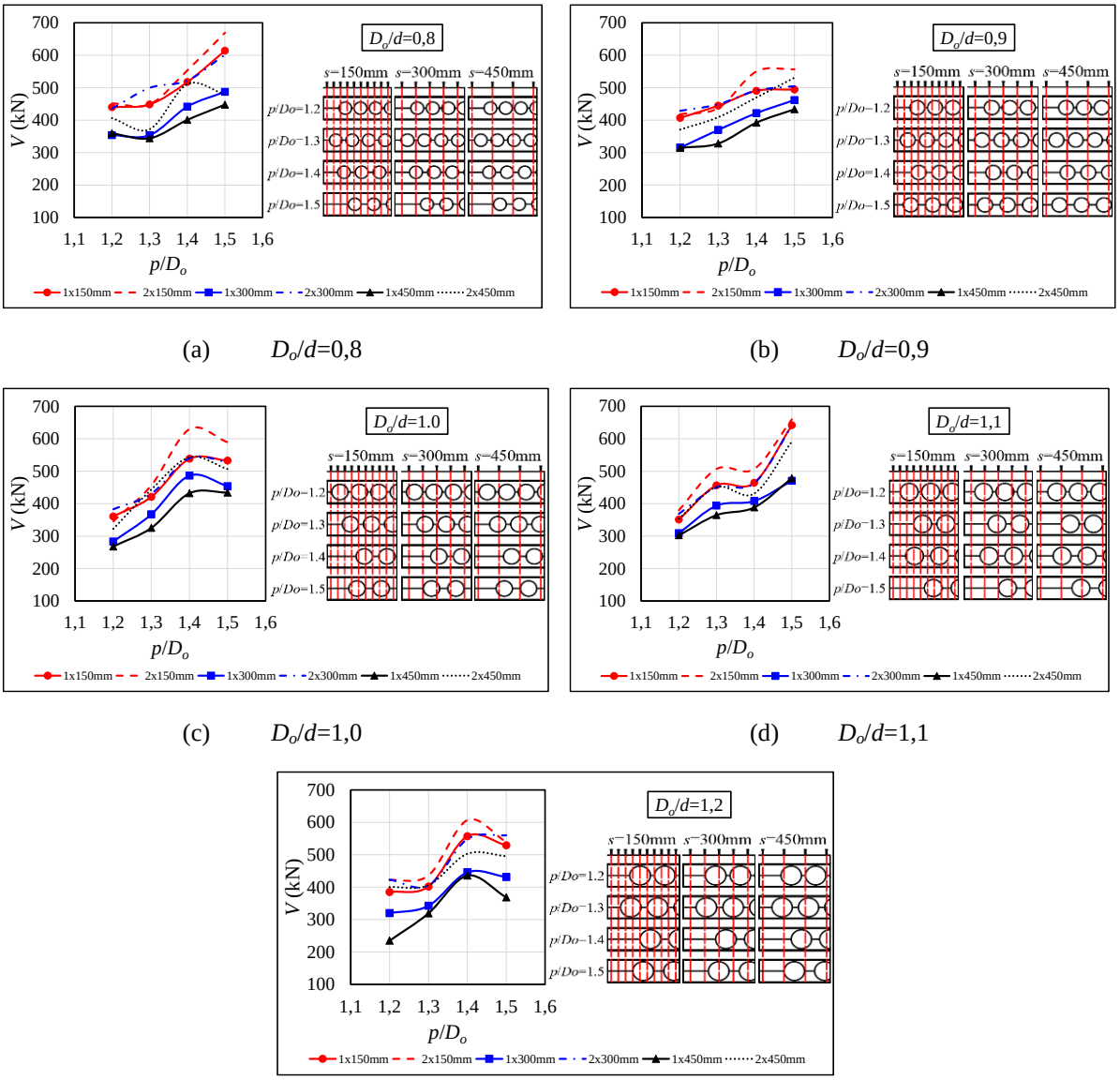

(a) D_o/d=0,8 (b) D_o/d=0,9

(c) D_o/d=1,0 (d) D_o/d=1,1

(e) D_o/d=1,2

Finalmente, os resultados apresentados nas **Figura 6.12c**, **Figura 6.12e**, **Figura 6.13c** e **Figura 6.13e** mostram a redução na capacidade resistente entre os modelos p/D_o=1,4 e modelos p/D_o=1,5. Tal redução é decorrente da largura do montante de extremidade, conforme discutido anteriormente, quanto maior for largura do montante de extremidade, maior será a capacidade resistente das vigas celulares mistas (FERREIRA; MARTINS; DE NARDIN, 2021a).

Na maioria dos modelos analisados foi observado que quanto maior o número de conectores maior a capacidade resistente, desde que sejam mantidas constantes as demais características. Em contraste, quanto menor o número de conectores, menor a capacidade resistente. Esse fato deixa clara a dependência que há entre capacidade resistente e interação aço-concreto ou ação mista em vigas celulares mistas.

Esses valores de capacidade resistente tendem a convergir uma vez que o modo de falha é limitado pela resistência da conexão. Outro fator importante em relação ao número de conectores de cisalhamento é a capacidade resistente equivalente. Por exemplo, a capacidade resistente dos modelos com um conector por linha e espaçados de 150 mm (1x150mm) foi semelhante à capacidade resistente dos modelos com duas linhas de conectores espaçados longitudinalmente de 300mm (2x300mm). Em ambos os casos, o número de conectores de cisalhamento é o mesmo contudo há variação da posição. Tal observação foi verificada nos modelos com capa e sem capa de concreto. Este apontamento também é válido para os modelos 1x300mm e 2x450mm. Porém, neste contexto, houve uma pequena diferença entre as capacidades resistentes devido à diferença entre o número de conectores, uma vez que os modelos 1x300mm e 2x450 possuem 10 e 14 conectores (desde o apoio até o meio do vão), respectivamente.

A seguir na seção 6.3 é apresentado um modelo analítico para previsão da capacidade resistente de vigas celulares mistas com lajes alveolares; esse modelo é fundamentado nos resultados do estudo paramétrico.

6.3 MODELOS ANALÍTICOS PARA A PREVISÃO DA CAPACIDADE RESISTENTE

Nesta seção é apresentada uma proposta para prever a capacidade resistente à instabilidade no montante de alma em vigas celulares mistas formadas por lajes alveolares pré-fabricadas de concreto.

6.3.1 Modelo do SCI P355

A publicação SCI P355 (LAWSON; HICKS, 2011) apresenta formulação para prever a força cortante global considerando interação parcial (**Eq. 6.1**) e interação total (**Eq. 6.2**). No

entanto, essas equações se referem a vigas celulares mistas formadas por lajes mistas de aço e concreto não havendo, até o momento, formulação para estimar a capacidade resistente quando a viga mista contém lajes pré-fabricadas.

$$V_{Rd} = \frac{V_{WPB}\left(D_o / p\right) + \left(4M_{bT,NV,Rd} / 0,45D_o\right)}{1 + h_{o,eff} / h_{eff}} + \frac{\Delta N_{sc,Rd}}{p}\left(y_t + h_s - 0,5h_c\right) \qquad \text{Eq. (6.1)}$$

$$V_{Rd} = \left[V_{WPB}\left(D_o / p\right) + \left(4M_{bT,NV,Rd} / 0,45D_o\right)\right]\frac{\left(h_{eff} + h_s - 0,5h_c\right)}{h_{eff} + D_o} \qquad \text{Eq. (6.2)}$$

A resistência à instabilidade no montante de alma (V_{WPB}) é calculada de acordo com as **Eqs. (6.3-6.9)**, conforme descrito no Capítulo 3. O parâmetro $M_{bT,NV,Rd}$ é o momento plástico resistente do tê inferior, reduzido devido ao esforço axial e multiplicado pelo fator aproximado $\left[1-\left(N / N_{pl}\right)^2\right]$. O parâmetro $\Delta N_{sc,Rd}$ é definido como o produto entre o número de conectores ($n_{sc,wp}$) no comprimento do montante de alma (p) e a resistência de cada conector de cisalhamento (P_{sc}).

$$\chi = \frac{1}{\phi + \sqrt{\phi^2 - \lambda_0^{\,2}}} \le 1,0 \qquad \text{Eq. (6.3)}$$

$$\phi = 0,5\left[1 + \alpha\left(\lambda_0 - 0,2\right) + \lambda_0^{\,2}\right] \qquad \text{Eq. (6.4)}$$

$$\lambda_0 = \sqrt{\frac{f_y}{f_{cr,w}}} \qquad \text{Eq. (6.5)}$$

$$f_{cr,w} = \frac{\pi^2 E}{\lambda_w^2} \qquad \text{Eq. (6.6)}$$

$$l_{eff} = 0,5\sqrt{b_w^2 + D_o^2} \le 0,7D_o \qquad \text{Eq. (6.7)}$$

$$\lambda_w = l_{eff}\sqrt{12} / t_w \qquad \text{Eq. (6.8)}$$

$$V_{WPB} = \chi f_y t_w b_w \qquad \text{Eq. (6.9)}$$

Tabela 6.5: Curvas de resistência

Curva de resistência	*a*	*b*	*c*	*d*
Fator de imperfeição (α)	0,21	0,34	0,49	0,76

O SCI P355 (LAWSON; HICKS, 2011) recomenda usar a curva de resistência *c* (**Tabela 6.5**) no cálculo do parâmetro χ correspondente à instabilidade. Porém, de acordo com as **Eqs (6.1-6.2)**, o grau de interação em vigas celulares mistas não está claramente definido, uma vez que o SCI P355 recomenda a escolha do menor valor entre as **Eqs (6.1-2)**, independentemente se a viga celular mista apresenta o grau de interação total ou parcial. Além disso, conforme apresentado por Sheehan et al. (2016), o espaçamento entre os conectores de cisalhamento influencia significativamente na capacidade resistente da viga mista pois está diretamente relacionado ao grau de interação aço-concreto. Isso mostra que o número de conectores de cisalhamento deve ser levado em consideração no cálculo da capacidade resistente. Outro fator importante a destacar é a verificação da combinação das falhas por instabilidade no montante de alma e mecanismo Vierendeel. No estudo paramétrico foi observada a ocorrência simultânea de ambos os modos de falha e assim, esses devem ser considerados na determinação da capacidade resistente.

6.3.2 Modelo Proposto

Nesse contexto, o presente estudo propõe uma forma simplificada para prever a força cortante resistente de vigas celulares mistas formadas por lajes alveolares pré-fabricadas (**Eqs. 6.10-12**). A presente proposta leva em conta a influência de três modos de falha e, para cada um deles, há uma parcela: força cortante resistente devido à instabilidade no montante de alma, força cortante resistente devido ao momento Vierendeel e força cortante resistente devido à ação mista. Vale ressaltar que a proposta aplica alguns fatores nas equações apresentadas pelo SCI P355 (LAWSON; HICKS, 2011).

$$V_{Rd} = V_{WPB} + V_{pl,T} + V_{VC} \qquad \text{Eq. (6.10)}$$

A força cortante resistente devido à instabilidade no montante de alma (V_{WPB}) é calculada de acordo com as **Eqs. (6.3-6.9)** e é idêntica à proposta pela SCI P355 (LAWSON; HICKS, 2011). A parcela da força cortante resistente devido ao momento Vierendeel ($V_{pl,T}$) é

calculada conforme **Eq. (6.11-6.12)**, levando em conta dois fatores (A_{wT}/A_T e D_o/d). Afirmar que ambos os tês estão completamente plastificados pode levar a resultados superestimados.

$$V_{pl,T} = 4\left[\frac{A_{wT} f_y \left(0,5h_{w,T} + t_f - z_{pl}\right) + A_{fT} f_y \left(0,5t_f - z_{pl} + z_{pl}^{\,2}/t_f\right)}{0,45D_o}\right]\left(\frac{A_{wT}}{A_T}\right)\left(\frac{Do}{d}\right) \qquad \text{Eq. (6.11)}$$

$$z_{pl} = A_f + A_{w,T}/2b_f \qquad \text{Eq. (6.12)}$$

A força cortante resistente devido a ação mista entre o tê superior e a laje de concreto é calculada conforme a SCI P355 (LAWSON; HICKS, 2011) (**Eq. 6.13**). Entretanto, o fluxo de cisalhamento é calculado pela razão da capacidade resistente do conector (P_{sc}) pelo espaçamento (s), multiplicada pelo fator k que considera o número de linhas de conectores. A resistência do conector foi calculada conforme a SCI P401 (GOUCHMAN, 2014), descrita na **Tabela 2.1** e Capítulo 4.

$$V_{VC} = k\frac{P_{sc}}{s}\left(y_t + 0,5h_c\right) \qquad \text{Eq. (6.13)}$$

Agora, uma questão a discutir é qual curva de resistência utilizar na previsão da força cortante resistente à instabilidade do montante de alma (**Eq. 6.4)**. Para auxiliar na definição da curva de resistência mais adequada, os resultados do estudo paramétrico foram comparados com resultados obtidos utilizando as curvas de resistência *c* (**Figura 6.14a**), *b* (**Figura 6.14b**) e *a* (**Figura 6.14c**).

Figura 6.14 – Análise estatística da influência da curva de resistência

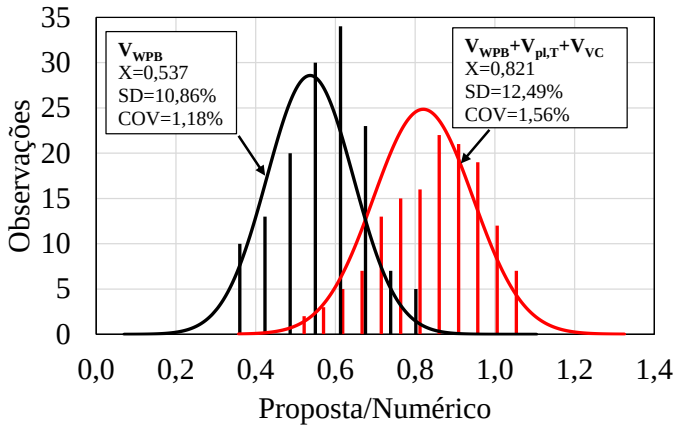

(a) V_{WPB} vs. $V_{WPB}+V_{pl,T}+V_{VC}$, considerando a curva de resistência *c*

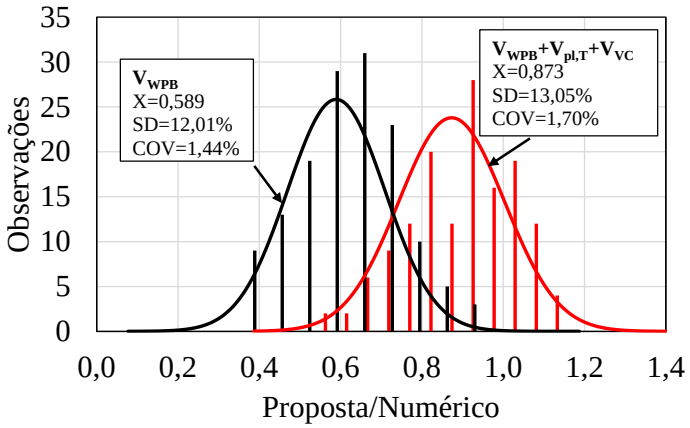

(b) V_{WPB} vs. $V_{WPB}+V_{pl,T}+V_{VC}$, considerando a curva de resistência *b*

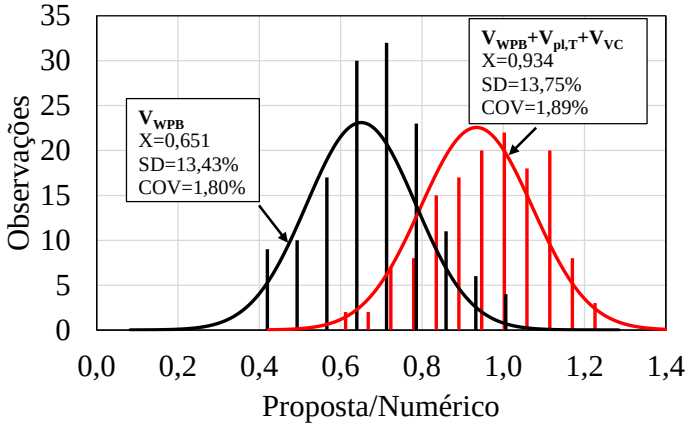

(c) V_{WPB} vs. $V_{WPB}+V_{pl,T}+V_{VC}$, considerando a curva de resistência *a*

Ao considerar apenas a resistência à instabilidade no montante de alma ($V_{Rd}=V_{WPB}$), os valores de força cortante resistente tendem a subestimar a capacidade resistente das vigas celulares mistas formadas por lajes alveolares pré-fabricadas. Nesse contexto, foi verificado que os valores médios da razão entre os modelos analíticos e numéricos (V_{FE}) são inferiores a 65%, ou seja, $V_{WPB}/V_{FE}<0,65$. Esses valores tendem a diminuir com o aumento do fator de imperfeição (α), que é função da curva de resistência.

Por outro lado, ao utilizar a **Eq. (6.10)**, os valores médios da razão entre os modelos analíticos e numéricos são superiores a 83% ($V_{Rd}/V_{FE}>0,83$). Esses valores tendem a aumentar, conforme o fator de imperfeição é diminuido e essa relação pode chegar a 93% ($V_{WPB}/V_{FE}>0,93$) ao se utilizar a curva de resistência *a*. Dos 240 modelos analisados via modelagem numérica, 142 deles apresentaram falha por instabilidade no montante de alma (59% dos modelos investigados). Considerando a curva de resistência *c*, apenas 10 observações superestimaram a capacidade resistente dos modelos o que corresponde a apenas 4% dos modelos investigados.

Nesse contexto, o máximo valor encontrado para a relação entre a força cortante resistente V_{Rd}, **Eq. (6.10),** e o modelo numérico foi 1,06. Ao considerar as curvas de resistência *b* e *a*, houve aumento da diferença entre os valores previstos e numéricos. Ao prever a força cortante resistente utilizando a curva de resistência *b*, apenas 30 previsões superestimaram o valor de referência (numérico) ou seja, apenas 12,5% e o valor máximo da razão foi 1,14. Para a curva de resistência *a*, 55 valores previstos foram superestimados (ou seja, 23%) e a máxima razão teórico/numérico foi 1,23. Portanto, a curva de resistência *c*, recomendada pela SCI P355 (LAWSON; HICKS, 2011) foi a que melhor representou a força cortante resistente do conjunto de dados numéricos considerado no estudo.

Não obstante, para verificar a eficácia do modelo analítico proposto para prever a capacidade resistente, os resultados do estudo paramétrico apresentados no Capítulo 5 são comparados aos valores previstos pelo modelo analítico. Vale ressaltar que na comparação são considerados apenas os modelos de vigas celulares mistas e lajes alveolares com capa (**Figura 6.15a**) e sem capa de concreto (**Figura 6.15b**), cuja capacidade resistente foi definida pela instabilidade no montante de alma, considerando apenas seção com dupla simetria, totalizando 38 modelos.

Figura 6.15 – Comparação: força cortante prevista pelo modelo analítico e força cortante advinda da modelagem numérica (resultados do Capítulo 5)

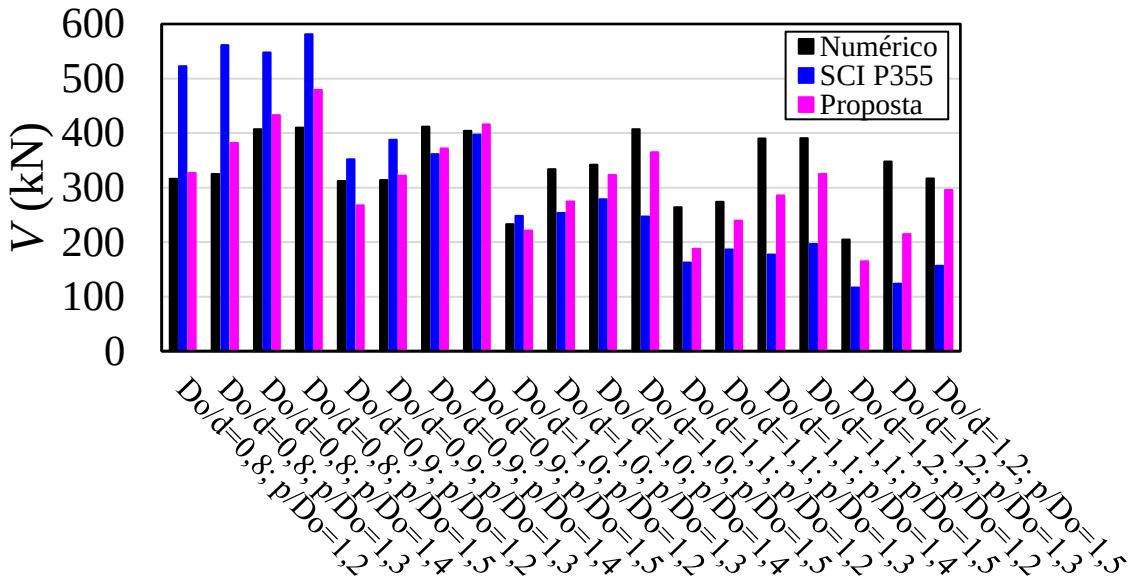

(a) Modelos sem capa de concreto

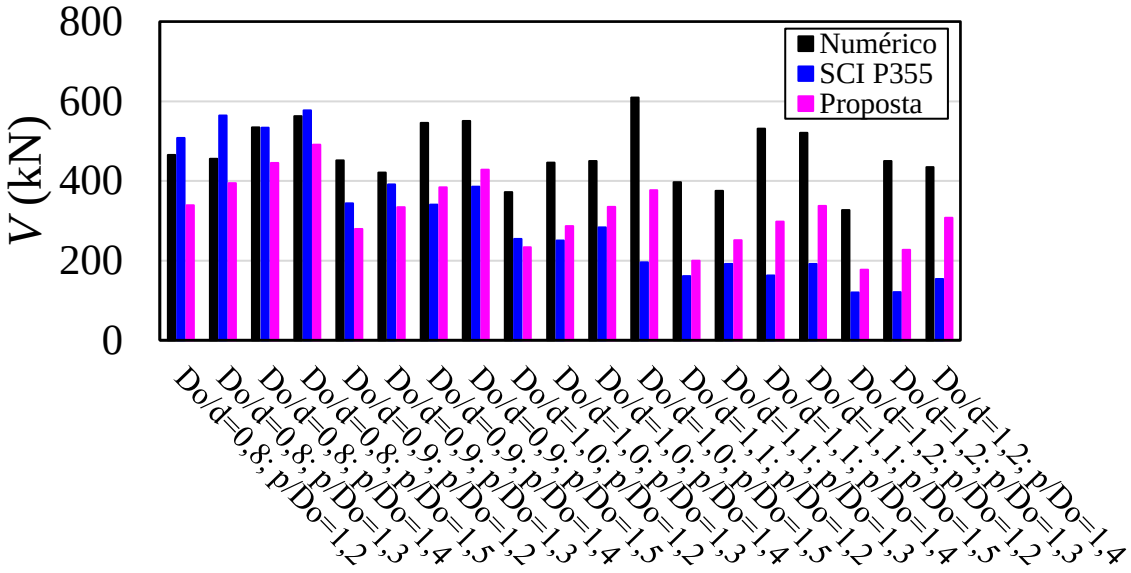

(b) Modelos com capa de concreto

A partir dos resultados apresentados na **Figura 6.15** e considerando a relação entre força cortante resistente prevista (modelo analítico) e obtida nas análises numéricas foram encontrados valores médios da razão analítico/numérico iguais a 91% e 68% para modelos com capa e sem capa de concreto, respectivamente. Isso significa que o modelo proposto apresentou uma maior precisão para os modelos sem capa de concreto. A explicação para isso é que a proposta foi desenvolvida em função dos modelos em que foi verificada a instabilidade no montante de alma. Nesse contexto, o maior número de observações em que ocorreu a instabilidade no montante de alma foi verificada para os modelos sem capa de concreto, conforme apresentado anteriormente nas **Tabelas 6.2-6.4**.

6.4 SÍNTESE E CONCLUSÕES

Os pontos mais importantes apresentados nesse capítulo são:

- A ruptura do conector de cisalhamento foi observada, principalmente nos modelos com capa de concreto. Nestes modelos, a capa de concreto proporcionou um aumento na resistência axial da laje, fator que limitou a capacidade resistente das vigas celulares mistas à capacidade resistente da conexão.
- Os modelos com capa de concreto apresentaram capacidade resistente maior (ou similar) em relação aos modelos sem capa de concreto. A capa de concreto contribuiu para o aumento da capacidade resistente. No entanto, conforme o número de conectores de cisalhamento diminuía, a capacidade resistente das vigas celulares mistas se tornava semelhante devido a falha ocorrer na interface aço-concreto;
- Em geral, os modelos com duas linhas de conectores de cisalhamento apresentaram capacidade resistente maior em relação aos modelos com uma única linha. Isso ocorreu porque quanto maior o número de conectores maior a resistência da interface aço-concreto (ação mista).
- Os modelos que apresentaram o mesmo número de conectores de cisalhamento, independente do espaçamento, obtiveram valores de capacidade resistente semelhantes;
- Houve queda da capacidade resistente devido à ausência de conectores de cisalhamento nas aberturas próximas ao apoio. Embora o número de conectores possa ter influência na capacidade resistente da viga mista, os resultados indicam que isso é menos importante que a presença de conectores sobre as aberturas mais próximas aos apoios.
- A resistência à ação mista é um fator importante a ser considerado no cálculo da capacidade resistente à instabilidade no montante de alma. Isso significa que quanto maior o número de conectores de cisalhamento maior a capacidade resistente à instabilidade no montante de alma.

7.

CONSIDERAÇÕES FINAIS

O presente trabalho teve como objetivo estudar a capacidade resistente de vigas celulares mistas associadas às lajes alveolares pré-fabricadas de concreto. Inicialmente, seriam utilizadas análises numéricas e experimentais. Contudo, devido às limitações impostas pela pandemia de covid-19, o estudo foi realizado utilizando simulações numéricas.

7.1 CONCLUSÕES

Com base nos resultados relacionados à "*Capacidade resistente de vigas celulares mistas com lajes alveolares*" concluiu-se que:

i. Com a variação dos parâmetros geométricos D_o/d e p/D_o e considerando seções de aço simétricas e assimétricas foram identificados quatro modos de falha: instabilidade no montante de alma, instabilidade do montante de alma combinado com algum mecanismo plástico, mecanismo plástico e mecanismo Vierendeel. Além disso, também foi verificada a combinação desses modos de falha com a ruptura do conector de cisalhamento. Nas seções simétricas, a instabilidade no montante de alma foi verificada para as séries com D_o/d variando entre 0,8 e 1,0. Isto significa que quanto maior a altura dos tês, maior será a

resistência a algum mecanismo plástico. Dessa forma, a partir da série D_o/d=1,1 e p/D_o=1,5 os modos de falha foram caracterizados pela combinação da instabilidade no montante de alma com algum mecanismo plástico ou até mesmo o mecanismo Vierendeel. Nesse contexto, o aumento do diâmetro de abertura implicava em redução nas alturas dos tês e, consequentemente, redução da capacidade resistente à formação de algum mecanismo plástico. Em contrapartida, nas seções assimétricas não foi observada a ocorrência exclusiva de instabilidade no montante de alma. Isso ocorreu porque o tê inferior apresenta rigidez maior que o tê superior. Assim, nas seções assimétricas foi predominante a ocorrência de instabilidade no montante de alma combinada com mecanismo plástico (séries D_o/d=0,8-1,1). Além disso, nos modelos com capa de concreto foi verificada, com predominância, a ruptura do conector de cisalhamento. A capa de concreto aumentou a resistência da laje à compressão axial e esse fator pode levar a falha da viga mista para a conexão aço-concreto ou, até mesmo, para o perfil celular.

ii. Em relação ao tipo de laje, vigas celulares com lajes alveolares pré-fabricadas apresentaram capacidade resistente maior ou igual às vigas celulares mistas com lajes mistas de aço e concreto. Contudo, nas vigas celulares mistas em que foi utilizada capa de concreto, houve aumento considerável da capacidade resistente evidenciando a contribuição da capa.

iii. Os resultados da modelagem numérica mostraram que a falha por instabilidade do montante de alma não é governada apenas pelas características do perfil de aço. Tal afirmação se deve à influência do tipo de laje, observada no presente estudo. Por exemplo, modelos com seção simétrica de aço e laje alveolar pré-fabricada com capa de concreto tiveram a capacidade resistente, de modo geral, governada pela instabilidade da alma. Esses modelos apresentaram maior capacidade resistente quando comparado com os modelos formados apenas pela laje alveolar e laje mista de aço e concreto. Isso significa que a capa de concreto contribuiu para a capacidade resistente da viga celular mista à força cortante global.

Quanto ao estudo referente à influência da "A*ção mista na capacidade resistente à instabilidade do montante de alma*" foi possível concluir:

iv. Ao variar os parâmetros geométricos do perfil celular (D_o/d; p/D_o) e o espaçamento entre os conectores de cisalhamento, considerando uma e duas linhas de conexão, foram identificados três modos de falhas: instabilidade no montante de alma combinada com mecanismo plástico, mecanismos plástico e Vierendeel. Além desses modos de falha, também foi verificada a combinação desses modos com a ruptura dos conectores de

cisalhamento. Nos modelos com capa de concreto, duas linhas de conexão e 150mm de espaçamento entre conectores de cisalhamento, não houve ruptura dos conectores. Para espaçamentos maiores (300mm e 450mm) foi registrada a combinação dos modos de falha com a ruptura do conector. Esse comportamento é explicado pelo fato de a altura da laje permanecer constante e ocorrer redução do número de conectores reduzindo a ação mista. Isso fez com que o modo de falha migrasse do perfil para a conexão aço-concreto uma vez que as contribuições da laje de concreto comprimida e do duplo tê de aço tracionado permaneciam constantes.

v. De modo geral, foi observado que os modelos com duas linhas de conectores apresentaram capacidade resistente maior que aqueles com uma única linha. Tal afirmação sustenta a contribuição da ação mista na capacidade resistente de vigas celulares mistas associadas a lajes alveolares pré-fabricadas de concreto.

vi. Os resultados do conjunto de modelos analisados permitiram identificar a capacidade resistente equivalente. O termo "capacidade resistente equivalente" utilizado no presente trabalho refere-se à comparação entre os modelos que apresentaram capacidades resistentes semelhantes. Essa afirmação foi fundamentada nos resultados dos modelos que possuíam o mesmo número de conectores, porém com espaçamentos diferentes. Por exemplo, modelos com duas linhas de conectores espaçados de 300mm e modelos com uma linha de conectores com espaçamento de 150mm e que apresentaram capacidades resistentes semelhantes. Ambos os modelos tinham 20 conectores de cisalhamento distribuídos entre o apoio e o meio do vão. Com isso, é possível afirmar que a contribuição da ação mista na capacidade resistente não é função do número de conectores acima da abertura, mas sim do fluxo de cisalhamento. Outro exemplo que sustenta essa afirmação: a resistência equivalente foi avaliada comparando modelos com uma linha de conectores espaçados de 300mm e modelos com duas linhas e espaçados de 450mm. Entre o apoio e o meio do vão foram alocados, respectivamente, nos modelos com 1x300m e 2x450mm, 10 e 14 conectores. Embora haja uma diferença de cerca de 29% no número de conectores, pouco significativa, não houve diferença significativa nas capacidades resistentes.

vii. Nos modelos analisados foram observadas reduções na capacidade resistente dos modelos em duas situações. A primeira situação ocorreu na variação da razão geométrica p/D_o em uma série D_o/d. Essa redução foi observada em alguns modelos que apresentavam largura do montante de extremidade menor que os demais. Isso ocorreu em função da transferência do cisalhamento até a primeira abertura, aquela que se encontra mais próxima do apoio.

Portanto, quanto maior o comprimento do montante de extremidade, maior será a capacidade resistente da viga celular mista. Isso foi válido para uma série cujo diâmetro de abertura foi mantido constante e o comprimento do montante de alma foi variado. Por outro lado, na segunda situação, a redução da capacidade resistente ocorreu nos modelos que não tinham conectores de cisalhamento posicionados acima das aberturas mais próximas do apoio. Portanto, recomenda-se a colocação de conectores acima das aberturas próximas ao apoio, independentemente do espaçamento adotado.

viii. Dentre os 240 modelos analisados, em nenhum deles foi registrado escorregamento superior a 6mm na interface aço-concreto. Contudo, todos os modelos analisados possuíam vão de 6m. Para vigas com maiores vãos, são esperados maiores valores de escorregamento na interface aço-concreto sendo possível que as vigas celulares mistas.

ix. Um modelo analítico para estimar a capacidade resistente de viga celulares mistas com lajes alveolares pré-fabricadas foi proposto. Tal modelo é constituído por três parcelas de resistência: instabilidade no montante de alma, mecanismo Vierendeel e ação mista. A resistência à instabilidade no montante de alma e ao mecanismo Vierendeel são calculados conforme as recomendações da SCI P355. Entretanto, no cálculo da resistência ao mecanismo Vierendeel foram introduzidos dois fatores (A_{wT}/A_T e D_o/d), pois não se pode afirmar que ambos os tês (superior e inferior) estão completamente plastificados. Por fim, a parcela de resistência correspondente à ação mista é calculada em função do fluxo de cisalhamento, ou seja, em função da razão da capacidade resistente do conector pelo espaçamento entre eles, multiplicada por um fator *k* que leva em consideração o número de linhas de conectores. O modelo proposto apresentou resultados satisfatórios quando comparado aos 180 resultados de vigas celulares mistas associadas às lajes alveolares com e sem capa de concreto e que tiveram a capacidade resistente governada pela instabilidade do montante de alma ou combinada a algum outro mecanismo.

7.2 SUGESTÕES PARA FUTUROS TRABALHOS

Com a realização do presente trabalho foram identificadas diversas questões que merecem ser investigadas em futuros trabalhos. Assim, visando dar continuidade ao estudo de vigas celulares mistas formadas por lajes alveolares pré-fabricadas de concreto são sugeridos os seguintes estudos:

- Análise experimental:

i. Avaliar o grau de interação por meio do perfil de deformação axial nas seções "duplo tê" próximas ao apoio e de momento fletor máximo;

ii. Investigar a influência do vão e do vão de cisalhamento na capacidade resistente da viga celular mista;

iii. Considerar materiais compósitos para o concreto de preenchimento das lajes alveolares como, por exemplo, concreto reforçado com fibras de aço;

iv. Avaliar a influência da altura da laje alveolar na capacidade resistente.

- Análise numérica:

i. Parametrizar a influência da resistência do concreto de preenchimento;

ii. Parametrizar a influência da resistência ao escoamento do perfil celular;

REFERÊNCIAS BIBLIOGRÁFICAS

ABAMBRES, M. et al. Neural Network-Based Formula for the Buckling Load Prediction of I-Section Cellular Steel Beams. **Computers**, v. 8, n. 1, p. 2, 26 dez. 2018.

ABREU, L. M. P. **Determinação do momento fletor resistente à flambagem lateral com torção de vigas de aço celulares**. [s.l.] 2011. Dissertação de Mestrado. Universidade Federal de Minas Gerais, 2011.

AGGELOPOULOS, E.; HANUS, F.; LAWSON, M. **Shear connection requirements for composite cellular beams**. Proceedings 12th international conference on Advances in Steel-Concrete Composite Structures - ASCCS 2018. **Anais**...Valencia: Universitat Politècnica València, 2018

AHMED, I. M.; TSAVDARIDIS, K. D. The evolution of composite flooring systems: applications, testing, modelling and eurocode design approaches. **Journal of Constructional Steel Research**, v. 155, p. 286–300, 2019.

AHMED K. EL-SAYED AND ABDULRAHMAN M. ALHOZAIMY, A. I. A.-N. Web Shear Resistance of Prestressed Precast Deep Hollow Core Slabs. **ACI Structural Journal**, v. 116, n. 1, [s.d.].

AMERICAN INSTITUTE OF STEEL CONSTRUCTION. **ANSI/AISC 360-16 - Specification for structural steel buildings.**Chicago, 2016.

ARAÚJO, D. L. et al. Headed steel stud connectors for composite steel beams with precast hollow-core slabs with structural topping. **Engineering Structures**, v. 107, p. 135–150, 2016.

ASSOCIAÇÃO BRASILEIRA DE NORMAS TÉCNICAS. **NBR 9062: Projeto e execução de estruturas de concreto pré-moldado**Rio de Janeiro, 2017.

BADKE-NETO, A.; CALENZANI, A. F. G.; FERREIRA, W. G. Estudo de

metodologias para o dimensionamento de vigas mistas de aço e concreto com perfil celular. **Revista IBRACON de Estruturas e Materiais**, v. 8, n. 6, p. 843–859, 2015.

BARAN, E. Effects of cast-in-place concrete topping on flexural response of precast concrete hollow-core slabs. **Engineering Structures**, v. 98, p. 109–117, set. 2015.

BATISTA, E. M.; LANDESMANN, A. **Análise experimental de vigas mistas de aço e concreto compostas por lajes alveolares e perfis laminados. COPPETEC, PEC-18541**Rio de Janeiro, 2016.

BEHNAM, H.; KUANG, J. S.; SAMALI, B. Parametric finite element analysis of RC wide beam-column connections. **Computers & Structures**, v. 205, p. 28–44, ago. 2018.

BENITEZ, M. A.; DARWIN, D.; DONAHEY, R. C. Deflections of composite beams with web openings. **Journal of Structural Engineering**, v. 124, n. 10, p. 1139–1147, out. 1998.

BOISSONNADE, N. et al. Design of cellular beams against lateral torsional buckling. **Proceedings of the Institution of Civil Engineers - Structures and Buildings**, v. 167, n. 7, p. 436–444, 2013.

BONILLA, J. et al. Review of stud shear resistance prediction in steel-concrete composite beams. **Steel and Composite Structures**, v. 27, n. 3, p. 355–370, 2018.

BRADFORD, M. A. Distortional buckling of monosymmetric I-beams. **Journal of Constructional Steel Research**, v. 5, n. 2, p. 123–136, jan. 1985.

BRADFORD, M. A. Inelastic distortional buckling of I-beams. **Computers and Structures**, v. 24, n. 6, p. 923–933, 1986.

BRADFORD, M. A. Buckling of elastically restrained beams with web distortions. **Thin-Walled Structures**, v. 6, n. 4, p. 287–304, 1988.

BRADFORD, M. A. Buckling of doubly-symmetric cantilevers with slender webs. **Engineering Structures**, v. 14, n. 5, p. 327–334, 1992.

BRINKHUS, R. N. **Análise de vigas casteladas e vigas casteladas mistas**. [s.l.] 2015. Dissertação de Mestrado. Universidade Federal do Rio Grande do Sul, 2015.

BRUNESI, E.; BOLOGNINI, D.; NASCIMBENE, R. Evaluation of the shear capacity of precast-prestressed hollow core slabs: numerical and experimental comparisons. **Materials and Structures**, v. 48, n. 5, p. 1503–1521, 28 maio 2015.

BYFIELD, M. P.; DAVIES, J. M.; DHANALAKSHMI, M. Calculation of the strain hardening behaviour of steel structures based on mill tests. **Journal of Constructional Steel Research**, v. 61, n. 2, p. 133–150, fev. 2005.

CARREIRA, D. J.; CHU, K. H. Stress-Strain Relationship for Plain Concrete in Compression. **ACI Journal Proceedings**, v. 82, n. 6, p. 797–804, 1985.

CARREIRA, D. J.; CHU, K. H. Stress-Strain Relationship for Reinforced Concrete in Tension. **ACI Journal Proceedings**, v. 83, n. 1, 1986.

CATOIA, B. **Lajes alveolares protendidas: cisalhamento em região fissurada por flexão**. [s.l.] 2011. Tese de Doutorado. Universidade de São Paulo, 2011.

CHAPMAN, J. C.; BALAKRISHNAN, S. Experiments on composite beams. **The Structural Engineer**, v. 42, n. 11, p. 369–383, 1964.

CHEN, S.; JIA, Y. Numerical investigation of inelastic buckling of steel–concrete composite beams prestressed with external tendons. **Thin-Walled Structures**, v. 48, n. 3, p. 233–242, mar. 2010.

CHEN, S.; LIMAZIE, T.; TAN, J. Flexural behavior of shallow cellular composite floor beams with innovative shear connections. **Journal of Constructional Steel Research**, v. 106, p. 329–346, 2015.

CHO, S. H. **An investigation on the strength of composite beams with web openings**. [s.l.] 1982. M.Sc. thesis. Hanyang University, 1982.

CHO, S. H. **Slab behaviour in composite beams at web openings**. [s.l.] 1990. Ph.D. thesis. McGill University, 1990.

CHO, S. H.; REDWOOD, R. G. Slab behavior in composite beams at openings. I: analysis. **Journal of Structural Engineering**, v. 118, n. 9, p. 2287–2303, 1992a.

CHO, S. H.; REDWOOD, R. G. Slab behavior in composite beams at openings. II: tests and verification. **Journal of Structural Engineering**, v. 118, n. 9, p. 2304–2322, 1992b.

CHUNG, K. .; LAWSON, R. . Simplified design of composite beams with large web openings to Eurocode 4. **Journal of Constructional Steel Research**, v. 57, n. 2, p. 135–164, fev. 2001.

CHUNG, K. F.; LIU, T. C. H.; KO, A. C. H. Investigation on vierendeel mechanism in steel beams with circular web openings. **Journal of Constructional Steel Research**, v. 57, n. 5, p. 467–490, 2001.

CLAWSON, W. C.; DARWIN, D. Composite beams with web openings. **ASCE Journal of the Structural Division**, v. 108, n. ST1, p. 145–162, 1982a.

CLAWSON, W. C.; DARWIN, D. Tests of composite beams with web openings. **ASCE Journal of the Structural Division**, v. 108, n. ST1, p. 145–162, 1982b.

CLAWSON, W. C.; DARWIN, D. Strength of composite beams at web openings. **ASCE Journal of the Structural Division**, v. 108, n. ST3, p. 623–641, 1982c.

CRISFIELD, M. A. A fast incremental/iterative solution procedure that handles "snap-through". **Computers & Structures**, v. 13, n. 1–3, p. 55–62, jun. 1981.

CRISFIELD, M. A. Snap-through and snap-back response in concrete structures and the dangers of under-integration. **International Journal for Numerical Methods in Engineering**, v. 22, n. 3, p. 751–767, mar. 1986.

DARWIN, D.; DONAHEY, R. C. LRFD for composite beams with unreinforced web openings. **Journal of Structural Engineering**, v. 114, n. 3, p. 535–552, mar. 1988.

DARWIN, D.; LUCAS, W. K. LRFD for steel and composite beams with web openings. **Journal of Structural Engineering**, v. 116, n. 6, p. 1579–1593, jun. 1990.

DAS, P. K.; SRIMANI, S. L. **Handbook for the design of castellated beams**. New Delhi, Delhi, India: Oxford & IBH Publishing Company, 1984.

DASSAULT SYSTÈMES SIMULIA. **Abaqus 6.18**Providence, RI, USA, 2016.

DE NARDIN, S.; DEBS, A. EL. State of the art of steel–concrete composite structures in Brazil. **Proceedings of the Institution of Civil Engineers - Civil Engineering**, v. 166, n. 6, p. 20–27, 2013.

DJEBLI, B.; KERDAL, D. E.; ABIDELAH, A. Additional and total deflection of composite symmetric cellular beams. **Journal of Constructional Steel Research**, v. 158, p. 99–106, 2019.

DONAHEY, R. C.; DARWIN, D. Web openings in composite beams with ribbed slabs. **Journal of Structural Engineering**, v. 114, n. 3, p. 518–534, mar. 1988.

DONOGHUE, C. M. Strength of composite beams with web openings. **ASCE Journal of the Structural Division**, v. 108, n. ST12, p. 2652–2667, 1982.

DU, H. et al. Effect of reinforcement on the strength of the web opening in steel-concrete composite beam. **Engineering Structures**, v. 235, p. 112038, maio 2021.

EARLS, C. J. Effects of material property stratification and residual stresses on single angle flexural ductility. **Journal of Constructional Steel Research**, v. 51, n. 2, p. 147–175, ago. 1999.

EL-LOBODY, E.; LAM, D. Finite Element Analysis of Steel-Concrete Composite Girders. **Advances in Structural Engineering**, v. 6, n. 4, p. 267–281, 7 out. 2003.

EL-SAWY, K. M.; SWEEDAN, A. M. I.; MARTINI, M. I. Moment gradient factor of cellular steel beams under inelastic flexure. **Journal of Constructional Steel Research**, v. 98, p. 20–34, 2014.

ELLOBODY, E. Nonlinear analysis of cellular steel beams under combined buckling modes. **Thin-Walled Structures**, v. 52, p. 66–79, 2012.

ELLOBODY, E.; LAM, D. Modelling of headed stud in steel-precast composite beams. **Steel and Composite Structures**, v. 2, n. 5, p. 355–378, 25 out. 2002.

ERDAL, F.; SAKA, M. P. Ultimate load carrying capacity of optimally designed steel cellular beams. **Journal of Constructional Steel Research**, v. 80, p. 355–368, 2013.

EUROPEAN COMMITTEE FOR STANDARDIZATION. **EN 1994-1-1: Eurocode 4 – Design of composite steel and concrete structures – Part 1-1: General rules for buildings.**Bruxelas, Bélgica, 2004.

EUROPEAN COMMITTEE FOR STANDARDIZATION. **EUROCODE 3: Design of steel structures - Part 1-1: General rules and rules buildings**Brussels, 2005.

EUROPEAN COMMITTEE FOR STANDARDIZATION. **EN 1993-1-5: Eurocode 3 – Design of steel structures – Part 1-5: Plated structural elements.**, 2006.

FAHMY, E. H. Analysis of composite beams with rectangular web openings. **Journal of Constructional Steel Research**, v. 37, n. 1, p. 47–62, mar. 1996.

FARES, S. S.; COULSON, J.; DINEHART, D. W. **AISC Steel Design Guide 31: Castellated and Cellular Beam Design**. [s.l.] American Institute of Steel Construction, 2016.

FERRARI, G. A. **Simulação numérica do comportamento estrutural de vigas alveolares mistas de aço e concreto**. [s.l.] 2013. Dissertação de Mestrado. Universidade Federal de Viçosa, 2013.

FERREIRA, F. P. V. et al. Buckling and post-buckling analyses of composite cellular beams. **Composite Structures**, v. 262, 2021a.

FERREIRA, F. P. V. et al. Steel–Concrete-Composite Beams with Precast Hollow-Core Slabs: A Sustainable Solution. **Sustainability**, v. 13, n. 8, p. 4230, 10 abr. 2021b.

FERREIRA, F. P. V. et al. Ultimate strength prediction of steel–concrete composite cellular beams with PCHCS. **Engineering Structures**, v. 236, p. 112082, jun. 2021c.

FERREIRA, F. P. V.; MARTINS, C. H.; DE NARDIN, S. Advances in composite beams with web openings and composite cellular beams. **Journal of Constructional Steel Research**, v. 172, p. 106182, set. 2020a.

FERREIRA, F. P. V.; MARTINS, C. H.; DE NARDIN, S. A parametric study of steel-concrete composite beams with hollow core slabs and concrete topping. **Structures**, v. 28, p. 276–296, dez. 2020b.

FERREIRA, F. P. V.; MARTINS, C. H.; DE NARDIN, S. Assessment of web post buckling resistance in steel-concrete composite cellular beams. **Thin-Walled Structures**, v. 158, p. 106969, jan. 2021a.

FERREIRA, F. P. V.; MARTINS, C. H.; DE NARDIN, S. Sensitivity Analysis of Composite Cellular Beams to Constitutive Material Models and Concrete Fracture. **International Journal of Structural Stability and Dynamics**, v. 21, n. 01, p. 2150008, 29 jan. 2021b.

FERREIRA, F. P. V.; ROSSI, A.; MARTINS, C. H. Lateral-torsional buckling of cellular beams according to the possible updating of EC3. **Journal of Constructional Steel Research**, v. 153, p. 222–242, fev. 2019.

FERREIRA, F. P. V. **Flambagem lateral com torção em vigas celulares de aço por meio da modificação da distribuição das tensões residuais**. [s.l.] 2019. Dissertação de Mestrado. Universidade Estadual de Maringá, 2019.

GENIKOMSOU, A. S.; POLAK, M. A. Finite element analysis of punching shear of concrete slabs using damaged plasticity model in ABAQUS. **Engineering Structures**, v. 98, p. 38–48, set. 2015.

GIZEJOWSKI, M. A.; KHALIL, W. A. S. **Stability and ductility of castellated composite beams subjected to hogging bending**. (E. Batista, P. Vellasco, L. de Lima, Eds.)SDSS'Rio 2010 STABILITY AND DUCTILITY OF STEEL STRUCTURES. **Anais**...Rio de Janeiro: 2010

GONÇALVES, A. B. **Modelo analítico para o dimensionamento de vigas alveolares mistas de aço e concreto**. [s.l.] 2015. Dissertação de Mestrado. Universidade Federal de Viçosa, 2015.

GOUCHMAN, G. H. **Design of composite beams using precast concrete slabs in accordance with EUROCODE 4. SCI P401.** [s.l.] The Steel Construction Institute, 2014.

GRANADE, C. J. **An investigation of composite beams having large rectangular openings in their webs**. [s.l.] 1968. Partial M.Sc. thesis. University of Alabama, 1968.

GRILO, L. F. **Formulação para determinação da força cortante resistente de flambagem do montante de alma em vigas celulares de aço**. [s.l.] 2018. Tese de Doutorado. Universidade Federal de Minas Gerais, 2018.

GRILO, L. F. et al. Design procedure for the web-post buckling of steel cellular beams. **Journal of Constructional Steel Research**, v. 148, p. 525–541, 2018.

GUEZOULI, S.; LACHAL, A. Numerical analysis of frictional contact effects in push-out tests. **Engineering Structures**, v. 40, p. 39–50, jul. 2012.

GUO, Z. **Principles of Reinforced Concrete**. First edit ed. [s.l.] Elsevier, 2014.

HAMILTON, T. R. **Composite steel and precast concrete slab construction**. [s.l.] 1989. Thesis for admission to corporate membership of Institution of Structural Engineers, 1989.

HASSAN, R.; MOHAREB, M. Distortional lateral torsional buckling for simply supported beams with web cleats. **Canadian Journal of Civil Engineering**, v. 42, n. 12, p. 1091–1103, 2015.

HECHLER, O.; MÜLLER, C.; SEDLACEK, G. **Investigations on Beams with Multiple Regular Web Openings**. Composite Construction in Steel and Concrete V. **Anais**...Reston, VA: American Society of Civil Engineers, 3 fev. 2006Disponível em: <http://ascelibrary.org/doi/abs/10.1061/40826%28186%2926>

HICKS, S. J.; LAWSON, R. M. **Design of composite beams using precast concrete slabs. SCI P287.** [s.l.] The Steel Construction Institute, 2003.

HILLERBORG, A.; MODÉER, M.; PETERSSON, P.-E. Analysis of crack formation and crack growth in concrete by means of fracture mechanics and finite elements. **Cement and Concrete Research**, v. 6, n. 6, p. 773–781, nov. 1976.

IBRAHIM, I. S. et al. Experimental study on the shear behaviour of precast concrete hollow core slabs with concrete topping. **Engineering Structures**, v. 125, p. 80–90, 2016.

JOO, H.-E. et al. Shear Tests of Deep Hollow Core Slabs Strengthened by Core-Filling. **Applied Sciences**, v. 10, n. 5, p. 1709, 2 mar. 2020.

KATWAL, U. et al. Load sharing mechanism between shear studs and profiled steel sheeting in push tests. **Journal of Constructional Steel Research**, v. 174, p. 106279, nov. 2020.

KERDAL, D.; NETHERCOT, D. A. Failure modes for castellated beams. **Journal of Constructional Steel Research**, v. 4, n. 4, p. 295–315, 1984.

LAM, D. **Composite steel beams using precast concrete hollow core floor slabs**. [s.l.] 1998. Ph.D. thesis. University of Nottingham, 1998.

LAM, D. Capacities of headed stud shear connectors in composite steel beams with precast hollowcore slabs. **Journal of Constructional Steel Research**, v. 63, n. 9, p. 1160–1174, 2007a.

LAM, D. Designing composite beams with precast hollowcore slabs to Eurocode 4. **Advanced Steel Construction**, v. 3, n. 2, p. 594–606, 2007b.

LAM, D.; EL-LOBODY, E. Behavior of Headed Stud Shear Connectors in Composite Beam. **Journal of Structural Engineering**, v. 131, n. 1, p. 96–107, jan. 2005.

LAM, D.; ELLIOTT, K. S.; NETHERCOT, D. A. Experiments on composite steel beams with precast concrete hollow core floor slabs. **Proceedings of the Institution of Civil Engineers - Structures and Buildings**, v. 140, n. 2, p. 127–138, 2000a.

LAM, D.; ELLIOTT, K. S.; NETHERCOT, D. A. Parametric study on composite steel beams with precast concrete hollow core floor slabs. **Journal of Constructional Steel Research**, v. 54, n. 2, p. 283–304, maio 2000b.

LAWSON, R. M.; CHUNG, K. F.; PRICE, A. M. Tests on composite beams with large web openings to justify existing design methods. **The Structural Enginee**, v. 70, n. 1, p. 1–7, 1992.

LAWSON, R. M.; HANUS, F.; SONCK, D. Large web openings in steel and composite beams. **Steel Construction**, v. 10, n. 2, p. 168–175, maio 2017.

LAWSON, R. M.; HICKS, S. J. **Design of composite beams with large web openings. SCI P355.** [s.l.] The Steel Construction Institute, 2011.

LAWSON, R. M.; LIM, J. B. P.; POPO-OLA, S. O. Pull-out forces in shear connectors in composite beams with large web openings. **Journal of Constructional Steel Research**, v. 87, p. 48–59, ago. 2013.

LAWSON, R. M. M. et al. Design of composite asymmetric cellular beams and beams with large web openings. **Journal of Constructional Steel Research**, v. 62, n. 6, p. 614–629, jun. 2006.

LAWSON, R. M.; SAVERIRAJAN, A. H. A. Simplified elasto-plastic analysis of composite beams and cellular beams to Eurocode 4. **Journal of Constructional Steel Research**, v. 67, n. 10, p. 1426–1434, 2011.

LEE, J.; FENVES, G. L. Plastic-Damage Model for Cyclic Loading of Concrete Structures. **Journal of Engineering Mechanics**, v. 124, n. 8, p. 892–900, ago. 1998.

LIU, X. et al. Finite element modelling of steel–concrete composite beams with high-strength friction-grip bolt shear connectors. **Finite Elements in Analysis and Design**, v. 108, p. 54–65, jan. 2016.

LUBLINER, J. et al. A plastic-damage model for concrete. **International Journal of Solids and Structures**, v. 25, n. 3, p. 299–326, 1989.

MAEWAL, A.; NACHBAR, W. Stable Postbuckling Equilibria of Axially Compressed, Elastic Circular Cylindrical Shells: A Finite-Element Analysis and Comparison With Experiments. **Journal of Applied Mechanics**, v. 44, n. 3, p. 475–481, 1 set. 1977.

MEGHARIEF, J. D. **Behavior of composite castellated beams**. [s.l.] 1997. Partial M.Sc. thesis. McGill University, 1997.

MENZIES, J. B. Cp 117 and Shear Connectors in Steel-Concrete Composite Beams

Made With Normal-Density of Lightweight Concrete. **Structural Engineer**, v. 49, n. 3, p. 137–154, 1971.

MICHELINI, E. et al. Experimental and Numerical Assessment of Flexural and Shear Behavior of Precast Prestressed Deep Hollow-Core Slabs. **International Journal of Concrete Structures and Materials**, v. 14, n. 1, p. 31, 7 dez. 2020.

MOY, S. S. J.; TAYLER, C. The Effect of Precast Concrete Planks on Shear Connector Strength. **Journal of Constructional Steel Research**, v. 36, n. 3, p. 201–213, 1996.

MÜLLER, C. et al. **Large web openings for service integration in composite floors. Technical Steel Research. European Comission, Contract No 7210-PR/315. Final report**, 2006.

NADJAI, A. **Performance of cellular composite floor beams at ambient temperature**. [s.l: s.n.].

NADJAI, A. et al. Performance of cellular composite floor beams at elevated temperatures. **Fire Safety Journal**, v. 42, n. 6–7, p. 489–497, set. 2007.

NARAYANAN, R.; AL-AMERY, R. I. M.; ROBERTS, T. M. Shear strength of composite plate girders with rectangular web cut-outs. **Journal of Constructional Steel Research**, v. 12, n. 2, p. 151–166, jan. 1989.

NGUYEN, T. N. H.; TAN, K. H.; KANDA, T. Investigations on web-shear behavior of deep precast, prestressed concrete hollow core slabs. **Engineering Structures**, v. 183, n. January, p. 579–593, 2019.

OLIVEIRA, L. B. **Definição da geometria de vigas alveolares de aço para sistemas de piso e de cobertura**. [s.l.] 2012. Dissertação de Mestrado. Universidade Federal de Viçosa, 2012.

OLLGAARD, J. G.; SLUTTER, R. G.; FISHER, J. W. Shear strength of stud connectors in lightweight and normal weight concrete. **AISC Engineering Journal**, v. 1971, n. April, p. 55–34, 1971.

PAJARI, M. Shear Resistance of PHC Slabs Supported on Beams. II: Analysis. **Journal of Structural Engineering**, v. 124, n. 9, p. 1062–1073, set. 1998.

PAJARI, M.; KOUKKARI, H. Shear Resistance of PHC Slabs Supported on Beams. I: Tests. **Journal of Structural Engineering**, v. 124, n. 9, p. 1050–1061, set. 1998.

PALMER, K. D.; SCHULTZ, A. E. Experimental investigation of the web-shear strength of deep hollow-core units. **PCI Journal**, v. Fall, p. 83–104, 2011.

PANEDPOJAMAN, P.; RONGRAM, T. Design Equations for Vierendeel Bending of Steel Beams with Circular Web Openings. **World Congress on Engineering 2014**, v. II, n. c, p. 0–5, 2014.

PANEDPOJAMAN, P.; SAE-LONG, W.; CHUB-UPPAKARN, T. Cellular beam design for resistance to inelastic lateral-torsional buckling. **Thin-Walled Structures**, v. 99, p. 182–194, 2016.

PANEDPOJAMAN, P.; THEPCHATRI, T.; LIMKATANYU, S. Novel design

equations for shear strength of local web-post buckling in cellular beams. **Thin-Walled Structures**, v. 76, p. 92–104, 2014.

PARK, J. W.; KIM, C. H.; YANG, S. C. Ultimate Strength of Ribbed Slab Composite Beams with Web Openings. **Journal of Structural Engineering**, v. 129, n. 6, p. 810–817, 2003.

PIASSI, A. D. et al. Lateral distortional buckling of cellular composite-beams. **Revista IBRACON de Estruturas e Materiais**, v. 11, n. 2, p. 331–356, 2018.

QUEIROZ, F. D.; VELLASCO, P. C. G. S.; NETHERCOT, D. A. Finite element modelling of composite beams with full and partial shear connection. **Journal of Constructional Steel Research**, v. 63, n. 4, p. 505–521, 2007.

REDWOOD, R.; CHO, S. H. Design of steel and composite beams with web openings. **Journal of Constructional Steel Research**, v. 25, n. 1–2, p. 23–41, jan. 1993.

REDWOOD, R. G.; POUMBOURAS, G. Tests of composite beams with web holes. **Canadian Journal of Civil Engineering**, v. 10, n. 4, p. 713–721, dez. 1983.

REDWOOD, R. G.; POUMBOURAS, G. Analysis of composite beams with web openings. **Journal of Structural Engineering**, v. 110, n. 9, p. 1949–1958, set. 1984.

REDWOOD, R. G.; WONG, P. K. **Web holes in composite beams with steel deck**. Canadian Structural Engineering Conference -1982. **Anais**...Ontario, Toronto: Canadian Steel Construction Council, 1982

ROBERTS, T. M.; AL-AMERY, R. I. M. Shear strength of composite plate girders with web cutouts. **Journal of Structural Engineering**, v. 117, n. 7, p. 1897–1910, jul. 1991.

SAMEER S. FARES; COULSON, J.; DAVID W. DINEHART. Castellated and Cellular Beam Design 31. **American Institute of Steel Construction**, 2016.

SHEEHAN, T. et al. Experimental study on long spanning composite cellular beam under flexure and shear. **Journal of Constructional Steel Research**, v. 116, p. 40–54, 2016.

SILVEIRA, E. G. **Avaliação do comportamento estrutural de vigas alveolares de aço com ênfase nos modos de colapso por plastificação**. [s.l.] 2011. Dissertação de Mestrado. Universidade Federal de Viçosa, 2011.

SJAARDA, M. et al. Fatigue Behavior of Welded Shear Studs in Precast Composite Beams. **Journal of Bridge Engineering**, v. 22, n. 11, p. 04017089, nov. 2017.

SONCK, D.; BELIS, J. Lateral-torsional buckling resistance of cellular beams. **Journal of Constructional Steel Research**, v. 105, p. 119–128, 2015.

SWEEDAN, A. M. I. Elastic lateral stability of I-shaped cellular steel beams. **Journal of Constructional Steel Research**, v. 67, n. 2, p. 151–163, 2011.

TAWADROUS, R.; MORCOUS, G. Shear Strength of Deep Hollow-Core Slabs. **ACI Structural Journal**, v. 115, n. 3, maio 2018.

TODD, D. M.; COOPER, P. B. Strength of composite beams with web openings. **ASCE Journal of the Structural Division**, v. 106, n. ST2, p. 431–444, 1980.

TSAVDARIDIS, K. D.; D'MELLO, C. Web buckling study of the behaviour and strength of perforated steel beams with different novel web opening shapes. **Journal of Constructional Steel Research**, v. 67, n. 10, p. 1605–1620, 2011.

TSAVDARIDIS, K. D.; D'MELLO, C. Vierendeel Bending Study of Perforated Steel Beams with Various Novel Web Opening Shapes through Nonlinear Finite-Element Analyses. **Journal of Structural Engineering**, v. 138, n. 10, p. 1214–1230, 2012.

VERÍSSIMO, G. .; FAKURY, R. . Design of steel and composite beams with web openings. **Journal of Constructional Steel Research**, v. 46, n. 1–3, p. 207, abr. 1998.

VERÍSSIMO, G. S. **Análise e comportamento de vigas de aço e vigas mistas com aberturas na alma**. [s.l.] 1996. Dissertação de Mestrado. Universidade Federal de Minas Gerais, 1996.

VERWEIJ, J. G. **Cellular beam-columns in portal frame structures**. [s.l.] 2010. M.Sc. thesis. Delft University of Technology Civil Engineering, 2010.

VIEIRA, H. C. **Análise numérica da flambagem do montante de alma devida ao cisalhamento em vigas de aço celulares**. [s.l.] 2014. Dissertação de Mestrado. Universidade Federal de Minas Gerais, 2014.

WALRAVEN, J. C.; MERCX, W. P. M. The bearing capacity of prestressed hollow core slabs. **Heron**, v. 28, n. 3, p. 1–46, 1983.

WARD, J. K. **Design of Composite and Non-Composite Cellular Beams**. Silwood Park, Ascot, UK: Steel Construction Institute, 1990.

WARREN, J. J. **Ultimate load and deflection behaviour of cellular beams**. [s.l.] 2001. M.Sc. thesis. University of Natal, 2001.

WIJESIRI PATHIRANA, S. et al. Flexural behaviour of composite steel–concrete beams utilising blind bolt shear connectors. **Engineering Structures**, v. 114, p. 181–194, maio 2016.

YUN, X.; GARDNER, L. Stress-strain curves for hot-rolled steels. **Journal of Constructional Steel Research**, v. 133, p. 36–46, jun. 2017.

ZHOU, W.-B.; YAN, W.-J. Refined nonlinear finite element modelling towards ultimate bending moment calculation for concrete composite beams under negative moment. **Thin-Walled Structures**, v. 116, p. 201–211, jul. 2017.

ZIRAKIAN, T.; SHOWKATI, H. Distortional buckling of castellated beams. **Journal of Constructional Steel Research**, v. 62, n. 9, p. 863–871, 2006.

APÊNDICES

Advances in composite beams with web openings and composite cellular beams

Felipe Piana Vendramell Ferreira*[a], Carlos Humberto Martins[b], Silvana De Nardin[a]

[a]Federal University of São Carlos, Rod. Washington Luiz, km 235, São Carlos, São Paulo, Brazil.

[b]State University of Maringá, Av. Colombo nº 5790, Maringá, Paraná, Brazil.

*Corresponding author

E-mail addresses: fpiana@live.com (F. P. V. Ferreira), chmartins@uem.br (C. H. Martins), snardin@ufscar.br (S. De Nardin)

Abstract

In the last two decades, civil construction has used steel elements to compose the structural framework. The use of composite elements of steel and concrete in multi-storey buildings has been gaining market share in several countries, mainly due to the possibility of reducing the height of the building, the structure's own weight and the speed of execution. In the early 1990s, due to the development of automated cutting and welding, beams with sequential web openings started to be manufactured. There are many challenges for multi-storey buildings design engineers, such as the height limitations that are stipulated by zoning and the need to match the height of the floors. In this context, the use of composite beams with web openings is an advantageous tool. The article aims to present the background that has been developed on composite beams with web openings and composite cellular beams, considering conventional floors, in which the concrete slab is placed on the upper flange of steel profile. Studies are presented, considering firstly composite beams with web openings, and later the composite cellular beams, formed by solid and composite slabs. Concluding remarks and future research directions of composite cellular beams are presented.

Keywords: Cellular beams. Web openings. Composite beams. Shear connectors. Solid slab. Composite slab.

NOTATION

The following notations and symbols are used in this paper

Asc the cross-sectional area of shear connector
b the width of the concrete slab
b_{eff} the effective width of the concrete slab
b_f the width of the flange
b_p the width of plastification line
b_w the width of the web post
b_{wc} the effective width of the concrete flange for shear
b_{we} the width of the web post at end
C the axial force in concrete of a composite section
C_1 the dimensionless constant in Eq. (19)
C_2 the dimensionless constant in Eq. (19)
C_3 the dimensionless constant in Eq. (19)
D_o the opening diameter
d the depth of parent section;
d_t the depth of tee section;
$d_{ef,comp}$ the effective depth of composite cellular beam
d_g the depth of cellular beam
d_{sc} the shear connector diameter
E the modulus of elasticity of the steel
E_c the modulus of elasticity of the concrete
f_c the compressive cylinder strength of concrete
f_u the ultimate strength
f_y the yield strength
H the overall depth of the slab
h_c the thickness of concrete above decking profile
h_o the height of the opening
h_p the depth of decking profile
h_{sc} the shear connector height
h_w the depth of the web of tee
L span
l_e effective length of opening
l_{eff} effective length of web-post
$l_{o,eff}$ effective length of opening for classification of tee
$l_{eff,P}$ effective length of web-post according Panedpojaman's model
M moment at opening
M_{vc} Vierendeel bending resistance due to local composite action
M_{vh} moment generated by horizontal shear force
$M_{pl,N}$ plastic bending resistance of tee section reduced for axial force
$M_{W,e}$ elastic bending moment of web post
$M_{W,Rk}$ flexural strength of Ward's model;
N axial tension force due to the global moment
N_{pl} plastic resistance of tee
n the number of shear connectors placed over the distance from the nearer support to the centreline of the opening
n_h the number of shear connectors placed over the opening
p the length between the opening diameter centers
Q the resistance of shear connector;
s spacing of the shear connectors
t_f the thickness of the flange
t_w the thickness of the web
T the axial force in steel
V the global shear force;
V_b the shear force in bottom tee
V_c the shear resistance of concrete slab
V_{ch} the shear force resisted by the concrete slab at the opening;
V_h the horizontal shear force
$V_{h,eff}$ the effective horizontal shear force
$V_{h,p}$ the horizontal plastic shear resistance
$V_{Gh,Rk}$ resistance to the horizontal shear force, according Grilo's model
$V_{Lv,Rk}$ resistance to the vertical shear force, according Lawson's model
V_{pl} the plastic shear resistance of tee
V_T and V_b the shear force in tee
$V_{Wh,Rk}$ resistance to the horizontal shear force, according Ward's model
x the distance from the nearer support to the centreline of the opening
y_o the distance from the geometric center of the bottom tee to bottom edge
y_p the depth of plastification line
y_t or y_b the depth of the centroid of the tee from the outer edge of the flange;
β_G the dimensionless constant in Eq. (38)
ε strain
θ angle
$\overline{\lambda}$ reduced slenderness factor
λ_w web slenderness ratio
σ stress
χ reduction factor

1. INTRODUCTION

The use of steel-concrete composite elements in multi-storey buildings has been gaining market share in several European countries, in the United States, Canada and Australia, mainly due to the possibility of reducing the height of the building, the structure's own weight and the speed of execution. Other advantages of the steel-concrete composite systems are the possibility of reducing or dispensing formworks and shoring, increasing the dimensional accuracy of structural elements, considerably reducing the consumption of structural steel and increasing the structure stiffness [1].

Steel-concrete composite structures are elements whose cross section is formed by structural concrete and steel profile, both working together to resist the applied loads. In the case of composite beams, the main advantage of this association is that concrete and steel work in a supportive manner: the concrete fundamentally resists compression, while steel resists tension. This results in steel savings and the mobilization of an effective width of the concrete slab that will contribute to the resistance.

In a composite beam, the steel profile and the concrete slab, precast[1] or not, are bonded by shear connectors, which are mechanical devices that connect the steel and concrete in order to promote the composite behavior. The steel-concrete bond, promoted by the shear connectors, is essential to resist the longitudinal shearing forces at the connection interface. The headed stud connectors are the most commonly used mechanical devices [2].

In multi-storey buildings with composite beams, composing floors here called conventional floors, the concrete slab is placed on the upper flange of the steel profile. In this context, the concrete slab can be executed in situ - solid or composite (with embedded steel sheets), or precast hollow core slabs. These elements have a higher quality than structural elements molded in situ, as they are produced in specific environments with monitoring and strict technological control. The use of precast concrete hollow core slabs offers advantages such as the possibility of overcoming large spans, speed and reduced construction costs. In general, a concrete topping is made for the purpose of smooth and uniform finish [3–5].

[1] It is called a precast element to that made in permanent installations far from the construction. This type of precast element may or may not reach the precast level, according to normative criteria.

In the early 1990s, due to the development of automated cutting and welding, beams with sequential web openings started to be manufactured at low costs, thus leading to the expansion of the product in the civil construction market. This advance allowed the alternative of using floor beams with web openings. Cellular or Castellated beams are those with sequential openings, manufactured from thermal cutting and welding, aiming at the expansion of the cross section and, consequently, greater flexural stiffness. Steel beams with sequential circular web openings are called cellular beams.

In the last two decades, civil construction has used steel elements to compose the structural framework. Steel has a much higher resistance than reinforced concrete, resulting in lighter structures with greater dimensional precision and faster execution, an extremely important characteristic of industrialized systems. Another important aspect is the need to use construction processes that result in the quick delivery of the project. In this scenario, the use of industrialized elements combines the speed of execution with the safety of working with structural elements that undergo rigorous quality control, avoiding waste of materials and meeting sustainability requirements. Included in this scope are steel profiles and precast concrete hollow core slabs. From the structural point of view, the good characteristics of the composite beams are unquestionable. It is a structural element with widespread use worldwide and with very consolidated calculation procedures.

There are many challenges for multi-storey buildings design engineers, such as the height limitations that are stipulated by zoning, aesthetic, economic requirements and the need to match the height of the floors [6]. In this context, the use of composite beams with web openings is an advantageous tool that can be used to reduce the height of the floor by solving problems of ducts passages [7,8].The demand for more economical and efficient structures, as in the case of composite cellular beams, has increased in civil construction, mainly in Europe and the United States [9]. However, in comparison with other composite elements, the use of cellular beams has been limited in many countries due to the lack of design specifications and practical analysis procedures [10]. For example, in Brazil the two main causes for the reduced use of composite cellular beams are the lack of knowledge on the part of structural engineers and architects and the failure to include cellular profiles and composite cellular beams in national and foreign technical standards.

The paper aims to present the background that has been developed on composite cellular beams, considering conventional floors. Studies are presented, considering firstly composite beams with rectangular

web openings, and later the composite cellular beams, formed by solid and composite slabs. Also, this paper presents the possible perspectives for composite cellular beams.

2. CELLULAR BEAMS

The first steel beams with expanded section and sequential web openings were widely used in the past in countries such as the USA, Japan, Germany, the United Kingdom, among others, for the construction of buildings, bridges, structures for industry and shipbuilding. The idea of cutting and expanding in order to increase the cross section stiffness was first used in 1910 by the company Chicago Bridge and Iron Works[1], founded in 1889 [11]. Later, this idea was also developed in 1935 by Geoffrey Murray Boyd in Argentina, as an interesting alternative to overcome larger spans without increasing steel consumption. As steel profiles with greater flexural stiffness were not available, Boyd thought of cutting the profile's web in the longitudinal direction, and then welding the parts in order to increase the height of the cross section [12]. Although the idea was patented in the United Kingdom, at that first moment the production of these beams came up against cutting and welding techniques.

In the 1940s, the use of beams with sequential web openings increased substantially due to the limited number of structural profiles that steelmakers could manufacture in Europe. In this way, with low labor costs, steel mills efficiently produced a series of profile sizes with the expansion of the cross section and the presence of openings. Although the beams with web openings were used in steel construction, these structural elements were not used frequently in North America due to high production costs [13].

With the evolution of cutting and welding processes, from the 1980s onwards, beams with web openings have been studied again. In Europe, the production process for these beams has gained popularity due to low manufacturing costs. At the beginning of the 1990s, with the development of automated cutting, there was a reduction in the costs of the manufacturing process and the beams with sequential web openings began to be produced in the United States. In this way, this advance allowed the alternative of using these beams as floor beams in composite elements, with lower production cost. Also, in that same decade, the patent for cellular steel beams was made effective, in the name of Peter A. Walker (US4894898A)[2].

[1] Currently known as Chicago Bridge and Iron Company (CBI®).
[2] PETER A. WALKER. **Method of making Castellated beams**, 1990.

2.1 MANUFACTURING PROCESS

The manufacturing process for cellular beams is illustrated in **Fig. 1**. The cellular beams are produced by means of two thermal cut lines, in the shape of semicircles, in the entire longitudinal web length. After the thermal cutting stage, the modules are separated and then welding. The result of this process is a beam with a cross section that varies between 130% to 160% the height of the original profile.

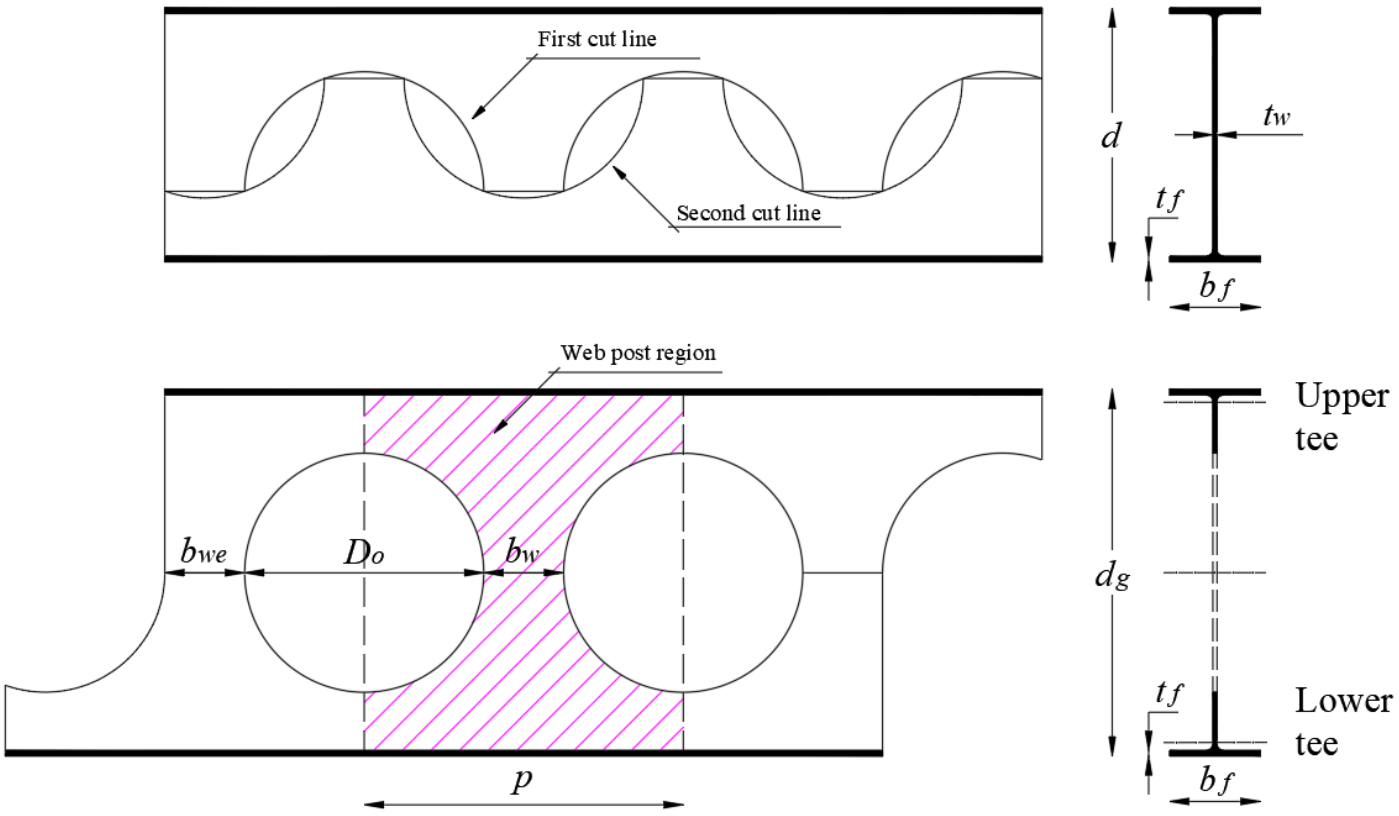

Fig. 1: Cellular beams manufacturing process

2.2 ADVANTAGES AND APPLICATIONS

Cellular beams are ideal for structures with open space requirements, such as parking garages, industries and warehouses, factories, office buildings, schools and hospitals, restoration, and also for the modernization of old buildings, factories and industries. As an example, there is the renovation of the Royal Vale Church (**Fig. 2**), built in 1873 in London, England.

Fig. 2: Restoration of Royal Vale Church [14]

Cellular beams are used as a solution to overcome large spans and reduce the structure's own weight. As an example, **Fig. 3a** shows the construction of Ballymore's Three Snowhill, the largest office development built outside London, and 1ST Manchester Street (**Fig. 3b**), in the same segment.

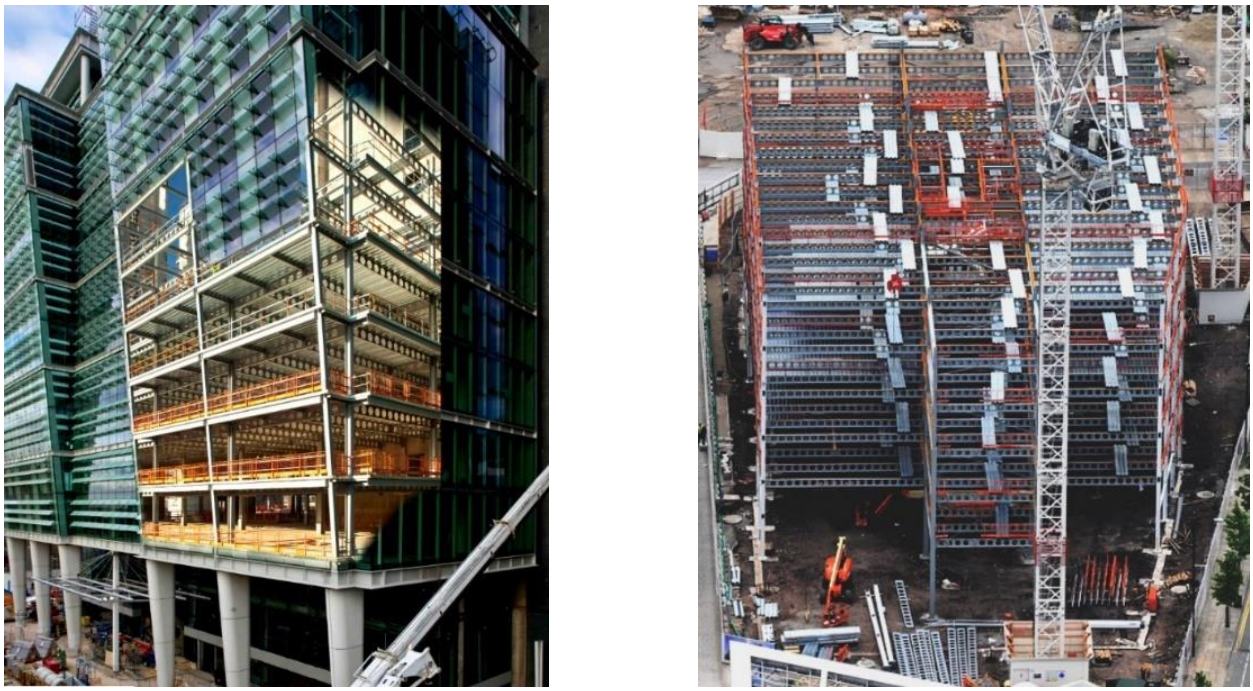

(a) Snowhill Development (b) 1ST Manchester Street

Fig. 3: Examples of buildings [14]

The main reasons for the use of cellular beams in parking beams are the ability to overcome larger spans, thus reducing the number of columns, favoring drainage and air flow, and presenting a better aesthetic aspect of the structure. As an example, the parking at the Altnagelvin Hospital is illustrated in **Fig.4**.

Fig. 4: Altnagelvin Hospital parking [14]

In the case of Offshore elements, the cellular beams reduce the structure's own weight and solve problems of passage of ducts for the integration of services (**Fig. 5)**.

Fig. 5: Ducts passage for the integration of services [14]

2.3 STRUCTURAL BEHAVIOR

Although the expansion of the cross section generates an increase in flexural stiffness, the presence of the openings makes the cellular beams more susceptible to lateral torsional buckling, web distortion, web post buckling, local web buckling, the Vierendeel mechanism, the web post rupture, the web post flexure, or even the combination of buckling modes [15–17].

Lateral torsional buckling (LTB) is a typical behavior of steel profiles, which are in bending about the strong axis without lateral restriction. Due to the cross-section expansion and the presence of openings, cellular beams are more vulnerable to LTB (**Fig. 6**).

Fig. 6: Lateral torsional buckling [18]

In cellular beams, the LTB occurs due to the fact that the compressed "tee" is insufficiently supported laterally [17–19]. In this scenario, the studies of Sweedan [20], Ellobody [15], Boissonnade et al. [19], El-Sawy et al. [16], Sonck and Belis [18], Panedpojaman et al. [17], Ferreira et al. [21], and Ferreira and Martins [22] stands out.

The web distortion, a phenomenon that allows the flange to deflect laterally with torsion, effectively reduces the torsion resistance of the steel profile. In this case, classical assumption that plain webbed sections remain plain after deflection is not valid due to the nature of the boundary conditions that can potentiate this phenomenon [23–27]. In this context, the work of Zirakian and Showkati [28] stands out.

The web post buckling (WPB) can be subdivided into two modes: shear and compression. WPB by shear (**Fig. 7**) becomes critical when the web post width is reduced [29].

Fig. 7: Web post buckling by shear [30]

According to the illustration, this mode of failure is characterized by a lateral displacement with torsion in the web post. The WPB resistance capacity depends on the cellular profile geometric characteristics such as the opening diameter, the web post width and the web thickness. Regarding the studies related to WPB on cellular beams, can be cited Tsavdaridis and D'mello [31], Erdal and Saka [32], Panedpojaman et al. [29], and Grilo et al. [30]. On the other hand, the web post buckling by compression can occur for beams with web

openings in which they are subjected by concentrated force in the region of the web post with the absence of stiffeners.

Local web buckling can occur for slender cross sections. The transfer of forces through the opening causes the web to be requested by compression, which can cause this buckling, if the parameter of slenderness of the web (height/web thickness) is relatively high. This type of instability has little influence on the resistance of composite beams with openings [33,34].

The Vierendeel mechanism is dependent on the presence of high magnitude shear force, and it is a phenomenon characterized by distortion and formation of plastic hinges in regions near to the opening, as illustrated in **Fig. 8**. Physically, the Vierendeel mechanism can be explained when the steel reaches the yield resistance at the ends of the tees due to the combination of normal and shear stresses. Still, this deformation can occur with the presence or not of reinforcements in regions close to the openings. The main parameters that affect this structural behavior are the web thickness and the opening diameter [34–36]. The main studies dealing with this phenomenon in cellular beams are Chung et al. [37], Warren [38], Tsavdaridis and D'Mello [36], Erdal and Saka [32], Panedpojaman et al. [39] and Panedpojaman and Rongram [40].

Fig. 8: Vierendeel mechanism [32]

In most cases, the weld in the web post between tee sections does not influence the local and global behavior of the cellular beams. This is due to the fact that the required thickness is determined in such a way that the horizontal shear force can be transmitted. In addition, fillet welding without chamfering on both sides of the web post proved to be the most efficient and economical solution. However, when the minimum design requirements are not met, the weld may reach to rupture (**Fig. 9**), especially when the web width is reduced [41].

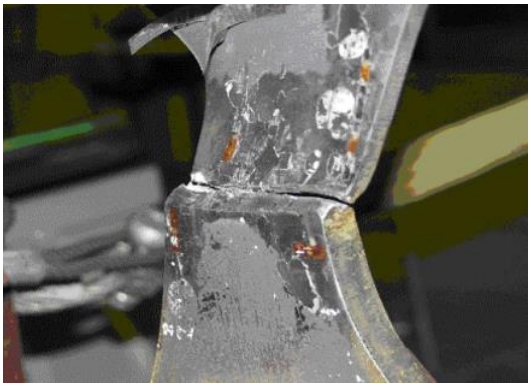

Fig. 9: Welding rupture of web post [41]

3. SHEAR CONNECTORS

Historically, the first studies of composite elements were carried out at the beginning of the 20th century. The researchers were concerned about the connection at the steel-concrete interface. At that time, no mechanical connectors were used. The first experimental test was reported by Mackay et al. [1]. Subsequently, until the end of the 1930s, further investigations were carried out to assess the interaction between the concrete slab and the steel profile. The main study on composite elements was carried out by Batho et al. [2], which verified the inefficiency of the connection at the steel-concrete interface due to the high slip values and suggested the use of mechanical connectors to increase the resistance of the composite action [42].

Lam [42] described that from the 1940s, all studies carried out on composite elements of steel and concrete considered mechanical connectors. As example in 1943, at the University of Lehigh a series of experimental tests were carried out. In this scenario, several studies of rigid connectors in the form of hooks, spiral, among others, were developed. The studies of stud connectors started with Viest[3], which performed pushout tests and found that this type of connection is suitable for shear strength due to its flexible behavior.

The first study considering the head stud connector was carried out by Chapman and Balakrishnan [43]. These authors reported that, although this type of connector was being widely used and studied in the

[1] MACKAY, H. M.; GILLESPIE, P.; LELUAU, C. Report on the strength of steel I-beams haunched with concrete. **Engineering Journal, Eng. Inst. of Canada**. v. 6, n. 8, p. 365-369, 1923.

[2] BATHO, C.; LASH, S. D.; KIRKHAM, R. H. H. The properties of composite beams, consisting of steel joists encased in concrete, under direct and sustained loading. **Journal Institution of Civil Engineering**, v. 11, n. 4, p. 6l-114, 1939.

[3] VIEST, I. M. Investigation of stud shear connectors for composite concrete and steel T-beams. **Journal of American Concrete Institute**, v. 27, n. 8, p. 875-891, 1956.

United States[1,2,3], there were no test results available on the behavior of composite beams with these connection elements. In this scenario, Chapman and Balakrishnan [43] carried out pushout tests, so that the results could be related to the results of bending tests on the composite beams, aiming to evaluate the effect of the height and diameter of the connectors, and also, an alternative device for vertical anchoring. In the tests, the authors described the flexible behavior of the head stud connector, based on the load-slip relationship. However, shear strength was still unknown and was only investigated later [44,45].

With the justification that previous investigations had limited results and it was not possible to provide project recommendations, Ollgaard et al. [45] determined the resistance and behavior of head stud connectors in concrete of normal and light density. For the evaluation, pushout tests were performed. In this study, the authors concluded that the shear strength of head stud, both in normal density and light density concrete, was mainly influenced by the compressive strength of the concrete.

In Menzies [44], comparisons of shear connector strengths were described between Codes of Practice, CP 117 Part 1[4] e Part 2[5], with pushout tests performed at the Building Research Station. Although the recommendations of CP 117 Part 1-2 showed satisfactory results, the author suggested the distinction between connectors embedded in normal density and light concrete.

Head stud connectors are the mechanical devices most commonly used in composite beams and this is due to their behavior. The behavior of the shear connectors is classified according to the capacity resistant to the shear flow that occurs at the steel-concrete interface, the relationship between force and slip, in flexible or rigid. A flexible connector close to reaching its maximum strength continues to deform without rupture, allowing neighboring connectors to increasingly absorb the shear flow. The flexible behavior of head stud connectors, which allows slipping between the concrete slab and the steel profile before reaching the ultimate

[1] BALDWIN, J. W.; HENRY, J. R.; SWEENEY, C. M. **Study of composite bridge stringers - Phase II**. University of Missouri, May, 1965.

[2] BUTTRY, K. E. **Behavior of stud shear connectors in lightweight and normal-weight concrete**. 1965. M.Sc. thesis. University of Missouri, August, 1965, Unpublished.

[3] CHINN, J. **The use of Nelson studs with idealite lightweight-aggregate concrete in composite construction - Part 1.** Engineering Experiment Station, University of Colorado, Boulder, Colorado, April, 1961 (Summarized in AISC Engineering Journal, Vol. 2, No.4, October, 1965).

[4] BRITISH STANDARDS INSTITUTION. CP117: Part 1 – Composite construction in structural steel and concrete: simply-supported beams in building, London, 1965.

[5] BRITISH STANDARDS INSTITUTION. CP117: Part 2 – Composite construction in structural steel and concrete: beams for bridges, London, 1967.

limit state, is one of the reasons for the wide use of this type of connector [2]. Unlike the flexible connector, the rigid connector does not have this ability to deform after the maximum force is reached. However, the resistance to shear stress and the stiffness of the steel-concrete connection depends not only on the resistance of the shear connector, but also on the resistance of the concrete slab against cracking caused by the high concentration of the shear stress in each connector [4,46]. Thus, composite beams are generally designed by partial interaction. This means that the combined strength of the shear connectors is less than the lowest compressive strength of concrete or the tensile strength of the steel profile. In this case, the connection may deform, resulting in relative movement along the steel-concrete interface, causing the elements to lose rigidity. Unlike total interaction, partial interaction favors ductility in the structural system as a whole [47].

There are recommendations for the case of composite beams with web openings and composite cellular beams, based on the EC4 [48] and ANSI/AISC 360-16 [49] standards, respectively. **Table 1** shows the strength calculation models of headed stud connectors.

Table 1: Shear strength of head stud (International System of Units: mm, mm², MPa and N, or cm, cm², kN/cm² and kN)

Ref.	Based on	Concrete failure (N or kN)	Steel Failure (N or kN)
[50]	EC4	$0.29\alpha_{sc}d_{sc}^2\sqrt{f_cE_c}$	$0.8f_uA_{sc}$
[51]	ANSI/AISC 360-16	$0.5A_{sc}\sqrt{f_cE_c}$	f_uA_{sc}

$\alpha_{sc}=0.2\left(h_{sc}/d_{sc}+1\right)$ for $3\le h_{sc}/d_{sc}\le 4$, or $\alpha_{sc}=1.0$ for $h_{sc}/d_{sc}>4$

4. COMPOSITE BEAMS WITH WEB OPENINGS

The initial studies, involving the composite beams with web openings, contemplated the beams with only one rectangular opening formed by solid or composite slabs.

4.1 WITH SOLIDS SLAB

The first study to be cited was fundamental in conducting analytical models of resistance calculations for the design of composite beams with rectangular web openings. Thus, Granade's work [52] stood out, in which tests were presented to predict the stresses based on the theory of the Vierendeel mechanism. The estimates of theoretical stresses in comparison with experimental tests proved to be inaccurate. Granade's work [52] was of paramount importance for the development of the analytical model by Todd and Cooper [53]. The authors presented a calculation methodology, considering moment-shear interaction diagrams, to

estimate the resistant capacity of composite beams in which the rectangular opening position was variable in the span length. The calculation model was based on hypotheses such as total interaction at the steel-concrete interface, the concrete compressive strength was assumed to be $0.85f_c$, the tensile strength of the concrete was disregarded, the shear that causes secondary moment was evenly distributed in the web, only the web of the steel section resists shear, the resistant capacity occurs through the formation of the Vierendeel mechanism (with four plastic hinges), the buckling has been disregarded, the yielding in the steel section due to the combination of normal and shear follows the von Mises criterion, applying the reduction of the web thickness and flange length in such a way that all the fibers of the cross section are yielding, and the neutral plastic axis lies in the concrete slab. According to Todd and Cooper [53] and **Fig. 10**, the calculation procedure can be summarized, assuming the yield criteria (**Eq. 1**):

$$\sigma^2 + 3\tau^2 = f_y^{\ 2} \tag{1}$$

In this scenario, the equivalent web thickness and flange width of the tee section are calculated according to the shear force (**Eqs. 2-3**):

$$t_{w,eq} = t_w \sqrt{1 - 3\left[\frac{V}{(d-2h)t_w f_y}\right]^2} \tag{2}$$

$$b_{f,eq} = b_f + t_{w,eq} - t_w \tag{3}$$

According to the authors, it is considered that the equivalent web thickness and flange width are subject only to normal stresses. In addition, the global shear force is considered to be divided between the lower and upper tee (**Eq. 4**):

$$V = V_T + V_B \tag{4}$$

For sections with double symmetry, V_T=V_B=0.5V. The moment generated by shear force of the tees is calculated according to the length of the rectangular opening, that is (**Eqs. 5-6**):

$$M_{VT} = V_T a \tag{5}$$

$$M_{VB} = V_B a \tag{6}$$

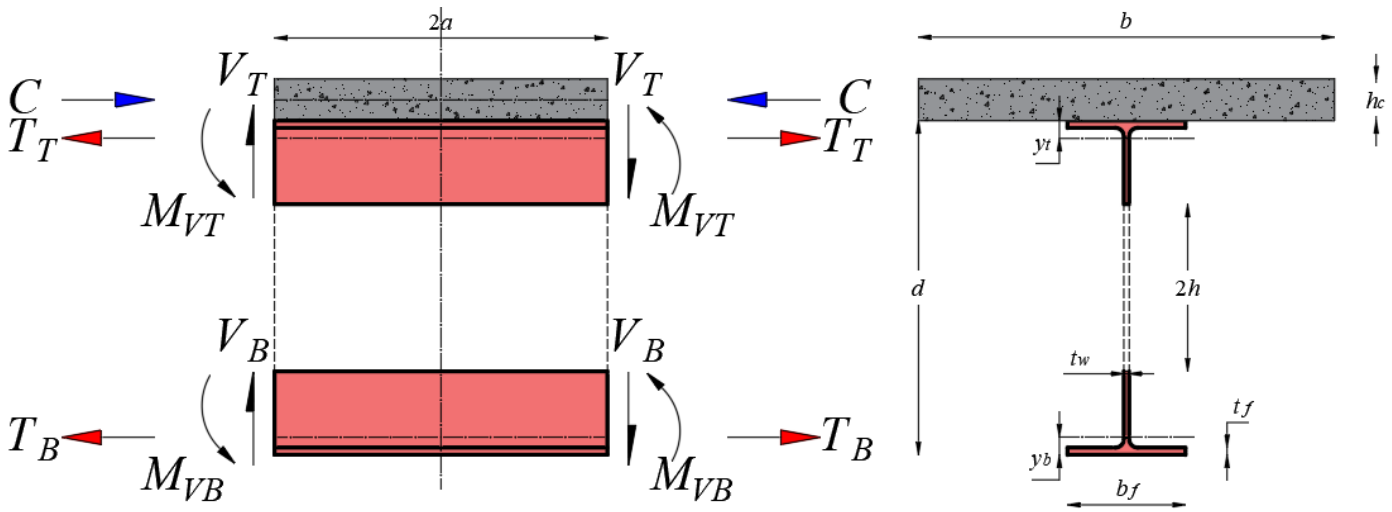

Fig. 10: Free body diagrams at opening, adapted from Todd and Cooper [53] with permission from ASCE

The axial forces in the upper (T_T) and lower (T_B) tees, and their respective positions in the geometric centers, can be calculated according to the moments generated by the shear forces in the tee section, as shown in **Eqs. (5-6)**. Considering the equilibrium of horizontal forces **(Eq. 7)**:

$$C = V_T + V_B \tag{7}$$

The plastic moment is calculated by summing the moments at the top of the slab (**Eq. 8**):

$$M_{pl} = T_B\left(d - y_b + h_c\right) + T_T\left(y_t + h_c\right) - C\left(\frac{1}{2}h_c\right) \tag{8}$$

It is important to note that when V=0, V_B=V_T=M_{VB}=M_{VT}=0. In this scenario, the resistant capacity is calculated as a function of bending. On the other hand, the maximum shear force that the section tee can support is obtained when the global bending moment is equal to zero. In this case, T_T=T_B=C=0. Axial forces are calculated according to the **Eqs. (9-11)**:

$$T_B = A_B f_y \tag{9}$$

$$T_T = A_T f_y \tag{10}$$

$$C = 0.85 f_c b h_c \tag{11}$$

The maximum shear force that the steel section can support (**Eq. 12**):

$$V_{pl} = \frac{f_y d t_w}{\sqrt{3}} \tag{12}$$

The calculation model presented by Todd and Cooper [53] was compared with the experimental results obtained by Granade [52], as illustrated in **Fig 11**. As shown in the illustration, the model underestimates the strength of composite beams with rectangular web openings, as the authors did not consider the contribution of the concrete slab to the shear strength. Another way used to investigate the moment-shear interaction diagrams was by varying parameters such as slab thickness, opening length, height and opening eccentricity. In this context, the theoretical results are conservative in their predictions of the resistant capacity, the variation in the thickness of the slab does not affect the interaction between the bending moment and the shear force and the larger the opening, the smaller the resistant capacity [53].

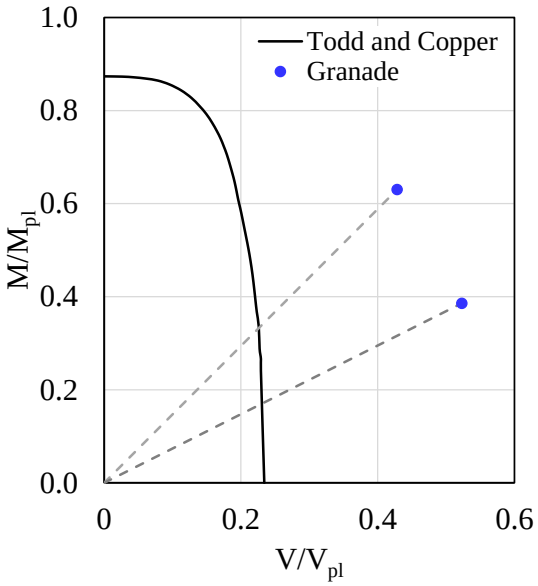

Fig. 11: Comparison of the Todd and Cooper model with the Granade tests, adapted from [53] with permission from ASCE

Concerning the disregard of the contribution of the concrete slab to the shear strength, the Donoghue [54] model also fits, which proposed a design approach that suggests reinforcing the rectangular web opening in order to provide the necessary shear strength. Unlike Todd and Cooper [53], the author considered partial interaction between the elements of steel and concrete. However, the contribution of the concrete flexural strength of the slab was neglected because it is relatively small when compared to the steel profile flexural strength. In view of this model, it was verified that the addition of reinforcement close to the opening region considerably increases the shear strength in the steel profile.

Notably, a greater number of investigations was necessary due to the shear strength, since until then the consideration of this strength was related only to the web, thus omitting the contribution of the concrete

slab in the composite action. In this context, the work of Clawson and Darwin [55] stands out. The authors tested steel beams of the same section used in composite beams with rectangular web openings, to assess the resistance of the steel profile to shear (**Fig 12**). Such methodology measured the contribution of the concrete slab to the shear strength, which in fact was fundamental for the adequacy of the calculation in the analytical models.

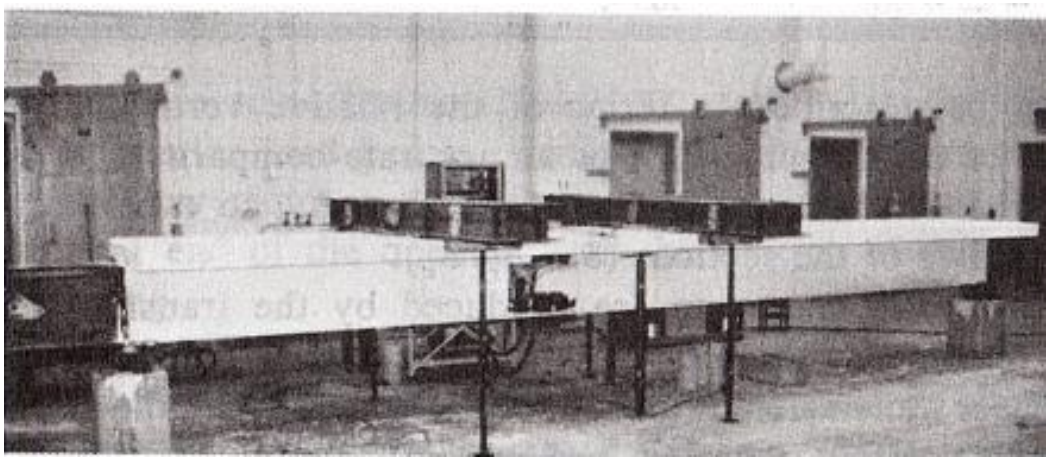

(a) General test arrangement

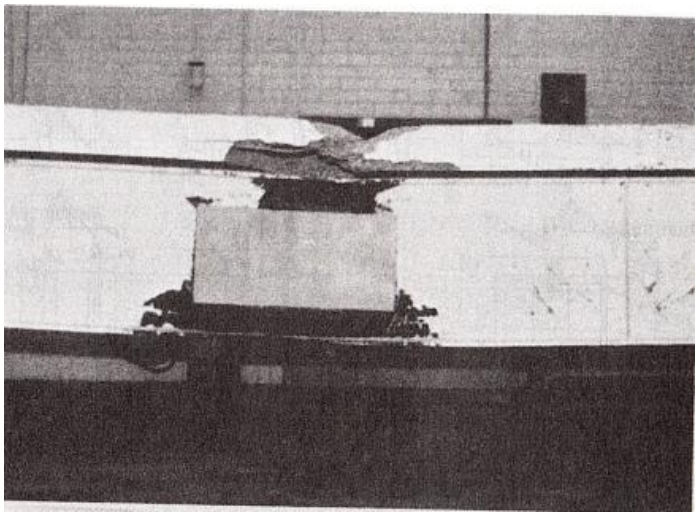

(b) Failure in Beam n.3

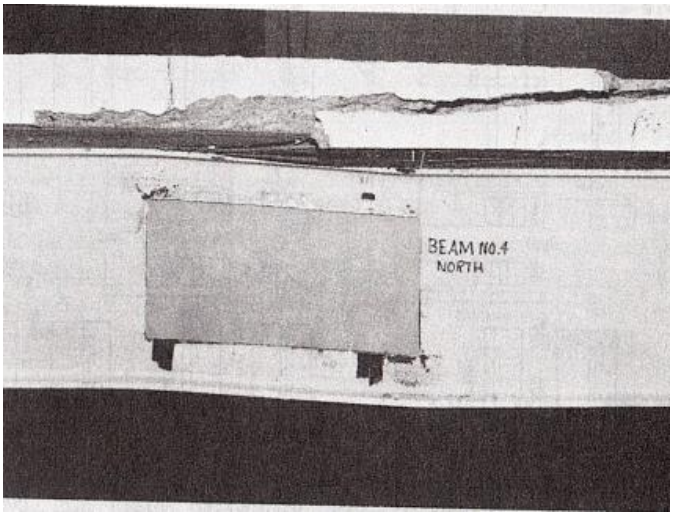

(c) Failure in Beam n.4

Fig. 12: Clawson and Darwin tests, adapted from [55] with permission from ASCE

The authors concluded that the presence of the rectangular web opening effectively reduces the strength of the composite beams; in the region of the opening, the compression strains in the concrete remain low, even after the steel has started to yield; the failure nature of composite beams with web openings was ductile (concrete failure occurs after the yield of steel in the opening region, according to **Fig. 13a**; the ultimate capacity was governed by the failure of the concrete; concrete and steel showed high slip values before the web opening failed; the moment-shear ratio in the opening had a pronounced effect on the ultimate behavior.

399 Beams that showed high values for this ratio failed due to steel yield and concrete crushing. On the other hand,
400 beams that present intermediate values of the moment-shear ratio failed due to the formation of plastic hinges
401 accompanied by failure by tension in the concrete (**Fig. 13b-d**).

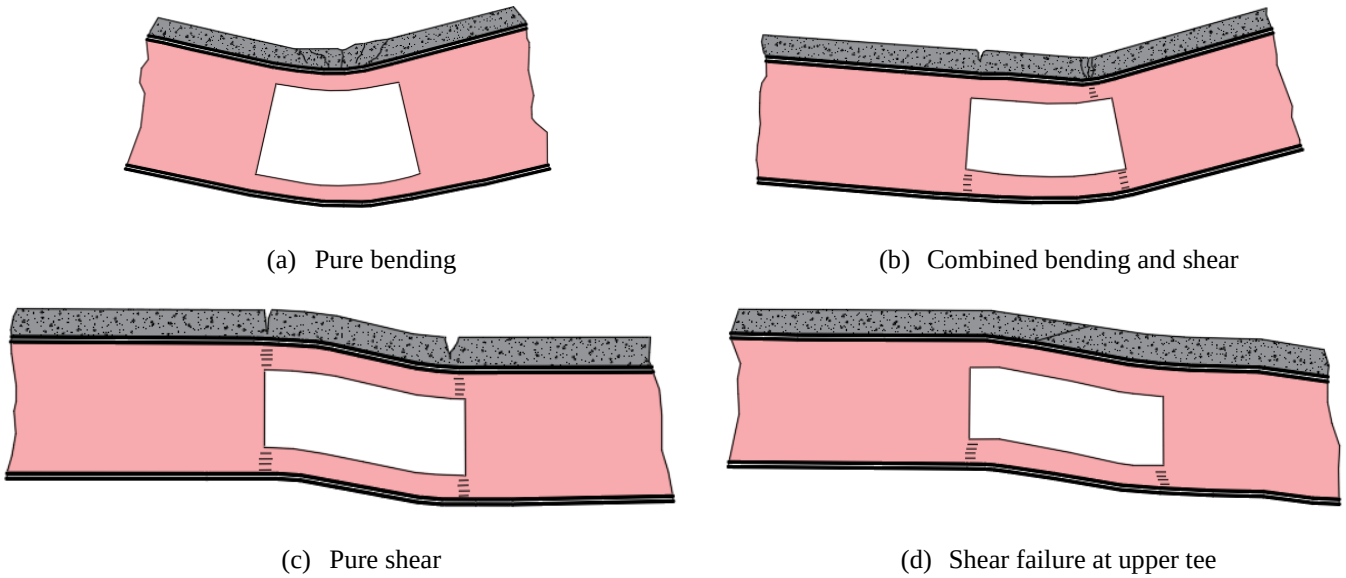

(a) Pure bending (b) Combined bending and shear

(c) Pure shear (d) Shear failure at upper tee

402 **Fig. 13: Modes of failure observed by Clawson and Darwin [56], with permission from ASCE**

403 As in the theory of reinforced concrete, the ultimate flexural strength in composite sections may occur
404 due to the yield of steel in tension or crushing of concrete in compression. For composite sections in which
405 the ductile rupture occurs, the ultimate flexural strength is given by the resistant capacity of the plastic moment
406 of the steel profile. However, for steel profiles that have high resistance values, crushing of the concrete slab
407 can occur before the steel profile has reached its strength. This is due to the position of the plastic neutral axis
408 in the web region, a factor that causes excessive compression stress in concrete slabs and low values of tensile
409 stress on the bottom flange of the steel profile.

410 In view of the previous observations, Clawson and Darwin [56] proposed a method to estimate the
411 resistant capacity of composite beams with rectangular web openings without the use of reinforcement,
412 considering the contribution of the concrete slab to the shear strength (**Fig. 14**). The proposed model predicted
413 the resistant capacity in the opening region by moment-shear interaction diagrams, as previously presented by
414 Todd and Cooper [53]. The procedure can be summarized, according to **Eqs. (13-17)**:

$$C = T_B \tag{13}$$

$$V = V_B + V_T \tag{14}$$

$$2V_B a = M_{VB,L} + M_{VB,H} \quad (15)$$

$$2V_T a = M_{VT,L} + M_{VT,H} \quad (16)$$

$$M_{pl} = T_B d_{eff} + M_{VB,H} + M_{VT,H} - Va \quad (17)$$

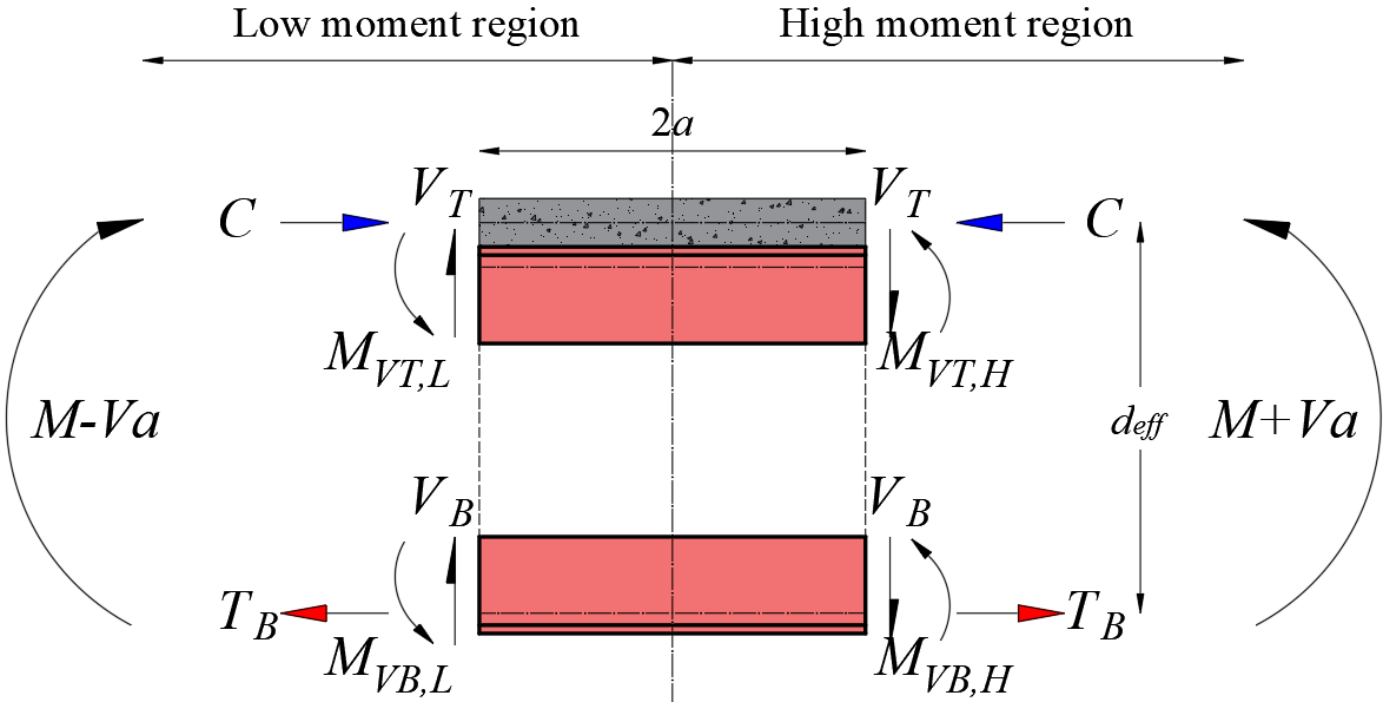

Fig. 14: Forces acting at web opening, adapted from [56] with permission from ASCE

To verify the accuracy of the model, Clawson and Darwin [56] made comparisons with the experimental models of Clawson and Darwin [55] and Granade [52]. However, in the latter case, the authors compared the results, also, with the analytical model previously proposed by Todd and Cooper [53]. Regarding the comparison of the analytical model with the tests by Clawson and Darwin [55], the model in question was conservative, as illustrated in **Fig. 15a** and **Fig. 15b**. On the other hand, when compared to the Granade [52] tests (**Fig. 15c**), the model was closer to the experimental values, unlike the calculation model by Todd and Cooper [53], who underestimate the resistance of these structural elements for neglecting the slab's contribution to shear strength. The calculation model presented by Clawson and Darwin [56] was subsequently supported based on the experimental tests of [57,58]. The comparison of the analytical model with the test results indicated that the forecast improved considerably when compared with Todd and Cooper [53], but still conservative, particularly for the Granade [52] tests.

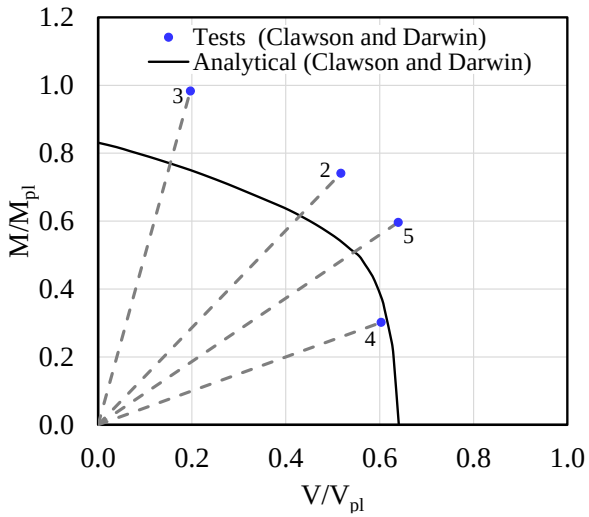

(a) tests of Clawson and Darwin

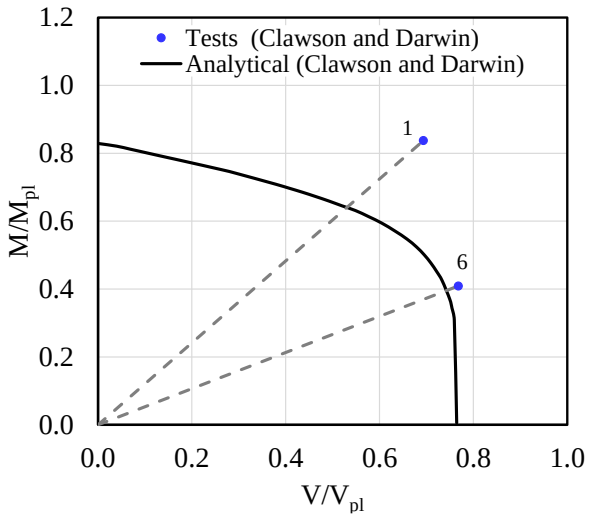

(b) tests of Clawson and Darwin

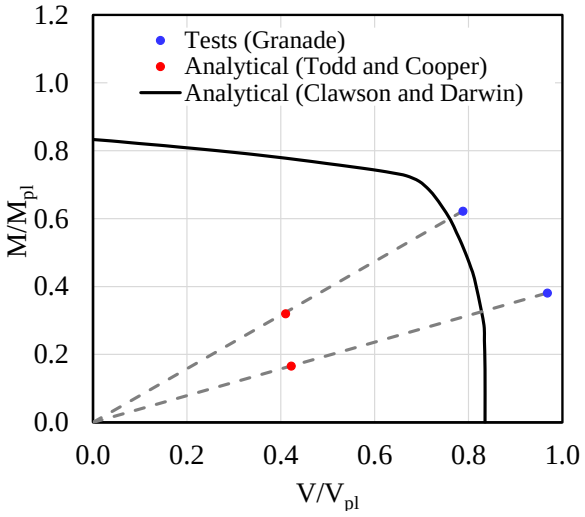

(c) tests of Granade and model of Todd and Cooper

Fig. 15: Comparisons of the Clawson and Darwin model, adapted from [56] with permission from ASCE

In Narayanan et al. [59] and Roberts and Al-amery [60] the shear strength in composite girders with rectangular web opening was investigated (**Fig. 16a-b**). The tests showed that if the steel-concrete interface develops tension in the shear connectors, the shear strength of composite girders with web openings was greater than that of the girder, alone. In addition, Roberts and Al-amery [60] maintained the importance of the pullout capacity of the connectors. The results of experimental tests were used for the development of an analytical model capable of predicting the shear strength of these structural elements. This procedure was based on experimental evidence, such as the behavior of slabs that exhibit a typical shear failure mode, the buckling in the web post of the girder and the Vierendeel mechanism.

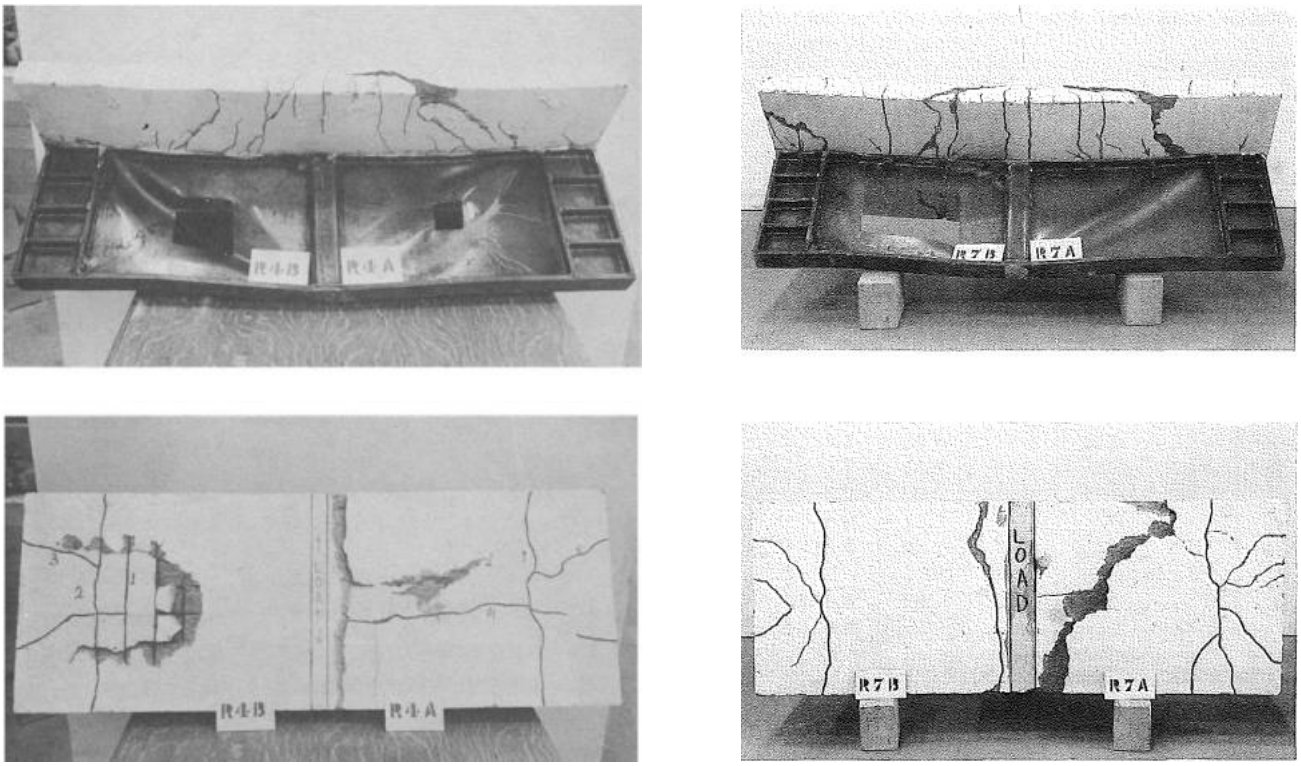

(a) Narayanan et al. [59]

(b) Roberts and Al-amery [60] with permission from ASCE

Fig. 16: Test on composite girders with web openings

Shanmugam et al. [61] carried out tests with steel-concrete composite girders with rectangular and circular web openings. In this study, the authors varied the height and the diameter of the openings. The ultimate behavior of the tests was characterized by the formation of plastic hinges with diagonal cracks in the concrete slabs. The results showed that the smaller the height or the opening diameter, the greater the shear strength. Subsequently, the authors developed a numerical model, considering non-linear analysis, using the finite element method. In this model, shell elements were implemented in the steel profile, solid elements for the slab and shear connectors, as well as contact elements between the steel-concrete surfaces. The model showed accuracy when compared with tests.

Regarding composite beams with rectangular web openings subject to negative moment, Chen et al. [62] and Li et al. [63] stands outs. Both authors performed tests and numerical analyses. Chen et al. [62] investigated the behavior of composite cantilever beams with web openings. Tests and non-linear analysis were conducted to investigate the effect of the opening size, the stiffening plates and the moment-shear ratio. The author's results indicated that the initial cracking loads of composite beams with web opening are lower

than that without web opening and the mechanical behavior of composite beam under negative moment can be improved significantly by applying stiffening steel plates around the opening.

Li et al. [63] performed tests on continuous steel-concrete composite beams with web openings. Subsequently, the authors performed geometrical nonlinear analyses in the software ANSYS to investigate the influence of slab thickness and reinforcement rate. Li et al. concluded that the openings decreased the stiffness of the structure; the failure mode was governed by the shear in the concrete slab near the opening, the increase in the concrete slab thickness and reinforcement rate contributed to the ultimate strength and ductile behavior. In addition, the numerical model developed by the authors was consistent with the tested models. In this study, the initial geometric imperfections were not considered.

In this same scenario, considering now composite cellular beams, Gizejowski and Khalil [64] presented the ultimate behavior in composite cellular beams subject to negative moment. In all situations, the authors observed the web distortion (**Fig. 17**), due to the fact that the boundary conditions potentiate this phenomenon, such negative moment. The web distortion occurs when the composite beam is subjected to a negative moment because, in this case, a result of compression appears on the bottom flange of the profile, which is unrestrained to leave out the plane of the beam.

Fig. 17: Web distortion [64]

Subsequently, the authors proposed a numerical model, considering geometrical and physical non-linear analyses in software ABAQUS. The analyses were carried out in two steps: elastic stability analysis and geometrical and physical non-linear analyses. In the latter case, the initial geometric imperfection was applied. The elastic stability analysis provides eigenvalues and eigenvectors as a response. Thus, geometric

imperfection is the association of an eigenvector with a scale factor, which is taken to the beginning of nonlinear analysis. Regarding the finite element discretization, shell elements were used, both for the slab and for the cellular profile. The authors' results were shown to be accurate when compared to physical models. **Table 2** presents the summary of the works developed in composite beams with web openings formed by solid slabs.

Table 2: Studies of composite beams with web openings formed by solid slabs

Model	Reference	Highlight
Experimental	Granade [52]	Investigated the stresses based on the Vierendeel mechanism
	Clawson and Darwin [55]	Observed the influence of the slab on shear strength
	Cho [57]	Sustained the slab's contribution to shear strength
	Narayanan et al. [59]	Observed the headed stud efficiency of on the steel-concrete interface
	Roberts and Al-Amery [60]	Investigated the bolted tension connectors efficiency on the steel-concrete interface
	Shanmugam et al. [61]	Carried out tests with steel-concrete composite girders with rectangular and circular web openings.
	Chen et al. [62]	Performed tests to verify the behavior of composite cantilever beams with web openings
	Li et al. [63]	Conducted tests on continuous steel-concrete composite beams with web openings
	Gizejowski and Kalil [64]	Observed the behavior of composite cellular beams subject to hogging moment
Analytical	Todd and Cooper [53]	Neglected the slab's contribution to shear strength
	Donoghue [54]	Suggested the use of reinforcements to contribute to shear strength
	Clawson and Darwin [56]	Considered the slab’s contribution to shear strength
Numerical	Shanmugam et al. [61]	Developed a numerical model, considering non-linear analysis, using the finite element method. In this model, shell elements were implemented in the steel profile, solid elements for the slab and shear connectors, as well as contact elements between the steel-concrete surfaces.
	Gizejowski and Kalil [64]	Performed geometrical and physical nonlinear analyses, considering shell elements for cellular beams and solid slab.
	Chen et al. [62]	Conducted non-linear analysis to investigate the effect of the size of the opening, the stiffening plates and the moment-shear ratio
	Li et al. [63]	Performed geometrical nonlinear analyses to investigate the influence of slab thickness and reinforcement rate.

4.2 WITH COMPOSITE SLAB

Redwood and Wong [65] performed tests on composite beams with larger rectangular web openings formed by composite slabs. The authors observed that high moment ratio values, failure modes were governed by flexure. A local bending, both upper and lower tees, caused the Vierendeel mechanism and became more evident as the moment-shear ratio had decreased. For low values of moment-shear ratio, the Vierendeel mechanism governed the failure mode and resulted in flexural cracks in the concrete slab (**Fig. 18**).

Fig. 18: Crack locations [65]

In addition, a displacement in the ribs occurred in all tests, causing a failure in the thickness of the concrete above the ribs in function of the medium and high values of the moment-shear ratio and the almost complete displacement in the steel-concrete interface above the opening for low values of the moment-shear ratio. The cracking of the concrete occurs due to deflections through the opening, with the progression of loading. In addition, near the ultimate strength, the concrete can develop transverse, longitudinal and diagonal cracks close to the opening region [9]. In solid slabs, transverse cracks are usually seen at the ends of the opening, both at the top and bottom of the slab. In composite slabs, however, the cracking starts near the top corner of the rib and advances diagonally to the top, as shown in **Fig. 19** [34].

Fig. 19: Cracking: composite slab [66]

In contrast to Clawson and Darwin [56], Redwood and Wong [65] provided a simplified analytical method considering the failure by Vierendeel mechanism with the formation of four plastic hinges, which represents a typical deformation of beams with rectangular web openings subjected to intense shear load [53–56]. It is important to note that Clawson and Darwin [56] used the failure criterion for concrete due to normal and shear stresses, while Redwood and Wong [65] considered the failure of the concrete slab by compression. The justification for this was that when the shear stress is intense, the average compression stress on the

concrete slab is limited to a low stress value, due to the shear connection between the concrete slab and the steel beam near the region of opening. In addition, the shear stress resisted by the composite action was limited to the shear resistant capacity of the steel beam with web openings, alone.

In Redwood and Poumbouras [67] two tests were carried out on composite beams with rectangular web openings (**Fig. 20**).

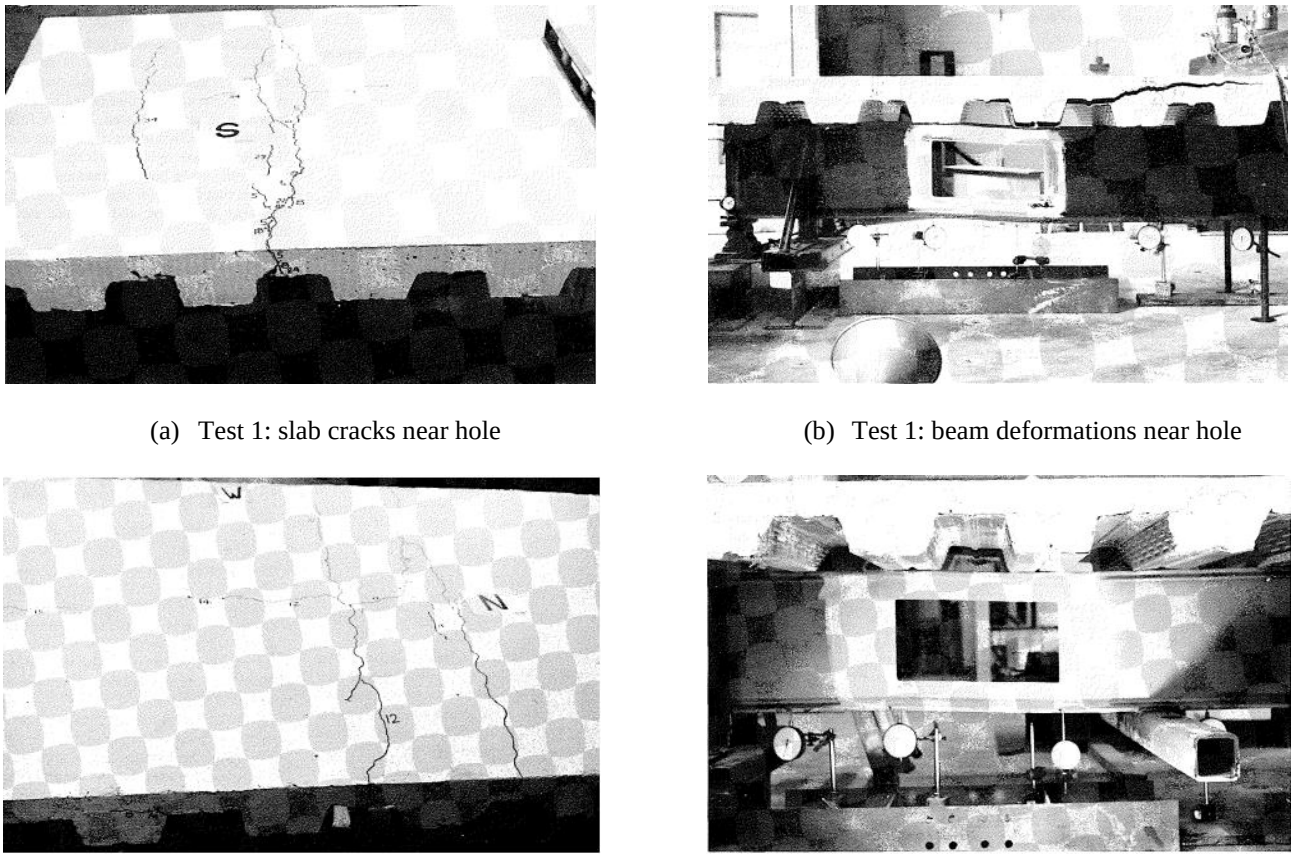

(a) Test 1: slab cracks near hole

(b) Test 1: beam deformations near hole

(c) Test 2: slab cracks near hole

(d) Test 2: beam deformations near hole

Fig. 20: Redwood and Poumbouras's tests, adapted from [67]

The first concerns the need for shear connectors in the length of the opening at the concrete slab and steel profile interface. The second considered the effect of the construction on the ultimate strength, since the unshored construction could produce severe conditions, before the composite action is carried out. The authors found that the absence of shear connectors, in the opening length, produces a significant reduction in the ultimate strength, and the effect of the construction loads acting on the steel form does not significantly affect the ultimate strength of the composite section when the beam is subjected to 60% of its predicted ultimate strength. Donahey and Darwin [9] performed tests, considering the composite slabs located both in the perpendicular and parallel directions to the longitudinal axis of the steel profile. The objectives of the

experiments were to investigate the effects of the moment-shear relationship, quantity and position of the shear connectors, orientation and position of the steel formwork. In view of the experimental results, the authors concluded that the concrete contributed significantly to the flexural and shear strength; as the moment-shear ratio decreases in an opening, the deflection through the opening increases accompanied by transverse cracking; the resistant capacity of the composite beams formed by composite slabs is ductile and the failure is preceded by cracks in the slab, steel yield and large deflections; concrete and steel exhibit high slip values before failure; the resistant capacity is governed by the failure of the concrete slab, and; as the number of shear connectors increases above the opening and between the opening and the support, the resistance in the opening increases. **Fig. 21** shows an example of ultimate behavior observed in tests.

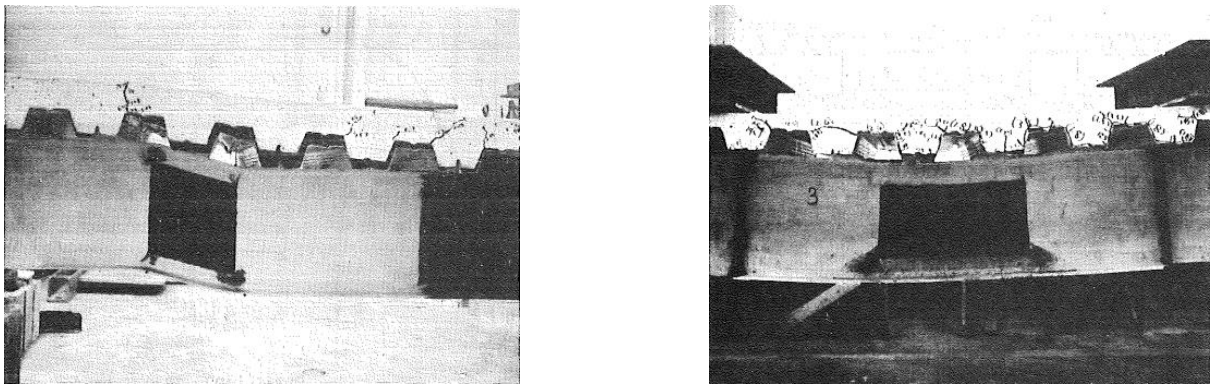

(a) Failure at web opening with low moment-shear ratio (b) Failure at web opening with high moment-shear ratio

Fig. 21: Example of ultimate behavior presented in [9], with permission from ASCE

Subsequently, in Darwin and Donahey [6] calculation methodologies were presented to determine the strength of composite beams with rectangular web openings, without the use of reinforcement. The procedure takes into account moment-shear diagrams, addressing the resistant capacity in the opening subjected to bending, pure shear and the combinations of bending and shear. In this method, the pure moment and shear resistant capacities are calculated separately and the two points are connected using a cubic interaction curve to represent the interaction between moment and shear. Also, the authors discussed the appropriate value of the Load Resistance Factor Design[1] (AISC/LRFD). The AISC/LRFD specification defines the design flexural strength as $\Phi_b M_n$, where Φ_b is the flexural strength factor. For compact composite sections, Φ_b was equal to 0.85. On the other hand, the design shear strength is defined as $\Phi_v V_n$, where Φ_v is the shear strength factor.

[1] **Load and resistance factor design manual of steel construction**. (1986). 1st Ed., American Institute of Steel Construction, Inc., Chicago, 1986.

For the design of composite sections, Φ_v was equal to 0.90. This value was based on the assumption that the shear was resisted only by the web of steel profile. The authors' calculation method was compared with the experimental results, considering solid and composite slab [9,52,55,57,65,67]. The results were accurate. In addition, the authors suggested the use of a resistance factor equal to 0.85, both for shear and flexure.

It was observed here that until then, in the 1980s, calculation procedures were developed with the use or not of reinforcement, since the authors have already considered the contribution of the concrete slab in the resistance of these structural elements. Although calculation methodologies were presented for different situations regarding the use or not of reinforcement in the rectangular web opening, there was no unified approach to such considerations. In this context, Darwin and Lucas [68] merged the method originally developed by Darwin and Donahey [6], unifying all considerations. The procedure provided a single equation to estimate shear strength at web openings for all types of beams. The method was compared with the experimental results, as previously presented. The method's accuracy was superior to previous calculation methods, such as the Redwood and Poumbouras [69]. In addition, Darwin and Lucas [68] suggested resistance factors equal to 0.90 and 0.85 for flexure and shear, respectively, differently from Darwin and Donahey [6], who suggested a value equal to 0.85, both for shear and flexure. Benitez and Darwin and Donahey [70] continued the work that was developed by Darwin and Donahey [6] and Donahey and Darwin [9], and described matrix procedures for determining maximum deflection in composite beams with web openings. The results were compared with tests [9,52,55,65]. The application of the matrix analysis stiffness method provided a reasonable estimate of the total deflection and deflection at the opening, when compared with the tests. The authors concluded that in most cases, a single web opening has little effect on total deflection, the effects of an opening and shear deflections are of the same order and ignoring the web opening 4 and shear deformation can lead to a significant error.

In the same decade, the AISC Steel Design Guide 2: steel and composite beams with rectangular web openings [71] was published. Although the methodology was limited to steels with yield strength not exceeding 450 MPa, the document gathers a series of information on the calculation of the strength of steel and concrete composite beams with web rectangular opening, considering solid and composite slabs, reinforced opening and eccentric openings.

Still, on the calculation of the maximum deflection in beams with openings, Djebli et al. [72] proposed an analytical model for calculating the total deflection of composite cellular beams subjected to concentrated or uniformly distributed loads. This model addresses the condition in which the opening is or is not in the center of the span, unlike previous models [7,33,50,70]. The maximum deflection is composed of two parts: the one in function of the global bending moment and the one of shear due to the Vierendeel mechanism. According to the authors, the analytical model directly provides additional deflection from the effect of vertical shear at the opening, the contribution of additional deflection is more significant in the case of beams with short lengths and the proposed approach can be used to calculate the deflections of composite cellular beams with various geometric characteristics.

Chung and Lawson [33] presented design procedures for composite beams with rectangular and circular web openings for application in EC4. Such procedures presented general information on the dimensioning of openings as a function of shear and bending strength, and the effect of these openings on deflections. According to the authors, although there were already design methodologies, such as Lawson[1], the main justification that was used for the publication was that the EC4, had not been prepared and it was suspended. Thus, there were no methods for designing composite beams with openings of various shapes and dimensions.

In Lawson et al. [73] tests were carried out, considering composite beams with rectangular web openings. Such tests aimed to observe the influence of longitudinal stiffeners in the action of global and local bending, local web buckling by compression and bending, shear transfer through the concrete slab, resistance to the formation of the Vierendeel mechanism and the increase in deflections resulting of the openings. The tests presented ductile behavior, without the occurrence of cracking and crushing of the concrete, and web buckling. The formation of the Vierendeel mechanism governed the resistant capacity of the experimental tests. The results were compared with Lawson's publication. The method was based on the previous experimental tests [9,67]. It was important to note that the method addresses the position of the opening in the span length, in the cross section and makes considerations regarding the reinforcements in the opening. In addition, the shear strength takes into account the contribution of the concrete slab. The authors concluded

[1] LAWSON, R. M. **Design for openings in the webs of composite beams**, SCI/CIRIA publication, SCI-P-068, 1987.

that the calculation method was conservative when compared to the experimental results. In addition, conservatism increases in the case of openings located within the intense shear zone. The tests also showed that welding of stiffeners, only on one side of the opening, does not affect the performance of the web and this can offer considerable savings in the execution of stiffened openings.

Cho and Redwood [74] presented the concept of truss analogy and a methodology capable of estimating the strength of composite beams with web openings, considering the shear connectors in the opening region as tensioned elements (**Fig. 22**). According to the authors, the basic concept of this analogy is that after cracking the concrete carries a set of compression stresses in diagonals (struts) and the reinforcement tensile stresses (struts). This approach related shear strength to the location of the connectors.

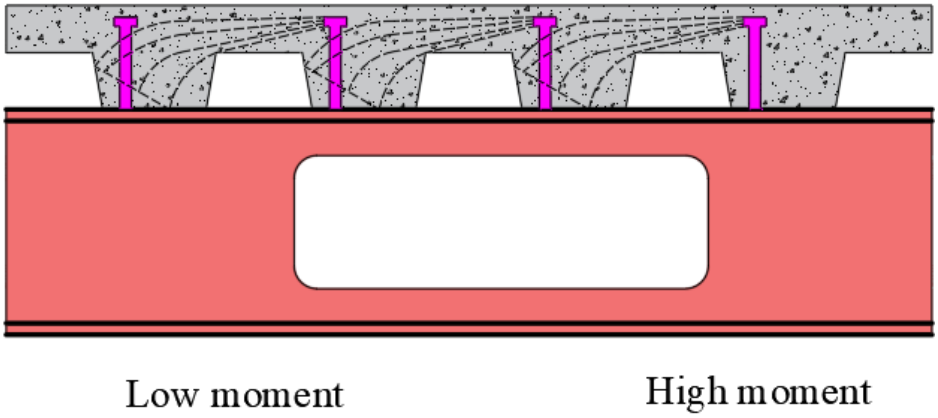

(a) Stress field

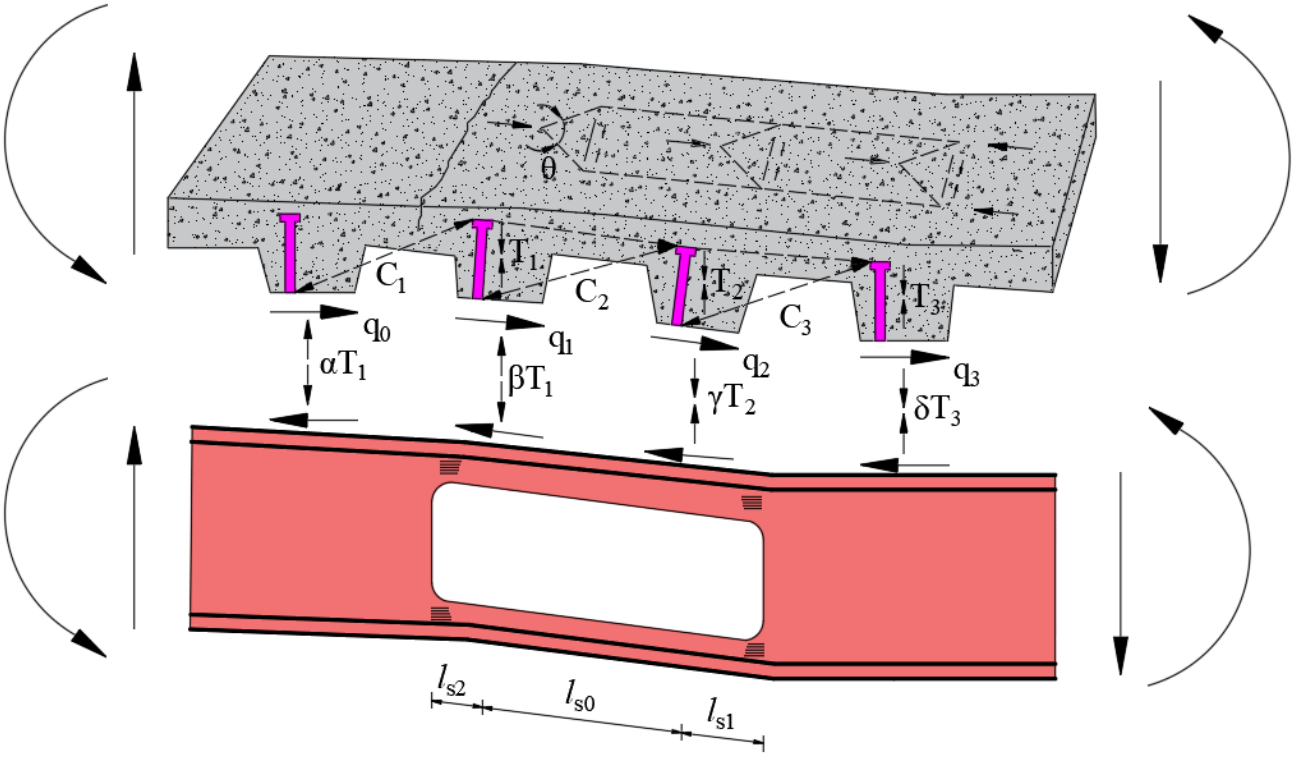

(b) Truss model

Fig. 22: Truss idealization for slab in composite beam at web hole, adapted from [74] with permission from ASCE

The solutions proposed by the authors provide for the strength of composite beams with openings in the web and information on the position of the connectors, in the region of the openings, capable of attributing the effectiveness of the truss when resisting vertical shear. An important observation reported by authors was a relation of contribution of the concrete slab to the shear strength. This observation relates a series of experimental tests, as illustrated in **Fig. 23**, which n_h is the number of shear connectors in the opening length, n the number of connectors, h_c is a height of the concrete slab, and d is the height of the steel profile.

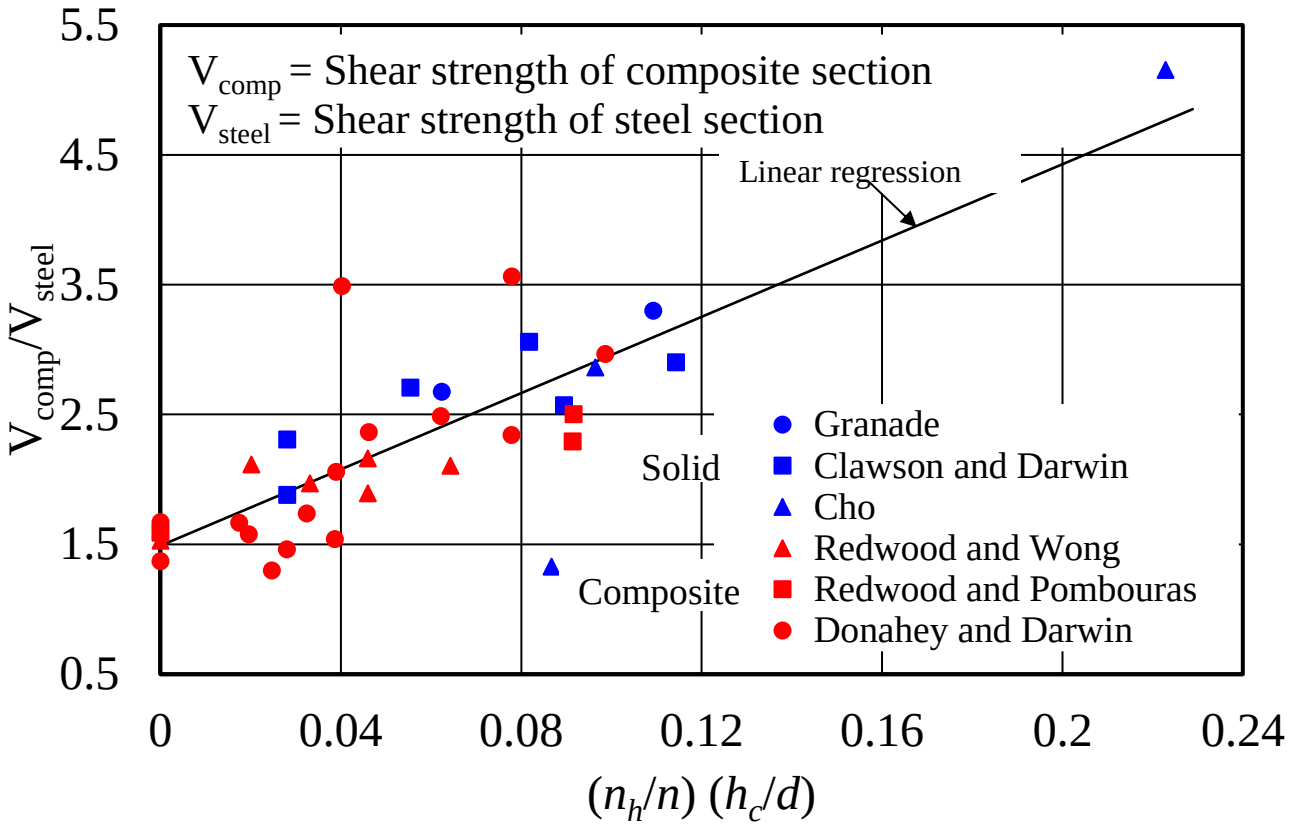

Fig. 23: Contribution of the concrete slab to the shear strength of composite beams with web openings, adapted from [74] with permission from ASCE

The tests indicated that the contribution of the concrete slab, in the shear strength in the opening region, can reach the order of 40% -420% for solid slabs [52,55,57] and 30% -260% for composite slabs [9,65,67], when compared with the steel profile, alone, maintaining the geometry of the openings. Thus, it was possible to conclude that when considering the concrete slab for calculating the shear strength, the use of reinforcements in the opening steel profile can be disregarded.

Later, to verify the calculation method using the truss analogy, in which the shear connectors were considered tensile elements and the compression diagonals that act on the concrete, Cho and Redwood [75]

615 carried out experimental tests. In addition, the authors considered the experimental tests previously performed
616 for verification [9,52,55,57,65,67]. Although the resistances estimated by the truss model were satisfactory,
617 in particular for composite beams with web openings formed by solid slabs, the model was not accurate. On
618 the other hand, for composite slabs, the truss model provides slightly more conservative predictions. As a
619 result, the truss model was more suitable for composite slabs. Regarding the results of the tests carried out by
620 the authors, the shear connectors, located within the length of the opening, were the main reason for the
621 contribution of the concrete slab to shear strength; experiments that included additional reinforcements welded
622 to the head stud, showed that the slab's resistant capacity to shear was dependent on the tensile strength of the
623 connectors; the width of the concrete slab was not a factor that affects the resistance of the slab to shear, and;
624 in solid slabs, the evidence indicated that the failure, at the bottom of the slab close to the opening, started
625 with a crack due to the diagonal traction through the thickness of the slab (**Fig 24**).

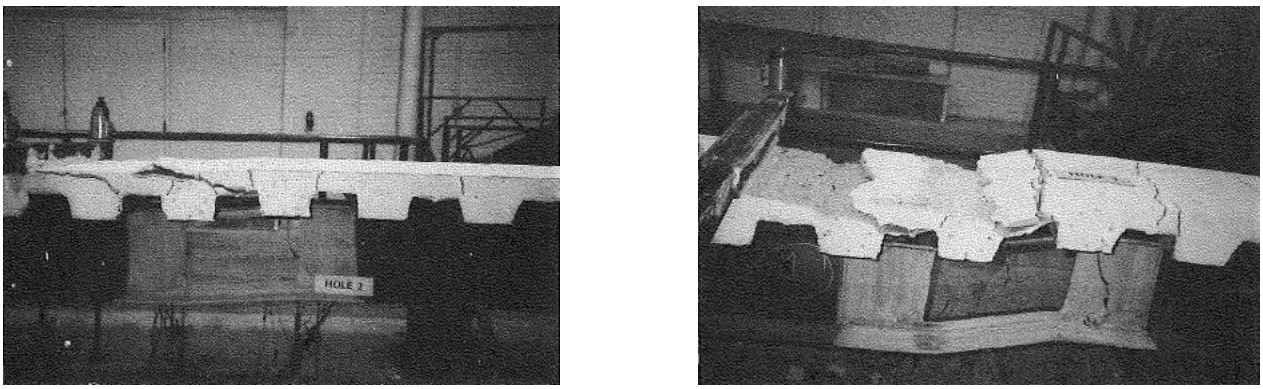

(a) Failure at web opening with low moment-shear ratio (b) Failure at web opening with high moment-shear ratio

626 **Fig. 24: Slab failure** [75] **with permission from ASCE**

627 In Redwood and Cho [34] a simplified calculation method was presented, considering composite
628 beams with reinforced web openings as the general case. The authors' justification was that the analyses that
629 provide particular solutions for composite beams with web openings, which were in general complex, as for
630 example in Clawson and Darwin [56]. The analysis was based on the tensions close to the four corners of the
631 opening that are in balance with the external loads and that satisfy the von Mises yield criterion. The method
632 was validated considering tests without reinforcement [9,55,57,65,67,73]. The authors concluded that the
633 average value of the ratio between the experimental tests and the analytical model was 1.064, with a variation
634 coefficient of 0.146.

Fahmy [76] proposed a method for calculating the resistant capacity using moment-shear interaction curves. Although for the development of the theoretical model the author considered the hypotheses of Todd and Cooper [53], the procedure in question considered the contribution of the concrete slab to the shear strength and complete interaction at the steel-concrete interface. Theoretical results were compared to experimental results [52,55,73] and were presented with accuracy.

So far, it has been observed that most studies carried out on composite beams with rectangular web openings were based on only one opening, that is, they disregarded beams that have sequential openings during the span, such as cellular beams. In this scenario, Park et al. [77] performed experimental tests. The observed parameters were the effects of the slab width and the moment-shear relationship of the resistance. The authors found that the failure modes, such as the diagonal in tension and pullout, depend on the slab width (**Fig. 25**).

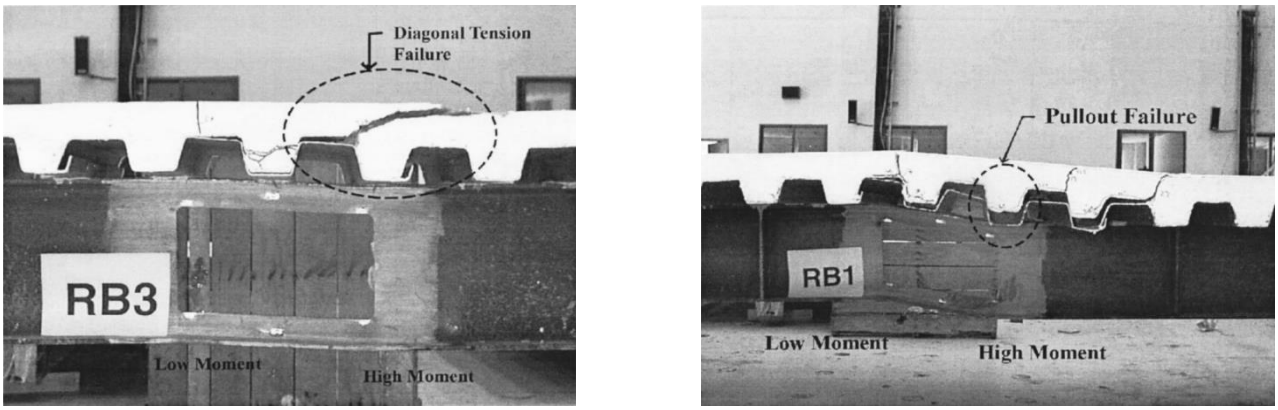

(a) (b)

Fig. 25: (a) Diagonal in tension e (b) pullout [77]**, with permission from ASCE**

The results of the experimental tests were used to develop an analytical model, with the combination of flexure and shear, to predict the strength of composite beams with web openings in the formed by composite slabs. The justification for this development was that the truss model, developed by Cho and Redwood [74], did not consider the effect of the dimension of the composite slabs, assuming that the cracking of the diagonal in tension does not occur before the failure by pulling out the connectors. The analytical model developed by Park et al. [77] presented accuracy, in comparison with the experimental tests and the Cho and Redwood model [74].

Some studies have stood out, considering numerical modeling, using the finite element method, in steel concrete composite beam with web openings. Chung et al. [78] and Chung and Wang [79] presented two

dimensional nonlinear analyses for composite beams with rectangular web openings, considering the tests by [67,80]. The shear connectors were modeled as vertical and horizontal springs with non-linear behavior. The authors' justification was that the principal mode of failure involves only in-plane deformation. The numerical results shown to be close to those of the tests. Ellobody and Young [81] investigated the behavior of composite beams with reinforced and unreinforced rectangular web openings. For this task, a numerical model was developed and calibrated by tests [65,77]. Non-linear analysis was performed, considering the steel beam, concrete slab, profiled steel sheeting, headed stud shear connectors, reinforcement bars as well as interfaces among these components. In parametric study, stiffened and unstiffened web opening sizes, moment-shear ratios at openings, web opening locations, beam lengths, concrete and steel beam strengths were varied. The ultimate load was compared with SCI P355 [50]. Ellobody and Young [81] concluded that the horizontal reinforcements located above and below the opening, and the strength of the steel beam are factors that can considerably increase the ultimate behavior of composite beams with rectangular web openings. The numerical results when compared with the SCI P355 prescriptions showed a maximum difference of 6%.

In Panedpojaman [82] was presented a simplified method for Vierendeel design calculations of steel concrete composite beams with rectangular web openings. The authors, also conducted a parametric study. The Non-linear analyses were calibrated by tests [66,80,83]. The stud properties, the geometric configuration of the steel beams, the web openings, and the concrete slab thickness were investigated. The results were compared with the SCI P355 and the method proposed by [82]. The author's calculation methodology proved to be less conservative when compared to the SCI P355 method.

In recent years, the asymmetric steel-concrete composite cellular beam has been widely used in construction. As the upper flange acts in conjunction with the slab, the bottom part of the beam is formed by a more rigid section than the upper part, to improve the efficiency in flexural and shear resistance. The proportion between the bottom and upper bottom areas is generally in the range of 1.5 to 2.5 [66]. Although asymmetric composite cellular beams are more efficient in strength when compared to those with double symmetry, EC4 recommends a higher degree of connection for asymmetric composite beams. However, in most situations it is impossible to achieve the desired degree of shear connection, as the spacing of the connectors is limited to the spacing of the steel form rib. Therefore, in design, it is often governed by obtaining

682 the minimum degree of shear connection [66]. In this context, several works investigated the behavior of these
683 elements [66,84,85].

684 Müller et al. [84,86], a European research project, carried out tests on composite cellular beams with
685 a double symmetry and asymmetric section. The authors investigated the non-composite (slab cut at end) and
686 composite actions at the supports of simply supported beams subjected to uniformly distributed loads. The
687 modes of failure observed were the web post buckling and Vierendeel mechanism for non-composite and
688 composite actions, respectively. Later, Müller et al. [84,86] developed parametric analysis focusing on the
689 influence of the resistance of steel-concrete materials on strength and failure modes of composite beam with
690 web openings. The authors concluded that the failure mechanism depends mainly on the type of steel. In
691 Nadjai [85], two experimental tests were presented considering asymmetry and double symmetry sections in
692 composite cellular beams formed by composite slabs. Both tests had the resistant capacity defined by web
693 post buckling. Sheehan et al. [66] carried out experiments on composite cellular beams of large spans formed
694 by asymmetric steel profiles and composite slabs. The degree of shear connection was 36%, less than half
695 recommended in EC4. Two tests were carried out. The composite cellular beams were subjected to uniformly
696 distributed loading. Slip, mid-span vertical displacement, shear connector capacity and stress distribution were
697 examined. Also, the effect of the unshored construction was observed. Unshored construction is popular as it
698 reduces time and cost during construction. However, there are differences in response depending on boundary
699 conditions. Unshored beams have a lower degree of slippage and require a lesser degree of shear connection.
700 EC4 does not address the advantages of composite beams in unshored construction [8,66]. In this study, the
701 authors observed that with the request for uniformly distributed loading, the composite cellular beam resisted
702 3.4 times the design loading, despite having a degree of shear connection considerably below the minimum
703 requirements of EC4; the bottom flange reached the yield resistance with the concrete deformations
704 considerably low; the ductile behavior of the shear connectors was confirmed by the observed end-slips of 8.5
705 mm and 13.5 mm under uniformly distributed load, which exceeded the minimum of 6 mm specified in EC4,
706 and no shear connector failed during the experimental tests; with the request for concentrated load, the beam
707 resisted a load 45% greater than the expected resistance of the steel cross section. This suggests the need for
708 modifications in the expected resistance to the Vierendeel mechanism for composite cellular beams.

Regarding the behavior of composite cellular beams at elevated temperature, some studies stand out, such as Nadjai et al. [87], Bihina et al. [88] and Bükülmez and Celik [89]. Nadjai et al. [87] presented experimental and numerical study. Four specimens were tested at elevated temperatures. According to the authors, the fire tests indicated that failure by web-post buckling, and the ultimate strength of composite cellular beams at elevated temperatures cannot be estimated by applying reduction factors on stiffness, as given in codes. Subsequentially, Nadjai et al. [87] developed a numerical model, considering geometrical non-linear analysis and shell elements, capable of representing the physical models that were tested. This analysis was observed by load-displacement relationship and failure modes. Bihina et al. [88] carried out full-scale fire tests on four specimens, considering, also, elongated web. The results of the physical models were used to calibrate a numerical model using the finite element method for the subsequent parametric study. In the parametric study, span, steel cross-section depth, diameter of the openings, composite slab, mechanical properties and loading conditions were varied. The results were compared with an existing analytical model[1] that proved to be conservative. In Bükülmez and Celik [89] was presented tests in protected and unprotected cellular beams at elevated temperature. The authors concluded that the deflections in the unprotected beam were more critical than those in the protected beam, and the difference between the protected and unprotected cellular beams is the fire resistance time, that means, protected beams had a longer duration because of the fire protection material.

Tables 3-5 present the experimental, analytical and numerical studies, respectively, in composite beams with web openings formed by composite slabs.

[1] Vassart O, Bouchaïr A, Muzeau JP. Analytical model for the web post buckling in cellular beams under fire. In: Proceedings of the COST C26 workshop (urban habitat constructions under catastrophic events), Prague; 30–31 March, 2007. p. 92–7.

734 **Table 3:** Experimental studies of composite beams with web openings formed by composite slabs

Reference	Highlight
Redwood and Wong [65]	Evaluated the moment-shear ratio in the region of the opening
Redwood and Poumburas [67]	Investigated the need for shear connectors in the opening length and the effects of unshored construction.
Donahey and Darwin [9]	Observed the behavior in function of the slab layout, located both in the perpendicular and parallel directions to the longitudinal axis of the steel profile.
Lawson et al. [73]	Evaluated the influence of longitudinal stiffeners in the action of global and local bending, web local buckling by compression and bending, shear transfer through the concrete slab, resistance to the formation of the Vierendeel mechanism and the increase in deflections resulting from the openings.
Cho and Redwood [75]	Verified the calculation model with truss analogy in which the shear connectors are considered tensile elements
Park et al. [77]	Observed the effects of the moment-shear ratio in slab width
Müller et al. [84]	Experimental tests were carried out on composite cellular beams with double symmetry and asymmetric section. The resistance was reached with the formation of the Vierendeel mechanism and web post buckling
Nadjai [85]	Observed that the resistance was defined by the web post buckling
Nadjai et al. [87]	The fire tests indicated that failure by web-post buckling, and the ultimate strength of composite cellular beams at elevated temperatures cannot be estimated by applying reduction factors on stiffness, as given in codes
Bihina et al. [88]	Carried out full-scale fire tests on four specimens, considering, also, elongated web
Bükülmez and Celik [89]	Presented tests in protected and unprotected cellular beams at elevated temperature
Sheehan et al. [66]	Investigated the effect of unscored construction and the interaction degree in composite cellular beams with large spans

735

736 **Table 4:** Analytical studies of composite beams with web openings formed by composite slabs

Reference	Highlight
Clawson and Darwin [56]	Used the failure criterion for concrete due to normal and shear stresses
Redwood and Wong [65]	Considered the failure of the concrete slab by compression
Redwood and Poumbouras [69]	Reported the increase in compression stresses due to the steel-concrete slip caused by the deformation of the shear connectors
Darwin and Donahey [6]	Determined the resistant capacity without the use of reinforcement
Cho and Redwood [74]	Presented the concept of truss analogy and a methodology to estimate the strength of composite beams with web opening, considering the shear connectors in the opening region as tensioned elements
Redwood and Cho [34]	Presented a simplified calculation model, considering composite beams with reinforced web opening as the general case
Fahmy [76]	Proposed a model for calculating the resistance of composite beams with web openings, considering full interaction
Benitez et al. [70]	Described matrix procedures for determining maximum deflection in composite beams with web openings
Chung and Lawson [33]	Presented design procedures for composite beams with rectangular and circular openings in the web for application in EN 1994-1-1 (2004)
Panedpojaman [82]	Presented a simplified method for Vierendeel design calculations of steel concrete composite beams with rectangular web openings.
Djebli et al. [72]	Proposed equations to estimate deflection in composite cellular beams

737

738

739

740

741

742

743 **Table 5:** Numerical studies of composite beams with web openings formed by composite slabs

Reference	Highlight
Chung et al. [78]	Presented two dimensional nonlinear analyses for composite beams with rectangular web openings, considering shear connectors as vertical and horizontal springs with non-linear behavior
Chung and Wang [79]	Carried out parametric analysis focusing on the influence of the resistance of steel-concrete materials on strength and failure modes of composite beam with web openings
Müller et al. [84]	Developed a numerical model, considering geometrical non-linear analysis and shell elements, capable of representing the physical models that were tested
Nadjai et al. [87]	Investigated the influence of span, steel cross-section depth, diameter of the openings, composite slab, mechanical properties and loading conditions
Bihina et al. [88]	Performed a parametric study, considering the stiffened and unstiffened web opening sizes, moment-shear ratios at openings, web opening locations, beam lengths, concrete and steel beam strengths;
Ellobody and Young [81]	Investigated the stud properties, the geometric configuration of the steel beams, the web openings, and the concrete slab thickness
Panedpojaman [82]	

744

745 ## 5. RESISTANCE OF COMPOSITE BEAMS WITH WEB OPENINGS AND COMPOSITE
746 ## CELLULAR BEAMS

747 This section presents calculation procedures that were developed to estimate the strength of composite
748 beams with rectangular web openings and composite cellular beams. As previously presented, the failure
749 modes of these structural elements can be characterized by failure in the steel profile by buckling or plastic
750 mechanism, followed by crushing or cracks in the concrete slab. In this context, the present study will focus
751 web post buckling and Vierendeel bending of tees. Generally, the shear resistance, both vertical and horizontal,
752 are calculated considering the net steel section with the contribution of the concrete slab, using classic
753 procedures for this. More information can be seen at [50,90]. Regarding the deflections of composite cellular
754 beams, calculation procedures can be seen in [72].

755 ### 5.1 WEB POST BUCKLING

756 Some analytical models have been developed to calculate the WPB resistance [7,29,30,50,91]. The methods are presented.
757 At the end of this section, the methods are compared, considering tests [84–86] as the object of comparison.

758 #### 5.4.1 Ward

759 The procedure [91] considers only symmetrical composite and non-composite cellular beams. The
760 method is found in Steel Design Guide 31 [51], also considering the asymmetric cellular beams via the most
761 critical situation between the upper and lower tees. In this method, three values are considered, such as C_1, C_2
762 and C_3, which are a function of the geometric properties of the web post and applicable for the intervals
763 $1.08 \leq p/D_o \leq 1.50$ and $1.25 \leq d_g/D_o \leq 1.75$.

764 The bending moment, which corresponds to the yielding in the critical section (**Eq. 18**), generated by
765 the horizontal shear force is equal to:

$$M_{vh} = 0.9\left(\frac{D_o}{2}\right)V_h \tag{18}$$

766 Thus, the WPB is calculated, according to **Eqs (19-24)**:

$$M_{W,\mathrm{Rk}} = M_{W,e}\left[C1\left(\frac{p}{D_o}\right) - C2\left(\frac{p}{D_o}\right)^2 - C3\right] \tag{19}$$

$$M_{W,e} = \frac{t_w\left(p - D_o + 0.564D_o\right)^2}{6} f_y \tag{20}$$

$$C1 = 5.097 + 0.1464\left(\frac{D_o}{t_w}\right) - 0.00174\left(\frac{D_o}{t_w}\right)^2 \tag{21}$$

$$C2 = 1.441 + 0.0625\left(\frac{D_o}{t_w}\right) - 0.000683\left(\frac{D_o}{t_w}\right)^2 \tag{22}$$

$$C3 = 3.645 + 0.0853\left(\frac{D_o}{t_w}\right) - 0.00108\left(\frac{D_o}{t_w}\right)^2 \tag{23}$$

767 Another form of calculation is to present the resistance to the horizontal shear force (**Eq. 8**):

$$V_{Wh,\mathrm{Rk}} = \frac{M_{W,e}}{0.45D_o}\left[C1\left(\frac{p}{D_o}\right) - C2\left(\frac{p}{D_o}\right)^2 - C3\right] \tag{24}$$

768 **Eq. (25)** shows the relationship between horizontal and vertical:

$$V = V_h\left(\frac{2y_o}{p}\right) \tag{25}$$

769 This relationship is obtained by summing the moments at point A (**Fig. 26**), in which F can be a
770 concentrated force, or even the result of a uniformly distributed load.

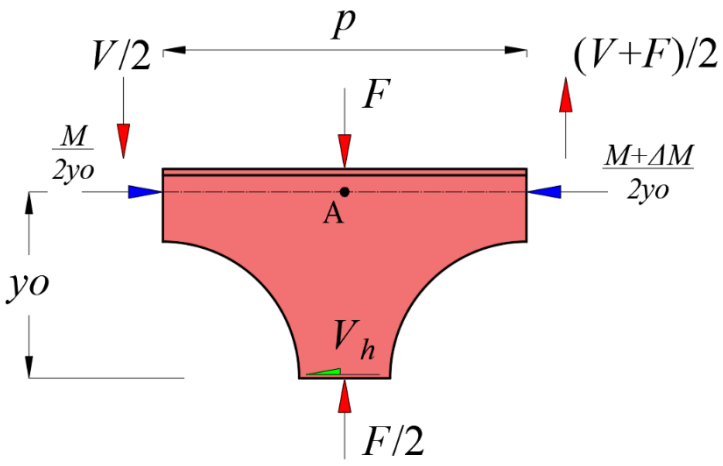

Fig. 26: Rigid body equilibrium in the tee section

5.4.2 Lawson et al.

The methodology of Lawson et al. [7,50], which consider symmetric and asymmetric sections, is based on strut theory, considering an effective length of a bar under compression. The method is presented in SCI P355 [50]. According to this method, the action of the horizontal shear force at half the height of the web causes tension and compression stresses due to the flexion between the upper and lower tees. These stresses vary around the opening (**Fig. 27**).

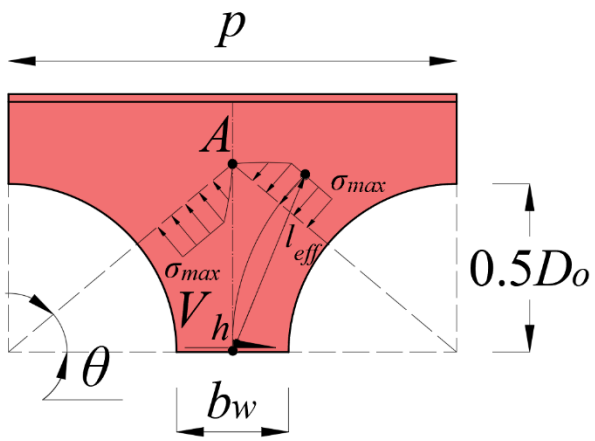

Fig. 27: Strut model, adapted from [7]

The effective length takes into account the variation of stresses around the opening, according to **Eq. (26)**.

$$l_{eff} = 0.5\sqrt{b_w^2 + D_o^2} \le 0.7D_o \quad (26)$$

Once the effective length has been determined, then the theory of compression bars, according to EN 1993-1-1 [92], is applied, considering slenderness in the web post length and using the buckling curve *c* (**Eqs. 27-32**):

$$\sigma_{Rk} = \chi f_y \tag{27}$$

$$\chi = \frac{1}{\phi + \sqrt{\phi^2 - \bar{\lambda}^2}} \leq 1.0 \tag{28}$$

$$\phi = 0.5\left[1 + 0.49\left(\bar{\lambda} - 0.2\right) + \bar{\lambda}^2\right] \tag{29}$$

$$\bar{\lambda} = \sqrt{\frac{f_y}{f_{cr,w}}} \tag{30}$$

$$f_{cr,w} = \frac{\pi^2 E}{\lambda_w^2} \tag{31}$$

$$\lambda_w = \frac{l_{eff}\sqrt{12}}{t_w} \tag{32}$$

Thus, the vertical shear strength can be calculated (**Eq. 33)**:

$$V_{Lv,Rk} = \sigma_{Rk} t_w b_w \tag{33}$$

5.4.3 Panedpojaman et al.

Panedpojaman et al. [29] made an adaptation in the effective length of the web post. In this model, the effective length of the web post is multiplied by a factor *k*, which is a factor that considers the partial restriction of the web post in relation to the buckling phenomenon (**Fig. 28**). According to the study, the coefficient presented in the **Eqs. (34-35)** considers the effect of the variation of the height of the tees with the values of the ratios D_o/d e p/D_o.

$$l_{eff,P} = k\left(0.5\sqrt{p^2 - D_o^2}\right) \tag{34}$$

$$k = 0.9\left(\frac{p}{D_o}\right)\left(\frac{D_o}{d}\right)^2 \leq \min\left(1.15\frac{D_o}{d}, 1.15\right) \tag{35}$$

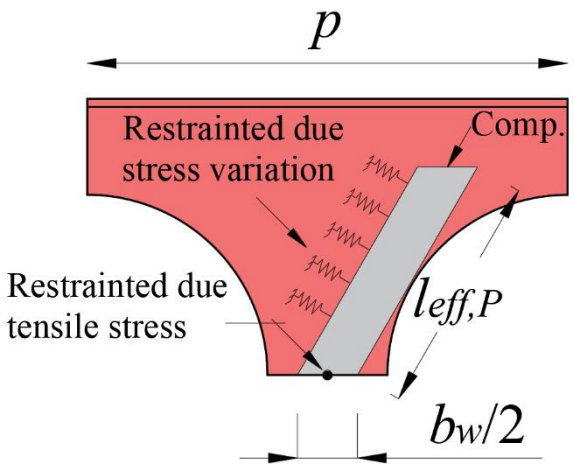

Fig. 28: The model of Panedpojaman et al., adapted from [29]

This method has also been modified for application in ANSI/AISC 360-16 specifications (**Eq. 36**):

$$\chi = \begin{cases} 0.658^{\left(f_y / f_{cr,w}\right)} & for \ \left(f_y / f_{cr,w}\right) > 2.25 \\ 0.877\left(f_y / f_{cr,w}\right) \le 1.0 & for \ \left(f_y / f_{cr,w}\right) \le 2.25 \end{cases} \quad (36)$$

5.4.4 Grilo et al.

The proposed formulation (**Eqs. 37-44**) takes into account a constant stress distribution (**Fig. 29**), and the reduction factor.

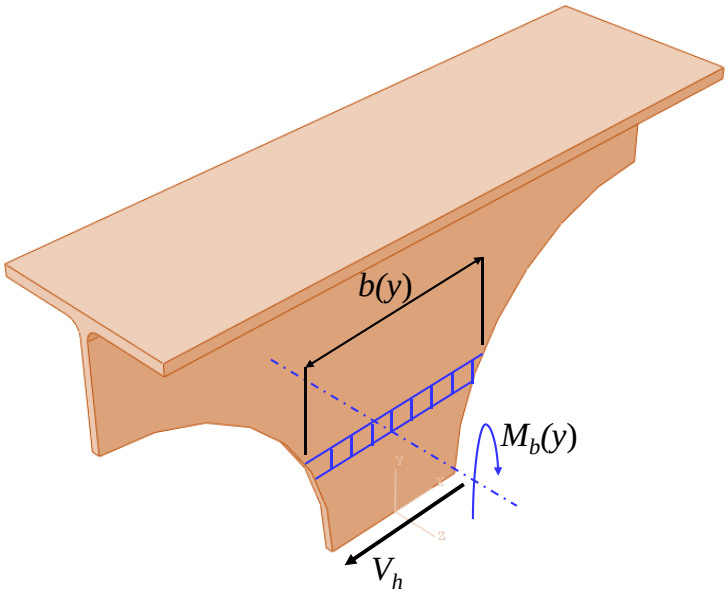

Fig. 29: The model of Grilo et al., adapted from [30]

$$V_{Gh,Rk} = V_{h,p}\chi \quad (37)$$

$$V_{h,p} = \beta_G f_y \frac{t_w b_p^{\,2}}{\sqrt{3b_p^{\,2} + 16y_p^{\,2}}} \quad (38)$$

$$\beta_G = 1.838 - 0.42\left(\frac{D_o}{d_g}\right) - \left(\frac{p}{3D_o}\right) \qquad for\left(p/Do\right) \geq 1.2 \tag{39}$$

$$y_p = \frac{D_o}{2}\left[0.445\left(\frac{p}{D_o}\right)^3 - 2.578\left(\frac{p}{D_o}\right)^2 + 4.770\left(\frac{p}{D_o}\right) - 2.475\right] \tag{40}$$

$$b_p = b_w\sqrt{1 - \frac{4{y_p}^2}{{D_o}^2}} \tag{41}$$

$$\lambda_{ma,0} = \sqrt{\frac{3\left(p^2 - D_o^2\right) f_y}{\pi^2 t_w^2 E}} \tag{42}$$

801 For $\lambda_{ma,0} \geq 1.0$:

$$\chi = \frac{m}{{\lambda_{ma,0}}^n} \leq 1.0 \tag{43}$$

802 For $\lambda_{ma,0} < 1.0$:

$$\chi = op^{\left({\lambda_{ma,0}}^q\right)} \leq 1.0 \tag{44}$$

803 With, *m*, *n*, *o*, *p* e *q*, according to **Table 6**.

804 **Table 6**: Values of *m* and *n*

D_o/d_g	p/D_o	*m*	*n*	*o*	*p*	*q*
	1.1	0.759	1.35	1.15	0.660	3.5
	1.2	0.730	1.39	1.42	0.514	2.1
0.5	1.3	0.780	1.40	1.16	0.672	3.5
	1.4	0.840	1.42	1.26	0.667	2.7
	1.5	0.916	1.40	1.09	0.840	5.0
	1.1	0.798	1.42	1.14	0.700	3.5
	1.2	0.791	1.42	1.13	0.700	3.8
0.6	1.3	0.836	1.40	1.10	0.760	4.5
	1.4	0.909	1.36	1.15	0.790	3.3
	1.5	0.970	1.31	1.09	0.890	4.5
	1.1	0.849	1.47	1.08	0.786	4.5
	1.2	0.844	1.44	1.11	0.760	3.9
0.7	1.3	0.903	1.39	1.15	0.785	4.0
	1.4	0.980	1.34	1.12	0.870	3.0
	1.5	1.130	1.33	-	-	-
	1.1	0.888	1.46	1.09	0.815	4.0
	1.2	0.901	1.42	1.14	0.790	3.5
0.8	1.3	1.020	1.42	-	-	-
	1.4	1.175	1.42	-	-	-
	1.5	1.285	1.36	-	-	-

According to the authors, some branches of the curves have not been determined, due to the failure occurring by a mechanism other than web post buckling, indicating that it will occur by a VM.

5.4.5 Comparison between Web Post Resistance Methods

Four tests on composite cellular beams, which had the ultimate capacity defined by web post buckling, are used to compare the calculation procedures (**Table 7**). Young's module was adopted equal to 200GPa. In the case of asymmetric sections, the most critical section between the upper tee and the lower tee is adopted.

Table 7: Details of the specimens (in mm and MPa)

Ref.				Upper tee				Lower tee			
	d_g	D_o	p	b_f	t_f	t_w	f_y	b_f	t_f	t_w	f_y
[87]	575	375	500	141.8	8.6	6.4	312[a]	141.8	8.6	6.4	312
[87]	630	450	630	141.8	8.6	6.4	312[a]	152.4	10.9	7.6	312
[84,86]	555	380	570	180	13.5	8.6	355	180	13.5	8.6	355
[84,86]	485	380	570	150	10.7	7.1	355	300	21.5	12	355

[a]It was adopted the average value between tensile tests of specimen 1 and 2 (Ulster);
[b]Shear force at opening, considering only the load;

The results are shown in **Table 8**. In this context, it is possible to observe that all procedures are conservative regarding the calculation of the web post buckling resistance.

Table 8: Tests vs. Analytical procedures

Ref.	Test			Analytical				Analytical/Test			
	P_{test} (kN)	V_{test} (kN)	$V_{h,test}$ (kN)	Horizontal shear (kN)		Vertical shear (kN)					
				W	G	L	P	W	G	L	P
[86]	370	185	141	96	67	91	108	0.68	0.48	0.49	0.59
[86]	430	215	190	118	79	96	90	0.62	0.41	0.45	0.42
[83,85]	806	403	365	239	217	263	237	0.66	0.59	0.65	0.59
[83,85]	658	329	333	176	150	166	136	0.53	0.45	0.51	0.41
							Average	0.62	0.48	0.52	0.50
							SD	2.43%	7.48%	8.89%	7.86%
							Cov.	0.32%	0.45%	0.60%	0.72%

*W=Ward; G= Grilo et al.; L= Lawson et al.; P=Panedpojaman et al.

5.2 VIERENDEEL BENDING OF TEES

As shown previously, the phenomenon occurs due to the transfer of shear through the opening. In this section, some calculation models for the verification of the Vierendeel mechanism are presented. In this way, the SCI P355 makes classifications in the lower tee (**Table 9**), which is tensioned, according to the web

824 opening length, considering rectangular web openings (**Eq. 45**), circular web openings (**Eq. 46**) and elongated
825 web openings (**Eq. 47**).

$$l_{o,eff} = l_o \tag{45}$$

$$l_{o,eff} = 0.7h_o \tag{46}$$

$$l_{o,eff} = l_o - 0.3h_o \tag{47}$$

826 **Table 9: Classification of tee webs** [50]

Class*	Limit on depth of web (h_w) according the length of the opening		
	$l_{o,eff} \leq 32\varepsilon t_w$	$32\varepsilon t_w < l_{o,eff} \leq 36\varepsilon t_w$	$l_{o,eff} > 36\varepsilon t_w$
2	No limit		$h_w \leq \frac{10\varepsilon t_w}{\sqrt{1-\left(\frac{32\varepsilon t_w}{l_{o,eff}}\right)^2}}$
3	No limit		$h_w \leq \frac{14\varepsilon t_w}{\sqrt{1-\left(\frac{36\varepsilon t_w}{l_{o,eff}}\right)^2}}$
4	No limit		

827 *$\varepsilon=(275/f_y)^{1/2}$
828

829 **5.4.1 Lawson et al.**

830 In this scenario, the opening can be represented by an equivalent rectangular opening (**Fig. 30**).

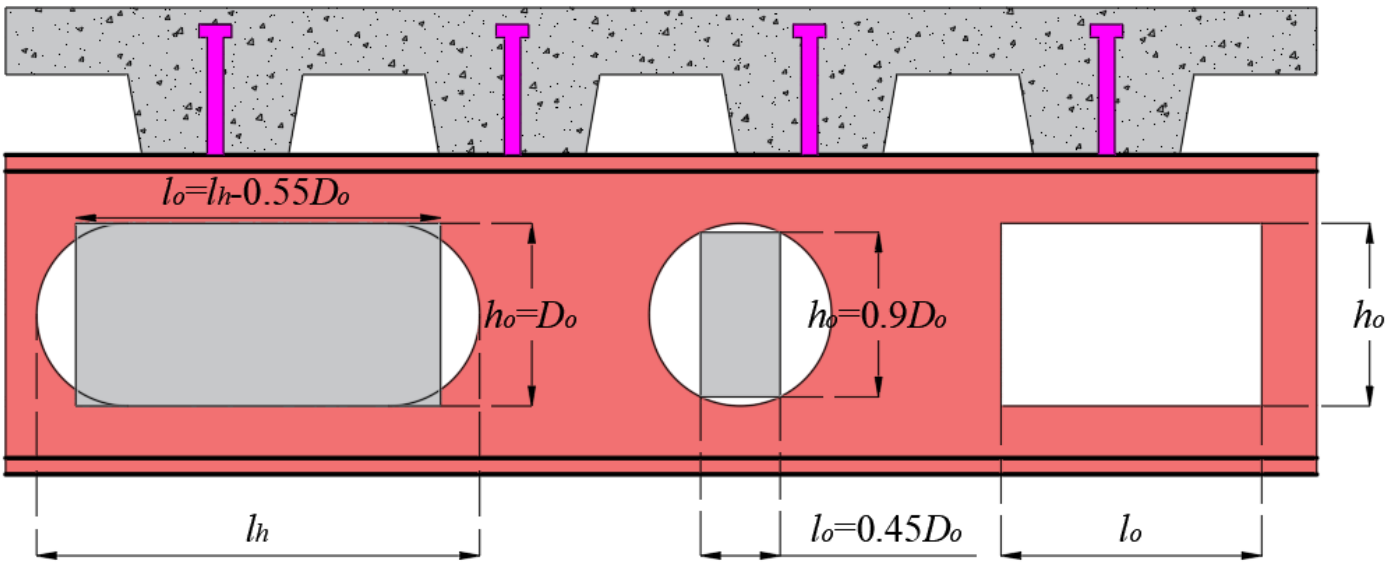

831

832 **Fig. 30: Equivalent openings**

The procedure takes into account the combination of the Vierendeel bending resistance of the steel sections combined with the bending resistance due to local composite action (**Eq. 48**):

$$\left(2M_{pl,N,B}+2M_{pl,N,T}+M_{VC}\right)/l_e \geq V \tag{48}$$

According to Lawson et al. [93], the bending resistances of the tees, are reduced due to axial tension by multiplying by the approximate factor $\left[1-\left(N/N_{pl}\right)^2\right]$. In the presence of shear high magnitude, i.e $\left[V/\left(V_{pl,b}+V_{pl,t}+V_c\right)\right]>0.5$, reduction of the web thickness of the tees should be applied. More information can be found at [50,93,94].

The contribution to Vierendeel bending resistance resulting from composite action above the opening is calculated according to **Eqs. (49-50)**:

$$M_{VC}=nQ\left(y_t+H-0.5h_c\right)k_1 \tag{49}$$

$$k_1=\left(1-\frac{l_o}{25d_t}\right) \tag{50}$$

Lawson et al. reports that k_1 can be taken equal to 1.0 when l_o <5d_t. Another way to calculate the contribution of composite action in resistance to the Vierendeel mechanism was presented in Lawson et al. [95]. In this model, the pull-out effect was considered (**Eqs. 51-52**):

$$V_{ch}=\frac{Q}{s}\left(h_p+0.5h_c\right)\left[1-\frac{\left(h_p+0.5h_c\right)}{l_o}\right]+0.25\,f_c{h_c}^2\frac{b_{eff}}{l_o} \tag{51}$$

$$b_{eff}=\begin{cases}3L/16, & for \quad x\leq L/4\\ L/4, & for \quad x>L/4\end{cases} \tag{52}$$

In addition, the authors presented a new coefficient of reduction (k_l) (**Eq. 53**), which is less conservative with that presented in **Eq. (50)**.

$$k_l=\left[1-\frac{l_o}{20\left(d-h_o\right)}\right] \tag{53}$$

5.4.2 Comparison between Vierendeel Mechanism Resistance Methods

Table 10 shows the tests that the ultimate behavior was governed by the Vierendeel mechanism. The data were obtained from Clawson and Darwin [55,80], Redwood and Wong [65], Redwood and Poumbouras

[67], Donahey and Darwin [9,83], Cho and Redwood [75], Lawson et al [73] and Sheehan et al. [66], with assistance of Hang [96]. These results are used to compare the following calculation methods:

i. SCI P355 [50];

ii. SCI P355 [50] with **Eq. (53)**;

iii. SCI P355 [50] with **Eq. (51)**;

Table 10: Tests (in mm and MPa)

Model	Ref.	Steel Profile															Slab					Shear connector		At opening		
		Upper tee				Lower tee				L	x	l	h	$f_{y,f}$	$f_{y,w}$	b	H	h_p	h_c	f_c	n	n_h	Q^a (kN)	V (kN)	M (kN.m)
		h_{wt}	t_w	b_f	t_f	h_{wb}	t_w	b_f	t_f																
CD-2	[55,80]	76	9	191	13	83	9	191	13	7315	2743	549	275	269	280	1219	102	0	102	29	16	2	98	161	440
CD-4		76	9	191	12	78	9	191	12	4572	914	549	275	295	336	1219	102	0	102	31	8	4	102	207	188
CD-5		78	10	152	16	80	10	152	16	6401	1829	549	275	286	272	1219	102	0	102	32	14	4	102	209	383
CD-6		60	8	170	11	60	8	170	11	4572	914	406	203	273	302	1219	102	0	102	28	8	4	95	173	157
RW-00	[65]	45	6	102	6	45	6	102	6	4000	1000	300	150	349	387	1000	141	76	65	26	4	1	93	81	81
RW-11		60	7	175	11	60	7	175	11	3890	945	426	213	277	311	1200	141	76	65	22	4	1	91	113	106
RW-15		25	7	175	11	96	7	175	11	3890	945	426	213	277	311	1200	141	76	65	22	4	1	91	120	113
RP-56	[67]	61	8	171	11	61	8	171	11	3787	945	426	213	302	325	1000	141	76	65	19	4	0	65	95	89
RP-57		61	8	171	11	61	8	171	11	3787	945	426	213	302	325	1000	141	76	65	19	6	4	65	136	129
RP-68		60	7	170	11	60	7	170	11	3787	945	426	213	304	303	1000	141	76	65	17	6	4	62	129	122
DD-1	[9,83]	94	9	165	11	94	9	165	11	5486	1067	629	314	349	357	1219	127	76	51	31	10	4	71	168	182
DD-2		94	9	166	11	94	9	166	11	5486	1981	629	314	338	350	1219	127	76	51	33	22	4	74	174	350
DD-4A		94	9	166	11	94	9	166	11	5791	1981	629	314	345	350	1219	127	76	51	33	5	0	106	146	294
DD-4B		94	9	166	11	94	9	166	11	5791	1981	629	314	345	350	1219	127	76	51	36	18	0	74	174	350
DD-5A		94	9	165	11	94	9	165	11	5791	1981	629	314	344	345	1219	127	76	51	33	7	2	106	154	313
DD-5B		94	9	165	11	43	9	165	11	5791	1981	629	366	344	345	1219	127	76	51	35	16	4	74	143	290
DD-6A		94	9	154	11	94	9	154	11	5334	2438	629	314	347	346	1219	127	76	51	28	12	4	67	182	0
DD-6B		94	9	167	11	94	9	167	11	5486	1067	629	314	347	346	1219	127	76	51	30	20	8	70	218	234
DD-7A		94	9	168	10	94	9	168	10	6706	1067	629	314	265	268	1219	127	76	51	29	22	10	69	194	209
DD-7B		94	9	168	10	94	9	168	10	6706	1981	629	314	265	268	1219	127	76	51	30	22	6	70	190	382
DD-8A		46	6	102	7	46	6	102	7	3658	924	300	151	311	329	1001	140	76	64	27	8	2	66	86	87
DD-8B		44	6	102	7	37	6	102	7	3658	749	473	162	311	329	1001	140	76	64	34	6	2	48	64	48
DD-9A		64	9	169	11	64	9	169	11	5182	1067	629	375	265	268	1219	178	76	102	29	10	4	68	154	167
DD-9B		67	9	169	11	60	9	169	11	5182	914	375	375	265	268	1219	178	76	102	30	8	2	70	210	201
CR-11	[75]	45	8	174	11	45	8	174	11	4000	3000	424	246	335	346	758	143	76	67	24	4	0	69	95	0
CR-22		44	7	171	12	44	7	171	12	4000	3000	424	247	301	348	750	145	76	69	25	4	2	102	73	0
CR-33		45	8	172	11	45	8	172	11	4000	3000	425	248	329	340	380	143	76	67	25	4	2	89	71	0
CR-44		43	7	171	12	43	7	171	12	4000	950	425	248	313	331	1005	144	76	68	23	6	2	81	94	89
CR-47		44	7	171	12	44	7	171	12	4000	1050	423	247	313	331	1005	144	76	68	23	6	2	81	103	108
CR-55		44	7	171	12	44	7	171	12	4000	950	424	247	304	334	1005	143	76	67	22	4	0	204	94	90
CR-58		44	7	171	12	44	7	171	12	4000	1050	424	248	304	334	1005	143	76	67	22	6	2	204	116	122
CR-66		45	7	172	12	45	7	172	12	4000	950	425	246	307	332	510	104	0	104	24	5	2	171	86	81
CR-69		44	7	172	12	44	7	172	12	4000	1050	425	247	307	332	510	104	0	104	24	5	2	171	93	98
L-3N	[73]	128	10	205	13	128	10	205	13	10000	825	450	250	309	341	2500	120	60	60	28	4	1	96	400	285
L-3S		153	10	205	13	153	10	205	13	10000	900	600	200	309	341	2500	120	60	60	28	4	2	96	400	306
S-2	[66]	78	9	190	15	25	13	300	23	15260	7630	1105	425	410	410	3000	150	80	70	24	25.5	3.7	68	153	1169

[a]For the models CD-2-6 and L-3N-S, the ultimate strength of the shear connector equal to 450 MPa was considered.

The results are shown in **Fig. 31**.

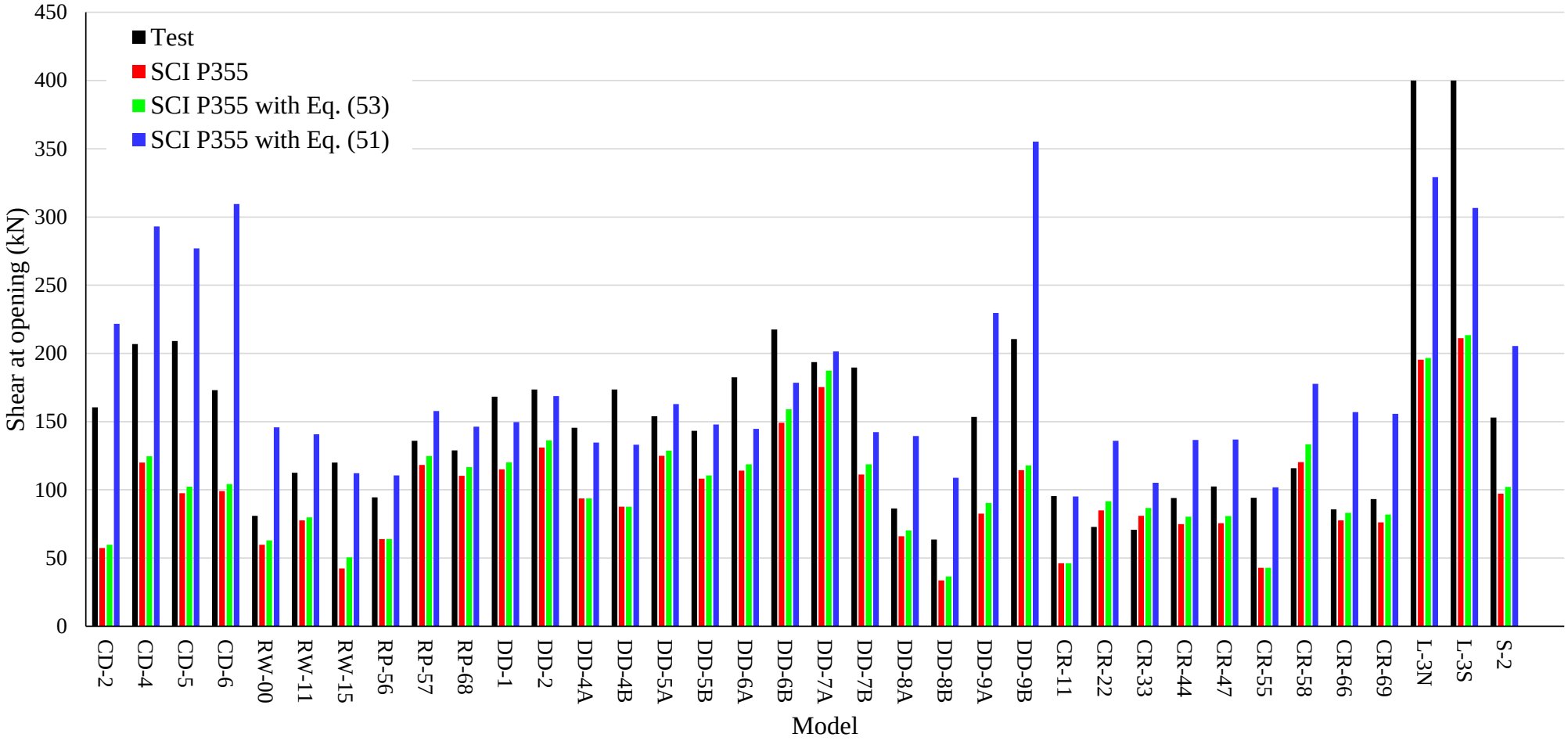

Fig. 31: Tests vs. analytical procedures

Overall, the models SCI P355 and SCI P355 with **Eq. (53)** presented conservative results. On the other hand, the model SCI P355 with **Eq. (51)** showed to overestimate the strength of composite beams with web openings, mainly for solid slabs, as is the case of CD-2-6. The statistical analysis is shown in **Table 11**.

Table 11: Statistical analysis

	Analytical/Test		
	SCI P355	SCI P355 with Eq. (53)	SCI P355 with Eq. (51)
Average	0.69	0.72	1.25
SD	0.19	0.21	0.34
COV.	3.8%	4.6%	11.9%

6. CONCLUDING REMARKS AND FUTURE RESEARCH DIRECTIONS

The composite beams formed by solid or composite slabs have disadvantages in relation to the high operational cost of welding the shear connector on site, the curing time of wet concrete in cold climates and short spans corresponding to the height of the floor. Thus, to improve some of these limitations, a new type of composite beam was proposed, using the precast hollow core slab [97].

Composite beams with precast concrete hollow slabs are used due to the technical and economic benefits they offer, such as the structural capacity as a function of the span/height ratio for a lower self-weight, reduction in the amount of concrete volume, making this system economical and ecologically correct, reducing the carbon emission, the shear connector is welded to the steel profile before taking it to the construction site, a factor that reduces the execution time and the favorable conditions of handling, transportation, storage. With these advantages, these elements have replaced the system of composite beams formed by solid and composite slabs and are common in the United Kingdom [98].

One of the common uses involving precast hollow core slabs is in floor systems in conjunction with a concrete topping molded in situ to provide resistance to actions and a smooth and uniform finish. Typically, the concrete topping has 40 to 100 mm of thickness, with strength ranges from 25 to 40 MPa and contain a small rate of reinforcement to control shrinkage. In the construction using hollow core slabs with concrete topping, there are no mechanical devices to promote the joint behavior of these elements. In this case, the shear strength of the interface depends on the natural adhesion between the precast and in situ concrete. The joint behavior between these structural elements is desired due to the increased strength and stiffness under

vertical loads, and also to resist and transmit forces resulting from the action of the diaphragm under lateral loads [5,99].

The first investigations related to composite beams with precast concrete slabs had an emphasis on shear connectors [100,101]. In Hamilton [100], the behavior of precast concrete slabs with a height of 150 mm and head stud with a 19 mm diameter were evaluated. The results of this study showed an increase in the resistance of composite element by 70%, when compared to the steel profile, alone. The ultimate behavior was due to the failure of the shear connectors. On the other hand, in Moy and Tayler [101], the resistance of head stud connectors in precast concrete slabs was presented. The results showed a drop in the strength of the connection with the reduction of the volume of cast concrete in situ. Still, the authors pointed out that the main factors that affect the resistant capacity of the connectors are the diameter of the connector, the concrete slab thickness, the connection length of the concrete slabs and the quantity and location of the transverse reinforcement. **Fig. 32** shows the typical behavior of head stud.

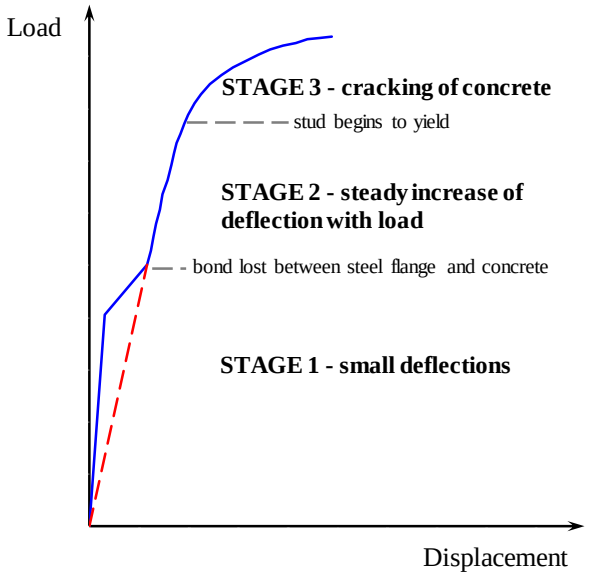

Fig. 32: Typical behavior of head stud, adapted from [101]

Both authors [100,101] were the precursors of composite beams with precast concrete slabs, as they validated the increased strength of this composition and the efficiency of the head stud. However, the evaluation of the behavior of the use of composite beams considering the prefabricated hollow core slabs was relatively new and unknown. In this context, Lam's work [4] fits in, which presented a new experimental procedure for determining the shear strength of composite beams with precast hollow core slabs. The

justification described by the author was that the standard pushout test, specified in EC4 [48], was not suitable for those structures, due to the differences in the construction processes. In **Fig. 33**, the positions of the transverse reinforcement and details of the experimental tests performed by the author are presented. In this study, the correlation between the results was verified, evaluating the influence of parameters such as the slab cut angle (square-ended or chanfred), reinforcement rate, connector diameter and contribution of transverse reinforcement. Such reinforcements assist in the transfer of forces from the profile to the slab and confine the concrete by reducing cracking.

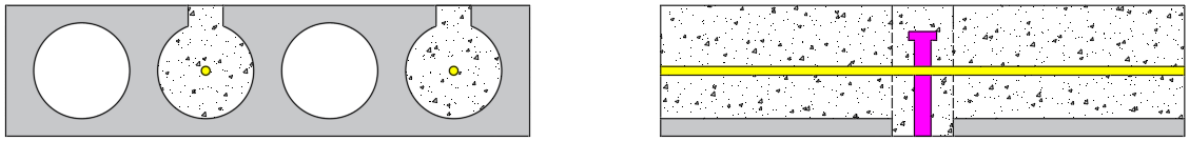

(a) a single transversal reinforcement per opening

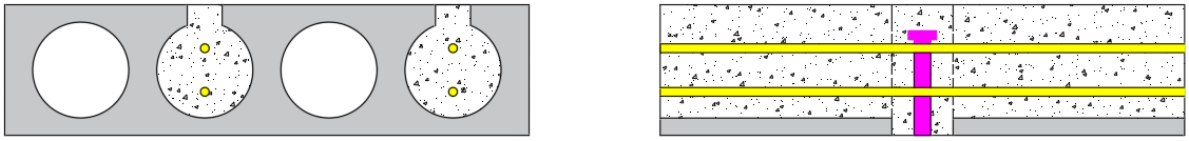

(b) two transversal reinforcement per opening

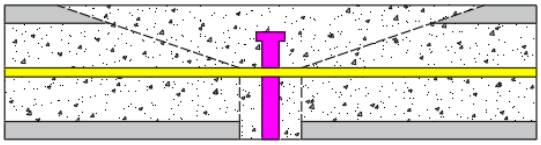

(c) chamfered ended with a single transversal reinforcement per opening

Fig. 33: Transverse reinforcement arrangement, adapted from [4]

Subsequently, Araújo et al. [2] evaluated the influence of the concrete topping strength and the reinforcement rate on the transfer of steel-concrete forces using head stud connectors. The author described that there may be changes in the resistant capacity of each connector due to the presence of concrete topping and other factors characteristic of this type of concrete slab. The authors concluded that the compressive strength of concrete executed in situ is the most important parameter for the resistant capacity of the connectors. In the specimen with more resistant concrete (40 MPa), the connector failed due to shear whereas for concrete with 30 MPa, the failure was characterized by the crushing of the concrete surrounding the connector.

Lam [42], pioneer in the study of composite beams formed by precast hollow core slabs, investigated the interaction between the steel and concrete elements, the determination of the flexural strength and stiffness

of the elements, and the capacity resistant to horizontal shear force of the floor element. In this study, two failure modes were observed: the sudden failure due to the rupture of the shear connectors associated with a high percentage of transverse reinforcement and the cracking of the concrete due to the yield of the transverse reinforcement which results in loss of stiffness and resistant capacity.

Consequently, there were several publications involving the author. In Lam et al. [102] experimental tests of composite beams with precast hollow core slabs were presented. The authors found that the composite action had a resistance three times greater than the resistance of the steel beam, alone, and mentioned that the type of failure was ductile and can be controlled by the correct use of transverse reinforcement and cast concrete in situ. Although with the experimental analysis it presented the flexural behavior, a greater number of investigations was necessary to evaluate the influence of the parameters on the structural behavior. In this context, Lam et al. [103] complemented the previous study by performing parametric analyses to assess the flexural behavior. The authors concluded that with an increase in the transverse reinforcement, the flexural strength significantly increased, but as ductility was reduced, fragile rupture due to crushing of the concrete slab was observed; the increase in the thickness of the slab lead to an increase in flexural strength, although the slab may fail due to traction, and; and when the ratio between the height of the steel beam and the height of the concrete slab is greater than 3, the composite beams are not effective, and failure can occur due to crushing of the concrete. Finally, the results of the numerical modeling allowed the determination of the effective width of the precast hollow core slab. It is observed here, that the authors verified parameters such as the slab height, profile height and transverse reinforcement rate. However, there were still no results of the flexural behavior due to the pin-type shear connectors with the head, the filling concrete and the distance between the slab panels in the vicinity of the connector. In this step, Ellobody and Lam [46] investigated such parameters. The authors performed numerical modeling based on pushout tests. On the results presented, the shear connector's resistant capacity increased with the increase of the width between the hollow core slabs with transverse reinforcement less than 16 mm. This increase was observed for a width of up to 80 mm. For opening widths greater than or equal to 80 mm, the effect on shear-resistant capacity was not observed. Also, both increases in the diameter of the reinforce bars and the width between the hollow core slabs had no

951 significant effect on the shear-resistant capacity of the head stud, but did affect the load-slip relationship. The
952 strength of concrete in situ had a considerable effect on the capacity of the shear connector.

953 In 2003, the Steel Construction Institute (SCI) published a manual containing design criteria for
954 composite beams with precast hollow core slabs [104]. Later in Gouchman [105], this publication is updated.
955 The document gathers recommendations of minimum dimensions, arrangement of shear connectors,
956 transverse reinforcement and recommendations for ultimate and service limit states in the construction phase
957 for cases of total and partial interaction. Later, with the explanation that the construction project in composite
958 elements considering precast hollow core slabs was outside the provisions of EC4, in Lam [106] some of the
959 specific issues that affect this new form of construction were presented. One of the main points addressed by
960 the author was in relation to the strength of the shear connectors, based on the tests performed [4]. In addition,
961 recommendations regarding the effective width of precast hollow core slabs, as well as the flexural strength
962 of composite beams were explained, based on EC4.

963 In Baran [99], the flexural behavior of precast hollow core slabs with concrete topping was
964 investigated. The results showed that the joint behavior between the hollow core slab and the concrete in situ
965 was valid at load levels corresponding to the non-cracked cross section. The presence of the concrete topping
966 resulted in improvements in the cracking moment and in the initial stiffness of the hollow core slabs. However,
967 the effect of the concrete topping on the strength was limited, mainly due to the loss of joint behavior before
968 reaching the ultimate strength. Ibrahim et al. [5] presented an experimental study of the shear-flexural strength
969 of precast hollow core slabs with concrete topping. The results of the experiment showed that the surface
970 condition of the hollow core slab and the longitudinal joint are factors that affect the stiffness and the flexural
971 and shear resistance of these structural elements. According to the authors, the ideal condition for the interface
972 of the hollow core slab and concrete topping that can produce greater stiffness and resistance to shear was
973 rough and wet.

974 From the scenario exposed so far, it appears that studies addressing composite beams with precast
975 hollow core slabs are quite recent. Since then, few researchers have dedicated themselves to this topic. In
976 Batista and Landesmann [107], experimental tests were carried out on composite steel and concrete beams
977 formed by hollow core slabs with concrete topping. Regarding the bending tests indicated a homogeneous

collapse mode, with the development of cracks initiated on the underside of the slab units, in the central region between the two applied loads. These cracks propagated along the full width of the slab unit, extending from the side face of the slab to the region of connection with the steel profile, a factor that reduces the stiffness of the structural element as a whole.

Thus, it appears that studies involving precast hollow core slabs in composite beams are relatively recent. In general, few researchers have devoted themselves to the theme of composite beams formed by precast hollow core slabs, and when we look at such a composition involving the use of cellular beams, studies are still scarce. In summary, the relevant points presented were:

i. Presenting solutions in civil construction due to the economy of materials and solving problems of passage of pipes, the composite beams with openings reduce the height of the floor;
ii. The main modes of failure in composite beams with openings are the web post buckling and the Vierendeel mechanism;
iii. The concrete slab contributes effectively to shear strength;
iv. The failure of the concrete slab occurs after the steel has reached the yield resistance;
v. The dimensioning of the shear connectors is of partial interaction, a factor that generates an increase in the ductility of the structure as a whole;
vi. The composite beams with precast concrete hollow core slabs can replaced the system of composite beams formed by solid and composite slabs;
vii. The failure modes of the composite beams formed by precast concrete hollow core slabs are: the sudden failure due to the rupture of the shear connectors, associated with a high percentage of transverse reinforcement and the cracking of the concrete due to the yield of the transverse reinforcement which results in loss of rigidity and resistant capacity.
viii. There is no study that describes the structural behavior of composite cellular beams with precast concrete hollow core slabs;

ACKNOWLEDGMENTS

This work was supported by the São Paulo Research Foundation (FAPESP) [grant number #2018/22803-1].

REFERENCES

[1] F.D. Queiroz, P.C.G.S. Vellasco, D.A. Nethercot, Finite element modelling of composite beams with full and partial shear connection, J. Constr. Steel Res. 63 (2007) 505–521. doi:10.1016/j.jcsr.2006.06.003.

[2] D.L. Araújo, M.W.R. Sales, S.M. Paulo, A.L.H.C. El Debs, Headed steel stud connectors for composite steel beams with precast hollow-core slabs with structural topping, Eng. Struct. 107 (2016) 135–150. doi:10.1016/j.engstruct.2015.10.050.

[3] S. De Nardin, A. El Debs, State of the art of steel–concrete composite structures in Brazil, Proc. Inst. Civ. Eng. - Civ. Eng. 166 (2013) 20–27. doi:10.1680/cien.2013.166.6.20.

[4] D. Lam, Capacities of headed stud shear connectors in composite steel beams with precast hollowcore slabs, J. Constr. Steel Res. 63 (2007) 1160–1174. doi:10.1016/j.jcsr.2006.11.012.

[5] I.S. Ibrahim, K.S. Elliott, R. Abdullah, A.B.H. Kueh, N.N. Sarbini, Experimental study on the shear behaviour of precast concrete hollow core slabs with concrete topping, Eng. Struct. 125 (2016) 80–90. doi:10.1016/j.engstruct.2016.06.005.

[6] D. Darwin, R.C. Donahey, LRFD for composite beams with unreinforced web openings, J. Struct. Eng. 114 (1988) 535–552. doi:10.1061/(ASCE)0733-9445(1988)114:3(535).

[7] R.M. Lawson, J. Lim, S.J. Hicks, W.I. Simms, Design of composite asymmetric cellular beams and beams with large web openings, J. Constr. Steel Res. 62 (2006) 614–629. doi:10.1016/j.jcsr.2005.09.012.

[8] R.M. Lawson, A.H.A. Saverirajan, Simplified elasto-plastic analysis of composite beams and cellular beams to Eurocode 4, J. Constr. Steel Res. 67 (2011) 1426–1434. doi:10.1016/j.jcsr.2011.03.016.

[9] R.C. Donahey, D. Darwin, Web openings in composite beams with ribbed slabs, J. Struct. Eng. 114 (1988) 518–534. doi:10.1061/(ASCE)0733-9445(1988)114:3(518).

[10] S. Chen, T. Limazie, J. Tan, Flexural behavior of shallow cellular composite floor beams with innovative shear connections, J. Constr. Steel Res. 106 (2015) 329–346. doi:10.1016/j.jcsr.2014.12.021.

[11] P.K. Das, S.L. Srimani, Handbook for the design of castellated beams, Oxford & IBH Publishing Company, New Delhi, Delhi, India, 1984.

[12] P.R. KNOWLES, Castellated Beams, in: Proc. Inst. Civ. Eng., 1991: pp. 521–536.

[13] J.D. Megharief, Behavior of composite castellated beams, 1997. Partial M.Sc. thesis. McGill University, 1997.

[14] Kloeckner Metals UK, No Title, (n.d.). https://www.kloecknermetalsuk.com.

[15] E. Ellobody, Nonlinear analysis of cellular steel beams under combined buckling modes, Thin-Walled Struct. 52 (2012) 66–79. doi:10.1016/j.tws.2011.12.009.

[16] K.M. El-Sawy, A.M.I. Sweedan, M.I. Martini, Moment gradient factor of cellular steel beams under inelastic flexure, J. Constr. Steel Res. 98 (2014) 20–34. doi:10.1016/j.jcsr.2014.02.007.

[17] P. Panedpojaman, W. Sae-Long, T. Chub-Uppakarn, Cellular beam design for resistance to inelastic lateral-torsional buckling, Thin-Walled Struct. 99 (2016) 182–194. doi:10.1016/j.tws.2015.08.026.

[18] D. Sonck, J. Belis, Lateral-torsional buckling resistance of cellular beams, J. Constr. Steel Res. 105 (2015) 119–128. doi:10.1016/j.jcsr.2014.11.003.

[19] N. Boissonnade, J. Nseir, M. Lo, H. Somja, Design of cellular beams against lateral torsional buckling, Proc. Inst. Civ. Eng. - Struct. Build. 167 (2013) 436–444. doi:10.1680/stbu.12.00049.

[20] A.M.I. Sweedan, Elastic lateral stability of I-shaped cellular steel beams, J. Constr. Steel Res. 67 (2011) 151–163. doi:10.1016/j.jcsr.2010.08.009.

[21] F.P.V. Ferreira, A. Rossi, C.H. Martins, Lateral-torsional buckling of cellular beams according to the possible updating of EC3, J. Constr. Steel Res. 153 (2019). doi:10.1016/j.jcsr.2018.10.011.

[22] F.P.V. Ferreira, C.H. Martins, LRFD for Lateral-Torsional Buckling Resistance of Cellular Beams, Int. J. Civ. Eng. (2019). doi:10.1007/s40999-019-00474-7.

[23] M.A. Bradford, Distortional buckling of monosymmetric I-beams, J. Constr. Steel Res. 5 (1985) 123–136. doi:10.1016/0143-974X(85)90010-0.

[24] M.A. Bradford, Inelastic distortional buckling of I-beams, Comput. Struct. 24 (1986) 923–933. doi:10.1016/0045-7949(86)90300-7.

[25] M.A. Bradford, Buckling of elastically restrained beams with web distortions, Thin-Walled Struct. 6

(1988) 287–304. doi:10.1016/0263-8231(88)90005-5.
[26] M.A. Bradford, Buckling of doubly-symmetric cantilevers with slender webs, Eng. Struct. 14 (1992) 327–334. doi:10.1016/0141-0296(92)90046-S.
[27] R. Hassan, M. Mohareb, Distortional lateral torsional buckling for simply supported beams with web cleats, Can. J. Civ. Eng. 42 (2015) 1091–1103. doi:10.1139/cjce-2015-0084.
[28] T. Zirakian, H. Showkati, Distortional buckling of castellated beams, J. Constr. Steel Res. 62 (2006) 863–871. doi:10.1016/j.jcsr.2006.01.004.
[29] P. Panedpojaman, T. Thepchatri, S. Limkatanyu, Novel design equations for shear strength of local web-post buckling in cellular beams, Thin-Walled Struct. 76 (2014) 92–104. doi:10.1016/j.tws.2013.11.007.
[30] L.F. Grilo, R.H. Fakury, A.L.R. de Castro e Silva, G. de S. Veríssimo, Design procedure for the web-post buckling of steel cellular beams, J. Constr. Steel Res. 148 (2018) 525–541. doi:10.1016/j.jcsr.2018.06.020.
[31] K.D. Tsavdaridis, C. D'Mello, Web buckling study of the behaviour and strength of perforated steel beams with different novel web opening shapes, J. Constr. Steel Res. 67 (2011) 1605–1620. doi:10.1016/j.jcsr.2011.04.004.
[32] F. Erdal, M.P. Saka, Ultimate load carrying capacity of optimally designed steel cellular beams, J. Constr. Steel Res. 80 (2013) 355–368. doi:10.1016/j.jcsr.2012.10.007.
[33] K.. Chung, R.. Lawson, Simplified design of composite beams with large web openings to Eurocode 4, J. Constr. Steel Res. 57 (2001) 135–164. doi:10.1016/S0143-974X(00)00011-0.
[34] R. Redwood, S.H. Cho, Design of steel and composite beams with web openings, J. Constr. Steel Res. 25 (1993) 23–41. doi:10.1016/0143-974X(93)90050-3.
[35] D. Kerdal, D.A. Nethercot, Failure modes for castellated beams, J. Constr. Steel Res. 4 (1984) 295–315. doi:10.1016/0143-974X(84)90004-X.
[36] K.D. Tsavdaridis, C. D'Mello, Vierendeel Bending Study of Perforated Steel Beams with Various Novel Web Opening Shapes through Nonlinear Finite-Element Analyses, J. Struct. Eng. 138 (2012) 1214–1230. doi:10.1061/(asce)st.1943-541x.0000562.
[37] K.F. Chung, T.C.H. Liu, A.C.H. Ko, Investigation on vierendeel mechanism in steel beams with circular web openings, J. Constr. Steel Res. 57 (2001) 467–490. doi:10.1016/S0143-974X(00)00035-3.
[38] J. Warren, Ultimate load and deflection behaviour of cellular beams, University of Natal, 2001.
[39] P. Panedpojaman, T. Thepchatri, S. Limkatanyu, Novel simplified equations for Vierendeel design of beams with (elongated) circular openings, J. Constr. Steel Res. 112 (2015) 10–21. doi:10.1016/j.jcsr.2015.04.007.
[40] P. Panedpojaman, T. Rongram, Design Equations for Vierendeel Bending of Steel Beams with Circular Web Openings, World Congr. Eng. 2014. II (2014) 0–5.
[41] J.G. Verweij, Cellular beam-columns in portal frame structures, 2010. M.Sc. thesis. Delft University of Technology Civil Engineering, 2010.
[42] D. Lam, Composite steel beams using precast concrete hollow core floor slabs, 1998. Ph.D. thesis. University of Nottingham, 1998.
[43] J.C. Chapman, S. Balakrishnan, Experiments on composite beams, Struct. Eng. 42 (1964) 369–383.
[44] J.B. MENZIES, Cp 117 and Shear Connectors in Steel-Concrete Composite Beams Made With Normal-Density of Lightweight Concrete, Struct. Eng. 49 (1971) 137–154.
[45] J.G. Ollgaard, R.G. Slutter, J.W. Fisher, Shear strength of stud connectors in lightweight and normal weight concrete, AISC Eng. J. 1971 (1971) 55–34.
[46] E. Ellobody, D. Lam, Modelling of headed stud in steel-precast composite beams, Steel Compos. Struct. 2 (2002) 355–378. doi:10.12989/scs.2002.2.5.355.
[47] E. Aggelopoulos, F. Hanus, M. Lawson, Shear connection requirements for composite cellular beams, in: Proc. 12th Int. Conf. Adv. Steel-Concrete Compos. Struct. - ASCCS 2018, Universitat Politècnica València, Valencia, 2018: pp. 153–159. doi:10.4995/ASCCS2018.2018.7161.
[48] EUROPEAN COMMITTEE FOR STANDARDIZATION, EN 1994-1-1: Eurocode 4 – Design of composite steel and concrete structures – Part 1-1: General rules for buildings., (2004).
[49] American Institute of Steel Construction, ANSI/AISC 360-16 - Specification for structural steel buildings., (2016).

[50] R.M. Lawson, S.J. Hicks, Design of beams with large web openings, The Steel Construction Institute, 2011.

[51] Sameer S. Fares, J. Coulson, David W. Dinehart, Castellated and Cellular Beam Design 31, Am. Inst. Steel Constr. (2016).

[52] C.J. Granade, An investigation of composite beams having large rectangular openings in their webs, 1968. Partial M.Sc. thesis. University of Alabama, 1968.

[53] D.M. Todd, P.B. Cooper, Strength of composite beams with web openings, ASCE J. Struct. Div. 106 (1980) 431–444.

[54] C.M. DONOGHUE, Strength of composite beams with web openings, ASCE J. Struct. Div. 108 (1982) 2652–2667.

[55] W.C. Clawson, D. Darwin, Tests of composite beams with web openings, ASCE J. Struct. Div. 108 (1982) 145–162.

[56] W.C. Clawson, D. Darwin, Strength of composite beams at web openings, ASCE J. Struct. Div. 108 (1982) 623–641.

[57] S.H. Cho, An investigation on the strength of composite beams with web openings, 1982. M.Sc. thesis. Hanyang University, 1982.

[58] S.H. Cho, Slab behaviour in composite beams at web openings, 1990. Ph.D. thesis. McGill University, 1990.

[59] R. Narayanan, R.I.M. Al-Amery, T.M. Roberts, Shear strength of composite plate girders with rectangular web cut-outs, J. Constr. Steel Res. 12 (1989) 151–166. doi:10.1016/0143-974X(89)90030-8.

[60] T.M. Roberts, R.I.M. Al-Amery, Shear strength of composite plate girders with web cutouts, J. Struct. Eng. 117 (1991) 1897–1910. doi:10.1061/(ASCE)0733-9445(1991)117:7(1897).

[61] N.E. Shanmugam, S.F. Darehshouri, S.A. Osman, Experimental study on composite plate girders with web opening, Proc. Inst. Civ. Eng. - Struct. Build. 167 (2014) 704–717. doi:10.1680/stbu.13.00043.

[62] T. Chen, X. Gu, H. Li, Behavior of steel-concrete composite cantilever beams with web openings under negative moment, Int. J. Steel Struct. 11 (2011) 39–49. doi:10.1007/S13296-011-1004-8.

[63] L. Li, W. Liao, J. Wang, D. Zhou, Behavior of continuous steel-concrete composite beams with web openings, Int. J. Steel Struct. 15 (2015) 989–997. doi:10.1007/s13296-015-1218-2.

[64] M.A. Gizejowski, W.A.S. Khalil, Stability and ductility of castellated composite beams subjected to hogging bending, in: E. Batista, P. Vellasco, L. de Lima (Eds.), SDSS'Rio 2010 Stab. DUCTILITY STEEL Struct., Rio de Janeiro, 2010: pp. 839–846.

[65] R.G. Redwood, P.K. Wong, Web holes in composite beams with steel deck, (1982) 41.

[66] T. Sheehan, X. Dai, D. Lam, E. Aggelopoulos, M. Lawson, R. Obiala, Experimental study on long spanning composite cellular beam under flexure and shear, J. Constr. Steel Res. 116 (2016) 40–54. doi:10.1016/j.jcsr.2015.08.047.

[67] R.G. Redwood, G. Poumbouras, Tests of composite beams with web holes, Can. J. Civ. Eng. 10 (1983) 713–721. doi:10.1139/l83-100.

[68] D. Darwin, W.K. Lucas, LRFD for steel and composite beams with web openings, J. Struct. Eng. 116 (1990) 1579–1593. doi:10.1061/(ASCE)0733-9445(1990)116:6(1579).

[69] R.G. Redwood, G. Poumbouras, Analysis of composite beams with web openings, J. Struct. Eng. 110 (1984) 1949–1958. doi:10.1061/(ASCE)0733-9445(1984)110:9(1949).

[70] M.A. Benitez, D. Darwin, R.C. Donahey, Deflections of composite beams with web openings, J. Struct. Eng. 124 (1998) 1139–1147. doi:10.1061/(ASCE)0733-9445(1998)124:10(1139).

[71] D. Darwin, Steel and Composite Beams with Web Openings, Chicago Am. Inst. Steel Contruction. (2003).

[72] B. Djebli, D.E. Kerdal, A. Abidelah, Additional and total deflection of composite symmetric cellular beams, J. Constr. Steel Res. 158 (2019) 99–106. doi:10.1016/j.jcsr.2019.03.015.

[73] R.M. Lawson, K.F. Chung, A.M. Price, Tests on composite beams with large web openings to justify existing design methods, Struct. Enginee. 70 (1992) 1–7.

[74] S.H. Cho, R.G. Redwood, Slab behavior in composite beams at openings. I: analysis, J. Struct. Eng. 118 (1992) 2287–2303. doi:10.1061/(ASCE)0733-9445(1992)118:9(2287).

[75] S.H. Cho, R.G. Redwood, Slab behavior in composite beams at openings. II: tests and verification, J. Struct. Eng. 118 (1992) 2304–2322. doi:10.1061/(ASCE)0733-9445(1992)118:9(2304).

166 [76] E.H. Fahmy, Analysis of composite beams with rectangular web openings, J. Constr. Steel Res. 37
167 (1996) 47–62. doi:10.1016/0143-974X(95)00022-N.
168 [77] J.W. Park, C.H. Kim, S.C. Yang, Ultimate Strength of Ribbed Slab Composite Beams with Web
169 Openings, J. Struct. Eng. 129 (2003) 810–817. doi:10.1061/(asce)0733-9445(2003)129:6(810).
170 [78] K.F. Chung, C.H. Ko, A.J. Wang, Design of steel and composite beams with web openings -
171 Verification using finite element method, Steel Compos. Struct. 5 (2005) 203–233.
172 doi:10.12989/scs.2005.5.2_3.203.
173 [79] A.J. Wang, K.F. Chung, Advanced finite element modelling of perforated composite beams with
174 flexible shear connectors, Eng. Struct. 30 (2008) 2724–2738. doi:10.1016/j.engstruct.2008.03.001.
175 [80] W.C. Clawson, D. Darwin, Composite beams with web openings, University of Kansas, Lawrence,
176 1980.
177 [81] E. Ellobody, B. Young, Behaviour and Design of Composite Beams with Stiffened and Unstiffened
178 Web Openings, Adv. Struct. Eng. 18 (2015) 893–918. doi:10.1260/1369-4332.18.6.893.
179 [82] P. Panedpojaman, Simplified equations for vierendeel design calculations of composite beams with
180 web openings, Steel Compos. Struct. (2018). doi:10.12989/scs.2018.27.4.401.
181 [83] R.C. Donahey, D. Darwin, Performance and design of composite beams with web openings. SM Report
182 No. 18, Lawrence, Kansas, 1986.
183 [84] C. MÜLLER, O. HECHLER, A. BUREAU, D. BITAR, D. JOYEUX, L.G. CAJOT, T. DEMARCO,
184 R.M. LAWSON, S. HICKS, P. DEVINE, O. LAGERQVIST, E. HEDMAN-PÉTURSSON, E.
185 UNOSSON, M. FELDMANN, Large web openings for service integration in composite floors.
186 Technical Steel Research. European Comission, Contract No 7210-PR/315. Final report, (2006).
187 [85] A. Nadjai, Performance of cellular composite floor beams at ambient temperature, 2005.
188 [86] O. Hechler, C. Müller, G. Sedlacek, Investigations on beams with multiple regular web openings, 2006.
189 [87] A. Nadjai, O. Vassart, F. Ali, D. Talamona, A. Allam, M. Hawes, Performance of cellular composite
190 floor beams at elevated temperatures, Fire Saf. J. 42 (2007) 489–497.
191 doi:10.1016/j.firesaf.2007.05.001.
192 [88] G. Bihina, B. Zhao, A. Bouchaïr, Behaviour of composite steel–concrete cellular beams in fire, Eng.
193 Struct. 56 (2013) 2217–2228. doi:10.1016/j.engstruct.2013.09.002.
194 [89] P. Sunar Bükülmez, O.C. Celik, Experimental Study on Fire Behavior of Steel–Concrete Composite
195 Cellular Beams with Large Opening Ratio, Int. J. Steel Struct. 20 (2020) 207–231. doi:10.1007/s13296-
196 019-00281-9.
197 [90] S.S. Fares, J. Coulson, D.W. Dinehart, AISC Steel Design Guide 31: Castellated and Cellular Beam
198 Design, American Institute of Steel Construction, 2016.
199 [91] J.K. Ward, Design of Composite and Non-Composite Cellular Beams, Steel Construction Institute,
200 Silwood Park, Ascot, UK, 1990.
201 [92] EUROPEAN COMMITTEE FOR STANDARDIZATION, EUROCODE 3: Design of steel structures
202 - Part 1-1: General rules and rules buildings, (2005).
203 [93] R.M. Lawson, F. Hanus, D. Sonck, Large web openings in steel and composite beams, Steel Constr. 10
204 (2017) 168–175. doi:10.1002/stco.201710020.
205 [94] R.M. Lawson, J. Lim, S.J. Hicks, W.I. Simms, Design of composite asymmetric cellular beams and
206 beams with large web openings, J. Constr. Steel Res. 62 (2006) 614–629.
207 doi:10.1016/j.jcsr.2005.09.012.
208 [95] R.M. Lawson, J.B.P. Lim, S.O. Popo-Ola, Pull-out forces in shear connectors in composite beams with
209 large web openings, J. Constr. Steel Res. 87 (2013) 48–59. doi:10.1016/j.jcsr.2013.03.025.
210 [96] K.C. Hang, A unified approach for steel and composite beams with web openings, The Hong Kong
211 Polytechnic University, 2002.
212 [97] I.M. Ahmed, K.D. Tsavdaridis, The evolution of composite flooring systems: applications, testing,
213 modelling and eurocode design approaches, J. Constr. Steel Res. 155 (2019) 286–300.
214 doi:10.1016/j.jcsr.2019.01.007.
215 [98] D. Lam, Composite steel beams with precast hollow core slabs: behaviour and design, Prog. Struct.
216 Eng. Mater. 4 (2002) 179–185. doi:10.1002/pse.128.
217 [99] E. Baran, Effects of cast-in-place concrete topping on flexural response of precast concrete hollow-core
218 slabs, Eng. Struct. 98 (2015) 109–117. doi:10.1016/j.engstruct.2015.04.017.
219 [100] T.R. Hamilton, Composite steel and precast concrete slab construction, 1989. Thesis for admission to

corporate membership of Institution of Structural Engineers, 1989.
[101] S.S.J. Moy, C. Tayler, The Effect of Precast Concrete Planks on Shear Connector Strength, J. Constr. Steel Res. 36 (1996) 201–213. doi:10.1016/0143-974X(95)00017-P.
[102] D. Lam, K.S. Elliott, D.A. Nethercot, Experiments on composite steel beams with precast concrete hollow core floor slabs, Proc. Inst. Civ. Eng. - Struct. Build. 140 (2000) 127–138. doi:10.1680/stbu.2000.140.2.127.
[103] D. Lam, K.S. Elliott, D.A. Nethercot, Parametric study on composite steel beams with precast concrete hollow core floor slabs, J. Constr. Steel Res. 54 (2000) 283–304. doi:10.1016/S0143-974X(99)00049-8.
[104] S.J. Hicks, R.M. Lawson, Design of composite beams using precast concrete slabs., The Steel Construction Institute, 2003.
[105] G.H. Gouchman, Design of composite beams using precast concrete slabs in accordance with EUROCODE 4, The Steel Construction Institute, 2014.
[106] D. Lam, Designing composite beams with precast hollowcore slabs to Eurocode 4, Adv. Steel Constr. 3 (2007) 594–606. doi:10.18057/IJASC.2007.3.2.
[107] E.M. Batista, A. Landesmann, Análise experimental de vigas mistas de aço e concreto compostas por lajes alveolares e perfis laminados. COPPETEC, PEC-18541, (2016).

Sensitivity analysis of composite cellular beams to constitutive material models and concrete fracture

Felipe Piana Vendramell Ferreira*[a], Carlos Humberto Martins[b], Silvana De Nardin[a]

[a]Federal University of São Carlos, Rod. Washington Luiz, km 235, São Carlos, São Paulo, Brazil.

[b]State University of Maringá, Av. Colombo nº 5790, Maringá, Paraná, Brazil.

*Corresponding author

E-mail addresses: fpiana@live.com (F. P. V. Ferreira), chmartins@uem.br (C. H. Martins), snardin@ufscar.br (S. De Nardin)

Abstract

Composite cellular beams are an advantageous solution that can be used to reduce floor height by solving service ducts problems. In previous literature, there is little information on numerical modeling that considers sensitivity analysis in composite cellular beams, varying the constitutive models of steel and concrete materials. The concrete, when submitted by external loading, undergoes volume variations caused by inelastic deformations. The parameter that measures dilatancy is known as the dilation angle. The present work aims to analyze sensitivity of the computed response of composite cellular beams to the constitutive models of steel and concrete materials, and the parameters that constitute concrete damage plasticity. Geometrical non-linear analyses are performed based on tests, considering solid elements for the composite slab and shear connectors, and shell elements for the cellular beam. It was concluded that the flexural behavior was not sensitive to dilation angles, unlike structures in which the resistance is governed by shear forces. For a dilation angle equal to 40º, a better post-peak behavior was observed in the load-displacement relationship. It was found that by varying the viscosity parameter (or relaxation time), the load-displacement behavior relationship is not affected.

Keywords: Cellular beams; Composite slab; Headed stud; Buckling; Fracture; Abaqus.

NOTATION

The following symbols are used in this paper:

A_{sc} the shear connector cross-sectional area

a the diameter of the opening

b_c the width of the concrete slab

b_f the width of the flange

b_w the width of the web post

D_0^{el} the initial elastic stiffness

d the elastic stiffness degradation variable

d_g the depth of cellular beam

d_{sc} the shear connector diameter

E_{cm} the modulus of elasticity of the concrete

f_{ck} the characteristic compressive cylinder strength of concrete

f_{cm} the compressive cylinder strength of concrete

f_t the concrete tension resistance

f_u the ultimate strength of cellular beam

$f_{u,sc}$ the ultimate strength of shear connector

f_y the yield strength of cellular beam

G flow potential function

h_F the depth of decking profile

h_{sc} the shear connector height

$\bar{I}_1$ the first invariant of the stress tensor

$\bar{J}_2$ the second invariant of the deviatory tensor

K_c the ratio of the second stress invariant on the tensile meridian to that on the compressive meridian, $0.5 \le K_c \le 1.0$ (the default value is 2/3).

$L_{b,cb}$ the unrestrained length of composite cellular beam

$L_{b,s}$ the unrestrained length of slab

L_p the distance between points of loads

$P_{FE,CC}$ the results obtained from Carreira and Chu model

$P_{FE,G}$ the results obtained from Guo model

p the length between the opening diameter centers

$\bar{p}$ the effective hydrostatic pressure ($\bar{I}_1/3$)

$q_{(CM)}$ the compressive meridian

$q_{(TM)}$ the tensile meridian

$\bar{q}$ the equivalent von Mises stress ($\sqrt{3\bar{J}_2}$)

t_c the thickness of concrete above decking profile

t_f the thickness of the flange

t_w the thickness of the web

V the global shear force

V_h the horizontal force

y_o the distance from the geometric center of the "tee" section to a weld

α the dimensionless constant in Eq. (2)

α_a the ascending branch parameter in Eq. (11)

α_d the descending branch parameter in Eq. (2)

α_{sc} the factor which takes into account the height of stud

α_t the descending branch parameter in Eq. (12)

β the dimensionless constant in Eq. (2)

β_c the stress-strain relationship form factor of concrete in compression

γ the dimensionless constant in Eq. (2)

ε strain

ε_c the compressive strain

ε_t the tensile strain

$\dot{\varepsilon}^{pl}$ the plastic strain rate

$\dot{\varepsilon}_v^{pl}$ the plastic strain rate

$\dot{\varepsilon}_v^{pl}$ the viscoplastic strain rate

$\tilde{\varepsilon}_v^{pl}$ the equivalent plastic strains

$\tilde{\varepsilon}_c^{pl}$ the equivalent plastic strains in compression

$\tilde{\varepsilon}_t^{pl}$ the equivalent plastic strains in tension

μ the viscosity parameter that represents the relaxation time

ξ the eccentricity (defines the rate at which the function approaches the asymptote, the default value is 0.1)

σ stress

σ_{b0} the initial equibiaxial compressive yield stress

σ_{c0} the initial uniaxial compressive yield stress

σ_{t0} the uniaxial tensile stress

$\bar{\sigma}$ the effective stress

$\bar{\sigma}_c\left(\tilde{\varepsilon}_c^{pl}\right)$ the effective compressive cohesion stress

$\bar{\sigma}_t\left(\tilde{\varepsilon}_t^{pl}\right)$ the effective tensile cohesion stress

$\hat{\bar{\sigma}}_{\max}$ the maximum principal effective stress

Ψ dilation angle

1. INTRODUCTION

Design engineers of multistorey buildings often face height limitations imposed by zoning or economic requirements [1]. Composite cellular beams are an advantageous solution that can be used in these scenarios. In general, the ultimate strength of composite cellular beams is associated with the concrete slab failure, such as cracking or crushing, which is combined with cellular beams failures, such web post buckling and Vierendeel mechanism. The cracking occurs as function of deflections through the opening, with the progression of loading. The concrete may develop transverse, longitudinal, and diagonal cracks near the opening region before it reaches the ultimate strength [2]. In composite slabs with embedded steel sheets, cracking begins near at top rib corner, and advances diagonally to the top [3]. Similar to the reinforced concrete theory, the ultimate flexural strength in composite beams can occur due to steel yielding or concrete crushing (**Fig. 1**). For composite sections in which ductile rupture occur, the ultimate flexural strength is given by the steel profile yielding moment resistance capacity. However, for steel profiles that have high yield strength values, concrete crushing may occur before the steel profile has reached its yielding resistance. This is due to the neutral plastic axis lies within the profile web region, which causes excessive compression stresses in concrete slab.

(a) (b) (c)

Fig. 1: Cracking or crushing, adapted from [4] (with permission from Elsevier)

The web post buckling failure is a local phenomenon characterized by a lateral displacement with torsion, and may occur due to the shear forces intensity (**Fig. 2)**. According to the illustration (**Fig. 2a)**, a horizontal force (V_h) acts along the welded joints. When the cellular beams are submitted to external loads, shear stresses develop in the web post, and bending tensions arise. In this scenario, the AB edge is requested by tensile stresses while the CD edge is requested by compression stresses, which may cause the phenomenon (**Fig. 2b)** [5]. The web post buckling resistance depends on cellular steel profile geometrical characteristics, such as opening diameter, spacing between openings, and web thickness [6–8]. On the other hand, the Vierendeel mechanism is characterized by the distortion and formation of plastic hinges in regions near the opening, and it can be explained when the steel reaches the yield strength at the tee's ends due to the combination of normal and tangential stresses [5,9]. Also, this deformation may occur with or without the presence of stiffeners in regions near the openings (**Fig. 3)**. This phenomenon is a typical mode of deformation in composite beams with web openings [10–13]. The main parameters affecting this structural behavior are web thickness and opening diameter.

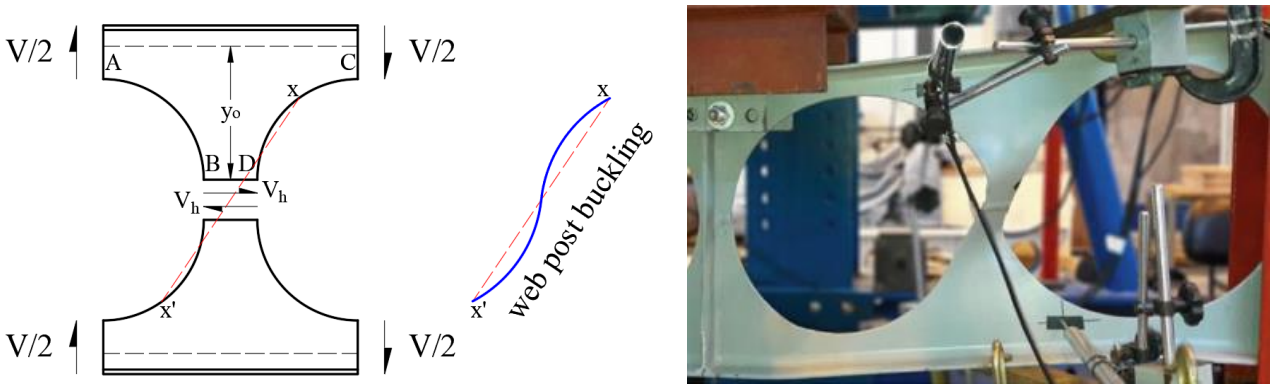

(a) Rigid body equilibrium of web post, adapted from [5] (with permission from Elsevier)

(b) Web post buckling phenomena [14] (with permission from Elsevier)

Fig. 2: Web post buckling

Fig. 3: Vierendeel mechanism [7] (with permission from Elsevier)

The initial studies involving steel beams with openings contemplated those with rectangular openings. Focusing on this type of steel beam, several experimental investigations were conducted [2,15–18], and analytical models were proposed [1,3,19–23]. More recently, a series of studies have been carried out in composite cellular beam, i.e., beams whose openings are distributed sequentially throughout the span. In this respect, it can be highlighted several experimental investigations [4,24–26] that resulted in procedures to predict the resistance of composite cellular beams [27–29]. Some studies that have developed numerical models in composite beams with web openings can be found in [25,30–32]. For example, Müller et al. [25] developed parametric analysis focusing on the influence of the resistance of steel-concrete materials on strength and failure modes. The authors concluded that the failure mechanism depends mainly on the type of steel. In this same regard, Chung [31] evaluated the influence of geometric parameters (i.e., opening shape) on the ultimate behavior. In this study, the author found out that both the cross-section stiffness and the strength of shear connectors were important for the ultimate behavior. Although the authors verified the influence of resistance of materials and geometric parameters on the ultimate behavior of composite beams with web openings, there are no investigations through sensitivity analysis regarding the behavior of these structural elements for different constitutive models. On the other hand, some authors performed sensitivity analysis varying the yield criterion parameters [33–35]. Although the authors observed that the structures behave differently to sensitivity analysis, none of them investigated such sensitivity in composite cellular beams.

The present study aims to investigate the behavior of composite cellular beams with the constitutive models of steel and concrete materials by varying yield criterion parameters of Concrete Damage Plasticity. For this task, geometrical non-linear analyses are performed in ABAQUS® [36]. Sensitivity analyses are calibrated by tests on composite cellular beams [24–26]. First, the concrete constitutive models are evaluated, considering stress-strain relationship proposed by Carreira and Chu [37,38] and Guo [39]. Then, the steel constitutive models are varied, considering the elastic perfectly plastic model, and the several multilinear stress-strain relationships [40–43]. In this scenario, the concrete damage plasticity model parameters are varied, such as the dilation angle and the viscosity (or relaxation time). Finally, with the numerical models calibrated, the present study proposes the final model for the simulation of composite cellular beams compared to tests results.

2. CONCRETE MATERIAL MODEL

The concrete damage plasticity (CDP) model is a criterion based on the models proposed by some authors [44–46], and has been widely used in modeling concrete, and other quasi-brittle materials. The model considers three hypotheses based on the plasticity theory: the initial yield surface determines when plastic deformation begins; the flow rule determines the direction of plastic deformation; and the softening/hardening rule defines how the surface flow evolves with plastic deformation [47]. Tensile cracking and compressive crushing of concrete are the main failure mechanisms of the CDP model. Due to this, the evolution of the yield surface is controlled by two hardening variables which cause failure under tensile and compressive loading. This damage model can be used to describe the irreversible damage that occurs during the fracture process [36].

2.1. STRESS-STRAIN RELATIONSHIP

The stress-strain relationship is governed by a damaged elastic quantity, according to **Eq. (1)**, in which : indicates Frobenius inner product. Therefore, damage associated with concrete failure mechanisms such as cracking and crushing results in degradation of material stiffness.

$$\sigma = \left(1-d\right) D_0^{el} : \left(\varepsilon - \varepsilon^{pl}\right) = \left(1-d\right)\bar{\sigma} \tag{1}$$

The tensile state or compressive damage is independently characterized by two variables, namely the tensile plastic strain and the compression plastic strain. Thus, microcracks and crushing in concrete are represented by the increasing values of these variables that control the yield surface evolution. The stiffness degradation is closely related to the dissipated fracture energy required to create the microcracks.

2.2. YIELD FUNCTION

The concrete damage plasticity model makes use of the strength function of [45], with the modifications proposed by [46] to explain the tensile and compressive strength surface evolution. In terms of the effective stresses, **Eq. (2–5)** describe the resistance function.

$$F = \frac{1}{1-\alpha}\left[\bar{q} - 3\alpha\bar{p} + \beta\left(\tilde{\varepsilon}^{pl}\right)\left\langle\hat{\bar{\sigma}}_{\max}\right\rangle - \gamma\left\langle\hat{\bar{\sigma}}_{\max}\right\rangle - \bar{\sigma}_c\left(\tilde{\varepsilon}_c^{pl}\right)\right] = 0 \tag{2}$$

$$\alpha = \frac{\left(\sigma_{b0}/\sigma_{c0}\right)-1}{2\left(\sigma_{b0}/\sigma_{c0}\right)-1}; 0 \le \alpha \le 0.5 \tag{3}$$

$$\beta = \frac{\bar{\sigma}_c\left(\varepsilon_c^{pl}\right)}{\bar{\sigma}_t\left(\varepsilon_t^{pl}\right)}\left(1-\alpha\right)-\left(1+\alpha\right) \tag{4}$$

$$\gamma = \frac{3\left(1-K_c\right)}{2K_c-1} \tag{5}$$

The yield surfaces are shown in **Fig. 4a** in the deviatoric plane and in plane stress (**Fig. 4b**).

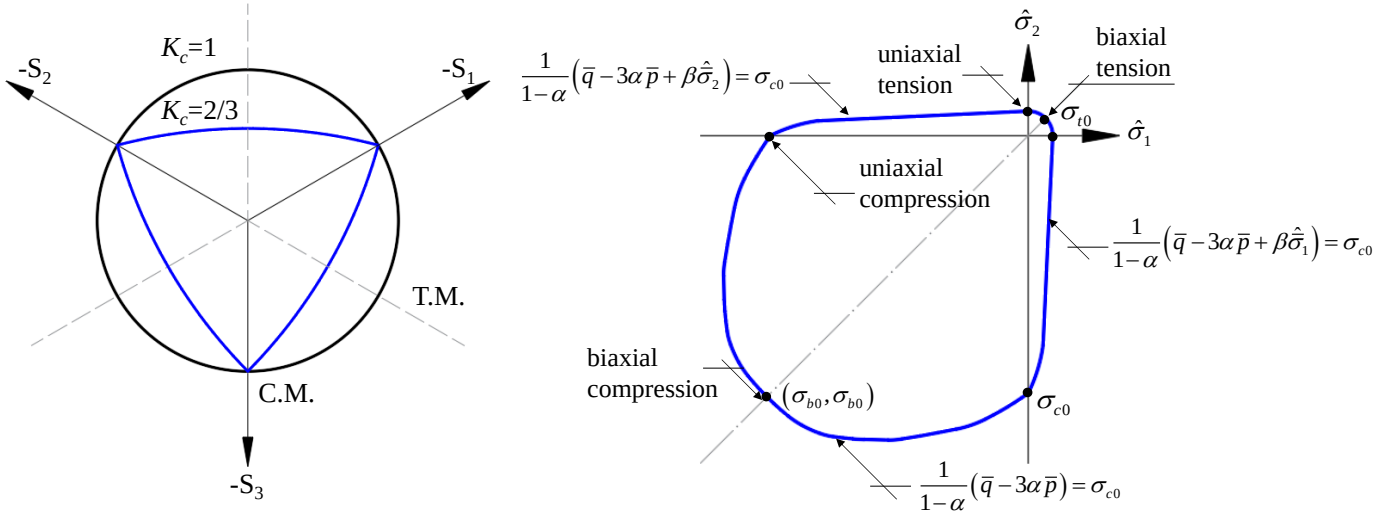

(a) in deviatoric plane **(b)** in plane stress

Fig. 4: Yield surfaces [36]

2.3. PLASTIC FLOW, ECCENTRICITY, AND DILATION ANGLE

Concrete as a brittle material undergoes considerable volume change caused by inelastic strains. This volume change is called dilatancy [33]. The flow rule in concrete damage plasticity model follows the Drucker-Prager model that establishes the hyperbolic function (**Eq. 6**), as shown in **Fig. 5**. The stress-strain relationship in the concrete and the yield surface are related by the flow rule, which corresponds to the function that defines the direction of deformations when the material reaches the state of plastic behavior.

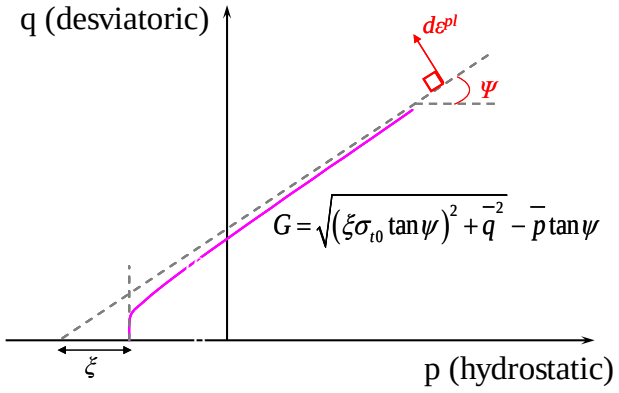

Fig. 5: Hyperbolic surface of the potential flow function in the meridian plane, adapted from [36]

$$G = \sqrt{(\xi \sigma_{t0} \tan\psi)^2 + \bar{q}^2} - \bar{p} \tan\psi \quad (6)$$

2.4. VISCOPLASTIC REGULARIZATION

A common technique for solving convergence difficulty problems is the use of viscoplastic regularization in constitutive equations, which causes the stiffness of the softening material to become positive for sufficiently little time increments. The concrete damage plasticity model can be regularized using viscoplasticity, allowing stresses to be outside the yield surface. For this purpose, the regularization of Duvaut-Lions [48] is used (**Eq. 7**).

$$\dot{\varepsilon}_v^{pl} = \frac{1}{\mu}\left(\varepsilon^{pl} - \varepsilon_v^{pl}\right) \quad (7)$$

3. THE NUMERICAL MODEL

The analyses are conducted using ABAQUS® software in two steps for each numerical model: buckle analysis and geometrical non-linear analysis. For this, the linear perturbation method is used to estimate the critical elastic stability load by obtaining eigenvalues and their eigenvectors. In this method, the elastic stability load is obtained by the product of the first positive eigenvalue (lower energy) by the external load applied to the structure in the initial state. Importantly, this type of analysis does not consider any imperfections in the structure. After this, the geometric nonlinear analysis is performed, considering the initial geometric imperfections. The structure shape in the buckle analysis, normalized to the initial imperfection value, was adopted as the shape at the beginning of the geometrical non-linear analysis. Thus, the implementation of geometric imperfection was performed by the *IMPERFECTION command, with the amplitude equal to d_g/1000. In the models, the residual stresses were not considered since these are not influential for composite beams submitted only to the positive moment. In this context, the residual stresses increase the effects of the negative moment and the beam can reach the lateral distortional buckling [49,50]. According Chen and Jia [49], when the slab is in tension and the bottom flange is in compression, lateral distortional buckling may occur. The lateral distortional buckling phenomenon is characterized by lateral displacement of the compressed bottom flange accompanied by web distortion outside the strong-axis plane. The Static Riks method was used to solve the geometric nonlinearity problem. This method, also known as modified Riks algorithm, can obtain equilibrium solutions for instability problems. This method was used in [51–55]. In the modified Riks algorithm, the size of the increment is limited by moving a certain distance along the tangent line of the curve to the current point of the solution, and the equilibrium search is performed on an orthogonal plane, passing through the obtained point [36]. In the setup of the procedure, it is necessary to implement the initial arc length, which refers to an initial percentage of the external load. Thus, in the next increments, the software automatically adjusts the load increments during analysis so that the problem of convergence occurs through a certain tolerance. A review of nonlinear analysis and modelling of steel and composite structures can be found in Thai et al. [56].

3.1. EXPERIMENTAL TESTS

The results of tests 1A (CCB1) and 1B (CCB2) [24] are considered to conduct the sensitivity analyses. Subsequently, with the results of the parameters provided via parametric study, an analysis is performed to verify the representation of the numerical

model, considering the test RWTH-1A (CCB3) [25,26]. Young's modulus of steel equal to 200 GPa was adopted in the numerical model. Importantly, although the profiled steel sheet was not considered in the numerical model, Holorib HR 51/150 geometry is used to represent the ribs. The headed studs' dimensions are 19x120mm (CCB1 and CCB2) and 19x100mm (CCB3), spaced 150mm. The mechanical properties of the headed studs are the same as presented in [57], i.e., the yield stress and the ultimate stress are 460 MPa and 559 MPa, respectively. The elongation at rupture is 18.8%. **Fig. 6** and **Table 1** show the details of the specimens, as well as the geometric and material properties, and boundary conditions.

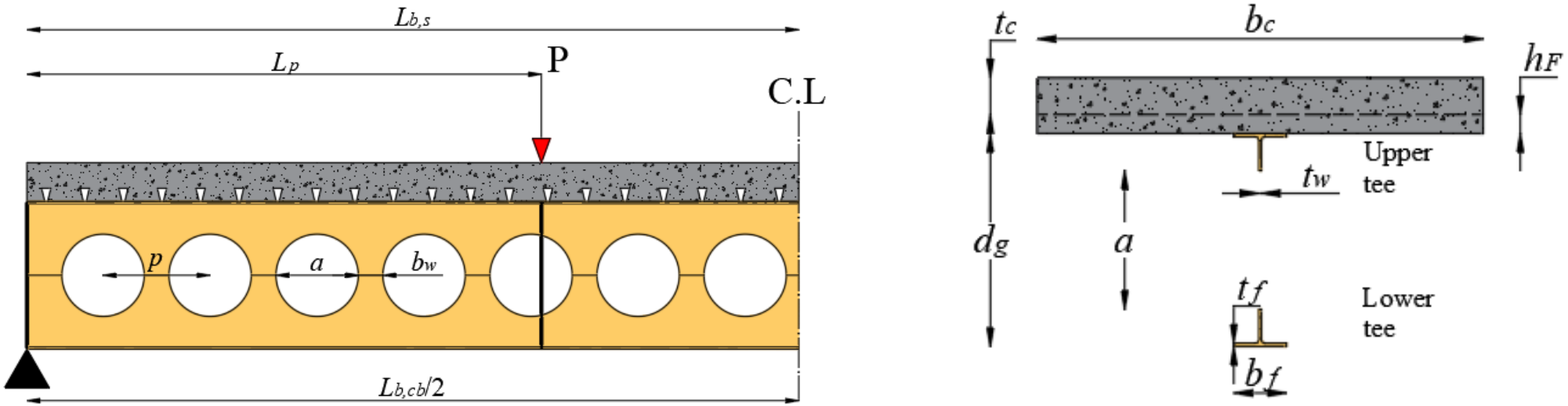

(a) Lateral view (b) Section

Fig. 6: Details of specimens

Table 1: Physical and geometric parameters of tested specimens (in mm and MPa)

Test	Ref.	d_g	a	p	b_w	Upper tee			Lower tee			f_y (flange/web)	f_u (flange/web)	b_c	t_c	h_F	f_{cm}	$L_{b,cb}$	$L_{b,s}$	L_p
						b_f	t_f	t_w	b_f	t_f	t_w									
CCB1	[24]	575	375	500	125	141.8	8.6	6.4	141.8	8.6	6.4	312[a]	438.5[a]	1200	99	51	28.6	4500	4500	1750[b]
CCB2	[24]	630	450	630	180	141.8	8.6	6.4	152.4	10.9	7.6	312[a]	438.5[a]	1200	99	51	28.6	4500	4500	2250
CCB3	[25,26]	555.2	380	570	190	180	13.5	8.6	180	13.5	8.6	451,489	541, 587[c,]	1800	79	51	33.6	6840	6555	1140[b] and 2850[b]

[a]It was adopted the average value between tensile tests of specimen 1 and 2 (Ulster)

[b]with symmetry

[c] $f_u \approx 1.2\, f_y$

3.2. MATERIALS

In Hillerborg et al. [44] was proposed a method in which fracture mechanics was introduced in the finite element method. According to the authors, it was assumed that the crack propagates when the stress reaches the concrete's tensile strength. A special feature of the proposed method was that it explains not only the growth of crack openings, but also the formation of new cracks. The implementation of the concept of stress-cracking requires the definition of a characteristic length associated with an integration point. This definition of the characteristic length is used because the direction in which the crack occurs is not known. Therefore, elements with large proportions will behave quite differently depending on the direction in which they crack. Some studies used the concrete constitutive model, considering the cracking opening and the characteristic length [33,34]. However, as the crack opening model is dependent on the characteristic length, that is, the finite element dimension, in the present study is adopted the stress-strain relationships. This is due to the presence of the slab ribs to be modeled (section 3.1), and also, the removal of volume from the slab for the application of the interaction (section 3.3). More information on how the mesh sensitivity affects the behavior of the concrete modelling can be found in Voyiadjis and Dorgan [58], and Skamniotis et al. [59]. In this paper, the discretization is discussed in section 3.4.

3.2.1. Concrete in Compression

Carreira and Chu [37] reported that the uniaxial stress-strain relationship is strongly affected by concrete characteristics such as water/cement factor, cement type, aggregate dimensions, cure type, and age at which the specimen was tested. The model described by **Eq. (8–9)** [37] presents a broad spectrum of experimental data and shows both the ascending and descending branches of the compressive concrete stress-strain relationship.

$$\frac{\sigma}{f_{cm}} = \frac{\beta_c \left(\varepsilon / \varepsilon_c\right)}{\beta_c - 1 + \left(\varepsilon / \varepsilon_c\right)^{\beta_c}} \tag{8}$$

$$\beta = \left(\frac{f_{cm}}{32.4}\right)^3 + 1.55 \quad (MPa) \tag{9}$$

Another stress-strain relationship showing the ascending and descending branches of stress-strain relationship of concrete in compression (**Eq. 10)** is shown in [39]. The ascending branch parameter (α_a) has its values ranging between 1.5 and 3.0 ($1.5 \leq \alpha_a \leq 3.0$), and α_d is the descending branch parameter ($0 \leq \alpha_d \leq \infty$). The GB-50010-2002 standard [60] describes the values of these parameters as a function of concrete strength. Some researchers [61,62] considered this constitutive model, and the results were in agreement with the test results, thus verifying their effectiveness.

$$\frac{\sigma}{f_{cm}} = \begin{cases} \alpha_a \left(\varepsilon / \varepsilon_c\right) + \left(3 - 2\alpha_a\right)\left(\varepsilon / \varepsilon_c\right)^2 + \left(\alpha_a - 2\right)\left(\varepsilon / \varepsilon_c\right)^3, & \varepsilon / \varepsilon_c \leq 1 \\ \dfrac{\varepsilon / \varepsilon_c}{\alpha_d \left[\left(\varepsilon / \varepsilon_c\right) - 1\right]^2 + \left(\varepsilon / \varepsilon_c\right)}, & \varepsilon / \varepsilon_c > 1 \end{cases} \tag{10}$$

3.2.2. Concrete in Tension

When the reinforcement embedded in the concrete is tested in pullout test, the stress-strain relationship shows that the concrete assists the reinforcement in the tensile stress flow even after cracking. The contribution of concrete is called tension stiffening [38]. This interaction can have a major impact on both the tension and stiffness of the structural element. The phenomenon results from the fact that with the formation of crack in the tensile or flexural reinforced concrete, the non-cracked concrete between each pair of adjacent tensile cracks allows the stress to transfer from the reinforcement to the surrounding concrete. As a result, the tensile stiffness of cracked reinforced concrete is greater than that of reinforcement alone. An important observation published by Cho and Redwood [20] was that a contribution ratio of concrete shear strength, which can range from 30% to 260%. Such an observation related to a range of tests on composite beams with web openings. Importantly, the web post buckling occurs as a function of shear stresses. Thus, concrete contributes significantly to bending and shear strength, and when concrete and steel exhibit high slip values prior to failure, the strength is governed by concrete slab failure [2]. In addition, according to Redwood and Wong [63], the composite beams with web openings are subjected to formation of flexural cracks in the concrete slab. Thus, if the tension stiffening is neglected, the stiffness of cracked reinforced concrete can be greatly underestimated [64]. Carreira and Chu [38] defined the tensile stress-strain relationship by **Eq. (11)**. Generally, the value of the parameter β_c is adopted as equal to the value of the strain compression stress relationship. Guo [39] also presents the tensile stress-strain relationship of the tensile concrete, according to **Eq. (12–13)**.

$$\frac{\sigma}{f_t} = \frac{\beta_c\left(\varepsilon/\varepsilon_t\right)}{\beta_c - 1 + \left(\varepsilon/\varepsilon_t\right)^{\beta_c}} \tag{11}$$

$$\frac{\sigma}{f_t} = \begin{cases} 1.2\left(\varepsilon/\varepsilon_t\right) - 0.2\left(\varepsilon/\varepsilon_t\right)^6, & \varepsilon/\varepsilon_t \le 1 \\ \dfrac{\varepsilon/\varepsilon_t}{\alpha_t\left[\left(\varepsilon/\varepsilon_t\right)-1\right]^{1.7} + \varepsilon/\varepsilon_t}, & \varepsilon/\varepsilon_t > 1 \end{cases} \tag{12}$$

$$\alpha_t = 0.312\, f_t^{\,2} \tag{13}$$

3.2.3. Steel

The stress-strain relationship of steel is particularly important in analytical, numerical, and design models for structures with large plastic deformations. Although several stress-strain models have been developed, many are applicable only to a limited strain range, or are too complex to be readily implemented in practice [43]. Thus, to investigate for better representation of steel strain-stress relationship, the models to be studied are present in **Fig. 7**.

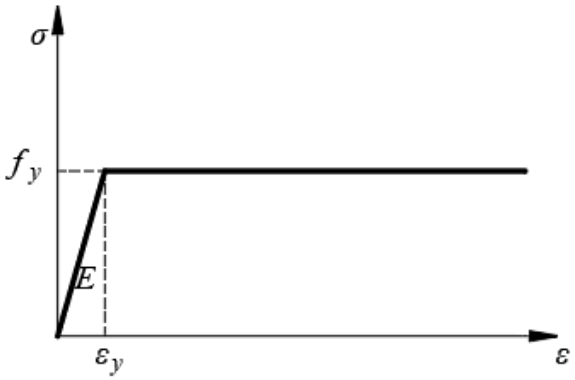

(a) Elastic-perfectly plastic

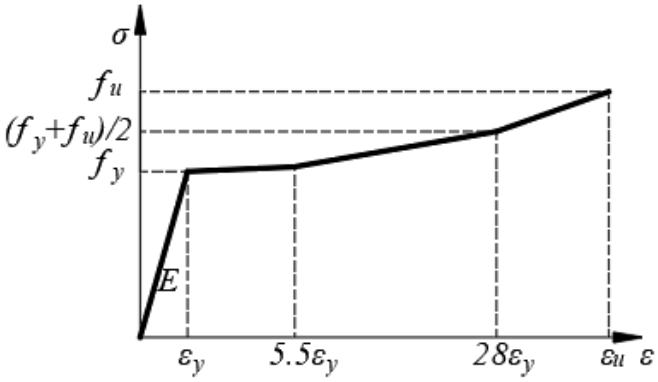

(b) Earls [40]

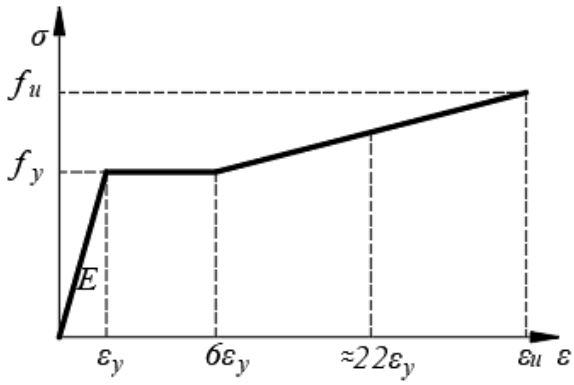

(c) Byfield el at. [41]

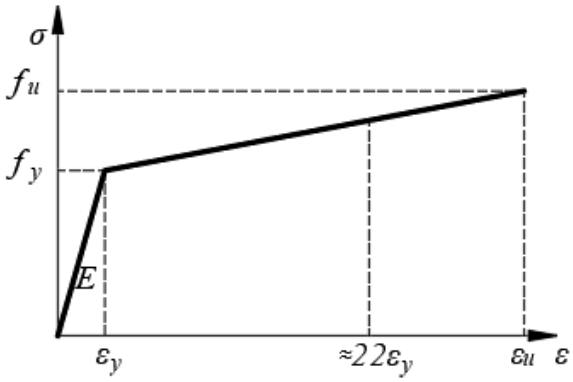

(d) BS EN 1993-1-5 [42]

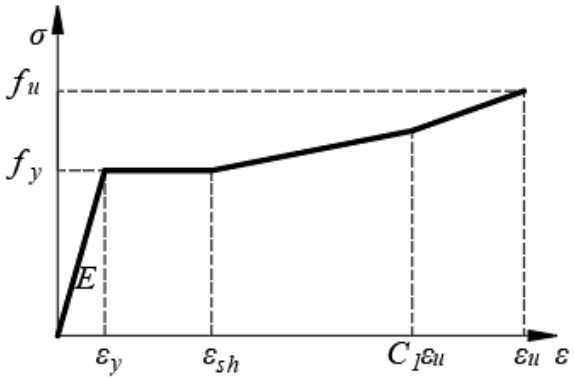

(e) Yun and Gardner [43]

Fig. 7: Steel stress-strain relationship

3.3. INTERACTION

Headed shear stud modeling is of great importance in the interaction between steel and concrete contact surfaces, as the shear stresses are transferred through the steel-concrete interface by the shear connectors' mechanical action [65,66]. Unlike the steel-concrete interface modeling, considering cohesive elements, which was presented in Sadeghi et al. [67], in the present study, the headed shear studs are modelled using solid elements embedded in the concrete slab [68–70]. The analysis strategy is illustrated in **Fig. 8**. The tie constraint is applied to the surface between the shear connectors and the upper flange of the steel cellular profile. This modeling technique allows representation of the perfect bond between steel profile surfaces and shear connectors. The interaction properties between the concrete slab and headed shear studs, and the concrete slab and the steel profile are defined by the normal and tangential behaviors. Therefore, the normal and tangential behavior between the slab-connector and slab-profile interfaces are applied. The friction coefficient for the connector-slab interface is assumed equal to 0.2, while for the slab-profile

interface, the adopted value was equal to 0.3. These adopted values are in accordance with the analyses of other researchers [69,71–73].

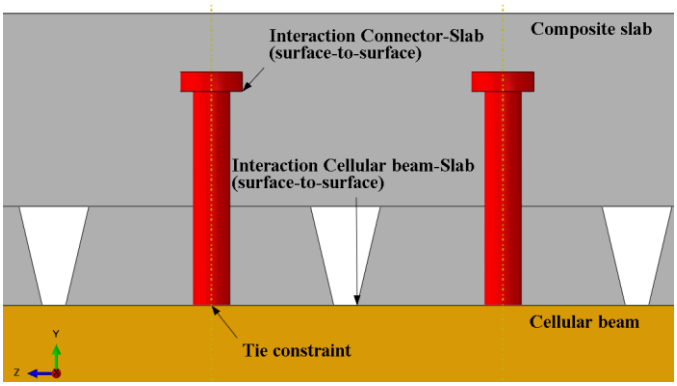

Fig. 8: Interaction between contact surfaces

3.4. BOUNDARY CONDITIONS

In order to reduce the computational cost, longitudinal axis symmetry is considered (**Fig. 9**). For this task, the vertical displacement (Uy=0) and the lateral displacement on the concrete slab (Ux=0) are restrained on the support. In the middle of the span, symmetry is considered (Uz=URx=URy=0) [54,55].

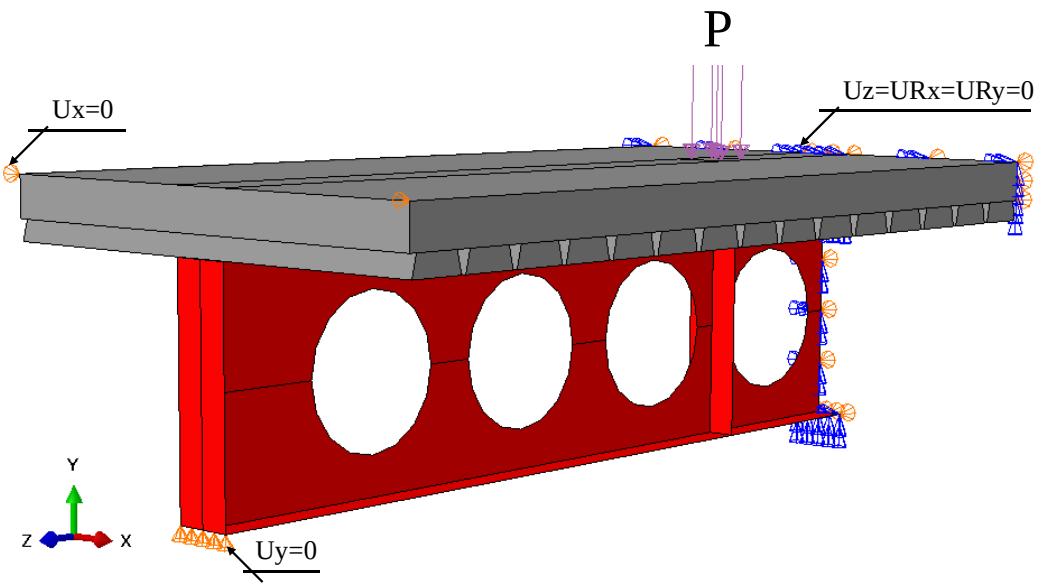

Fig. 9: Boundary conditions, considering symmetry

3.5. DISCRETIZATION

The dimension values of the elements is adopted according to the literature [35,52,53,69,73]. Regarding the steel beam, Dias et al. [74] reported that dimensions smaller than one sixth of the flange width, no significant differences was obtained. However, in Ferreira et al. [52,53], mesh sensitivity analyses were carried out on cellular beams. The results showed that there were no significant differences in the response between the dimensions of 5mm and 10mm. However, the finite element dimension of 5mm obtained a higher computational cost. Regarding the finite element dimension of concrete slab, as performed by Sjaarda et al. [69], Liu et al. [73] and Nguyen et al. [35], the maximum dimension of 30mm was adopted, with respect to the master and slave surfaces.

Besides, the size of the finite element was taken with respect to the master/slave surfaces. As the shear connectors surface are slave, both for the cellular beam and slab, to avoid convergence problems, the dimension of $d_{sc}/8$ was taken. The assignment of master and slave roles can have a significant effect on performance with surface-to-surface contact if the two surfaces have dissimilar mesh refinement; the solution can become quite expensive if the slave surface is much coarser than the master surface [36]. A four-node, doubly curved thin shell element with reduced integration (S4R) was used to model the web and flanges of the cellular beam. This quadrilateral element reduces the processing time. Solid elements with eight nodes and reduced integration (C3D8R) were implemented to model shear connectors and concrete slab. These finite elements support plastic analysis with large deformations and allow crack visualization in the concrete damage plasticity (CDP) model. Both elements have six degrees of freedom per node – three rotations and three translations. The discretization of the steel profile, concrete slab, and headed studs is presented in **Fig. 10**.

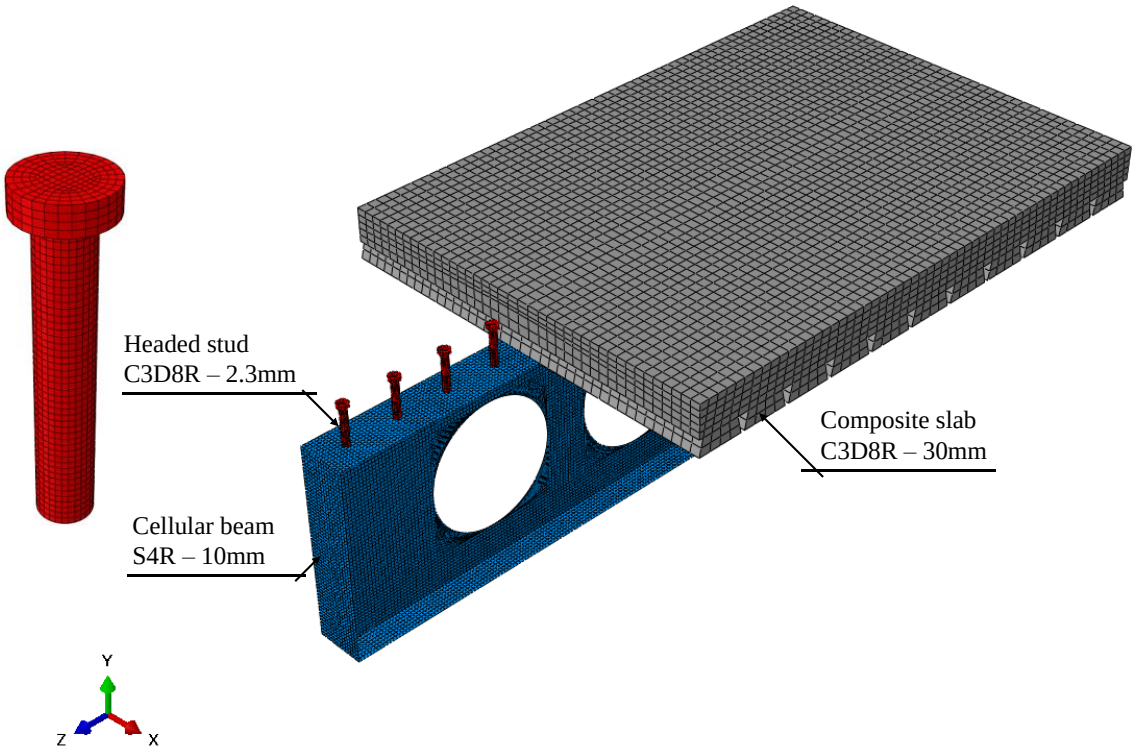

Fig. 10: Discretization

4. RESULTS AND DISCUSSION

A total of 120 numerical models were analyzed considering the combination of the constitutive models of materials shown in **Fig. 11,** and the results were compared with test results of specimens CCB1 and CCB2 [24]. According to Nadjai et al. [75], both tests CCB1 and CCB2 presented the ultimate behavior governed by web-post buckling with an S-shaped double curvature, as shown diagonally xx' (**Fig. 2**). Moreover, it was verified that the development of tensile stresses was above the openings, indicating that the plastic neutral axis was near or in the concrete slab, and after the web-post buckling took place, plastic hinges developed around the openings. The maximum deflection of both tests immediately before failure was 10 mm. In this scenario, the numerical models presented the same ultimate behavior (**Fig. 29**). However, there were differences in post-peak behavior.

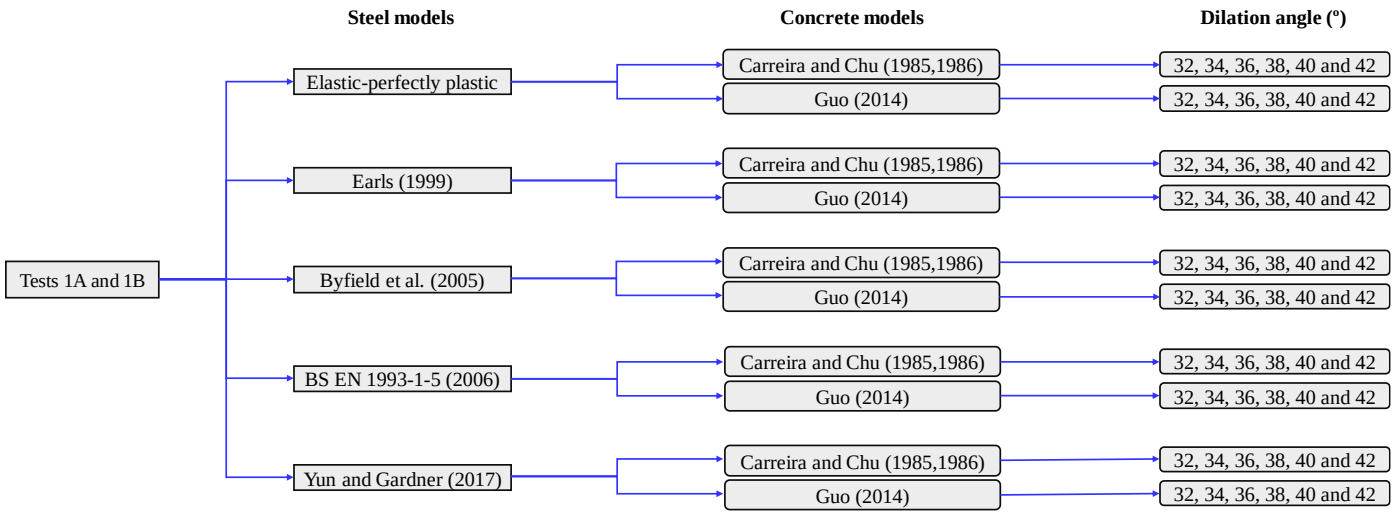

Fig. 11: Numerical models and methodology of analysis

4.1. Test CCB1

Regarding the computed response, with the variation of steel and concrete constitutive models as a function of the dilation angle, although there were no significant differences in the load response, the same cannot be said for post-peak behavior. In general, the steel elastic-perfectly plastic model did not show post-peak behavior. Therefore, this model (**Fig. 7a**) can be a suitable simplification for when hardening was not expected and the resistance is determined by buckling [43], such as web post buckling. On the other hand, scenarios that may present hardening were cited by Yun and Gardner [43], i.e., the simulation of section forming, the response of structures under extreme loads, the modelling and design of connections, and the design of structural elements incorporating inelastic behavior, and strain hardening. It can be seen in steel-concrete composite beam without opening subjected to positive moment. In this situation, there is no possibility of instability. In addition, the steel models [41,43] do not show such behavior either, since the test presented large deformations before reaching instability. The steel models [39,41] showed the loss of stiffness in post-peak behavior. Yun and Gardner [43] point out that the quadrilinear stress-strain relationship is more accurate and in agreement with the experimental stress-strain relationship across the tensile stress range. Although the BS EN 1993-1-5 [42] model is not quadrilinear, such models present hardening after the structure has reached the yield strength, such as steel model [39].

In accordance with von Mises stresses distribution, the maximum value of stress occurred at the headed studs placed in the region above the opening, near to the support (**Fig. 12a**). In addition, according to Cho and Redwood [17], headed studs allocated within the opening length are responsible for the concrete slab contribution to the shear strength. However, in most situations, it is impossible to achieve the desired degree of shear connection, as the connectors spacings are limited to the steel sheets rib spacings [4]. The ultimate strength of shear connector, which was presented by [57], was compared with the numerical results. The ratio between the maximum von Mises stress and the ultimate shear connector strength was approximately 0.848 and 0.853 for the model CCB1 and CCB2, respectively. Thus, it can be concluded that the shear connector would still have a utilization of 15% of the ultimate strength until reaching the rupture. However, this was not possible because both models reached the resistance capacity by web post buckling.

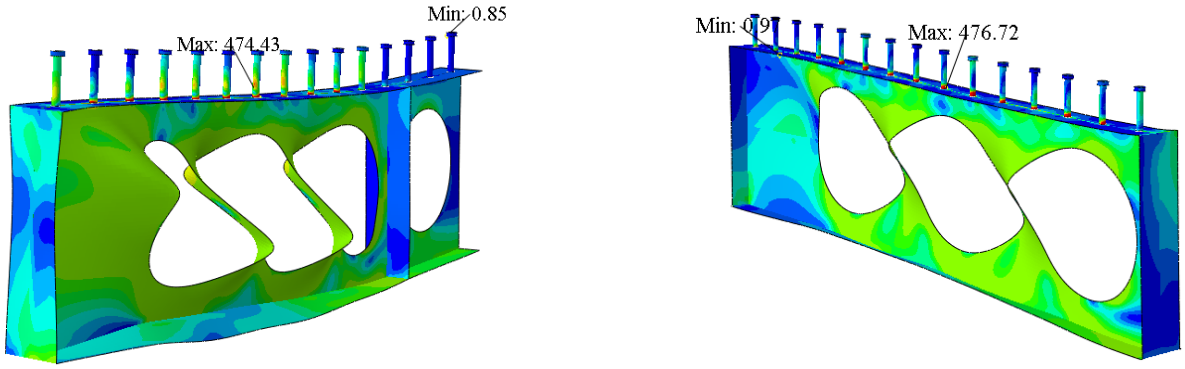

(a) Test CCB1 **(b)** Test CCB2

Fig. 12: Maximum stress of von Mises (in MPa)

Regarding the constitutive models of concrete [37–39] and dilation angle variation evaluated in the present study, the flexural behavior did not show sensitivity, unlike sensitivity analysis performed by others researchers [33–35]. The Mohr-Coulomb friction angle was replaced by the dilation angle for the concrete damage plasticity model [45] and therefore, greater the dilation angle, greater the shear strength. This was verified by previous studies that have performed sensitivity analyses on structures in which the ultimate capacity is governed by shear, such as column-slab connection [33], beam-column connection [34], and precast hollow core slabs [35]. The numerical results have been presented by load-displacements relationship and were compared to the test results [24] (**Figs. 13–17)**.

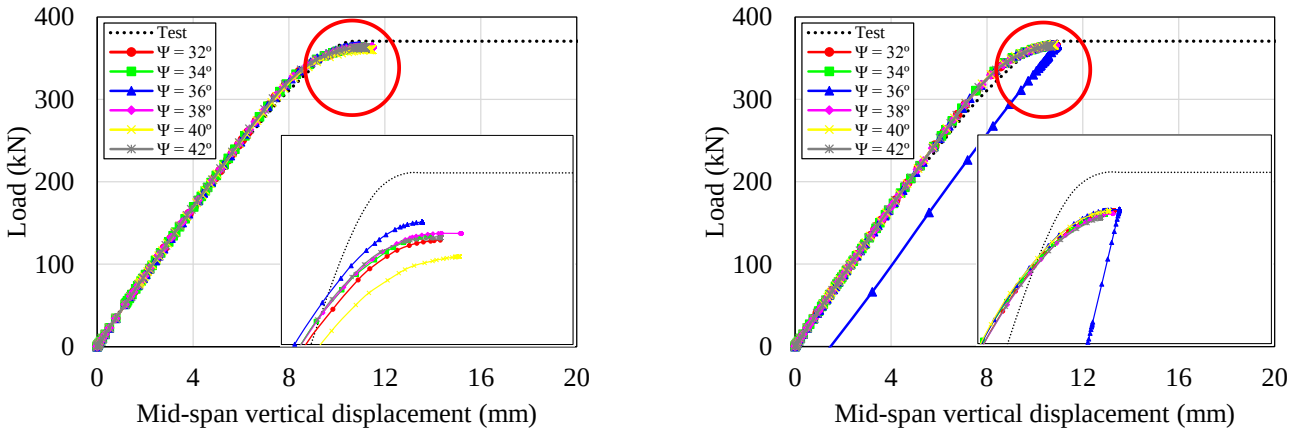

(a) Carreira and Chu [37,38] **(b)** Guo [39]

Fig. 13: CCB1 and elastic-perfectly plastic steel model combined with concrete models

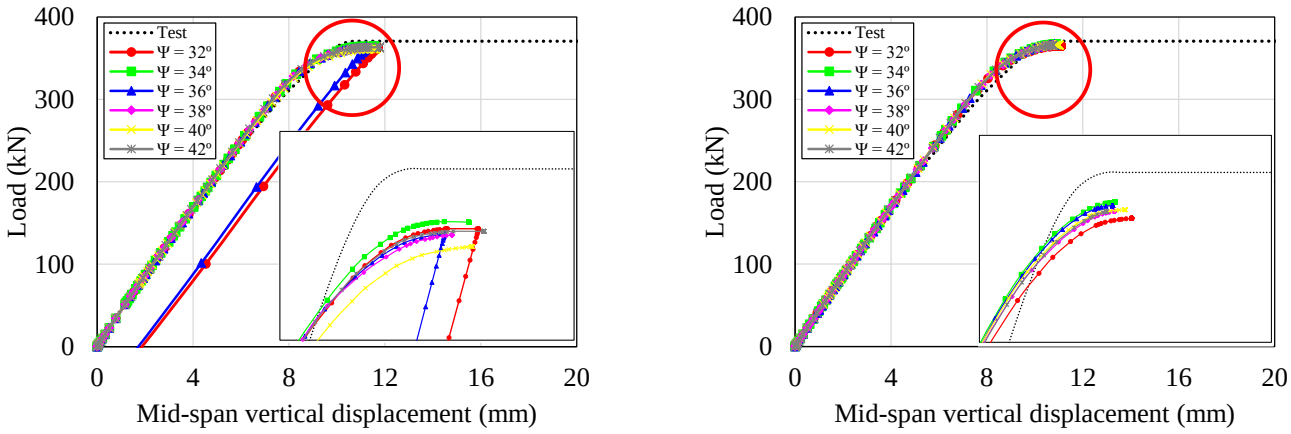

(a) Carreira and Chu **(b)** Guo [39]

Fig. 14: CCB1 and Earls [40] steel model combined with concrete models

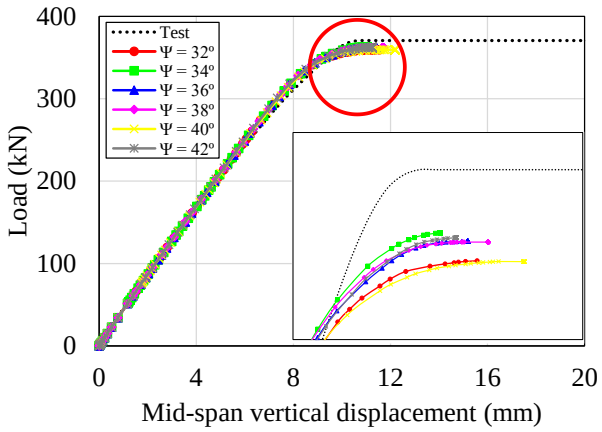

(a) Carreira and Chu

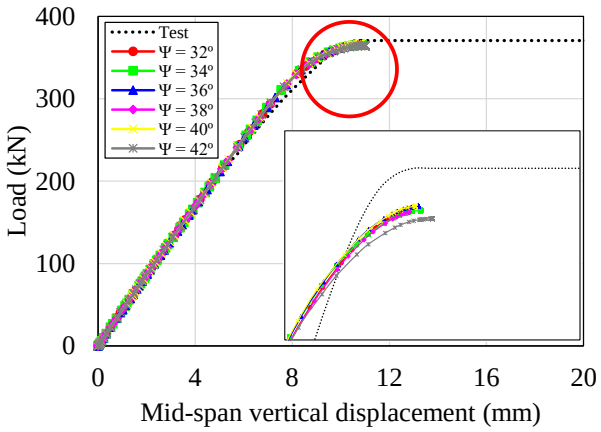

(b) Guo [39]

Fig. 15: CCB1 and Byfield et al. [41] steel model combined with concrete models

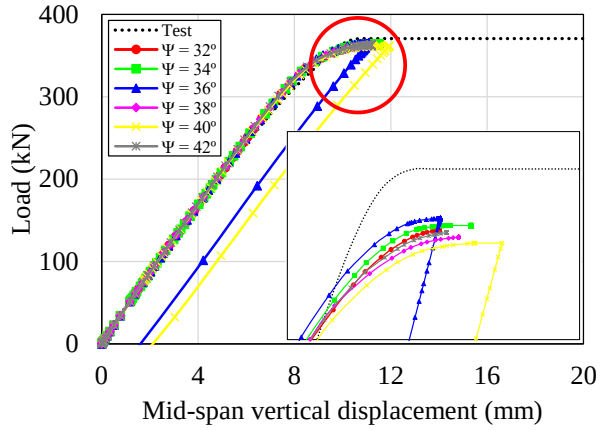

(a) Carreira and Chu

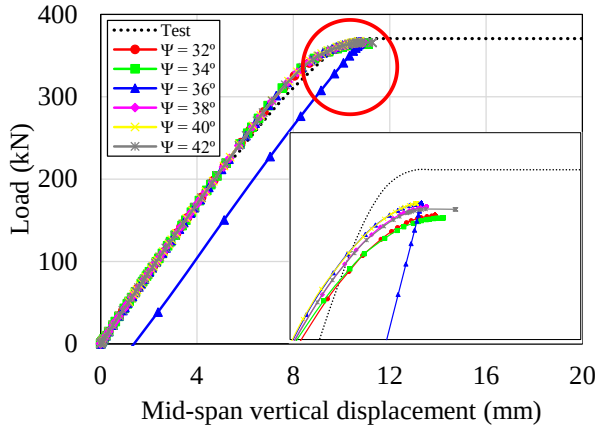

(b) Guo [39]

Fig. 16: CCB1 and BS EN 1993-1-5 [42] steel model combined with concrete models

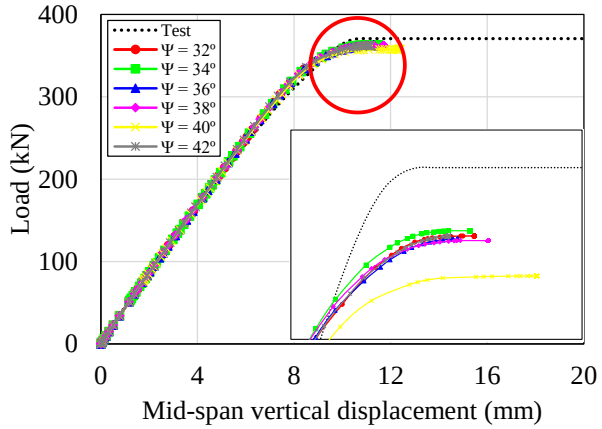

(a) Carreira and Chu

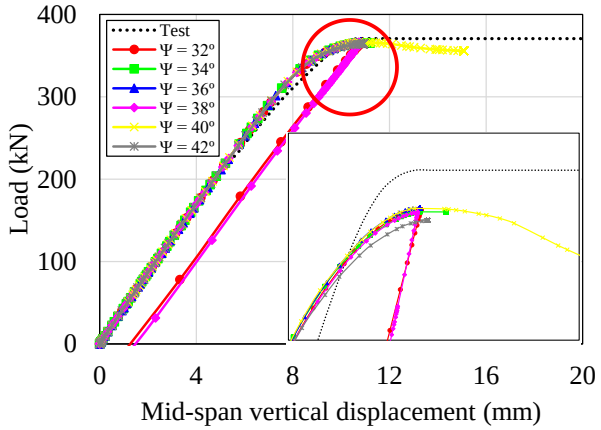

(b) Guo [39]

Fig. 17: CCB1 and Yun and Gardner [43] steel model combined with concrete models

It can be observed through illustrations that in some situations, it was possible to present post peak and unloading behavior (**Fig. 14a, 16a, 16b, and 17b**). This was due to the convergence of the nonlinearity equations in the arc-length method. On the other hand, there were situations wherein it was possible to present only the ultimate strength. In this scenario, the material calculations

either failed to converge or were not attempted at one or more points as notified by the software at the end of the analysis. Thus, these results showed the influence of the constitutive models of materials in numerical modeling.

Another observation that can be raised was that higher values of the dilation angle produce ductile behavior while lower values produce brittle behavior [34,76]. In this scenario, it was found that the greater the dilation angle, the greater the mid-span vertical displacement values in the ultimate behavior of the models analyzed. Malm [76] reported that the choice of a greater dilation angle, which can vary by 25-40º, will result in a lower grade and pressure confinement in the compressed concrete. **Fig. 18** shown the influence of the dilation angle, considering the damage to compression.

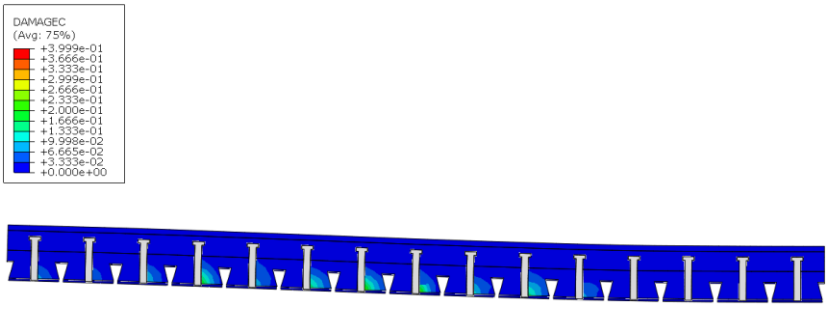

(a) Ψ=32º

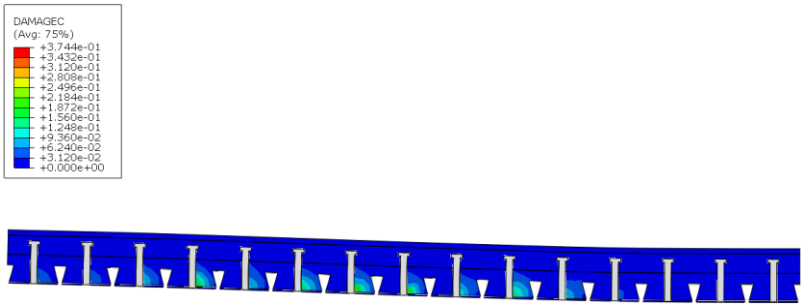

(b) Ψ=36º

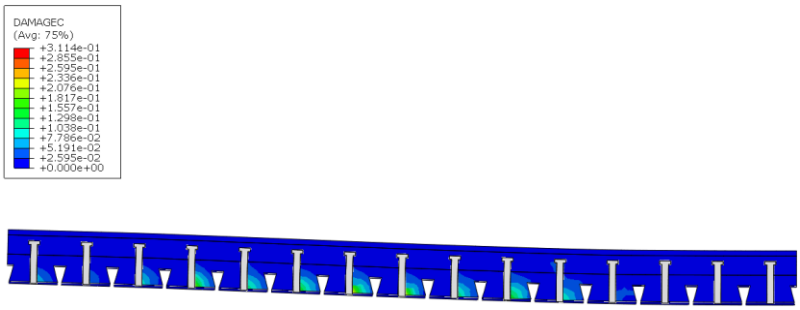

(c) Ψ=42º

Fig. 18: The influence of dilation angle on concrete crushing

Other issues that can be cited due to the problem of convergence in the post-peak behavior are local instabilities, local yield, surface wrinkling, localized material failure and snap-through [76]. The last one can be explained by a more convenient representation of the equilibrium trajectory (**Fig. 19)**. The following explanation was reported in Crisfield [77,78]. The load value associated with point B is called the limit load. In practice, this would be the maximum load the structure would support under regime stable in static equilibrium. The response beyond point B is called post-buckling behavior. Moreover, in the illustration, an

important phenomenon stands out, the snap-through. This involves a dynamic jump to a new state of displacement at a fixed load level (from point B to D). In the analysis of concrete elements, a softening is generally provided in the material model, according to the descending branch of the stress-strain relationship of the concrete presented previously. The softening material induces the location of deformation, in which a local region softens (or cracks) (**Fig. 26-27**) while adjacent materials unload elastically [78]. As verified by Crisfield [78], these locations may accompany snap-through as a result of softening and under load control that would lead to instantaneous instability. In addition, Wang [79] pointed out that analyzing unstable models through static analysis with Abaqus can result in convergence difficulties. This is because the static Riks solution may close at the limit load due to softening. The snap-through phenomenon presents some of the most difficult problems in nonlinear structural analysis. In numerical analysis, limit loads are often associated with a failure to achieve convergence with the iterative solution procedure [78]. Nonlinear static analysis techniques have considerable difficulties with these phenomena and this may explain the convergence difficulties that are often encountered. Load-controlled analysis equates structure failure with iterative solution technique failure as a convergence problem. As a result, structures may fail to establish cracks, in the case of concrete, or specific mechanisms that initiate collapse because there is no convergent equilibrium state [77,78], as verified in **Fig 13a**, **13b**, **14b, 15a** and **17a**. In this context, the complexities of nonlinear analysis can be avoided by applying a simple form of displacement control. The application of displacement control loading can simulate an experimental testing procedure such as the hydraulic actuator. For example, referring to **Fig. 19**, if displacement control was prescribed, the limit point B could be exceeded, and the equilibrium trajectory BC could be plotted. Therefore, a characteristic of the structural response at the limit point is that if the process is performed by load control rather than displacement, a small increase in applied force intensity causes snap-through and may lead to convergence problems. However, as presented by Crisfield [77], the disadvantages in displacement control are related to the selection of the appropriate displacement variable, which may result in computational cost or divergence from the iterative solution procedure [80]. Therefore, one way to avoid the convergence problem and to seek the equilibrium trajectory with post-peak behavior is by applying displacement-controlled loading. It is noteworthy that there are no works of numerical analyses in composite cellular beams that use this tool.

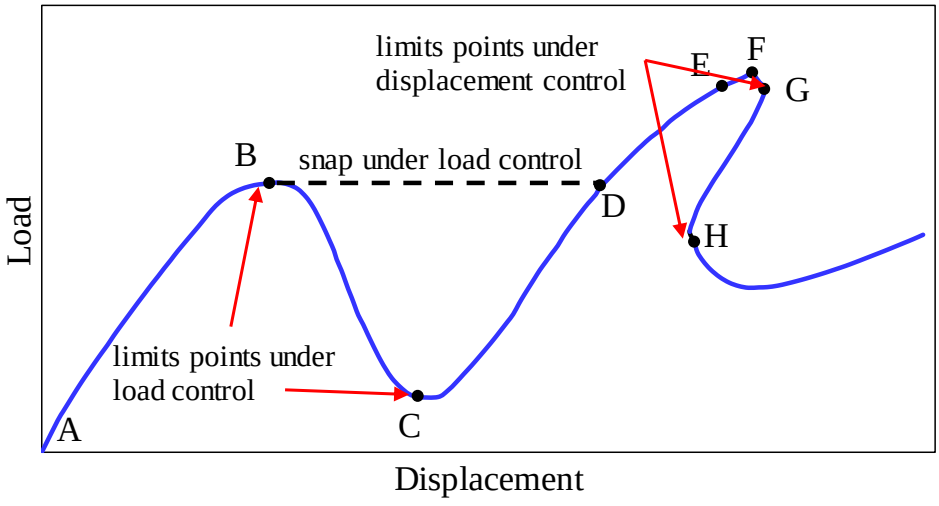

Fig. 19: Snap buckling, adapted from [77] (with permission from Elsevier)

4.2. Test CCB2

The maximum von Mises stress was observed at the shear connector above the opening in the support region **(Fig.12b)**, such as the Test CCB1 specimen. However, the load-displacement relationships were not similar to the Test CCB1 specimen because the Test CCB2 specimen's lower tee was more rigid than the upper one. In **Figs. 20–25**, the load-displacements relationship in function of the several steel and concrete constitutive models have been compared to the test results [24].

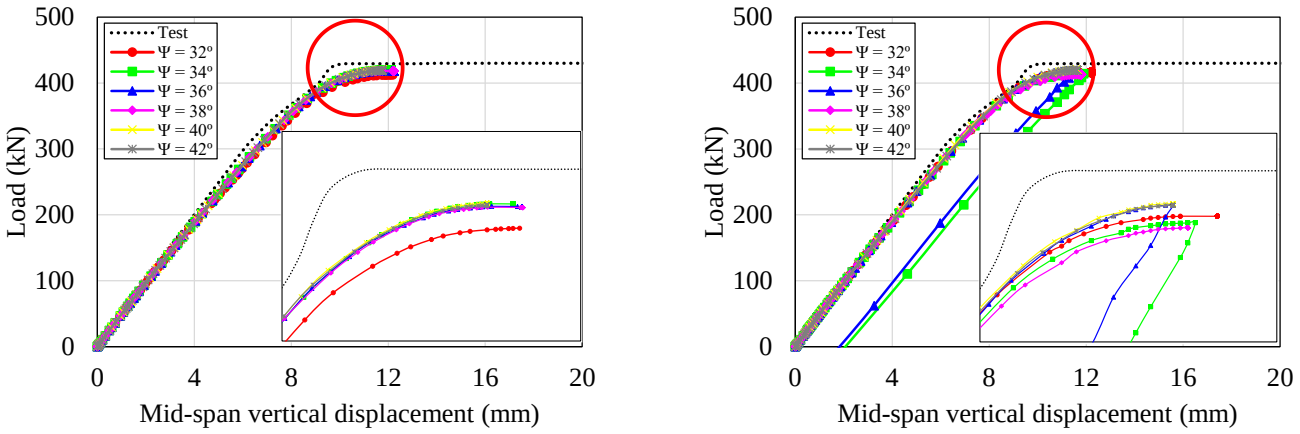

(a) Carreira and Chu [37,38] **(b)** Guo [39]

Fig. 20: CCB2 and elastic-perfectly plastic steel model combined with concrete models

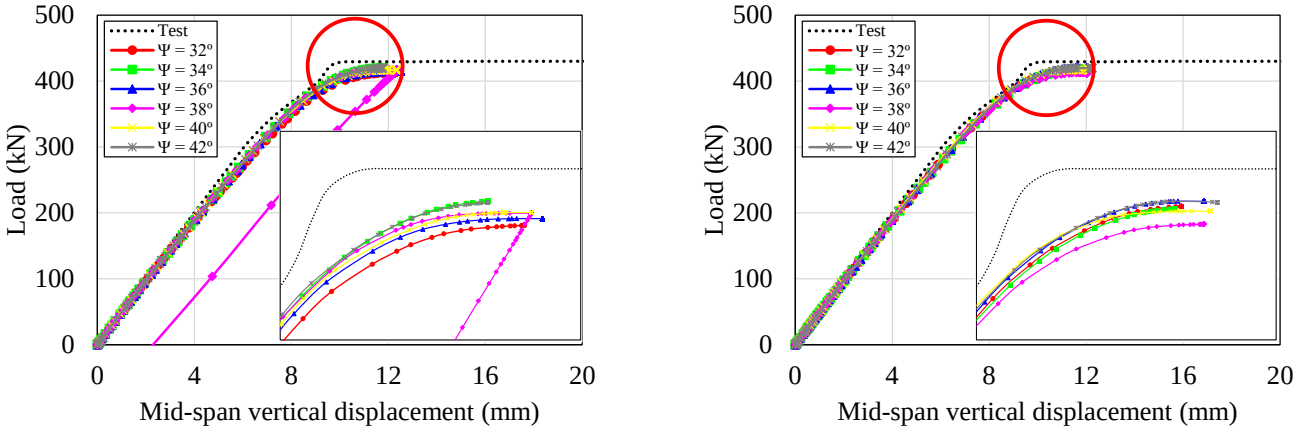

(a) Carreira and Chu [37,38] **(b)** Guo [39]

Fig. 21: CCB2 and Earls [40] steel model combined with concrete models

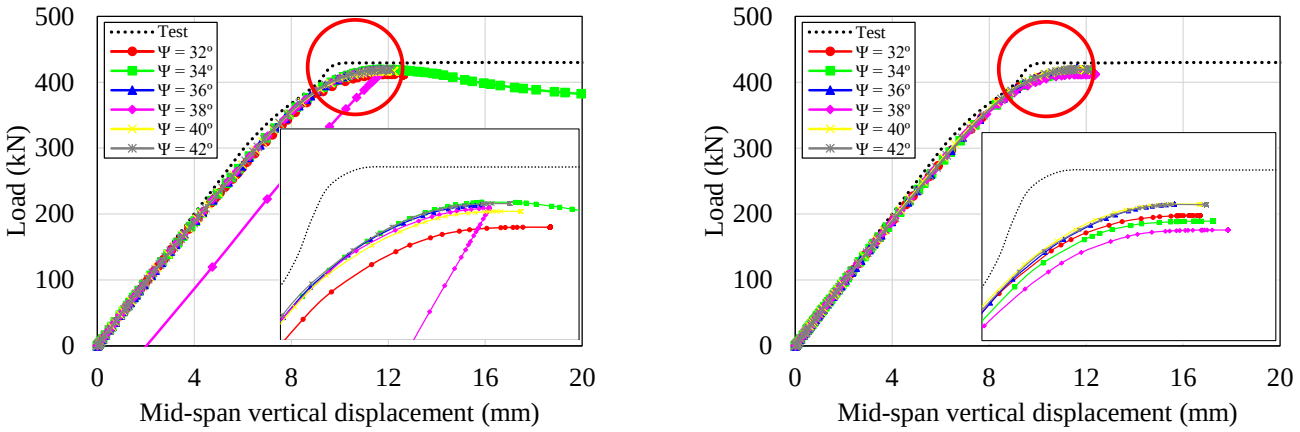

(a) Carreira and Chu [37,38] **(b)** Guo [39]

Fig. 23: CCB2 and Byfield et al. [41] steel model combined with concrete models

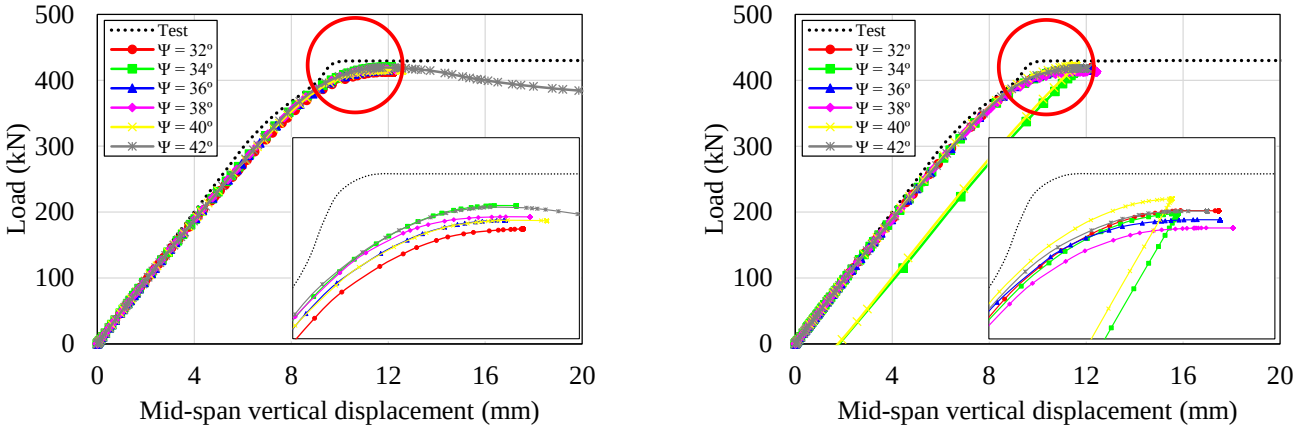

(a) Carreira and Chu [37,38] **(b)** Guo [39]

Fig. 24: CCB2 and BS EN 1993-1-5 [42] steel model combined with concrete models

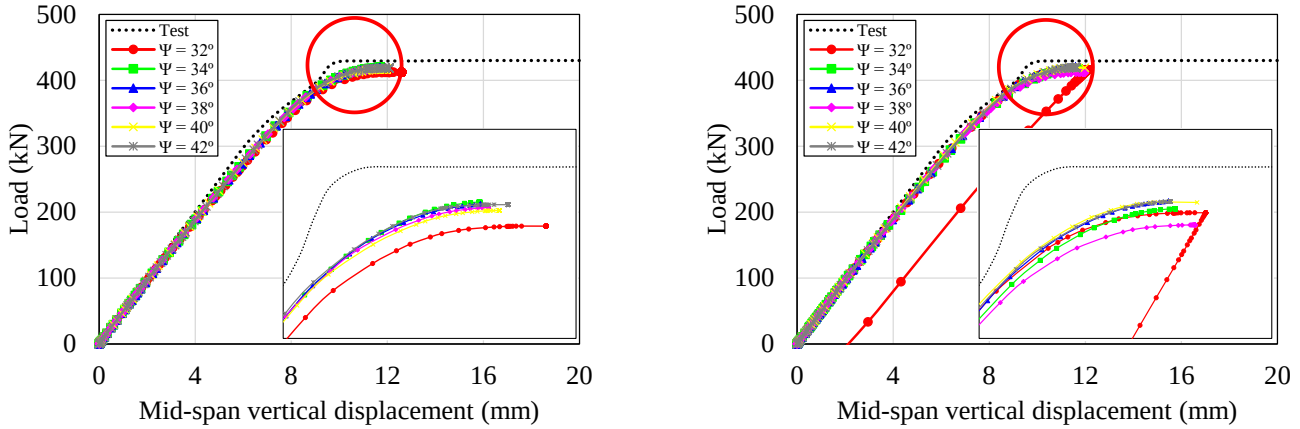

(a) Carreira and Chu [37,38] **(b)** Guo [39]

Fig. 25: CCB2 and Yun and Gardner [43] steel model combined with several concrete models

When the elastic-perfectly plastic model was used, it was able to represent the post-peak behavior. Unlike Test CCB1, in Test CCB2, when it reached the WPB, the steel section stresses were lower than the yield strength. Asymmetric composite cellular beams have a higher resistance efficiency as compared to those with double symmetry [4]. In this context, there were no excessive

plastic deformations other than those caused by concrete due to the shear connector. However, regarding post-peak behavior, situations that did not obtain this behavior (**Fig. 21b** and **22b**) owed it to the failure of material calculations and snap-through problem. The results showed that the steel constitutive model influences the computed response.

4.3. SUMMARY OF RESULTS

A summary of the results is presented in **Table 2.** Considering the results discussed in the previous section, the model that represents the best post-peak behavior of specimens Test CCB1 (**Fig. 26a)** and CCB2 (**Fig. 26b)** is the combination of Guo's [39] and Yun and Gardner's [43] models for concrete and steel materials, respectively. The criterion adopted for choosing the constitutive models was to evaluate the differences between the numerical model load response with the experimental result, verify post-peak behavior, and finally, to find out whether the chosen constitutive models meet both CCB1 and CCB2 models. In addition, as noted, there were no significant differences in numerical model responses compared to experimental models. The mean value of the P_{FE}/P_{EXP} ratio, the standard deviation, and the variance were below 2.5%, 0.73%, and 0.0043%, respectively. The concrete was represented by the concrete damage plasticity model and although no significance difference was found during the investigation on the influence of damage parameters, the best results were obtained when the dilation angle Ψ was taken equal to 40º.

Table 2: Summary of results

Test	Ψ (º)	Elastic-perfectly plastic		Earls [40]		Byfield et al. [41]		BS EN 1993-1-5 [42]		Yun and Gardner [43]	
		$\frac{P_{FE,CC}}{P_{EXP}}$	$\frac{P_{FE,G}}{P_{EXP}}$	$\frac{P_{FE,CC}}{P_{EXP}}$	$\frac{P_{FE,G}}{P_{EXP}}$	$\frac{P_{FE,CC}}{P_{EXP}}$	$\frac{P_{FE,G}}{P_{EXP}}$	$\frac{P_{FE,CC}}{P_{EXP}}$	$\frac{P_{FE,G}}{P_{EXP}}$	$\frac{P_{FE,CC}}{P_{EXP}}$	$\frac{P_{FE,G}}{P_{EXP}}$
CCB1	32	0.978	0.987	0.982	0.986	0.972	0.988	0.982	0.986	0.979	0.989
	34	0.980	0.988	0.984	0.992	0.981	0.988	0.983	0.986	0.981	0.988
	36	0.965	0.979	0.980	0.991	0.978	0.989	0.985	0.990	0.978	0.989
	38	0.980	0.986	0.980	0.989	0.978	0.987	0.979	0.989	0.978	0.988
	40	0.970	0.986	0.976	0.989	0.971	0.989	0.977	0.990	0.966	0.989
	42	0.973	0.985	0.981	0.989	0.979	0.985	0.981	0.989	0.979	0.985
	X	0.974	0.985	0.981	0.989	0.976	0.988	0.981	0.988	0.977	0.988
	SD	0.614%	0.336%	0.266%	0.183%	0.399%	0.150%	0.283%	0.200%	0.532%	0.148%
	COV	0.0038%	0.0011%	0.0007%	0.0003%	0.0016%	0.0002%	0.0008%	0.0004%	0.0028%	0.0002%
CCB2	32	0.957	0.961	0.960	0.973	0.958	0.968	0.960	0.973	0.959	0.968
	34	0.975	0.969	0.976	0.972	0.975	0.964	0.976	0.971	0.975	0.970
	36	0.972	0.971	0.965	0.977	0.973	0.975	0.966	0.966	0.973	0.975
	38	0.970	0.962	0.968	0.961	0.971	0.958	0.968	0.961	0.971	0.960
	40	0.974	0.968	0.969	0.970	0.969	0.975	0.966	0.981	0.969	0.975
	42	0.973	0.963	0.975	0.976	0.974	0.975	0.975	0.972	0.973	0.975
	X	0.970	0.966	0.969	0.971	0.970	0.969	0.969	0.971	0.970	0.970
	SD	0.654%	0.422%	0.616%	0.570%	0.612%	0.730%	0.613%	0.680%	0.587%	0.617%
	COV	0.0043%	0.0018%	0.0038%	0.0032%	0.0037%	0.0053%	0.0038%	0.0046%	0.0035%	0.0038%

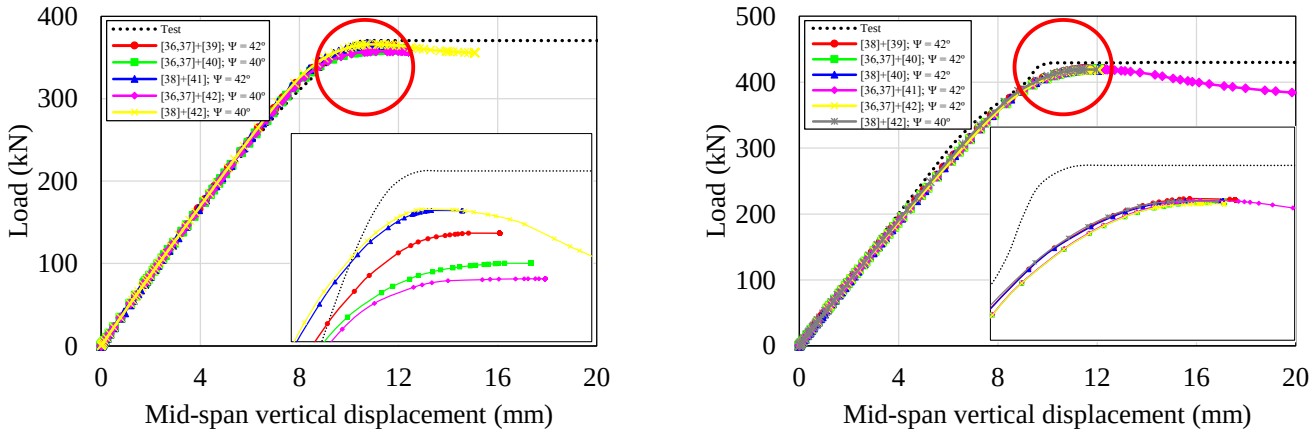

(a) Test CCB1 **(b)** Test CCB2

Fig. 26: Results for dilation angle

4.4. VISCOSITY SENSITIVITY

To investigate the viscosity sensitivity or relaxation time, the steel model of Yun and Gardner [43], dilation angle Ψ=40º, and the concrete model of Guo [39] were considered in this analysis. **Figs. 27–28** present Test CCB1 and Test CCB2 models' results. According to the illustrations, the load-displacement relationship was plotted as a function of arc length, which is a technique that seeks the convergence of results in the solution of nonlinear problems, as mentioned in section 3. In this case, it was observed that the variation of the viscosity parameter influences the arc length method, i.e., the smaller the viscosity parameter, the smaller the arc length required for convergence at the equilibrium surface point. Furthermore, as shown in the figures, when the viscosity parameter was increased, the damage caused by the external load was distributed over a larger area; that is, the damage was not located at the integration point. Krahl [81] stated that the viscosity parameter is a mathematical tool for decreasing mesh sensitivity for constitutive models that suffer from softening behavior, such as concrete. Furthermore, the author pointed out that the basic idea of the viscosity parameter is to distribute or homogenize the damage located at an integration point to a region of influence. Unlike the Test CCB2 model, for values less than μ=0.0001 in Test CCB1 model, convergence problems occurred due to material calculations failure. Thus, the lower the viscosity parameter, the greater the area of influence of the damage. The present study verified that the value μ=0.001 was closer to the experimental values. Finally, as observed in the load-displacement relationship as a function of the arc length method, it can be concluded that the dependence of the viscosity parameter provides additional ductility in the model, and it was an efficient method to overcome the simulation algorithm convergence problems of cracking [82]. **Fig. 29** presents the results of the viscosity variation with the load-displacements relationship. It can be observed through the illustrations, as confirmed in [34], that the viscosity parameter variation does not affect the load-displacement behavior. However, the computational cost is affected, for example, as there was a difference of approximately one hour between the processing time of μ=0.00001 and μ=0.00005. In addition, in situations where it was not possible to present post-peak behavior, it was due to the convergence problems regarding material and the viscosity parameter.

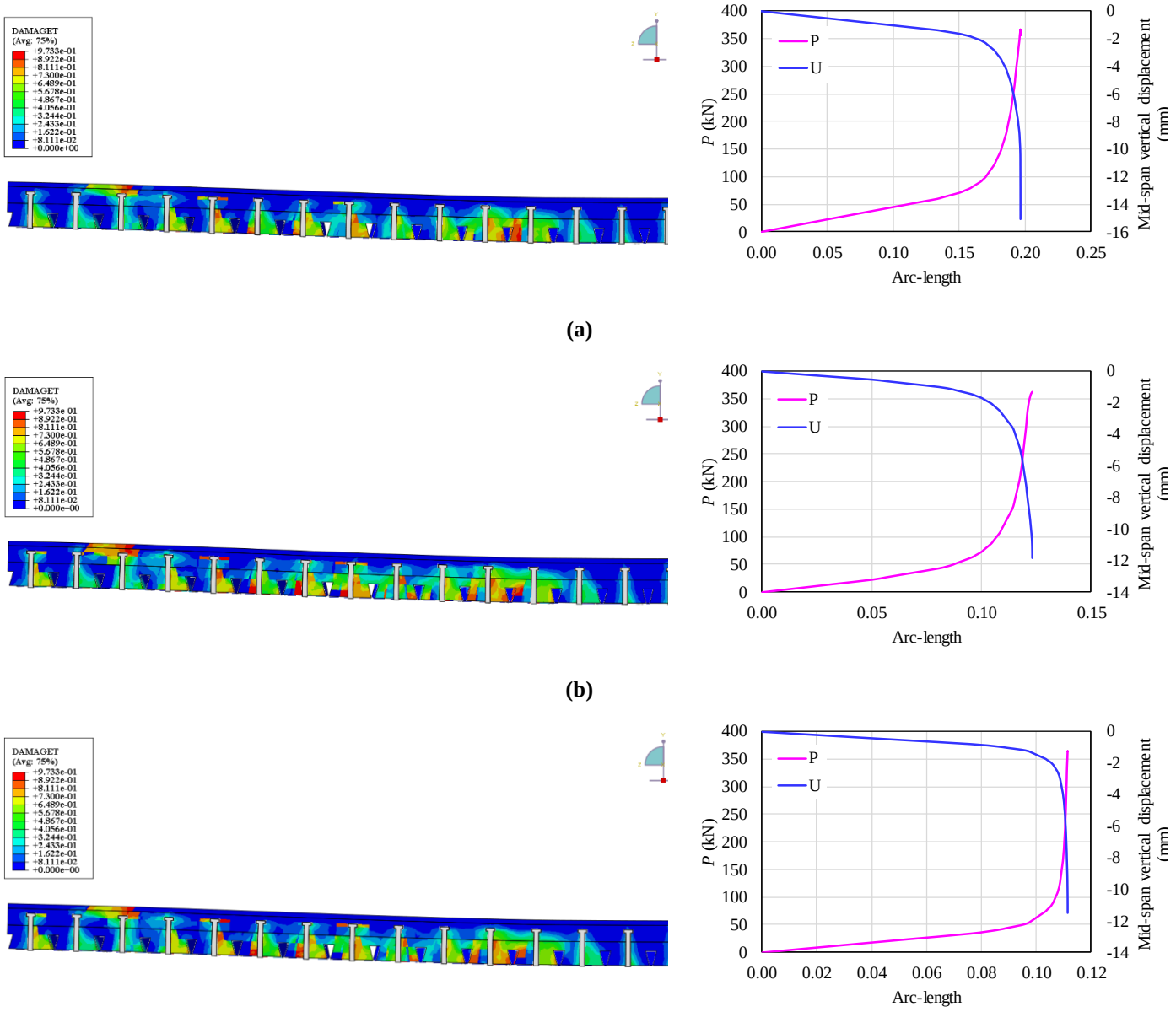

Fig. 27: Test CCB1 **(a)** μ=0.001; **(b)** μ=0.0005; **(c)** μ=0.0001

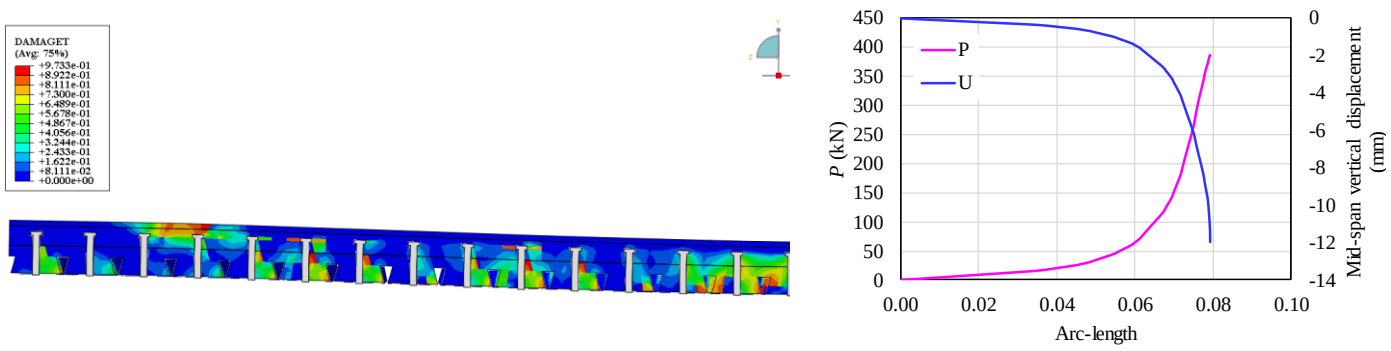

(a)

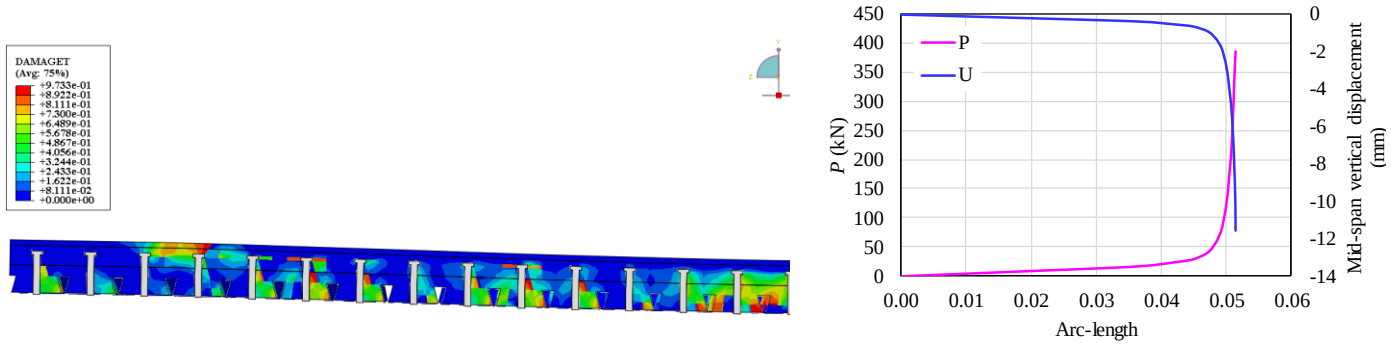

(b)

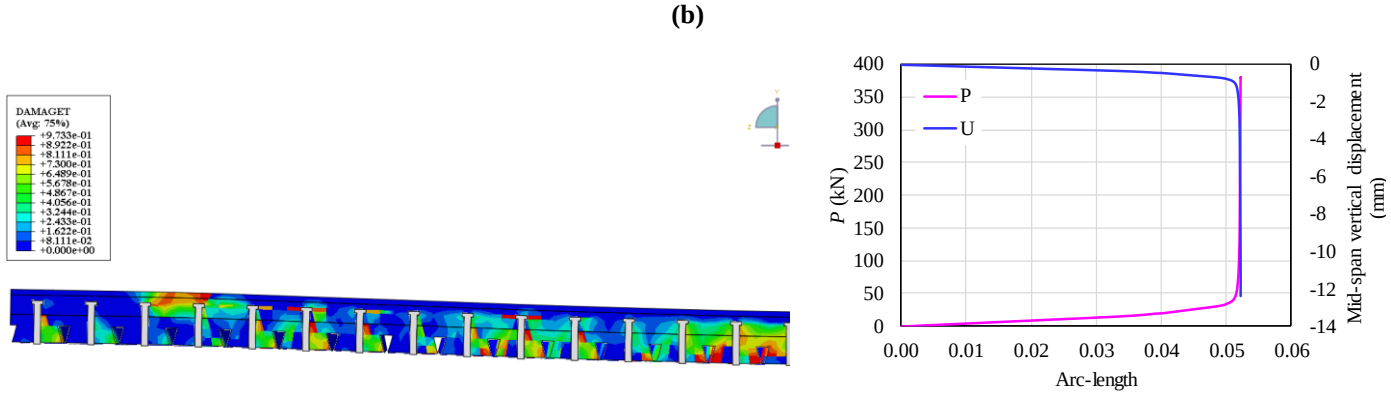

(c)

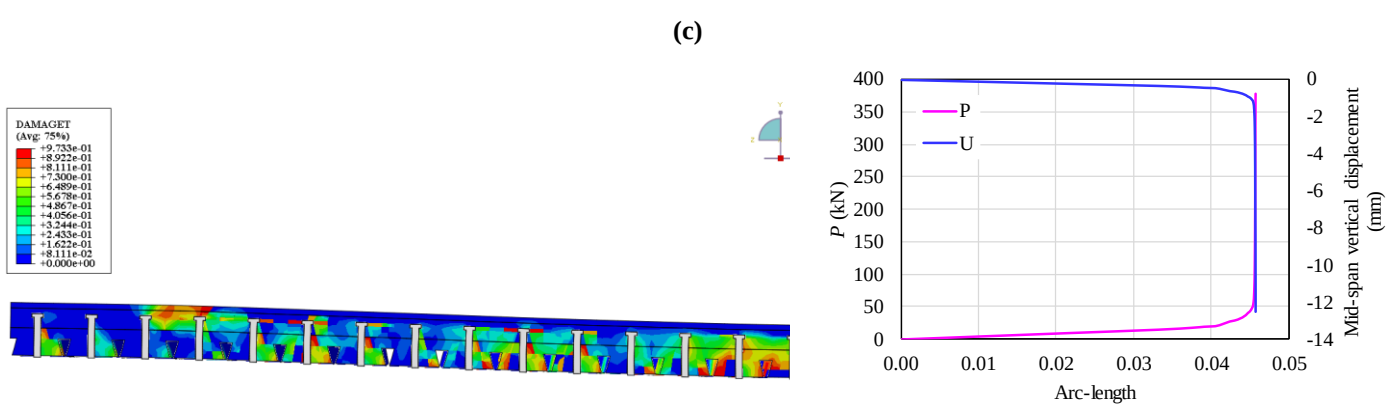

(d)

Fig. 28: Test CCB2 **(a)** μ=0.001; **(b)** μ=0.0001; **(c)** μ=0.00001; **(d)** μ=0.000005

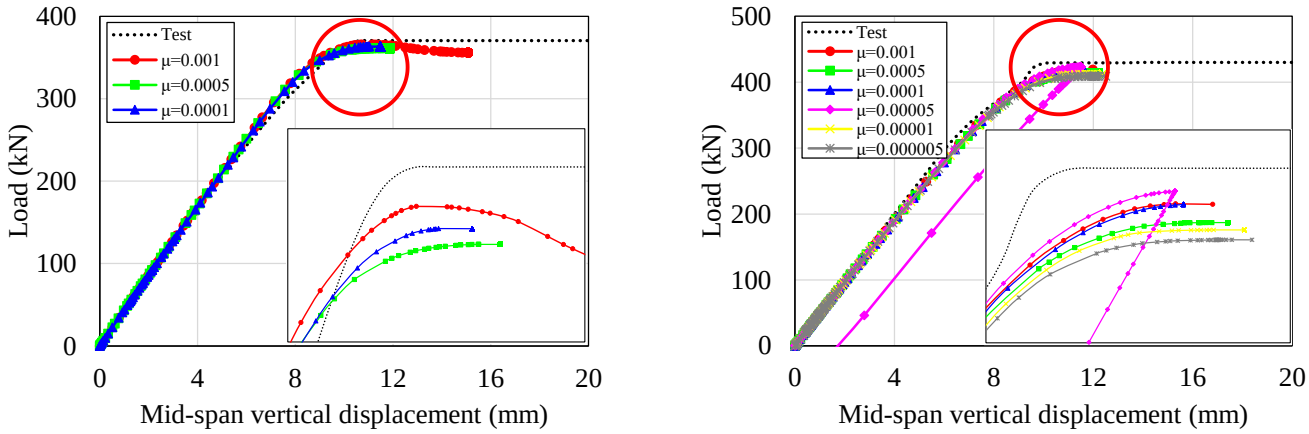

(a) CCB1 **(b)** CCB2

Fig. 29: Viscosity sensitivity

4.5. FINAL MODELS

According to the analyses performed, the steel and concrete models exposed by Yun and Gardner [43] and Guo [39], respectively, were considered as final models. This is due to the fact that the models could predict the composite cellular beam response, including the post-peak behavior, with minor error compared to the experimental tests. The final modes are presented in **Fig. 30** for both Tests CCB1 and CCB2.

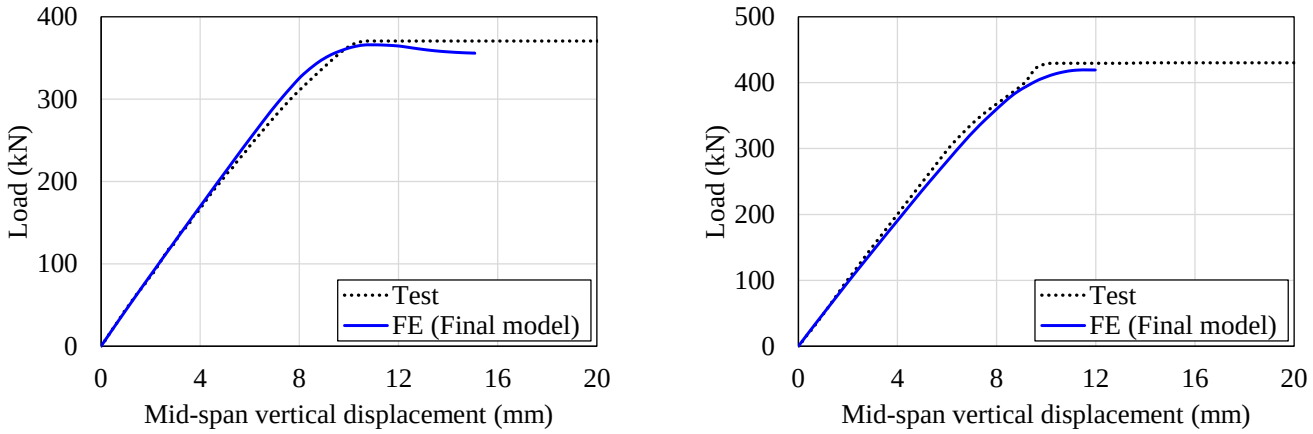

(a) **(b)**

Fig. 30: Final models: **(a)** Test CCB1 **(b)** Test CCB2

Table 3 presents the final model parameters of concrete damage plasticity compared to some models found in the literature. In **Fig. 31**, the results of the final numerical models are compared to the tests [24].

Table 3: Final models

Ref.	**Model**	**Ψ (°)**	**μ (s^{-1})**
[33]	Column-slab connection	40	0.00001
[34]	Beam-column connection	40	0.00001
[35]	Precast hollow core slabs	28	-
Present study	Composite cellular beams	40	0.001

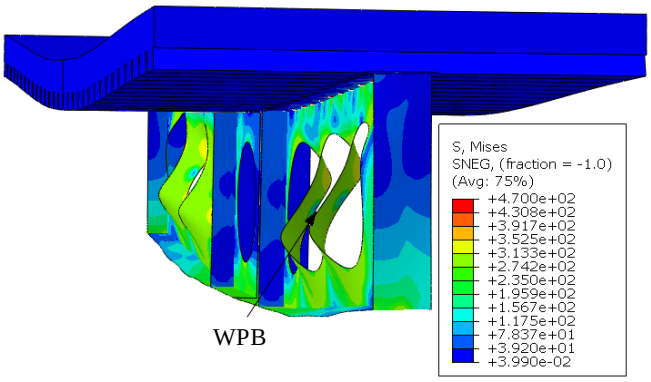

(a) FE CCB1

(b) Test CCB1 [24]

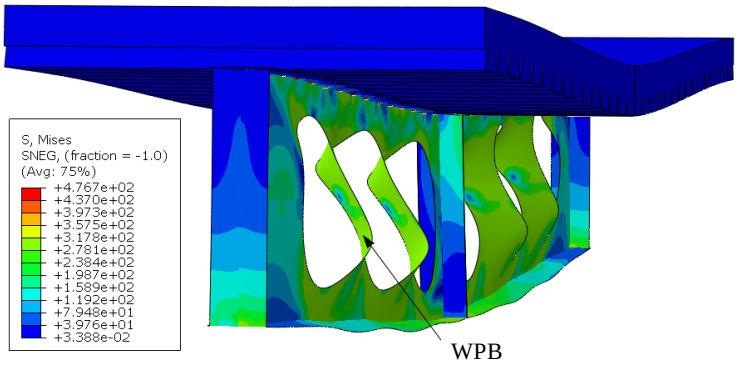

(c) FE CCB5

(d) Test CCB2 [24]

Fig. 31: Final models

4.6. REPRESENTATION OF THE NUMERICAL MODEL

In this section, the representation of the numerical models is presented, considering the CCB3 test, as shown in **Table 2**. According to Muller et al. [25] and Hechler et al. [26], the objective of the CCB3 test was to investigate the composite action at the end, that means, the slab was cut back by 285 mm at end of cellular beam. The failure mechanism was characterized by web post buckling between 11^{th} and 12^{th} opening at 805.6 kN of load. This happened due to the absence of the slab, a factor that reduced the resistance. Although this test had different objectives than those performed by Nadjai [24], the CCB3 model showed the representativity with final numerical model (**Table 4**), which makes the model even more robust. The load value of the numerical model was 808.6 kN, a value that differs in approximately 0.31% from the experimental model. The load-displacement relationship (**Fig. 32a**) and the deformed shape (**Fig. 32b**) are shown below.

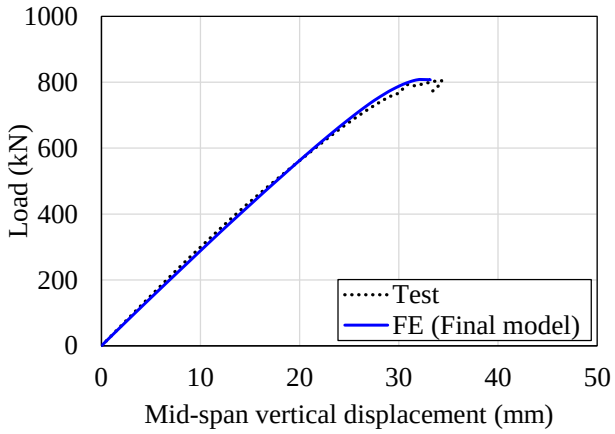

(a) Load-displacement relationship

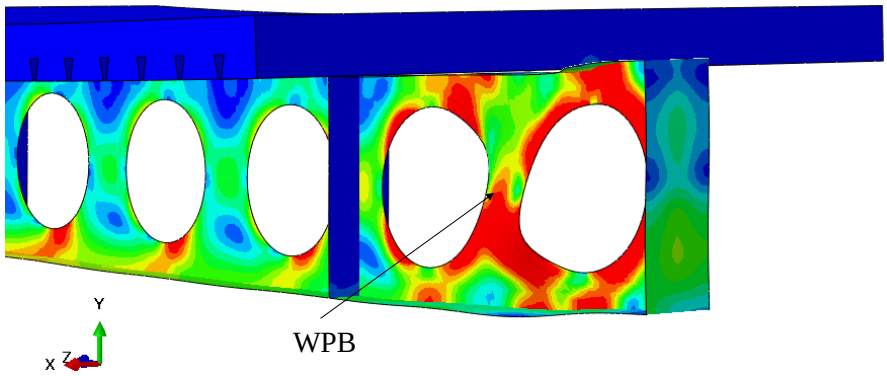

(b) WPB

Fig. 32: CCB3 model

CONCLUSIONS

This study presented a sensitivity analyses in composite cellular beams, considering the influence of constitutive models of steel-concrete materials, and the parameters of Concrete Damage Plasticity. The constitutive models of steel and concrete, the dilation angle, and viscosity were varied. Geometrical non-linear analyses were performed, considering solid elements for the composite slab and shear connector, and shell elements for the cellular beam. The numerical results were compared with tests results. The results were discussed, due to convergence problems that may occur in the analysis processing. A solution that has been presented and can be used for instability problems, such as web post buckling or crack opening, is the control of loading by displacement. Considering the parameters that were analyzed, it was concluded that the quadrilinear steel model presented the best post-peak behavior when compared to the experimental results. The shear connectors above the opening in the region near the support reached the maximum von Mises stresses. The flexural behavior was not sensitive to dilation angles, unlike structures in which the ultimate behavior is governed by shear forces. The best post-peak behavior was verified by load-displacements relationship for the dilation angle as equal to 40º. With varying viscosity or relaxation time, the behavior of the load-displacement relationship remained unaffected, and it was found that the lower the viscosity, the greater the finite element damage area and the higher the computational cost.

ACKNOWLEDGMENTS

This work was supported by the São Paulo Research Foundation (FAPESP) [grant number #2018/22803-1].

REFERENCES

[1] D. Darwin, R.C. Donahey, LRFD for composite beams with unreinforced web openings, J. Struct. Eng. 114 (1988) 535–552. https://doi.org/10.1061/(ASCE)0733-9445(1988)114:3(535).

[2] R.C. Donahey, D. Darwin, Web openings in composite beams with ribbed slabs, J. Struct. Eng. 114 (1988) 518–534. https://doi.org/10.1061/(ASCE)0733-9445(1988)114:3(518).

[3] R. Redwood, S.H. Cho, Design of steel and composite beams with web openings, J. Constr. Steel Res. 25 (1993) 23–41. https://doi.org/10.1016/0143-974X(93)90050-3.

[4] T. Sheehan, X. Dai, D. Lam, E. Aggelopoulos, M. Lawson, R. Obiala, Experimental study on long spanning composite cellular beam under flexure and shear, J. Constr. Steel Res. 116 (2016) 40–54. https://doi.org/10.1016/j.jcsr.2015.08.047.

[5] D. Kerdal, D.A. Nethercot, Failure modes for castellated beams, J. Constr. Steel Res. 4 (1984) 295–315. https://doi.org/10.1016/0143-974X(84)90004-X.

[6] K.D. Tsavdaridis, C. D'Mello, Web buckling study of the behaviour and strength of perforated steel beams with different novel web opening shapes, J. Constr. Steel Res. 67 (2011) 1605–1620. https://doi.org/10.1016/j.jcsr.2011.04.004.

[7] F. Erdal, M.P. Saka, Ultimate load carrying capacity of optimally designed steel cellular beams, J. Constr. Steel Res. 80 (2013) 355–368. https://doi.org/10.1016/j.jcsr.2012.10.007.

[8] P. Panedpojaman, T. Thepchatri, S. Limkatanyu, Novel design equations for shear strength of local web-post buckling in cellular beams, Thin-Walled Struct. 76 (2014) 92–104. https://doi.org/10.1016/j.tws.2013.11.007.

[9] K.D. Tsavdaridis, C. D'Mello, Vierendeel Bending Study of Perforated Steel Beams with Various Novel Web Opening Shapes through Nonlinear Finite-Element Analyses, J. Struct. Eng. 138 (2012) 1214–1230. https://doi.org/10.1061/(asce)st.1943-541x.0000562.

[10] W.C. Clawson, D. Darwin, Strength of composite beams at web openings, ASCE J. Struct. Div. 108 (1982) 623–641.

[11] W.C. Clawson, D. Darwin, Tests of composite beams with web openings, ASCE J. Struct. Div. 108 (1982) 145–162.

[12] C.M. DONOGHUE, Strength of composite beams with web openings, ASCE J. Struct. Div. 108 (1982) 2652–2667.

[13] D.M. Todd, P.B. Cooper, Strength of composite beams with web openings, ASCE J. Struct. Div. 106 (1980) 431–444.

[14] L.F. Grilo, R.H. Fakury, A.L.R. de Castro e Silva, G. de S. Veríssimo, Design procedure for the web-post buckling of steel cellular beams, J. Constr. Steel Res. 148 (2018) 525–541. https://doi.org/10.1016/j.jcsr.2018.06.020.

[15] R.G. Redwood, G. Poumbouras, Tests of composite beams with web holes, Can. J. Civ. Eng. 10 (1983) 713–721. https://doi.org/10.1139/l83-100.

[16] R.M. Lawson, K.F. Chung, A.M. Price, Tests on composite beams with large web openings to justify existing design methods, Struct. Enginee. 70 (1992) 1–7.

[17] S.H. Cho, R.G. Redwood, Slab behavior in composite beams at openings. II: tests and verification, J. Struct. Eng. 118 (1992) 2304–2322. https://doi.org/10.1061/(ASCE)0733-9445(1992)118:9(2304).

[18] J.W. Park, C.H. Kim, S.C. Yang, Ultimate Strength of Ribbed Slab Composite Beams with Web Openings, J. Struct. Eng. 129 (2003) 810–817. https://doi.org/10.1061/(asce)0733-9445(2003)129:6(810).

[19] R.G. Redwood, G. Poumbouras, Analysis of composite beams with web openings, J. Struct. Eng. 110 (1984) 1949–1958. https://doi.org/10.1061/(ASCE)0733-9445(1984)110:9(1949).

[20] S.H. Cho, R.G. Redwood, Slab behavior in composite beams at openings. I: analysis, J. Struct. Eng. 118 (1992) 2287–2303. https://doi.org/10.1061/(ASCE)0733-9445(1992)118:9(2287).

[21] E.H. Fahmy, Analysis of composite beams with rectangular web openings, J. Constr. Steel Res. 37 (1996) 47–62. https://doi.org/10.1016/0143-974X(95)00022-N.

[22] M.A. Benitez, D. Darwin, R.C. Donahey, Deflections of composite beams with web openings, J. Struct. Eng. 124 (1998)

1139–1147. https://doi.org/10.1061/(ASCE)0733-9445(1998)124:10(1139).

[23] K.F. Chung, R.M. Lawson, Simplified design of composite beams with large web openings to Eurocode 4, J. Constr. Steel Res. 57 (2001) 135–164. https://doi.org/10.1016/S0143-974X(00)00011-0.

[24] A. Nadjai, Performance of cellular composite floor beams at ambient temperature, 2005.

[25] C. MÜLLER, O. HECHLER, A. BUREAU, D. BITAR, D. JOYEUX, L.G. CAJOT, T. DEMARCO, R.M. LAWSON, S. HICKS, P. DEVINE, O. LAGERQVIST, E. HEDMAN-PÉTURSSON, E. UNOSSON, M. FELDMANN, Large web openings for service integration in composite floors. Technical Steel Research. European Comission, Contract No 7210-PR/315. Final report, (2006).

[26] O. Hechler, C. Müller, G. Sedlacek, Investigations on beams with multiple regular web openings, 2006.

[27] R.M. Lawson, S.J. Hicks, Design of beams with large web openings, The Steel Construction Institute, 2011.

[28] Sameer S. Fares, J. Coulson, David W. Dinehart, Castellated and Cellular Beam Design 31, Am. Inst. Steel Constr. (2016).

[29] B. Djebli, D.E. Kerdal, A. Abidelah, Additional and total deflection of composite symmetric cellular beams, J. Constr. Steel Res. 158 (2019) 99–106. https://doi.org/10.1016/j.jcsr.2019.03.015.

[30] K.F. Chung, C.H. Ko, A.J. Wang, Design of steel and composite beams with web openings - Verification using finite element method, Steel Compos. Struct. 5 (2005) 203–233. https://doi.org/10.12989/scs.2005.5.2_3.203.

[31] K.F. Chung, Recent Advances in Design of Steel and Composite Beams with Web Openings, Adv. Struct. Eng. 15 (2012) 1521–1536. https://doi.org/10.1260/1369-4332.15.9.1521.

[32] F.P.V. Ferreira, C.H. Martins, S. De Nardin, Advances in composite beams with web openings and composite cellular beams, J. Constr. Steel Res. 172 (2020) 106182. https://doi.org/10.1016/j.jcsr.2020.106182.

[33] A.S. Genikomsou, M.A. Polak, Finite element analysis of punching shear of concrete slabs using damaged plasticity model in ABAQUS, Eng. Struct. 98 (2015) 38–48. https://doi.org/10.1016/j.engstruct.2015.04.016.

[34] H. Behnam, J.S. Kuang, B. Samali, Parametric finite element analysis of RC wide beam-column connections, Comput. Struct. 205 (2018) 28–44. https://doi.org/10.1016/j.compstruc.2018.04.004.

[35] T.N.H. Nguyen, K.H. Tan, T. Kanda, Investigations on web-shear behavior of deep precast, prestressed concrete hollow core slabs, Eng. Struct. 183 (2019) 579–593. https://doi.org/10.1016/j.engstruct.2018.12.052.

[36] Dassault Systèmes Simulia, Abaqus 6.18, (2016).

[37] D.J. CARREIRA, K.H. CHU, Stress-Strain Relationship for Plain Concrete in Compression, ACI J. Proc. 82 (1985) 797–804. https://doi.org/10.14359/10390.

[38] D.J. Carreira, K.H. Chu, Stress-Strain Relatonship for Reinforced Concrete in Tension., J. Am. Concr. Inst. 83 (1986) 21–28.

[39] Z. Guo, Principles of Reinforced Concrete, Elsevier, 2014. https://doi.org/10.1016/C2013-0-13698-7.

[40] C.J. Earls, Effects of material property stratification and residual stresses on single angle flexural ductility, J. Constr. Steel Res. 51 (1999) 147–175. https://doi.org/10.1016/S0143-974X(99)00024-3.

[41] M.P. Byfield, J.M. Davies, M. Dhanalakshmi, Calculation of the strain hardening behaviour of steel structures based on mill tests, J. Constr. Steel Res. 61 (2005) 133–150. https://doi.org/10.1016/j.jcsr.2004.08.001.

[42] EUROPEAN COMMITTEE FOR STANDARDIZATION, EN 1993-1-5: Eurocode 3 – Design of steel structures – Part 1-5: Plated structural elements., (2006).

[43] X. Yun, L. Gardner, Stress-strain curves for hot-rolled steels, J. Constr. Steel Res. 133 (2017) 36–46. https://doi.org/10.1016/j.jcsr.2017.01.024.

[44] A. Hillerborg, M. Modéer, P.-E. Petersson, Analysis of crack formation and crack growth in concrete by means of fracture mechanics and finite elements, Cem. Concr. Res. 6 (1976) 773–781. https://doi.org/10.1016/0008-8846(76)90007-7.

[45] J. Lubliner, J. Oliver, S. Oller, E. Oñate, A plastic-damage model for concrete, Int. J. Solids Struct. 25 (1989) 299–326. https://doi.org/10.1016/0020-7683(89)90050-4.

[46] J. Lee, G.L. Fenves, Plastic-Damage Model for Cyclic Loading of Concrete Structures, J. Eng. Mech. 124 (1998) 892–900. https://doi.org/10.1061/(ASCE)0733-9399(1998)124:8(892).

[47] T. Yu, J.G. Teng, Y.L. Wong, S.L. Dong, Finite element modeling of confined concrete-I: Drucker–Prager type plasticity model, Eng. Struct. 32 (2010) 665–679. https://doi.org/10.1016/j.engstruct.2009.11.014.

[48] G. Duvaut, J.L. Lions, Inequalities in Mechanics and Physics, Springer Berlin Heidelberg, Berlin, Heidelberg, 1976. https://doi.org/10.1007/978-3-642-66165-5.

[49] S. Chen, Y. Jia, Numerical investigation of inelastic buckling of steel–concrete composite beams prestressed with external tendons, Thin-Walled Struct. 48 (2010) 233–242. https://doi.org/10.1016/j.tws.2009.10.009.

[50] W.-B. Zhou, W.-J. Yan, Refined nonlinear finite element modelling towards ultimate bending moment calculation for concrete composite beams under negative moment, Thin-Walled Struct. 116 (2017) 201–211. https://doi.org/10.1016/j.tws.2017.02.011.

[51] A. Rossi, F.P.V. Ferreira, C.H. Martins, E.C. Mesacasa Júnior, Assessment of lateral distortional buckling resistance in welded I-beams, J. Constr. Steel Res. 166 (2020) 105924. https://doi.org/10.1016/j.jcsr.2019.105924.

[52] F.P.V. Ferreira, A. Rossi, C.H. Martins, Lateral-torsional buckling of cellular beams according to the possible updating of EC3, J. Constr. Steel Res. 153 (2019) 222–242. https://doi.org/10.1016/j.jcsr.2018.10.011.

[53] F.P.V. Ferreira, C.H. Martins, LRFD for Lateral-Torsional Buckling Resistance of Cellular Beams, Int. J. Civ. Eng. (2019). https://doi.org/10.1007/s40999-019-00474-7.

[54] F.P.V. Ferreira, C.H. Martins, S. De Nardin, A parametric study of steel-concrete composite beams with hollow core slabs and concrete topping, Structures. (n.d.). https://doi.org/10.1016/j.istruc.2020.08.045.

[55] F.P.V. Ferreira, C.H. Martins, S. De Nardin, Assessment of web post buckling resistance in steel-concrete composite cellular beams, Thin-Walled Struct. (2020) 106969. https://doi.org/10.1016/j.tws.2020.106969.

[56] H.-T. Thai, T.-K. Nguyen, S. Lee, V.I. Patel, T.P. Vo, Review of Nonlinear Analysis and Modeling of Steel and Composite Structures, Int. J. Struct. Stab. Dyn. 20 (2020) 2030003. https://doi.org/10.1142/S0219455420300037.

[57] D. de L. Araújo, M.W.R. Sales, S.M. de Paulo, A.L.H. de C. El Debs, Headed steel stud connectors for composite steel beams with precast hollow-core slabs with structural topping, Eng. Struct. 107 (2016) 135–150. https://doi.org/10.1016/j.engstruct.2015.10.050.

[58] G.Z. Voyiadjis, R.J. Dorgan, Bridging of length scales through gradient theory and diffusion equations of dislocations, Comput. Methods Appl. Mech. Eng. 193 (2004) 1671–1692. https://doi.org/10.1016/j.cma.2003.12.021.

[59] C.G. Skamniotis, M. Elliott, M.N. Charalambides, On modelling the constitutive and damage behaviour of highly non-linear bio-composites – Mesh sensitivity of the viscoplastic-damage law computations, Int. J. Plast. 114 (2019) 40–62. https://doi.org/10.1016/j.ijplas.2018.10.001.

[60] NATIONAL STANDARD OF THE PEOPLE'S REPUBLIC OF CHINA, GB 50010-2002: Code for Design Concrete Structures, (2002).

[61] C. Xu, K. Sugiura, C. Wu, Q. Su, Parametrical static analysis on group studs with typical push-out tests, J. Constr. Steel Res. 72 (2012) 84–96. https://doi.org/10.1016/j.jcsr.2011.10.029.

[62] M. Pavlović, Z. Marković, M. Veljković, D. Buđevac, Bolted shear connectors vs. headed studs behaviour in push-out tests, J. Constr. Steel Res. 88 (2013) 134–149. https://doi.org/10.1016/j.jcsr.2013.05.003.

[63] R.G. Redwood, P.K. Wong, Web holes in composite beams with steel deck, (1982) 41.

[64] G.A. Hegemier, H. Murakami, L.J. Hageman, On tension stiffening in reinforced concrete, Mech. Mater. 4 (1985) 161–179. https://doi.org/10.1016/0167-6636(85)90014-6.

[65] D. Lam, E. El-Lobody, Behavior of Headed Stud Shear Connectors in Composite Beam, J. Struct. Eng. 131 (2005) 96–107. https://doi.org/10.1061/(ASCE)0733-9445(2005)131:1(96).

[66] E. Ellobody, B. Young, Performance of shear connection in composite beams with profiled steel sheeting, J. Constr. Steel Res. 62 (2006) 682–694. https://doi.org/10.1016/j.jcsr.2005.11.004.

[67] F. Sadeghi, J. Li, X. Zhu, A steel-concrete composite beam element for structural damage identification, Int. J. Struct. Stab. Dyn. (2020) S0219455420420158. https://doi.org/10.1142/S0219455420420158.

555 [68] S. Wijesiri Pathirana, B. Uy, O. Mirza, X. Zhu, Flexural behaviour of composite steel–concrete beams utilising blind bolt
556 shear connectors, Eng. Struct. 114 (2016) 181–194. https://doi.org/10.1016/j.engstruct.2016.01.057.

557 [69] M. Sjaarda, T. Porter, J.S. West, S. Walbridge, Fatigue Behavior of Welded Shear Studs in Precast Composite Beams, J.
558 Bridg. Eng. 22 (2017) 04017089. https://doi.org/10.1061/(ASCE)BE.1943-5592.0001134.

559 [70] U. Katwal, Z. Tao, M.K. Hassan, B. Uy, D. Lam, Load sharing mechanism between shear studs and profiled steel sheeting
560 in push tests, J. Constr. Steel Res. 174 (2020) 106279. https://doi.org/10.1016/j.jcsr.2020.106279.

561 [71] S. Guezouli, A. Lachal, Numerical analysis of frictional contact effects in push-out tests, Eng. Struct. 40 (2012) 39–50.
562 https://doi.org/10.1016/j.engstruct.2012.02.025.

563 [72] S. Ebrahimi, S.M. Zahrai, S.R. Mirghaderi, Cyclic Performance Evaluation of Hollow Structural Section (HSS) and
564 Concrete-Filled Tube (CFT) Braces, Int. J. Struct. Stab. Dyn. 19 (2019) 1950140.
565 https://doi.org/10.1142/S0219455419501402.

566 [73] X. Liu, M.A. Bradford, Q.-J. Chen, H. Ban, Finite element modelling of steel–concrete composite beams with high-strength
567 friction-grip bolt shear connectors, Finite Elem. Anal. Des. 108 (2016) 54–65. https://doi.org/10.1016/j.finel.2015.09.004.

568 [74] J.V.F. Dias, J.P.S. Oliveira, A.F.G. Calenzani, R.H. Fakury, Elastic Critical Moment of Lateral-Distortional Buckling of
569 Steel-Concrete Composite Beams under Uniform Hogging Moment, Int. J. Struct. Stab. Dyn. 19 (2019) 1950079.
570 https://doi.org/10.1142/S0219455419500792.

571 [75] A. Nadjai, O. Vassart, F. Ali, D. Talamona, A. Allam, M. Hawes, Performance of cellular composite floor beams at elevated
572 temperatures, Fire Saf. J. 42 (2007) 489–497. https://doi.org/10.1016/j.firesaf.2007.05.001.

573 [76] R. Malm, Predicting shear type crack initiation and growth in concrete with non-linear finit element method, Royal Institute
574 of Technology, 2009.

575 [77] M.A. Crisfield, A fast incremental/iterative solution procedure that handles “snap-through,” Comput. Struct. 13 (1981) 55–
576 62. https://doi.org/10.1016/0045-7949(81)90108-5.

577 [78] M.A. Crisfield, Snap-through and snap-back response in concrete structures and the dangers of under-integration, Int. J.
578 Numer. Methods Eng. 22 (1986) 751–767. https://doi.org/10.1002/nme.1620220314.

579 [79] Y.C. Wang, Steel and Composite Structures, Routledge, Manchester, 2007. https://doi.org/10.1201/9780203738351.

580 [80] A. Maewal, W. Nachbar, Stable Postbuckling Equilibria of Axially Compressed, Elastic Circular Cylindrical Shells: A
581 Finite-Element Analysis and Comparison With Experiments, J. Appl. Mech. 44 (1977) 475–481.
582 https://doi.org/10.1115/1.3424103.

583 [81] P.A. Krahl, Lateral stability of ultra-high performance fiber-reinforced concrete beams with emphasis in transitory phases,
584 Universidade de São Paulo, 2018. https://doi.org/10.11606/T.18.2018.tde-27082018-125631.

585 [82] A. Wosatko, J. Pamin, M.A. Polak, Application of damage–plasticity models in finite element analysis of punching shear,
586 Comput. Struct. 151 (2015) 73–85. https://doi.org/10.1016/j.compstruc.2015.01.008.

587

Assessment of web post buckling resistance in steel-concrete composite cellular beams

Felipe Piana Vendramell Ferreira*[a], Carlos Humberto Martins[b], Silvana De Nardin[a]

[a]Federal University of São Carlos, Rod. Washington Luiz, km 235, São Carlos, São Paulo, Brazil.

[b]State University of Maringá, Av. Colombo nº 5790, Maringá, Paraná, Brazil.

*Corresponding author

E-mail addresses: fpiana@live.com (F. P. V. Ferreira), chmartins@uem.br (C. H. Martins), snardin@ufscar.br (S. De Nardin)

Abstract

This paper aims to investigate the ultimate strength of steel-concrete composite cellular beams, considering the web post buckling. The numerical model is calibrated via experimental tests consolidated in the literature by geometrical non-linear analyses. Asymmetric and symmetric sections are investigated. For each section, the ratio of the web-post width to opening diameter, and opening diameter to the depth of the parent section are varied. The results are compared with analytical procedures. In the models, web post buckling and the Vierendeel mechanism were observed. The end post width affected the ultimate behavior of the concrete slab. The calculation procedures proved to be conservative.

Keywords: Composite cellular beams; Shear connectors; Web post buckling; Geometrical nonlinear analyses; ABAQUS.

NOTATION

The following symbols are used in this paper:

b_c the width of the concrete slab
b_f the width of the flange
b_p the width of plastification line
b_w the width of the web post
b_{we} the width of the end post
C_i the axial force in concrete of a composite section
C_1 the dimensionless constant in Eq. (3)
C_2 the dimensionless constant in Eq. (3)
C_3 the dimensionless constant in Eq. (3)
D_0^{el} the initial elastic stiffness
D_o the opening diameter
d the depth of parent section;
d_e the elastic stiffness degradation variable
$d_{ef,comp}$ the effective depth of composite cellular beam
d_g the depth of cellular beam
f_{cm} the compressive cylinder strength of concrete
f_{cubic} the compressive cubic strength of concrete
f_t the concrete tension resistance
f_u the ultimate strength of cellular beam
f_y the yield strength of cellular beam
G flow potential function
h_F the depth of decking profile
$\bar{I}_1$ the first invariant of the stress tensor
$\bar{J}_2$ the second invariant of the deviatory tensor
K_c the ratio of the second stress invariant on the tensile meridian to that on the compressive meridian, $0.5 \le K_c \le 1.0$ (the default value is 2/3).
l_{eff} effective length of web-post
$l_{eff,P}$ effective length of web-post according Panedpojaman's model
$L_{b,cb}$ the unrestrained length of composite cellular beam
$L_{b,s}$ the unrestrained length of slab
L_p the distance between points of loads
M_i moment at i opening
M_{vh} moment generated by horizontal shear force
$M_{W,e}$ elastic bending moment of web post
$M_{W,Rk}$ flexural strength of Ward's model;
p the length between the opening diameter centers
$\bar{p}$ the effective hydrostatic pressure ($\bar{I}_1/3$)
$\bar{q}$ the equivalent von Mises stress ($\sqrt{3\bar{J}_2}$)
t_c the thickness of concrete above decking profile
t_f the thickness of the flange
t_w the thickness of the web
T_i the axial force in bottom tee
V_b the shear force in bottom tee
V_h the horizontal shear force
$V_{h,eff}$ the effective horizontal shear force
$V_{h,p}$ the horizontal plastic shear resistance
$V_{Gh,Rk}$ resistance to the horizontal shear force, according Grilo's model
$V_{Wv,Rk}$ resistance to the vertical shear force, according to SCI P355 model
V_t the shear force in top tee
$V_{Wh,Rk}$ resistance to the horizontal shear force, according Ward's model
$y_{o,inf}$ the distance from the geometric center of the bottom tee to bottom edge
y_p the depth of plastification line
α the dimensionless constant in Eq. (37)
α_a the ascending branch parameter in Eq. (42)
α_d the descending branch parameter in Eq. (42)
α_t the descending branch parameter in Eq. (43)
β the dimensionless constant in Eq. (37)
β_G the dimensionless constant in Eq. (27)
γ the dimensionless constant in Eq. (37)
ε strain
ε_c the compressive strain
ε^{pl} the plastic strain rate
ε_t the tensile strain
$\tilde{\varepsilon}_c^{pl}$ the equivalent plastic strains in compression
$\tilde{\varepsilon}_t^{pl}$ the equivalent plastic strains in tension
θ angle
$\bar{\lambda}$ reduced slenderness factor
λ_w web slenderness ratio
μ the viscosity parameter that represents the relaxation time
ξ the eccentricity (defines the rate at which the function approaches the asymptote, the default value is 0.1)
σ stress
σ_{b0} the initial equibiaxial compressive yield stress
σ_{c0} the initial uniaxial compressive yield stress
σ_{max} the maximum compression stress, relative to the horizontal shear stress at half height in the web post;
σ_{t0} the uniaxial tensile stress
$\bar{\sigma}$ the effective stress
$\bar{\sigma}_c\left(\tilde{\varepsilon}_c^{pl}\right)$ the effective compressive cohesion stress
$\bar{\sigma}_t\left(\tilde{\varepsilon}_t^{pl}\right)$ the effective tensile cohesion stress
$\hat{\bar{\sigma}}_{\max}$ the maximum principal effective stress
τ the horizontal shear stress at mid-height of the web-post
χ reduction factor
Ψ dilation angle

1. INTRODUCTION

In the early 1990s, due to the development of automated cutting and welding, steel beams with sequential web openings started to be manufactured at low costs. This advance allowed the alternative of using these structural elements as floors beams in composite elements. Cellular beams are those with sequential web openings, in the shape of a circumference, manufactured from thermal cutting and welding, aiming the expansion of the cross section and, consequently, greater flexural stiffness (**Fig. 1**). In order to support high shear forces (i.e. in close proximity of supports or point loads), it can be necessary to infill certain openings (**Fig. 2**), thus increasing the end post width (b_{we}) [1].

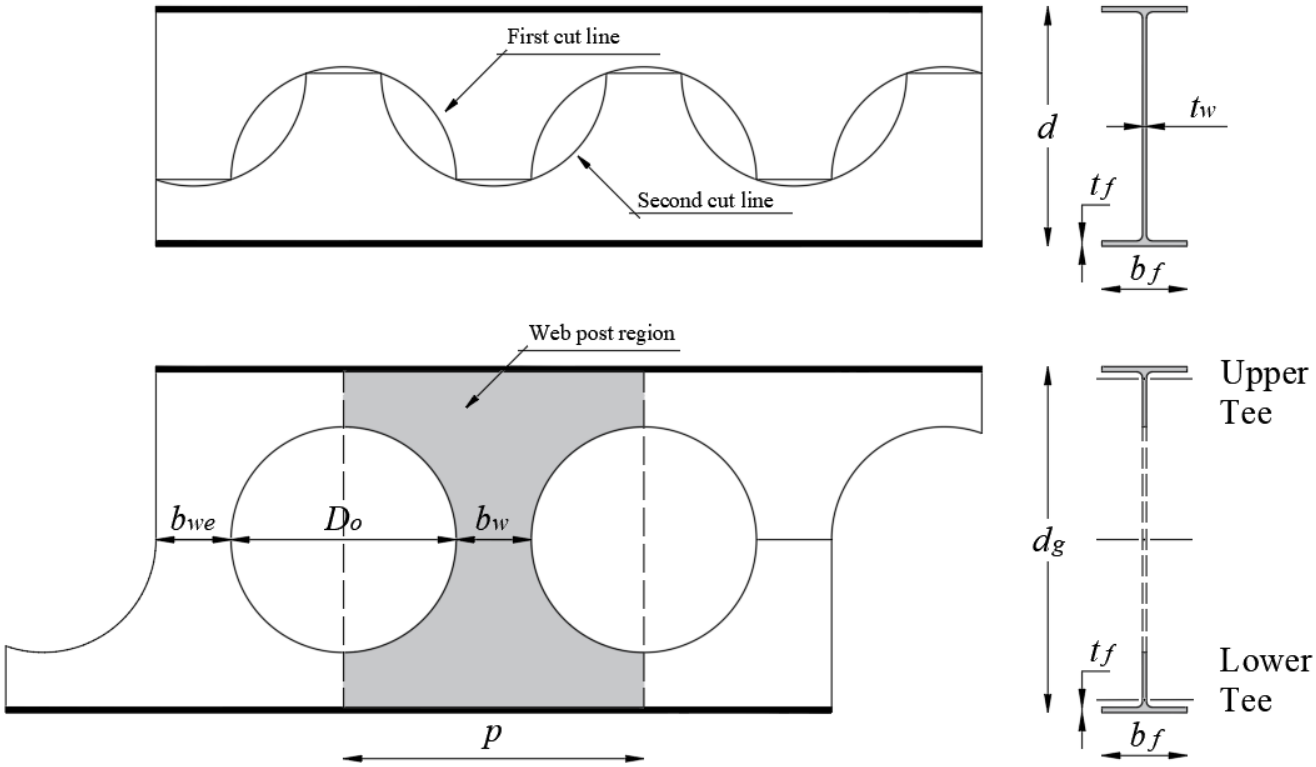

Fig. 1: Manufacturing process

Fig. 2: Filled openings at support [1]

Design engineers of multi-storey buildings are often faced with height limitations imposed by zoning, aesthetic, economic requirements and the need to match the height of the floors. In this context, the use of steel beams with web openings is an advantageous tool that can be used to reduce the height of the floor by solving problems of ducts passages [2]. The demand for more economical and efficient structures, as in the case of composite beams with web openings, has increased in construction, especially in several European countries, United States, Canada and Australia, mainly due to the possibility of reducing the height of the building, the structure's own weight, speed of execution, possibility of reducing or dispensing forms and shoring, increasing the dimensional accuracy of structural elements, and considerably reducing the consumption of structural steel [3–5]. Cellular beams are ideal for structures with open space requirements, such as parking, industries and warehouses, factories, office buildings, schools and hospitals. The main reasons for the use of cellular beams in parking are the ability to overcome larger spans, thus reducing the number of columns, favoring drainage and air flow, and presenting a better aesthetic aspect of the structure. In the case of offshore elements, the cellular beams reduce the structure's own weight and solve piping problems for the integration of services.

Although the expansion of the cross section generates an increase in flexural stiffness, the presence of openings makes cellular beams more susceptible to lateral torsional buckling, web distortion, the web post buckling (WPB), the Vierendeel mechanism (VM), or even the combination of the buckling modes [6–8]. In the case of composite cellular beams, the ultimate strength is associated with the concrete slab failure, such as cracking or crushing, which is combined with cellular beams failures, such VM and the WPB. However, the concrete slab failure is dependent on the opening position and the type of steel sheets of the composite slab. Cracking, crushing were more observed in composite slabs with trapezoidal decking [5,9–12] .

VM is dependent on the presence of high magnitude shear, and it is a phenomenon characterized by distortion and formation of plastic hinges in regions close to the opening. Physically, the VM occurs when the steel reaches the yield resistance due to the combination of normal and tangential stresses, caused by both the global (primary) and Vierendeel (secondary) bending moments, respectively. The Vierendeel moment results from the action of shear force in the t-sections over the horizontal length of the web opening [13]. In this way, the interaction between the primary and secondary bending moments with local axial forces forms plastic hinges in the tee section. This occurs through the transfer of shear force through the web opening [14]. Cellular beams are able to resist additional load until the formation of four plastic hinges in critical locations [15,16]. Still, the VM can occur with the presence or not of stiffeners placed in regions close to the openings. The main parameters that affect this structural behavior are the web thickness, the opening diameter and the depth of tee [13,17,18], and the most important parameters that contribute to the resistance of the Vierendeel mechanism in composite beams with web openings are the shape of the opening, the opening length and the number of shear connectors above the opening (composite action) [19,20]. In Akrami and Erfani [21] was presented comparisons between calculation procedures, such as ASCE 23-97 [22], Chung et al [23], Tsavdaridis and D'Mello [13], SCI P100 [24], SCI P355 [25], considering the Vierendeel mechanism in non-composite beams with web openings. The procedures proved to be conservative.

On the other hand, the WPB becomes critical when the web post width is reduced [26]. The WPB resistance depends on the geometric characteristics of the cellular profile, such as the opening diameter, the web post width and the web thickness. This phenomenon is characterized by a lateral displacement with torsion in web post. Some analytical models have been developed to calculate the WPB resistance [19,24–27]. The first method to be cited was developed by Ward [24]. In this context, the procedure considers only symmetrical composite and non-composite cellular beams. The method is found in Steel Design Guide 31 [28], also considering the asymmetric cellular beams via the most critical situation between the upper and lower tees. The model is based on a series of experimental tests carried out at the Steel Construction Institute of the United Kingdom, and structured by investigations considering the finite element method, via non-linear analyses. The methodology of SCI P355 [19,25], which consider symmetric and asymmetric sections, is based on strut theory, considering an effective length of a bar under compression. The method does not comment on the slab's contribution to WPB resistance. In Abambres et al. [29] was proposed an artificial neural network (ANN) to estimate an elastic buckling load in non-composite cellular beams. According to the authors, the web post buckling will always govern the ultimate behavior for slender web posts, according to the SCI P355 criteria, which underestimates the web post buckling resistance in cellular beams. Panedpojaman et al. [26] made an adaptation in the effective length of the web post. In this model, the effective length of the web post is multiplied by a factor *k*, which is a factor that considers the partial restriction of the web post in relation to the buckling phenomenon. The procedure was developed, considering the web post model of symmetric cellular beams, via parametric study and geometrical nonlinear analysis. However, this model can be applied in asymmetric sections, considering the critical section between the upper and lower tee sections. Tsavdaridis and D'Mello [30] and Tsavdaridis et al. [31] proposed an empirical formulation to estimate the web post vertical shear strength, considering the absence and the presence of stiffeners, respectively. The studies were developed by numerical simulations. The first study investigated non-composite beams with different web openings shapes, while the second focused on non-composite cellular beams. Considering circular web openings, as is the case of cellular beams, the estimate by Tsavdaridis and D'Mello [30] for web post buckling resistance proved to be conservative. In addition, the authors found that the greater the web post width, the greater the vertical shear resistance. On the other hand, in Tsavdaridis et al. [31] was concluded that the transverse stiffeners were effective for up to $p/D_o<1.3$, while for $p/D_o\geq1.3$ they were almost ineffective. For this range, the web post buckling occurred. Grilo et al [27] developed a web post model, considering only symmetric cellular beams. The procedure considers the von Mises criterion, taking into account the equivalent stresses. The procedure is based on the results of numerical simulations and calibrated by non-linear regression curves of resistance.

All the aforementioned procedures do not consider the contribution of the concrete slab to the WPB resistance in composite cellular beams. The present work aims to investigate the behavior of composite cellular beams, considering the web post buckling. For this task, geometrical nonlinear analyses are performed. The numerical model is calibrated via experimental tests consolidated in the literature, considering the initial geometric imperfection. Solid elements are considered for the slab and the shear connectors, and shell elements for the cellular beam. Cellular beams are subjected to two points of loads spaced symmetrically. Asymmetric

and symmetric sections are investigated. For each section, the ratio of the web-post width to opening diameter, and opening diameter to the depth of the parent section are varied. The results are compared with the analytical models [19,24–27].

2. LITERATURE REVIEW

Initial studies involving composite beams with web openings contemplated beams with only one opening, in rectangular shape, formed by solid slabs. In this scenario, some experimental studies were developed [32–34]. Granade [32] studied the stresses that cause the Vierendeel mechanism. Clawson and Darwin [33] observed the influence of the slab on shear strength. The authors tested six composite beams with web openings and two steel beams, bare, which the same section, to assess shear resistance. With these tests it was possible to evaluate the contribution of the concrete slab to the shear strength, which is fundamental for the adequacy of calculation models. Cho [34] sustained the slab's contribution to shear strength. Other authors contributed to the development of analytical models, for example, Todd and Cooper [35] neglected the slab's contribution to shear strength, Donoghue [36] suggested the use of reinforcements in the opening to contribute to shear strength, and Clawson e Darwin [37] considered the contribution of the slab to shear strength.

Regarding the composite beams with web openings formed by composite slabs, several studies were developed in experimental analysis [5,9–11,38,39]. In this scenario, composite beams with only one web opening, with rectangular shape, were still studied. Redwood and Wong [9] evaluated the moment-shear ratio in the opening region. Redwood and Poumbouras [10] investigated the need for connectors in the opening length and the effects of unshored construction. Donahey and Darwin [5] observed the ultimate behavior due to the slab layout, located both in the perpendicular and parallel directions to the longitudinal axis of the steel profile. Lawson et al. [38] observed the influence of longitudinal stiffeners in the action of global and local bending, local web buckling by compression and bending, shear transfer through the concrete slab, resistance to the formation of the Vierendeel mechanism and the increase in deflections resulting from the openings. Cho and Redwood [39] investigated the width of the slab and the position of the connector above the opening, making an analogy to the truss in which the shear connectors are considered tensile elements. Park et al. [11] observed the effects of the slab width and the moment-shear relationship on the ultimate strength. In this scenario, some authors developed prediction models of the ultimate strength, considering composite beams with web openings formed by composite slabs [2,9,18,40–44]. Redwood and Wong [9] considered the failure of the concrete slab by compression, and in Redwood and Poumbouras [40] an increase in compression stresses due to the slip effect caused by the deformation of the shear connectors was predicted. Darwin and Donahey [2] unified the strength of composite beams with web openings, without the use of reinforcement, formed by solid and composite slabs. Cho and Redwood [41] predicted the concept of analogy to the truss and presented a methodology capable of estimating the strength of composite beams with web openings, considering the shear connectors in the opening region as tensioned elements. Another important observation that confirmed the contribution of the concrete slab to the shear strength was published in Cho and Redwood [41]. Although these beams had only a rectangular web opening, such observation related a range of experimental tests of composite beams with rectangular web opening [5,9,10,32]. According to the authors, the tests indicated that the contribution of the concrete slab to the shear strength in the web

opening region can reach the order of 30%-260%, when compared to the isolated steel profile, maintaining the geometry of the openings. Redwood and Cho [18] presented a simplified calculation method, considering composite beams with reinforced web openings as the general case. Fahmy [42] proposed a method for the calculation of the resistant capacity considering full interaction in the steel-concrete interface. Benitez et al. [43] described matrix procedures for determining maximum deflection in composite beams with web openings. Chung and Lawson [44] presented design procedures for composite beams with rectangular and circular web openings.

Now, considering composite cellular beams, those with sequential web openings, produced by thermal cutting and welding (**Fig. 1**), some studies were developed in the experimental analysis [12,45–47]. Müller et al. and Hechler et al. [45,46] performed tests on composite cellular beams with symmetric and asymmetric section. The resistance was reached by WPB. Such experimental studies were complemented with the parametric study, varying the resistance of the materials. The authors concluded that the failure mechanism depends mainly on the type of steel. In this same scenario, Nadjai [47] studied composite symmetric and asymmetric cellular beams. The author verified that the ultimate strength was defined by the WPB. Sheehan et al. [12] investigated the effect of unshored construction on composite cellular beams with large spans, considering cyclical loads. It is observed here that there are few studies that consider composite cellular beams, which shows the need for further investigation. More information on the literature review can be found at [48].

3. WEB POST BUCKLING RESISTANCE

This section presents the calculation procedures that will be used as objects of comparison with the parametric study.

3.1 WARD [24]

In this method, three values are considered, such as C_1, C_2 and C_3, which are a function of the geometric properties of the web post and applicable for the intervals $1.08 \leq p/D_o \leq 1.50$ and $1.25 \leq d_g/D_o \leq 1.75$. The horizontal shearing force in the web post between the openings *i* e *i+1* (**Fig. 3**) is calculated (**Eq. 1**):

$$V_h = \left| \frac{M_{(i+1)} - M_{(i)}}{d_{ef,comp}} \right| \tag{1}$$

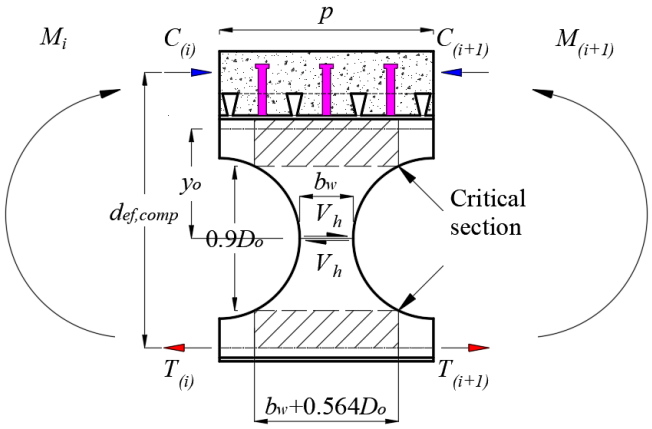

Fig. 3: Ward's model, adapted from [28]

The bending moment, which corresponds to the yielding in the critical section (**Eq. 2**), generated by the horizontal shear force is equal to:

$$M_{vh} = 0.9\left(\frac{D_o}{2}\right)V_h \tag{2}$$

Thus, the WPB is calculated, according to **Eqs (3-7)**:

$$M_{W,\mathrm{Rk}} = M_{W,e}\left[C1\left(\frac{p}{D_o}\right) - C2\left(\frac{p}{D_o}\right)^2 - C3\right] \tag{3}$$

$$M_{W,e} = \frac{t_w\left(p - D_o + 0.564D_o\right)^2}{6} f_y \tag{4}$$

$$C1 = 5.097 + 0.1464\left(\frac{D_o}{t_w}\right) - 0.00174\left(\frac{D_o}{t_w}\right)^2 \tag{5}$$

$$C2 = 1.441 + 0.0625\left(\frac{D_o}{t_w}\right) - 0.000683\left(\frac{D_o}{t_w}\right)^2 \tag{6}$$

$$C3 = 3.645 + 0.0853\left(\frac{D_o}{t_w}\right) - 0.00108\left(\frac{D_o}{t_w}\right)^2 \tag{7}$$

Another form of calculation is to present the resistance to the horizontal shear force (**Eq. 8**):

$$V_{Wh,\mathrm{Rk}} = \frac{M_{W,e}}{0.45D_o}\left[C1\left(\frac{p}{D_o}\right) - C2\left(\frac{p}{D_o}\right)^2 - C3\right] \tag{8}$$

3.2 SCI P355 [25]

According to this method, the action of the horizontal shear force at half the height of the web causes tension and compression stresses due to the flexion between the upper and lower tees. These stresses vary around the opening (**Fig. 4**).

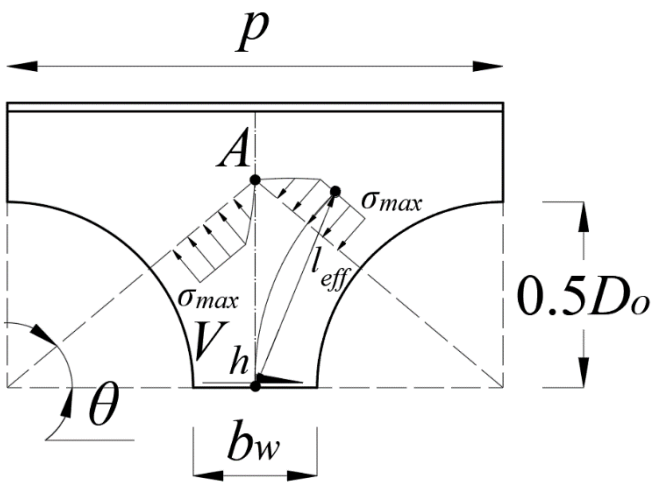

Fig. 4: Strut model, adapted from [19]

The effective length takes into account the variation of stresses around the opening, according to **Eq. (9)**.

$$l_{eff} = 0.5\sqrt{b_w^2 + D_o^2} \leq 0.7D_o \tag{9}$$

Once the effective length has been determined, then the theory of compression bars, according to EN 1993-1-1 [49], is applied, considering slenderness in the web post length and using the buckling curve *c* (**Eqs. 10-15**):

$$\sigma_{Rk} = \chi f_y \tag{10}$$

$$\chi = \frac{1}{\phi + \sqrt{\phi^2 - \bar{\lambda}^2}} \leq 1.0 \tag{11}$$

$$\phi = 0.5\left[1 + 0.49\left(\bar{\lambda} - 0.2\right) + \bar{\lambda}^2\right] \tag{12}$$

$$\bar{\lambda} = \sqrt{\frac{f_y}{f_{cr,w}}} \tag{13}$$

$$f_{cr,w} = \frac{\pi^2 E}{\lambda_w^2} \tag{14}$$

$$\lambda_w = \frac{l_{eff}\sqrt{12}}{t_w} \tag{15}$$

Thus, the vertical shearing strength can be calculated (**Eq. 16)**:

$$V_{Lv,Rk} = \sigma_{Rk} t_w b_w \tag{16}$$

3.3 PANEDPOJAMAN et al. [26]

With the justification that the method of SCI P355 presents conservative results, Panedpojaman et al. [26] made an adaptation in the effective length of the web post. In this model, the effective length of the web post is multiplied by a factor *k* (**Fig. 5**).

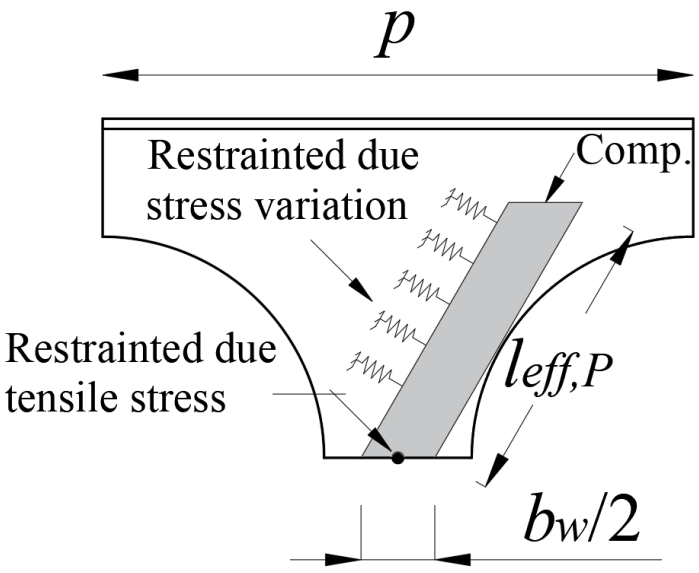

Fig. 5: The model of Panedpojaman et al., adapted from [26]

According to the study, the coefficient presented in the **Eqs. (17-18)** considers the effect of the variation of the height of the tees with the values of the ratios D_o/d e p/D_o.

$$l_{eff,P} = k\left(0.5\sqrt{p^2 - D_o^2}\right) \tag{17}$$

$$k = 0.9\left(\frac{p}{D_o}\right)\left(\frac{D_o}{d}\right)^2 \leq \min\left(1.15\frac{D_o}{d}, 1.15\right) \tag{18}$$

3.4 GRILO et al. [27]

The proposed formulation (**Eqs. 19-26**) takes into account a constant stress distribution (**Fig. 6**), and the reduction factor.

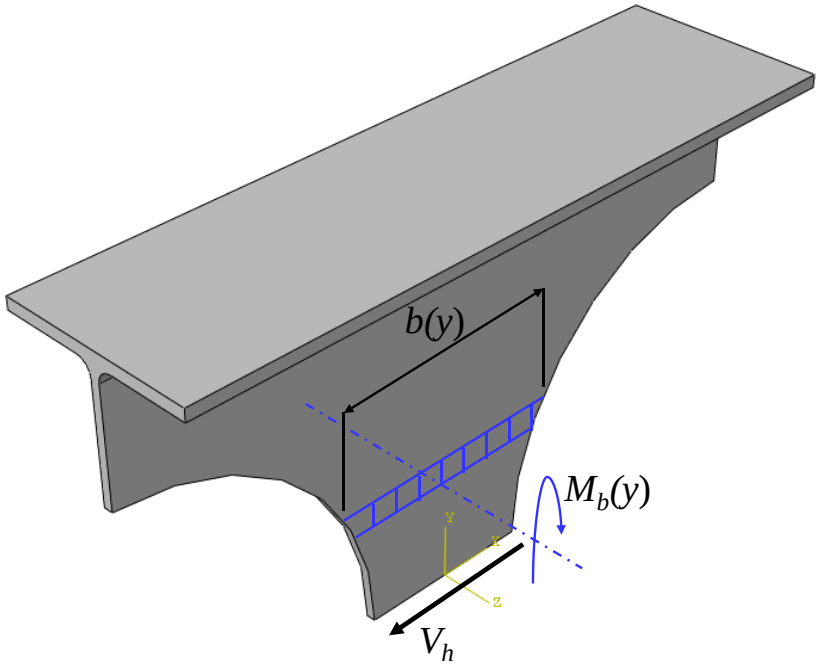

Fig. 6: The model of Grilo et al., adapted from [27]

$$V_{Gh,Rk} = V_{h,p}\chi \tag{19}$$

$$V_{h,p} = \beta_G f_y \frac{t_w b_p^{\,2}}{\sqrt{3b_p^{\,2} + 16y_p^{\,2}}} \tag{20}$$

$$\beta_G = 1.838 - 0.42\left(\frac{D_o}{d_g}\right) - \left(\frac{p}{3D_o}\right) \qquad for\,(p/Do) \geq 1.2 \tag{21}$$

$$y_p = \frac{D_o}{2}\left[0.445\left(\frac{p}{D_o}\right)^3 - 2.578\left(\frac{p}{D_o}\right)^2 + 4.770\left(\frac{p}{D_o}\right) - 2.475\right] \tag{22}$$

$$b_p = b_w\sqrt{1 - \frac{4y_p^{\,2}}{D_o^{\,2}}} \tag{23}$$

$$\lambda_{ma,0} = \sqrt{\frac{3\left(p^2 - D_o^2\right) f_y}{\pi^2 t_w^2 E}} \quad (24)$$

For $\lambda_{ma,0} \geq 1.0$:

$$\chi = \frac{m}{\lambda_{ma,0}^{\ n}} \leq 1.0 \quad (25)$$

For $\lambda_{ma,0} < 1.0$:

$$\chi = op^{\left(\lambda_{ma,0}{}^{q}\right)} \leq 1.0 \quad (26)$$

With, *m*, *n*, *o*, *p* e *q*, according to **Table 1**.

Table 1: Values of *m* and *n*

D_o/d_g	p/D_o	*m*	*n*	*o*	*p*	*q*
	1.1	0.759	1.35	1.15	0.660	3.5
	1.2	0.730	1.39	1.42	0.514	2.1
0.5	1.3	0.780	1.40	1.16	0.672	3.5
	1.4	0.840	1.42	1.26	0.667	2.7
	1.5	0.916	1.40	1.09	0.840	5.0
	1.1	0.798	1.42	1.14	0.700	3.5
	1.2	0.791	1.42	1.13	0.700	3.8
0.6	1.3	0.836	1.40	1.10	0.760	4.5
	1.4	0.909	1.36	1.15	0.790	3.3
	1.5	0.970	1.31	1.09	0.890	4.5
	1.1	0.849	1.47	1.08	0.786	4.5
	1.2	0.844	1.44	1.11	0.760	3.9
0.7	1.3	0.903	1.39	1.15	0.785	4.0
	1.4	0.980	1.34	1.12	0.870	3.0
	1.5	1.130	1.33	-	-	-
	1.1	0.888	1.46	1.09	0.815	4.0
	1.2	0.901	1.42	1.14	0.790	3.5
0.8	1.3	1.020	1.42	-	-	-
	1.4	1.175	1.42	-	-	-
	1.5	1.285	1.36	-	-	-

According to the authors, some branches of the curves have not been determined, due to the failure occurring by a mechanism other than web post buckling, indicating that it will occur by a VM.

3.5 FINITE ELEMENT HORIZONAL SHEAR FORCE

As previously mentioned, the calculation procedures are compared with the results of the numerical analyses. In this way, the extraction of the horizontal shear value will be respected, according to the **Eqs. (27-28)** and **Fig. 7**:

$$V_{h,FE} = \left| \frac{M_{FE(i+1)} - M_{FE(i)}}{d_{ef,comp}} \right| \quad (27)$$

$$d_{ef,comp} = d_g - y_{o,\inf} + h_F + 0.5t_c \quad (28)$$

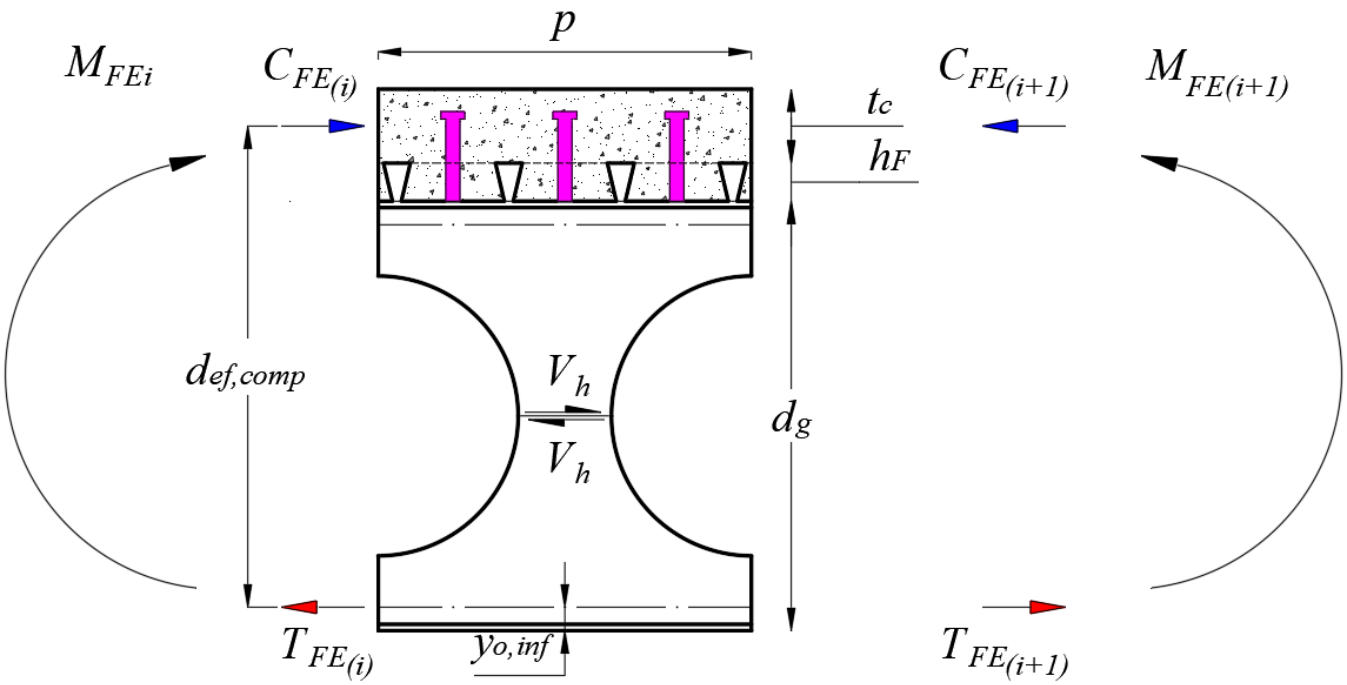

Fig. 7: Finite element horizontal shear

4. NUMERICAL MODEL: VALIDATION STUDY

The analyses are performed in the ABAQUS software [50] in two steps: elastic stability and geometrical and physical nonlinear analyses. This procedure was previously used in [51–53]. The elastic stability analysis is used to estimate critical buckling loads in structures, and can also be used as the shape associated with an initial geometric imperfection for the beginning of the geometrical non-linear analysis. To perform this analysis, the linear perturbation method ("*Buckle*") is used, which is possible to estimate the critical loads by obtaining eigenvalues and their respective eigenvectors. The geometrical non-linear analysis is performed considering the initial geometric imperfection in the cellular beam. The implementation of the geometric imperfection is made by *IMPERFECTION. The shape of the structure in the elastic stability analysis normalized to the initial imperfection value in the cellular beam is adopted as the shape at the beginning of this analysis. To solve the problem of geometric nonlinearity, the "*Static Riks*" method is used. Also known with a *modified Riks* algorithm, the method is able to obtain equilibrium solutions for unstable problems. When configuring the procedure, it is necessary to implement the initial arc length, which refers to an initial percentage of the external load. In this way, the next increments are automatically adjusted for convergence to occur.

4.1 EXPERIMENTAL TESTS

For the calibration of the numerical model, experimental tests 1A (CCB1) and 1B (CCB2) performed by Nadjai [54], and the tests RWTH-1A (CCB3) and RWTH-3 (CCB4) performed by por Müller et al. [45] e Hechler et al. [46] are considered. **Fig. 8** and **Table 2** show the details of the specimens, as well as the geometric properties, material properties, and boundary conditions. Importantly, although the profiled steel sheet was not considered in the numerical model, Holorib HR 51/150 geometry was used to represent the ribs in the concrete slab. The Young's modulus is equal to 200 GPa for CCB1 and CCB2 models, and 195 GPa for

CCB3 and CCB4 models. The headed studs had dimensions 19x120mm (CCB1 and CCB2) and 19x100mm (CCB3 and CCB4), spaced 150mm. The mechanical properties of the shear connectors are in accordance with what was presented in [55], i.e., the yield stress and the ultimate stress were 460 MPa and 559 MPa, respectively. The elongation at rupture was 18.8%.

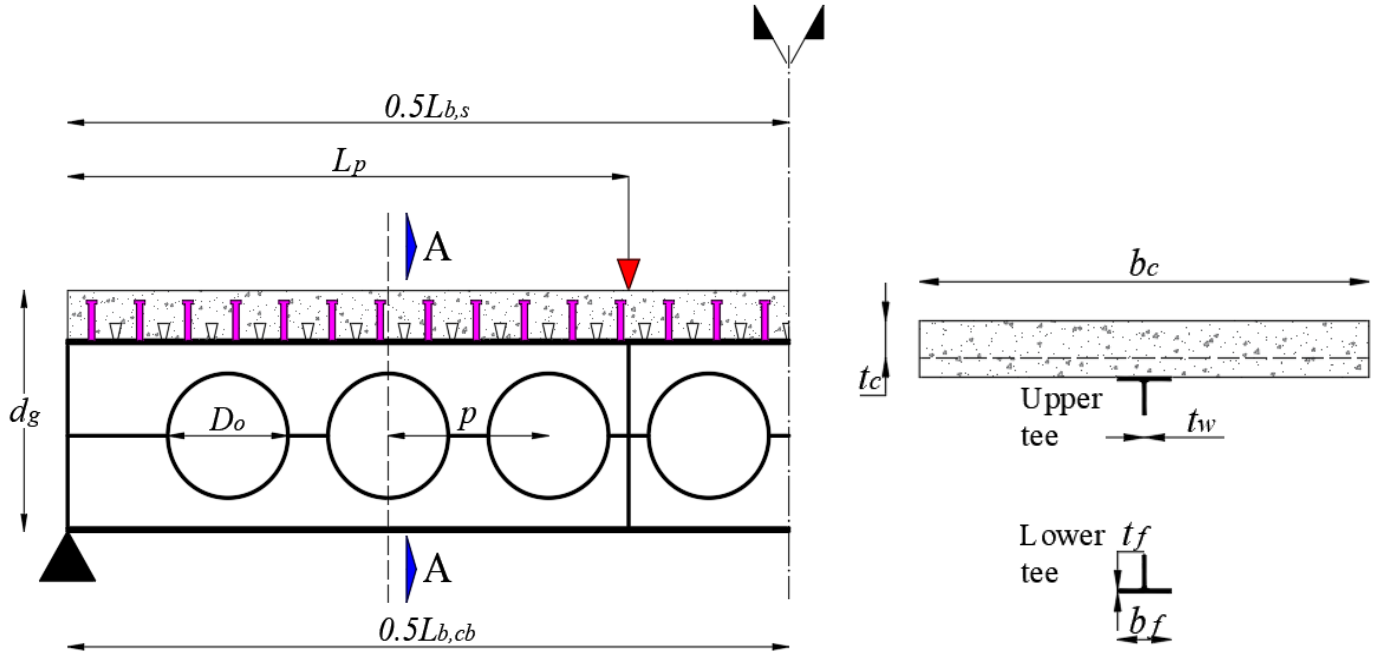

(a) Lateral view (b) Section A-A

Fig. 8: Details of specimens

Table 2: Details of the specimens (in mm and MPa)

Model	Ref.	d_g	D_o	p	Upper tee					Lower tee					$L_{b,cb}$	f_{cubic}	b_c	t_c	$L_{b,s}$	L_p
					b_f	t_f	t_w	f_y (flange/web)	f_u (flange/web)	b_f	t_f	t_w	f_y (flange/web)	f_u (flange/web)						
CCB1	[54]	575	375	500	141.8	8.6	6.4	312	438.5	141.8	8.6	6.4	312	438.5	4500	35	1200	99	4500	1750
CCB2	[54]	630	450	630	141.8	8.6	6.4	312	438.5	152.4	10.9	7.6	312	438.5	4500	35	1200	99	4500	2250
CCB3	[45,46]	555	380	570	180	13.5	8.6	451/489	541/587	180	13.5	8.6	451/489	541/587	6840	42	1800	79	6555	1140/2850
CCB4	[45,46]	485	380	570	150	10.7	7.1	407/467	524/588	300	21.5	12	453/488	519/582	6840	30	1800	79	6555	1140/2850

4.2 MATERIALS

4.2.1 **Concrete**

The Concrete Damage Plasticity (CDP) [56–58] is adopted. The model takes into account hypotheses based on the theory of plasticity [59], and the stress-strain relationship is governed by a damaged elastic variable, according to **Eq. (29)**.

$$\sigma = \left(1-d_e\right) D_0^{el} : \left(\varepsilon - \varepsilon^{pl}\right) = \left(1-d_e\right)\overline{\sigma} \tag{29}$$

The CDP makes use of the resistance function of Lubliner et al. [57] (**Eqs. 30-33**), with the modifications proposed by Lee and Fenves [58] to explain the different evolution of resistance under tension and compression:

$$F = \frac{1}{1-\alpha}\left[\overline{q} - 3\alpha\overline{p} + \beta\left(\varepsilon^{pl}\right)\left\langle\overline{\sigma}_{\max}\right\rangle - \gamma\left\langle-\overline{\sigma}_{\max}\right\rangle - \overline{\sigma}_c\left(\varepsilon_c^{pl}\right)\right] = 0 \tag{30}$$

$$\alpha = \frac{\left(\sigma_{b0}/\sigma_{c0}\right)-1}{2\left(\sigma_{b0}/\sigma_{c0}\right)-1}; 0 \le \alpha \le 0.5 \tag{31}$$

$$\beta = \frac{\overline{\sigma}_c\left(\varepsilon_c^{pl}\right)}{\overline{\sigma}_t\left(\varepsilon_t^{pl}\right)}\left(1-\alpha\right) - \left(1+\alpha\right) \tag{32}$$

$$\gamma = \frac{3\left(1-K_c\right)}{2K_c - 1} \tag{33}$$

The flow potential function is described in **Eq. (34)**. This function defines the direction of the deformations, when the material reaches the state of plastic behavior.

$$G = \sqrt{\left(\xi\sigma_{t0}\tan\psi\right)^2 + \overline{q}^2} - \overline{p}\tan\psi \tag{34}$$

The input parameters to characterize the plasticity are: dilation angle (ψ), eccentricity (ξ), the ratio of initial equibiaxial compressive yield stress to initial uniaxial compressive yield stress (σ_{b0}/σ_{c0}), the ratio of the second stress invariant on the tensile meridian to that on the compressive meridian (K_c), and the viscosity parameter that represents the relaxation (μ). Some of these parameters mentioned, the ABAQUS software suggests values per default. However, the dilation angle and the viscosity parameter are sensitive, depending on the model to be used [60,61]. **Table 3** presents the input parameters for defining the plastic behavior.

Table 3: CDP input parameters

Parameter	**Value**
Ψ (º)	40
ξ	0.1 (default)
σ_{b0}/σ_{c0}	1.16 (default)
K_c	2/3 (default)
μ (s^{-1})	0.001

To fully represent the stress-strain relationship of compressed and tensile concrete, the Guo model is used [62]. In this model, the behavior of concrete under compression and tension is defined by branches, with different functions (**Eq. 35-37**). Some authors [63,64] verified the effectiveness of this model with the results of experimental analyses. Such a model is also found in the GB-50010-2002 standard [65].

$$\frac{\sigma}{f_{cm}}=\begin{cases}\alpha_a\left(\varepsilon/\varepsilon_c\right)+\left(3-2\alpha_a\right)\left(\varepsilon/\varepsilon_c\right)^2+\left(\alpha_a-2\right)\left(\varepsilon/\varepsilon_c\right)^3, & \varepsilon/\varepsilon_c\le 1\\ \dfrac{\varepsilon/\varepsilon_c}{\alpha_d\left[\left(\varepsilon/\varepsilon_c\right)-1\right]^2+\left(\varepsilon/\varepsilon_c\right)}, & \varepsilon/\varepsilon_c>1\end{cases} \tag{35}$$

$$\frac{\sigma}{f_t}=\begin{cases}1.2\left(\varepsilon/\varepsilon_t\right)-0.2\left(\varepsilon/\varepsilon_t\right)^6, & \varepsilon/\varepsilon_t\le 1\\ \dfrac{\varepsilon/\varepsilon_t}{\alpha_t\left[\left(\varepsilon/\varepsilon_t\right)-1\right]^{1.7}+\varepsilon/\varepsilon_t}, & \varepsilon/\varepsilon_t>1\end{cases} \tag{36}$$

$$\alpha_t=0.312\,f_t^2 \tag{37}$$

4.2.2 **Steel**

The quadrilinear diagrams are more accurate and they are in accordance with the experimental stress-strain curves across the tensile stress range. In addition, this curve is suitable for incorporation into analytical, numerical and design models. Therefore, for cellular beams, the quadrilinear model (**Fig. 9**) of Yun and Gardner [66].

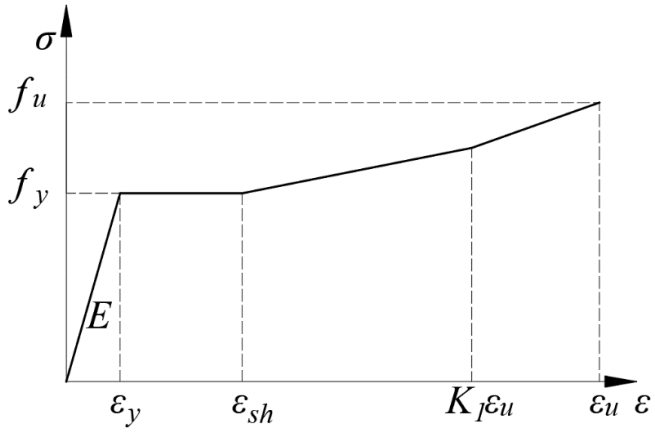

Fig. 9: Stress-strain relationship for steel

The model parameters are calculated, according to the **Eqs. (38-42)**:

$$f\left(\varepsilon\right)=\begin{cases}E\varepsilon,\varepsilon\le\varepsilon_y\\ f_y,\varepsilon_y<\varepsilon\le\varepsilon_{sh}\\ f_y+E_{sh}\left(\varepsilon-\varepsilon_{sh}\right),\varepsilon_{sh}<\varepsilon\le C_1\varepsilon_u\\ f_{C_1\varepsilon_u}+\left(\dfrac{f_u+f_{C_1\varepsilon_u}}{\varepsilon_u-C_1\varepsilon_u}\right),C_1\varepsilon_u<\varepsilon\le\varepsilon_u\end{cases} \tag{38}$$

$$\varepsilon_u=0.6\left(1-\frac{f_y}{f_u}\right),\varepsilon_u\ge 0.06 \tag{39}$$

$$\varepsilon_{sh}=0.1\frac{f_y}{f_u}-0.055,0.015<\varepsilon_{sh}\le 0.03 \tag{40}$$

$$K_1=\frac{\varepsilon_{sh}+0.25\left(\varepsilon_u-\varepsilon_{sh}\right)}{\varepsilon_u} \tag{41}$$

$$E_{sh} = \frac{f_u - f_y}{0.4\left(\varepsilon_u - \varepsilon_{sh}\right)} \tag{42}$$

The implementation of the stress- strain relationship must be done with the real values, according to the **Eqs. (43-44):**

$$\sigma^{true} = \sigma^{nom}\left(1+\varepsilon^{nom}\right) \tag{43}$$

$$\varepsilon^{true} = \ln\left(1+\varepsilon^{nom}\right) \tag{44}$$

4.3 INTERACTION

In a composite beam, the steel profile and the concrete slab are associated by shear connectors, which are mechanical devices that promote the composite behavior, and this is essential to resist the longitudinal shear forces at the connection interface. The headed studs are the most commonly used mechanical devices in composite beams and this is due to their flexible behavior, that is, the connector close to reaching its maximum strength continues to deform without rupture, allowing neighboring connectors increasingly absorb the shear flow. However, the resistance to shear stress and the stiffness of the steel-concrete connection depends not only on the strength of the shear connector, but also on the strength of the concrete slab against cracking caused by the high concentration of the shear stress in each connector [55,67,68].

The shear connectors were implemented within a volume cut from the slab, according to the technique used by Pathirana et al. [69]. The analysis strategy is illustrated in **Fig. 10.** The tie constraint restriction was applied to the surface between the shear connectors and the upper flange. This modeling technique allows to represent the perfect bond between the surfaces of the cellular beam and the shear connector. Regarding the surface-to-surface interaction, the normal and tangential behavior between the slab-connector and slab-beam interfaces is considered. For the interface between the connector and the concrete slab, the value of the friction coefficient was equal to 0.2. On the other hand, for the slab-beam interface, it is considered the value of the coefficient and friction equal to 0.3. These values are in accordance with the analyses performed by Guezouli and Lachal [70].

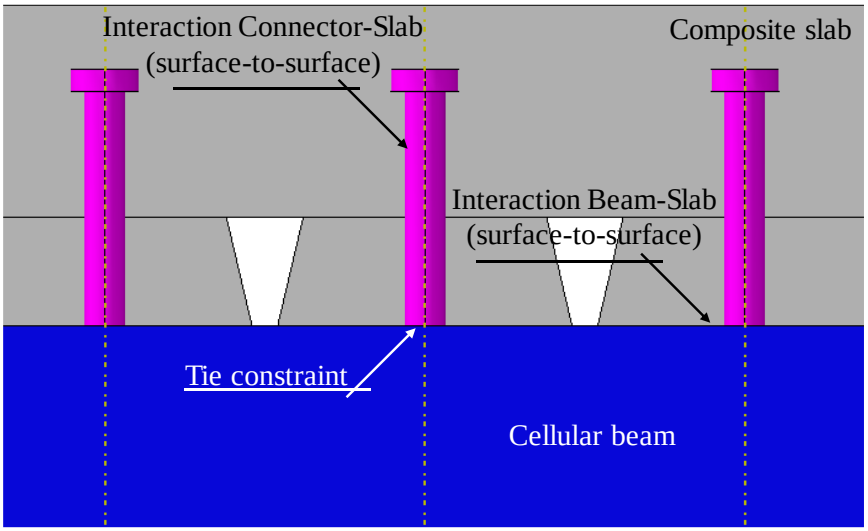

Fig. 10: Interaction

4.4 BOUNDARY CONDITIONS

As shown **Fig. 11**, the vertical displacement (Uy=0) and the lateral displacement on the concrete slab (Ux=0) were restrained on the support. In the middle of the span, symmetry was considered (Uz=URx=URy=0).

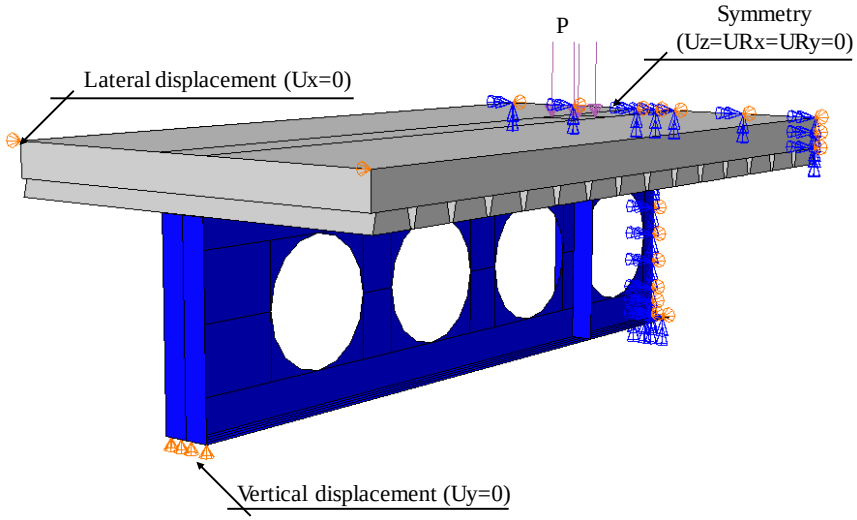

Fig. 11: Boundary conditions

4.5 DISCRETIZATION

The shell elements were implemented in cellular beams. The S4R element is a quadrilateral element with four nodes and reduced integration, a factor that reduces processing time. On the other hand, on the shear connector and the concrete slab, the solid element C3D8R was implemented, which has eight nodes, reduced integration and supports plastic analysis with large deformations, and allows the visualization of the crack in the CDP yield criterion. Both elements have six degrees of freedom per node - three rotations and three translations - referenced in a three-axis system (X, Y and Z). The discretization of the steel profile, concrete slab, and headed studs is presented in **Fig. 12**.

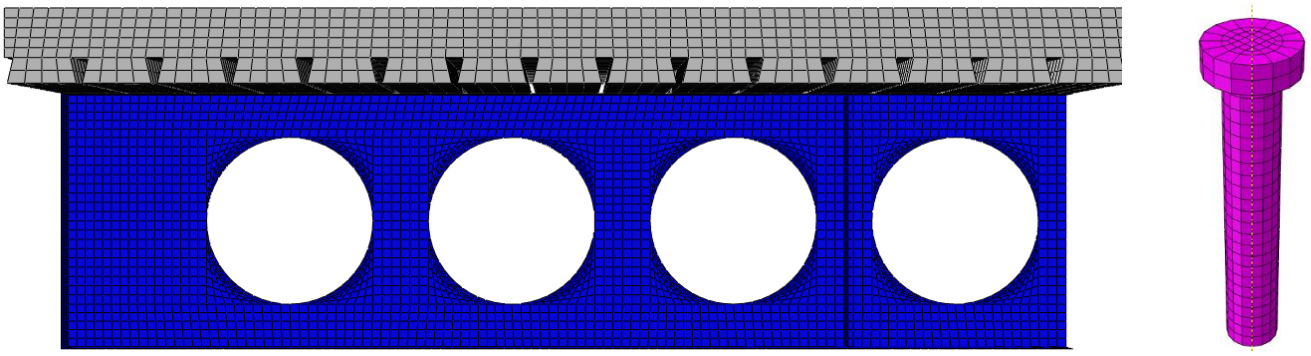

(a) Composite cellular beams (b) Headed stud

Fig. 12: Discretization

4.6 INITIAL GEOMETRIC IMPERFECTIONS

In the models, the residual stresses were not considered since these are not influential for composite beams submitted only to the positive moment. In this context, the residual stresses increase the effects of the negative moment and the beam can reach the lateral distortional buckling [71,72]. However, due to the process of cutting and fabrication, imperfection is inevitable and realistic

cellular beams are typically difficult to make. The imperfection contributes to initiation of buckling in the cellular beams. Real imperfection is hardly determined [26]. The lack of straightness of the cellular beam, both in the height of the cross section and in the span length, causes the eccentricities in the loads, a factor that intensifies the bending moment and reduces the resistance of the cross section. The ACB® [1] recommends that the geometric imperfection limit on the web post should not be more than 4mm for sections with d_g<600mm and d_g/100 for sections with d_g>600 mm. Therefore, in numerical models, only the initial geometric imperfection is considered, as well as performed in [26,27].

4.7 SENSIVITY ANALYSES

Parametric analyses were performed to investigate the influence of the initial geometric imperfection. For this, the initial geometric imperfection was varied. The results are shown in **Fig. 13** and **Table 4**. Although the variation of the initial geometric imperfection showed little sensitivity, that is, the maximum relative error between the largest and smallest amplitude was 8%, it is possible to observe that the greater the initial geometric imperfection, the lower the ultimate load. This behavior was also observed by Chen and Jia [71], and Couto and Vila Real [73]. This small relative error, which was observed in the sensitivity analyses, occurred due to the fact that the composite cellular beams presented the ultimate behavior governed by WPB, which is a type of local buckling. In this scenario, for the initial geometric imperfection value equal to d_g/1000, the numerical models showed agreement with the tests. Thus, it can be verified that the numerical model was calibrated via sensitivity analysis.

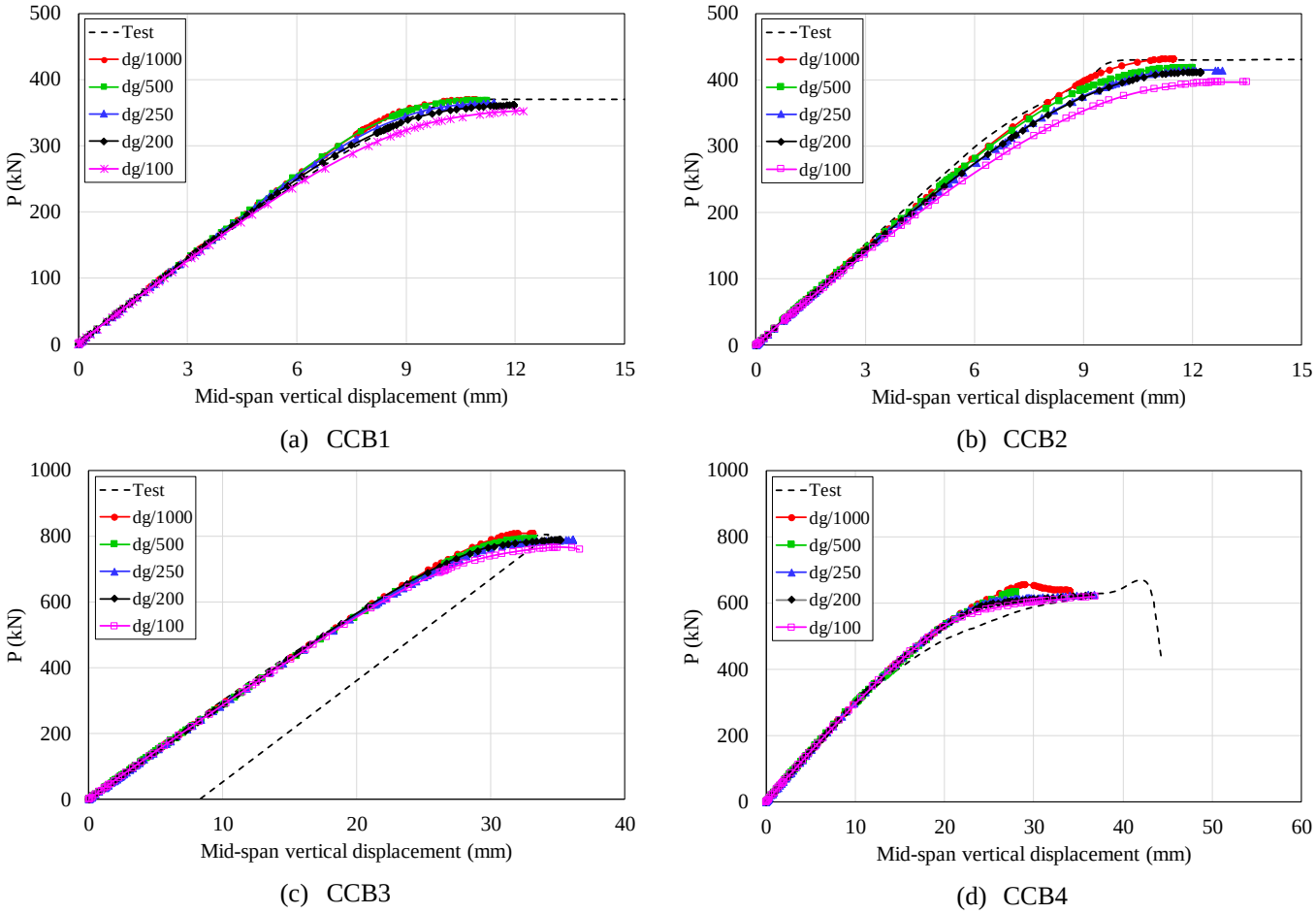

Fig. 13: Sensivity analyses

Table 4: Sensivity analyses

Model	P_{Test} (kN)	$P_{dg/1000}$ (kN)	$P_{dg/500}$ (kN)	$P_{dg/250}$ (kN)	$P_{dg/200}$ (kN)	$P_{dg/100}$ (kN)	$\frac{P_{(d_g/1000)}}{P_{Test}}$	$\frac{P_{(d_g/500)}}{P_{Test}}$	$\frac{P_{(d_g/250)}}{P_{Test}}$	$\frac{P_{(d_g/200)}}{P_{Test}}$	$\frac{P_{(d_g/100)}}{P_{Test}}$
CCB1	370	370.71	369.73	364.64	361.22	352.48	1.00	1.00	0.99	0.98	0.95
CCB2	430	431.36	418.14	414.66	412.12	397.07	1.00	0.97	0.96	0.96	0.92
CCB3	806	808.06	791.74	789.23	789.17	766.49	1.00	0.98	0.98	0.98	0.95
CCB4	658	656.03	633.30	626.23	623.28	620.04	1.00	0.96	0.95	0.95	0.94
						Average	1.00	0.98	0.97	0.97	0.94
						SD	0.28%	1.57%	1.52%	1.51%	1.34%
						COV	0.00%	0.02%	0.02%	0.02%	0.02%

5. NUMERICAL MODEL: PARAMETRIC STUDY

The following are the general considerations for the parametric study:

i. The cross sections of models CCB1, CCB2, CCB3 and CCB4 are considered;

ii. It is considered that the end post width (b_{we}) shall not be smaller than the other web posts width (b_w);

iii. The length of the composite cellular beam is equal 6m, and the effective slab width is $L/4$;

iv. The slab depth is equal to 150mm, and the Holorib HR 51/150 geometry was used;

v. The headed stud dimension is 19x120mm;

vi. The surface/surface contact properties were applied as [70];

vii. The ratios p/D_o and D_o/d are varied, considering symmetric and asymmetric sections (**Table 5-6**);

Table 5: Symmetric sections (in mm)

Section	***d***	***d_g***	***D_o/d***	***D_o***	***i***	***p/D_o***	***p***	**Section**	***d***	***d_g***	***D_o/d***	***D_o***	***i***	***p/D_o***	***p***
UB 406x140x39	398	575	0.8	320	14	1.2	384	IPE 400	400	555.2	0.8	320	14	1.2	384
					14	1.3	416						14	1.3	416
					12	1.4	448						12	1.4	448
					12	1.5	480						12	1.5	480
			0.9	360	12	1.2	432				0.9	360	12	1.2	432
					12	1.3	468						12	1.3	468
					10	1.4	504						10	1.4	504
					10	1.5	540						10	1.5	540
			1	400	12	1.2	480				1	400	12	1.2	480
					10	1.3	520						10	1.3	520
					10	1.4	560						10	1.4	560
					8	1.5	600						8	1.5	600
			1.1	440	10	1.2	528				1.1	440	10	1.2	528
					10	1.3	572						10	1.3	572
					8	1.4	616						8	1.4	616
					8	1.5	660						8	1.5	660
			1.2	480	10	1.2	576				1.2	480	10	1.2	576
					8	1.3	624						8	1.3	624
					8	1.4	672						8	1.4	672
					8	1.5	720						8	1.5	720

Table 6: Asymmetric sections (in mm)

Section	d^a	d_g	D_o/d	D_o	i	p/D_o	p	Section	d^a	d_g	D_o/d	D_o	i	p/D_o	p
UB 406x140x39 UB 406x152x42	398	630	0.8	320	14	1.2	384	IPE 300 HEB 340	300	484.6	0.8	240	20	1.2	288
					14	1.3	416						18	1.3	312
					12	1.4	448						16	1.4	336
					12	1.5	480						16	1.5	360
			0.9	360	12	1.2	432				0.9	270	18	1.2	324
					12	1.3	468						16	1.3	351
					10	1.4	504						14	1.4	378
					10	1.5	540						14	1.5	405
			1	400	12	1.2	480				1	300	16	1.2	360
					10	1.3	520						14	1.3	390
					10	1.4	560						14	1.4	420
					8	1.5	600						12	1.5	450
			1.1	440	10	1.2	528				1.1	330	14	1.2	396
					10	1.3	572						12	1.3	429
					8	1.4	616						12	1.4	462
					8	1.5	660						10	1.5	495
			1.2	480	10	1.2	576				1.2	360	12	1.2	432
					8	1.3	624						12	1.3	468
					8	1.4	672						10	1.4	504
					8	1.5	720						10	1.5	540

[a]the lowest value between the depths of the parent sections

viii. The ASTM A572 Grade 50 steel is adopted, whose yield strength is equal 345 MPa and the ultimate strength is equal 450 MPa. The Young's modulus is equal to 200 GPa;

ix. The concrete resistance is 35 MPa;

x. The initial geometric imperfection factor is equal to d_g/1000, according to sensitivity analyses performed;

xi. Four-point bending with symmetry is considered (**Fig. 14**). The composite cellular beams are simply supported and subjected to two points of loads, spaced symmetrically in 2m from supports. Stiffeners were provided at the point of load and support.

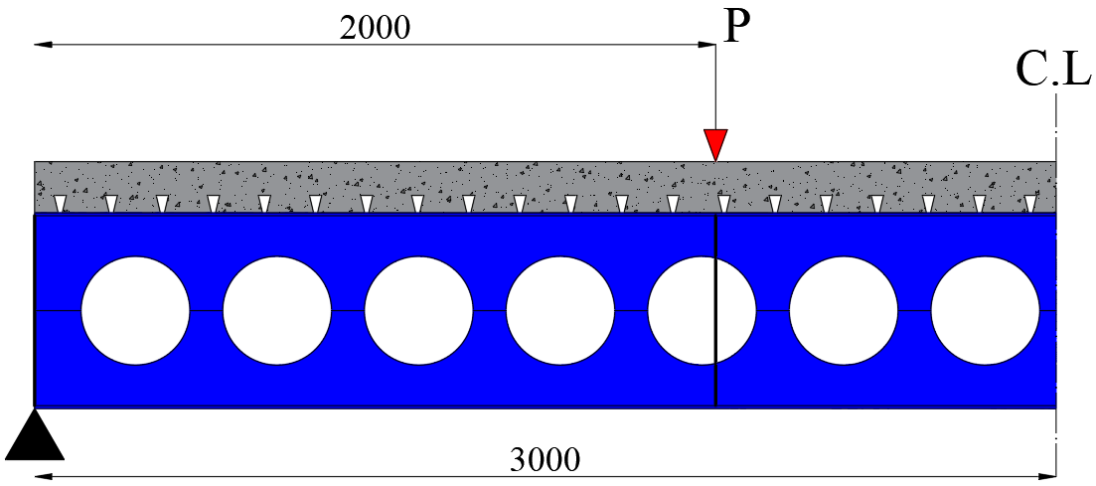

Fig. 14: Four-point bending with symmetry (dimensions in mm)

6. RESULTS AND DISCUSSION

A total of 80 numerical models were analyzed, considering the methodology illustrated **Fig. 15**. In the first step, the pre-processing, for each section, the D_o/d ratio was varied by 0.8, 0.9, 1.0, 1.1 and 1.2, and for each D_o/d ratio value, the p/D_o ratio was varied by 1.2, 1.3, 1.4 and 1.5. In the second step, the post-processing, the failure mode of the composite cellular beams is observed. If the ultimate behavior was not governed by the WPB, even so, the horizontal shear force will be calculated and computed, according to **Eq. (27)**. Otherwise, when the ultimate behavior has been achieved by WPB, the horizontal shear force value will be used for the comparison between the calculation procedures. The results are discussed, considering symmetric sections, asymmetric sections and the analytical procedures, such as Ward [24], SCI P355 [19,25], Panedpojaman et al. [26] and Grilo et al [27].

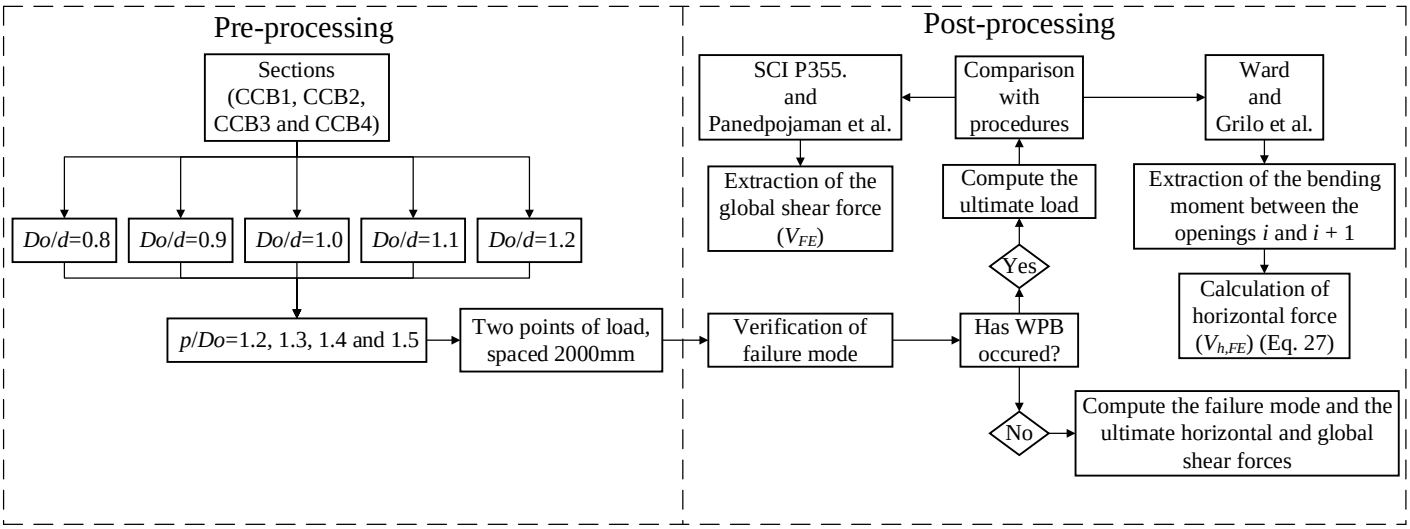

Fig. 15: Numerical models and methodology of analysis

6.1 SYMMETRIC SECTIONS

Regarding the behavior of the symmetric composite cellular sections, three points were monitored to investigate the behavior during the analyses: 25% and 50% of the applied load, and ultimate load.

Considering the cellular beams constituted by the parent section UB 406x140x39 with the D_o/d ratio equal to 0.8, in general, considering 25% of the applied external loading, there was no beginning of the steel yielding. The maximum stresses of von Mises were found close to the openings, in the region where there is a variation in the bending moment, close to the support. In addition, the slab was damaged in the region of the contact surfaces. With the value of 50% of the external loading applied, the cellular profile had already reached the yielding resistance, showing that in some regions they were already in plastic regime. In this scenario, the values of stresses in the shear connectors had already reached the yield strength. There was also an increase in the damaged area on the slab, in the region between two consecutive ribs close to the point of application of the loading. The upper part of the slab, close to the support, was also damaged, especially for situations in which the cellular beams had the end post width (b_{we}) greater than the width of the other web posts (b_w). Unlike the web post models presented by Panedpojaman [26], Grilo et al. [27], Tsavdaridis and D'Mello [30] and Tsavdaridis et al. [31], the analyzed models did not show a trend behavior. It is important to emphasize that the web post models, which were analyzed by the authors, do not consider the composite action, the number of shear connectors above

the opening, the concrete slab and the end post. In the present study, full models of composite cellular beams were simulated, that is, the end post, shear connector and concrete slab were considered. The end post has been shown to influence the resistant capacity of composite cellular beams. With the presence of the slab, shear connectors, and the end post, the analyses presented a different behavior from that observed in [26]. For example, according to the authors, the buckling shear strength increased with smaller value of D_o/d, and with larger value of p/D_o. The relations of the analyzed models are presented (**Fig. 16**).

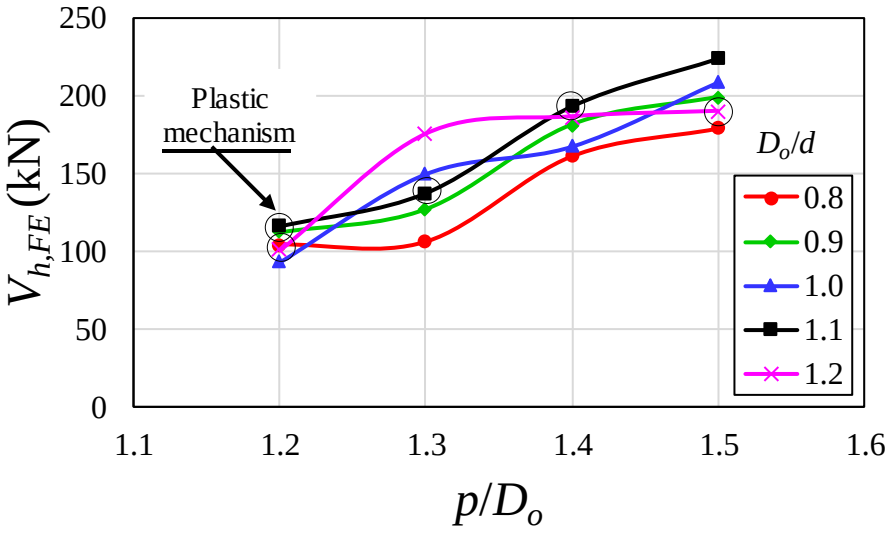

Fig. 16: Influence of the parameters on the shear strength for UB 406x140x39

In order to better verify the width effect of the end post width, a parameter that directly influences the formation of the plastic mechanism, **Tables 7-8** show the ultimate behaviors in relation to cellular beams and slabs, respectively. As shown in the illustrations, the WPB failure is a local phenomenon characterized by a lateral displacement with torsion and may occur due to the shear forces intensity. When the cellular beams are submitted to external loads, shear stress develops in the web post and bending tensions arise, which may cause the phenomenon. With the progression of loading until the composite cellular beams reach their ultimate strength, the maximum von Mises tension is found around the openings near to the support. The maximum stresses in the shear connector was 464MPa. The WPB was characterized for the composite cellular beams that showed the p/D_o=1.3, 1.4 and 1.5, although there were regions that started the formation of the plastic mechanism, according to the model that presented p/D_o=1.2 (**Fig. 17**).

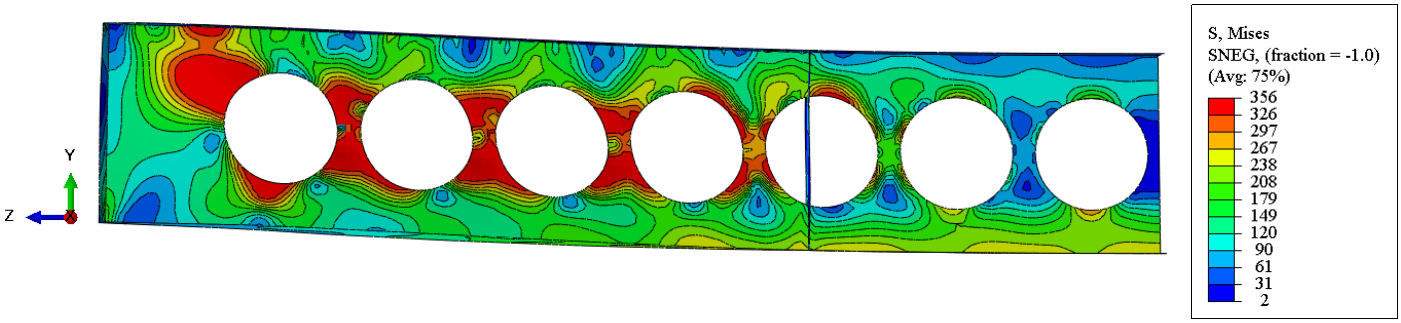

Fig. 17: Plastic mechanism, von Mises stresses in MPa

In the situations that were observed the WPB, there was the development of bending tensions in the web post. In general, all models presented null sliding values between the slab and the cellular profile. In this scenario of ultimate capacity, on the slab there was an increase in the damaged region between the ribs and in the upper part, close to the support. Donahey and Darwin [5] described that concrete cracking occurs due to deflections through the opening, with the progression of loading. In addition, near the ultimate strength, the concrete can develop transverse, longitudinal and diagonal cracks close to the opening region.

Regarding composite cellular beams with D_o/d=0.9, 1.0, 1.1 and 1.2, the behavior was similar to the previous situation. However, the von Mises stresses in the shear connectors were higher, but did not reach rupture, that is, the higher the D_o/d ratio, the greater the von Mises stresses in the shear connectors.

452

Table 7: UB 406x140x39 parent section, considering the section moment (SM)

D_o/d	p/D_o = 1.2	1.3	1.4	1.5
0.8	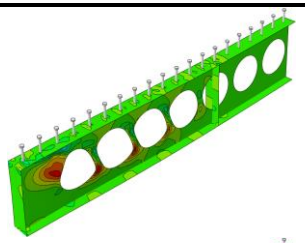	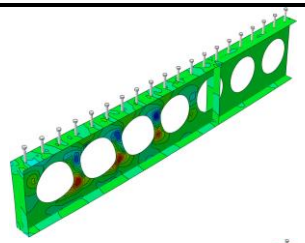	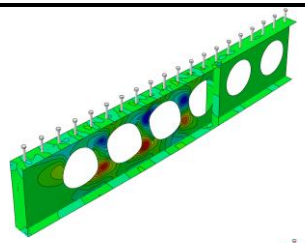	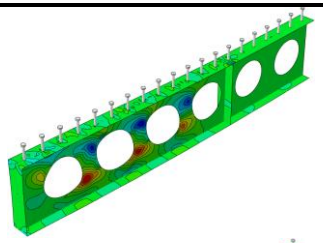
0.9	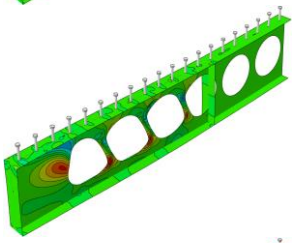	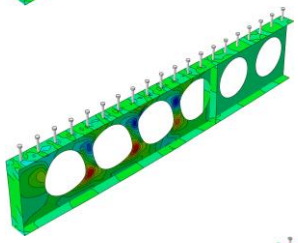	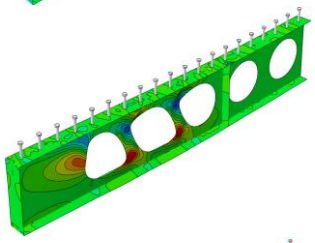	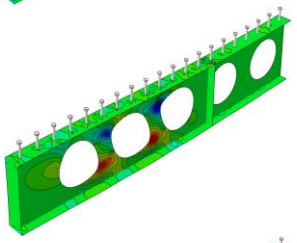
1.0	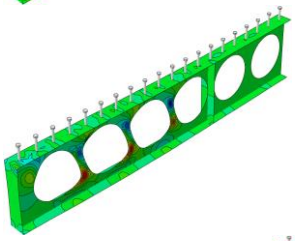	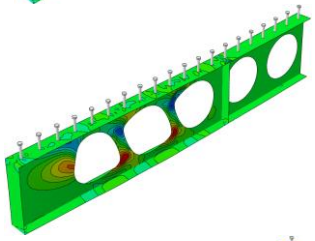	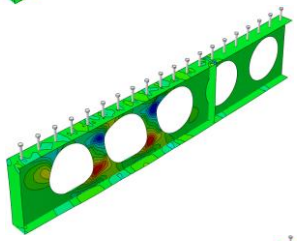	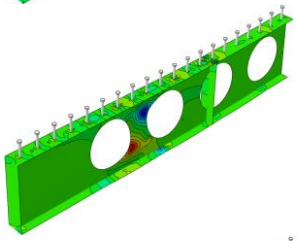
1.1	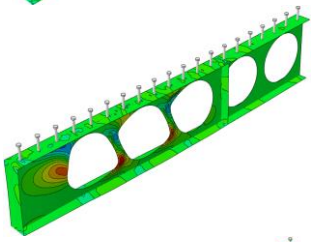	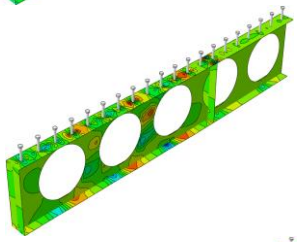	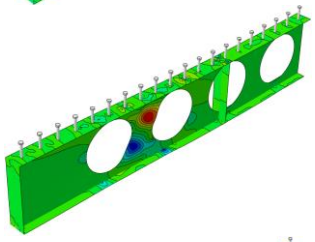	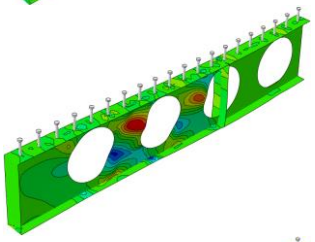
1.2	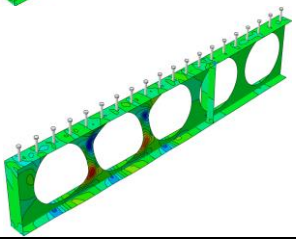	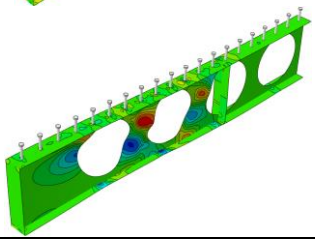	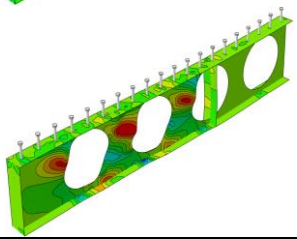	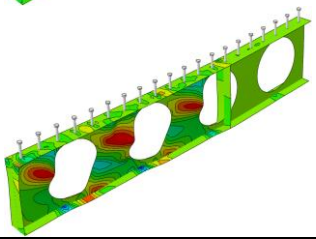

453

Table 8 – UB 406x140x39 parent section, considering the damage (DAMAGET)

D_o/d \ p/D_o	1.2	1.3	1.4	1.5
0.8	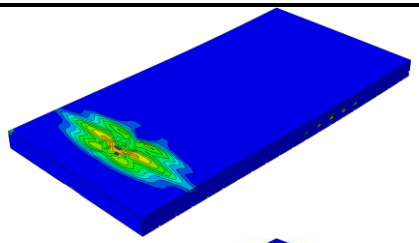	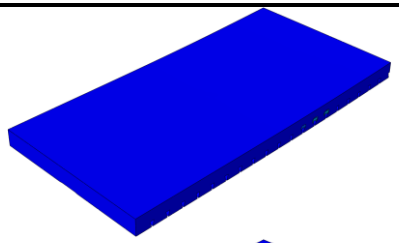	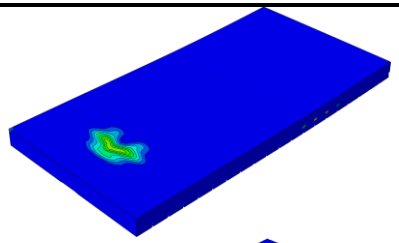	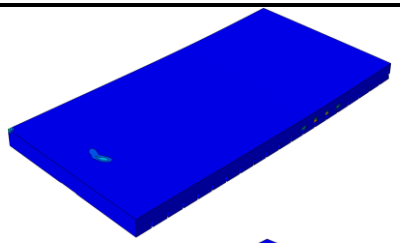
0.9	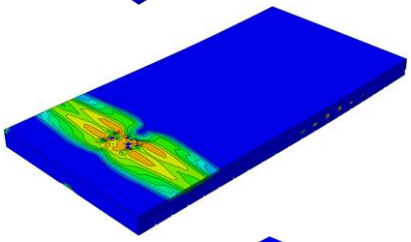	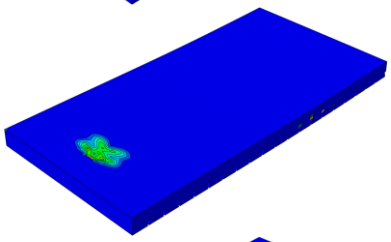	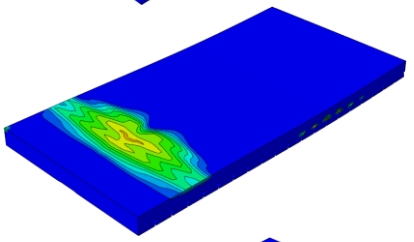	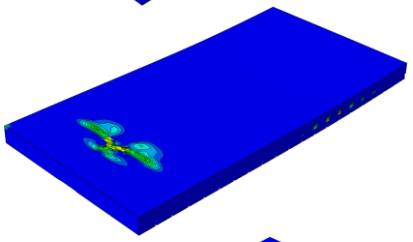
1.0	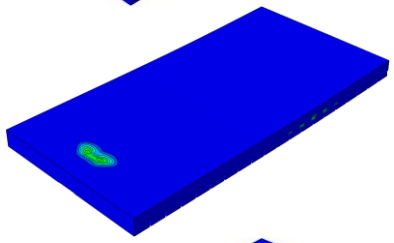	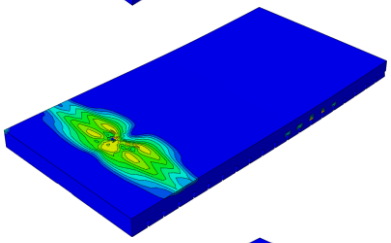	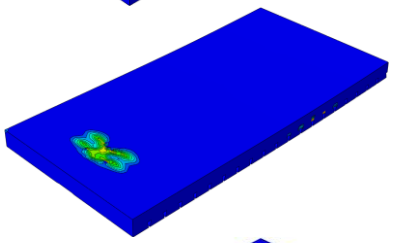	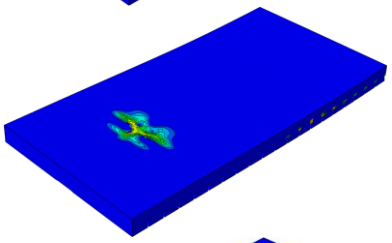
1.1	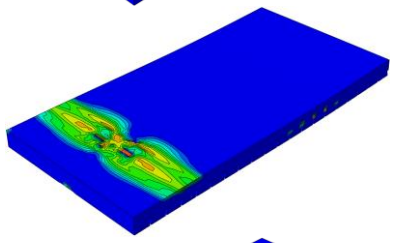	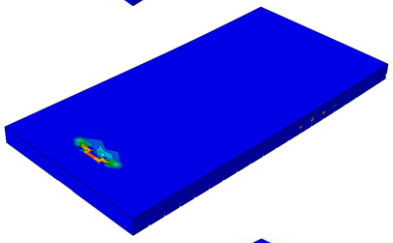	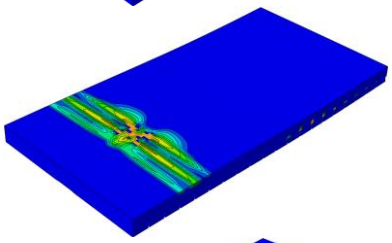	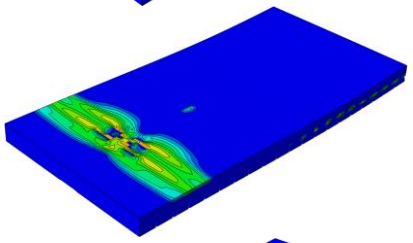
1.2	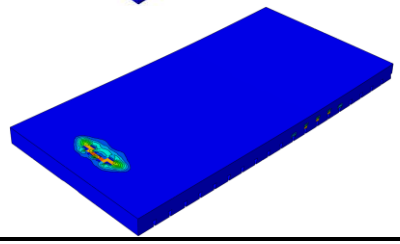	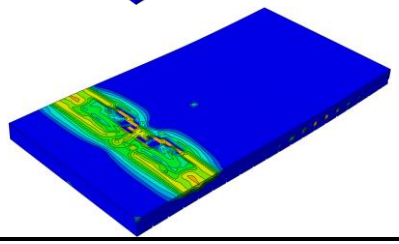	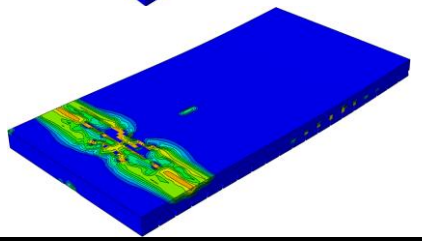	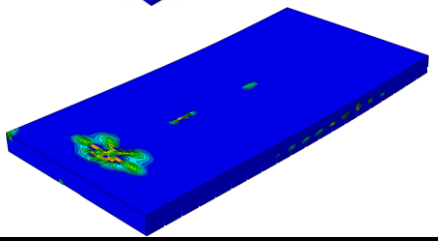

454

Considering the composite cellular beams formed by the parent section IPE 400, in some situations, considering 25% of the applied external loading, the steel had already reached the plastic regime in the openings close to the support, for the parameters D_o/d=0.8 and p/D_o=1.2, D_o/d=1.0 and p/D_o≥1.4, D_o/d=1.1 and p/D_o=1.3-1.5, and D_o/d=1.2 and p/D_o≥1.2. In this scenario, the slab was damaged, in the region between two consecutive ribs close to the loading application point, and also, at the upper edge, close to the support. With the loading progression at 50% of the applied external loading, the maximum von Mises stresses were found between the openings i=2-3, and i=3-4. Also, there was an increase in the damaged region. In the ribs, the damage started from the axis of the slab and spread to the ends. With the progression of the loading, until ultimate strength, the maximum von Mises stress was found around all the openings and web posts. In this scenario, the formation of the Vierendeel mechanism was observed, and the stresses in the shear connectors almost reached rupture. In particular, for the model D_o/d=1.1 and p/D_o=1.4, there was a rupture of the shear connector (**Fig. 18**). It is possible to reach this conclusion by relating the constitutive model of the shear connector, presented in section 4.1, with **Eq. (43)**.

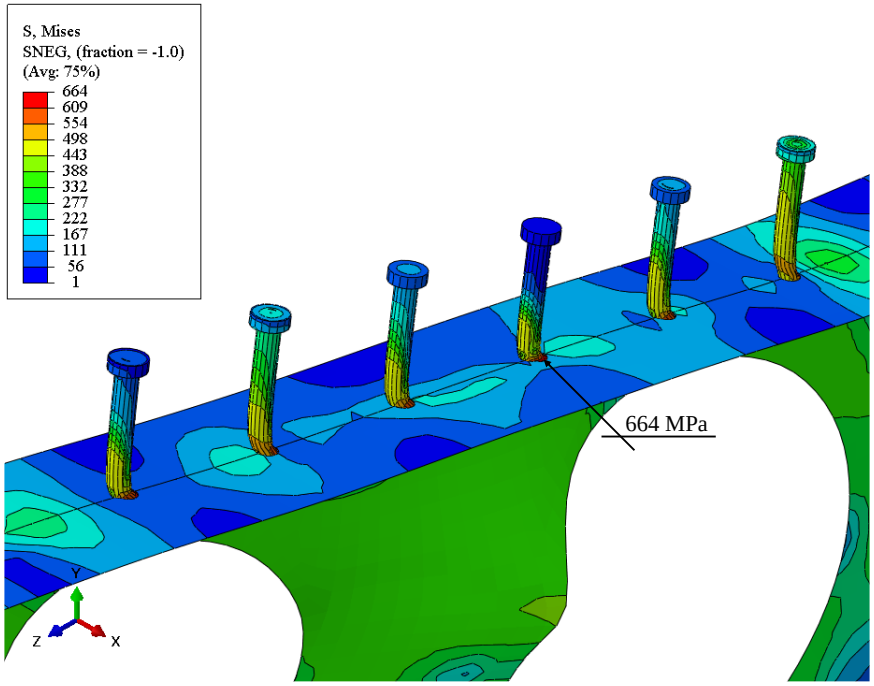

Fig. 18: Shear connector rupture, von Mises stresses (in MPa)

In general, the structure presented a low sliding value, almost null. In this context, there was an increase in the damaged area on the slab. As reported by Panedpojaman et al. [26], the compressed diagonal in the web post causes the WPB, and the yielding in the tee section causes failure by Vierendeel mechanism. In addition, it was also verified in these analyses that the web post width increases the resistance to the shear force, causing the resistant capacity to be reached by the formation of the plastic mechanism.

On the other hand, regarding the composite cellular beams that had their resistant capacity reached by WPB, the behavior was analogous to that previously presented. In **Fig. 19** the results are presented, and in **Tables 9-10** the final configuration of the simulated models.

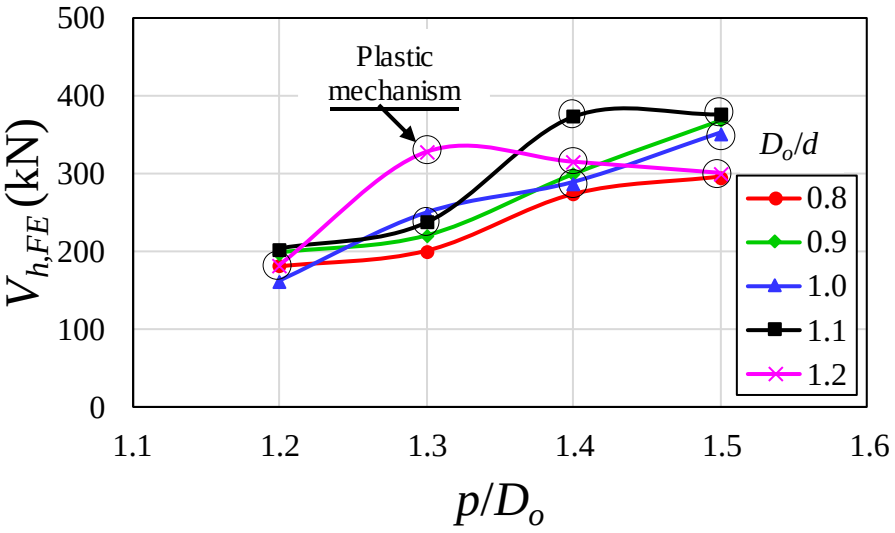

Fig. 19: Influence of the parameters on the shear strength for IPE 400

493

Table 9: IPE 400 parent section, considering the section moment (SM)

D_o/d	p/D_o = 1.2	1.3	1.4	1.5
0.8	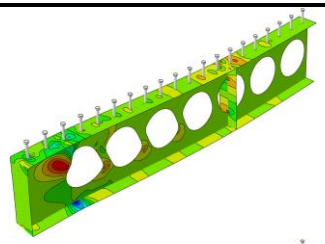	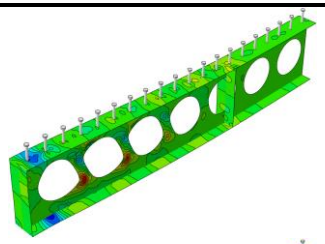	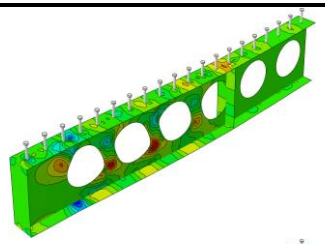	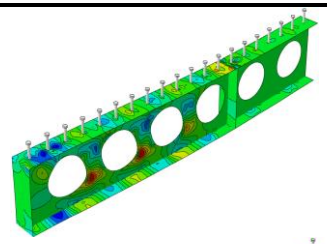
0.9	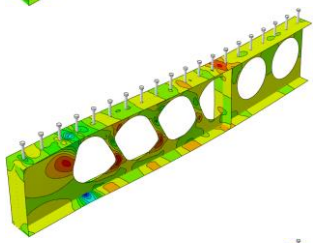	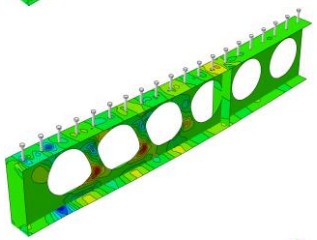	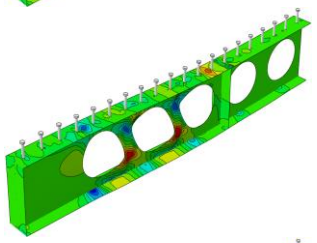	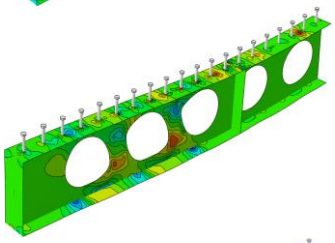
1.0	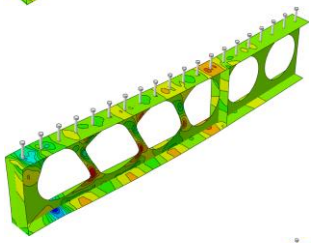	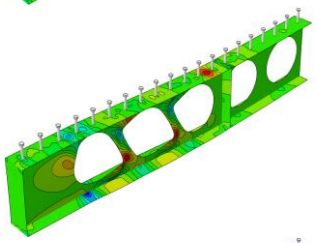	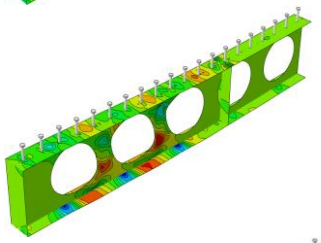	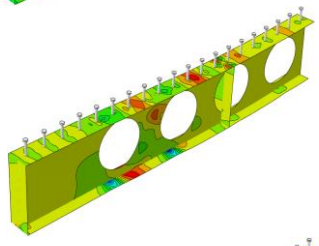
1.1	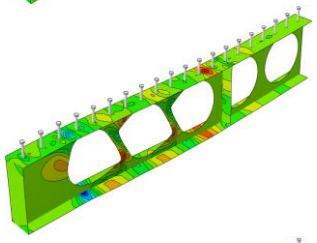	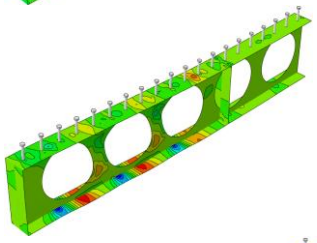	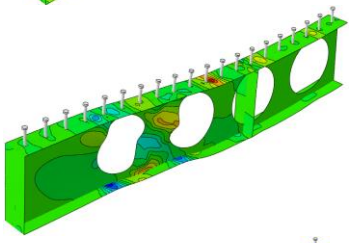	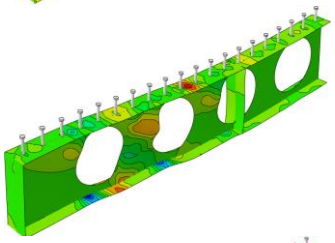
1.2	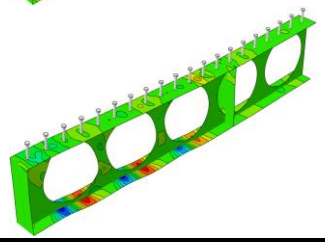	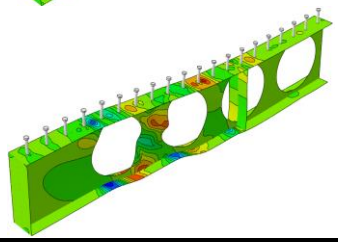	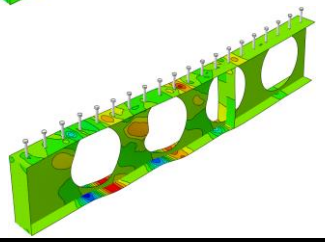	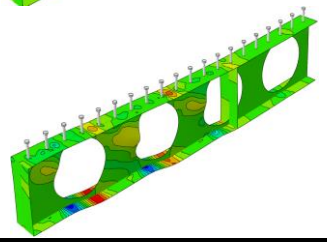

494

Table 10 – IPE 400 parent section, considering the damage (DAMAGET)

D_o/d	p/D_o = 1.2	1.3	1.4	1.5
0.8	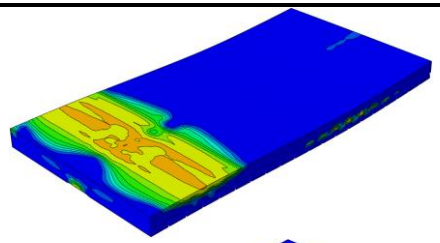	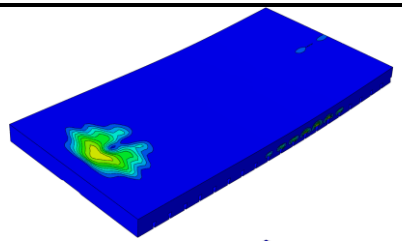	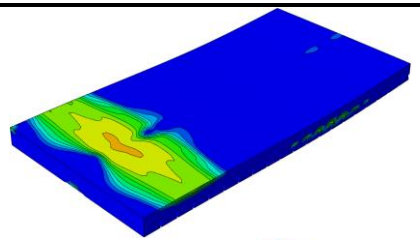	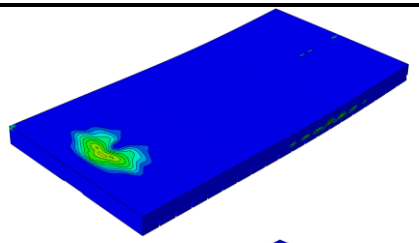
0.9	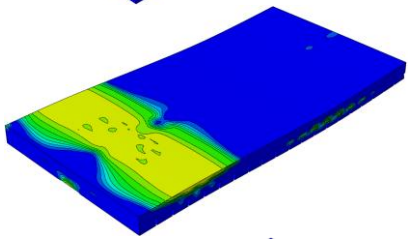	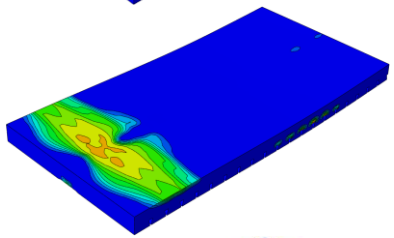	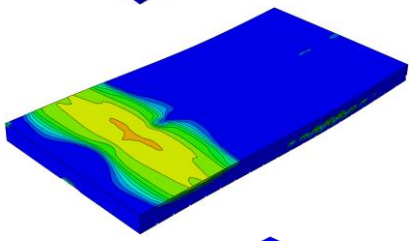	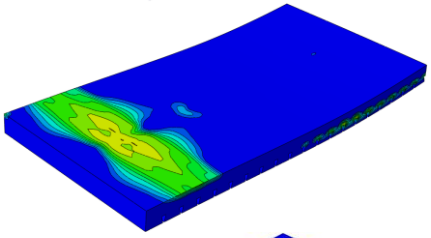
1.0	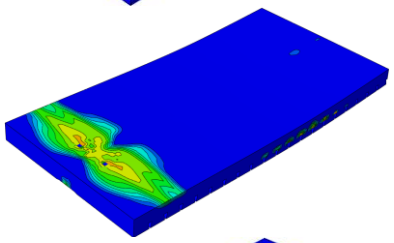	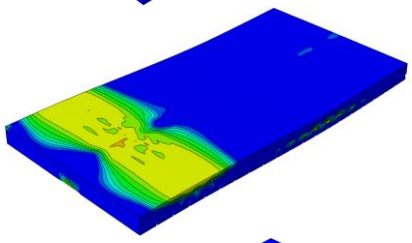	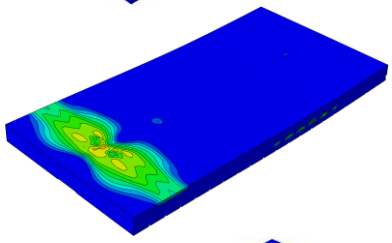	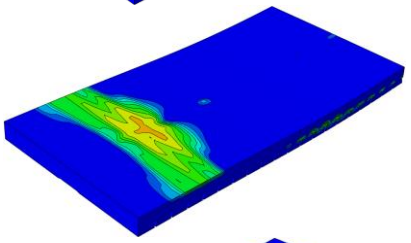
1.1	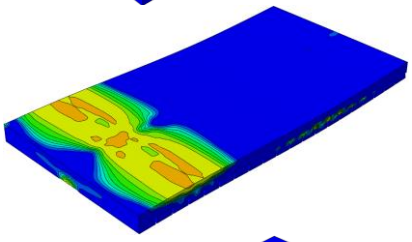	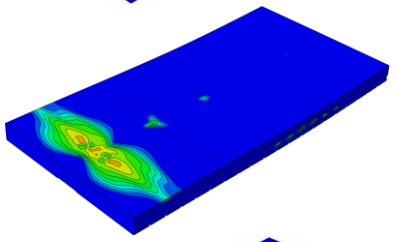	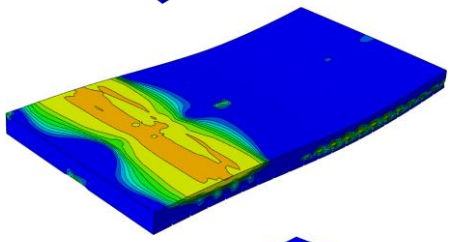	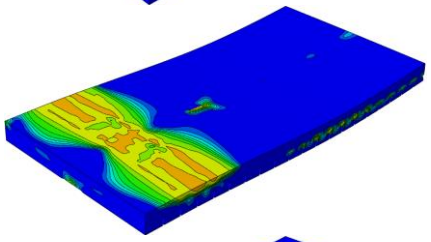
1.2	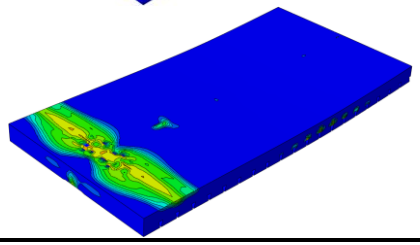	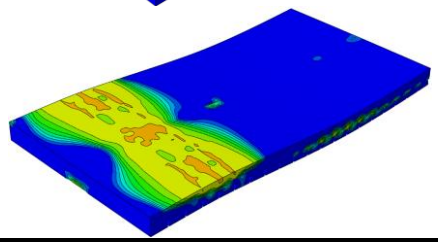	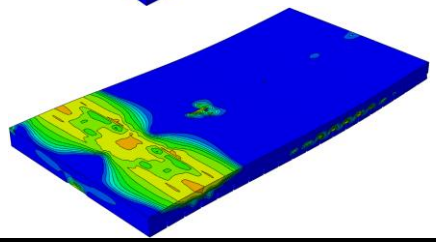	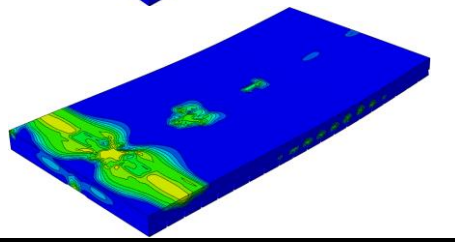

495

6.2 ASYMMETRIC SECTIONS

Regarding the behavior of the asymmetric composite cellular sections, three points were also monitored to investigate the behavior during the analyses, as previously presented.

Considering the cellular beams formed by parent sections UB 406x140x39 and UB 406x152x42 with D_o/d=0.8, for the loading prescribed in 25%, no resistance to yielding was achieved in any region of the cellular profile. The maximum stresses of von Vises were close to the opening i=2, close to the support region. In this scenario, the slab is damaged in the region of the contact surfaces. With the loading progression in 50%, for the beams that presented the ratio p/D_o=1.2, 1.3 and 1.4, the cellular profile had already reached the yield resistance, close to the openings i=2,3 and 4. The maximum von Mises stresses are found between the openings i=2-3, and i=3-4. In this loading step, the yielding of the shear connector started, and also, there was an increase in the damaged area in the region of the contact surfaces. On the other hand, in relation to the beam that presented the p/D_o=1.5 ratio, for this prescribed loading situation (50%), no resistance to yielding was achieved in any region of the cellular profile. The maximum von Mises stress was found around the openings i=1. With the progression of loading, until the composite cellular beams reach the ultimate behavior, in general the maximum von Mises stress was found close to the openings i=2-3. The maximum stress in the shear connector was equal to 465MPa. The ultimate strength, in general, was characterized by WPB, although there were regions that started the formation of the plastic mechanism. In general, the structures showed low slip values, almost null. In this context, the slab was damaged, in the region between two consecutive ribs close to the loading application point. The upper part of the slab, close to the support, was also damaged, mainly for the cellular beams that had the end post width (b_{we}) greater than the width of the others web post (b_w). Regarding the D_o/d beams equal to 0.9, 1.0, 1.1 and 1.2, the behavior was similar to the previous situation, considering symmetric sections. However, with the increase in the D_o/d ratio, for the loading prescribed in 50% of the loading applied, the cellular profile had not yet reached the yield resistance. **Fig. 20** shows the numerical response as a function of the geometric parameters of the cellular beams.

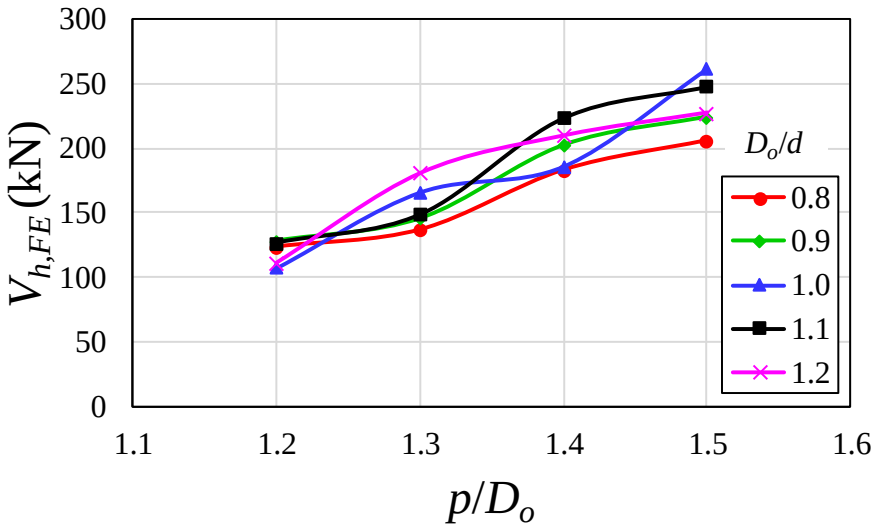

Fig. 20: Influence of the parameters on the shear strength for UB 406x140x39 and UB 406x152x42

As reported by Sheehan et al. [12], in the asymmetrical cellular sections, as the upper flange acts in conjunction with the slab, the lower part of the beam is formed by a more rigid section than the upper part, to improve the efficiency in flexural and shear resistance, presenting thus greater efficiency in resistance when compared to those with symmetry. **Tables 11-12** illustrate the ultimate behavior of cellular beams and slabs, respectively.

Table 11: UB 406x140x39 and UB 406x152x42 parent sections, considering the section moment (SM)

D_o/d	p/D_o = 1.2	1.3	1.4	1.5
0.8	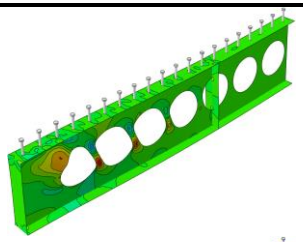	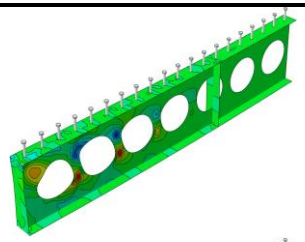	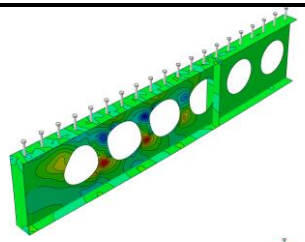	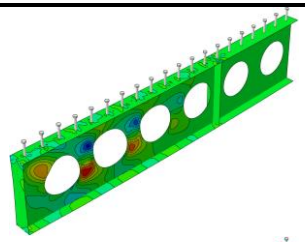
0.9	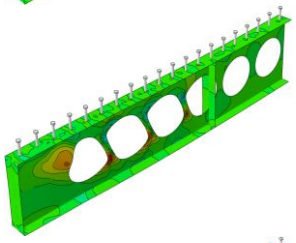	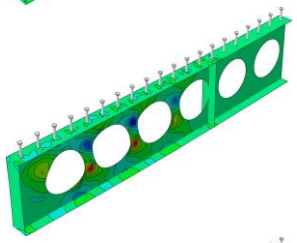	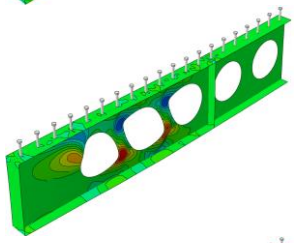	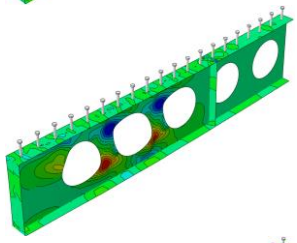
1.0	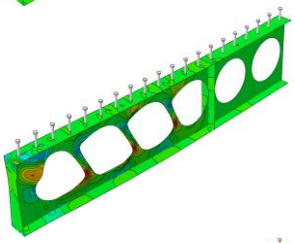	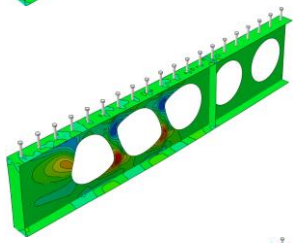	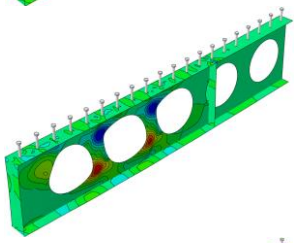	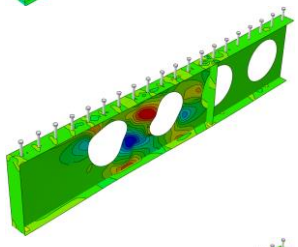
1.1	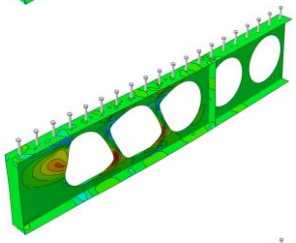	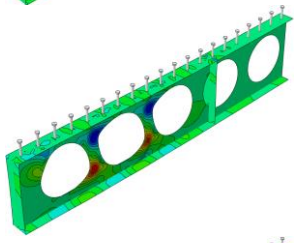	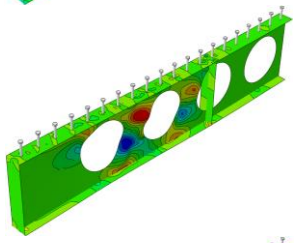	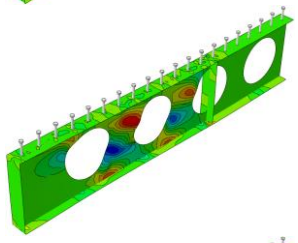
1.2	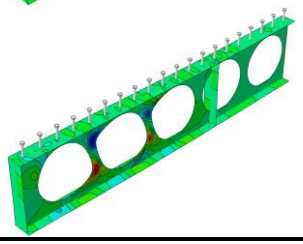	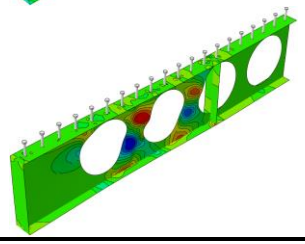	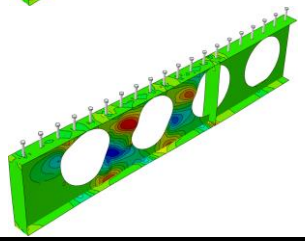	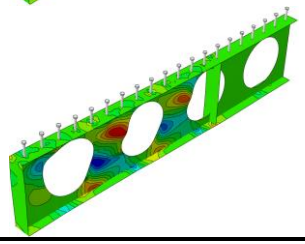

538

Table 12: UB 406x140x39 and UB 406x152x42 parent sections, considering the damage (DAMAGET)

D_o/d \ p/D_o	1.2	1.3	1.4	1.5
0.8	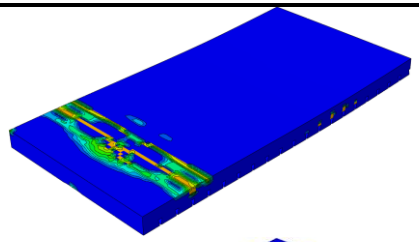	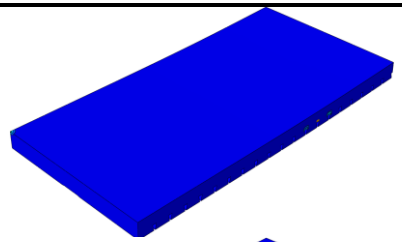	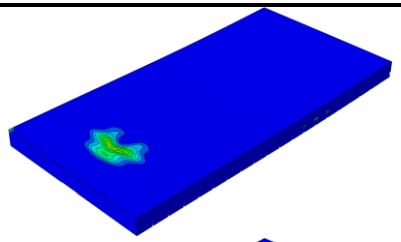	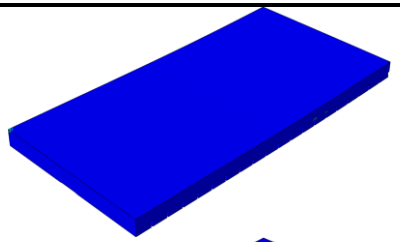
0.9	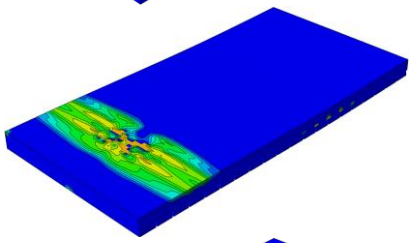	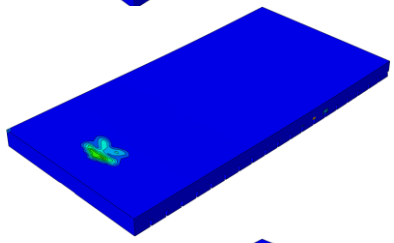	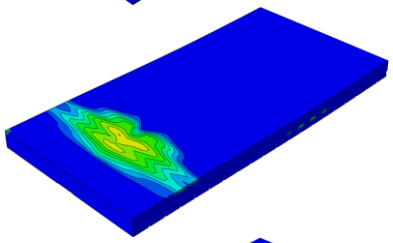	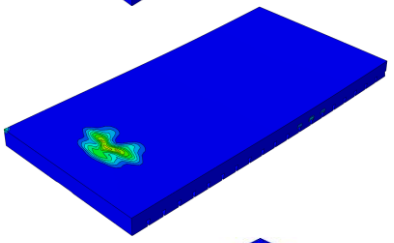
1.0	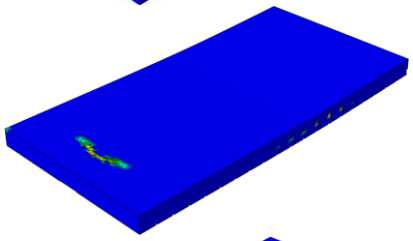	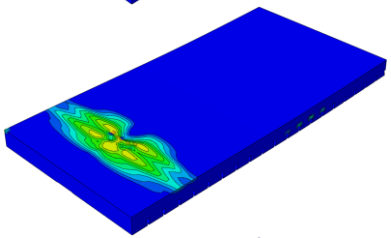	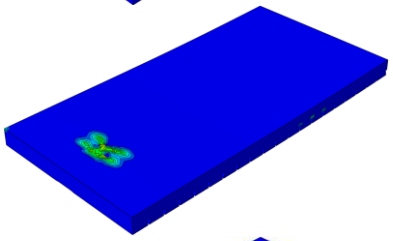	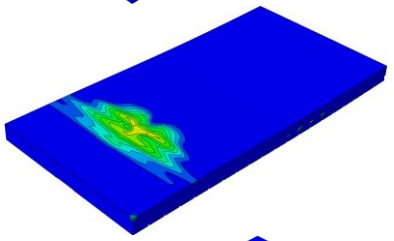
1.1	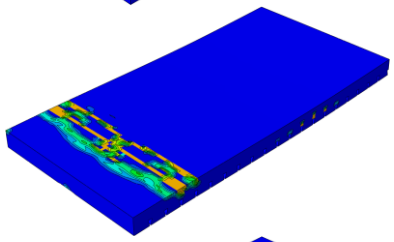	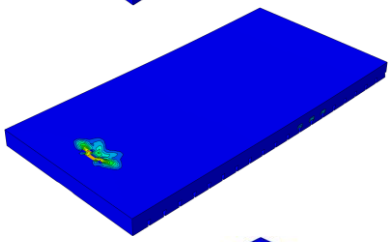	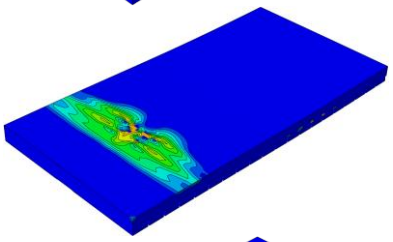	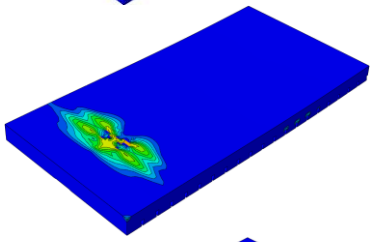
1.2	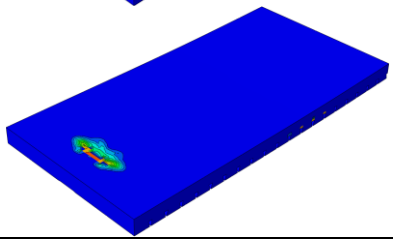	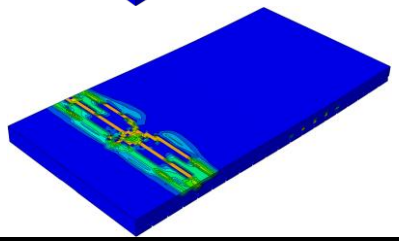	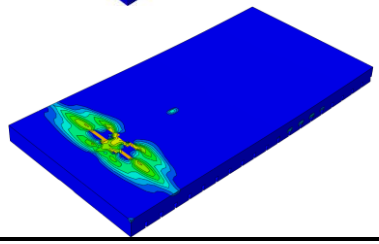	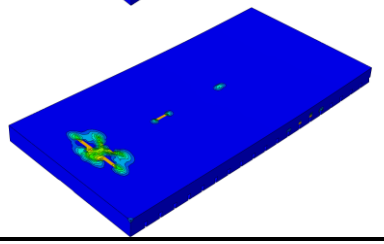

539

Regarding the cellular beams formed by the parent sections IPE 300 and HEB 340, the Vierendeel mechanism occurred in all situations. **Fig. 21** illustrates the behavior of the composite cellular beams with ratios D_o/d=1.2 and p/D_o=1.5. **Tables 13-14** illustrate the ultimate behavior of cellular beams and slabs, respectively.

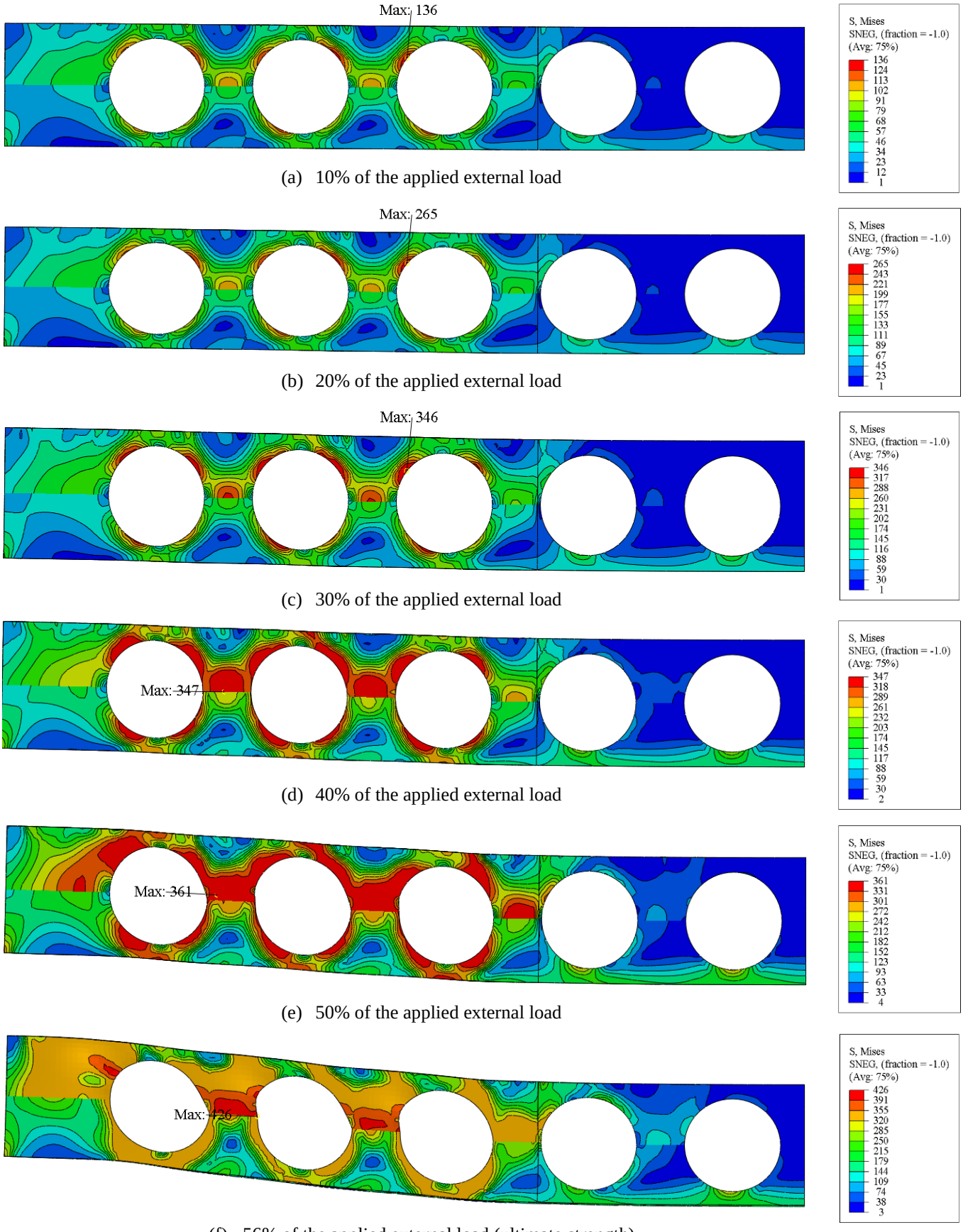

(a) 10% of the applied external load

(b) 20% of the applied external load

(c) 30% of the applied external load

(d) 40% of the applied external load

(e) 50% of the applied external load

(f) 56% of the applied external load (ultimate strength)

Fig. 21: Vierendeel mechanism (von Mises stresses in MPa)

Another important observation presented in **Fig. 21** is the distribution of stresses in the web post. In this context, the distribution of stresses occurs in a discontinuous way, since the cellular section is asymmetrical, formed by the profiles IPE 300 and HEB 340. In the case of **Fig. 21**, the asymmetric section shows the ratio of the area of the lower tee to the area of the upper tee approximately equal to 3. This means that when the ultimate behavior is defined by a plastic mechanism, for each loading increment, the stress level in the lower tee will be less than the stress level in the upper tee. Other examples are presented in **Fig. 22**. It can be seen in **Fig. 22a-b** that for symmetrical sections the stress distribution in the web post is continuous. On the other hand, according to **Fig. 22c**, which is a section that has a low degree of asymmetry, a situation in which the ratio of the area of the lower tee to area of the upper tee is approximately equal to 1.3, there are discontinuities in the distribution of stresses in the web post, although this discontinuity is less than in the situation shown in **Fig. 22d**. Thus, it is possible to conclude that the greater the degree of asymmetry of the cross section, the greater the discontinuity of stresses in the web post, due to the area of the lower tee being greater than the area of the upper tee. This proves the contribution of the lower tee in the ultimate behavior of composite cellular beams [12].

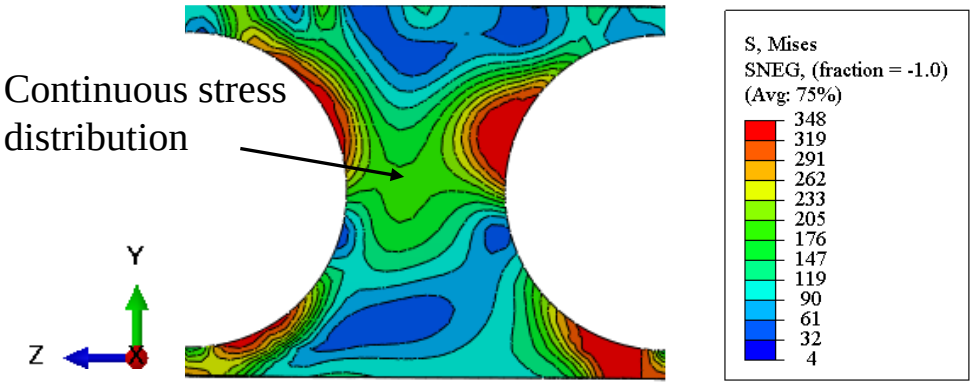

(a) Symmetrical section: UB 406x140x39

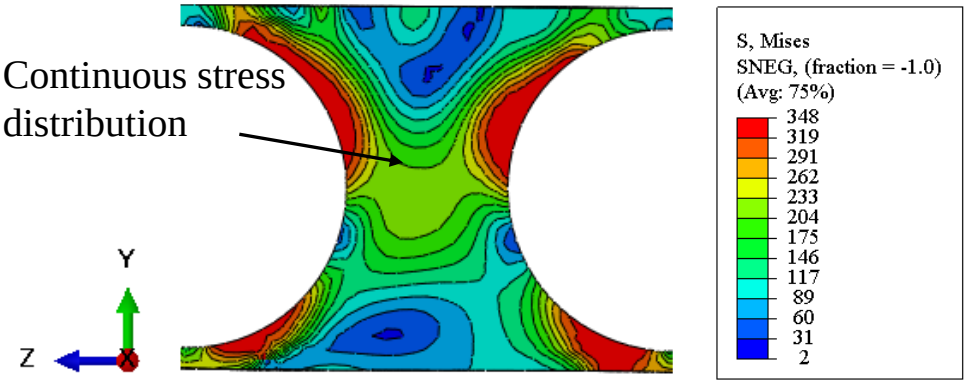

(b) Symmetrical section: IPE 400

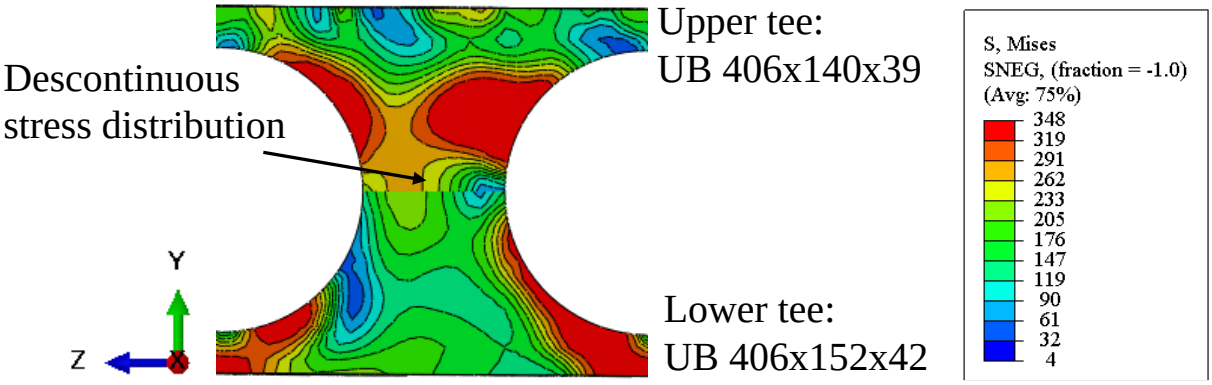

(c) Asymmetrical section: UB 406x140x39 and UB 406x152x42

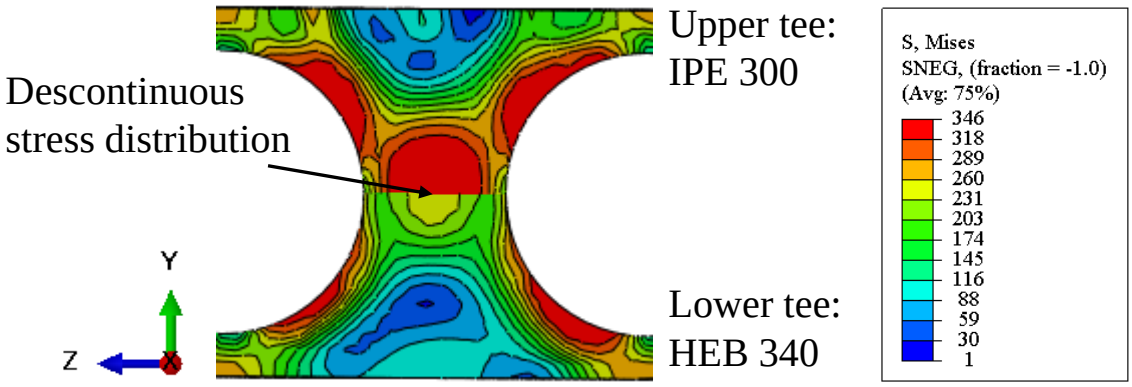

(d) Asymmetrical section: IPE 300 and HEB 340

575 **Fig. 22: Distribution of stresses in the web post, cellular beams with ratios D_o/d=1.2 and p/D_o=1.5 (von Mises**

576 **stresses in MPa)**

577

Table 13: IPE 300 and HEB 340 parent sections, considering the section moment (SM)

D_o/d	p/D_o = 1.2	1.3	1.4	1.5
0.8	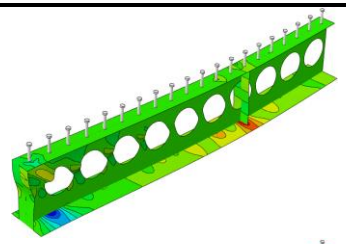	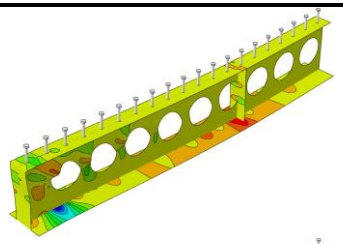	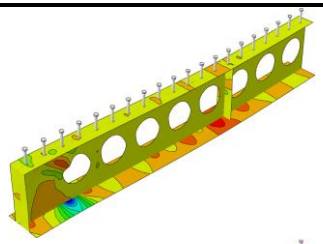	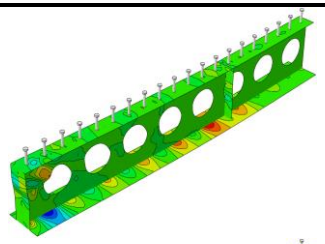
0.9	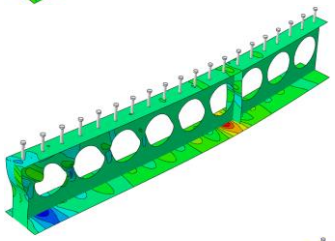	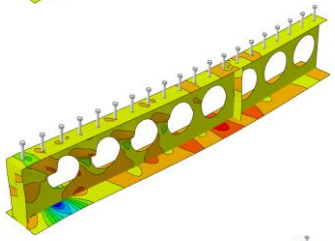	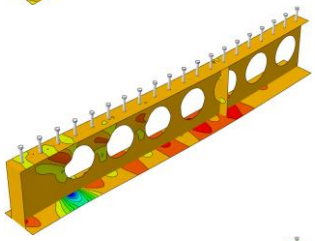	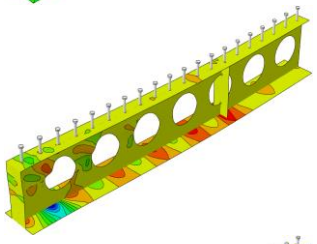
1.0	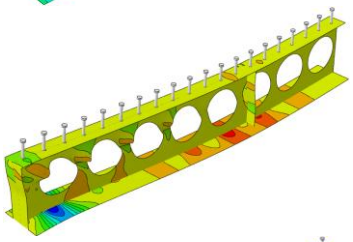	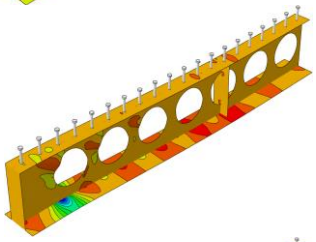	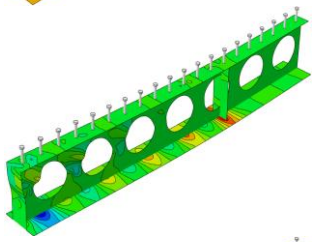	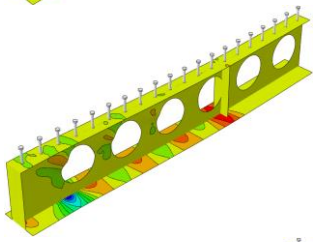
1.1	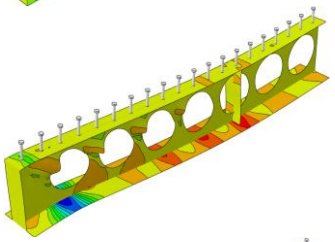	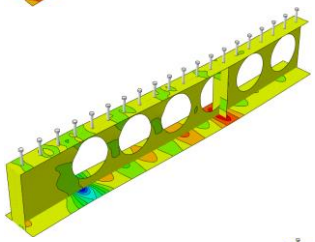	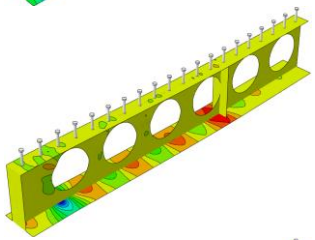	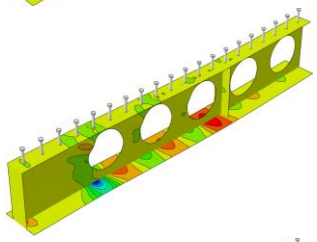
1.2	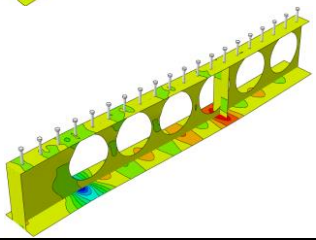	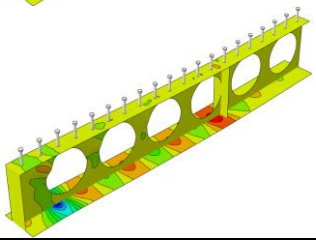	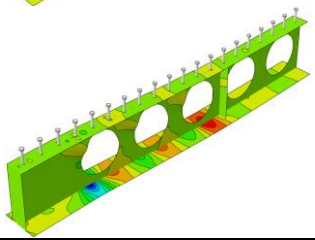	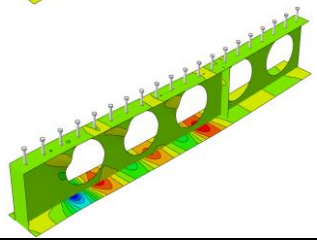

578

Table 14: IPE 300 and HEB 340 parent sections, considering the damage (DAMAGET)

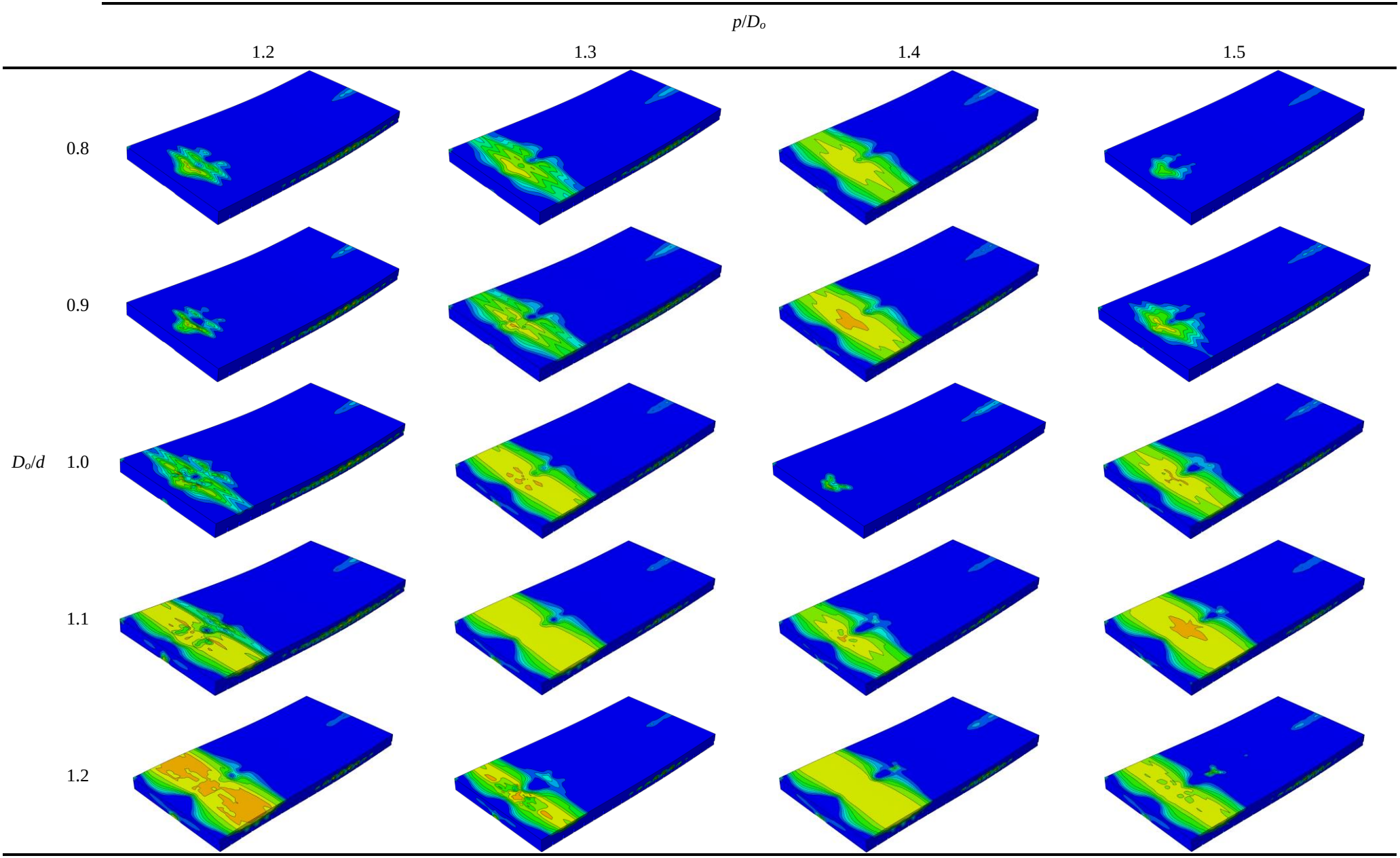

579

In relation to the sections that present the relation D_o/d=0.8, considering the prescribed loading in 25%, for all situations the cellular profile was already reached the yield strength, close to the openings, in the upper tee, since the area of the lower tee is three times larger than the area of the upper tee. In addition, the slab was damaged in the region between the contact surfaces. With the progression of loading, considering 50% of the prescribed loading, the yielding area increased, close to the openings i=2,3 and 4. The maximum stresses of von Mises are found between the openings i=2 and 3, and i=3 and 4. In this scenario, the shear connector also exhibited plastic behavior. In the slab, there was an increase in the damaged area, in the region between two consecutive ribs close to the loading application point. The upper part of the slab, close to the support, was also damaged. With the progression of loading, until the beams reached the resistant capacity, the maximum stress of von Mises was present around all the openings and web posts. In all situations, the shear connector rupture occurred, similar to that shown in **Fig. 18**. The failure was characterized by the formation of the plastic mechanism. In general, the structures presented low sliding values, almost null. In the ultimate behavior, in relation to the slab, there was an increase in the damaged area, in the region between two consecutive ribs close to the loading application point. The upper part of the slab, close to the support, was also damaged. Considering the cellular profiles that present the ratios D_o/d=0.9, 1.0, 1.1 and 1.2, the behavior was similar. However, for situations D_o/d=0.9 and p/D_o=1.2-1.5, D_o/d=1.0 and p/D_o=1.2, D_o/d=1.1 and p/D_o=1.5, there was the shear connector rupture. Next, in **Fig. 23**, the values of the forces developed in the web post are shown as a function of the ratio p/D_o.

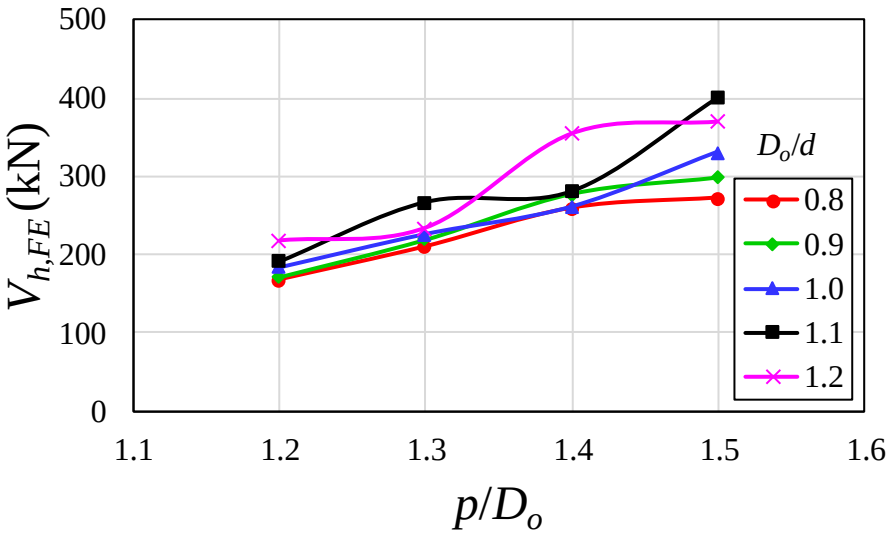

Fig. 23: Influence of the parameters on the shear strength for IPE 300 and HEB 340

6.3 SUMMARY OF RESULTS

The summary of results is presented in **Table 15**.

Table 15: Summary of results

Section	D_o/d_g	p/D_o	D_o/d	$V_{h,FE}$ (kN)	Failure	Section	D_o/d_g	p/D_o	D_o/d	$V_{h,FE}$ (kN)	Failure
UB 406x140x39	0.56	1.2	0.8	103.99	VM	UB 406x140x39 UB 406x152x42	0.51	1.2	0.8	123.72	WPB
	0.56	1.3	0.8	105.84	WPB		0.51	1.3	0.8	137.04	WPB
	0.56	1.4	0.8	161.12	WPB		0.51	1.4	0.8	183.48	WPB
	0.56	1.5	0.8	179.09	WPB		0.51	1.5	0.8	206.37	WPB
	0.63	1.2	0.9	112.63	VM		0.57	1.2	0.9	128.26	WPB
	0.63	1.3	0.9	127.45	WPB		0.57	1.3	0.9	145.77	WPB
	0.63	1.4	0.9	181.28	WPB		0.57	1.4	0.9	202.70	WPB
	0.63	1.5	0.9	198.84	WPB		0.57	1.5	0.9	224.69	WPB
	0.70	1.2	1.0	93.60	WPB		0.63	1.2	1.0	107.20	WPB
	0.70	1.3	1.0	150.08	WPB		0.63	1.3	1.0	166.01	WPB
	0.70	1.4	1.0	167.64	WPB		0.63	1.4	1.0	186.15	WPB
	0.70	1.5	1.0	208.67	WPB		0.63	1.5	1.0	261.97	WPB
	0.77	1.2	1.1	116.14	VM		0.70	1.2	1.1	126.74	WPB
	0.77	1.3	1.1	137.54	VM		0.70	1.3	1.1	148.82	WPB
	0.77	1.4	1.1	193.36	WPB		0.70	1.4	1.1	224.03	WPB
	0.77	1.5	1.1	224.07	WPB		0.70	1.5	1.1	248.46	WPB
	0.83	1.2	1.2	101.03	WPB		0.76	1.2	1.2	111.73	WPB
	0.83	1.3	1.2	175.32	WPB		0.76	1.3	1.2	180.90	WPB
	0.83	1.4	1.2	186.32	VM		0.76	1.4	1.2	209.98	WPB
	0.83	1.5	1.2	189.80	VM		0.76	1.5	1.2	227.69	WPB
IPE 400	0.58	1.2	0.8	181.81	VM	IPE 300 HEB 340	0.50	1.2	0.8	167.80	VM*
	0.58	1.3	0.8	201.81	WPB		0.50	1.3	0.8	210.23	VM*
	0.58	1.4	0.8	274.29	WPB		0.50	1.4	0.8	259.56	VM*
	0.58	1.5	0.8	296.56	WPB		0.50	1.5	0.8	272.48	VM*
	0.65	1.2	0.9	198.94	WPB		0.56	1.2	0.9	171.86	VM*
	0.65	1.3	0.9	220.97	WPB		0.56	1.3	0.9	219.64	VM
	0.65	1.4	0.9	300.18	WPB		0.56	1.4	0.9	278.07	VM
	0.65	1.5	0.9	369.25	WPB		0.56	1.5	0.9	298.98	VM*
	0.72	1.2	1.0	162.18	WPB		0.62	1.2	1.0	184.22	VM*
	0.72	1.3	1.0	249.66	WPB		0.62	1.3	1.0	226.31	VM
	0.72	1.4	1.0	288.92	VM		0.62	1.4	1.0	260.99	VM
	0.72	1.5	1.0	352.29	VM		0.62	1.5	1.0	330.31	VM
	0.79	1.2	1.1	204.49	WPB		0.68	1.2	1.1	191.88	VM
	0.79	1.3	1.1	238.10	VM		0.68	1.3	1.1	267.90	VM
	0.79	1.4	1.1	374.75	VM*		0.68	1.4	1.1	281.77	VM
	0.79	1.5	1.1	377.75	VM		0.68	1.5	1.1	401.45	VM*
	0.86	1.2	1.2	183.43	VM		0.74	1.2	1.2	218.20	VM
	0.86	1.3	1.2	328.09	VM		0.74	1.3	1.2	234.74	VM
	0.86	1.4	1.2	315.36	VM		0.74	1.4	1.2	355.79	VM
	0.86	1.5	1.2	301.07	VM		0.74	1.5	1.2	371.13	VM

*Shear connector rupture was observed.

6.4 COMPARASION WITH ANALYTICAL PROCEDURES

All the composite cellular beams analyzed are within the ranges $1.1 \leq p/D_o \leq 1.5$, $0.8 \leq D_o/d \leq 1.2$, and $0.5 \leq D_o/d_g \leq 0.86$. In this section, the results of the numerical modeling that reached the ultimate behavior by WPB are compared with the calculation procedures by analytical/numerical ratio (**Fig. 24**).

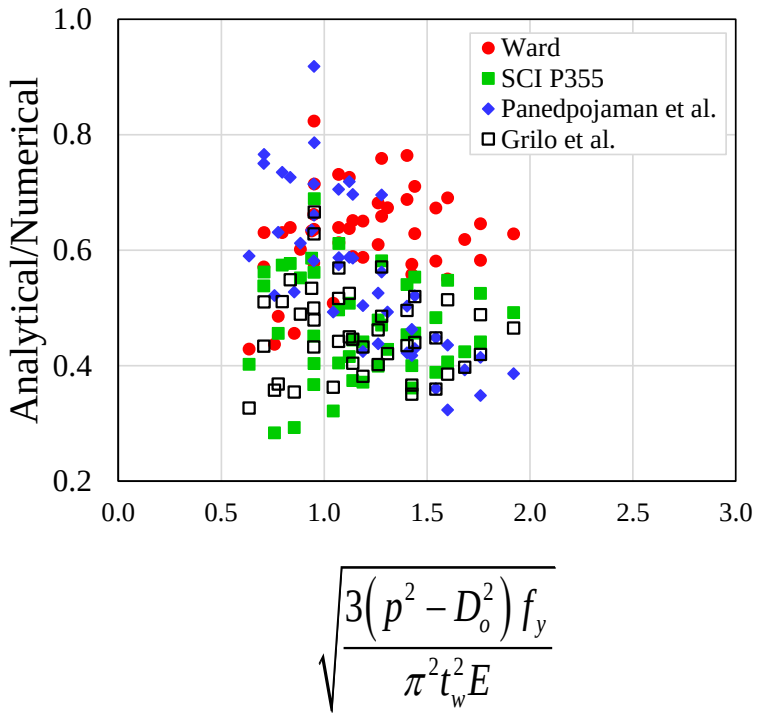

Fig. 24: Comparison between analytical procedures and numerical results

Considering the procedure prescribed by Ward [24], which meets the intervals $1.08 \leq p/D_o \leq 1.5$ and $0.57 \leq D_o/d_g \leq 0.80$, conservative results were presented in all situations. The procedure in question obtained an average, standard deviation and variance equal to 0.63, 8.29% and 0.69%, respectively. In this case, it is observed that the maximum and minimum relative error presented were 57% and 18%, respectively. Regarding the procedure by SCI P355 [19,25], which meets the range $1.2 \leq p/D_o \leq 2.0$, the results presented were more conservative than Ward's procedure [24], with average, standard deviation and variance equal to 0.47, 8.91% and 0.69%, respectively. In this situation, the maximum and minimum relative errors presented were 72% and 31%, respectively.

On the other hand, on the adapted formulation of Panedpojaman et al. [26], which meets the range $1.1 \leq p/D_o \leq 1.8$ and $0.8 \leq D_o/d \leq 1.2$, the results presented were less conservative than the procedure by SCI P355 [19,25]. However, when compared to the Ward procedure [24], Panedpojaman et al.'s model [26], was more conservative. This calculation model obtained an average value, standard deviation and variance equal to 0.56, 13.79% and 1.90%, respectively. The value of the standard deviation presented is in agreement with the value presented by Panedpojaman et al. [26], when the authors compared their analytical model with tests. The authors reported the shear strength was underestimated by up to 53% for small values of D_o/d and p/D_o. The maximum and minimum relative error presented were 68% and 8%, respectively. Finally, regarding the formulation of Grilo et al. [27], which is applied for the $1.1 \leq p/D_o \leq 1.5$ and $0.5 \leq D_o/d_g \leq 0.8$, the results presented were also conservative. According to the procedure, the

628 average, standard deviation and variance were equal to 0.46, 7.63% and 0.58%, respectively. The maximum and minimum relative
629 error presented were 67% and 33%, respectively. The statistical analyses are shown in **Fig. 25**.

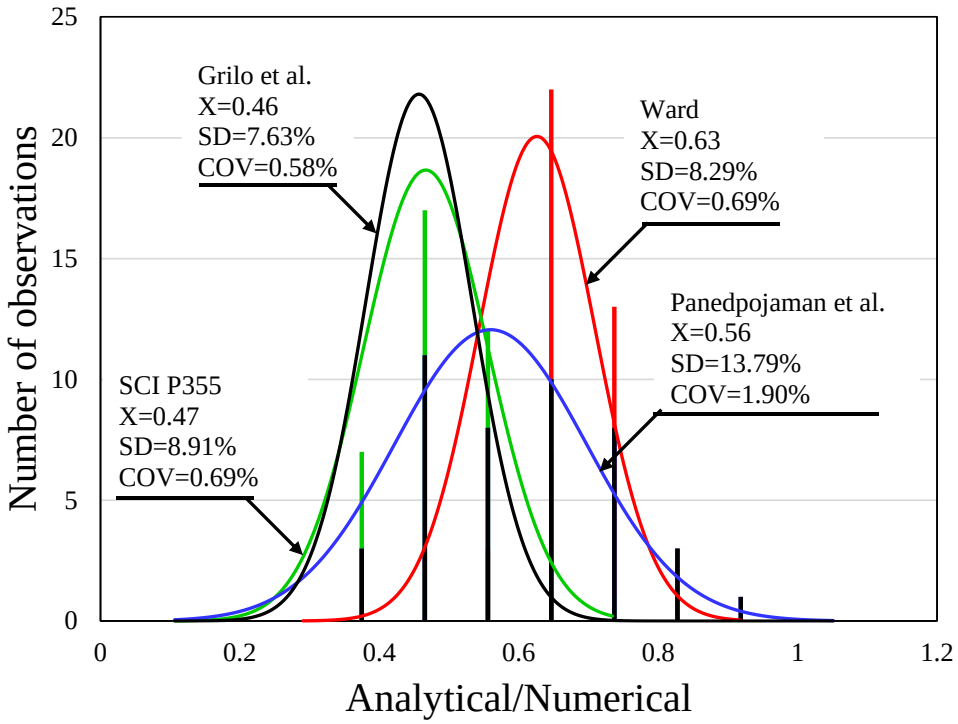

630

631 **Fig. 25: Statistical analysis**

632 As shown, all the procedures mentioned underestimate the WPB resistance of composite cellular beams. According to the
633 analyses carried out, it was possible to conclude that both the presence of the concrete slab and the end post width contributed to
634 the WPB resistance. The calculation models presented do not consider the contribution of these two factors. As observed in the
635 analyses carried out in the present work, this increase in length generated an increase in the strength of the composite cellular beams,
636 a factor that differs from the models that consider only the web post model.

637 **CONCLUSIONS**

638 This paper investigated the strength of steel-concrete composite cellular beams, considering the web post buckling. A
639 parametric study was carried out. The ratios p/D_o and D_o/d were varied. Asymmetric and symmetric sections were investigated. The
640 results were compared with existing analytical procedures. It was concluded:

641 1. For symmetric sections, the Virendeel mechanism was characterized for the ratios p/D_o=1.2 and D_o/d=0.8, p/D_o=1.2 and
642 D_o/d=0.9, p/D_o=1.4, 1.5 and D_o/d=1.0, p/D_o=1.2, 1.3, 1.4, 1,5 and D_o/d=1.1, and p/D_o=1.2, 1.3, 1.4, 1.5 and D_o/d=1.2. For the
643 other ratios, web post buckling was characterized;
644 2. For the section with a low degree of asymmetry, for all situations (p/D_o=1.2, 1.3, 1.4 and 1.5; D_o/d=0.8, 0.9, 1.0, 1.1 and 1.2),
645 the ultimate behavior was characterized by web post buckling;

3. For the section with a high degree of asymmetry, for all situations (p/D_o=1.2, 1.3, 1.4 and 1.5; D_o/d=0.8, 0.9, 1.0, 1.1 and 1.2), the ultimate behavior was reached by the Vierendeel mechanism. In addition, when the ultimate behavior is governed by the formation of the plastic mechanism, the shear connector rupture can occur;
4. The end post width and the concrete slab contributed significantly to the ultimate behavior of composite cellular beams;
5. The greater the end post width, the greater the damaged area on the slab;
6. In general, the relative slips between the slab and the cellular profile were almost null;
7. The analytical procedures underestimate the web post buckling resistance of composite cellular beams;

ACKNOWLEDGMENTS

This work was supported by the São Paulo Research Foundation (FAPESP) [grant number #2018/22803-1].

REFERENCES

[1] ArcelorMittal, ACB® and Angelina® beams - A New Generation of Cellular Beams, (2018).

[2] D. Darwin, R.C. Donahey, LRFD for composite beams with unreinforced web openings, J. Struct. Eng. 114 (1988) 535–552. doi:10.1061/(ASCE)0733-9445(1988)114:3(535).

[3] W.C. Clawson, D. Darwin, Composite beams with web openings, University of Kansas, Lawrence, 1980.

[4] F.D. Queiroz, P.C.G.S. Vellasco, D.A. Nethercot, Finite element modelling of composite beams with full and partial shear connection, J. Constr. Steel Res. 63 (2007) 505–521. doi:10.1016/j.jcsr.2006.06.003.

[5] R.C. Donahey, D. Darwin, Web openings in composite beams with ribbed slabs, J. Struct. Eng. 114 (1988) 518–534. doi:10.1061/(ASCE)0733-9445(1988)114:3(518).

[6] K.M. El-Sawy, A.M.I. Sweedan, M.I. Martini, Moment gradient factor of cellular steel beams under inelastic flexure, J. Constr. Steel Res. 98 (2014) 20–34. doi:10.1016/j.jcsr.2014.02.007.

[7] E. Ellobody, Nonlinear analysis of cellular steel beams under combined buckling modes, Thin-Walled Struct. 52 (2012) 66–79. doi:10.1016/j.tws.2011.12.009.

[8] P. Panedpojaman, W. Sae-Long, T. Chub-Uppakarn, Cellular beam design for resistance to inelastic lateral-torsional buckling, Thin-Walled Struct. 99 (2016) 182–194. doi:10.1016/j.tws.2015.08.026.

[9] R.G. Redwood, P.K. Wong, Web holes in composite beams with steel deck, (1982) 41.

[10] R.G. Redwood, G. Poumbouras, Tests of composite beams with web holes, Can. J. Civ. Eng. 10 (1983) 713–721. doi:10.1139/l83-100.

[11] J.W. Park, C.H. Kim, S.C. Yang, Ultimate Strength of Ribbed Slab Composite Beams with Web Openings, J. Struct. Eng. 129 (2003) 810–817. doi:10.1061/(asce)0733-9445(2003)129:6(810).

[12] T. Sheehan, X. Dai, D. Lam, E. Aggelopoulos, M. Lawson, R. Obiala, Experimental study on long spanning composite cellular beam under flexure and shear, J. Constr. Steel Res. 116 (2016) 40–54. doi:10.1016/j.jcsr.2015.08.047.

[13] K.D. Tsavdaridis, C. D'Mello, Vierendeel Bending Study of Perforated Steel Beams with Various Novel Web Opening Shapes through Nonlinear Finite-Element Analyses, J. Struct. Eng. 138 (2012) 1214–1230. doi:10.1061/(asce)st.1943-541x.0000562.

[14] F. Erdal, M.P. Saka, Ultimate load carrying capacity of optimally designed steel cellular beams, J. Constr. Steel Res. 80 (2013) 355–368. doi:10.1016/j.jcsr.2012.10.007.

[15] K.F. Chung, T.C.H. Liu, A.C.H. Ko, Investigation on vierendeel mechanism in steel beams with circular web openings, J. Constr. Steel Res. 57 (2001) 467–490. doi:10.1016/S0143-974X(00)00035-3.

[16] P. Panedpojaman, T. Rongram, Design Equations for Vierendeel Bending of Steel Beams with Circular Web Openings, World Congr. Eng. 2014. II (2014) 0–5.

[17] D. Kerdal, D.A. Nethercot, Failure modes for castellated beams, J. Constr. Steel Res. 4 (1984) 295–315. doi:10.1016/0143-974X(84)90004-X.

[18] R. Redwood, S.H. Cho, Design of steel and composite beams with web openings, J. Constr. Steel Res. 25 (1993) 23–41. doi:10.1016/0143-974X(93)90050-3.

[19] R.M. Lawson, J. Lim, S.J. Hicks, W.I. Simms, Design of composite asymmetric cellular beams and beams with large web openings, J. Constr. Steel Res. 62 (2006) 614–629. doi:10.1016/j.jcsr.2005.09.012.

[20] R.M. Lawson, J.B.P. Lim, S.O. Popo-Ola, Pull-out forces in shear connectors in composite beams with large web openings, J. Constr. Steel Res. 87 (2013) 48–59. doi:10.1016/j.jcsr.2013.03.025.

[21] V. Akrami, S. Erfani, Review and Assessment of Design Methodologies for Perforated Steel Beams, J. Struct. Eng. 142 (2016) 04015148. doi:10.1061/(ASCE)ST.1943-541X.0001421.

[22] Proposed Specification for Structural Steel Beams with Web Openings, J. Struct. Eng. 118 (1992) 3315–3324. doi:10.1061/(ASCE)0733-9445(1992)118:12(3315).

[23] K.F. Chung, C.H. Liu, A.C.H. Ko, Steel beams with large web openings of various shapes and sizes: an empirical design method using a generalised moment-shear interaction curve, J. Constr. Steel Res. 59 (2003) 1177–1200. doi:10.1016/S0143-974X(03)00029-4.

[24] J.K. Ward, Design of Composite and Non-Composite Cellular Beams, Steel Construction Institute, Silwood Park, Ascot, UK, 1990.

[25] R.M. Lawson, S.J. Hicks, Design of beams with large web openings, The Steel Construction Institute, 2011.

[26] P. Panedpojaman, T. Thepchatri, S. Limkatanyu, Novel design equations for shear strength of local web-post buckling in cellular beams, Thin-Walled Struct. 76 (2014) 92–104. doi:10.1016/j.tws.2013.11.007.

[27] L.F. Grilo, R.H. Fakury, A.L.R. de Castro e Silva, G. de S. Veríssimo, Design procedure for the web-post buckling of steel cellular beams, J. Constr. Steel Res. 148 (2018) 525–541. doi:10.1016/j.jcsr.2018.06.020.

[28] Sameer S. Fares, J. Coulson, David W. Dinehart, Castellated and Cellular Beam Design 31, Am. Inst. Steel Constr. (2016).

[29] M. Abambres, K. Rajana, K. Tsavdaridis, T. Ribeiro, Neural Network-Based Formula for the Buckling Load Prediction of I-Section Cellular Steel Beams, Computers. 8 (2018) 2. doi:10.3390/computers8010002.

[30] K.D. Tsavdaridis, C. D'Mello, Web buckling study of the behaviour and strength of perforated steel beams with different novel web opening shapes, J. Constr. Steel Res. 67 (2011) 1605–1620. doi:10.1016/j.jcsr.2011.04.004.

[31] K.D. Tsavdaridis, G. Galiatsatos, Assessment of cellular beams with transverse stiffeners and closely spaced web openings, Thin-Walled Struct. 94 (2015) 636–650. doi:10.1016/j.tws.2015.05.005.

[32] C.J. Granade, An investigation of composite beams having large rectangular openings in their webs, 1968. Partial M.Sc. thesis. University of Alabama, 1968.

[33] W.C. Clawson, D. Darwin, Tests of composite beams with web openings, ASCE J. Struct. Div. 108 (1982) 145–162.

[34] S.H. Cho, An investigation on the strength of composite beams with web openings, 1982. M.Sc. thesis. Hanyang University, 1982.

[35] D.M. Todd, P.B. Cooper, Strength of composite beams with web openings, ASCE J. Struct. Div. 106 (1980) 431–444.

[36] C.M. DONOGHUE, Strength of composite beams with web openings, ASCE J. Struct. Div. 108 (1982) 2652–2667.

[37] W.C. Clawson, D. Darwin, Strength of composite beams at web openings, ASCE J. Struct. Div. 108 (1982) 623–641.

[38] R.M. Lawson, K.F. Chung, A.M. Price, Tests on composite beams with large web openings to justify existing design methods, Struct. Enginee. 70 (1992) 1–7.

[39] S.H. Cho, R.G. Redwood, Slab behavior in composite beams at openings. II: tests and verification, J. Struct. Eng. 118 (1992) 2304–2322. doi:10.1061/(ASCE)0733-9445(1992)118:9(2304).

[40] R.G. Redwood, G. Poumbouras, Analysis of composite beams with web openings, J. Struct. Eng. 110 (1984) 1949–1958. doi:10.1061/(ASCE)0733-9445(1984)110:9(1949).

[41] S.H. Cho, R.G. Redwood, Slab behavior in composite beams at openings. I: analysis, J. Struct. Eng. 118 (1992) 2287–2303. doi:10.1061/(ASCE)0733-9445(1992)118:9(2287).

[42] E.H. Fahmy, Analysis of composite beams with rectangular web openings, J. Constr. Steel Res. 37 (1996) 47–62. doi:10.1016/0143-974X(95)00022-N.

[43] M.A. Benitez, D. Darwin, R.C. Donahey, Deflections of composite beams with web openings, J. Struct. Eng. 124 (1998) 1139–1147. doi:10.1061/(ASCE)0733-9445(1998)124:10(1139).

[44] K.F. Chung, R.M. Lawson, Simplified design of composite beams with large web openings to Eurocode 4, J. Constr. Steel Res. 57 (2001) 135–164. doi:10.1016/S0143-974X(00)00011-0.

[45] C. MÜLLER, O. HECHLER, A. BUREAU, D. BITAR, D. JOYEUX, L.G. CAJOT, T. DEMARCO, R.M. LAWSON, S. HICKS, P. DEVINE, O. LAGERQVIST, E. HEDMAN-PÉTURSSON, E. UNOSSON, M. FELDMANN, Large web openings for service integration in composite floors. Technical Steel Research. European Comission, Contract No 7210-PR/315. Final report, (2006).

[46] O. Hechler, C. Müller, G. Sedlacek, Investigations on beams with multiple regular web openings, 2006.

[47] A. Nadjai, Performance of cellular composite floor beams at ambient temperature, 2005.

[48] F.P.V. Ferreira, C.H. Martins, S. De Nardin, Advances in composite beams with web openings and composite cellular beams, J. Constr. Steel Res. 172 (2020) 106182. doi:10.1016/j.jcsr.2020.106182.

[49] EUROPEAN COMMITTEE FOR STANDARDIZATION, EUROCODE 3: Design of steel structures - Part 1-1: General rules and rules buildings, (2005).

[50] Dassault Systèmes Simulia, Abaqus 6.18, (2016).

[51] F.P.V. Ferreira, A. Rossi, C.H. Martins, Lateral-torsional buckling of cellular beams according to the possible updating of EC3, J. Constr. Steel Res. 153 (2019) 222–242. doi:10.1016/j.jcsr.2018.10.011.

[52] F.P.V. Ferreira, C.H. Martins, LRFD for Lateral-Torsional Buckling Resistance of Cellular Beams, Int. J. Civ. Eng. (2019). doi:10.1007/s40999-019-00474-7.

[53] A. Rossi, F.P.V. Ferreira, C.H. Martins, E.C. Mesacasa Júnior, Assessment of lateral distortional buckling resistance in welded I-beams, J. Constr. Steel Res. 166 (2020) 105924. doi:10.1016/j.jcsr.2019.105924.

[54] A. Nadjai, O. Vassart, F. Ali, D. Talamona, A. Allam, M. Hawes, Performance of cellular composite floor beams at elevated temperatures, Fire Saf. J. 42 (2007) 489–497. doi:10.1016/j.firesaf.2007.05.001.

[55] D.L. Araújo, M.W.R. Sales, S.M. Paulo, A.L.H.C. El Debs, Headed steel stud connectors for composite steel beams with precast hollow-core slabs with structural topping, Eng. Struct. 107 (2016) 135–150. doi:10.1016/j.engstruct.2015.10.050.

[56] A. Hillerborg, M. Modéer, P.-E. Petersson, Analysis of crack formation and crack growth in concrete by means of fracture mechanics and finite elements, Cem. Concr. Res. 6 (1976) 773–781. doi:10.1016/0008-8846(76)90007-7.

[57] J. Lubliner, J. Oliver, S. Oller, E. Oñate, A plastic-damage model for concrete, Int. J. Solids Struct. 25 (1989) 299–326. doi:10.1016/0020-7683(89)90050-4.

[58] J. Lee, G.L. Fenves, Plastic-Damage Model for Cyclic Loading of Concrete Structures, J. Eng. Mech. 124 (1998) 892–900. doi:10.1061/(ASCE)0733-9399(1998)124:8(892).

[59] T. Yu, J.G. Teng, Y.L. Wong, S.L. Dong, Finite element modeling of confined concrete-I: Drucker–Prager type plasticity model, Eng. Struct. 32 (2010) 665–679. doi:10.1016/j.engstruct.2009.11.014.

[60] H. Behnam, J.S. Kuang, B. Samali, Parametric finite element analysis of RC wide beam-column connections, Comput. Struct. 205 (2018) 28–44. doi:10.1016/j.compstruc.2018.04.004.

[61] A.S. Genikomsou, M.A. Polak, Finite element analysis of punching shear of concrete slabs using damaged plasticity model in ABAQUS, Eng. Struct. 98 (2015) 38–48. doi:10.1016/j.engstruct.2015.04.016.

[62] Z. Guo, Principles of Reinforced Concrete, Elsevier, 2014. doi:10.1016/C2013-0-13698-7.

[63] W. Xue, M. Ding, H. Wang, Z. Luo, Static behavior and theoretical model of stud shear connectors, J. Bridg. Eng. 13 (2008) 623–634. doi:10.1061/(ASCE)1084-0702(2008)13:6(623).

[64] M. Pavlović, Z. Marković, M. Veljković, D. Buđevac, Bolted shear connectors vs. headed studs behaviour in push-out tests, J. Constr. Steel Res. 88 (2013) 134–149. doi:10.1016/j.jcsr.2013.05.003.

[65] NATIONAL STANDARD OF THE PEOPLE'S REPUBLIC OF CHINA, GB 50010-2002: Code for Design Concrete Structures, (2002).

[66] X. Yun, L. Gardner, Stress-strain curves for hot-rolled steels, J. Constr. Steel Res. 133 (2017) 36–46. doi:10.1016/j.jcsr.2017.01.024.

[67] E. Ellobody, D. Lam, Modelling of headed stud in steel-precast composite beams, Steel Compos. Struct. 2 (2002) 355–378. doi:10.12989/scs.2002.2.5.355.

[68] D. Lam, Capacities of headed stud shear connectors in composite steel beams with precast hollowcore slabs, J. Constr. Steel

Res. 63 (2007) 1160–1174. doi:10.1016/j.jcsr.2006.11.012.

[69] S. Wijesiri Pathirana, B. Uy, O. Mirza, X. Zhu, Flexural behaviour of composite steel–concrete beams utilising blind bolt shear connectors, Eng. Struct. 114 (2016) 181–194. doi:10.1016/j.engstruct.2016.01.057.

[70] S. Guezouli, A. Lachal, Numerical analysis of frictional contact effects in push-out tests, Eng. Struct. 40 (2012) 39–50. doi:10.1016/j.engstruct.2012.02.025.

[71] S. Chen, Y. Jia, Numerical investigation of inelastic buckling of steel–concrete composite beams prestressed with external tendons, Thin-Walled Struct. 48 (2010) 233–242. doi:10.1016/j.tws.2009.10.009.

[72] W.-B. Zhou, W.-J. Yan, Refined nonlinear finite element modelling towards ultimate bending moment calculation for concrete composite beams under negative moment, Thin-Walled Struct. 116 (2017) 201–211. doi:10.1016/j.tws.2017.02.011.

[73] C. Couto, P. Vila Real, Numerical investigation on the influence of imperfections in the lateral-torsional buckling of beams with slender I-shaped welded sections, Thin-Walled Struct. 145 (2019) 106429. doi:10.1016/j.tws.2019.106429.

Buckling and post-buckling analyses of composite cellular beams

Felipe Piana Vendramell Ferreira*[a], Konstantinos Daniel Tsavdaridis[b], Carlos Humberto Martins[c], Silvana De Nardin[a]

[a]Department of Civil Engineering, Federal University of São Carlos, Rod. Washington Luiz, km 235, São Carlos, São Paulo, Brazil.

[b]School of Civil Engineering, Faculty of Engineering and Physical Sciences, University of Leeds, Woodhouse Lane, LS2 9JT Leeds, UK.

[c]Department of Civil Engineering, State University of Maringá, Av. Colombo nº 5790, Maringá, Paraná, Brazil.

*Corresponding author

E-mail address: fpiana@live.com (F. P. V. Ferreira), K.Tsavdaridis@leeds.ac.uk (K. D. Tsavdaridis), chmartins@uem.br (C. H. Martins), snardin@ufscar.br (S. De Nardin)

Abstract

This paper aims to investigate the buckling and post-buckling analyses of composite cellular beams. For this, the numerical model is calibrated by experimental tests via post-buckling analysis. A parametric study is developed, considering six cross sections. For each section, the opening diameter and web post length are varied. Regarding the buckling analyses for the symmetrical sections, it was concluded that the end post is an important parameter in the strength of composite cellular beams that presents high web slenderness. The smaller the opening diameter, the greater the critical global shear. The variation in the height of the cellular beam had a little influence on larger diameters and web posts widths. Considering asymmetric sections, it was verified that the web post buckling did not happen for the first buckling mode. In this scenario, local web buckling of the upper tee was observed. With the height variation, there was an increase in the global shear. This is due to the fact that with the increase in height, the buckling mode was transferred to the WPB, instead of local web buckling. Finally, there was a conservatism in the SCI P355 calculation recommendations, a factor that needs to be revised.

Keywords: Composite cellular beams; Critical global shear; Finite element analysis; Buckling; Post-buckling.

NOTATION

The following symbols are used in this paper:

b	the width of the concrete slab	l_{eff}	effective length of web-post
b_f	the width of the flange	V	the global shear
b_w	the width of the web post	V_{cr}	the critical global shear
b_{we}	the width of the end post	L_b	the unrestrained length of composite cellular beam
D_o	the opening diameter	L_p	the distance between support and load
E	Young's modulus	p	the length between the opening diameter centers
d	the depth of parent section;	t_f	the thickness of the flange
d_g	the depth of cellular beam	t_w	the thickness of the web
f_c	the compressive cylinder strength of concrete	α	the imperfection factor
$f_{cr,w}$	the critical stress at web post	λ_w	the web slenderness ratio
f_t	the concrete tension resistance	$\overline{\lambda}$	the reduced slenderness factor
f_u	the ultimate strength of cellular beam	χ	the reduction factor
f_y	the yield strength of cellular beam		

1. INTRODUCTION

Cellular beams are those with circular sequential openings along the web, manufactured from thermal cutting and welding, aiming at the expansion of the cross section. Such beams are used in the design of parking garages, industries and warehouses, factories, office buildings, schools, hospitals and offshore elements. The presence of the openings influences the air flow, as well as the integration of services through ducts. However, due to the presence of openings, cellular beams are more susceptible to buckling modes, such as lateral torsional buckling, web distortion, web post buckling (WPB) or even the combination of the buckling modes [1–3], although the formation of the plastic mechanism, such as the Vierendeel mechanism (VM), can also occur. In the case of composite cellular beams, due to the compressed cellular beam flange being restrained by the concrete slab, the ultimate strength of these structures occur through the association of the failure mechanisms of the cellular beams, in this case VM or WPB, with the mechanisms of the concrete slab, i.e. cracking or crushing [4–8]. VM occurs when the tees reach the yield strength, caused by the combination of normal and tangential stresses. This phenomenon is characterized by the formation of plastic hinges near to the opening [9]. The main parameters that affect this structural behavior are the web thickness and the depth of tee [10–12]. On the other hand, the WPB is characterized by a double curvature, in the shape of an "S", which occurs in the web post according to the geometric characteristics of the cellular profile, such as opening diameter, the web post width and the web thickness [13].

In Abrambes et al. [14] the elastic buckling analyses of non-composite cellular beams were estimated using an artificial neural network (ANN). In this study, the authors found that WPB occurred for sections with slender web posts. In Rajana et al. [15] elastic and inelastic analyses were presented in non-composite cellular beams, the purpose of which was to illustrate the influence

of geometric parameters on the resistance of these structural elements based on the requirements of SCI P355 [15]. Such a study is the motivation for carrying out analyses on composite cellular beams. With a focus on WPB, the SCI P355 [15] recommendations address a truss model for calculating resistance. In this model, which is based on the EC3 [16], it starts by elastic analysis, and then the buckling curves are associated (**Fig. 1**). Regarding the selection of the buckling curves, for the case of double symmetrical hot-rolled sections, the buckling curves *a*, *b* and *c* can be used in the design of sections that have d/b_f>1.2. In this context, for sections with t_f≤40mm, the buckling curves *a* and *b* are used when the buckling occurs around the strong and weak axes, respectively. For hot-rolled sections that have d/b_f≤1.2 and 40mm≤t_f ≤100mm, the buckling curves *b* and *c* are recommended for the occurrence of buckling around the strong and weak axes, respectively. On the other hand, for doubly symmetrical welded sections, the classification of the use of buckling curves is limited only in the flange thickness. For sections with t_f≤40mm, buckling curves *b* and *c* are recommended for the occurrence of buckling around strong and weak axes, respectively. For t_f>40mm, buckling curves *c* and *d* are recommended, depending on the strong and weak axes. In the case of cellular beams, it is recommended to use the buckling curves *b* and *c* for hot-rolled and welded sections, respectively, considering the web post buckling. **Table 1** shows the imperfection factor (α) values for each buckling curve.

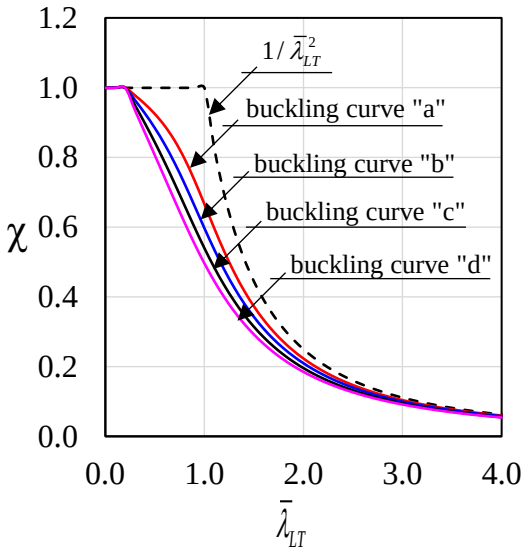

Fig. 1: EC3 buckling curves

Table 1: Imperfection factors for buckling curves according EC3

Buckling curve	*a*	*b*	*c*	*d*
Imperfection factor (α)	0.21	0.34	0.49	0.76

The paper aims to investigate numerically elastic analyses in composite cellular beams. The finite element model is calibrated, considering tests via inelastic analyses. The model is represented, considering the structural system of composite cellular beams formed by cellular beams, headed stud connectors and composite slabs (with Holorib HR 51/150 geometry). Subsequently, a parametric study is developed, varying the key parameters such as the opening diameter and web post width. In this study, six

geometric sections are considered, that is, three symmetric sections and three asymmetric sections. In total, 120 elastic analyses are performed. The results are presented and discussed, considering the buckling modes and the critical global shear that causes WPB. Also, the results are compared with the inelastic analyses, previously presented in Ferreira et al. [17], and with the calculation of the critical global shear presented in [13,18].

2. BACKGROUND

There are studies on composite beams with only a rectangular web opening, considering solid [19–26] or composite slabs [4,5,32–34,6,7,11,27–31]. The present paper focuses on studies of composite cellular beams, which are recent; mainly those initiated in the 2000s. In this scenario, there are several experimental and numerical investigations that evaluated the behavior of composite cellular beams [8,17,35–39]. Hechler et al. [35] and Müller et al. [36] presented test from two models: composite symmetric and asymmetric cellular beams. Both specimens were designed in such a way that at one end it was possible to investigate the composite action, at the other end, only the cellular beam. According to the authors, the VM was observed for low loading values at the end corresponding to the composite cellular beam. However, at the end where there was only the cellular steel profile, the strength was reached by WPB. In the same way, Nadjai et al. [37] presented tests results of composite symmetric and asymmetric cellular beams. Both models had the strength governed by WPB. Gizejowski and Khalil [39] performed a set of tests on composite cellular beams subjected to negative bending moment. In all situations, the authors observed failure modes associated with web distortion. Sheehan et al. [8] tested composite asymmetric cellular beams, situation in which the lower tee consists of a section heavier than the upper tee, with large spans. The authors observed that the composite cellular beam requested for uniformly distributed loads resisted 3.4 times the estimated design load, despite the degree of interaction considerably less than the minimum required by EC4 [40]. In Ferreira et al. [17] the resistance of steel-concrete composite cellular beams was investigated by inelastic analyses. In this study it was found that the procedures for calculating WPB are conservative [13,18,41,42]. Although there are several analytical calculation models in the literature, considering the WPB, as presented in Ferreira et al. [43], the present study focuses on the SCI P355 procedure [17,42]. Such a model is based on strut, considering the effective length, which takes into account the variation of stresses around the opening, according to **Eq. (1)**. Once the effective length has been determined, then the theory of compression bars, according to EN 1993-1-1 [44], is applied, considering slenderness in the web post length and using the buckling curve *b* and *c* (**Fig. 1**) for hot-rolled and welding members, respectively (**Eqs. 2-8**):

$$l_{eff} = 0.5\sqrt{b_w^2 + D_o^2} \leq 0.7D_o \tag{1}$$

$$\sigma_{Rk} = \chi f_y \tag{2}$$

$$\chi = \frac{1}{\phi + \sqrt{\phi^2 - \bar{\lambda}^2}} \leq 1.0 \tag{3}$$

$$\phi = 0.5\left[1 + \alpha\left(\bar{\lambda} - 0.2\right) + \bar{\lambda}^2\right] \tag{4}$$

$$\bar{\lambda} = \sqrt{\frac{f_y}{f_{cr,w}}} \tag{5}$$

$$f_{cr,w} = \frac{\pi^2 E}{\lambda_w^2} \tag{6}$$

$$\lambda_w = \frac{l_{eff}\sqrt{12}}{t_w} \tag{7}$$

In which l_{eff} is the effective length of web-post, b_w is the width of the web post, D_o is the opening diameter, χ is the reduction factor, $\bar{\lambda}$ is the reduced slenderness factor, λ_w is the web slenderness ratio and $f_{cr,w}$ is the critical stress at web post. Thus, the vertical shear strength can be calculated (**Eq. 8)**:

$$V_{Lv,Rk} = \sigma_{Rk} t_w b_w \tag{8}$$

Panedpojaman et al. [13] made an adaptation in the effective length of the web post. In this model, the web post effective length is multiplied by a factor k (**Eqs. 9-10**):

$$l_{eff,P} = k\left(0.5\sqrt{p^2 - D_o^2}\right) \tag{9}$$

$$k = 0.9\left(\frac{p}{D_o}\right)\left(\frac{D_o}{d}\right)^2 \leq \min\left(1.15\frac{D_o}{d}, 1.15\right) \tag{10}$$

3. FINITE ELEMENT MODEL: VALIDATION STUDY

The numerical models are developed in two steps: elastic (buckling) and inelastic (post-buckling) [15,17,45–49]. The first step is used to estimate critical buckling loads on structures, and it can also be used as the first step to start the inelastic analysis. In the elastic analysis, no imperfections, physical and geometrical, are considered. The inelastic analysis is performed considering an initial geometric imperfection of d_g/1000. Using this imperfection factor (d_g/1000), in Ferreira et al. [17] sensitivity analyses were carried out using the finite element method, with the imperfection factor varying from d_g/100, d_g/200, d_g/250, d_g/500 and d_g/1000. The authors concluded that there was little sensitivity in the results, since the ultimate behavior was determined by the WPB. This low sensitivity in the results was assessed, also in Chen and Jia [50], and Couto and Vila Real [51]. The true initial imperfections of the cellular beams are a difficult task to determine, due to the manufacturing process [13]. In addition, in the case of cellular beams, the initial geometric imperfection in the web amount must not be greater than 4mm for sections with d_g<600mm and d_g/100 for sections with d_g>600 mm [52]. Therefore, for the present study, the factor of d_g/1000 is considered, according to the study presented in [17]. In this scenario, the deformed structure in the elastic analysis multiplied by an initial geometric imperfection scale factor is adopted as the shape at the beginning of this analysis. The implementation of geometric imperfection is performed using the command *INITIAL CONDITIONS of the ABAQUS® computational package [53]. **Table 2** shows the physical and geometric properties of the tests that are used in the validation study.

Table 2: Models (in mm, MPa and GPa)

Model	Ref	d_g	D_o	p	Upper tee					Lower tee				
					b_f	t_f	t_w	f_y (flange/web)	f_u (flange/web)	b_f	t_f	t_w	f_y (flange/web)	f_u (flange/web)
CCB1	[37]	575	375	500	141.8	8.6	6.4	312	438.5	141.8	8.6	6.4	312	438.5
CCB2	[37]	630	450	630	141.8	8.6	6.4	312	438.5	152.4	10.9	7.6	312	438.5
CCB3	[36]	555	380	570	180	13.5	8.6	451/489	541/587	180	13.5	8.6	451/489	541/587
CCB4	[36]	485	380	570	150	10.7	7.1	407/467	524/588	300	21.5	12	453/488	519/582

Model	Ref	E	Slab		L_b	L_p
			f_c	b		
CCB1	[37]	200	28.6	1200	4500	1750
CCB2	[37]	200	28.6	1200	4500	2250
CCB3	[36]	195	33.6	1800	6840*	1140/2850
CCB4	[36]	195	24.0	1800	6840*	1140/2850

*Slab cut back by 285 mm at end of cellular beam

3.1 MATERIALS

Regarding the constitutive material models, the quadrilinear model (**Fig. 2**) presented in Yun and Gardner [54] was used for steel **Eqs. (11-15)**. The implementation of the stress- strain relationship must be done with the real values, according to the **Eqs. (16-17).**

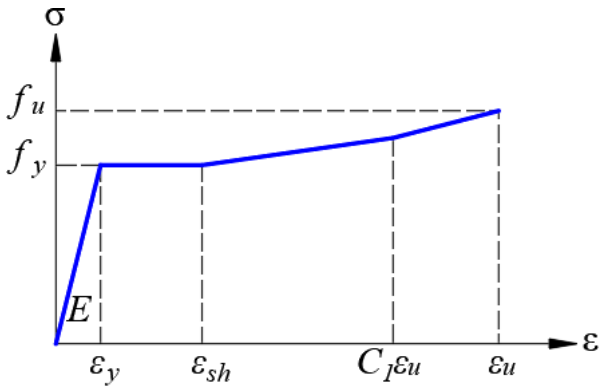

Fig. 2: Stress-strain relationship for steel [54]

$$f(\varepsilon)=\begin{cases} E\varepsilon, \varepsilon \le \varepsilon_y \\ f_y, \varepsilon_y < \varepsilon \le \varepsilon_{sh} \\ f_y + E_{sh}(\varepsilon - \varepsilon_{sh}), \varepsilon_{sh} < \varepsilon \le C_1\varepsilon_u \\ f_{C_1\varepsilon_u} + \left(\dfrac{f_u + f_{C_1\varepsilon_u}}{\varepsilon_u - C_1\varepsilon_u}\right), C_1\varepsilon_u < \varepsilon \le \varepsilon_u \end{cases} \quad (11)$$

$$\varepsilon_u = 0.6\left(1-\frac{f_y}{f_u}\right), \varepsilon_u \ge 0.06 \quad (12)$$

$$\varepsilon_{sh} = 0.1\frac{f_y}{f_u} - 0.055, 0.015 < \varepsilon_{sh} \le 0.03 \quad (13)$$

$$C_1 = \frac{\varepsilon_{sh} + 0.25\left(\varepsilon_u - \varepsilon_{sh}\right)}{\varepsilon_u} \quad (14)$$

$$E_{sh} = \frac{f_u - f_y}{0.4\left(\varepsilon_u - \varepsilon_{sh}\right)} \quad (15)$$

$$\sigma^{true} = \sigma^{nom}\left(1 + \varepsilon^{nom}\right) \quad (16)$$

$$\varepsilon^{true} = \ln\left(1 + \varepsilon^{nom}\right) \quad (17)$$

For concrete, the Carreira and Chu [55,56] model was adopted (**Eqs. 18-20**). The parameters that control plasticity yield criteria were similar to those presented in [17,48], according to **Table 3**.

$$\frac{\sigma}{f_c} = \frac{\beta_c\left(\varepsilon / \varepsilon_c\right)}{\beta_c - 1 + \left(\varepsilon / \varepsilon_c\right)^{\beta_c}} \quad (18)$$

$$\frac{\sigma}{f_t} = \frac{\beta_c\left(\varepsilon / \varepsilon_t\right)}{\beta_c - 1 + \left(\varepsilon / \varepsilon_t\right)^{\beta_c}} \quad (19)$$

$$\beta_c = \left(\frac{f_c}{32.4}\right)^3 + 1.55 \ \ (MPa) \quad (20)$$

Table 3: CDP input parameters

Parameter	Value
Ψ (º)	40
ξ	0.1 (default)
σ_{b0}/σ_{c0}	1.16 (default)
K_c	2/3 (default)
μ (s^{-1})	0.001

3.2 INTERACTION

About the interaction between the contact surfaces, the same strategy applied in [17,48,49,57,58] was used (**Fig. 3**). According to illustration, tie constraint, which is a restriction that represent the perfect bond between the surfaces, was applied to the surface between the shear connectors and the upper flange. Normal and tangential behavior (surface-to-surface) between the slab-connector and slab-beam are considered. The value of the friction coefficients was to 0.2 and 0.3 for slab-connector and slab-beam, respectively [59].

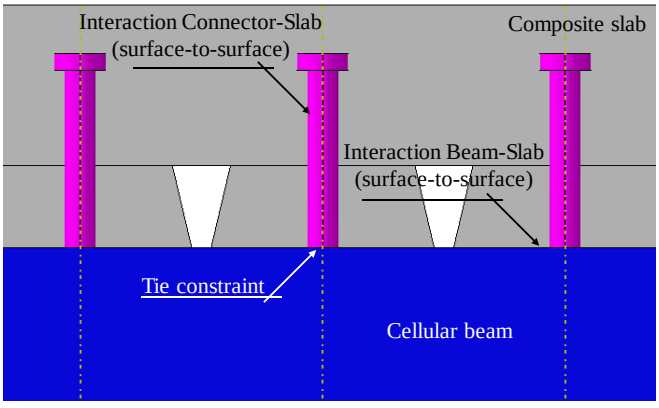

Fig. 3: Interaction of contact surfaces [17]

3.3 BOUNDARY CONDTIONS AND DISCRETIZATION

The boundary conditions were applied considering the symmetry at the longitudinal axis. **Fig. 4** illustrate the boundary conditions and discretization. The vertical displacement (U_y=0) in the support, and lateral displacement (Ux=0) at the ends of the slab were restrained. Longitudinal symmetry was applied at mid-span (U_z=U_{Rx}=U_{Ry}=0). About the discretization, the dimension of the elements was taken according to previous studies [60–62] respecting the master and slave surfaces. The cellular beam was discretized with shell-type finite elements (S4R). The headed stud connectors and the concrete slab were discretized by the solid element (C3D8R). Both elements have six degrees of freedom per node - three rotations and three translations. The validation results are presented by global shear curves by mid-span vertical displacement. Both the results of the elastic and inelastic analysis are illustrated.

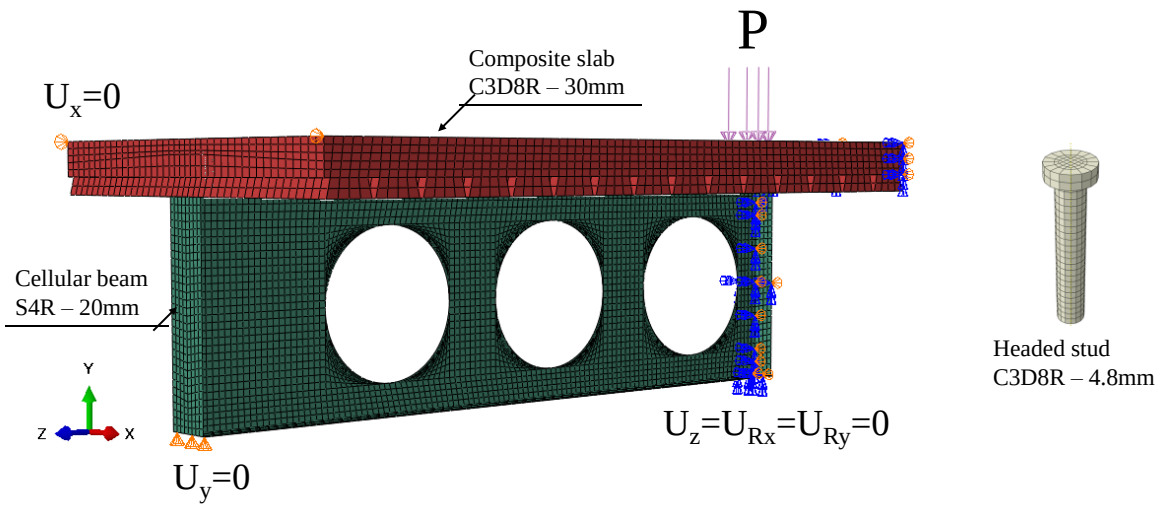

Fig. 4: Boundary conditions and discretization

3.4 VALIDATION RESULTS

The results of the validation study are presented below, considering the elastic and inelastic results (**Table 4** and **Fig. 5**). It is noteworthy that the elastic analysis is the first step to carry out the inelastic analysis, as previously described. It is observed in **Table 4** that the difference between the two analyses can reach up to 50%, since in the elastic analysis no initial imperfections are considered. In **Fig. 5** the curves of both analyses are shown compared to the tests. The response of the elastic analysis is presented by means of a constant line of blue color, since the ABAQUS software provides, for this type of analysis, eigenvalues and eigenvectors. According to the presentation of the results, it is possible to state that the numerical model is validated.

Table 4: Summary of results

Model	V_{Test} (kN)	$V_{FE,ELASTIC}$ (kN)	$V_{FE,INELASTIC}$ (kN)	$V_{FE,ELASTIC}/V_{FE,INELASTIC}$	$V_{FE}/V_{INELASTIC}$
CCB1	185	240	187	1.28	1.01
CCB2	215	263	213	1.23	0.99
CCB3	403	551	404	1.36	1.00
CCB4	329	492	328	1.50	1.00

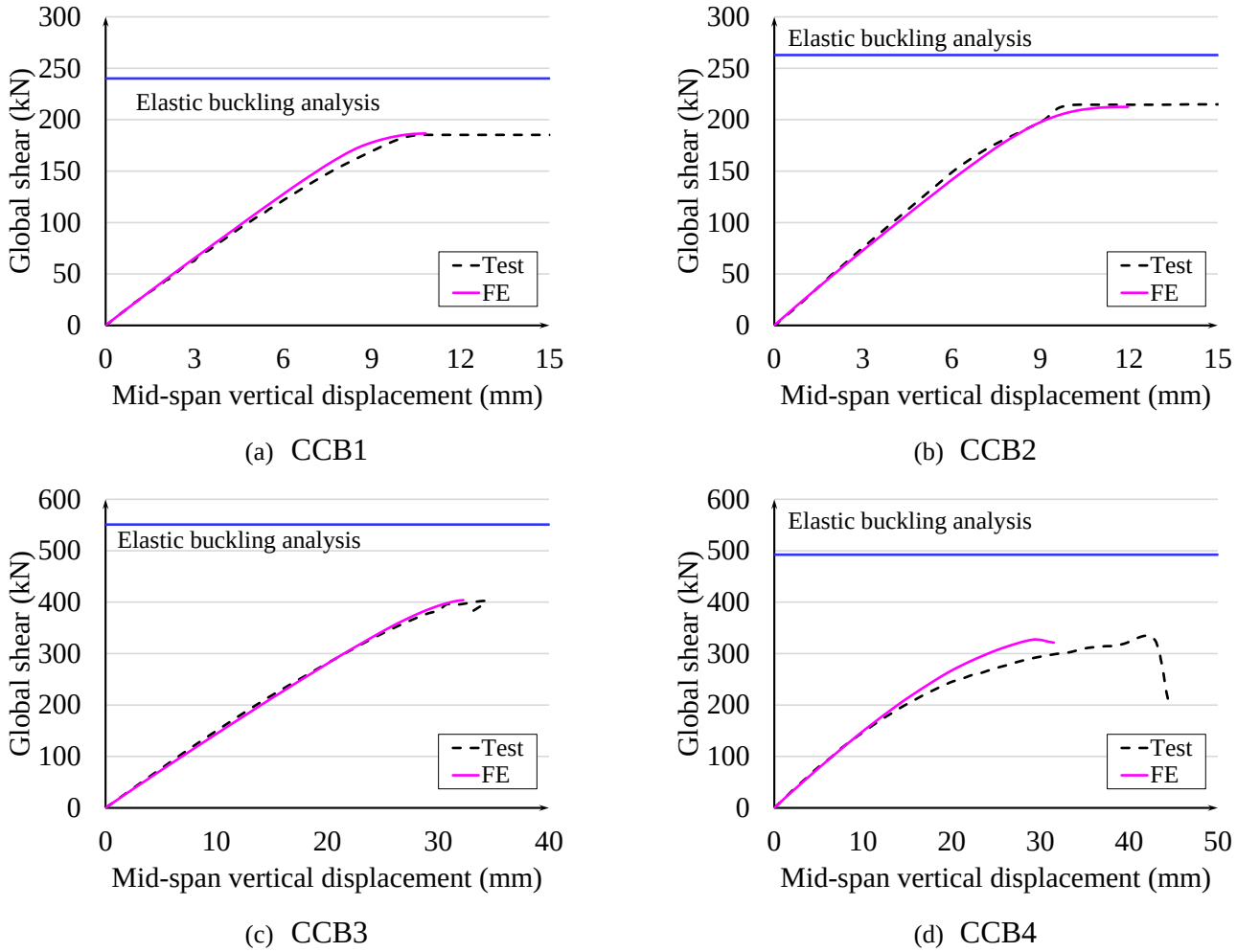

Fig. 5: Validation results

4. FINITE ELEMENT MODEL: PARAMETRIC STUDY

The following are the general considerations:

1. Six sections are considered (**Table 5**);

Table 5: Sections analyzed

Model	d_g	Upper tee			Lower tee		
		b_f	t_f	t_w	b_f	t_f	t_w
CCB1	575	141.8	8.6	6.4	141.8	8.6	6.4
CCB2	630	141.8	8.6	6.4	152.4	10.9	7.6
CCB3	555	180	13.5	8.6	180	13.5	8.6
CCB4	485	150	10.7	7.1	300	21.5	12
CCB5	580	180	13.5	8.6	180	13.5	8.6
CCB6	580	180	13.5	8.6	300	21.5	12

2. The ratios p/D_o and D_o/d are varied in 1.2-1.5 and 0.8-1.2, respectively;
3. The end post width (b_{we}) shall not be smaller than the other web posts width (b_w);
4. The length of the composite cellular beam is equal 6m, and the effective slab width is L/4;
5. The slab depth is equal to 150mm, with Holorib HR 51/150 geometry;
6. The headed stud dimension is 19x120mm;

7. The ASTM A572 Grade 50 steel is adopted (f_y=345 MPa and f_u=450 MPa). The Young's modulus is equal to 200 GPa;
8. The concrete resistance is 35 MPa for CCB1-4 sections, and 30 MPa for CCB5-6 sections;
9. The composite cellular beams are simply supported and subjected to two points of loads, spaced symmetrically in 2m from supports. Stiffeners were provided at the point of load and support.

5. RESULTS AND DISCUSSION

In total 120 analyses were performed. The results are discussed considering symmetric and asymmetric sections. At the end of each section, the results of elastic analysis are compared with the results of inelastic analysis [17]. At the end of the results and discussion section, a comparison between the numerical results with the critical global shear of the procedures is performed.

5.1. SYMMETRIC SECTION

This section discusses the results presented by sections CCB1, CCB3 and CCB4. In general, the buckling modes presented by section CCB1 were characterized by WPB. **Fig. 6** illustrates some examples. An important observation to be noted in **Fig. 6a** was the local web buckling at the end post. This phenomenon was observed for situations in which the end post width was much longer than the web post width.

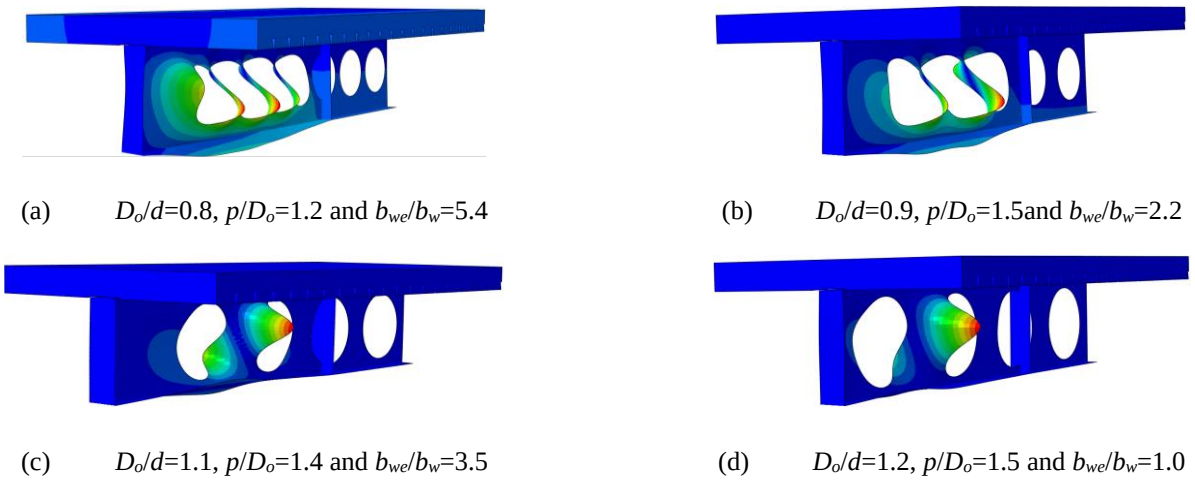

(a) D_o/d=0.8, p/D_o=1.2 and b_{we}/b_w=5.4 (b) D_o/d=0.9, p/D_o=1.5and b_{we}/b_w=2.2

(c) D_o/d=1.1, p/D_o=1.4 and b_{we}/b_w=3.5 (d) D_o/d=1.2, p/D_o=1.5 and b_{we}/b_w=1.0

Fig. 6: Buckling modes for CCB1 models

In **Fig. 7** the critical global shear curves (V_{cr}) are shown as a function of the key parameters ($D_o/d$and p/D_o). As noted, the curves for D_o/d=0.8, 0.9 and 1.1 showed a pattern. This is explained by the end post width, which presented similar values. In addition, the graph shows for these situations that the smaller the opening diameter, the greater the critical global shear that causes WPB. Also, as the web post width increases, the critical global shear tends to increase. On the other hand, for situations D_o/d=1.0 and 1.2, these values are divergent. In this scenario, the end post width was an important parameter that showed variability in the critical global shear. Such observations were measured for the b_{we}/b_w ratio approximately equal to 4.0.

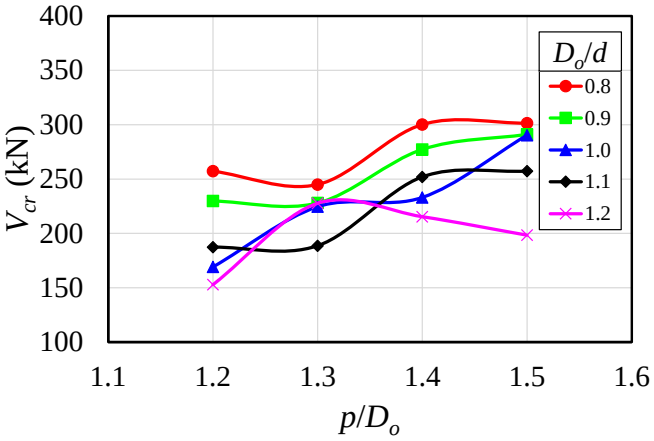

Fig. 7: Critical global shear vs. key parameters for CCB1 models

The behavior of the CCB3 (**Fig 8a-b**) and CCB5 (**Fig 8c-d**) models were similar to the behavior of the CCB1 model. This difference between the height of sections CCB3 and CCB5is 25mm, which was enough to change the buckling mode. As shown in **Fig. 8a**, the CCB3 model presented a buckling mode in which the local web buckling at the end post has been characterized. On the other hand, the CCB5 model did not show such buckling (**Fig. 8c**). This is explained by the fact that the model CCB5 presents the web slenderness greater than the model CCB3; a factor that transfers the local web buckling to the WPB. The results of the global critical shear as a function of the key parameters for the models CCB3 (**Fig. 9a**) and CCB5 are presented below (**Fig. 9b**). In this scenario, it is observed that the curve behaviors are similar to the CCB1 model. This is due to the fact that the diameter and the web post width have the same values as in the parametric study. For better visualization, in **Fig. 10** the results of each variation are presented for sections CCB1, CCB3 and CCB5. A difference of approximately 300kN is observed among sections CCB1 and CCB3 and CCB1 and CCB5. This difference is due to the fact that the CCB1 section has a higher slenderness value than the other sections. In addition, sections CCB3 and CCB5 have a web thickness equal to 8.6mm, while section CCB1 has a web thickness value of 6.4mm. Both parameters discussed are fundamental for the resistance to WPB, as presented in [13,18,63]. In relation to sections CCB3 and CC5, it is noted that the total height of the cellular beam causes small differences in critical global shear from the parameters D_o/d=0.9, p/D_o=1.4 (**Fig. 10b**). From this situation to the other parameters, the CCB3 model presented higher critical global shear results than the CCB5 section, due to the web slenderness of the CCB3 section being smaller than the CCB5 section.

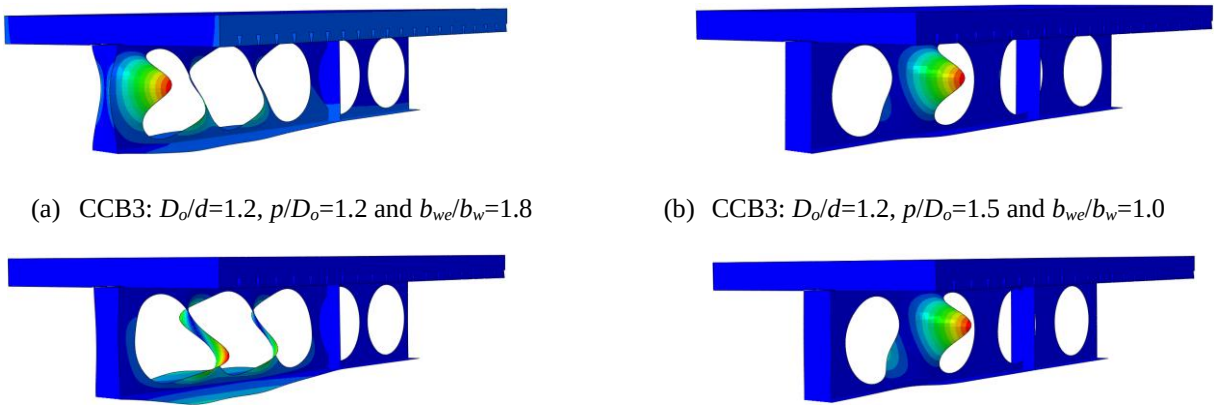

(a) CCB3: D_o/d=1.2, p/D_o=1.2 and b_{we}/b_w=1.8

(b) CCB3: D_o/d=1.2, p/D_o=1.5 and b_{we}/b_w=1.0

(c) CCB5: D_o/d=1.2, p/D_o=1.2 and b_{we}/b_w=1.8

(d) CCB5: D_o/d=1.2, p/D_o=1.5 and b_{we}/b_w=1.0

Fig. 8: Buckling modes for models CCB3 and CCB5

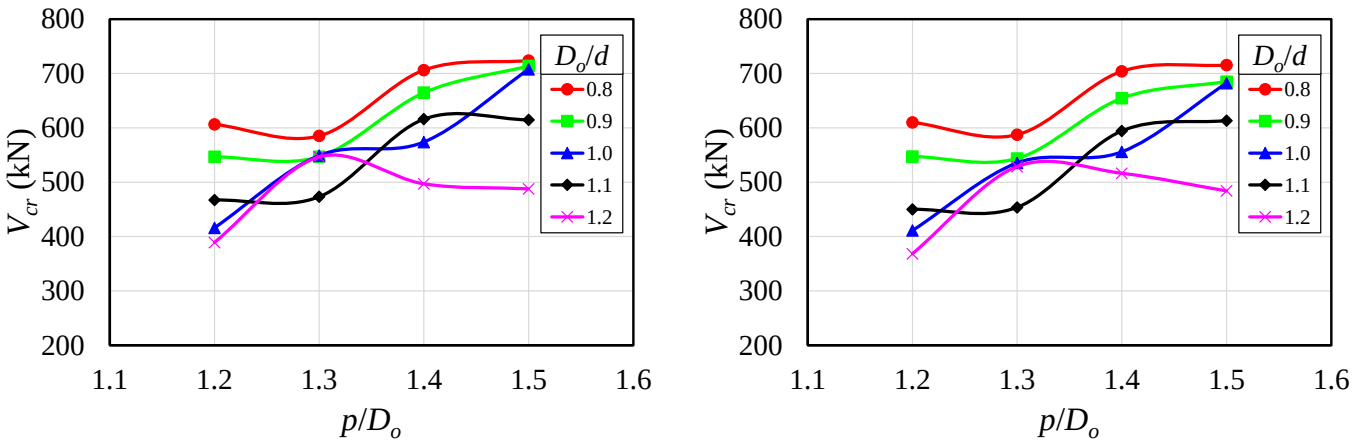

(a) CCB3 model

(b) CCB5 model

Fig. 9: Critical global shear vs. key parameters for CCB3 and CCB5 models

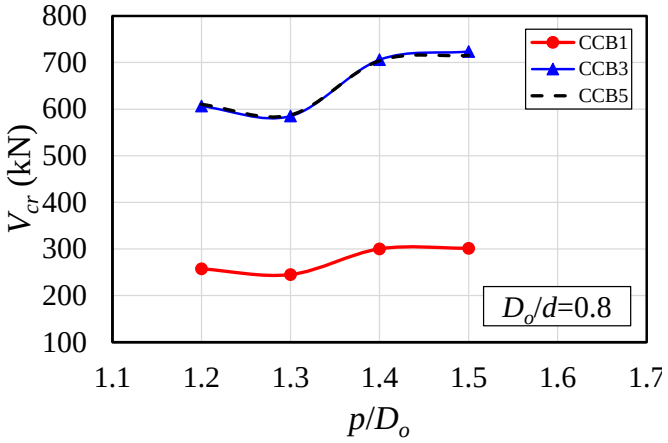

(a) D_o/d=0.8

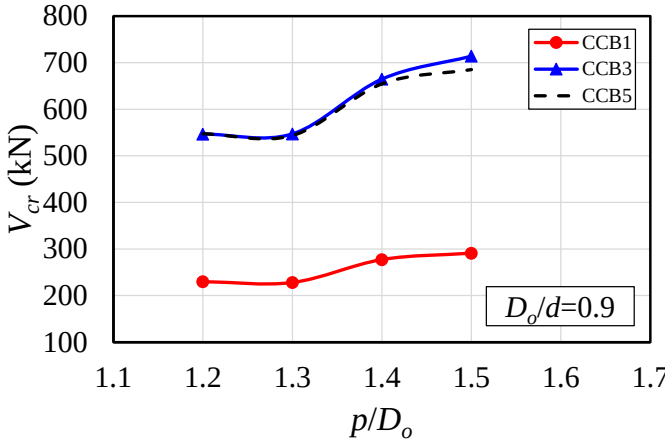

(b) D_o/d=0.9

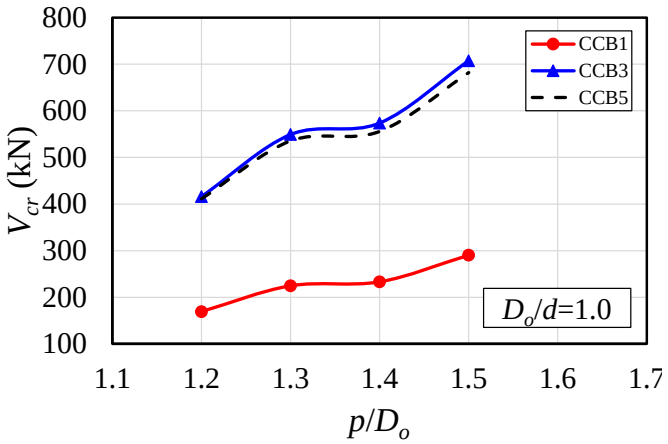

(c) D_o/d=1.0

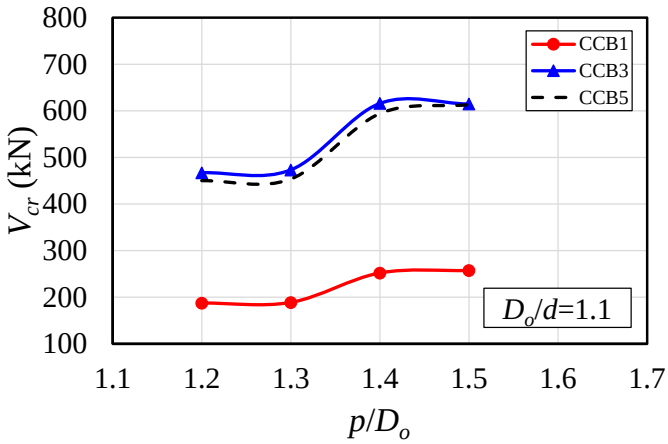

(d) D_o/d=1.1

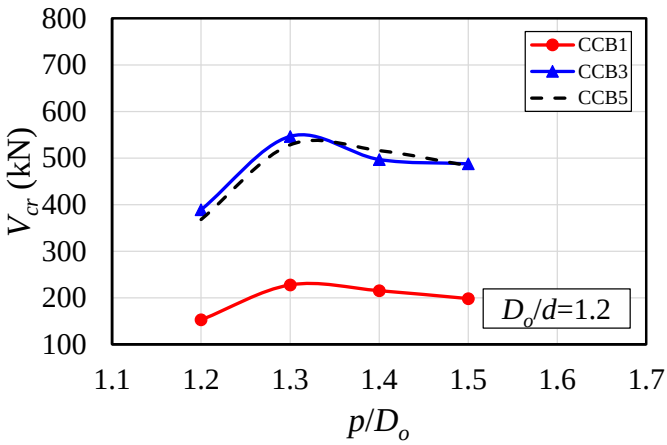

(e) D_o/d=1.2

Fig. 10: Comparative analyses for symmetric composite cellular beams

In **Fig. 11**, comparisons are presented between the elastic analyses of the present work, with the inelastic analyses presented by Ferreira et al. [17]. The differences, minimum, maximum and average were 11%, 51% and 36%, respectively. It is worth mentioning that in the elastic analysis, no physical and geometric imperfections are considered.

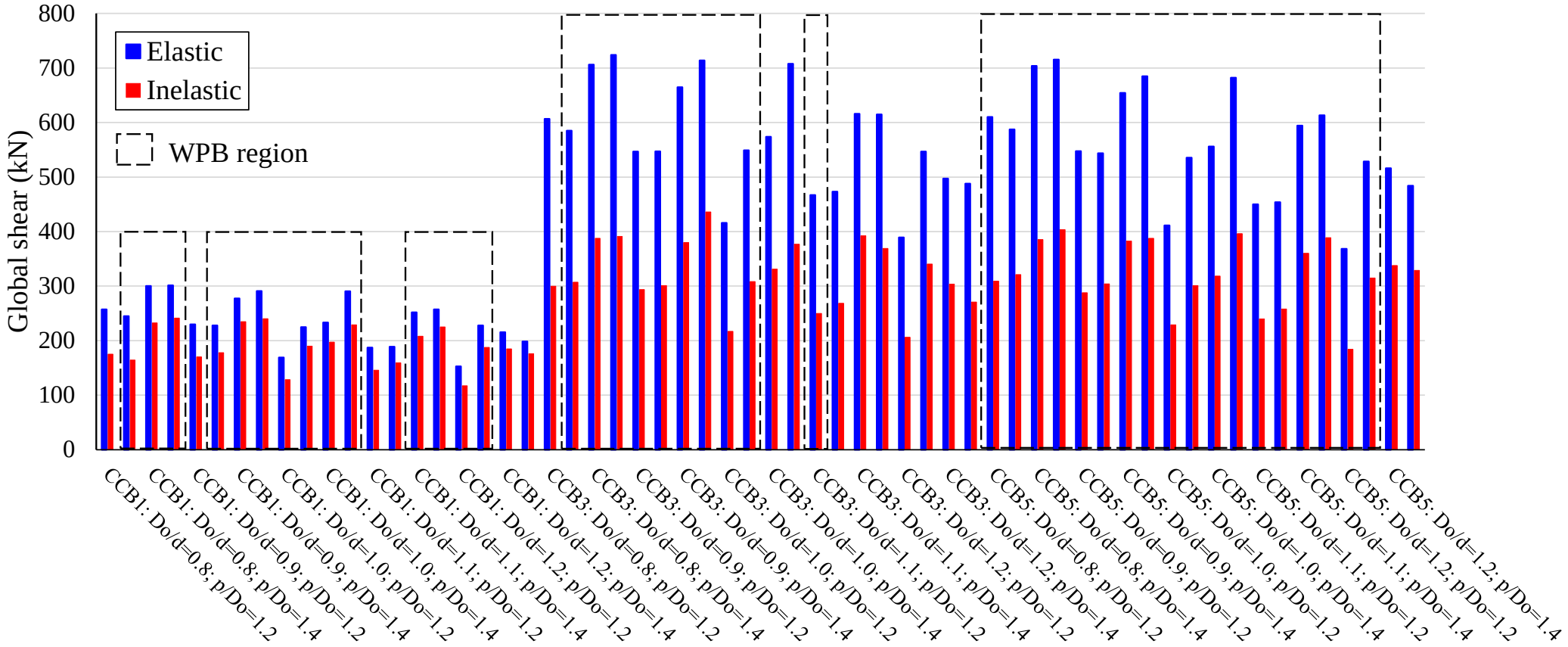

Fig. 11: Elastic and inelastic analyses for composite symmetric cellular beams

5.2. ASYMMETRIC SECTION

This section discusses the results presented by sections CCB2, CCB4 and CCB6. Regarding the CCB2 section, for some situations, the first buckling mode was not characterized by WPB (**Fig. 12**). As noted, the first buckling mode was characterized by local web buckling, specifically in the upper tee. This can be explained in relation to the lower tee being more rigid than the upper tee. Such buckling modes were observed for D_o/d=0.8. For other situations, WPB was verified. In **Fig. 13** some examples are presented. In **Fig. 14** the critical global shear curves (V_{cr}) are shown as a function of the key parameters (D_o/d and p/D_o). In the illustration, it is possible to observe a trend analogous to that previously presented for the symmetrical sections. This is possible due to the ratio between the areas of the upper tee to the lower tee being approximately 1.3, that is, a cross section with a low degree of asymmetry.

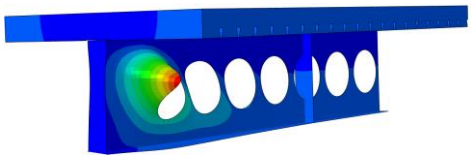

(a) D_o/d=0.8, p/D_o=1.2, b_{we}/b_w=5.4 and mode 1

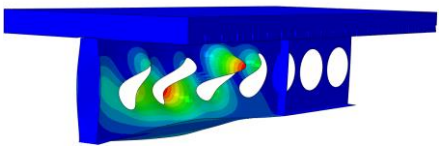

(b) D_o/d=0.8, p/D_o=1.2, b_{we}/b_w=5.4 and mode 2

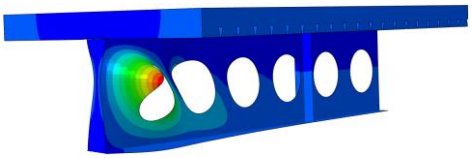

(c) D_o/d=0.8, p/D_o=1.5, b_{we}/b_w=1.3 and mode 1

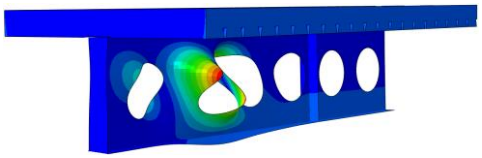

(d) D_o/d=0.8, p/D_o=1.5, b_{we}/b_w=1.3 and mode 2

Fig. 12: Buckling modes for CCB2 model

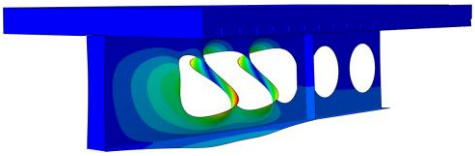

(a) D_o/d=0.9, p/D_o=1.4 and b_{we}/b_w=3.8

(b) D_o/d=1.0, p/D_o=1.2 and b_{we}/b_w=3.8

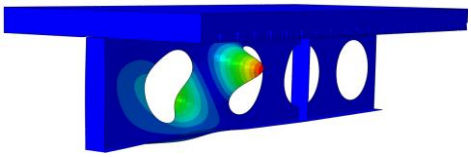

(c) D_o/d=1.1, p/D_o=1.5 and b_{we}/b_w=2.1

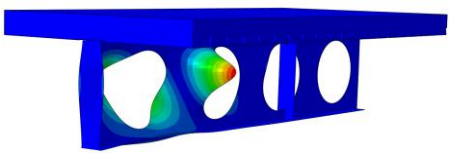

(d) D_o/d=1.5, p/D_o=1.5 and b_{we}/b_w=1.0

Fig. 13: WPB for CCB2 models

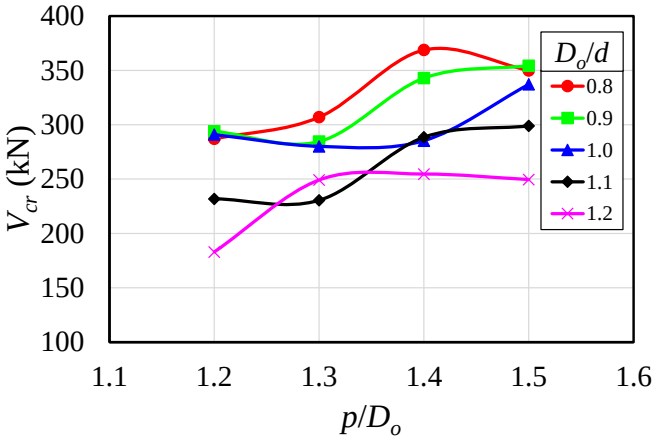

Fig. 14: Critical global shear vs. key parameters for CCB2 models

The buckling modes for sections CCB4 and CCB6, considering WPB, are illustrated below **(Fig. 15)**. The sections CCB4 and CCB6 have the upper and lower tees formed by the sections IPE 300 and HEB 340, respectively. As shown in **Fig. 15a**, **Fig. 15c** and **Fig. 15d**, the WPB for the CCB4 section was characterized by the formation of a C-shaped buckling curvature in the upper tee, due to the lower tee being more rigid. Notably, for section CCB6 (**Fig. 15b**, **Fig. 15d** and **Fig. 15f**), the WPB was characterized by a double "S" shaped buckling curvature. What differs the section CCB4 and CCB6 is a variation of the total height of the cellular profile in approximately 100mm, that is, the section CCB6 is slenderer than the section CCB4.

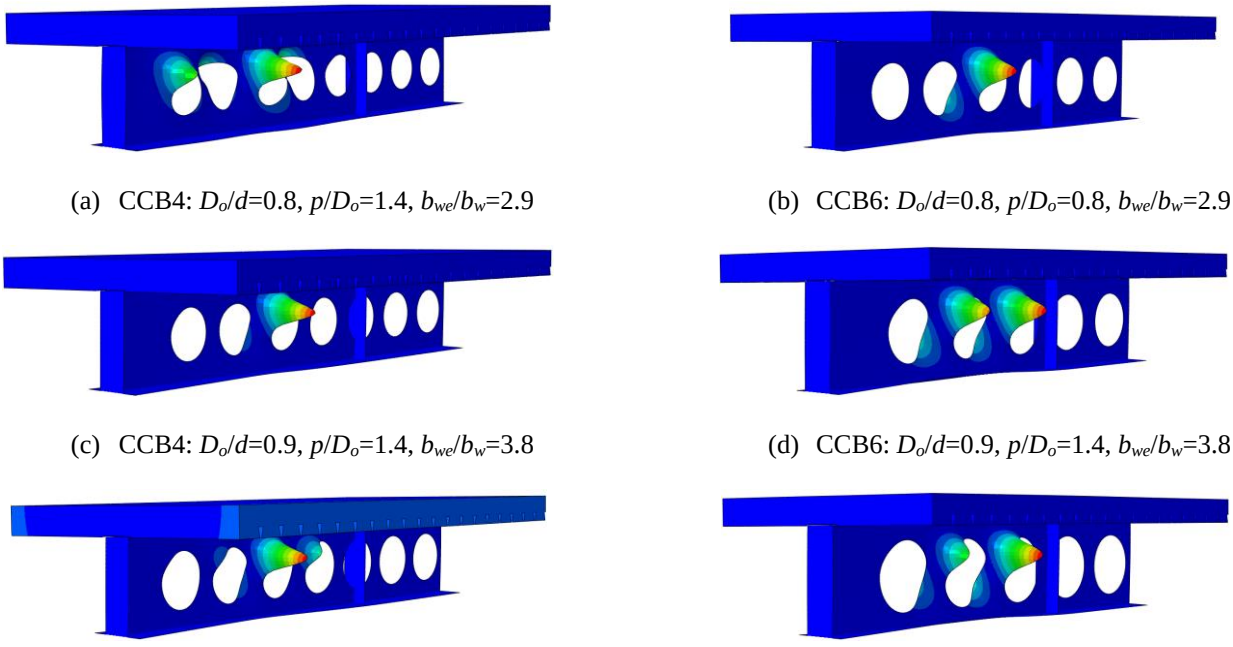

(a) CCB4: D_o/d=0.8, p/D_o=1.4, b_{we}/b_w=2.9

(b) CCB6: D_o/d=0.8, p/D_o=0.8, b_{we}/b_w=2.9

(c) CCB4: D_o/d=0.9, p/D_o=1.4, b_{we}/b_w=3.8

(d) CCB6: D_o/d=0.9, p/D_o=1.4, b_{we}/b_w=3.8

(e) CCB4: D_o/d=1.0, p/D_o=1.3, b_{we}/b_w=3.8

(f) CCB6: D_o/d=1.0, p/D_o=1.3, b_{we}/b_w=3.8

Fig. 15: WPB for CCB4 and CCB6 sections

Another important observation to be highlighted is in relation to the buckling modes. Alike section CCB2, for sections CCB4 and CCB6, it was verified that WPB did not occur in the first buckling mode. This occurred for several situations in section CCB4 (D_o/d=0.8, p/D_o=1.2-1.3 and 1.5; D_o/d=0.9, p/D_o=1.2-1.3 and 1.5; D_o/d=1.0, p/D_o=1.2 and 1.4-1.5; D_o/d=1.1-1.2, p/D_o=1.2-1.5), which is less slender than the CCB6 section. For the CCB6 section, these situations were observed only for D_o/d=0.8 and

p/D_o=1.2-1.3 and 1.5 models. **Fig. 16 and Fig. 17** illustrates some examples. When this occurs, the ultimate behavior of inelastic analysis is governed by a plastic mechanism or even the rupture of the shear connectors [17]. The results of the global critical shear as a function of the key parameters for the models CCB4 (**Fig. 18a**) and CCB6 are presented below (**Fig. 18b**).

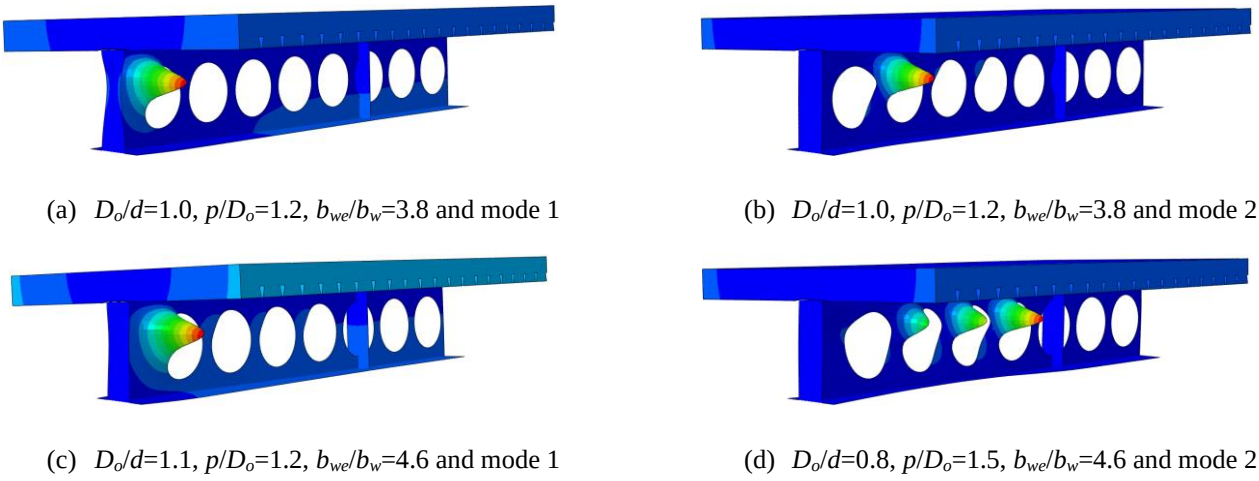

(a) D_o/d=1.0, p/D_o=1.2, b_{we}/b_w=3.8 and mode 1

(b) D_o/d=1.0, p/D_o=1.2, b_{we}/b_w=3.8 and mode 2

(c) D_o/d=1.1, p/D_o=1.2, b_{we}/b_w=4.6 and mode 1

(d) D_o/d=0.8, p/D_o=1.5, b_{we}/b_w=4.6 and mode 2

Fig. 16: Buckling modes for CCB4 model

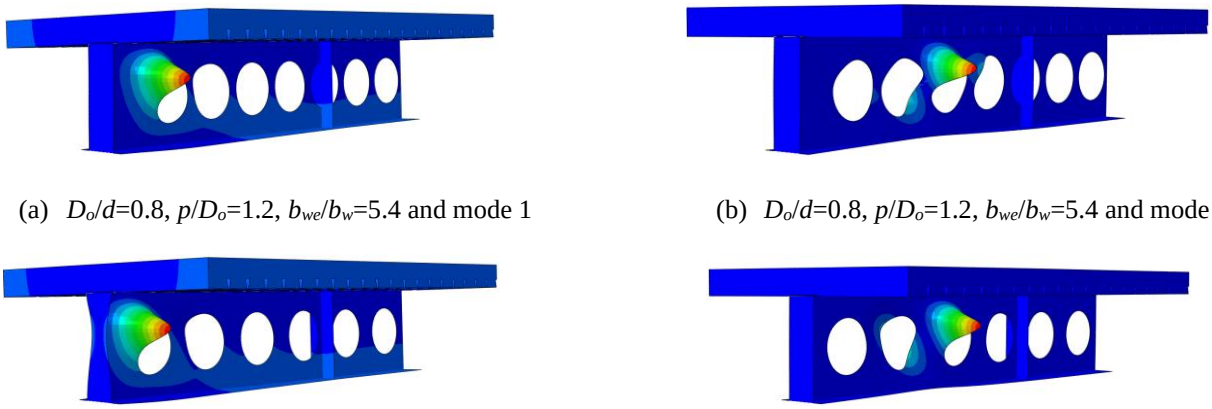

(a) D_o/d=0.8, p/D_o=1.2, b_{we}/b_w=5.4 and mode 1

(b) D_o/d=0.8, p/D_o=1.2, b_{we}/b_w=5.4 and mode 2

(c) D_o/d=0.8, p/D_o=1.5, b_{we}/b_w=1.3 and mode 1

(d) D_o/d=0.8, p/D_o=1.5, b_{we}/b_w=1.3 and mode 2

Fig. 17: Buckling modes for CCB6 model

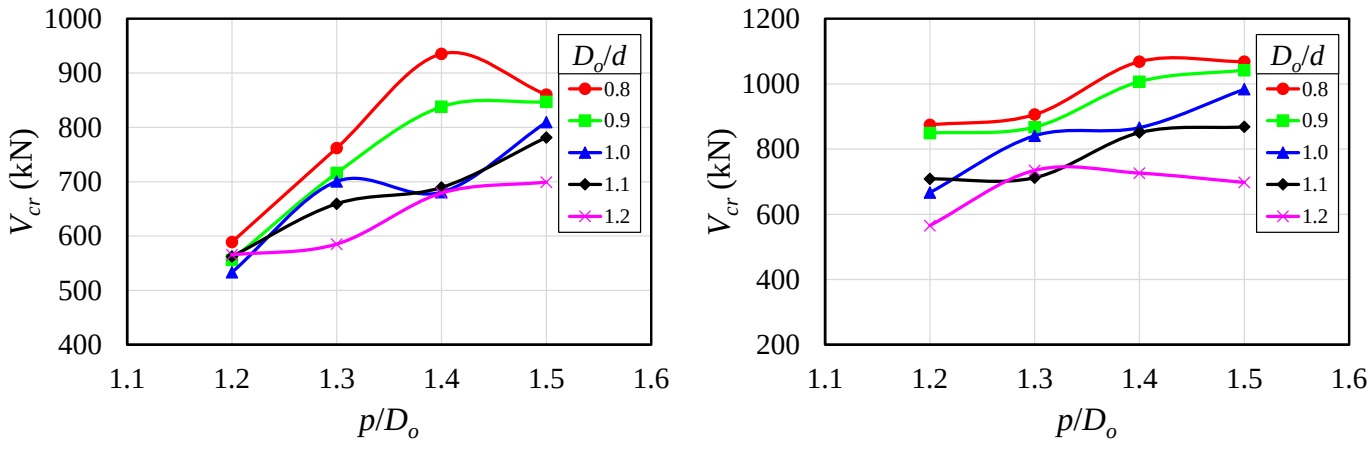

(a) CCB4 model

(b) CCB6 model

Fig. 18: Critical global shear vs. key parameters for CCB4 and CCB6 models

As noted, the CCB4 section, which is less slender than the CCB6 section, showed lower values of critical global shear (**Fig. 18a**). This is explained by the occurrence of local web buckling of the upper tee. Notably, for section CCB6 (**Fig. 18b**) the values of the critical global shear were higher, because in most situations the WPB was verified, thus requesting both the upper and lower tees. **Fig. 19** shows the comparisons between sections CCB2, CCB4 and CCB6, and **Fig. 20**, comparisons are presented between the elastic analyses of the present work, with the inelastic analyses presented by Ferreira et al. [17].

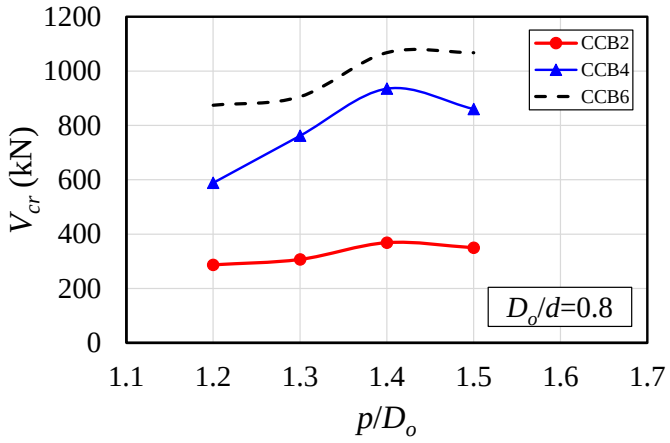

(a) D_o/d=0.8

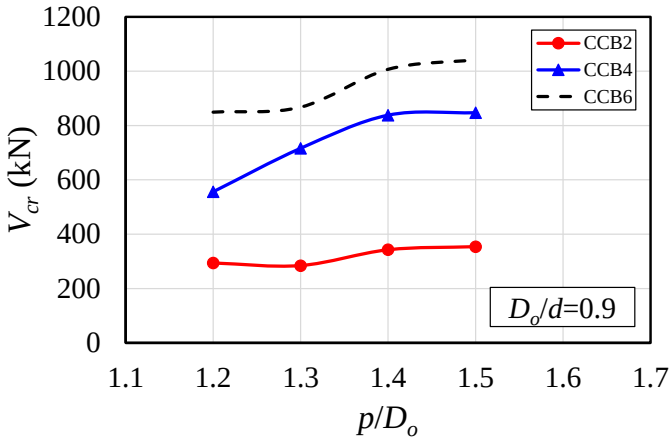

(b) D_o/d=0.9

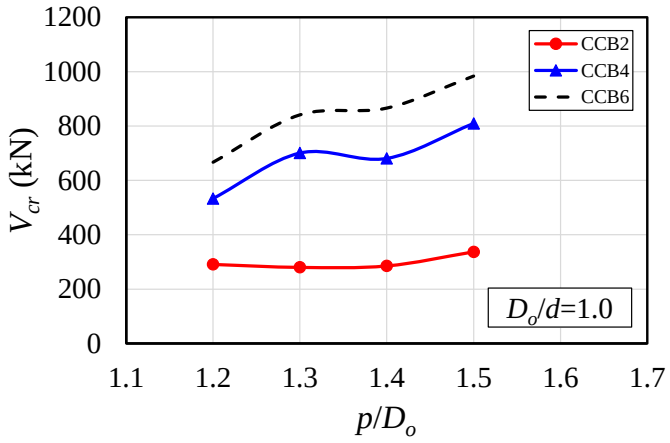

(c) D_o/d=1.0

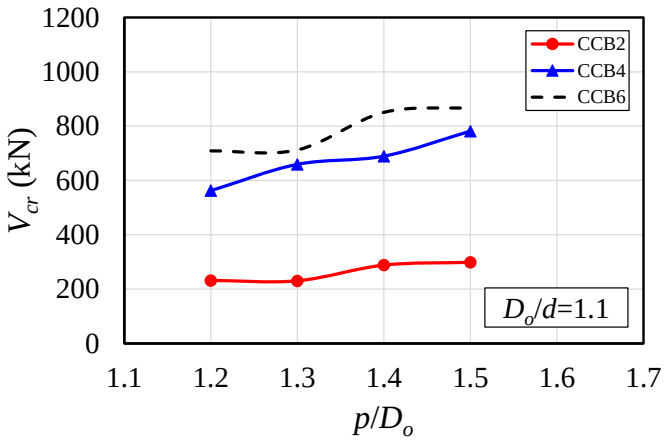

(d) D_o/d=1.1

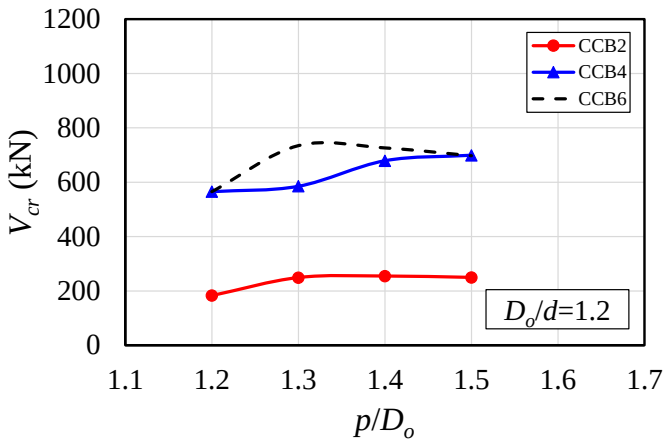

(e) D_o/d=1.2

Fig. 19: Comparative analyses for asymmetric composite cellular beams

The differences, minimum, maximum and average were 8%, 53% and 39%, respectively. It is worth mentioning that in the elastic analysis, no physical and geometric imperfections are considered.

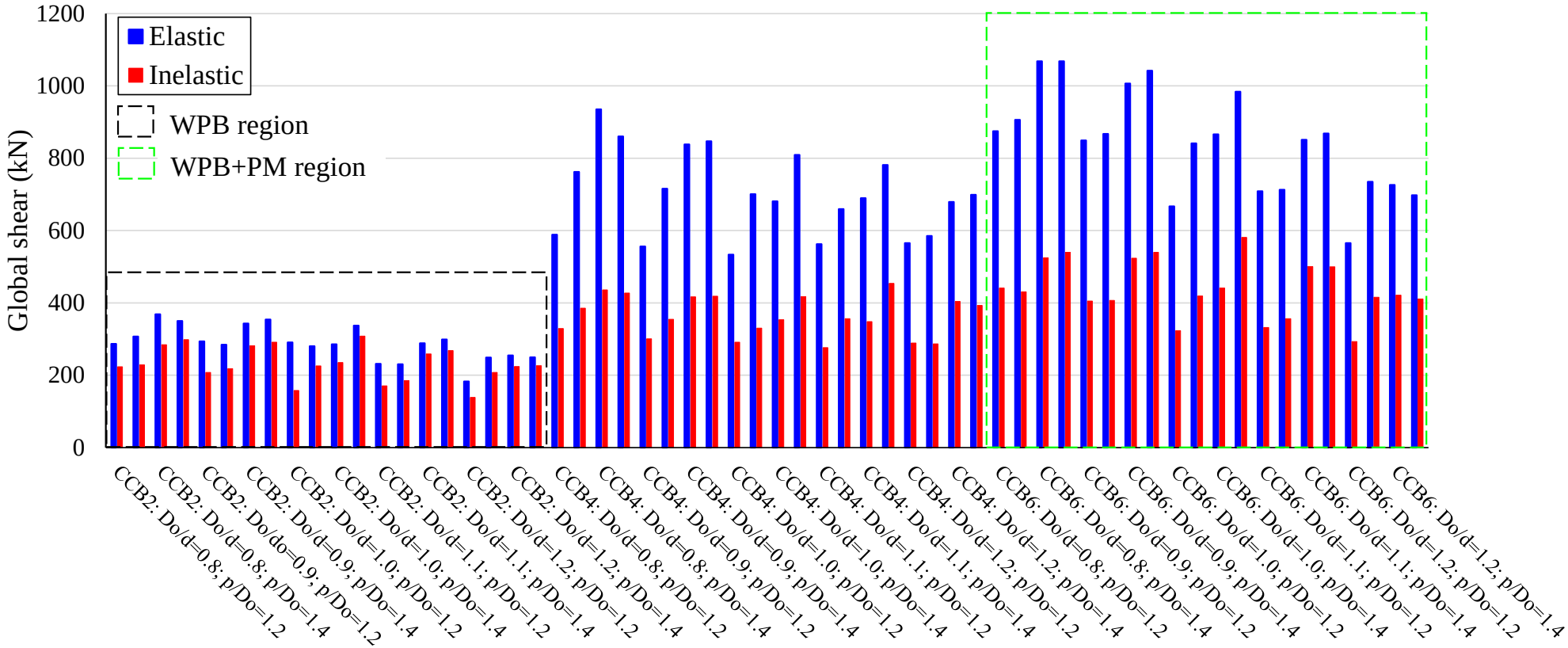

Fig. 20: Elastic and inelastic analyses for composite asymmetric cellular beams

5.3. STATISTICAL ANALYSIS

The results of the elastic analyses are presented according to each key parameter, such as the relationships D_o/d, p/D_o and b_{we}/b_w, considering all sections analyzed (**Fig. 21**). As shown in **Fig. 21a**, in general, the smaller the opening diameter, the greater the critical global shear that causes WPB. It is noteworthy that the smaller the opening diameter, the larger the tees sections. According to **Fig. 21b**, the greater the web post width, the greater the critical global shear response. Finally, on the variation of the end post (**Fig. 21c**), the greatest influence was measured for the sections that presented greater web thickness (CCB3-CCB6) and asymmetry (CCB4 and CCB6).

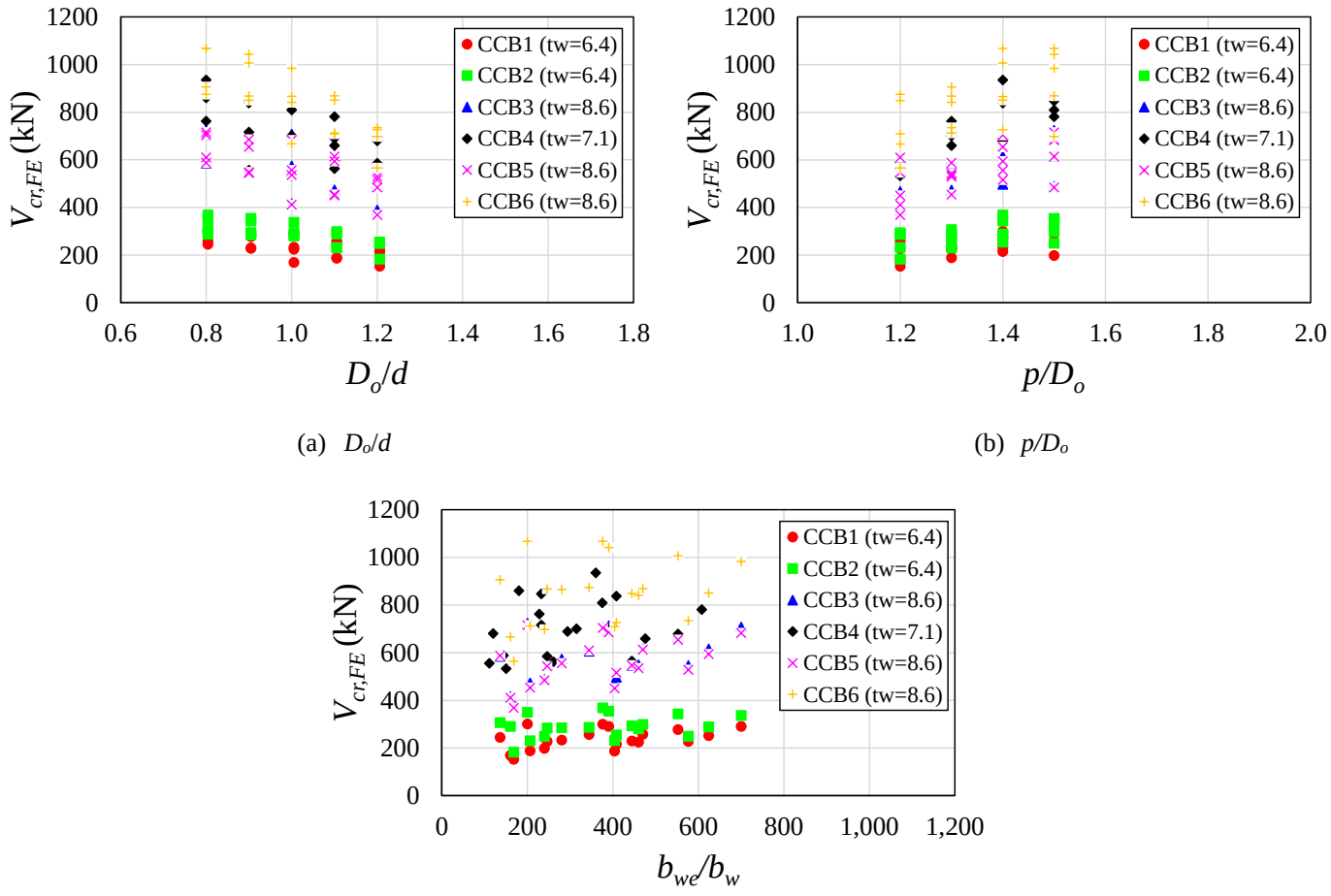

(a) D_o/d (b) p/D_o

(c) b_{we}/b_w

Fig. 21: The influence of key parameters on critical global shear

Fig. 22 depicts a comparison of the critical global shear with the analytical procedures presented in section 2. As shown, a greater conformity between the elastic numerical values was verified with the procedure of Panedpojaman et al. [13]. This meant that in total 101 observations were in the conservative zone ($V_{cr}/V_{cr,FE} \leq 1.0$). Thus, such a procedure, which takes into account the k factor for the calculation of the effective length, is a good approximation for the estimation of the elastic buckling. On the other hand, the procedure prescribed in SCI P355 [18] overestimated the elastic analysis, since all results showed $V_{cr}/V_{cr,FE} > 1.0$. This conclusion, also, was stated in Abrambes et al. [14] and Rajana et al. [15], considering non-composite cellular beams.

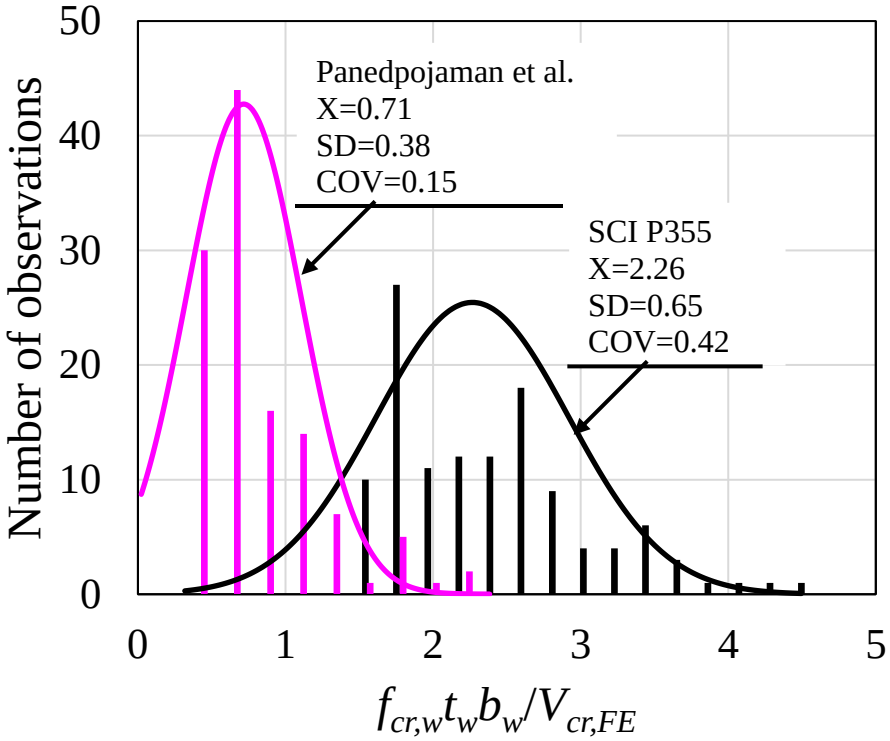

Fig. 22: Statistical analysis

Another observation to be considered is illustrated in **Fig. 23**. Such an illustration normalizes the results of the elastic and inelastic analyses [17] for comparison with the EC3 buckling curves. As previously presented, the use of buckling curves *b* and *c* may underestimate the strength of composite cellular beams, since most of the results presented were above the buckling curve *a*.

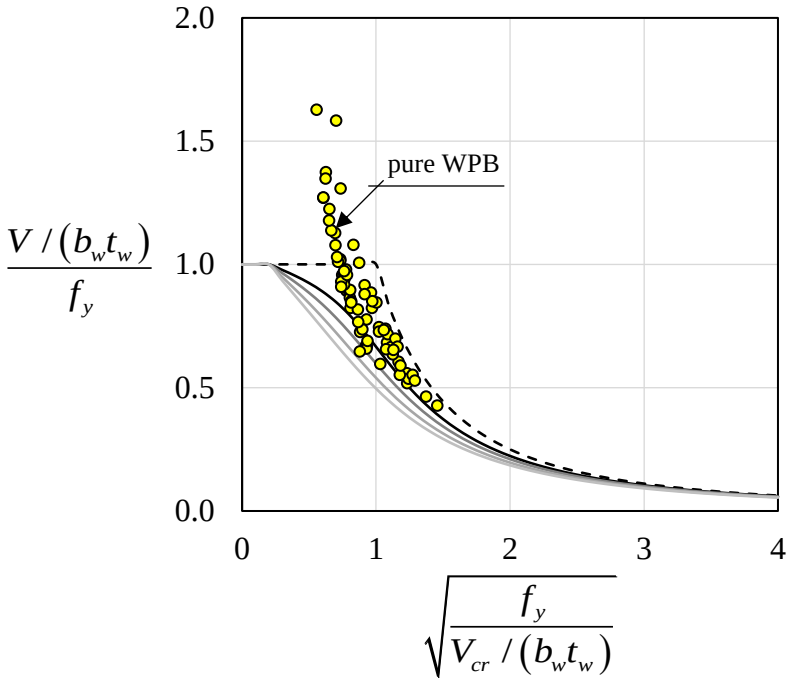

Fig. 23: Elastic and Inelastic analyses vs. EC3 buckling curves

CONCLUDING REMARKS

This paper presented a numerical model capable of representing experimental models of composite cellular beams. A parametric study was carried out, varying the cross sections as well as the D_o/d, p/D_o and b_{we}/b_w ratios. In total, 120 models were processed. The elastic analyses were compared with inelastic analyses and analytical procedures, considering the critical global shear that causes the web post buckling. It was concluded:

1. In composite cellular beams with a less slender web, local web buckling is observed in the upper tee close to the support;
2. Increasing the web slenderness, the buckling mode changed from local web buckling to web post buckling. This effect generated an increase in the critical global shear, as both upper and lower tees were utilized;
3. The smaller the opening diameter is, the greater the critical global shear that causes WPB;
4. The greater the web post width is, the greater the critical global shear;
5. The end post width is an expressive parameter that influences the critical global shear in composite asymmetric cellular beams with slender web;
6. The differences between elastic and inelastic analyses show an average value of 36% and 39%, for the composite symmetric and asymmetric sections, respectively.
7. The calculation procedure recommended by SCI P355 overestimates the elastic analyses, while the procedure that presents the modification of the effective length is a good approximation for the estimation of the elastic buckling.

ACKNOWLEDGMENTS

This work was supported by the São Paulo Research Foundation (FAPESP) [grant number #2018/22803-1].

REFERENCES

[1] El-Sawy KM, Sweedan AMI, Martini MI. Moment gradient factor of cellular steel beams under inelastic flexure. J Constr Steel Res 2014;98:20–34. https://doi.org/10.1016/j.jcsr.2014.02.007.

[2] Ellobody E. Nonlinear analysis of cellular steel beams under combined buckling modes. Thin-Walled Struct 2012;52:66–79. https://doi.org/10.1016/j.tws.2011.12.009.

[3] Panedpojaman P, Sae-Long W, Chub-Uppakarn T. Cellular beam design for resistance to inelastic lateral-torsional buckling. Thin-Walled Struct 2016;99:182–94. https://doi.org/10.1016/j.tws.2015.08.026.

[4] Redwood RG, Wong PK. Web holes in composite beams with steel deck. Can. Struct. Eng. Conf. -1982, Ontario, Toronto: Canadian Steel Construction Council; 1982, p. 1–41.

[5] Redwood RG, Poumbouras G. Tests of composite beams with web holes. Can J Civ Eng 1983;10:713–21. https://doi.org/10.1139/l83-100.

[6] Donahey RC, Darwin D. Web openings in composite beams with ribbed slabs. J Struct Eng 1988;114:518–34. https://doi.org/10.1061/(ASCE)0733-9445(1988)114:3(518).

[7] Park JW, Kim CH, Yang SC. Ultimate Strength of Ribbed Slab Composite Beams with Web Openings. J Struct Eng 2003;129:810–7. https://doi.org/10.1061/(asce)0733-9445(2003)129:6(810).

[8] Sheehan T, Dai X, Lam D, Aggelopoulos E, Lawson M, Obiala R. Experimental study on long spanning composite cellular beam under flexure and shear. J Constr Steel Res 2016;116:40–54. https://doi.org/10.1016/j.jcsr.2015.08.047.

[9] Erdal F, Saka MP. Ultimate load carrying capacity of optimally designed steel cellular beams. J Constr Steel Res 2013;80:355–68. https://doi.org/10.1016/j.jcsr.2012.10.007.

[10] Kerdal D, Nethercot DA. Failure modes for castellated beams. J Constr Steel Res 1984;4:295–315. https://doi.org/10.1016/0143-974X(84)90004-X.

[11] Redwood R, Cho SH. Design of steel and composite beams with web openings. J Constr Steel Res 1993;25:23–41. https://doi.org/10.1016/0143-974X(93)90050-3.

[12] Tsavdaridis KD, D'Mello C. Vierendeel Bending Study of Perforated Steel Beams with Various Novel Web Opening Shapes through Nonlinear Finite-Element Analyses. J Struct Eng 2012;138:1214–30. https://doi.org/10.1061/(asce)st.1943-541x.0000562.

[13] Panedpojaman P, Thepchatri T, Limkatanyu S. Novel design equations for shear strength of local web-post buckling in cellular beams. Thin-Walled Struct 2014;76:92–104. https://doi.org/10.1016/j.tws.2013.11.007.

[14] Abambres M, Rajana K, Tsavdaridis K, Ribeiro T. Neural Network-Based Formula for the Buckling Load Prediction of I-Section Cellular Steel Beams. Computers 2018;8:2. https://doi.org/10.3390/computers8010002.

[15] Rajana K, Tsavdaridis KD, Koltsakis E. Elastic and inelastic buckling of steel cellular beams under strong-axis bending. Thin-Walled Struct 2020;156:106955. https://doi.org/10.1016/j.tws.2020.106955.

[16] EUROPEAN COMMITTEE FOR STANDARDIZATION. Eurocode 3: Design of steel structures—Part 1-1: General rules and rules for buildings 2005.

[17] Ferreira FPV, Martins CH, De Nardin S. Assessment of web post buckling resistance in steel-concrete composite cellular beams. Thin-Walled Struct 2020:106969. https://doi.org/10.1016/j.tws.2020.106969.

[18] Lawson RM, Hicks SJ. Design of beams with large web openings. The Steel Construction Institute; 2011.

[19] Granade CJ. An investigation of composite beams having large rectangular openings in their webs. 1968. Partial M.Sc. thesis. University of Alabama, 1968.

[20] Clawson WC, Darwin D. Tests of composite beams with web openings. ASCE J Struct Div 1982;108:145–62.

[21] Cho SH. An investigation on the strength of composite beams with web openings. 1982. M.Sc. thesis. Hanyang University, 1982.

[22] Narayanan R, Al-Amery RIM, Roberts TM. Shear strength of composite plate girders with rectangular web cut-outs. J Constr Steel Res 1989;12:151–66. https://doi.org/10.1016/0143-974X(89)90030-8.

[23] Roberts TM, Al-Amery RIM. Shear strength of composite plate girders with web cutouts. J Struct Eng 1991;117:1897–910. https://doi.org/10.1061/(ASCE)0733-9445(1991)117:7(1897).

[24] Todd DM, Cooper PB. Strength of composite beams with web openings. ASCE J Struct Div 1980;106:431–44.

[25] DONOGHUE CM. Strength of composite beams with web openings. ASCE J Struct Div 1982;108:2652–67.

[26] Clawson WC, Darwin D. Strength of composite beams at web openings. ASCE J Struct Div 1982;108:623–41.

[27] Lawson RM, Chung KF, Price AM. Tests on composite beams with large web openings to justify existing design methods. Struct Enginee 1992;70:1–7.

[28] Cho SH, Redwood RG. Slab behavior in composite beams at openings. II: tests and verification. J Struct Eng 1992;118:2304–22. https://doi.org/10.1061/(ASCE)0733-9445(1992)118:9(2304).

[29] Redwood RG, Poumbouras G. Analysis of composite beams with web openings. J Struct Eng 1984;110:1949–58. https://doi.org/10.1061/(ASCE)0733-9445(1984)110:9(1949).

[30] Darwin D, Donahey RC. LRFD for composite beams with unreinforced web openings. J Struct Eng 1988;114:535–52. https://doi.org/10.1061/(ASCE)0733-9445(1988)114:3(535).

[31] Cho SH, Redwood RG. Slab behavior in composite beams at openings. I: analysis. J Struct Eng 1992;118:2287–303. https://doi.org/10.1061/(ASCE)0733-9445(1992)118:9(2287).

[32] Fahmy EH. Analysis of composite beams with rectangular web openings. J Constr Steel Res 1996;37:47–62. https://doi.org/10.1016/0143-974X(95)00022-N.

[33] Benitez MA, Darwin D, Donahey RC. Deflections of composite beams with web openings. J Struct Eng 1998;124:1139–47. https://doi.org/10.1061/(ASCE)0733-9445(1998)124:10(1139).

[34] Chung K. F, Lawson R. M. Simplified design of composite beams with large web openings to Eurocode 4. J Constr Steel Res 2001;57:135–64. https://doi.org/10.1016/S0143-974X(00)00011-0.

[35] Hechler O, Müller C, Sedlacek G. Investigations on Beams with Multiple Regular Web Openings. Compos. Constr. Steel Concr. V, Reston, VA: American Society of Civil Engineers; 2006, p. 270–81. https://doi.org/10.1061/40826(186)26.

[36] MÜLLER C, HECHLER O, BUREAU A, BITAR D, JOYEUX D, CAJOT LG, et al. Large web openings for service integration in composite floors. Technical Steel Research. European Comission, Contract No 7210-PR/315. Final report 2006.

[37] Nadjai A. Performance of cellular composite floor beams at ambient temperature. 2005.

[38] Nadjai A, Vassart O, Ali F, Talamona D, Allam A, Hawes M. Performance of cellular composite floor beams at elevated temperatures. Fire Saf J 2007;42:489–97. https://doi.org/10.1016/j.firesaf.2007.05.001.

[39] Gizejowski MA, Khalil WAS. Stability and ductility of castellated composite beams subjected to hogging bending. In: Batista E, Vellasco P, Lima L de, editors. SDSS'Rio 2010 Stab. DUCTILITY STEEL Struct., Rio de Janeiro: 2010, p. 839–46.

[40] EUROPEAN COMMITTEE FOR STANDARDIZATION. EN 1994-1-1: Eurocode 4 – Design of composite steel and concrete structures – Part 1-1: General rules for buildings. 2004.

[41] Fares SS, Coulson J, Dinehart DW. AISC Steel Design Guide 31: Castellated and Cellular Beam Design. American Institute of Steel Construction; 2016.

[42] Grilo LF, Fakury RH, Castro e Silva ALR de, Veríssimo G de S. Design procedure for the web-post buckling of steel cellular beams. J Constr Steel Res 2018;148:525–41. https://doi.org/10.1016/j.jcsr.2018.06.020.

[43] Ferreira FPV, Martins CH, De Nardin S. Advances in composite beams with web openings and composite cellular beams. J Constr Steel Res 2020;172:106182. https://doi.org/10.1016/j.jcsr.2020.106182.

[44] EUROPEAN COMMITTEE FOR STANDARDIZATION. EUROCODE 3: Design of steel structures - Part 1-1: General rules and rules buildings 2005.

[45] Ferreira FPV, Martins CH. LRFD for Lateral-Torsional Buckling Resistance of Cellular Beams. Int J Civ Eng 2020;18:303–23. https://doi.org/10.1007/s40999-019-00474-7.

[46] Ferreira FPV, Rossi A, Martins CH. Lateral-torsional buckling of cellular beams according to the possible updating of EC3. J Constr Steel Res 2019;153:222–42. https://doi.org/10.1016/j.jcsr.2018.10.011.

[47] Rossi A, Ferreira FPV, Martins CH, Mesacasa Júnior EC. Assessment of lateral distortional buckling resistance in welded I-beams. J Constr Steel Res 2020;166:105924. https://doi.org/10.1016/j.jcsr.2019.105924.

[48] Ferreira FPV, Martins CH, De Nardin S. Sensitivity Analysis of Composite Cellular Beams to Constitutive Material Models and Concrete Fracture. Int J Struct Stab Dyn 2020:2150008. https://doi.org/10.1142/S0219455421500085.

[49] Ferreira FPV, Martins CH, De Nardin S. A parametric study of steel-concrete composite beams with hollow core slabs and concrete topping. Structures 2020;28:276–96. https://doi.org/10.1016/j.istruc.2020.08.045.

[50] Chen S, Jia Y. Numerical investigation of inelastic buckling of steel–concrete composite beams prestressed with external tendons. Thin-Walled Struct 2010;48:233–42. https://doi.org/10.1016/j.tws.2009.10.009.

[51] Couto C, Vila Real P. Numerical investigation on the influence of imperfections in the lateral-torsional buckling of beams with slender I-shaped welded sections. Thin-Walled Struct 2019;145:106429. https://doi.org/10.1016/j.tws.2019.106429.

[52] ArcelorMittal. ACB® and Angelina® beams - A New Generation of Cellular Beams 2018.

[53] Dassault Systèmes Simulia. Abaqus 6.18 2016.

[54] Yun X, Gardner L. Stress-strain curves for hot-rolled steels. J Constr Steel Res 2017;133:36–46. https://doi.org/10.1016/j.jcsr.2017.01.024.

[55] Carreira DJ, Chu KH. Stress-Strain Relatonship for Reinforced Concrete in Tension. J Am Concr Inst 1986;83:21–8.

[56] CARREIRA DJ, CHU KH. Stress-Strain Relationship for Plain Concrete in Compression. ACI J Proc 1985;82:797–804. https://doi.org/10.14359/10390.

[57] Wijesiri Pathirana S, Uy B, Mirza O, Zhu X. Flexural behaviour of composite steel–concrete beams utilising blind bolt shear connectors. Eng Struct 2016;114:181–94. https://doi.org/10.1016/j.engstruct.2016.01.057.

[58] Katwal U, Tao Z, Hassan MK, Uy B, Lam D. Load sharing mechanism between shear studs and profiled steel sheeting in push tests. J Constr Steel Res 2020;174:106279. https://doi.org/10.1016/j.jcsr.2020.106279.

[59] Guezouli S, Lachal A. Numerical analysis of frictional contact effects in push-out tests. Eng Struct 2012;40:39–50. https://doi.org/10.1016/j.engstruct.2012.02.025.

[60] Sjaarda M, Porter T, West JS, Walbridge S. Fatigue Behavior of Welded Shear Studs in Precast Composite Beams. J Bridg Eng 2017;22:04017089. https://doi.org/10.1061/(ASCE)BE.1943-5592.0001134.

[61] Liu X, Bradford MA, Chen Q-J, Ban H. Finite element modelling of steel–concrete composite beams with high-strength friction-grip bolt shear connectors. Finite Elem Anal Des 2016;108:54–65. https://doi.org/10.1016/j.finel.2015.09.004.

[62] Nguyen TNH, Tan KH, Kanda T. Investigations on web-shear behavior of deep precast, prestressed concrete hollow core slabs. Eng Struct 2019;183:579–93. https://doi.org/10.1016/j.engstruct.2018.12.052.

[63] Lawson RMM, Lim J, Hicks SJJ, Simms WII. Design of composite asymmetric cellular beams and beams with large web openings. J Constr Steel Res 2006;62:614–29. https://doi.org/10.1016/j.jcsr.2005.09.012.

A parametric study of steel-concrete composite beams with hollow core slabs and concrete topping

Felipe Piana Vendramell Ferreira*[a], Carlos Humberto Martins[b], Silvana De Nardin[a]

[a]Federal University of São Carlos, Rod. Washington Luiz, km 235, São Carlos, São Paulo, Brazil.

[b]State University of Maringá, Av. Colombo nº 5790, Maringá, Paraná, Brazil.

*Corresponding author

E-mail addresses: fpiana@live.com (F. P. V. Ferreira), chmartins@uem.br (C. H. Martins), snardin@ufscar.br (S. De Nardin)

Abstract

The use of industrialized elements results in the speed of execution, it avoids waste of materials, and it meets sustainability requirements. The steel profiles and hollow core slabs are included in this scope. The hollow core slab presents superior quality than cast in-situ structural elements, and it is produced in specific environments with technological control and monitoring. In general, a concrete topping is made for smooth and uniform finishing. Studies addressing the structural behavior of steel-concrete composite beams with hollow core slabs with concrete topping are scarce. The present work aims to investigate the behavior of steel-concrete composite beams with hollow core slabs with concrete topping, considering full and partial interaction. Geometric nonlinear analyses are performed based on experimental tests. The steel-concrete composite beams with hollow core slabs with concrete topping are simply supported and subjected to two points loads symmetrically spaced. The influence of concrete topping (50mm of thickness), the in situ concrete strength (25 MPa, 30 MPa and 40 MPa), the rate of transverse reinforcement (10mm, 12.5mm and 16mm), the interaction degree (shear connectors spaced at 120mm, 175mm and 225mm), and the steel cross section (W360x51, W460x74 and W530x72) are the parameters investigated. The results are discussed, considering these parameters. It was concluded that the concrete topping increased the strength of the composite beams with precast hollow core slabs, the lower the degree of interaction, the greater the ductile behavior of the composite element as a whole. The in-situ infill concrete strength was directly influenced by the steel cross-sectional area, reinforcement rate and interaction degree. The resistance of steel-concrete composite beams with precast hollow core slabs may vary depending on the transverse reinforcement rate and interaction degree. Ductile behavior was observed for all situations, considering partial interaction.

Keywords: Composite beams; Hollow core slabs; Concrete topping; Geometric nonlinear analyses.

NOTATION

The following notations and symbols are used in this paper:

HCU Hollow core unit;
PCHCS Precast hollow core slab;
P.N.A Plastic neutral axis;
A_a the steel section cross-sectional area;
A_{sc} the headed stud cross-sectional area;
A_s the transversal reinforcement cross-sectional area;
b the effective slab width;
b_f the steel flange width;
C_c the concrete flange axial resistance;
C_s the axial resistance of the steel section in compression;
c the concrete topping thickness;
d the steel beam depth;
d_{sc} the headed stud diameter;
E_c the modulus of elasticity of the concrete;
E_s the modulus of elasticity of the steel;
f_c the compressive concrete strength;
$f_{c,in\text{-}situ}$ the in-situ infill compressive strength;
$f_{c,HCU}$ the HCU compressive strength;
f_t the concrete tensile strength;
$f_{u,sc}$ the head stud ultimate strength;
f_y the steel section yield strength;
$f_{y,f}$ the flange yield strength;
f_{ys} the transverse reinforcement yield strength;
$f_{y,w}$ yield strength of the web;
g gap;
h_w clear depth of the steel web;
h_{sc} overall length of the headed stud connector;
k coefficient applied to take account the influence of the shear connectors confinement due to the transverse reinforcement, and the shear connectors geometry relative to the hollow core units;
K_c the ratio of the second stress invariant on the tensile meridian to that on the compressive meridian;
L composite beam length;
L_φ transverse reinforcement;
M_{FE} Bending moment of finite element model;
$M_{FE,0}$ Bending moment of finite element model without concrete topping;
$M_{FE,50}$ Bending moment of finite element model with concrete topping;
M_{Test} Bending moment of experimental tests;
M_{pl} the plastic moment of the composite section;
$M_{pl,a}$ the plastic moment of the steel section;
$M_{pl,FULL}$ the plastic moment of the composite section with full shear connection;
n number of shear connectors;
s shear connectors spacing;
t_c overall depth of the concrete flange (including the concrete topping);
t_f the steel flange thickness;
t_w the steel web thickness;
T_a the axial resistance of the steel section in tension;
$T_{a,flange}$ the axial resistance of the steel flange;
$T_{a,web}$ the axial resistance of the steel web;
Z_x plastic modulus of steel section;
α_{sc} factor which takes into account the height of stud;
β_c the stress-strain relationship form factor of concrete in compression;
β_{sc} factor that takes into account the in-situ infill gap;
δ_{FE} Mid-span vertical displacement of the finite element models;
δ_{Test} Mid-span vertical displacement of the tests;
Δ_{CB1} Slip of CB1 model;
Δ_{CB1} Slip of CB2 model;
ε strain;
ε_c the strain corresponding to concrete compressive strength;
ε_t the strain corresponding to concrete tensile strength;
ε_{sc} factor that takes into account the transverse reinforcement;
η the ratio of the sum of the resistances of the shear connectors provided to the sum of the resistances of the shear connectors needed for full shear connection;
λ_{sc} factor for lightweight concrete and for the hollow-core slab height;
μ viscosity parameter;
ξ eccentricity;
σ stress;
σ_{b0} the initial equibiaxial compressive yield stress;
σ_{c0} the initial uniaxial compressive yield stress;
φ diameter of the transverse reinforcement;
ψ dilation angle

1. INTRODUCTION

Composite beams with solid or composite slabs have disadvantages in relation to the high operational cost of welding the shear connector on site, the curing time of wet concrete in cold climates and short spans corresponding to the floor height. Thus, to improve some of these limitations, a new type of composite beam was proposed, using the precast concrete hollow core slab (PCHCS) [1]. Composite beams with PCHCS are used due to the technical and economic benefits they offer, such as structural capacity as a function of span/height for a lower self-weight, reduction in the amount of concrete volume, making this system economical and ecologically correct, the shear connector is welded on the steel profile before taking it to the construction site, a factor that reduces the execution time, and the favorable conditions of handling, transportation, storage. Composite beams with PCHCS are common in the United Kingdom [2].

One of the common uses involving PCHCS is in floor systems in composite action with a cast in-situ concrete topping to provide resistance to actions and a smooth and uniform finish. Typically, the cast in-situ concrete topping is 40 to 100 mm of thickness, with strength ranges from 25 to 40 MPa and contain a small amount of transverse reinforcement to control shrinkage. In the construction of PCHCS with concrete topping there are no mechanical devices to promote the joint behavior of these elements [3]. In this case, the interface shear strength depends on the natural bond between the PCHCS and cast in-situ concrete topping. The composite behavior between PCHCS and concrete topping is desired due to the increased strength and stiffness under vertical loads, and also to resist and transmit forces resulting from the action of the diaphragm under lateral loads [4]. Baran [4] investigated the flexural behavior of PCHCS with concrete topping. The results showed that the composite behavior between these elements was valid at load levels corresponding to the non-cracked cross section. The presence of the concrete topping resulted in improvements in the cracking moment and in the initial stiffness of the PCHCS. However, the effect of concrete topping on strength was limited, mainly due to the loss of composite behavior before reaching the ultimate strength. In this scenario, Ibrahim et al [3] presented an experimental study of the shear-flexural strength of PCHCS with concrete topping. The results showed that the surface condition of the PCHCS and the longitudinal joint were factors that affect the stiffness and shear-flexural strength of these structural elements.

Regarding the studies of composite beams with PCHCS, Lam [5] stands out. The author investigated the interaction between the steel beam and PCHCS, the determination of the flexural strength and stiffness, and the horizontal shear stress resistance. Note that in this study the concrete topping was not considered. The author observed two failure modes: the sudden failure due to the rupture of the shear connectors associated with a high rate of transverse reinforcement, and the cracking of the concrete due to the yielding of the transverse reinforcement which resulted in loss of stiffness. Hence, there were several publications involving the author. Lam et al. [6] presented flexural tests, in which the composite beams with PCHCS were subjected to two points loads symmetrically spaced. The authors found that the composite action had a resistance three times greater than the steel beam resistance, bare, and the type of failure was ductile and can be controlled by the correct use of transverse reinforcement and in-situ infill concrete. Lam et al. [7] complemented the previous study by parametric analyses, considering the finite element method. In the numerical model, the author considered the shear connectors as spring elements. The authors concluded that with an increase

in the transverse reinforcement rate, the flexural strength significantly increased. However, the ductility was reduced, observing the fragile rupture due to the concrete slab crushing, and with the increase in the depth of PCHCS, there was an increase in the flexural strength, although the slab may fail due to tension. Due to the presence of the openings and low tensile strength of the concrete, the PCHCS are naturally susceptible to shear collapses. This factor becomes more critical for slabs that have non-circular opening and heights greater than 300mm [8]. It was observed here, that the authors verified parameters such as the slab and profile height, and transverse reinforcement rate. However, there were still no results of the flexural behavior due to the shear connectors, and the distance between the slab panels, which is called gap. In this context, Ellobody and Lam [2] investigated such parameters. The results showed that the shear connectors resistance increased with the increase of the gap, which is the distance between the HCU, the region where the shear connector is placed. Head studs are the mechanical devices most commonly used in composite beams and this is due to their behavior. A flexible connector close to reaching its maximum strength continues to deform without rupture, allowing neighboring connectors to increasingly absorb the shear flow. The flexible behavior of the head studs, which allows slipping between the concrete slab and the steel profile before reaching the ultimate limit state, is one of the reasons for the wide use of this type of connector in composite beams [9]. However, the resistance to shear stress and the stiffness of the steel-concrete connection depends not only on the strength of the shear connector, but also on the strength of the concrete slab against cracking caused by the high concentration of the shear stress in each connector [2,10]. In this scenario, Lam [10] presented a new experimental procedure for determining the shear strength of headed studs in composite beams with PCHCS. The justification described by the author was that the standard pushout test, specified in EC4 [11], it was not suitable as the dimensions specified for the slab were small to represent the construction of PCHCS; the reinforcement specified in the standard test was not suitable, since only the transverse reinforcement was used for the construction with PCHCS. The author [10] studied the influence of parameters such as the slab cutting angle (squared or chamfered), reinforcement rate, connector diameter and contribution of transverse reinforcements were evaluated. Such reinforcements assist in the transfer of forces from the profile to the slab and confine the concrete by reducing cracking. As observed so far, previous studies have not investigated the behavior of the concrete topping in the PCHCS subjected to pushout tests. In this scenario, Araújo et al. [9] performed pushout tests to assess such behavior. Unlike previous studies, the authors investigated the influence of the concrete topping, and the reinforcement rate on the transfer of steel-concrete forces using head studs. The authors concluded that the in-situ concrete compressive strength was the most important parameter for the strength of the shear connectors. **Table 1** presents the strength of head stud, considering PCHCS. In Batista and Landesmann [12], which is technical report, experimental tests on composite beams with PCHCS with concrete topping were performed. The tests indicated a homogeneous collapse mode, with the development of cracks initiated on the underside of the PCHCS units, in the central region between the two applied loads. These cracks propagated along the full width of the slab panel, extending from the side face of the slab to the region of connection with the steel profile, a factor that reduces the stiffness of the structural element as a whole.

Table 1: Headed stud strength, considering PCHCS with concrete **topping**

Ref.	Concrete crushing	Steel yielding
[13]	$0.29k\alpha_{sc}d_{sc}^{2}\sqrt{f_cE_c}$	$0.8f_{u,sc}A_{sc}$
[9]	$0.29\alpha_{sc}\beta_{sc}\varepsilon_{sc}\lambda_{sc}d_{sc}^{2}\sqrt{f_cE_c}$ $\varepsilon_{sc}=(\phi/23+1)\le 1.0 \rightarrow 8\le\phi\le 16$ $\lambda_{sc}=0.43(t_c/150+1)$	$0.75f_{u,sc}A_{sc}$

$\alpha_{sc}=0.2(h_{sc}/d_{sc}+1)\le 1.0$

$\beta_{sc}=0.5(g/71+1)\le 1.0$

$k=0.9$

From the scenario exposed so far, it appears that studies on composite beams with PCHCS are quite recent (**Table 2**). As presented, it is possible to observe that few researchers have dedicated to this theme, and there are no parametric studies that consider the flexural behavior of composite beams with PCHCS with concrete topping. This subject, being relatively new, was also addressed in the concluding remarks and future research directions section in Ferreira et al. Thus, the paper aims to investigate the behavior of composite beams with PCHCS with concrete topping. A parametric study is performed, considering nonlinear geometric analyses. The numerical model is calibrated, considering experimental tests [5,12]. For this task, symmetry on the longitudinal axis and displacement control are used. The composite beams with PCHCS with concrete topping are simply supported and subjected to two symmetrically spaced load points. The influence of concrete topping (50mm of thickness), the in situ concrete strength (25 MPa, 30 MPa and 40 MPa), the rate of transverse reinforcement (10mm, 12.5mm and 16mm), the interaction degree (shear connectors spaced at 120mm, 175mm and 225mm), and the steel cross section (W360x51, W460x74 and W530x72) are the parameters investigated. The results are discussed and compared with resistance calculation procedures, which are described in section 2.

Table 2: Studies of composite beams with PCHCS

Ref.	Parameters studied							
	Concrete topping	**In situ infill concrete strength**	**Transverse reinforcement rate**	**Interaction degree**	**Headed Stud**	**Steel section**	**Slab cutting angle**	**Gap**
[2,5–7,10,14][a]	No	Yes	Yes	Yes	Yes	Yes	Yes	Yes
[12][b]	Yes	No	No	No	No	No	No	No
Present study	Yes	Yes	Yes	Yes	No	Yes	No	No

[a]Experimental tests and parametric studies;
[b]Experimental tests;
[c]Parametric studies.

2. RESISTANCE OF COMPOSITE BEAMS WITH HOLLOW CORE SLABS

In 2003, the Steel Construction Institute published a manual containing design criteria for composite beams with PCHCS [15]. Further, Gouchman [13] updated such publication. The manual gathers recommendations of minimum dimensions, arrangement of shear connector, transverse reinforcement and recommendations for ultimate and service limit states in the

construction phase for cases of total and partial interaction. The total interaction refers to the case where the connection between the elements is able to fully resist the forces applied to it. This is possibly the most common situation. In this case, the sum of the resistance of the shear connectors is greater than the lowest resistance between concrete slab and steel. In this situation, it is observed that the position of the plastic neutral axis (P.N.A) can be located in the slab, in the upper flange or in the web of steel profile (**Fig. 1**). The calculation of the strength of composite beams with PCHCS is based on the prescriptions of Gouchman [13], considering total and partial interaction. The flexural strength is calculated according to the position of the P.N.A.

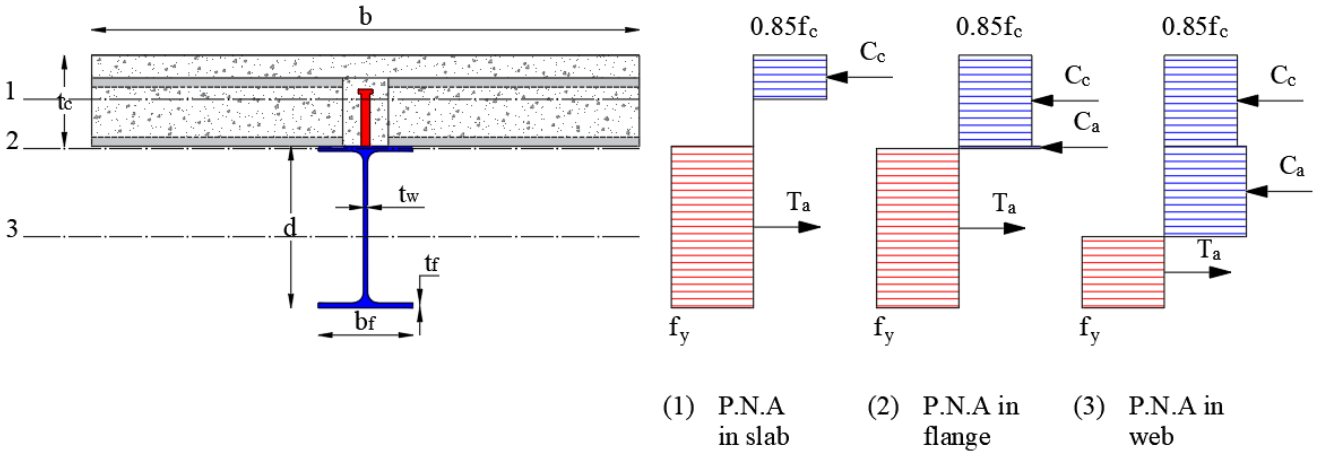

Fig. 1: Plastic neutral axis position: full interaction

Gouchman [13] mentions that for the case of composite beams with PCHCS, the P.N.A is not allowed to be located in the concrete slab. When this occurs, it is necessary to increase the height of the steel profile, otherwise the alternative solution would be to consider the partial interaction. Thus, when the P.N.A lies within the upper flange ($C_c \geq T_{a,web}$ and $T_a > C_c$), the flexural strength of composite beams with PCHCS is calculated, according to **Eqs. (1-7)**:

$$M_{pl} = T_a\left(\frac{d}{2}\right) + C_c\left(\frac{t_c}{2}\right) - \left[\frac{\left(T_a - C_c\right)^2}{T_{a,\,flange}}\right]\left(\frac{t_f}{4}\right) \tag{1}$$

$$C_c = 0.85\, f_c b t_c \tag{2}$$

$$b \leq \begin{cases} L/4 \\ 2L_\phi + g \end{cases} \tag{3}$$

$$T_{a,\,flange} = b_f t_f f_y \tag{4}$$

$$T_{a,web} = h_w t_w f_y \tag{5}$$

$$h_w = d - 2t_f \tag{6}$$

$$T_a = A_a f_y \tag{7}$$

When the P.N.A lies within the web ($T_{a,web}>C_c$), the flexural strength of composite beams with PCHCS is calculated **(Eqs. 8-9)**:

$$M_{pl} = M_{pl,a} + C_c\left(\frac{d+t_c}{2}\right) - \frac{C_c^{\,2}}{T_{a,web}}\left(\frac{h_w}{4}\right) \tag{8}$$

$$M_{pl,a} = Z_x f_y \tag{9}$$

However, in the last two decades, the use of composite beams in civil construction has led to many cases in which the connection could not withstand all the forces applied. In this case, the connection may fail by shear before any of the other elements reach their strength [16]. This means that the combined strength of the shear connectors is less than the lowest compressive strength of concrete or the tensile strength of the steel profile **(Fig. 2)**. In this case, the connection may deform, resulting in relative movement along the steel-concrete interface, causing the elements to lose stiffness. Unlike total interaction, partial interaction favors ductility in the structural system as a whole [17].

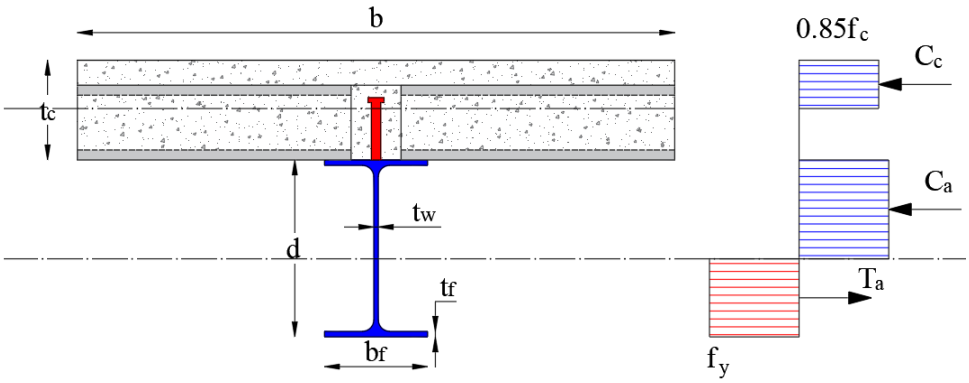

Fig. 2: Plastic neutral axis position: partial interaction

The simplest method of determining the bending resistance of a composite section with partial shear connection is the 'linear interaction' (**Eq. 10**) approach, covered by EC4 [11]:

$$M_{pl} = M_{pl,a} + \left(M_{pl,FULL} - M_{pl,a}\right)\eta \tag{10}$$

3. NUMERICAL MODEL: VALIDATION STUDY

Geometric nonlinear analyses are processed using the ABAQUS® software [18]. To solve the problem of geometric non-linearity, the Static Riks method is used. This method, also known with a modified Riks algorithm. When configuring the procedure, it is necessary to implement the initial arc length, which refers to an initial percentage of the external load. Thus, in the next increments, the software, automatically during the analysis, adjusts the load increments so that the problem converges through a certain tolerance or stopping criterion, such as values of load or displacement. This is called automatic incrementation control. By default, the software automatically adjusts the size of the increments to solve nonlinear problems efficiently [18]. This is an advantageous tool for solving non-linear problems, a factor that reduces computational cost and time. This method has already been used in other studies [19–21]. In the models, residual stresses were not considered, since they do not influence the ultimate behavior

of composite beams subjected to only positive moment. In this context, the residual stresses increase the effects of the negative moment and the composite beam can reach the lateral distortional buckling [22,23].

3.1. EXPERIMENTAL TESTS

The calibration of the numerical model is based on experimental tests, considering PCHCS units with 150mm of height [5,12]. All the elements that made up the experimental tests are shown in **Fig. 3**. However, due to lack of information, it was not possible to present the shape of the openings of the tests performed by Lam [5]. Thus, as presented in [24], the dimensions of the opening in the rectangular shape were considered.

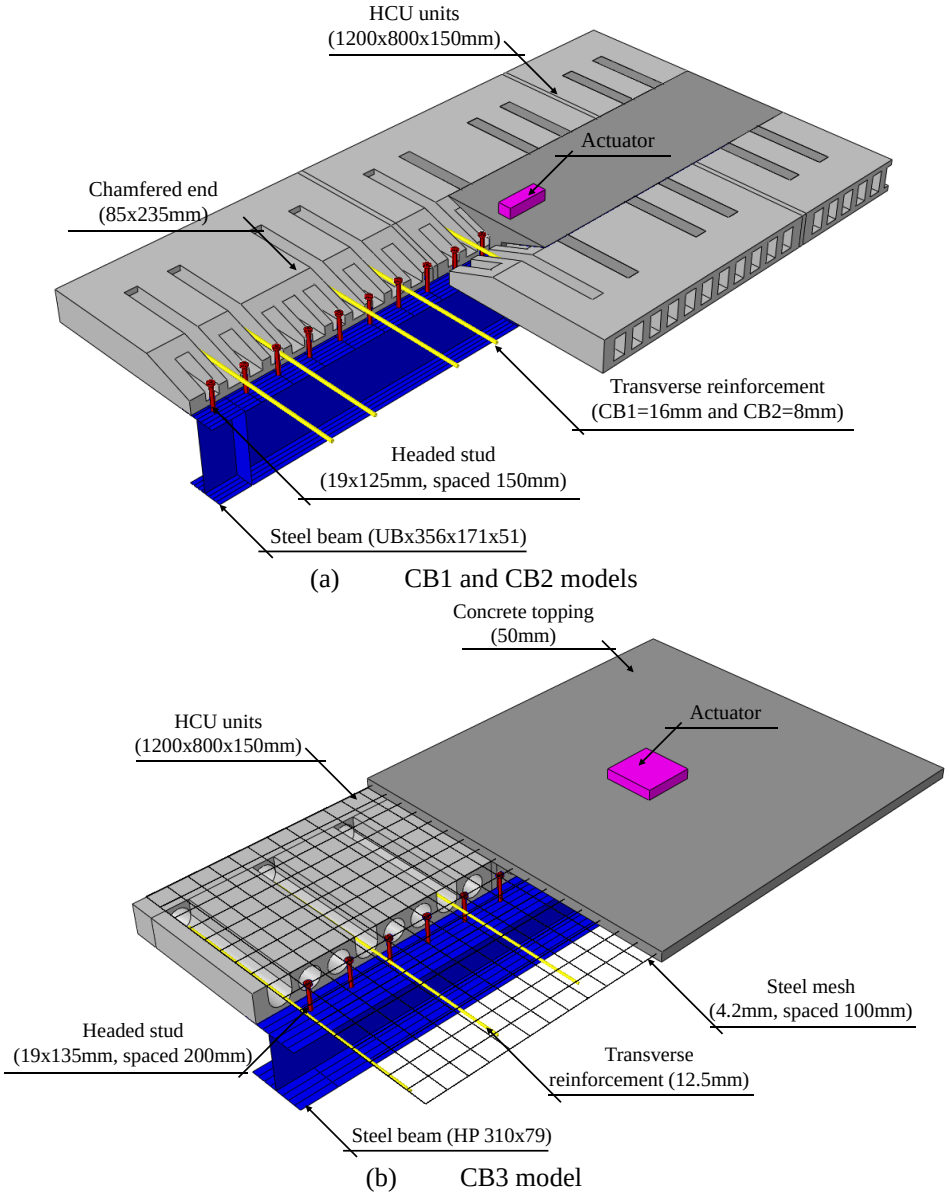

Fig. 3: Numerical model parts

Regarding the tests performed by Lam [5], the supports were spaced at 5700mm and the loads were applied symmetrically with the distance of 1500mm from the supports **(Fig. 4a)**. More information can be seen in [5,7,24,25]. On the other hand, regarding the experimental test performed by Batista and Landesman [12], the supports were spaced at 5830mm and the loads were applied symmetrically with the distance of 1915mm from the supports **(Fig. 4b)**. **Table 3** shows some of the physical characteristics of the tests.

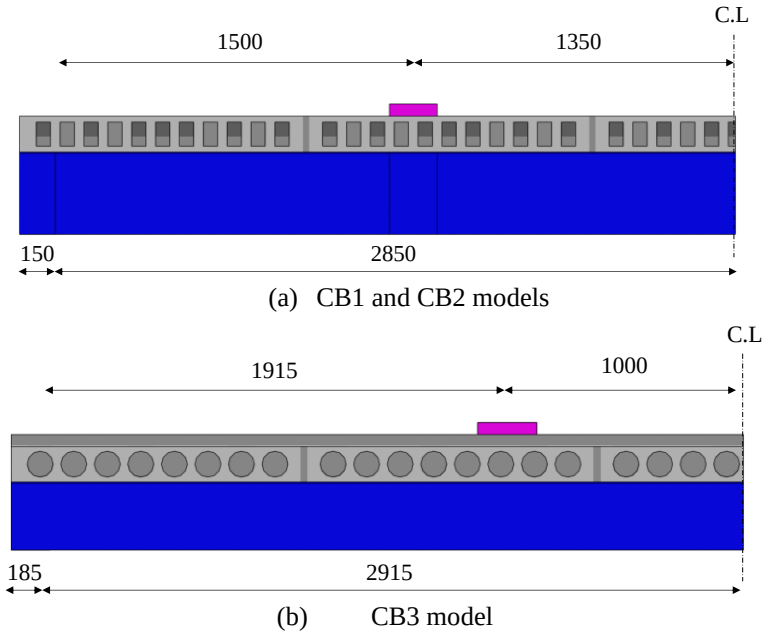

Fig. 4: Distance between supports and loads (in mm)

Table 3: Physical properties of experimental tests

Model	Ref.	Steel beam			Concrete		Reinforcement	
		$f_{y,f}$ (MPa)	$f_{y,w}$ (MPa)	E_a (GPa)	$f_{c,HCU}$ (MPa)	$f_{c,in\text{-}situ}$ (MPa)	f_{ys} (MPa)	E_s (GPa)
CB1	[24]	310	355	205	50[a]	32[a]	585	205
CB2						26[a]	473	
CB3	[12]	345	345	200	45[b]	30[b]	500	200

[a]Cubic resistance
[b]Cylindric resistance

3.2. MATERIALS MODELS

For steel, the perfect elasto-plastic behavior was considered (**Fig. 5**). Regarding the concrete, the Concrete Damage Plasticity (CDP) [26–28] is adopted for carrying out the analyses. The model takes into account hypotheses based on the theory of plasticity [29]. In this context, the relationship between stress and deformation is governed by a damaged elastic variable. Thus, the damage associated with concrete failure mechanisms, such as cracking and crushing, results in the degradation of the material's stiffness. The CDP makes use of the resistance function of Lubliner et al. [27], with the modifications proposed by Lee and Fenves [28] to explain the different evolution of resistance under tension and compression. The stress-strain relationship in concrete and the yield surface are related through the plastic flow, which corresponds to the function that defines the direction of the deformations, when the material reaches the state of plastic behavior. In addition, concrete, as a brittle material, undergoes considerable volume changes caused by inelastic deformations, and this volume change is called dilatancy [30]. The input parameters to characterize the plasticity are: dilation angle (ψ), eccentricity (ξ), the ratio of initial equibiaxial compressive yield stress to initial uniaxial compressive yield stress (σ_{b0}/σ_{c0}), the ratio of the second stress invariant on the tensile meridian to that on the compressive meridian (K_c), and the viscosity parameter that represents the relaxation (μ). Some of these parameters mentioned, the ABAQUS software suggests values per default. However, the dilation angle and the viscosity parameter are sensitive, depending on the model to be used. For example, Behnam et al. [31] and Genikomsou and Polak [30] found that the value of 40º for the dilation angle showed

agreement between the experimental and numerical models for in-situ concrete. On the other hand, the value of 28º for the dilation angle represented the ideal behavior for the modeling of PCHCS [8]. A common technique to solve problems of convergence difficulties is the use of a viscoplastic regularization in the constitutive equations, which makes the stiffness of the softening material positive for sufficiently small increments of time. In this scenario, as in the models of the present study there are many contact elements, the value of 0.001 for viscosity will be adopted, in order to avoid the loss of convergence in the models. **Table 4** presents the input parameters for defining the plastic behavior. The Carreira and Chu models were used [32,33], according to **Fig 6** and **Eqs. (11-13)**. The values of stresses and strains are calculated according to EN 1992-1-1 (2004) [11].

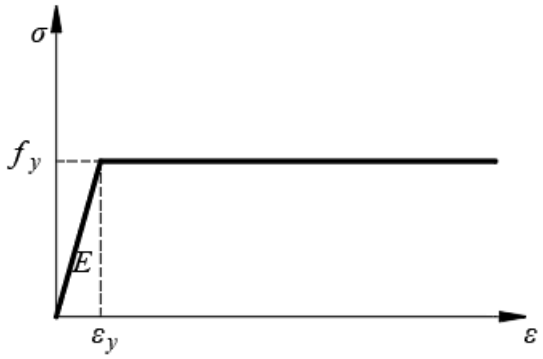

Fig. 5: Perfect elasto-plastic behavior of steel components

Table 4: CDP input parameters

Parameter	Value	Ref.
Ψ (º) (In-loco concrete)	40	[30,31]
Ψ (º) (HCU concrete)	28	[8]
ξ	0.1 (default)	[8,18,30,31]
σ_{b0}/σ_{c0}	1.16 (default)	[8,18,30,31]
K_c	2/3 (default)	[8,18,30,31]
μ (s^{-1})	0.001	-

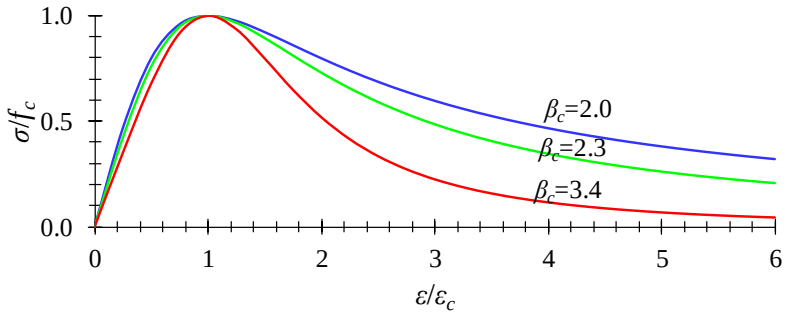

Fig. 6: Concrete model [32,33]

$$\frac{\sigma}{f_c}=\frac{\beta_c\left(\varepsilon/\varepsilon_c\right)}{\beta_c-1+\left(\varepsilon/\varepsilon_c\right)^{\beta_c}} \tag{11}$$

$$\frac{\sigma}{f_t}=\frac{\beta_c\left(\varepsilon/\varepsilon_t\right)}{\beta_c-1+\left(\varepsilon/\varepsilon_t\right)^{\beta_c}} \tag{12}$$

$$\beta_c = \left(\frac{f_c}{32.4}\right)^3 + 1.55 \ \ (MPa) \tag{13}$$

3.3. INTERACTION

The shear connectors were located in the concrete volume of the slab, using the same technique of Wijesiri Pathirana et al. [34]. In this interaction methodology, the same volume of the shear connector is extracted from the slab. The purpose of this removal of volume is such that there is an interaction between the contact surfaces of the slab and shear connector. The interaction scheme is illustrated in **Fig. 7**. The tie constraint was applied to the surface between on the bottom surfaces of the shear connectors and the upper flange, and between the precast and in-situ infill concrete. This modeling technique allows to simulate the perfect bond between the contact surfaces. In this case, each node on the slave surface will have the same values for its degrees of freedom as the point on the master surface. The contact between the concrete and the transverse reinforcement, as well as the concrete and steel mesh, were made through the embedded region, which is used to specify that an element is embedded in another element. As for the surface-to-surface interaction, the normal and tangential behavior between the slab-connector and slab-profile surfaces were considered. The friction coefficient is based on the Coulomb friction model. According to the literature, the coefficient of friction between the steel and concrete surfaces varies between 0.2 to 0.83. For example, in Liu et al. [35] was adopted the coefficient of friction value equal 0.45. In Sjaarda et al. [36] was adopted the value equal 0.83. According the authors, this friction coefficient was determined from past experimental work by Chen [37]. On the other hand, Guezouli and Lachal [38] recommended using the value of the coefficient equal 0.2 and 0.3 for the connector-slab and slab-profile interfaces, respectively. The authors performed sensitivity analyses, considering pushout tests. Thus, in the CB1 model, the friction coefficient equal to 0.4 was adopted. In the CB2 model, on the other hand, for having presented a relatively greater slip between the contact surfaces in the experimental model, when compared with the CB1 experimental model ($\Delta_{CB2}/\Delta_{CB1}$=6.5), as presented in [5], the friction coefficient equal to 0.2 was adopted. In the CB3 model, the friction coefficient for the connector-slab interface was assumed equal to 0.2, while for the slab-profile interface, the adopted value was equal to 0.3. All these values are within the range investigated by Guezouli and Lachal [38]. In all types of interactions, it is important to differentiate the master from the slave surface. According to ABAQUS® software [18]: the larger of the two surfaces should act as the master surface, if the surfaces are of comparable size, the surface on the stiffer body should act as the master surface and if the surfaces are of comparable size and stiffness, the surface with the coarser mesh should act as the master surface. **Table 5** presents the pairs of interaction.

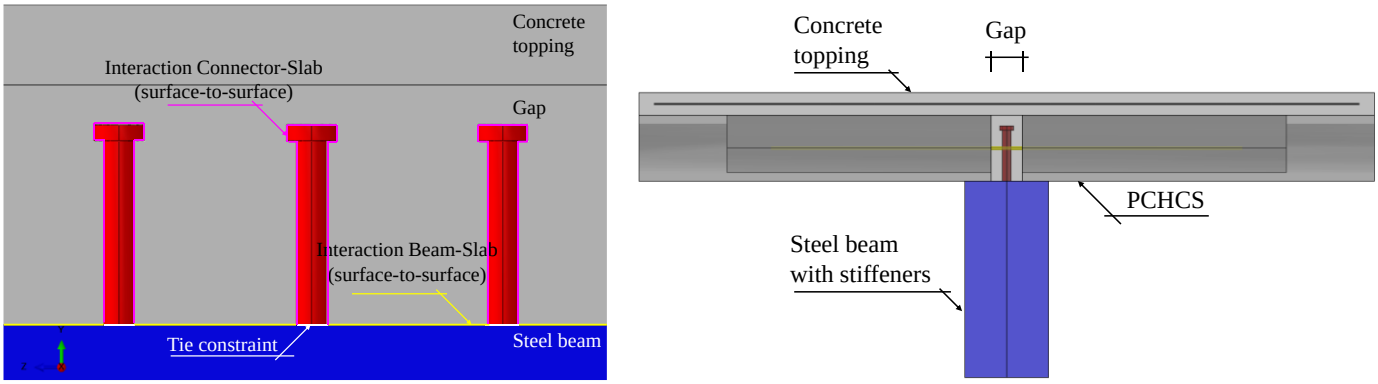

(a) Lateral view (b) Section

Fig. 7: Interactions

Table 5: Pairs of interaction

Interaction	Surfaces		Type
	Master	Slave	
Concrete topping and actuator	Topping	Actuator	Normal/Tangential
Gap and shear connector	Gap	Shear connector	Normal/Tangential
PCHCS and steel profile	PCHCS	Steel profile	Normal/Tangential
Gap and steel profile	Steel profile	Gap	Normal/Tangential
Steel profile and shear connector	Steel profile	Shear connector	Tie
PCHCS and gap	PCHCS	Gap	Tie
PCHCS and concrete infill	PCHCS	Concrete infill	Tie
PCHCS and concrete topping	Concrete topping	PCHCS	Tie
Concrete topping and gap	Concrete topping	Gap	Tie
Steel mesh and concrete topping	-	-	Embedded
Transverse reinforcement and concrete infill	-	-	Embedded

3.4. BOUNDARY CONDITIONS

The boundary conditions were applied in a manner similar to that presented in Ellobody and Lam [24], according to **Fig. 3a**. However, it was decided to make the displacement control instead of applying the load. Crisfield [39,40] reported that, in numerical analysis, limit loads are often associated with a failure to achieve convergence with the iterative solution procedure. In addition, the author pointed out that nonlinear static analysis techniques have considerable difficulties with softening materials, such as concrete, and this may explain the convergence difficulties that are often encountered. Load-controlled analysis equates structure failure with iterative solution technique failure as a convergence problem. As a result, structures may fail to establish cracks, in the case of concrete, or specific mechanisms that initiate collapse because there is no convergent equilibrium state. In this context, the complexities of nonlinear analysis can be avoided by applying a simple form of displacement control, according to present study. The application of displacement control loading can simulate an experimental testing procedure such as the hydraulic actuator. However, as presented by Crisfield [39,40], the disadvantages in displacement control are related to the selection of the appropriate displacement variable, which may result in computational cost or divergence from the iterative solution procedure, as observed by Maewal and Nachbar [41]. Thus, the variable for the displacement control of the present study was the mid-span vertical displacement. **Fig. 8** shows the boundary conditions. The vertical displacement was restricted on the support (Uy=0), the lateral displacement on the concrete slab (Ux=0). In the middle of the span, symmetry was considered (Uz=URx=URy=0).

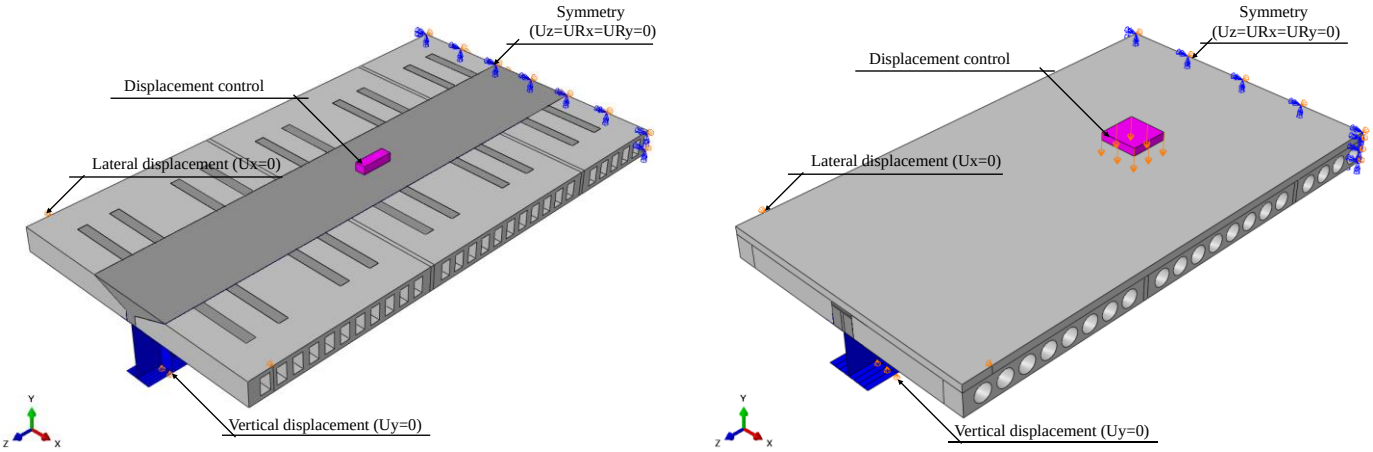

(a) CB1 and CB2 (b) CB3

Fig. 8: Boundary conditions of specimens

3.5. DISCRETIZATION

Although there are sensitivity analyses in the literature in only one type of structure, sensitivity analyses were not performed to define the mesh size. This is due to the fact that there are many parts to carry out the modeling, a factor that makes the study unfeasible. However, as performed by Sjaarda et al. [36], it was assumed, that the mesh sizes and element types would provide accurate results based on previous similar simulations by Liu et al. [35] and Nguyen et al. [8]. In these studies, the approximate overall mesh scale was 40 mm, with the smallest mesh scale being about 5 mm. Besides, the size of the finite element was taken with respect to the master/slave surfaces (**Table 5**). According to software ABAQUS [18], the assignment of master and slave roles can have a significant effect on performance with surface-to-surface contact if the two surfaces have dissimilar mesh refinement; the solution can become quite expensive if the slave surface is much coarser than the master surface. **Fig. 9** shows the discretization of finite elements with the approximate global size. Shell-type elements have been implemented to the geometry of the steel beams. The S4R element is a quadrilateral element with four nodes and reduced integration, a factor that reduces processing time. On the other hand, on the shear connector and the elements that form the concrete slab, the solid element C3D8R was implemented. This element has eight nodes, reduced integration and supports plastic analysis with large deformations, and allows the visualization of the crack in the CDP yield criteria. Both elements have six degrees of freedom per node - three rotations and three translations - referenced in a three-axis system (X, Y and Z). For transverse reinforcement, T3D2 truss elements, 2-node linear displacement were considered.

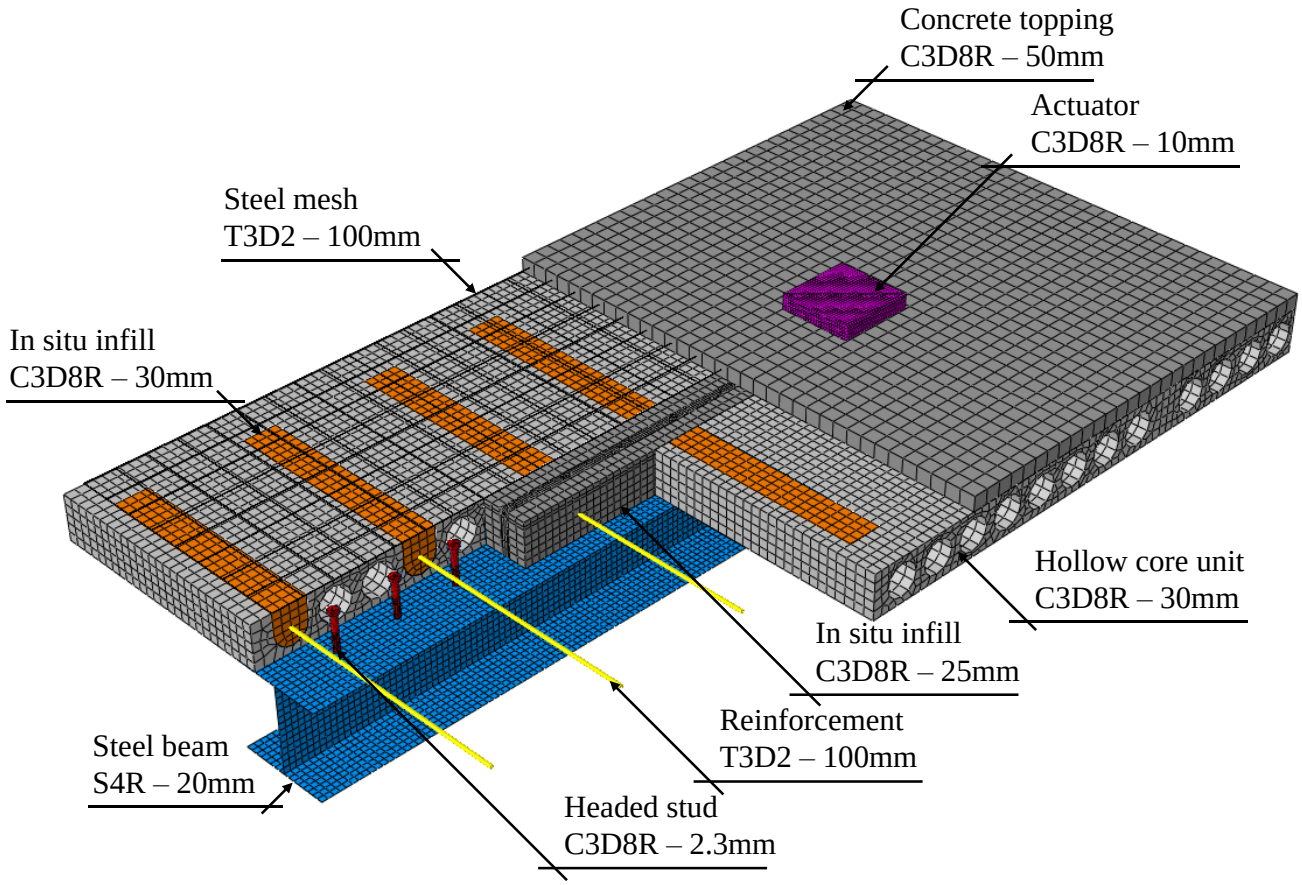

345

346 **Fig. 9: Discretization with approximate global size with T3D2 elements rendered**

347 3.6. RESULTS

348 The results were presented by load-displacement relationships (**Fig. 10**).

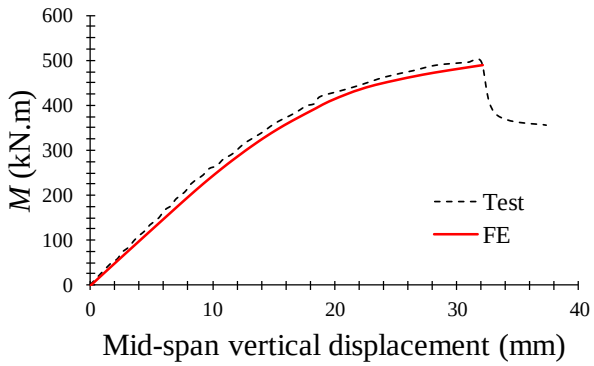

(a) CB1

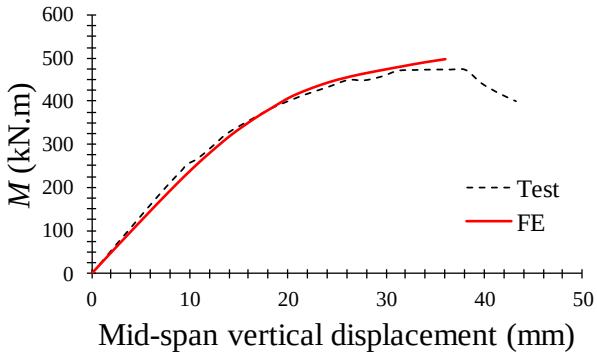

(b) CB2

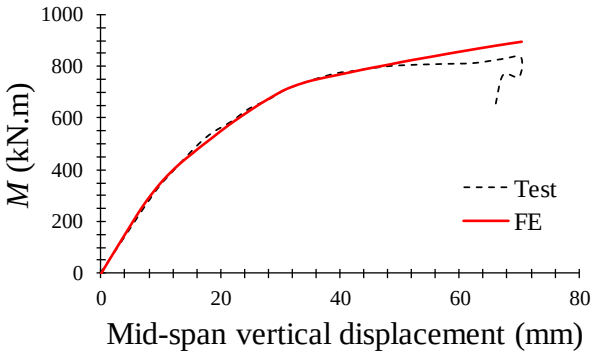

(c) CB3

349 **Fig. 10: Validation results**

In models CB1 and CB2 (**Fig. 11a**), it was possible to observe the yielding of the steel profile at lower flange and the cracking in the lower part of the PCHCS, as observed in experiments [5]. The behavior of the CB3 model (**Fig. 11b**) was also similar to test [12]. In this scenario, cracks started to develop on lower part PCHCS and in the central region between the load application point. According to the authors, these cracks propagated along the PCHCS width, extending from the side face of the slab to the region of connection with the steel profile.

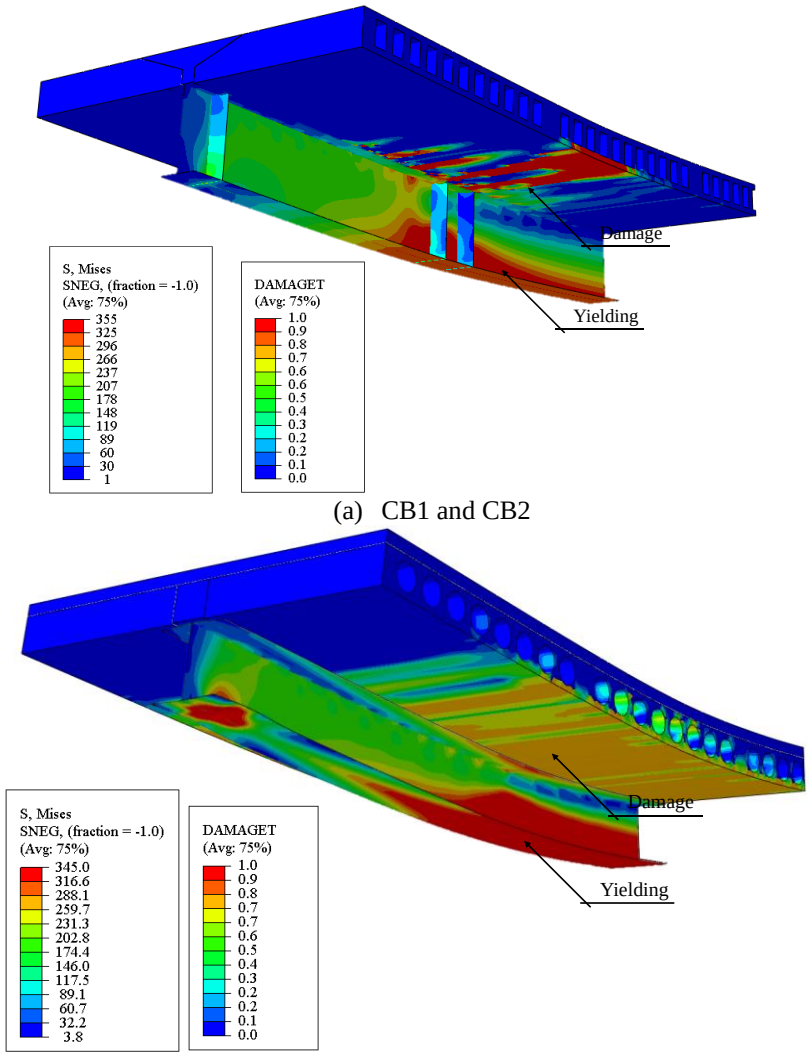

(a) CB1 and CB2

(b) CB3

Fig. 11: Final configuration and failure mode of numerical models, von Mises stresses in MPa

Table 6 presents the values of the results in comparison with the experimental results performed by [5,12]. As shown, it was possible to state that the numerical model was calibrated according to the experimental models.

Table 6: Comparison of numerical and experimental results: model validation

Test	M_{test} (kN.m)	δ_{test} (mm)	M_{FE} (kN.m)	δ_{FE} (mm)	M_{FE}/M_{test}	$\delta_{FE}/\delta_{test}$
CB1	497.3	32	490.8	32.1	1.00	1.00
CB2	474.0	35	498.80	36.0	0.95	1.03
CB3	846.3	70.3	895.4	70.5	0.95	1.00

4. PARAMETRIC STUDY

The following are the general considerations for the parametric study:

i. For the profile, ASTM A572 Gr.50 steel was adopted, whose yield strength is 345 MPa. The modulus of elasticity and the Poisson's ratio were equal to 200 GPa and 0.3, respectively;

ii. Three cross sections of steel profile of the W series were considered: W360x51, W460x74 and W530x72;

iii. The degree of interaction was varied depending on the spacing of the shear connectors (**Fig 12a-b** and **Table 7**), whose dimensions are 19x125mm;

iv. LP15 PCHCS units (**Fig. 12c**), with f_c equal to 40 MPa, without chamfer and gap (g) equal to 70mm were considered;

v. For each model, the in-situ concrete resistance (f_c) were varied from 25, 30 and 40 MPa;

vi. The thickness of the concrete topping was 50mm, with reference models being those that do not have the concrete topping;

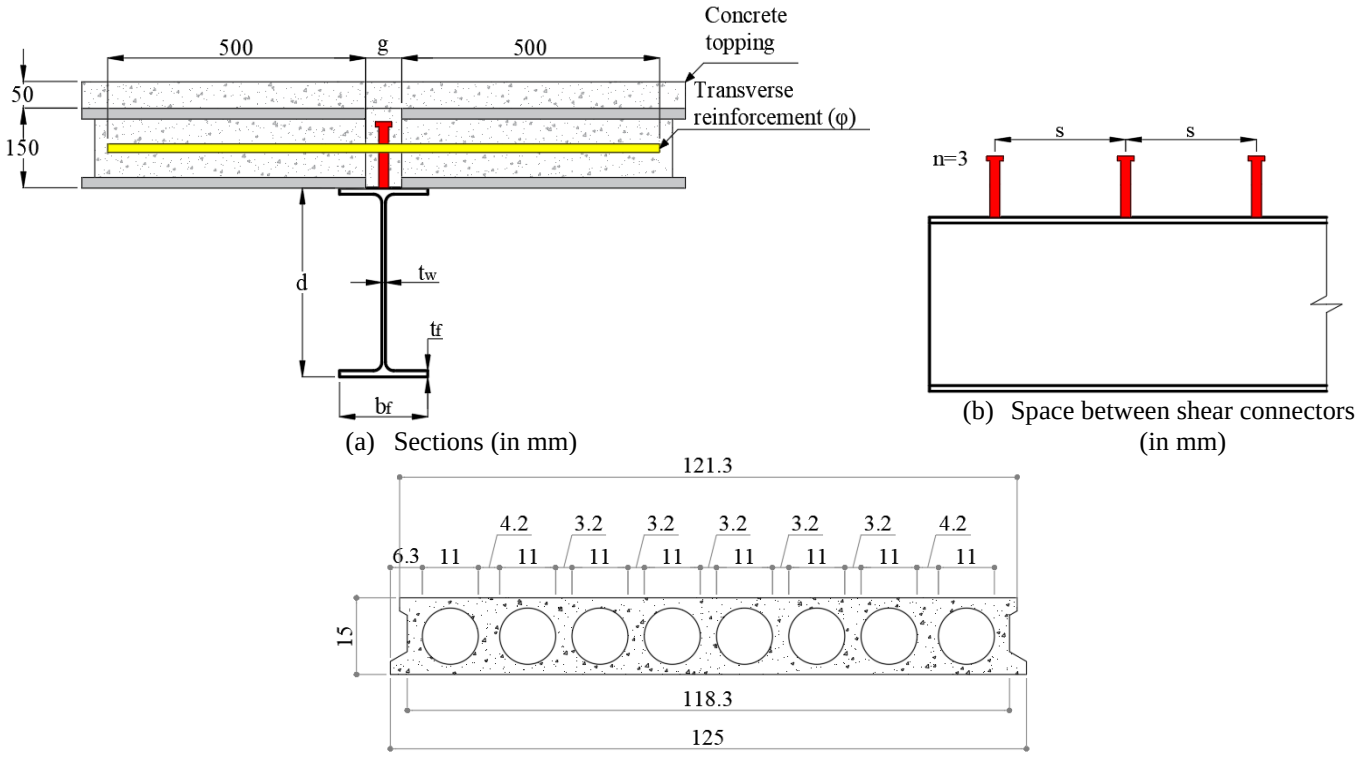

(a) Sections (in mm)

(b) Space between shear connectors (in mm)

(c) HCU LP15 (in cm)

Fig. 12: Geometry of parametric study

Table 7: Characteristics of models for interaction degree analysis: parametric study

Section	d (mm)	b_f (mm)	t_f (mm)	t_w (mm)	L (mm)	s* (mm)	n/2	η
W360x51	355	171	11.6	7.2	6000	120	24	1.0
						175	17	0.7
						225	13	0.5
W460x74	457	190	14.5	9.0	6000	120	24	1.0
						175	17	0.7
						225	13	0.5
W530x72	524	207	10.9	9.0	6000	120	24	1.0
						175	17	0.7
						225	13	0.5

*According to Gouchman [13], the shear connectors are often placed at 120 to 225 mm centres along the beam. In the present study it is considered that the minimum distance of 120mm between the shear connectors will provide total interaction. Thus, the calculation of interaction degree is taken based on the number of connectors (n/2)=24.

vii. Welded steel mesh with wires of 4.2 mm in diameter and with 100 mm spacing was considered [9];

viii. For each model, the diameters of the transverse reinforcement were varied by 10mm, 12.5mm and 16mm. The length of the transverse reinforcement was 1000+g, in mm;

ix. The filling of the 1st, 3rd, 5th and 7th core was considered;

x. The beams were considered to be simply supported and subjected to two load points spaced L/4 from each support;

xi. The surface/surface contact properties were applied as [30];

xii. The mid-span vertical displacement of maximum value equal to L/100 was adopted as a stopping criterion.

5. RESULTS AND DISCUSSION

In total, 162 numerical analyses were performed (**Fig. 13**). The results are discussed, considering the influence of the concrete topping, the influence in-situ concrete strength, the interaction degree, the transverse reinforcement rate, and finally, the analytical procedures, according to sections 2 (resistance of composite beams with hollow core slabs) and **Table 1**.

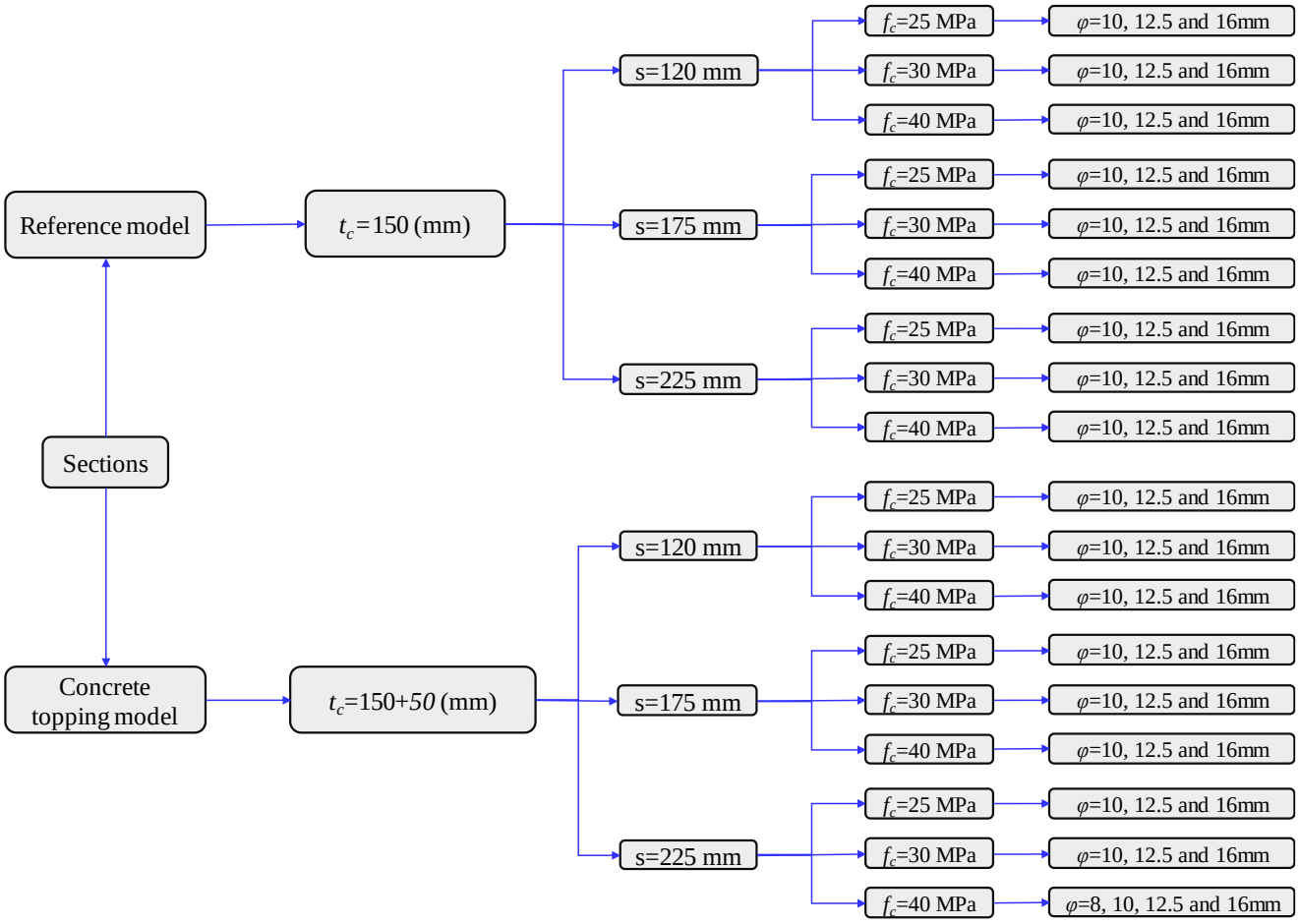

Fig. 13: Numerical models evaluated in parametric study

5.1. INFLUENCE OF THE CONCRETE TOPPING

The failure mode of the composite beams with PCHCS, considering the maximum mid-span vertical displacement equal to L/100, was analogous to that presented by Batista and Landesmann [12], that is, the appearance of cracks initiated on the bottom edge of the PCHCS and at the point load application. As the loading progressed, the cracks propagated along the entire width of the slab, extending from the side of the slab to the upper edge (**Fig. 14**).

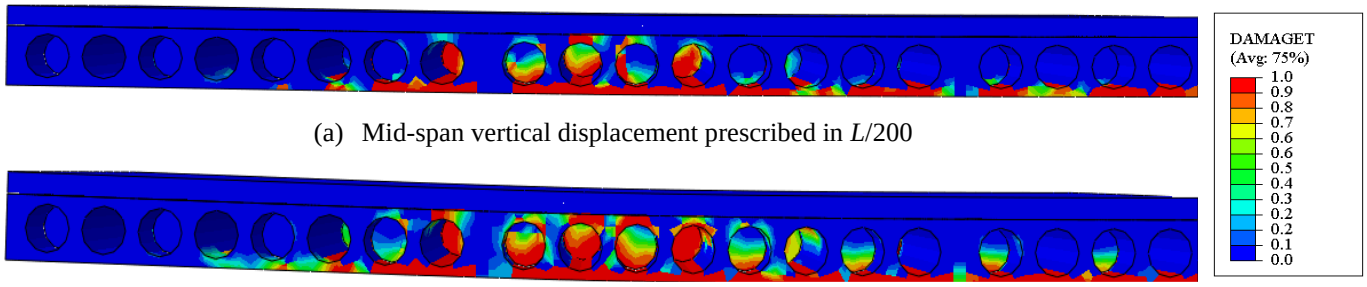

(a) Mid-span vertical displacement prescribed in $L/200$

(b) Mid-span vertical displacement prescribed in $L/100$

Fig. 14: Damage in PCHCS with concrete topping

To assess the influence of the concrete topping, the ratio of the numerical model with and without concrete topping was calculated ($M_{FE,50}/M_{FE,0}$), according to **Fig. 15**. By means this ratio, two points of displacement were monitored, considering the maximum mid-span vertical displacement ($L/200$) [13], as well as twice that value ($L/100$).

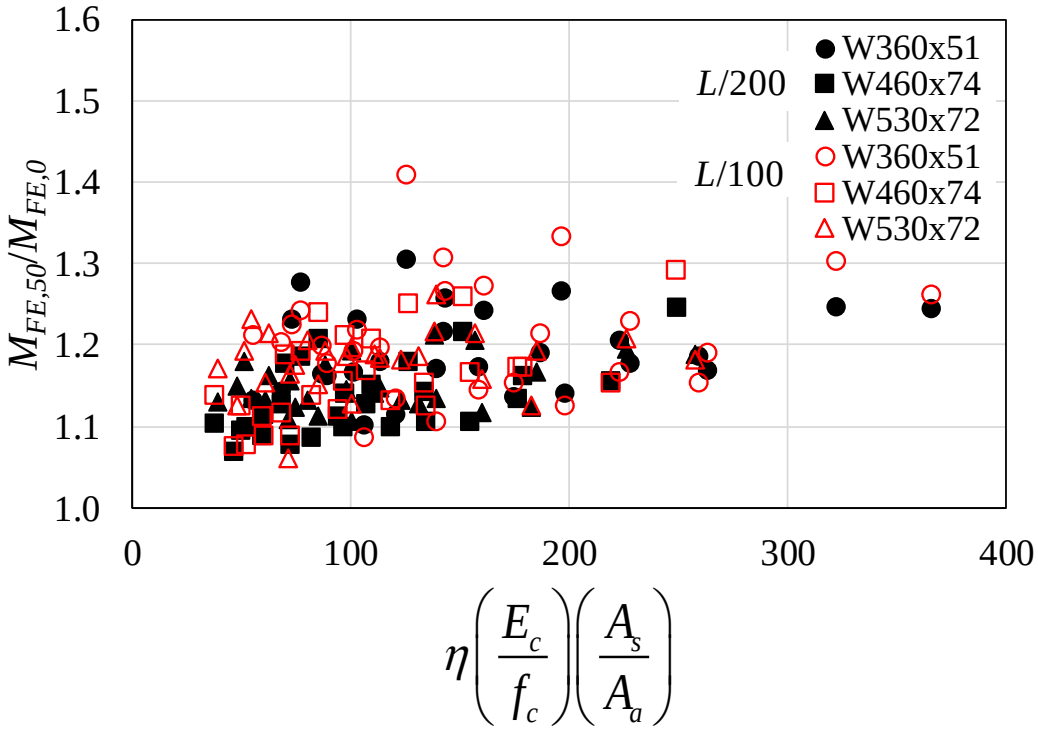

Fig. 15: Influence of the concrete topping

An increase of at least 7% in the strength of the composite beams with PCHCS with concrete topping was observed. In addition, the presence of the concrete topping resulted in improvements in the cracking moment and in the initial stiffness of the PCHCS. Such an increase in strength was previously evaluated by Baran [4], considering only PCHCS with concrete topping. Some examples are illustrated in **Fig. 16.** In addition, it was possible to observe that with the reduction of the degree of interaction, there was a reduction in the strength of the composite beams with PCHCS with concrete topping.

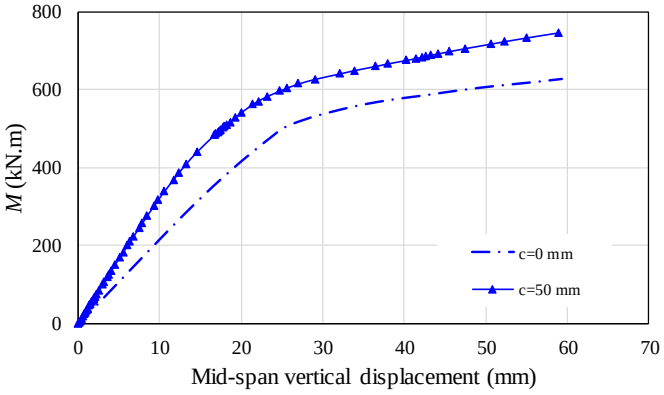

(a) W360: (n/2)=24, f_c=25 MPa and φ=16 mm

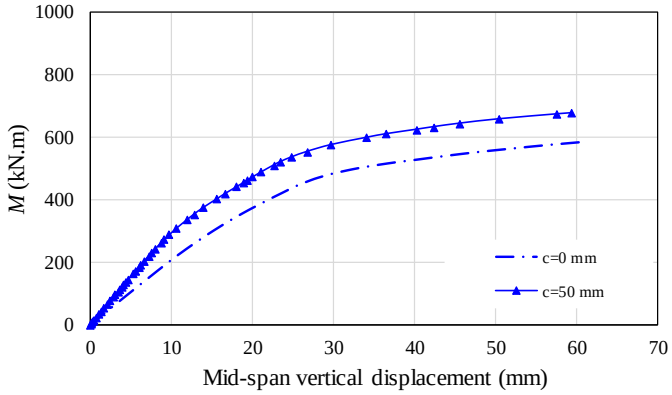

(b) W360: (n/2)=17, f_c=25 MPa and φ=16 mm

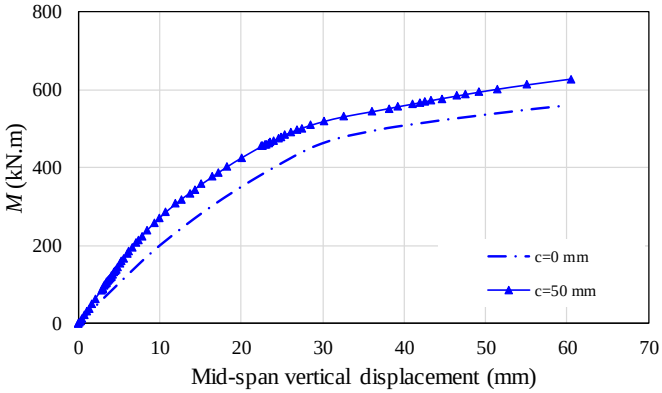

(c) W360: (n/2)=13, f_c=25 MPa and φ=16 mm

Fig. 16: Influence of concrete topping on the initial stiffness of the composite beams

5.2. INFLUENCE OF STEEL SECTION

Considering the steel profile W360x51 and 120mm spacing between shear connectors (n/2=24), in general, with the mid-span vertical displacement prescribed in L/400, the yield resistance was not achieved in any region of the steel profile. In this scenario, the maximum von Mises stresses in the bottom flange, web and upper flange were 256 MPa, 280 MPa and 100 MPa, respectively (**Fig. 17a**). These values decreased with increasing spacing between shear connectors, for example, for 175mm of spacing (n/2=17), these values reached 243 MPa, 252 MPa and 147 MPa, for the bottom flange, web and upper flange, respectively, while for 225mm of spacing (n/2=13), these values reached 225 MPa, 230 MPa and 177 MPa, for the bottom flange, web and upper flange, respectively. Note that, in this case, the greater the spacing between shear connectors, the greater the slip in the steel and concrete interface, a factor that generated an increase in von Mises stresses in the upper flange. For the steel profiles W460x74 and W530x72, which present approximately the same cross-sectional area, in general, no region of the steel profile was reached the yield strength. However, the stresses were higher than in the previous situation, considering the W360x51 profile. In the case of profiles W460x74 and W530x72, considering 120mm spacing between shear connectors (n/2=24), the maximum von Mises stresses in the bottom flange, web and upper flange were 272 MPa, 325 MPa and 208 MPa, respectively. These values also decrease with increasing spacing between shear connectors. For 175mm of spacing (n/2=17), these values reached 249 MPa, 291 MPa and 206 MPa, for the bottom flange, web and upper flange, respectively, while for 225mm of spacing (n/2=13), these values reached 234 MPa, 268 MPa and 223 MPa, for the bottom flange, web and upper flange, respectively.

With the progression of loading, considering the steel profile W360x51, for mid-span vertical displacement prescribed in *L*/200 (**Fig. 17b**), the bottom flange and approximately 1/4 of the web height had already reached the yield strength. In no region where the shear connectors were located reached the yield strength. The maximum von Mises stresses in the upper flange were approximately 240 MPa. The behavior of steel profiles W460x74 and W530x72 were similar to W360x51. In the final step, considering all sections, for the mid-span vertical displacement prescribed in *L*/100 (**Fig. 17c**), in the bending region and close to the supports were yielding (across the bottom flange and practically the entire web region). The maximum von Mises stresses in the upper flange was 324 MPa, only some regions where the shear connectors were located. In the rest, the upper flange stresses had not yet reached the yield strength, with values of approximately 240 MPa.

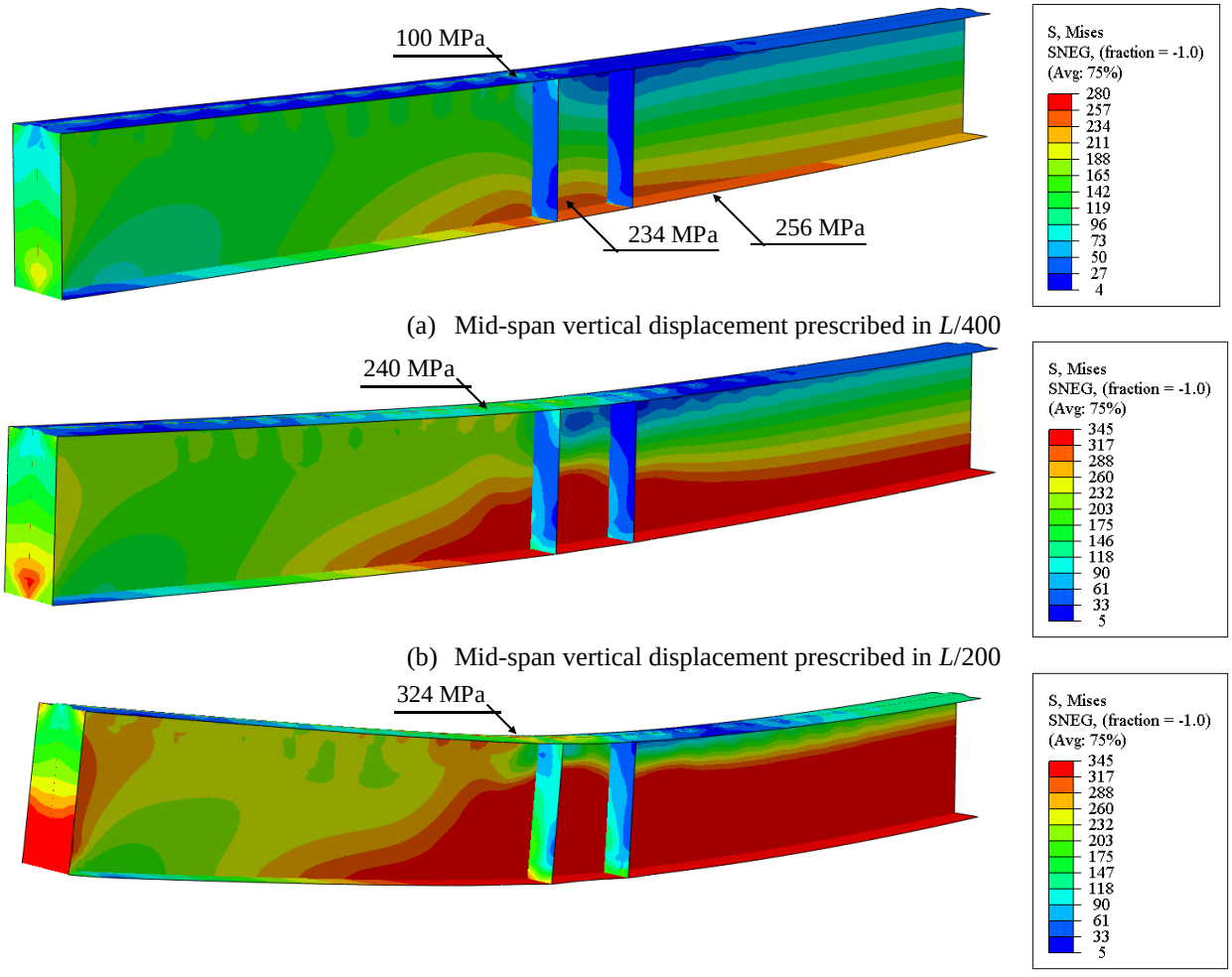

(a) Mid-span vertical displacement prescribed in *L*/400

(b) Mid-span vertical displacement prescribed in *L*/200

(c) Mid-span vertical displacement prescribed in *L*/100

Fig. 17: Flexural behavior of W360x51 section, considering (*n*/2)=24, f_c=25 MPa and φ=16 mm (in MPa)

In addition, it was possible to evaluate, by means of shear-slip and load-displacement relationships (**Fig. 18)**, that the steel area influences the ductility of the composite beams with PCHCS with concrete topping.

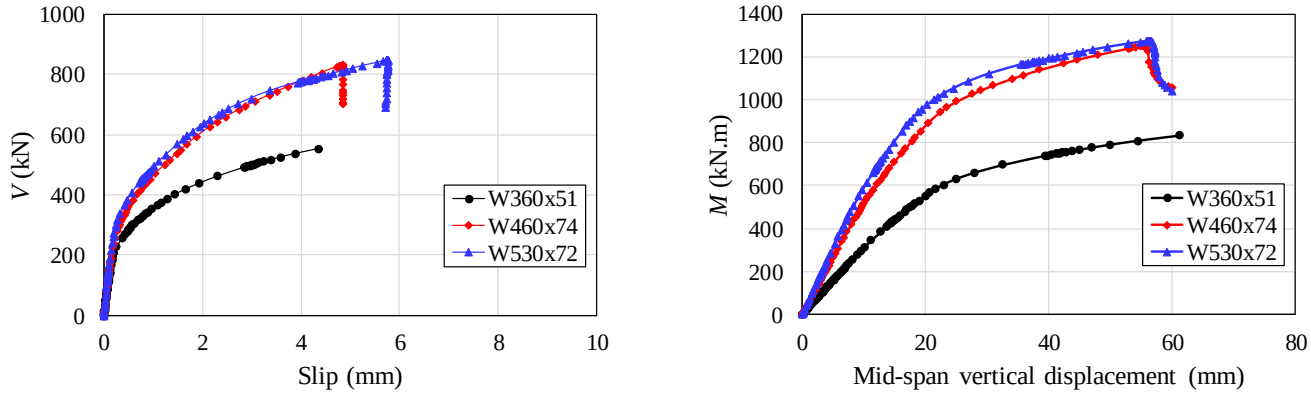

(a) (b)

Fig. 18: Influence of the steel section, considering (n/2)=24, f_c=25 MPa and φ=16 mm

As observed, the composite beam formed by the W360x51 profile did not reach its ultimate strength before the stopping criterion, which means that the composite beam could be subjected to a higher level of loading. In this model, the propagation of damage in the PCHCS was observed, with plastification of web of the steel profile, as shown in **Fig.17c**. On the other hand, the composite beams, whose sections were formed by the profiles W460x74 and W530x72 reached their resistant capacity before the stopping criterion adopted (L/100). In this scenario, the steel sections were fully plasticized in the region close to the loading application point. Lam et al. [7] pointed out when the ratio between the height of the steel beam to the height of the PCHCS is greater than 3, the composite beams are not effective, and failure may occur due to crushing of the concrete, such as the steel profiles W460x74 (**Fig. 19a**) and W530x72 (**Fig. 19b**), in this case. This was observed for situations in which total interaction was considered. As for the situations in which the degree of interaction varied, it was not observed such a phenomenon.

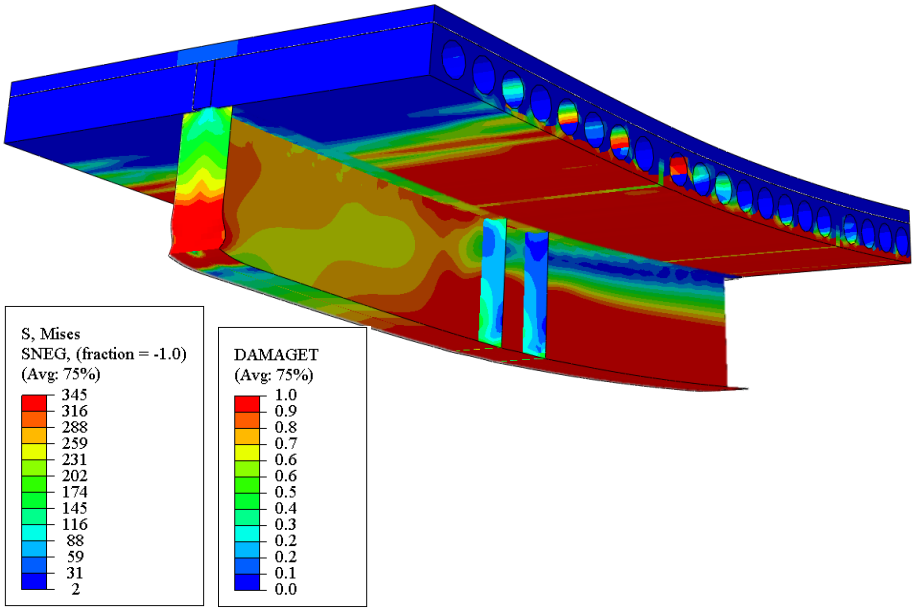

(a) W460x74

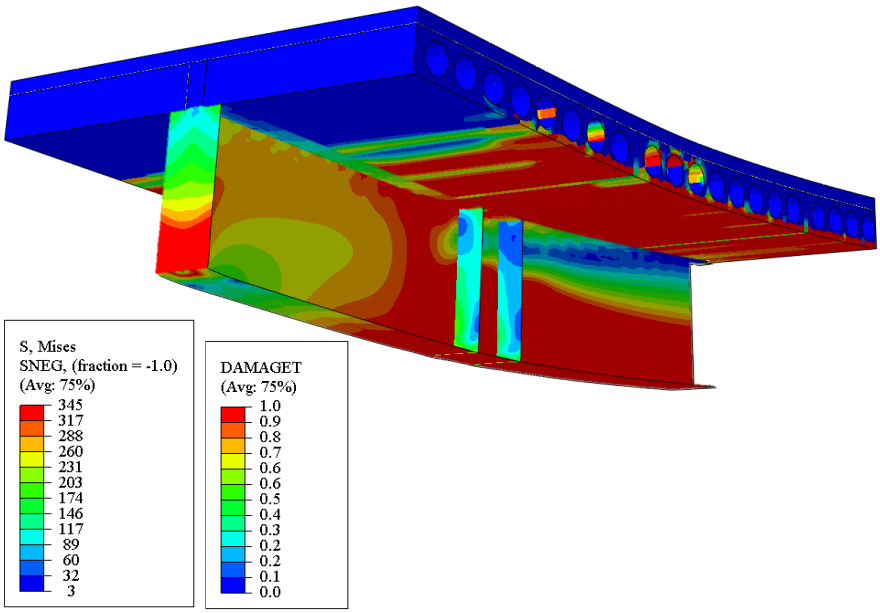

(b) W530x72

Fig. 19: Final configuration of the composite beam, considering (n/2)=24, f_c=25 MPa and φ=16 mm

5.3. INFLUENCE OF THE IN-SITU CONCRETE STRENGTH

The compressive strength of concrete parameter was directly influenced by the steel cross section, transverse reinforcement rate and degree of interaction (**Fig. 20**). As presented by Araujo et al. [9], the in-situ concrete compressive strength is the most important parameter for the resistant capacity of the shear connectors. This was observed in the present study. For example, considering the composite beam formed by the W360x51 section, total iteration and in-situ concrete compressive strength equal to 30 MPa, presented with greater resistance (**Fig. 20a**), for any value of the transverse reinforcement rate. On the other hand, considering the in-situ concrete compressive strength equal to 40 MPa, the models presented a fragile behavior, showing a difference in resistance due to the prescribed displacements. The composite beam formed by the W460x74, considering in-situ concrete compressive strength equal to 25 MPa, presented with greater resistance (**Fig. 20b**). Regarding the composite section formed by the W530x72 profile, the differences in the load-displacement relationship were not significant (**Fig. 20c**). Thus, the differences are greater for the W360x51 section, which has a smaller cross-sectional area than the other sections. With the reduction of the interaction degree, there were no significant differences with the variation of the in-situ concrete compressive strength (**Fig. 21**). It can be seen in the illustrations that for total interaction, with the variation of the in-situ concrete compressive strength, as well as the transverse reinforcement rate, depending on the cross section, there were differences in the numerical response, specifically for the section W360x51 (**Fig. 21a**). As the cross-sectional area is increased, in relation to the sections W460x74 (**Fig. 21b**) and W530x72 (**Fig. 21c**), these differences decrease. This occurs depending on the position of P.N.A. With the increase in the area of the steel section, the P.N.A tends to be located in the steel profile. This factor can cause excessive compressive stress on the PCHCS, especially when the P.N.A is located in the steel profile web. When this occurs, there is a tendency for the ultimate behavior to be achieved by concrete crushing. Considering partial interaction, as the interaction degree is reduced, these differences in the numerical response are not significant, in particular for situations in which the interaction degree is equal 50%. In this scenario, as

shown in section 2 (resistance of composite beams with hollow core slabs), there are two P.N.A located in the composite beam. This situation causes both the slab and the steel profile to be subjected to compression and tension. Thus, as the PCHCS has low tensile strength, the ultimate behavior tends to occur due to the cracking of the concrete with yielding of steel profile, as shown in **Fig. 17.** Finally, it was found that the greater the in-situ concrete compressive strength, the greater the value of the von Mises stresses in the shear connectors. **Fig. 22** shows some examples, considering (n/2)=24. According to Araujo et al. [9], when the average concrete compressive strength was greater than 40 MPa, the failure mode can occurs by cut off of the headed stud, and when the average concrete compressive strength was reduced to less than 30 MPa, the failure was governed by the in situ concrete strength. In the numerical model, it was only possible to observe the cracking of the concrete caused by the high stress in the connectors, and also by the point of loading application, as shown in [12].

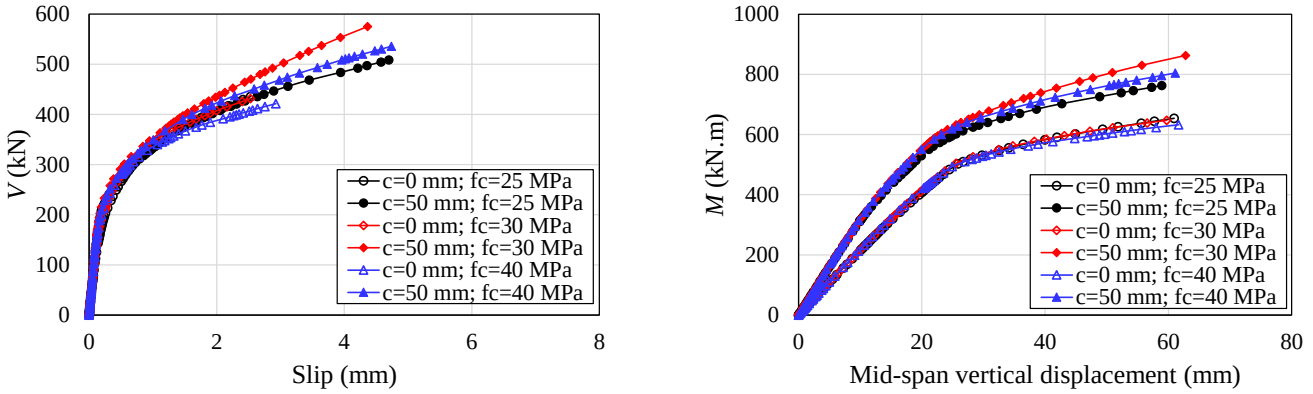

(a) W360x51

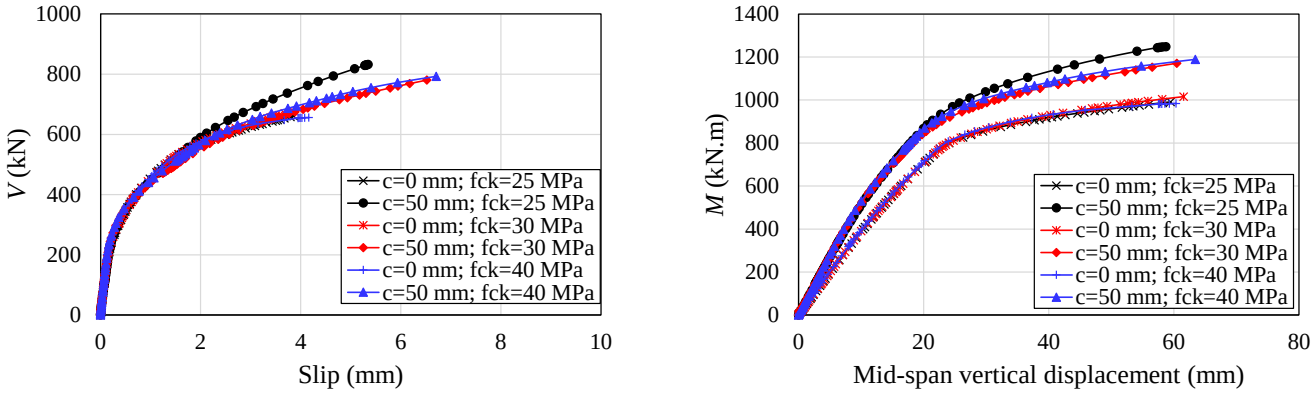

(b) W460x74

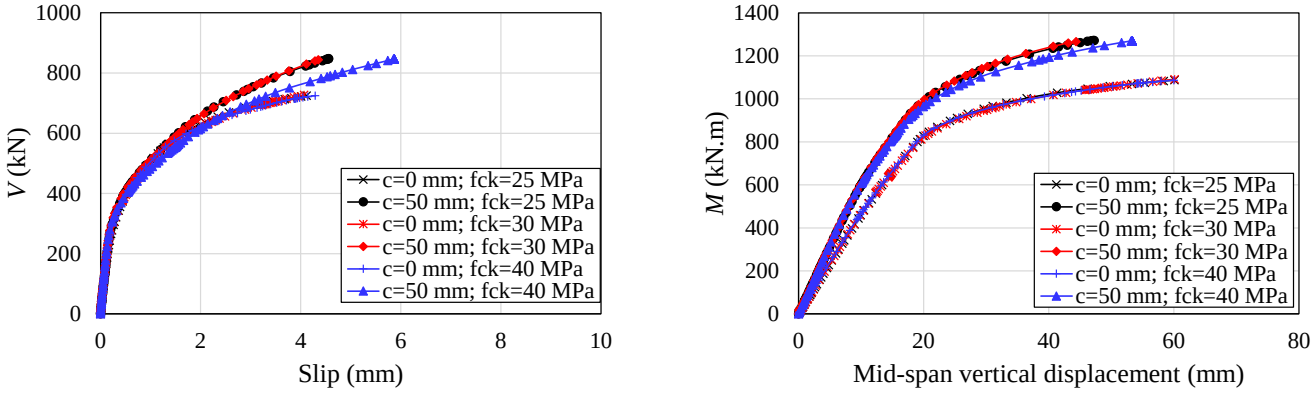

(c) W530x72

Fig. 20: Behavior of composite beam, (n/2=24) and φ=12.5 mm

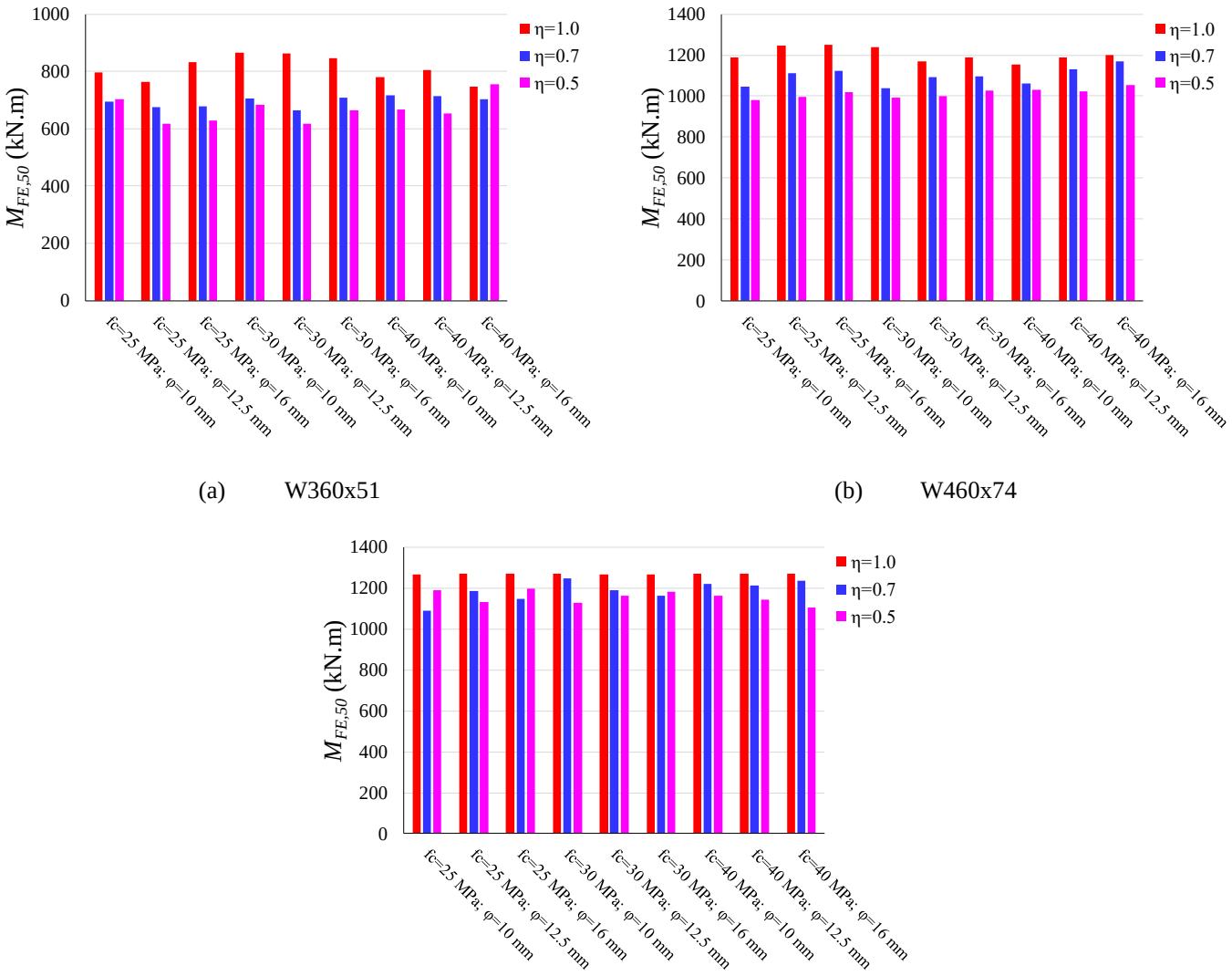

476 **Fig. 21: Influence of the interaction degree and in-situ concrete strength on moment**

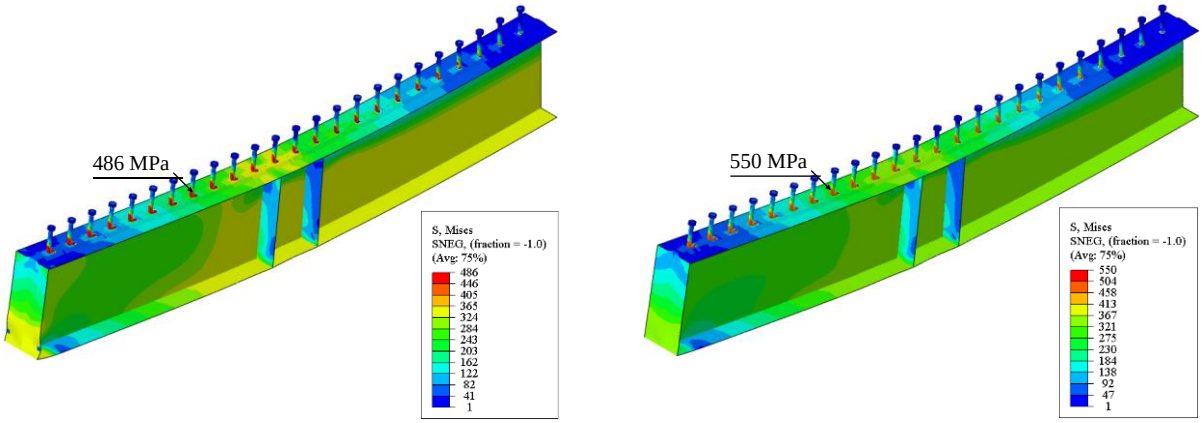

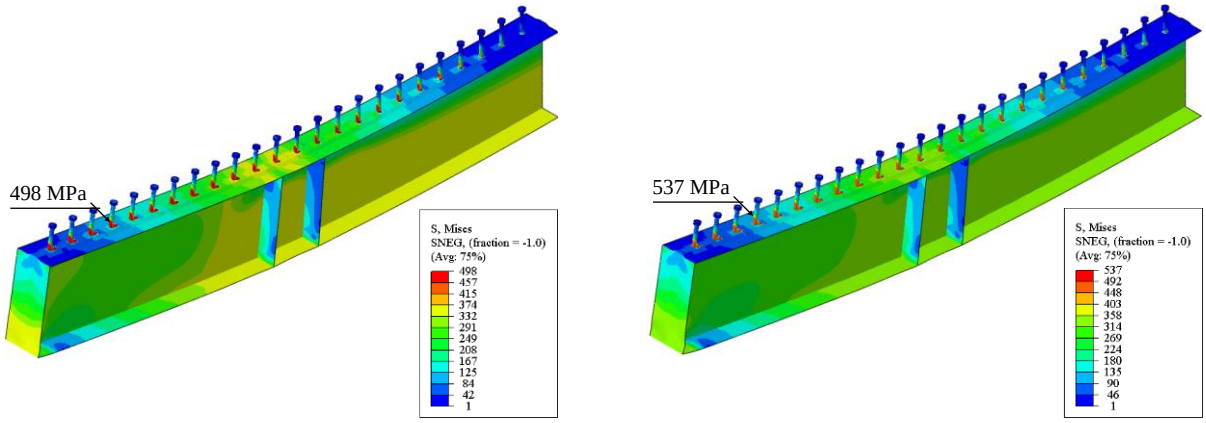

(c) f_c =30 MPa and φ =16mm (d) f_c =40 MPa and φ =16mm

Fig. 22: von Mises stresses in headed studs, considering W360 and (*n*/2)=24

5.4. INFLUENCE OF TRANSVERSE REINFORCEMENT RATE

Considering the variation in the reinforcement rate, the shear-slip and moment-deflection relationships were more affected in situations where there was total interaction and lower in-situ concrete compressive strength. Some examples are illustrated (**Fig. 23-24**). According to the illustration, the transverse reinforcement rate, considering the diameter of 16mm, provided greater resistance in the composite beams with PCHCS with concrete topping, considering total interaction. On the other hand, with increasing spacing between shear connectors, the diameter of 10mm, provided greater resistance. Also, it was possible to evaluate the ductile behavior with the variation of the reinforcement rate, considering the spacing between connectors (**Fig. 25**). For the composite beam to be classified with ductile behavior, the EC4 [11] points out that there must be a slip of at least 6mm at the steel-concrete interface. According to the illustration, the ductile behavior was observed in the total interaction, only for the W460x74 and W530x72 profiles. For the profile W460x74, such behavior was assessed from the situations in which the composite beams had the in-situ concrete compressive strength of 30 MPa and a transverse reinforcement diameter equal to 12.5mm. The W530x72 profile presented only one situation, as shown in **Fig. 25c**. On the other hand, the ductile behavior was observed for all situations, considering the reduction in the interaction degree, that is, the increase in spacing between the shear connectors. In addition, as previously verified in the studies by Lam et al. [6,7] the type of failure of steel-concrete composite beams with PCHCS can be ductile with control of the transverse reinforcement rate, and with an increase in the transverse reinforcement rate, there was a significant increase in flexural strength. However, the ductility was reduced, observing the fragile rupture due to the crushing of the concrete slab. Also, Araújo et al. [9] reported that the transverse reinforcement is the dominant factor affecting both the shear capacity of the headed stud connectors and the maximum slip at the interface, as observed in **Fig. 22**. Besides, it was observed in the present study, as noted earlier, the cross section of the steel directly influences the ductile behavior. Thus, in general, it was found that the area of the steel cross section influenced the von Mises stresses in the transverse reinforcement (**Fig. 26**). As example, for section W360x51, the maximum von Mises stress was 51 MPa, and for W530x72 section, the maximum von Mises stress was 104 MPa. These values decrease with increasing spacing between shear connectors.

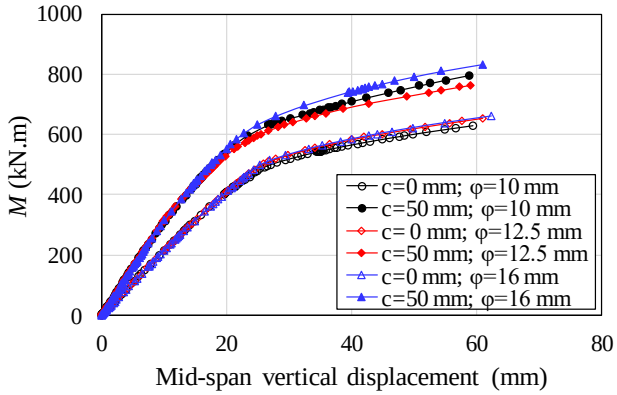

(a) W360x51 and (n/2)=24

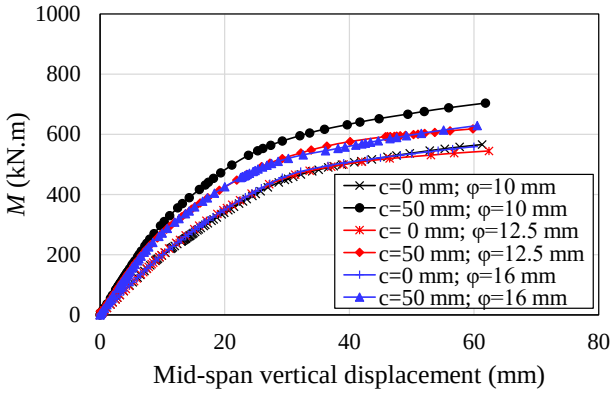

(b) W360x51 and (n/2)=13

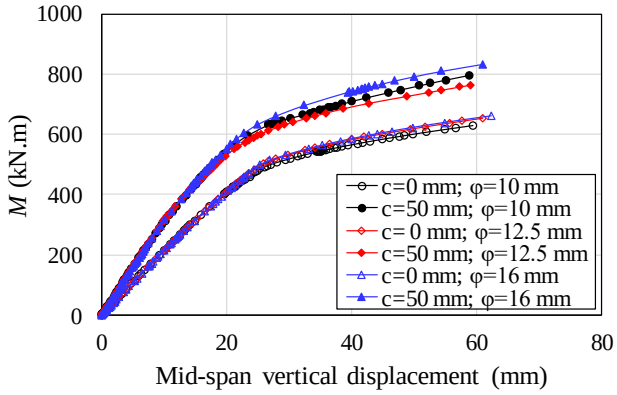

(c) W460x74 and (n/2)=24

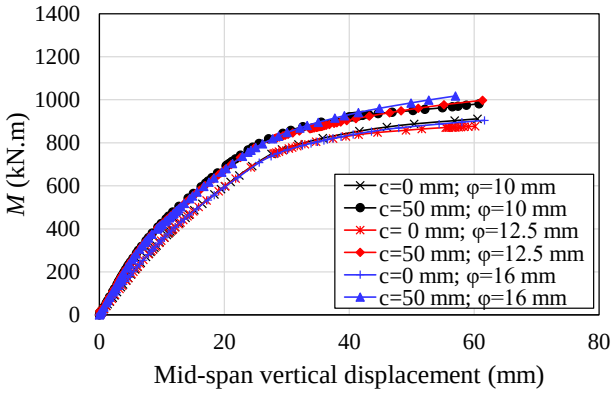

(d) W460x74 and (n/2)=13

Fig. 23: Influence of transverse reinforcement rate on behavior of composite beam with f_c=25MPa, considering moment-displacement relationship

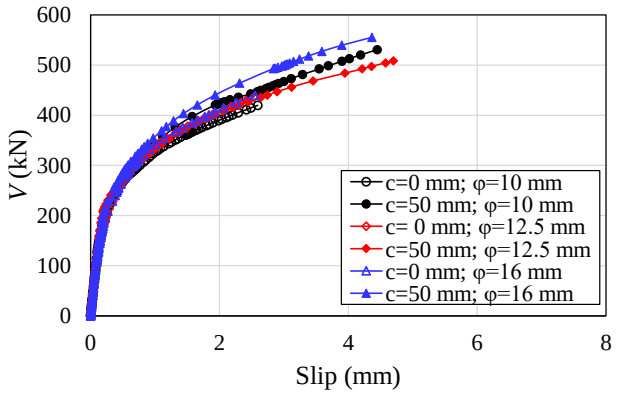

(a) W360x51 and (n/2)=24

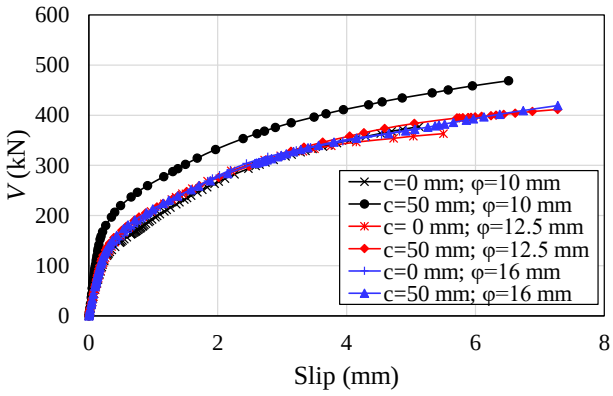

(b) W360x51 and (n/2)=13

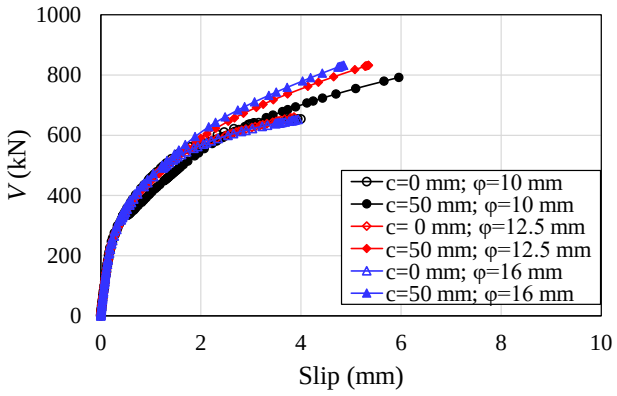

(c) W460x74 and (n/2)=24

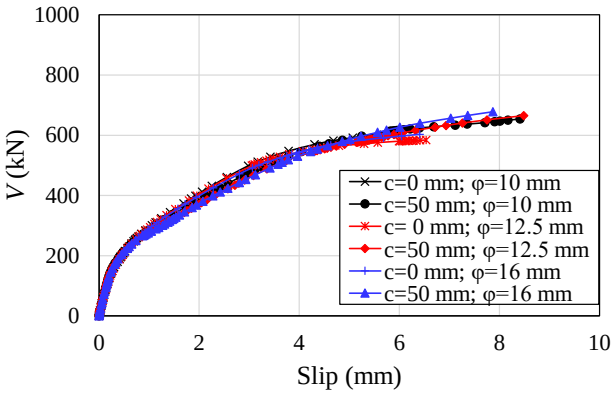

(d) W460x74 and (n/2)=13

Fig. 24: Influence of transverse reinforcement rate on behavior of composite beam with f_c=25MPa, considering shear-slip relationship

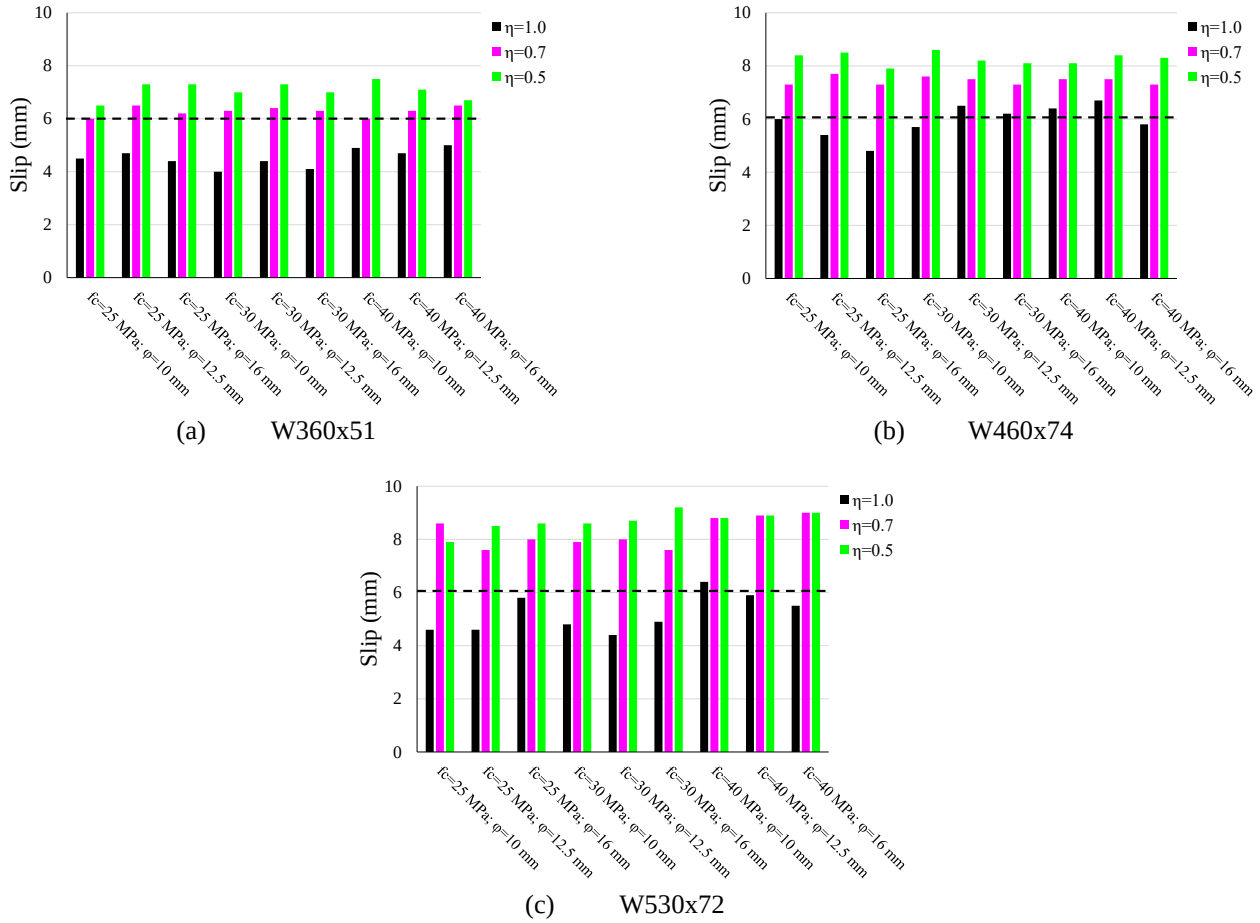

(a) W360x51 (b) W460x74

(c) W530x72

506 **Fig. 25: Values of slip on slab-profile interface**

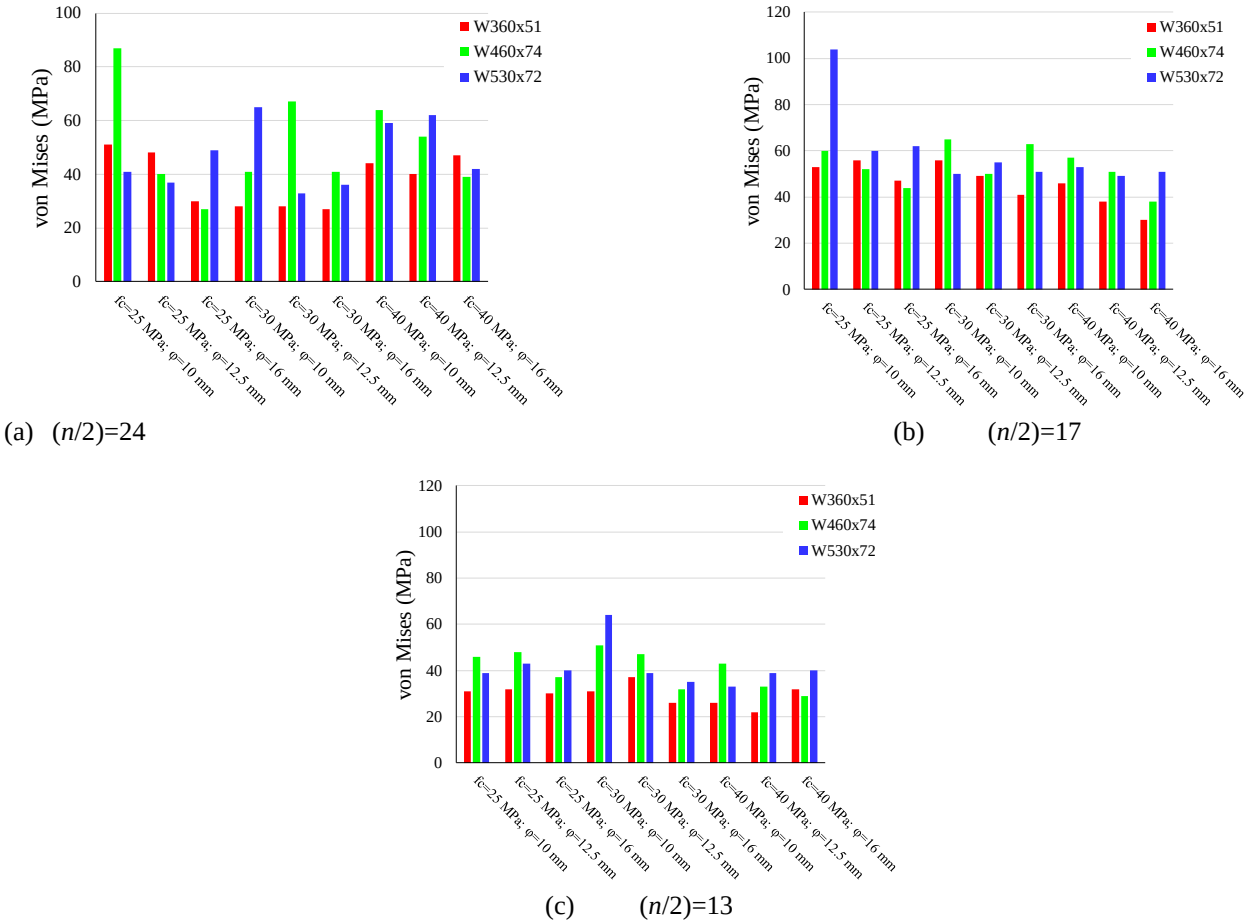

(a) (*n*/2)=24 (b) (*n*/2)=17

(c) (*n*/2)=13

507 **Fig. 26: Values of von Mises stress on transversal reinforcements**

5.5. COMPARASION WITH ANALYTICAL PROCEDURES

The results of the parametric study were compared with the resistance equations presented in section 2 (resistance of composite beams with hollow core slabs), considering the models of shear connectors resistance [9,13] (**Table 1)**. For this purpose, the displacement prescriptions in *L*/200 and *L*/100 were considered (**Fig. 27**). As shown in the illustration, considering the displacement limit equal to *L*/200, some situations were found in the non-conservative zone. It is worth mentioning that although the authors' models take into account in their equations the parameters that influence the strength of the shear connectors, there is no data of any parametric study, considering the composite beams with PCHCS with concrete topping. Therefore, for this displacement limit, according to Gouchman's prescriptions [13], the flexural behavior, specifically the bending moment of the numerical models, presented values lower than such recommendations. It is important to note that the recommendations lead to the hypothesis that the composite section is completely in plastic behavior. On the other hand, considering the stopping criterion, that is, the displacement prescribed in *L*/100, the models presented themselves in the conservative zone. This means that the bending moment values of the numerical models were higher than the recommendations.

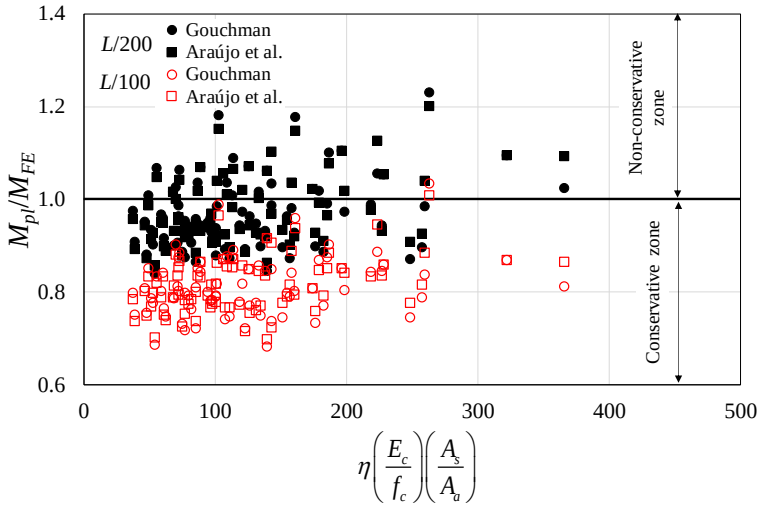

Fig. 27: Resistance of composite beams with PCHCS and concrete topping

In **Fig. 28**, the relations of statics are presented, considering both models studied, with the displacement prescriptions in *L*/200 and *L*/100. Considering the displacement prescribed in *L*/200, the number of 30 observations of each model appeared to be against safety. However, it is important to note that for this analysis with the displacement prescribed in *L*/200, the steel section showed plastic behavior only on the lower flange and the lower part of the web, unlike the equations presented in section 2, which consider that the entire steel section is in plastic behavior. (**Fig.17b**). On the other hand, considering the displacement prescribed in *L*/100, the number of observations that were against safety, for both models, was almost null. This means that both prescriptions for calculating strength, considering the strength of the shear connectors, shown in **Table 1**, are similar. This statement is validated through the mean, standard deviation and variance, shown in **Fig. 28**.

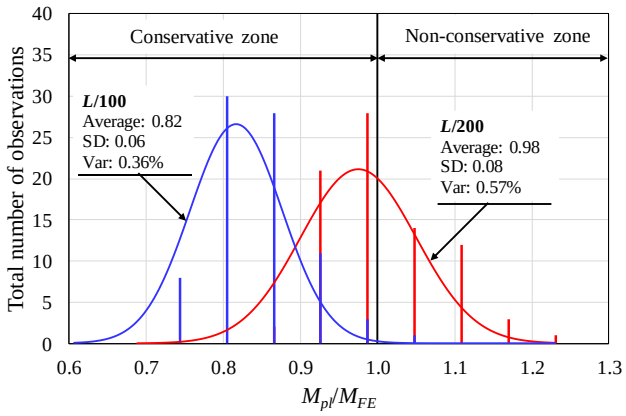

(a) Araújo et al. [9]

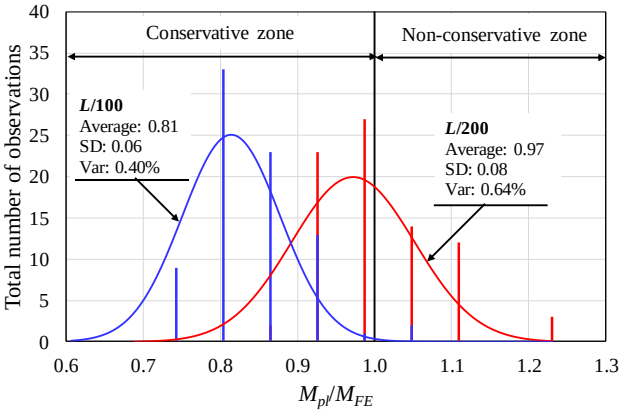

(b) Gouchman [13]

Fig. 28: Total number of observations vs. analytical procedures distributions

CONCLUSIONS

This study investigated the behavior of steel-concrete composite beams with hollow core slabs with concrete topping, considering full and partial interaction. A parametric study was conducted to investigate the in-situ concrete compressive strength, transverse reinforcement rate, shear connector spacing and steel cross section. The results of the parametric study were compared with analytical procedures. It was concluded that the presence of the concrete topping increased the strength of the composite beams with precast hollow core slabs, by at least 7%. The greater the in-situ concrete compressive strength, the greater the value of the von Mises stresses in the shear connectors. The in-situ concrete compressive strength was directly influenced by the steel cross-sectional area, reinforcement rate and degree of interaction. The area of the steel cross section influenced the magnitude of von Mises stresses in the transverse reinforcement. Considering the stopping criterion, that is, the mid-span vertical displacement prescribed in *L*/100, the results were presented in the conservative zone when compared to analytical procedures. Regarding the spacing of the shear connectors, for:

- **Full interaction (n/2=24):**

1. The steel-concrete composite beams with precast hollow core slab and concrete topping showed greater strength when compared to the other degrees of interaction;

2. The ductile behavior was not observed in any situation, that is, the results presented for slip values in the steel-concrete interface were less than 6mm;

3. The transverse reinforcement rate, considering the diameter of 16mm, provided greater resistance in the composite beams with PCHCS with concrete topping;

- **Partial interaction (n/2=17 and 13):**

1. With the reduction in the degree of interaction, there was a reduction in the strength of the composite beams with precast hollow core slabs;

2. In all situations, the ductile behavior was observed, that is, the results presented for slip values in the steel-concrete interface were greater than or equal to 6mm, and the lower the degree of interaction, the greater the ductile behavior of the composite element as a whole;

3. There were no significant differences in resistance of composite beams with PCHCS and concrete topping, considering the variation of the in-situ concrete compressive strength;

4. With increasing spacing between shear connectors, the diameter of 10mm, provided greater resistance;

ACKNOWLEDGMENTS

The authors would like to thank Construção Metálica – Gerdau Aços Brasil for making available the data related to COPPETEC, PEC-18541. This work was supported by the São Paulo Research Foundation (FAPESP) [grant number #2018/22803-1].

REFERENCES

[1] Ahmed IM, Tsavdaridis KD. The evolution of composite flooring systems: applications, testing, modelling and eurocode design approaches. J Constr Steel Res 2019;155:286–300. doi:10.1016/j.jcsr.2019.01.007.

[2] Ellobody E, Lam D. Modelling of headed stud in steel-precast composite beams. Steel Compos Struct 2002;2:355–78. doi:10.12989/scs.2002.2.5.355.

[3] Ibrahim IS, Elliott KS, Abdullah R, Kueh ABH, Sarbini NN. Experimental study on the shear behaviour of precast concrete hollow core slabs with concrete topping. Eng Struct 2016;125:80–90. doi:10.1016/j.engstruct.2016.06.005.

[4] Baran E. Effects of cast-in-place concrete topping on flexural response of precast concrete hollow-core slabs. Eng Struct 2015;98:109–17. doi:10.1016/j.engstruct.2015.04.017.

[5] Lam D. Composite steel beams using precast concrete hollow core floor slabs. 1998. Ph.D. thesis. University of Nottingham, 1998.

[6] Lam D, Elliott KS, Nethercot DA. Experiments on composite steel beams with precast concrete hollow core floor slabs. Proc Inst Civ Eng - Struct Build 2000;140:127–38. doi:10.1680/stbu.2000.140.2.127.

[7] Lam D, Elliott KS, Nethercot DA. Parametric study on composite steel beams with precast concrete hollow core floor slabs. J Constr Steel Res 2000;54:283–304. doi:10.1016/S0143-974X(99)00049-8.

[8] Nguyen TNH, Tan KH, Kanda T. Investigations on web-shear behavior of deep precast, prestressed concrete hollow core slabs. Eng Struct 2019;183:579–93. doi:10.1016/j.engstruct.2018.12.052.

[9] Araújo D de L, Sales MWR, Paulo SM de, El Debs ALH de C. Headed steel stud connectors for composite steel beams with precast hollow-core slabs with structural topping. Eng Struct 2016;107:135–50. doi:10.1016/j.engstruct.2015.10.050.

[10] Lam D. Capacities of headed stud shear connectors in composite steel beams with precast hollowcore slabs. J Constr Steel

Res 2007;63:1160–74. doi:10.1016/j.jcsr.2006.11.012.

[11] EUROPEAN COMMITTEE FOR STANDARDIZATION. EN 1994-1-1: Eurocode 4 – Design of composite steel and concrete structures – Part 1-1: General rules for buildings. 2004.

[12] Batista EM, Landesmann A. Análise experimental de vigas mistas de aço e concreto compostas por lajes alveolares e perfis laminados. COPPETEC, PEC-18541 2016.

[13] Gouchman GH. Design of composite beams using precast concrete slabs in accordance with EUROCODE 4. The Steel Construction Institute; 2014.

[14] Lam D. Designing composite beams with precast hollowcore slabs to Eurocode 4. Adv Steel Constr 2007;3:594–606. doi:10.18057/IJASC.2007.3.2.

[15] Hicks SJ, Lawson RM. Design of composite beams using precast concrete slabs. The Steel Construction Institute; 2003.

[16] Queiroz FD, Vellasco PCGS, Nethercot DA. Finite element modelling of composite beams with full and partial shear connection. J Constr Steel Res 2007;63:505–21. doi:10.1016/j.jcsr.2006.06.003.

[17] Aggelopoulos E, Hanus F, Lawson M. Shear connection requirements for composite cellular beams. Proc. 12th Int. Conf. Adv. Steel-Concrete Compos. Struct. - ASCCS 2018, Valencia: Universitat Politècnica València; 2018, p. 153–9. doi:10.4995/ASCCS2018.2018.7161.

[18] Dassault Systèmes Simulia. Abaqus 6.18 2016.

[19] Ferreira FPV, Rossi A, Martins CH. Lateral-torsional buckling of cellular beams according to the possible updating of EC3. J Constr Steel Res 2019;153. doi:10.1016/j.jcsr.2018.10.011.

[20] Ferreira FPV, Martins CH. LRFD for Lateral-Torsional Buckling Resistance of Cellular Beams. Int J Civ Eng 2019. doi:10.1007/s40999-019-00474-7.

[21] Rossi A, Ferreira FPV, Martins CH, Mesacasa Júnior EC. Assessment of lateral distortional buckling resistance in welded I-beams. J Constr Steel Res 2020;166:105924. doi:10.1016/j.jcsr.2019.105924.

[22] Chen S, Jia Y. Numerical investigation of inelastic buckling of steel–concrete composite beams prestressed with external tendons. Thin-Walled Struct 2010;48:233–42. doi:10.1016/j.tws.2009.10.009.

[23] Zhou W-B, Yan W-J. Refined nonlinear finite element modelling towards ultimate bending moment calculation for concrete composite beams under negative moment. Thin-Walled Struct 2017;116:201–11. doi:10.1016/j.tws.2017.02.011.

[24] El-Lobody E, Lam D. Finite Element Analysis of Steel-Concrete Composite Girders. Adv Struct Eng 2003;6:267–81. doi:10.1260/136943303322771655.

[25] Lam D. Composite steel beams with precast hollow core slabs: behaviour and design. Prog Struct Eng Mater 2002;4:179–85. doi:10.1002/pse.128.

[26] Hillerborg A, Modéer M, Petersson P-E. Analysis of crack formation and crack growth in concrete by means of fracture mechanics and finite elements. Cem Concr Res 1976;6:773–81. doi:10.1016/0008-8846(76)90007-7.

[27] Lubliner J, Oliver J, Oller S, Oñate E. A plastic-damage model for concrete. Int J Solids Struct 1989;25:299–326. doi:10.1016/0020-7683(89)90050-4.

[28] Lee J, Fenves GL. Plastic-Damage Model for Cyclic Loading of Concrete Structures. J Eng Mech 1998;124:892–900. doi:10.1061/(ASCE)0733-9399(1998)124:8(892).

[29] Yu T, Teng JG, Wong YL, Dong SL. Finite element modeling of confined concrete-I: Drucker–Prager type plasticity model. Eng Struct 2010;32:665–79. doi:10.1016/j.engstruct.2009.11.014.

[30] Genikomsou AS, Polak MA. Finite element analysis of punching shear of concrete slabs using damaged plasticity model in ABAQUS. Eng Struct 2015;98:38–48. doi:10.1016/j.engstruct.2015.04.016.

[31] Behnam H, Kuang JS, Samali B. Parametric finite element analysis of RC wide beam-column connections. Comput Struct 2018;205:28–44. doi:10.1016/j.compstruc.2018.04.004.

[32] CARREIRA DJ, CHU KH. Stress-Strain Relationship for Plain Concrete in Compression. ACI J Proc 1985;82:797–804. doi:10.14359/10390.

[33] Carreira DJ, Chu KH. Stress-Strain Relatonship for Reinforced Concrete in Tension. J Am Concr Inst 1986;83:21–8.

[34] Wijesiri Pathirana S, Uy B, Mirza O, Zhu X. Flexural behaviour of composite steel–concrete beams utilising blind bolt shear connectors. Eng Struct 2016;114:181–94. doi:10.1016/j.engstruct.2016.01.057.

[35] Liu X, Bradford MA, Chen Q-J, Ban H. Finite element modelling of steel–concrete composite beams with high-strength friction-grip bolt shear connectors. Finite Elem Anal Des 2016;108:54–65. doi:10.1016/j.finel.2015.09.004.

[36] Sjaarda M, Porter T, West JS, Walbridge S. Fatigue Behavior of Welded Shear Studs in Precast Composite Beams. J Bridg Eng 2017;22:04017089. doi:10.1061/(ASCE)BE.1943-5592.0001134.

[37] Chen Y. Innovative shear connections for the accelerated construction of composite bridges. 2013. Ph.D. thesis. University of Waterloo, 2013.

[38] Guezouli S, Lachal A. Numerical analysis of frictional contact effects in push-out tests. Eng Struct 2012;40:39–50. doi:10.1016/j.engstruct.2012.02.025.

[39] Crisfield MA. Snap-through and snap-back response in concrete structures and the dangers of under-integration. Int J Numer Methods Eng 1986;22:751–67. doi:10.1002/nme.1620220314.

[40] Crisfield MA. A fast incremental/iterative solution procedure that handles “snap-through.” Comput Struct 1981;13:55–62. doi:10.1016/0045-7949(81)90108-5.

[41] Maewal A, Nachbar W. Stable Postbuckling Equilibria of Axially Compressed, Elastic Circular Cylindrical Shells: A Finite-Element Analysis and Comparison With Experiments. J Appl Mech 1977;44:475–81. doi:10.1115/1.3424103.

Steel-Concrete Composite Beams with Precast Hollow Core Slabs: A Sustainable Solution

Felipe Piana Vendramell Ferreira[a], Konstantinos Daniel Tsavdaridis[b], Carlos Humberto Martins*[c], Silvana De Nardin[a]

[a]Federal University of São Carlos, Rod. Washington Luiz, km 235, São Carlos, São Paulo, Brazil.

[b]School of Civil Engineering, Faculty of Engineering and Physical Sciences, University of Leeds, Woodhouse Lane, LS2 9JT Leeds, UK.

[c]State University of Maringá, Av. Colombo nº 5790, Maringá, Paraná, Brazil.

*Corresponding author

E-mail addresses: fpiana@live.com (F. P. V. Ferreira), K.Tsavdaridis@leeds.ac.uk (K. D. Tsavdaridis), chmartins@uem.br (C. H. Martins), snardin@ufscar.br (S. De Nardin).

Abstract

Industrialization of construction makes building operation more environmental friendly and sus-tainable. This change is necessary as it is an industry that demands large consumption of water and energy as well as being responsible for the disposal of high volume of waste. However, the trans-formation of the construction sector is a big challenge worldwide. It is also well known, that the largest proportion of the material used in a multi-story building, thus its carbon impact, is attributed to its slabs being the main contributor of weight. Steel-concrete composite beams with precast hollow core slabs (PCHCS) are developed due to their technical and economic benefits owing to their high strength and concrete self-weight reduction, making this system economical and with lower environmental footprint, thus reducing carbon emissions. Significant research has been car-ried out on deep hollow core slabs due to the need to overcome larger spans that resist high loads. The publication SCI P401, in accord with EC4, is limited to hollow core slabs with depths from 150 to 250mm, with or without concrete topping. This paper aims to investigate hollow core slabs with concrete topping to understand its effect on the flexural behavior of steel-concrete composite beams, considering the hollow core slab depth is greater than the SCI P401 recommendation. For this task, 150mm and 265mm hollow core units with concrete topping are considered to assess if the increase of the hollow core unit deep (or consumption of precast concrete) provides greater resistance to the structural system. An experimentally validated finite element model is developed and calibrated by geometrical nonlinear analyses. A comprehensive parametric study was conducted varying the in-situ infill concrete strength, the transverse reinforcement rate, the shear connector spacing and the cross-section of steel are varied. All observations showed a homogeneous collapse mode, that is, excessive cracking of the PCHCS. The results showed that increasing the hollow core unit deep is not advantageous, since the strength gain is low, the ultimate strength is fragile and the consump-tion of concrete is higher. This last factor intensifies the emission of CO2. For full interaction, a sit-uation in which there is a greater number of shear studs, therefore, a greater consumption of energy for execution, there were no differences with the variation of the transverse reinforcement rate, and the in-situ concrete strength. On the other hand, for partial interaction, some models provided re-sistance equivalent to full interaction models. This means that the same strength can be obtained for a smaller number of shear studs, less energy consumption, and consequently, a reduction in the embodied energy. Besides, the calculation procedure according to Eurocode 4, was in favor of safety for the partial interaction hypothesis.

Keywords: Composite beams; Hollow core slabs; Sustainable; Finite element analyses.

1 INTRODUCTION

It has been observed so far that researchers have been studying the impact that civil construction causes on the environment. In this context a concept that has been studied is embodied energy in materials buildings [1]. In Whitworth and Tsavdaridis [2,3] optimization studies were presented in steel-concrete composite beams with the objective of presenting sustainable structural designs by minimizing the embodied energy. The study showed that it is possible to reduce the embodied energy of these structural systems, considering the design recommendations of EC4 [4].

Conventional steel-concrete composite beams have a concrete slab which is placed at the upper flange of the downstand steel profile. In this context, three types of slabs can be used: solid, composite or precast hollow core slabs (PCHCS). In composite beams with PCHCS, a cast in-situ concrete topping is usually made to provide smooth and uniform finish [5]. The concrete topping can increase strength and stiffness of the structural system [6,7]. Other factors influence the strength of PCHCS, such as the intensity of the actual prestress, the prestress transmission length, the depth of slab, and filled cores [8]. PCHCS are widely used in countries with cold climates in the construction of residential or industrial buildings due to their fast installation. In Albero et al. [9] the estimate of the number of PCHCS floors installed in Europe was estimated close to 1,000 million square meters. The use of PCHCS offers advantages, i.e. large spans, speed and reduced construction costs [5,10–14]. In the European Union, according to Ahmed and Tsavdaridis [15], the construction and building are responsible for about 40% of the environmental impact. In Dong et al. [16] the precast and cast in-situ construction methods were compared using a study of case. The authors concluded that the precast construction can lead to 10% carbon reduction for one cubic meter concrete. PCHCS is an industrialized structural element which consumes less energy to be constructed in-house in comparison to in-situ slabs, and with minimum waste of concrete, thus with overall lower carbon footprint. In terms of sustainability, the PCHCS is a structural element that contributes not only to the speed in construction, but also to the significant reduction of CO2 emissions due to the lower consumption of concrete.

The present study aims to examine the flexural behavior of steel-concrete composite beams with PCHCS and concrete topping, considering the HCU depth greater than the SCI P401 recommendation. The finite element (geometrical non-linear analysis) model is developed based on tests [17,18]. The results are compared with the SCI P401 procedure [19], thus analytical models of shear studs resistance capacity are employed [19,20].

2 BACKGROUND

Lam [17] and Lam et al. [21] presented flexural tests on steel-concrete composite beams with PCHCS. A four-point bending was considered. In these studies, the concrete topping was not considered. The experimental results of the authors showed the sudden failure due to the shear studs rupture, and the concrete cracking, resulting in loss of stiffness. Lam et al. [22] complemented the previous studies and carried out a parametric study. In this study, the authors observed that with an increase in the depth of PCHCS (150mm to 200-250mm), there was an increase in the ultimate strength. However, the slab may fail due due to excessive cracking. Ellobody and Lam [23] investigated the shear studs, and the gap, considering the flexural behavior. The authors concluded that the shear stud resistance increased with the increase of the gap, and the in-situ infill concrete strength influenced the

strength of the shear study. In 2003, the SCI P287 [24] was published. It is a design criteria for composite beams with PCHCS [17]. This publication was subsequently updated to SCI P401 [19]. The document gathers recommendations of minimum dimensions, such as arrangement of the shear studs and transverse reinforcement. However, some limitations are observed, such as application only for 150-250mm HCU depths; 12mm or 16 mm transverse reinforcement diameter are recommended for composite construction; for partial shear connection, 16 mm diameter bars should be provided; for HCU up to 260mm, 16 mm diameter bars should be considered, spaced in 200-350mm, and; for full interaction, if the plastic neutral axis (P.N.A.) lies within the slab, the interaction degree must be reduced, or the size of the steel profile increased. A technical report (COPPETEC, PEC-18541/2016), which was presented by Batista and Landesmann [18], described tests on composite beams with PCHCS and concrete topping. According to the authors, in the ultimate strength, the loss of stiffness was due to excessive cracking. In Ferreira et al. [25] a parametric study was presented, considering PCHCS with 150mm of depth and 50mm of concrete topping. In this study, the presence of the concrete topping increased the strength of the composite beams by at least 7%. As observed, few studies have investigated the behavior of steel-concrete composite beams with PCHCS [26]. Besides, Tawadrous and Morcous [4] and El-Sayed et al. [5] described that due to the successful use of PCHCS, deeper HCUs were developed to resist higher loads and to support longer spans. In this scenario, some researchers carried out tests to investigate the behavior of deeper PCHCS [12,13,27–32]. However, such investigation did not consider the composite behavior, i.e. steel-concrete composite beams.

3 NUMERICAL MODEL: VALIDATION STUDY

In this section, the methodology of the validation study is described. The ABAQUS® software [33] is used. Three types of steel concrete composite beams are modeled, considering symmetry:

1. 150mm of HCU depth with chamfered end (**Fig. 1a**);
2. 150mm of HCU depth and 50mm of concrete topping with squared end (**Fig. 1b**);
3. 265mm of HCU depth and 50mm of concrete topping with squared end (**Fig.1c**);

Geometrical nonlinear analyses are processed, using the Static Riks method. This method was previously used in [25,34–40]. This method is based on the arc length method. Residual stresses were not considered. These stresses do not influence the ultimate strength of composite beams subjected to only positive moment. The residual stresses increase the effects of the negative moment [41,42].

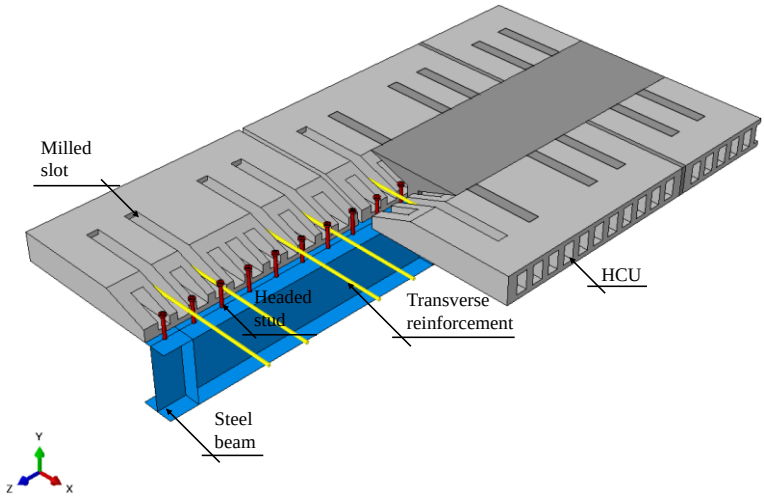

(a) 150mm of hollow core slab depth with chamfered end

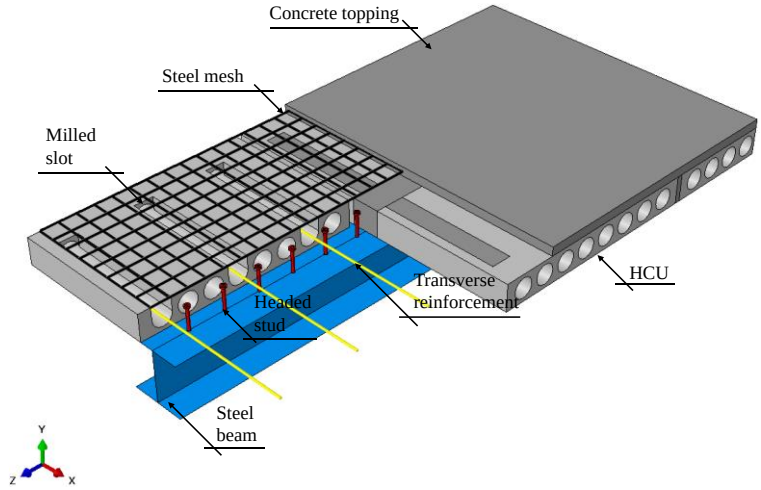

(b) 150mm of hollow core slab depth and 50mm of concrete topping with squared end

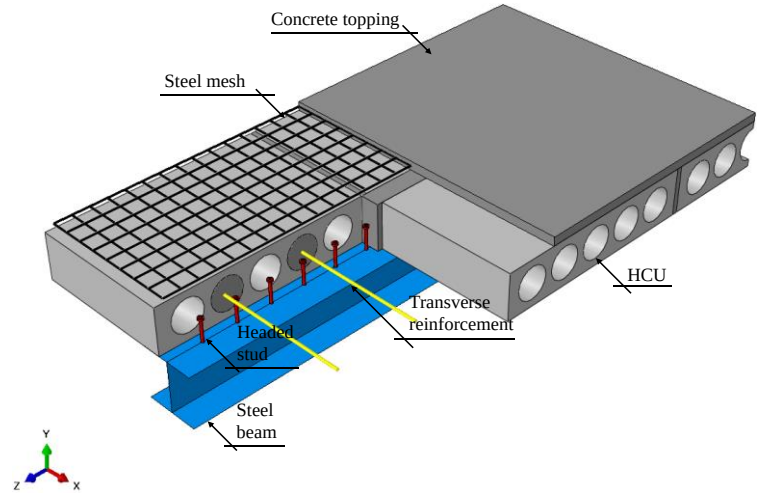

(c) 265mm of hollow core slab depth and 50mm of concrete topping with squared end

Fig. 1: Parts of steel-concrete composite beams with hollow core slab

3.1 TESTS

The numerical models are calibrated considering tests on steel-concrete composite beams with PCHCS, with 150mm and 265mm of depth, with and without concrete topping. **Fig. 2** and **Table 1** show the details of the tests [18,43], in which d is the steel beam depth, b_f is the steel flange width, t_f is the steel flange thickness, t_w is the steel web thickness, b is the effective slab width, g is the gap, h_c is the depth of the HCU, c is the concrete topping thickness, L_e is the distance between the end of the beam and the

support, L_p is the distance between the load application point and the support, L_b is the unrestrained length, φ is the diameter of the transverse reinforcement, $f_{y,f}$ is the yield strength of the flange, $f_{y,w}$ is the yield strength of the web, $f_{y,s}$ is the transverse reinforcement yield strength, $f_{c,HCU}$ is the HCU compressive strength and $f_{c,in}$ is the in-situ infill compressive strength.

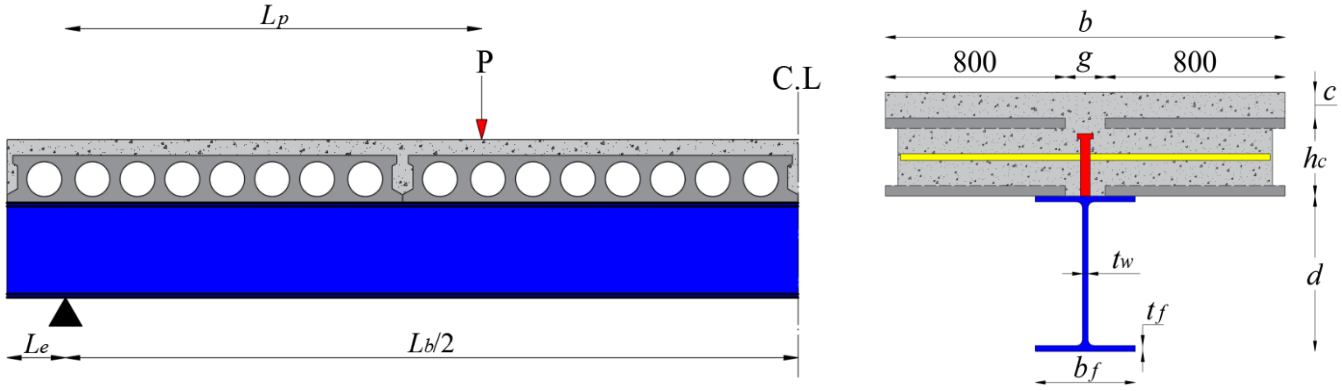

(a) Lateral view (b) Section

Fig. 2: Geometric details of tests (in mm)

Table 1: Details of specimens

Model	d (mm)	b_f (mm)	t_f (mm)	t_w (mm)	b (mm)	g (mm)	h_c (mm)	c (mm)	L_e (mm)	L_p (mm)	L_b (mm)	φ (mm)	$f_{y,f}$ (MPa)	$f_{y,w}$ (MPa)	$f_{y,s}$ (MPa)	$f_{c,HCU}$ (MPa)	$f_{c,in}$ (MPa)
CB1	355	171.5	11.5	7.4	1665	65	150	-	150	1500	5700	16	310	355	585	50[a]	32[a]
CB2	355	171.5	11.5	7.4	1665	65	150	-	150	1500	5700	8	310	355	473	50[a]	26[a]
CB3	299	306	11	11	1756	156	150	50	185	1915	5830	12.5	345	345	500	45[b]	30[b]
CB4	299	306	11	11	1756	106	265	50	185	1915	5830	12.5	345	345	500	45[b]	30[b]

[a]Cubic resistance;
[b]Cylindric resistance.

3.2 MATERIALS

The concrete damage plasticity (CDP) [44–46] model is used. The model is based on the plastic theory. Thi model can be used to describe the irreversible damage that occurs during the fracture process [33], such cracking and crushing. The concrete damage plasticity model makes use of the yield function of Lubliner et al. [45], with the modifications proposed by Lee and Fenves [46]. The concrete as a brittle material undergoes considerable volume change, called dilatancy [47], caused by inelastic strains. The flow rule in follows the Drucker-Prager model. The concrete damage plasticity model can be regularized using viscoplasticity. The regularization of Duvaut-Lions [48] is used. The input parameters for defining the plastic behavior are presented in **Table 2**, in which ψ is the dilation angle, ξ is the eccentricity, σ_{b0} is the initial equibiaxial compressive yield stress, σ_{c0} is the initial uniaxial compressive yield stress, K_c is the ratio of the second stress invariant on the tensile meridian to that on the compressive meridian and μ is the viscosity parameter. The concrete model of Carreira and Chu [49,50] is used for both compression and tension **Eqs. (1–3)**. For steel, the perfect elasto-plastic behavior is considered. In which ε_c is the strain corresponding to concrete compressive strength, ε_t is the strain corresponding to concrete tensile strength, f_c is the compressive concrete strength, f_t is the concrete tensile strength and β_c is the stress-strain relationship form factor of concrete in compression.

$$\frac{\sigma}{f_c} = \frac{\beta_c\left(\varepsilon/\varepsilon_c\right)}{\beta_c - 1 + \left(\varepsilon/\varepsilon_c\right)^{\beta_c}} \quad (1)$$

$$\frac{\sigma}{f_t} = \frac{\beta_c\left(\varepsilon/\varepsilon_t\right)}{\beta_c - 1 + \left(\varepsilon/\varepsilon_t\right)^{\beta_c}} \quad (2)$$

$$\beta_c = \left(\frac{f_c}{32.4}\right)^3 + 1.55 \ \ (MPa) \quad (3)$$

Table 2: CDP input parameters

Parameter	Value	Ref.
Ψ (º) (In-situ concrete)	40	[47,51]
Ψ (º) (HCU concrete)	28	[28]
ξ	0.1 (default)	[28,33,47,51]
σ_{b0}/σ_{c0}	1.16 (default)	[28,33,47,51]
K_c	2/3 (default)	[28,33,47,51]
μ (s^{-1})	0.001	-

3.3 INTERACTION

Fig. 3 shows the pairs of interactions. The tie constraint technique allows to simulate the perfect bond between the contact surfaces. The contact between the concrete and the transverse reinforcement, as well as the concrete and steel mesh, were made through the embedded region. The normal/tangential behavior is considered between steel beam and PCHCS, steel beam and gap, actuator and concrete topping, and headed stud and gap. The headed studs are located in the gap, using the same technique presented in [52]. The friction coefficient is based on the Coulomb friction model. The literature reports some values of the friction coefficient [53–55]. The friction coefficient equals 0.2 and 0.3 were adopted for gap and headed stud and steel beam and slab interfaces, respectively [55].

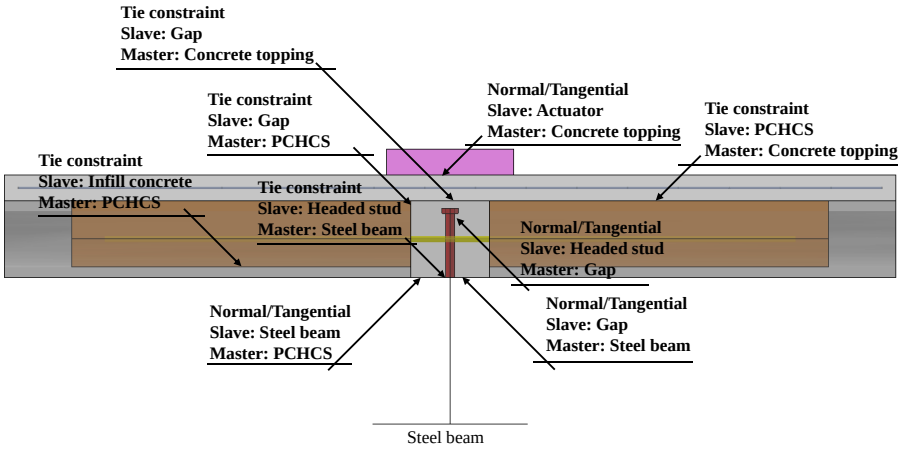

Fig. 3: Surface-to-surface interactions

3.4 BOUNDARY CONDITIONS

The boundary conditions (**Fig. 4**) were applied considering the symmetry at mid-span (Uz=URx=URy=0). The vertical displacement was restricted at the supports (Uy=0) and the lateral displacement at the ends of the slab (Ux=0). Displacement control is used. Nonlinear static analysis techniques have considerable difficulties with softening materials, such as concrete, and it can be

avoided by applying a simple form of displacement control [56,57]. The disadvantages in displacement control are related to the selection of the appropriate displacement variable, which may result in computational cost or divergence from the iterative solution procedure [58]. Thus, the variable selected for the stopping criterion is the mid-span vertical displacement.

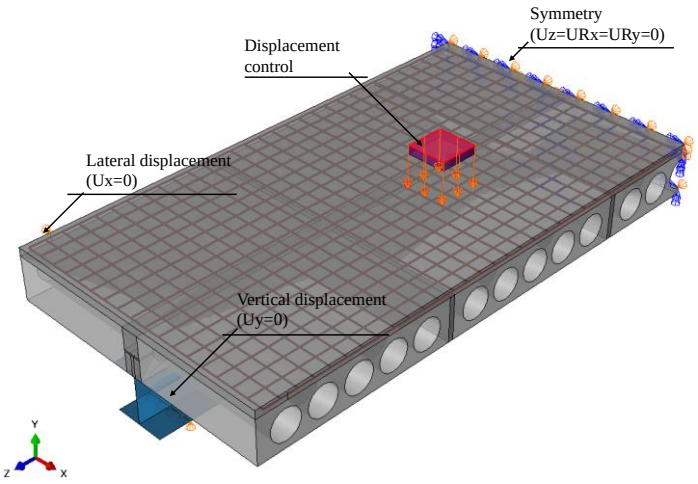

Fig. 4: Boundary conditions (CB3 model)

3.5 DISCRETIZATION

The discretization of the elements is shown in **Fig. 5**. The dimension values of the elements were adopted according to the literature [28,53,54], and with respect to the master and slave surfaces. The S4R element is a quadrilateral element with four nodes and reduced integration, a factor that reduces processing time. The C3D8R element has eight nodes, reduced integration and supports plastic analysis with large deformations, and allows the visualization of the crack in the CDP model. T3D2 element has 2-node linear displacement.

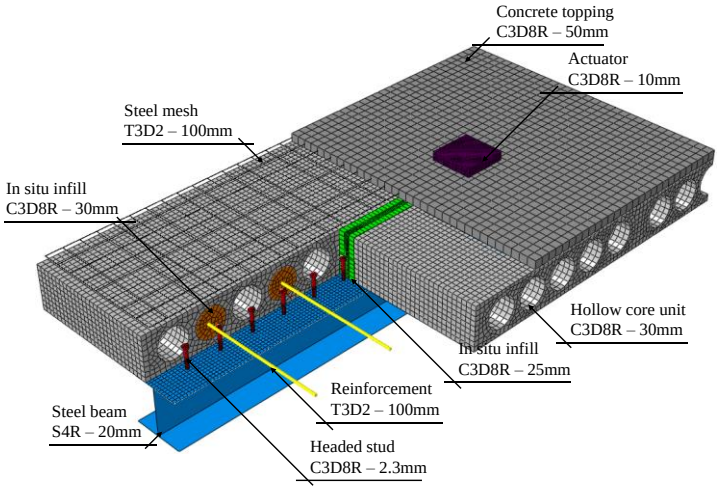

Fig. 5: Discretization (CB4 model)

3.6 RESULTS

The results are presented in **Figure 6** and **Table 3**, in which M_{FE} is the bending moment of finite element model, M_{Test} is the bending moment of experimental tests; δ_{FE} is the mid-span vertical displacement of the finite element models and δ_{Test} is the mid-span vertical displacement of the tests. It was possible to observe the yielding at lower flange, and in the models CB1 and CB2, the cracking was observed in the lower part of the PCHCS, according to Lam [17]. The behavior of CB3 and CB4 models were

similar to presented in Batista and Landesmann [18], that means, there was the propagation of cracks, which started in the central part of PCHCS and extended over the entire width.

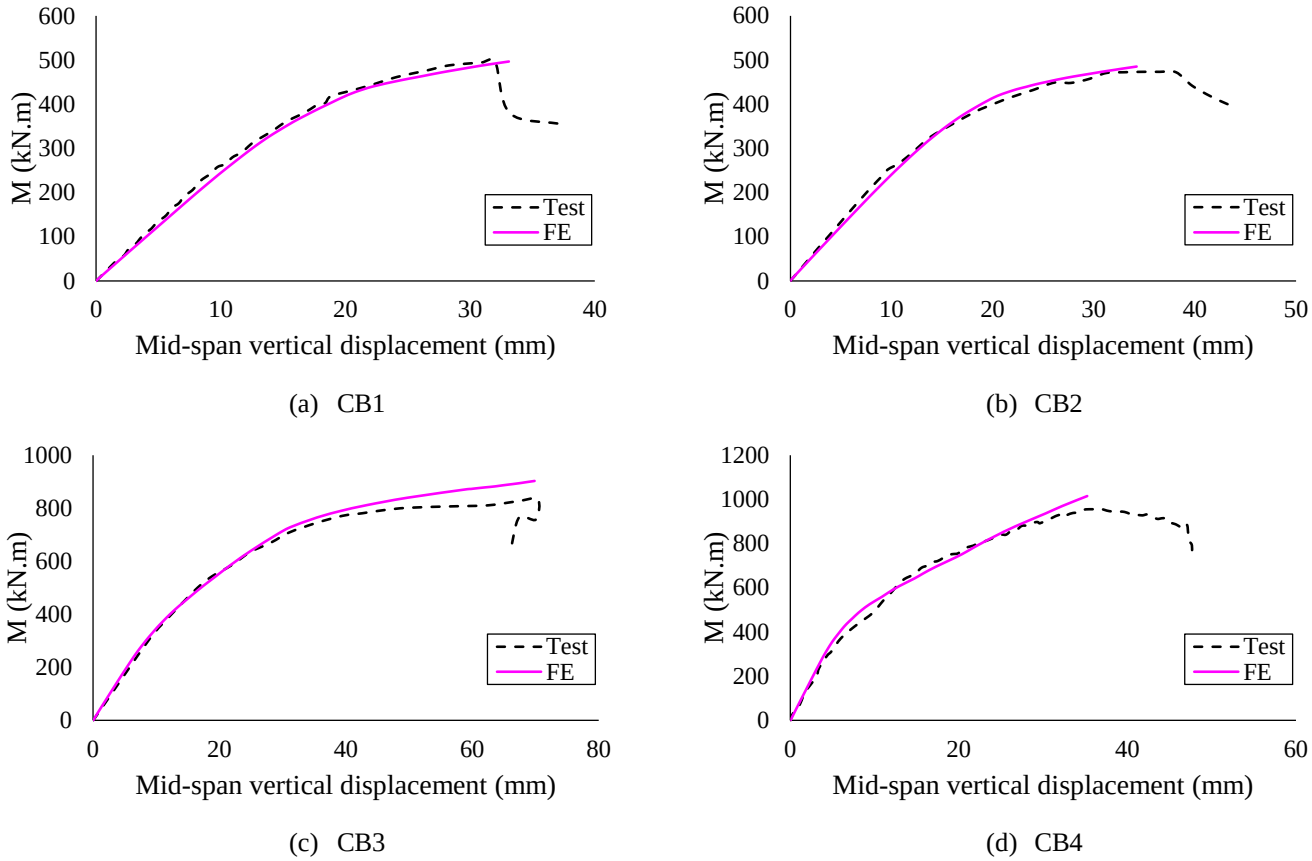

Fig. 6: Validation results

Table 3: Comparison of finite element analysis and tests results

Model	M_{Test} (kN.m)	δ_{Test} (mm)	M_{FE} (kN.m)	δ_{FE} (mm)	M_{FE}/M_{test}	$\delta_{FE}/\delta_{test}$
CB1	497	32	496	33	1.00	1.03
CB2	474	35	485	34	0.95	0.97
CB3	846	70	895	71	0.95	1.00
CB4	985	37	1015	35	1.03	0.95

4 NUMERICAL MODEL: PARAMETRIC STUDY

The studied parameters are shown in **Table 4**. The following are the general considerations for the parametric study:

1. The thickness of the concrete topping was 50mm;
2. The length of the transverse reinforcement was 1000+g, in mm;
3. Welded steel mesh with wires of 4.2 mm in diameter and with 100 mm spacing was considered [20];
4. LP26 units (**Fig. 7**), with f_c equal to 40 MPa, and gap (g) equal to 70mm were considered;
5. For the steel beam, ASTM A572 Gr.50 steel was adopted, whose yield strength is 345 MPa. The modulus of elasticity and the Poisson's ratio were equal to 200 GPa and 0.3, respectively;
6. The composite beams were simply supported and subjected to two load points spaced $L/4$ from each support. Stiffeners are placed at support and point of load;

7. The mid-span vertical displacement of maximum value equal to *L*/100 was adopted as a stopping criterion.

Table 4: Parametric study

Parameters	Variation
Section	W360x51, W460x74 and W530x72
In situ concrete strength (MPa)	25, 30 and 40
Transverse reinforcement diameter (mm)	10, 12.5 and 16
Shear connectors spacing (mm)	125, 175 and 275

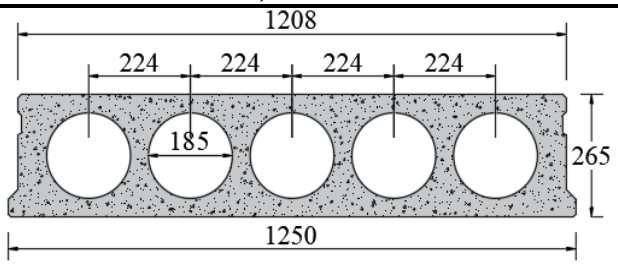

Fig. 7: PCHCS units

5 RESULTS AND DISCUSSION

In this section, the results are discussed, according to steel cross section analyzed. At the end of this section, the results are compared with the resistant calculation procedures for steel-concrete composite beams as well as with the results presented in Ferreira et al. [25], considering a 150mm of PCHCS with concrete topping.

5.1 SECTION W360x51

Considering the spacing between shear studs in 120mm, for the mid-span vertical displacement at 15mm, only the region where the beam was supported has reached the yield strength. The maximum von Mises stresses in the lower flange, web and upper flange were, approximately, 290MPa, 260MPa and 115MPa, respectively. When the composite beam reached the ultimate strength, for the mid-span vertical displacement at 26mm, the lower flange and approximately 1/4 of the web depth were in plastic regime. In no region where the shear studs were located, the yield strength was reached. The von Mises stresses in the upper flange were, approximately, 200MPa. The ultimate strength was governed by excessive cracking of the PCHCS (**Fig.8**). With the variation of the transverse reinforcement rate and in situ concrete strength, there were no differences in the shear-slip and moment-deflection relationships (**Fig. 9**). This can be explained as a function of the depth and area of the steel cross-section in relation to the depth and effective area of the PCHCS and concrete topping. Upon reaching the ultimate strength, as shown in **Fig. 8**, the N. P. A. was in the concrete topping, a factor that generates excessive tensile stresses in the PCHCS. This observation can be concluded, since in the final configuration, the upper part of the PCHCS, which were in the region of pure bending, was damaged. Another important observation was the fragile behavior of the composite beams, since the slip values at the steel-concrete interface were less than 6mm, a parameter that EC4 [4] considers to characterize the ductile behavior (**Fig. 9**). Due to this fragile behavior, with the variation of parameters, such as transverse reinforcement rate and in situ concrete strength, there were no significant differences in terms of stresses, both in the shear studs and in the transversal reinforcement, considering the ultimate strength. Some examples are illustrated in **Fig. 10**. For the models with f_c=25 MPa, it was observed that the smaller the transverse reinforcement diameter, the lower the von Mises stresses in the shear stud. The von Mises stresses in the shear studs, for f_c=25 MPa, showed a variation of only 6MPa.

On the other hand, for f_c=40 MPa, there were no variations between the von Mises stresses in the shear studs with the variation of the transverse reinforcement diameter. The observations for f_c=30MPa were similar.

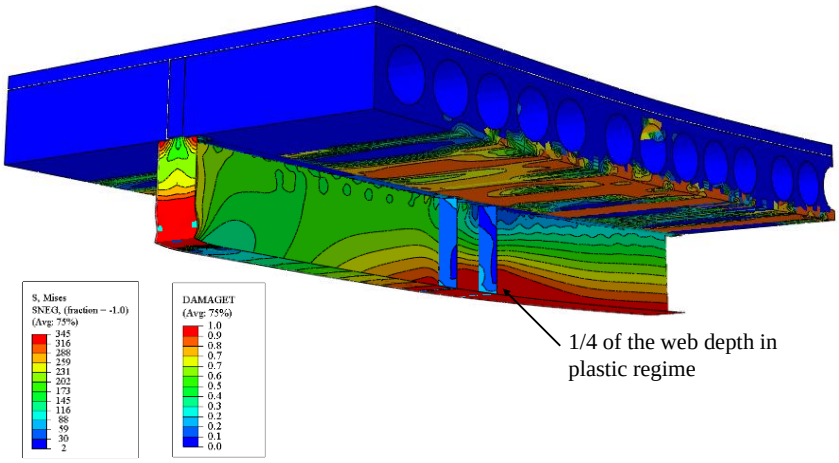

Fig. 8: Final configuration for W360x51, considering f_c=25 MPa, φ=10mm, and 120mm of spacing

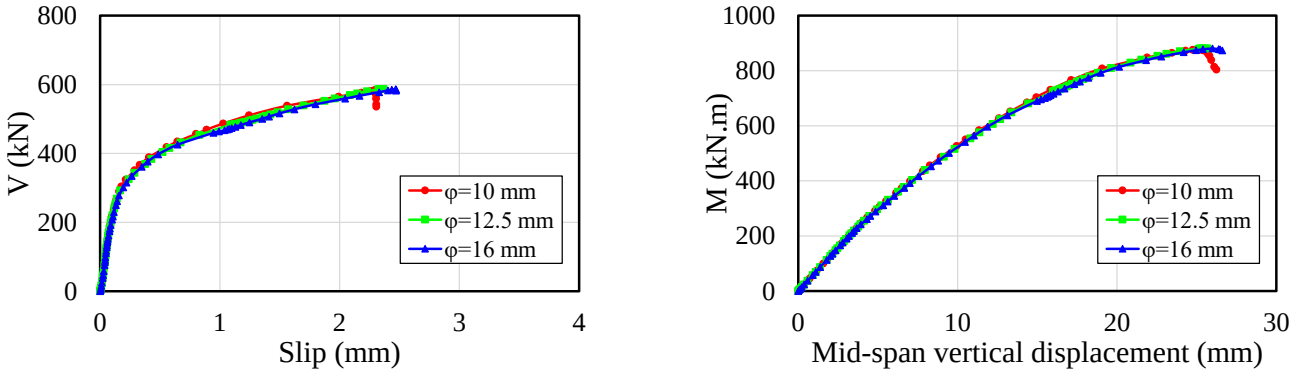

(a) Shear-slip relationship for f_c=25 MPa (b) Moment-deflection relationship for f_c=25 MPa

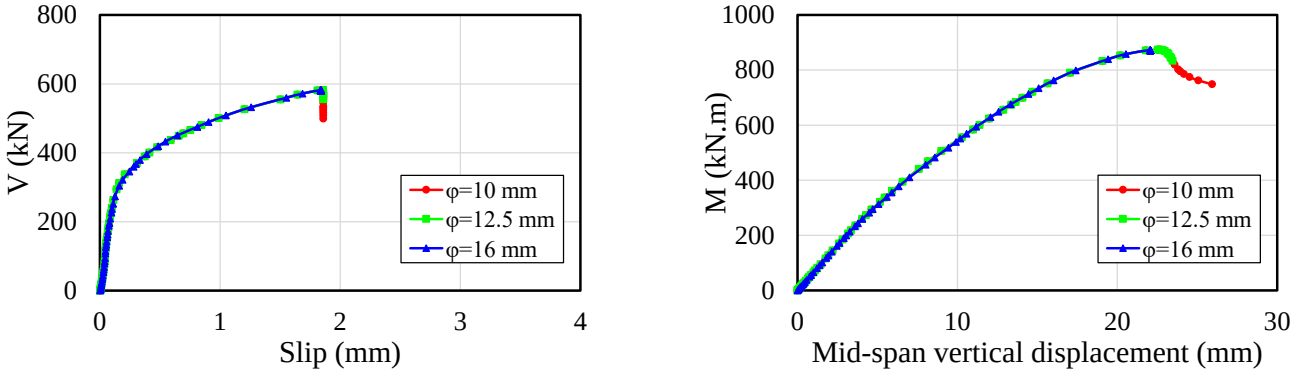

(c) Shear-slip relationship for f_c=40 MPa (d) Moment-deflection relationship for f_c=40 MPa

Fig. 9: Influence of transverse reinforcement, W360x51 and 120mm of spacing

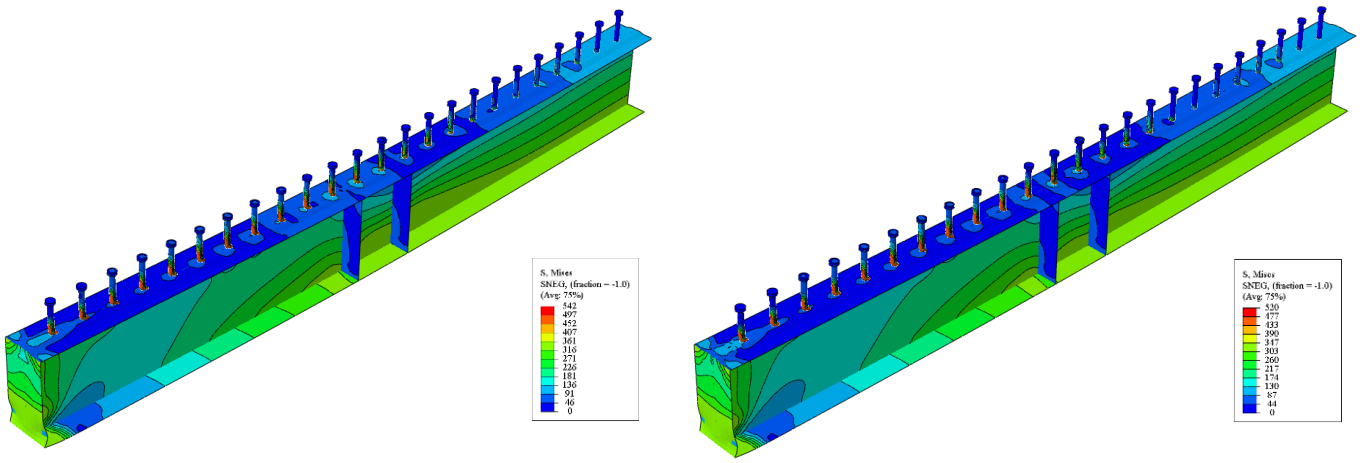

(a) f_c=25 MPa and φ=10mm (b) f_c=40 MPa and φ=16mm

Fig. 10: Von Mises stresses in headed studs, W360x51 and spacing of 120mm

On the other hand, for the shear studs spacing in 175mm and 225mm, for the mid-span vertical displacement at 15mm, the behavior was similar to the 120mm of spacing models. However, in the ultimate strength, the mid-span vertical displacements were greater than the previous situation, with the maximum value equal to 36mm, considering φ=16mm, f_c=40MPa and 175mm of spacing. For the situation in which the spacing was 225mm, the mid-span vertical displacement reached 42mm, considering φ=10mm and f_c=25MPa. Regarding the ultimate strength, the composite beams with shear studs spacing in 175mm and 225mm made better use of the steel section, that is, approximately half the web depth reached the plastification (**Fig. 11**). Then, the greater the spacing between the shear studs, the better the use of the steel section.

The variation in both the transverse reinforcement rate (**Fig. 12 and Fig. 13**) and the in situ concrete strength showed significant differences in the shear-slip and moment-deflection relationships. It was observed in the illustrations, that even with the variation of the transverse reinforcement rate and in situ concrete strength, the initial stiffness of the composite beams modeled were similar, showing that the differences of these relations were significant in non-linear branch. Although the ultimate moment has an approximate value for the models illustrated (φ=10mm, φ=12.5mm and φ=16mm), the models φ=10mm and φ=12.5mm showed similar behavior in the shear-slip and moment-deflection relationships, differently from the model φ=16mm (**Fig. 12 and Fig. 13**). This behavior, according to Lam et al. [22], it can be explained that with the increase in the transverse reinforcement rate, the flexural strength capacity increases, but reduces the ductility leading to fragile rupture.

Another important observation was that in no model presented, for W360x51 section, the composite beams showed ductile behavior. Thus, it is possible to conclude that in all models analyzed for W360x51 section, the ultimate strength was characterized as fragile. In the most observations for both 175mm and 225mm of spacing, the von Mises stresses in the shear studs were less than the models with 120mm of spacing. For example, for f_c=25MPa, considering 175mm and 225mm models, the von Mises stresses in the shear studs were lower than the model with 120 mm of spacing. A similar situation occurred for f_c=30MPa. On the other hand, for f_c=40MPa, there were models in which the von Mises stresses in the shear studs, considering 175mm and 225mm of spacings, were greater than the 120mm of spacing model. This was observed specifically for transversal reinforcement diameter equal to 10mm and 12.5mm.

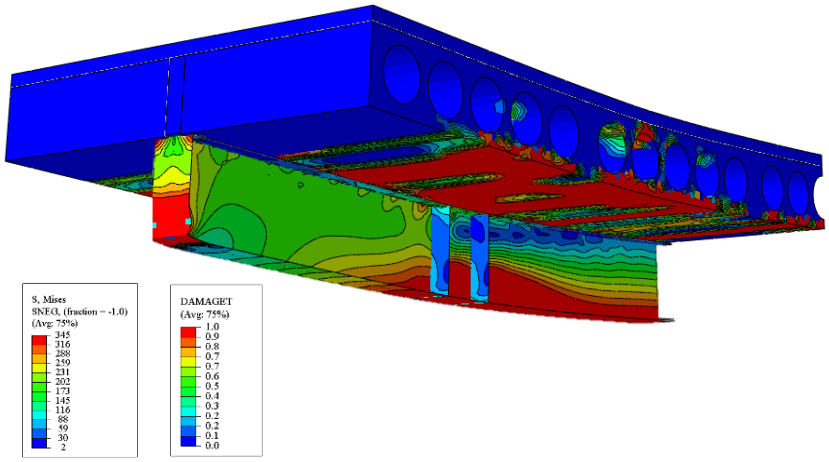

(a) 175mm of spacing, f_c=40 MPa and φ=16mm

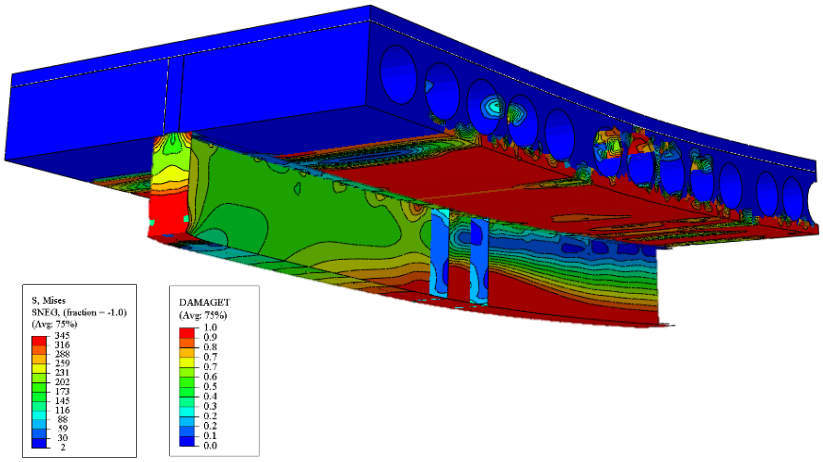

(b) 225mm of spacing, f_c=25 MPa and φ=10mm

Fig. 11: Final configuration for W360x51 section

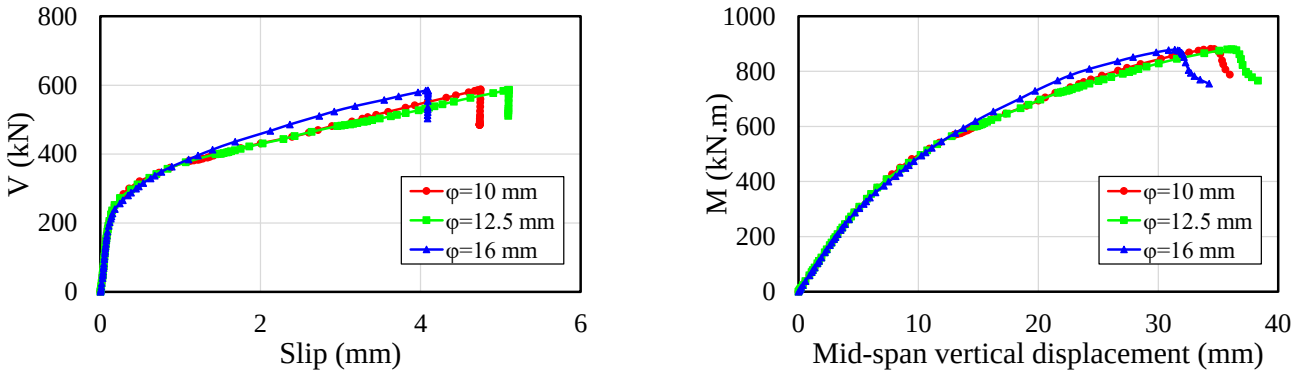

(a) Shear slip relationship (b) Moment-deflection relationship

Fig. 12: Influence of transverse reinforcement, W360x51, f_c=40 MPa 175mm of spacing

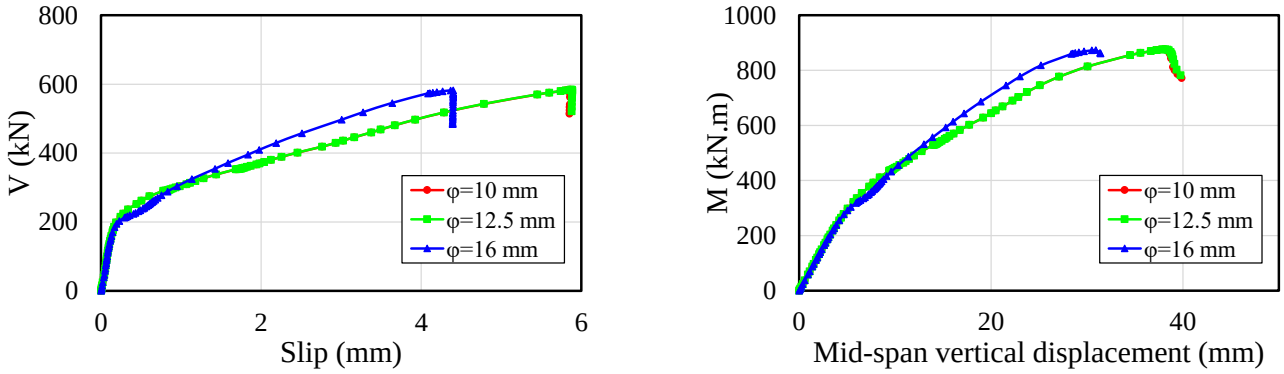

(a) f_c=40 MPa (b) f_c=40 MPa

Fig. 13: Influence of transverse reinforcement, W360x51 f_c=40 MPa 225mm of spacing

5.2 SECTION W460x74

Considering 120mm of spacing between shear studs, for the mid-span vertical displacement at 15mm, only the region in which the beam was supported has reached the yield strength. The von Mises stresses in the lower flange, web and upper flange were 290MPa, 290MPa and 120MPa, respectively. When the composite beam reached its ultimate strength, the upper flange and approximately 1/4 of the web depth were in plastic regime. The von Mises stresses in the upper flange were 230MPa. The ultimate strength was governed by excessive cracking of the PCHCS (**Fig. 14**).

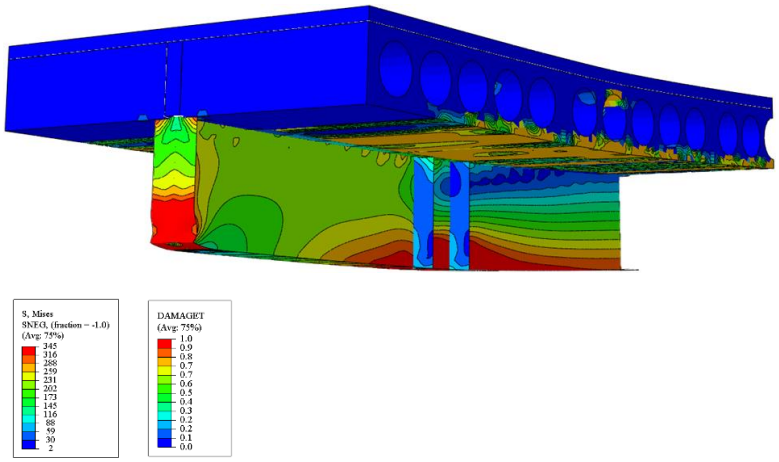

With the transverse reinforcement rate variation and in situ concrete strength, there were no differences in the shear-slip and moment-deflection relationships (**Fig. 15**). As noted, there are no significant differences in the behavior of these analyzed composite beams, because the ultimate strength was achieved by excessive cracking of the PCHCS. Situation analogous to W360x51 section. Another important observation was the fragile behavior of the composite beams, a situation similar to section W360x51. Due to this fragile behavior, with the variation of the parameters, such as transverse reinforcement rate and in situ concrete strength, there were small differences in the magnitude of the von Mises stresses, specifically in the shear studs. Some examples are illustrated in **Fig. 16**.

For f_c=25MPa models, the smaller the transverse reinforcement diameter, the lower the von Mises stresses in the shear studs. There was no variation in the stresses in the shear studs for f_c=25MPa. A similar situation occurred for f_c=30MPa models. For f_c=40MPa models, the von Mises stresses in the shear studs varied with the variation of the transverse reinforcement diameter.

Unlike the f_c=25MPa models, the smaller the transverse reinforcement diameter, the greater the von Mises stresses in the shear studs. This variation reached approximately 20MPa between φ=10mm and φ=16mm.

Fig. 14: Final configuration for W460x74, considering f_c=25 MPa, φ=10mm, and 120mm of spacing

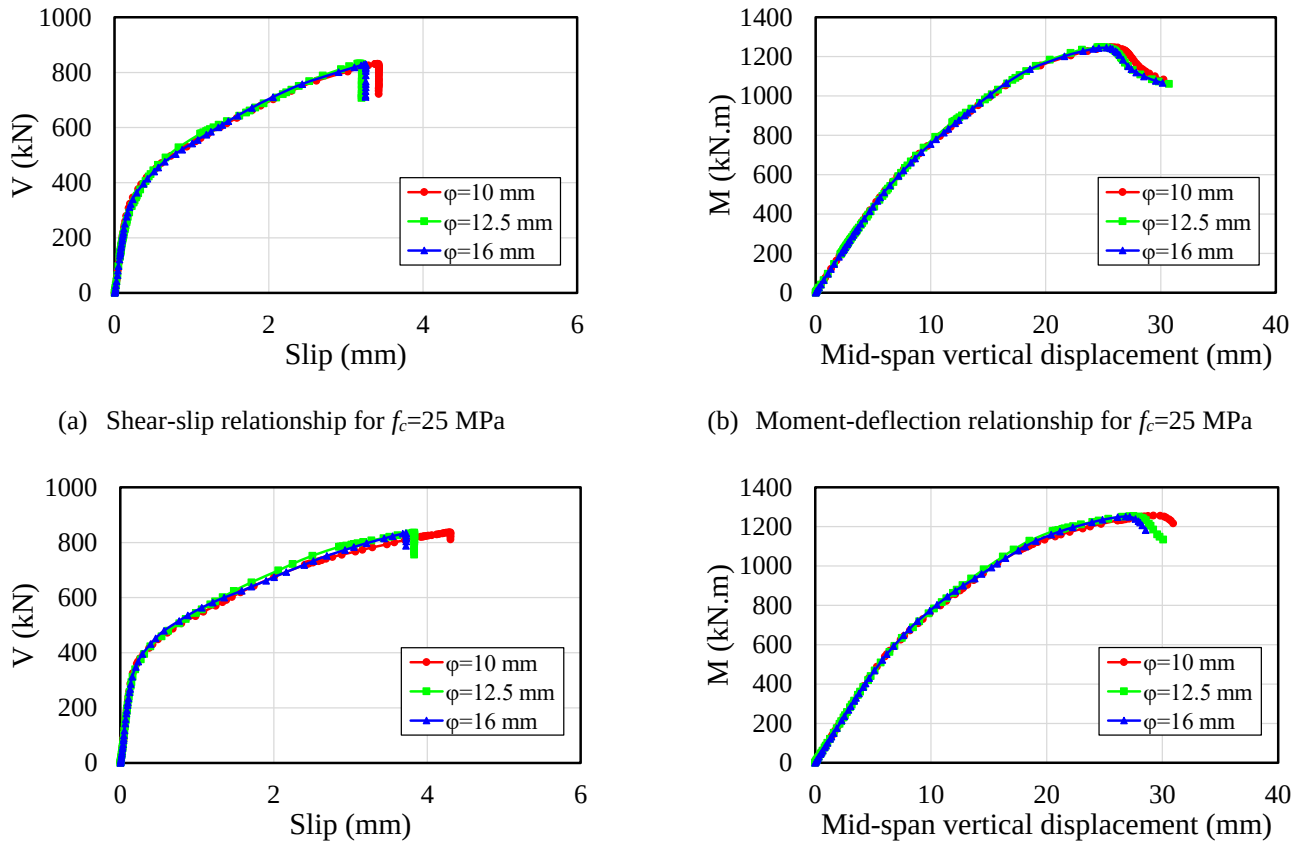

(a) Shear-slip relationship for f_c=25 MPa

(b) Moment-deflection relationship for f_c=25 MPa

(c) Shear-slip relationship for f_c=40 MPa

(d) Moment-deflection relationship for f_c=40 MPa

Fig. 15: Influence of transverse reinforcement, W460x74 and 120mm of spacing

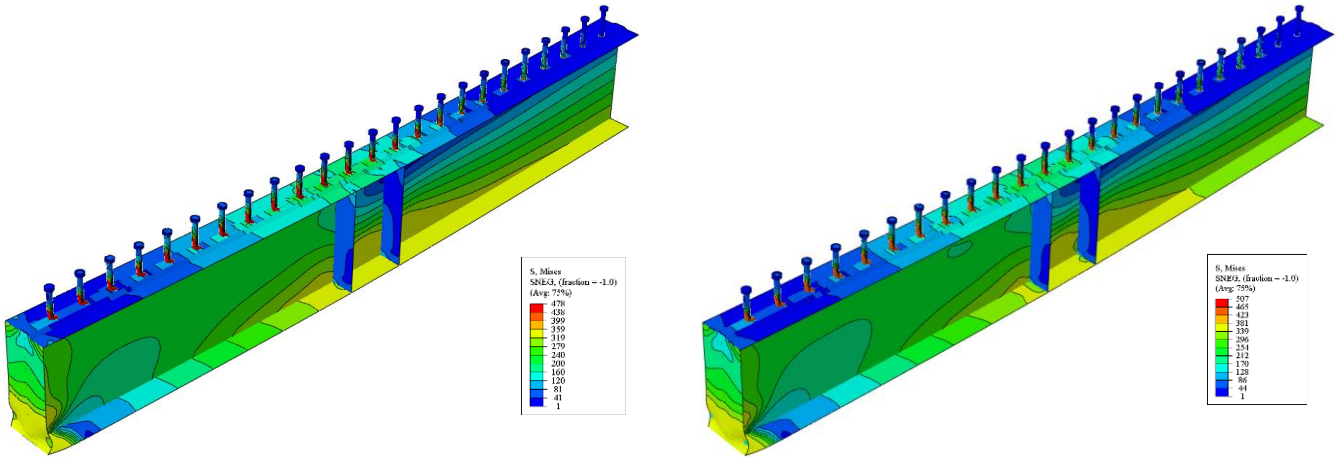

(a) f_c=25 MPa and φ=10mm

(b) f_c=40 MPa and φ=16mm

Fig. 16: Von Mises stresses in headed studs, W460x74 and spacing of 120mm

Considering both 175mm and 225mm of spacing models, it was possible to observe two different situations. In relation to the 175mm of spacing, for the mid-span vertical displacement at 15mm, the yield strength was not reached in any region of the steel

profile. The maximum von Mises stresses in the lower flange, web and upper flange were 290MPa, 290MPa and 120MPa, respectively. When the composite beams reached the ultimate strength, only part of the lower flange was in plastic regime (**Fig. 17a**). For 225mm of spacing between shear studs, the ultimate strength was characterized with the lower flange, half the web depth, and part of the upper flange, which were in the region of the loading application point, in plastic regime (**Fig. 17b**). This was the model in which the composite action took advantage of the strength of the steel profile.

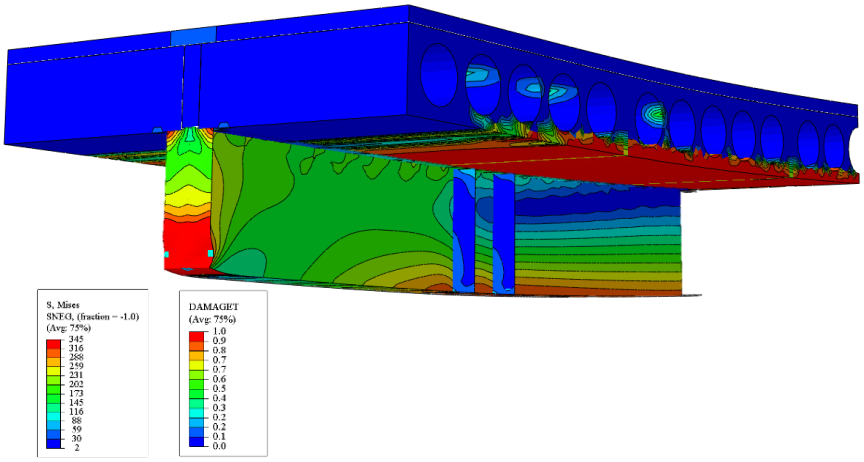

(a) 175mm of spacing, f_c=40 MPa and φ=10mm

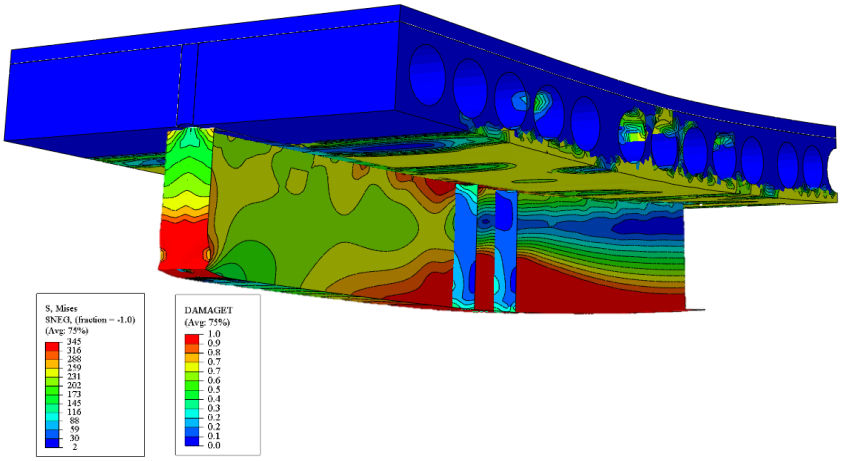

(b) 225mm of spacing, f_c=40 MPa and φ=16mm

Fig. 17: Final configuration for W460x74 section

The variation in both the transverse reinforcement rate and the in situ concrete strength (**Fig. 18** and **19**) showed significant differences in the shear-slip and moment-deflection relationships. These differences were observed for the concrete with the highest strength and transversal reinforcement diameters equal to 12.5mm and 16mm. **Fig. 18** shows that the greater the concrete strength, the greater the initial stiffness of the composite beam, although the values for the ultimate moment are analogous, since the ultimate strength is governed by the slab. However, as the spacing between the connectors is increased, that is, the interaction degree is reduced, as illustrated in **Fig. 19**, the model f_c=30MPa showed a different behavior in the shear-slip and moment-deflection relationships. This change in behavior was previously presented in Araújo et al. [20] and Ferreira et al [25]. The authors reported that when the compressive strength of the in situ concrete was close to 40MPa, the failure mode can occur in the shear stud, and resistance values below 30MPa, the failure can be governed by the in situ concrete.

Another important observation was that for models with 225mm of spacing, considering the W460x51 section, the composite beams showed ductile behavior, that is, the slip at the steel-concrete interface was greater than 6mm. Thus, it is possible to conclude that in all models analyzed for the W460x51 section and 225mm of spacing, the behavior at the steel-concrete interface was characterized as ductile, according to prescriptions of EC4. For f_c=25MPa models, the von Mises stresses in the shear studs, considering 175mm and 225mm of spacings, were greater than the 120mm of spacing models. A similar behavior occurred for f_c=30MPa models. For f_c=40MPa, there were models in which the von Mises stresses in the shear studs, considering 175mm and 225mm of spacings, were much higher than the 120mm of spacing models. This was observed for all transverse reinforcement diameters analyzed.

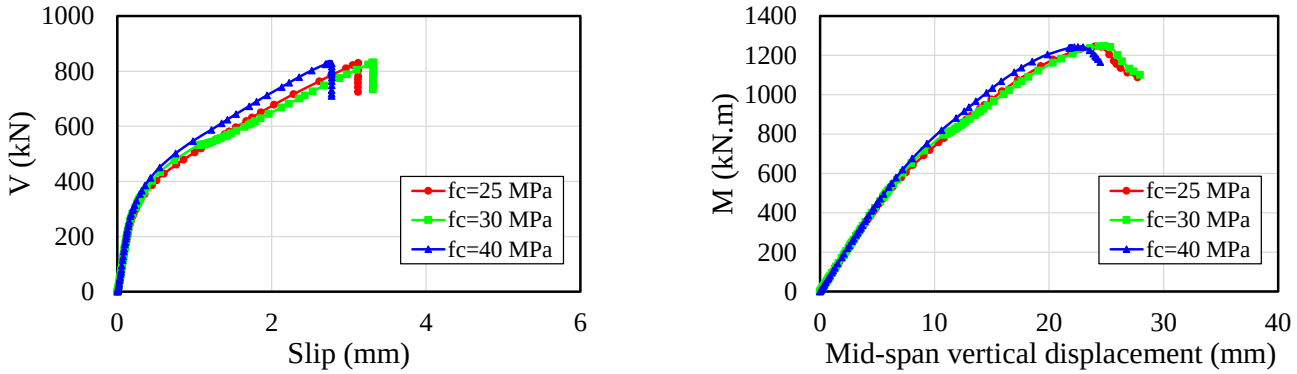

(a) Shear-slip relationship for (b) Moment-deflection relationship

Fig. 18: Influence of in situ concrete strength for W460x74 section, φ=12.5mm and 175mm of spacing

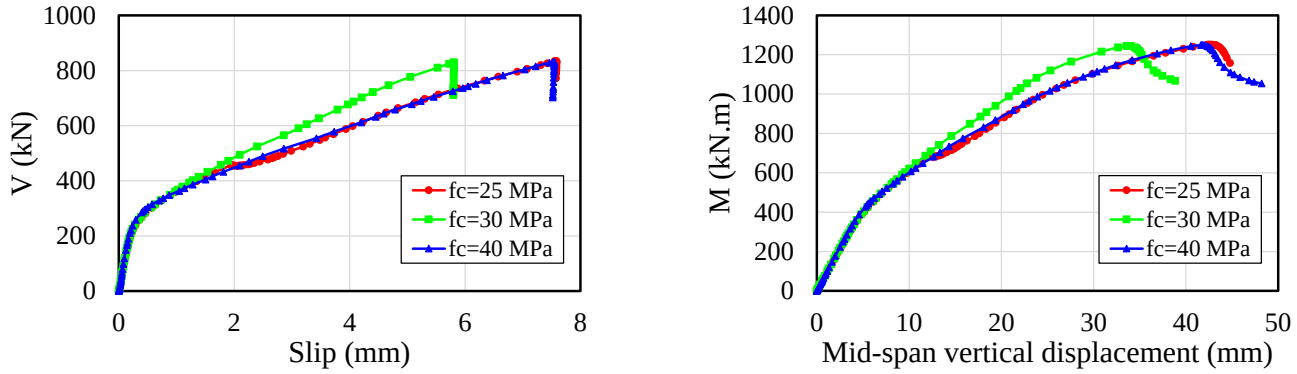

(a) Shear-slip relationship (b) Moment-deflection relationship

Fig. 19: Influence of in situ concrete strength for W460x74 section, φ=16mm and 225mm of spacing

5.3 SECTION W530x72

Considering 120mm of spacing, for the mid-span vertical displacement at 15mm, the region where the composite beam was supported and the lower flange reached the yield resistance. The maximum von Mises stresses in the lower flange, web and upper flange were 345MPa, 316MPa and 230MPa, respectively. When the composite beam reached the ultimate strength (**Fig. 20**), for the mid-span vertical displacement at 22mm, the lower flange and approximately 1/4 of the web depth were in plastic regime.

The ultimate strength was governed by excessive cracking of the slab. It is important to note that in these models there were a better use of the steel section, in comparison with the previous cross sections. This is due to the fact that the steel section has a depth and area greater than the other steel sections studied. So, the N.P.A. tends to move in the direction of the steel section, a factor that favors the resistance of the hollow core slab, thus reducing tension stresses. With the variation of the transverse

reinforcement rate and in situ concrete strength, there were no differences in the shear-slip and moment-deflection relationships (similar to previously situations). Regarding the von Mises stresses in the shear studs, there were no significant differences, reaching values between 556-570MPa.

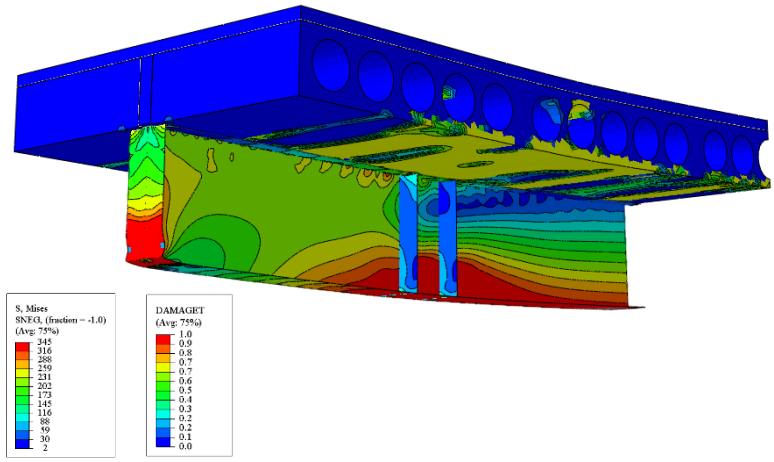

Fig. 20: Final configuration for W530x72, considering f_c=40 MPa, φ=16mm, and 120mm of spacing

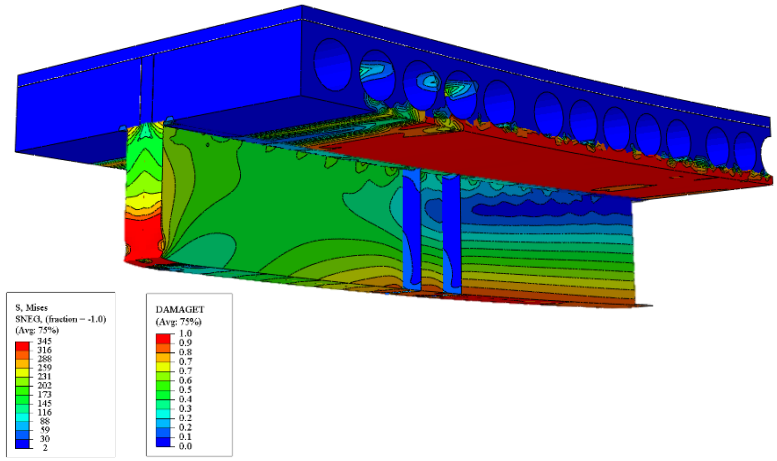

(a) 175mm of spacing, f_c=40 MPa and φ=16mm

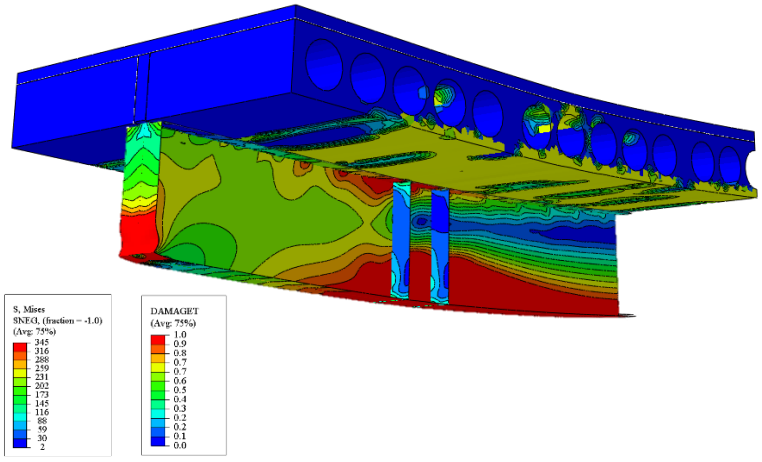

(b) 225mm of spacing, f_c=40 MPa and φ=16mm

Fig. 21: Final configuration for W530x72 section

On the other hand, considering 175mm of spacing between shear studs, for the mid-span vertical displacement at 15mm, only the support region reached the yield strength. The von Mises stresses in the lower flange, web and upper flange were 316MPa,

288MPa and 116MPa, respectively. In the ultimate strength (**Fig. 21a**), the mid-span vertical displacement was 21mm. In this loading stage, the lower flange was in plastic regime.

For 225mm of spacing, with the mid-span vertical displacement at 15mm, the results were similar to the previous one. However, the maximum von Mises stresses in the lower flange, web and upper flange were 288 MPa, 288MPa and 116MPa, respectively. In the ultimate strength (**Fig. 21b**), with the mid-span vertical displacement at 38mm, the lower flange, half the web depth and the upper flange were in plastic regime. With the variation of the transverse reinforcement rate and the in situ concrete strength, it was possible to verify some differences in the shear-slip and moment-deflection relationships (**Figs. 22-23**).

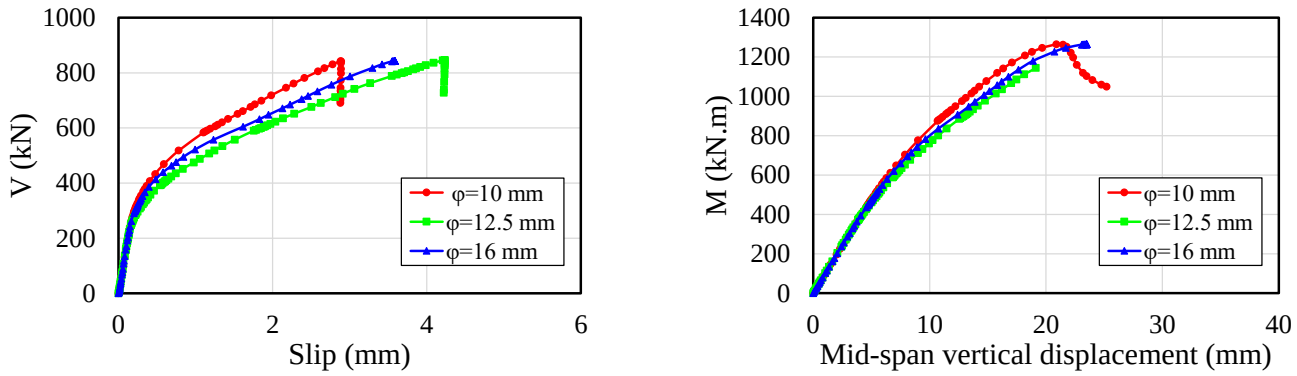

(a) Shear-slip relationship (b) Moment-deflection relationship

Fig. 22: Influence of transverse reinforcement for W530x72 section, f_c=25 MPa and 175mm of spacing

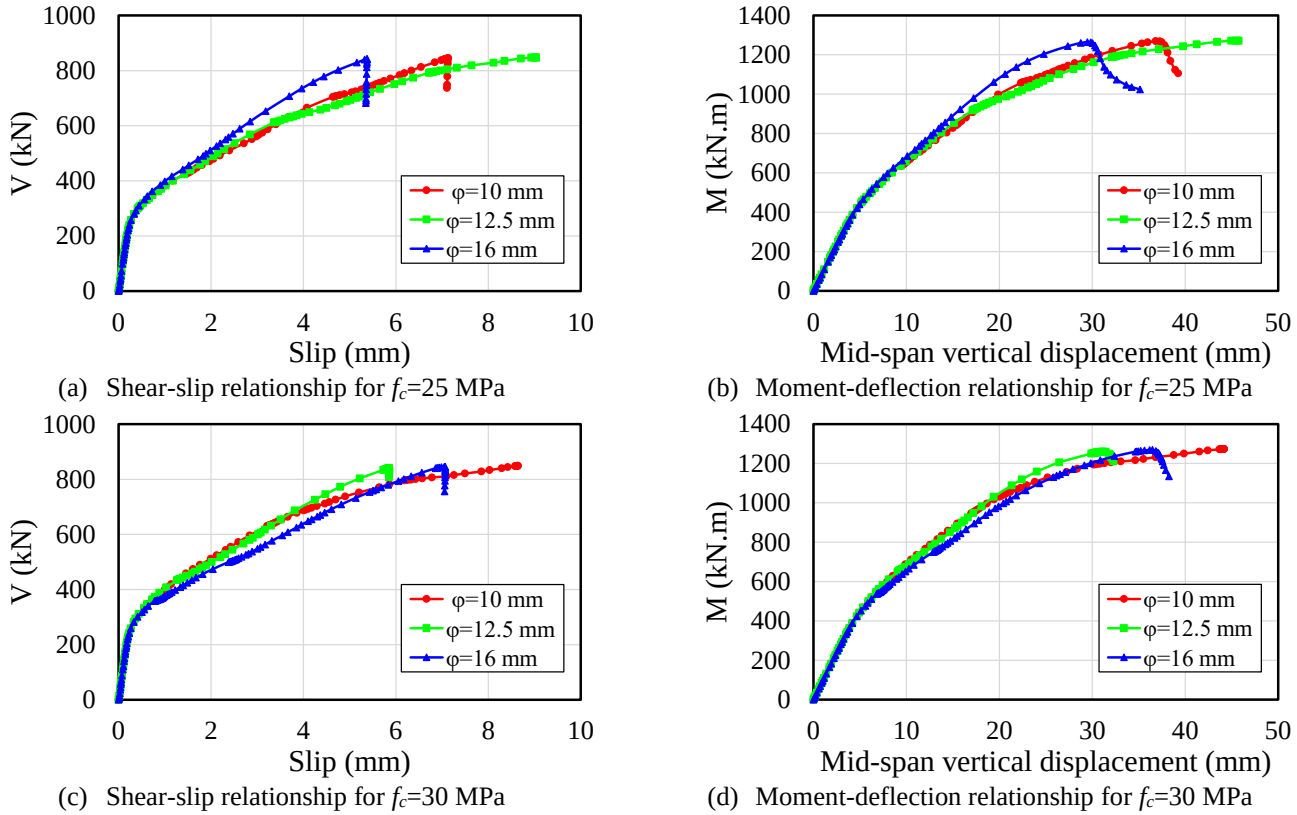

(a) Shear-slip relationship for f_c=25 MPa (b) Moment-deflection relationship for f_c=25 MPa

(c) Shear-slip relationship for f_c=30 MPa (d) Moment-deflection relationship for f_c=30 MPa

Fig. 23: Influence of transverse reinforcement for W530x72 section and 225mm of spacing

313 It was observed that for the models with 175mm of spacing, there were some differences in the relationships presented in
314 **Fig. 22**, considering the transverse reinforcement diameter equal 12.5mm and f_c=25-30MPa. On the other hand, for the models with
315 225mm of spacing, these differences were observed, according **Fig. 23**, for the transverse reinforcement diameter equal 16mm and
316 similar strength values for concrete. It is important to note that the behavior of the illustrations (**Fig. 22** and **Fig. 23**) is similar to
317 that discussed in the **Fig. 12** and **Fig. 13**.

318 5.4 DESIGN

319 In this section, the results are presented in a summarized way, considering the ductile behavior (**Fig. 24**), the maximum
320 mid-span vertical displacement for the service limit state for composite floors (**Fig. 25**) and SCI P401 [19] procedure (**Fig. 26**),
321 considering for that strength models of shear studs presented in [19,20]. Considering full interaction and N.P.A lies in concrete slab
322 (**Eqs. 4-10**), in which A_a is the steel section cross-sectional area, C_c is the concrete flange axial strength, f_y is the steel section yield
323 strength, L is the composite beam length, M_{pl} is the plastic moment of the composite section, Q_R is the shear connector strength, t_c
324 is overall depth of the concrete flange (including the concrete topping), T_a is the axial strength of the steel section in tension and L_φ
325 is the transverse reinforcement length.

$$\sum Q_R \geq A_a f_y \tag{4}$$

$$0.85 f_c b t_c \geq A_a f_y \tag{5}$$

$$C_c = 0.85 f_c b a \tag{6}$$

$$b \leq \begin{cases} L/4 \\ 2L_\phi + g \end{cases} \tag{7}$$

$$T_a = A_a f_y \tag{8}$$

$$a = \frac{T_a}{0.85 f_c b} \leq t_c \tag{9}$$

$$M_{pl} = T_a \left(\frac{d}{2} + t_c - \frac{a}{2} \right) \tag{10}$$

326 For partial interaction, the linear method is used, according to EC4 (**Eq. 11**), in which $M_{pl,a}$ is the plastic moment of the
327 steel section, $M_{pl,FULL}$ is the plastic moment of the composite section with full shear connection, and η is the ratio of the sum of the
328 strength of the shear studs provided to the sum of the strength of the shear studs needed for full shear connection.

$$M_{pl} = M_{pl,a} + \left(M_{pl,FULL} - M_{pl,a} \right) \eta \tag{11}$$

329

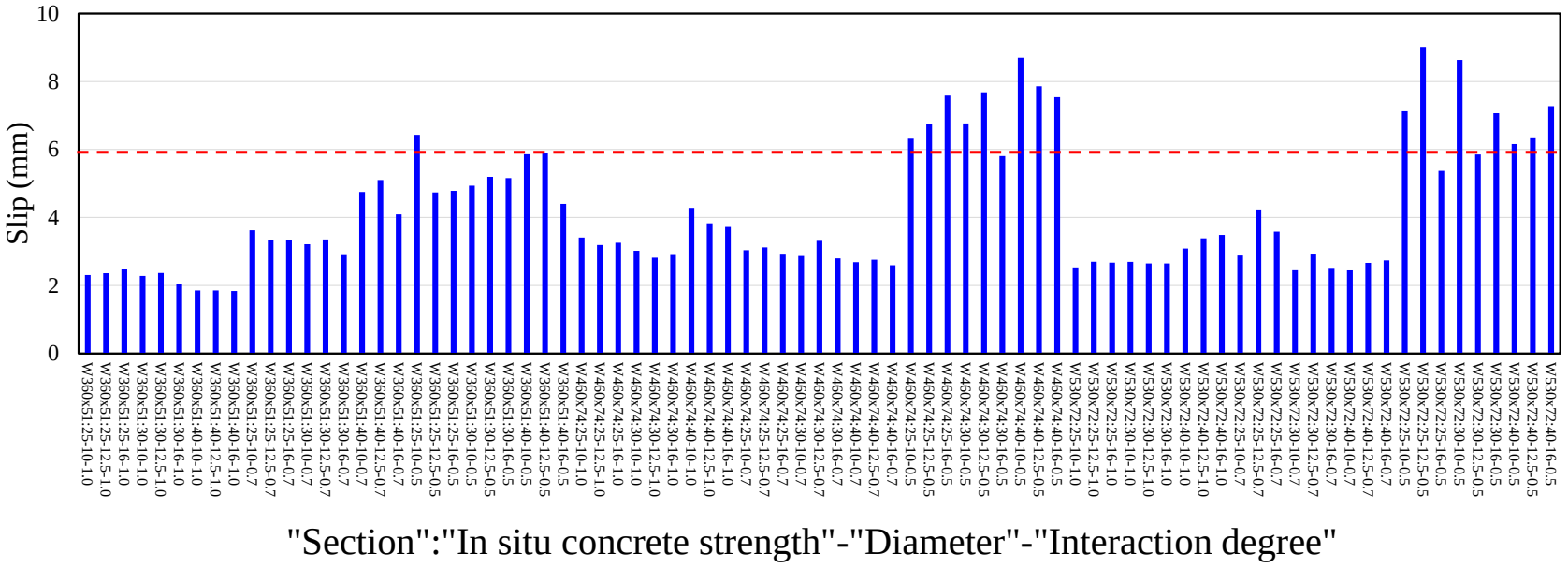

330
331

Fig. 24: Maximum steel-concrete interface slips on ultimate behavior

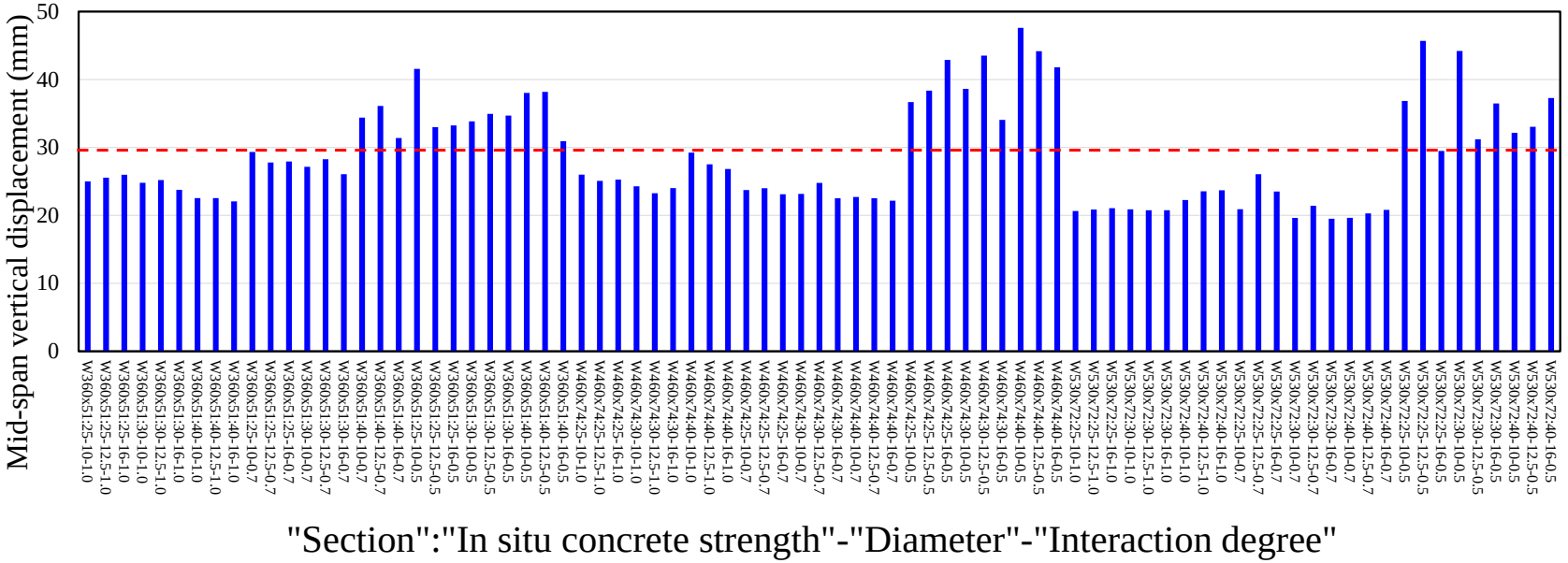

332
333

Fig. 25: Maximum mid-span vertical displacement on ultimate behavior

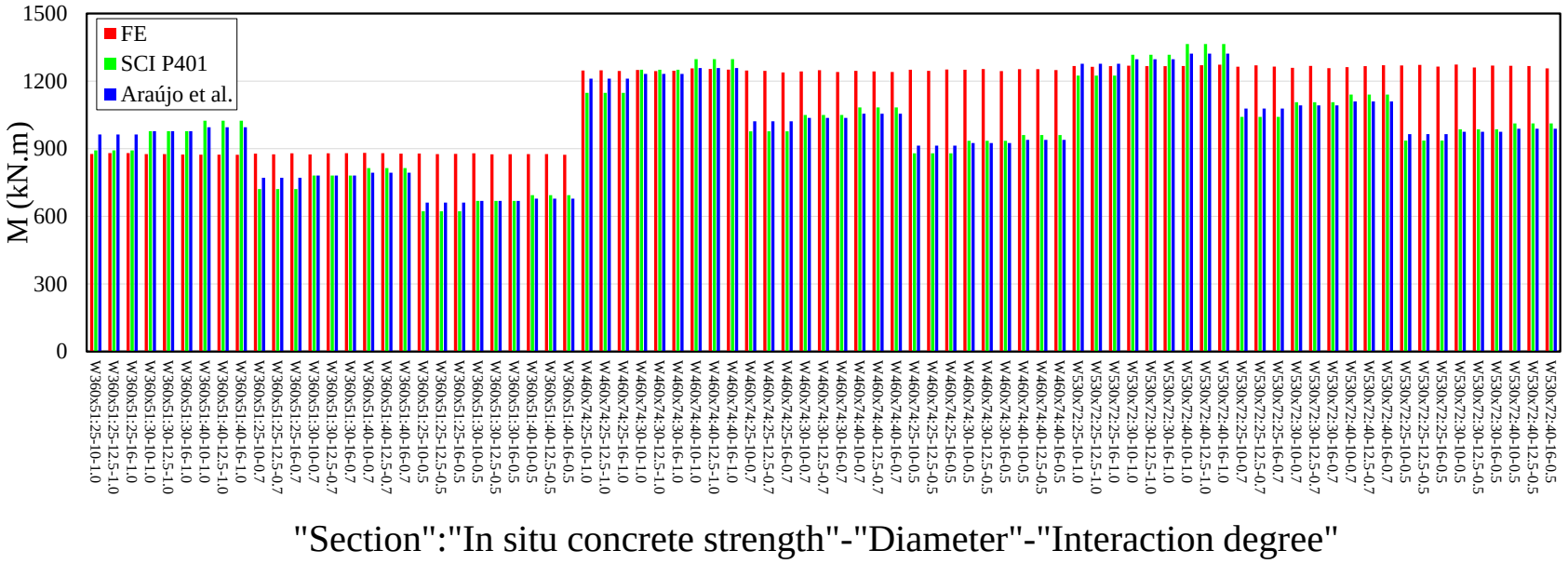

Fig. 26: Comparison of finite element models vs. analytical procedures

For a presentation of the results, a hypothesis of the minimum space is made, i.e., 120mm, providing full interaction. On the other hand, for the other spaces, partial interaction is considered. Therefore, for the spacings of 120mm, 175mm, 225mm and the degree of interaction are: 1.0, 0.7 and 0.5, respectively. As shown in **Fig. 24**, only one situation for section W360x51 presented a ductile behavior (fc=25 MPa, φ=10mm and spacing of 225mm). On the other hand, for all situations of W460x74 and W530x72 sections, considering 225mm of spacing, it was observed ductile behavior. This means that the greater the area of the steel cross section and the greater the spacing between the shear connectors, the greater the sliding in the steel-concrete interface. Respecting the mid-span vertical displacement limit for floors (L/200), according to EC4, 52 observations were found below the limit value, specifically for all situations of full interaction (**Fig. 25**). Therefore, another observation is what is the smallest degree of interaction, the greater the mid-span vertical displacement. Finally, considering the calculation procedures, mentioned in this section, a total of 60 observations it was found in conservative zone ($M_{FE} \leq M_{Rk}$). The observations that were shown to be against safety ($M_{FE} > M_{Rk}$) were verified for situations in which full interaction was considered (**Fig. 26**).

5.5 COMPARATIVE ANALYSES

In this section, a comparison of the resistance of the models developed in the present work is performed with that presented by Ferreira et al. [25] (**Fig. 27**). As noted, in some models the higher PCHCS provided greater strength. This difference reached a maximum of 30%, considering the ratio of the 150mm PCHCS depth models to the 265mm PCHCS depth models. These values were measured considering the section W360x51. With the increase in the steel cross section (sections W460x74 and W530x72), this difference is not so significant. This demonstrated that for the models studied, it is not advantageous to increase the depth of the PCHCS, since the collapse is determined by the slab. In addition, the greater the depth of the hollow core slab, the greater the weight of the structural system due to the higher consumption of concrete, and thus the costs. Therefore, from a sustainable point of view and structural efficiency, the 150mm depth PCHCS is the best option for the models studied.

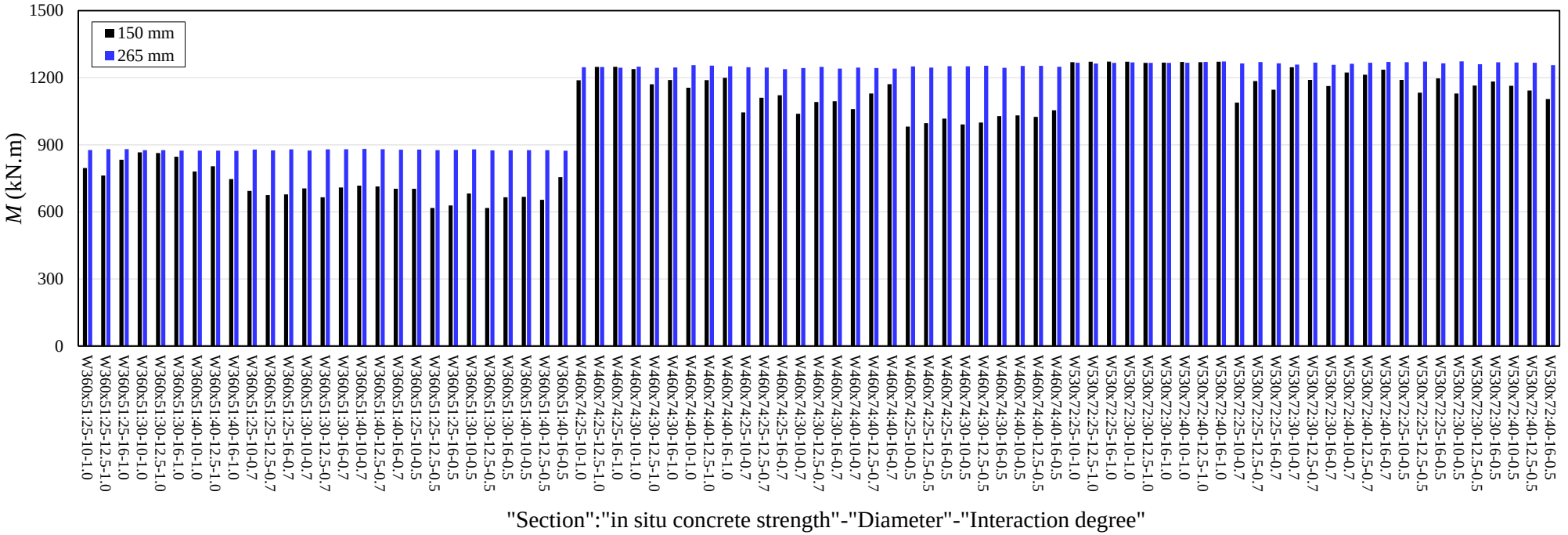

Fig. 27: Comparative analyses between 150mm and 265mm PCHCS with concrete topping (+50mm)

CONCLUSIONS

Steel-concrete composite beams with precast hollow core slabs is a sustainable solution and the better understanding of its parameters will yield to more efficient designs. The present study developed a reliable finite element model to investigate some limitations imposed in the design recommendations of steel-concrete composite beams with precast hollow core slabs, such hollow core slab depth, transverse reinforcement rate, and shear studs spacing. A parametric study was carried out, considering a 265mm hollow core unit with concrete topping, since the SCI P401 recommendation is only applicable for 150-250mm deep hollow core units. The parameters investigated were the in situ concrete strength, the transverse reinforcement rate, the interaction degree, and the steel cross section. 81 models were analyzed. The numerical results were compared with steel-concrete composite beams models, considering a 150mm hollow core unit with concrete topping. In general, for the models that were considered the partial interaction hypothesis, there was a better efficiency of the structural system, providing greater deformations. Therefore, designing steel-concrete composite beams hollow core slabs considering partial interaction is a viable option, since it reduces the cost of the project, due to the smaller number of shear studs to be used, as well as the labor. Specifically, considering the parameters analyzed, it was concluded:

1. In all models, the ultimate strength was reached by excessive cracking of the precast hollow core slab. This occurs because the neutral plastic axis lies within the hollow core slab, a factor that generates tensile stresses. Thus, dimensioning steel-concrete composite beams with deeper hollow core slabs is not advantageous. This is because the resistance is governed by the concrete slab, a factor that does not take advantage of the steel section. Therefore, in these analyzed models, there was a waste of material.
2. The greater the area of the steel cross section, the greater the use of the steel section. When there is a larger steel cross section, there is an increase in the plastic axial strength of the steel profile. This increase causes the neutral plastic axis to descend towards the steel profile, causing only compression stresses in the hollow core slab.
3. The greater the spacing of the shear studs, the greater the use of the steel section. When considering the hypothesis of partial interaction, as presented for the 175mm and 225mm of spacing models, the structural system can achieve ductile behavior, a factor that favors the ability of the structural elements to deform without reaching the ultimate strength. The use of a smaller number of shear connectors (175mm and 225mm models) provided resistance equivalent to the 120mm models. Therefore, using a lower amount of material for the design of a structural system, as is the case with modeled steel-concrete composite beams, from the point of view of sustainability there is a reduction in the embodied energy, since a smaller number of installed connectors will require a smaller amount of electricity consumption.
4. The transverse reinforcement rate had little influence on the ultimate strength of the models analyzed. This is because in most models the fragile behavior was verified.
5. With the variation of the in situ concrete strength, there were no significant differences in the ultimate strength. Therefore, the use of less in situ concrete strength can be advantageous, that is, the lower the concrete resistance, the greater the possibility of the plastic neutral axis lies within steel section. However, it is worth mentioning that the strength of concrete is also related to

durability, factor that certainly influences the life cycle of the structural element. The greater the durability of the structural system, the less the need for excessive maintenance, thus contributing to the reduction of waste and embodied energy.

6. Ductile behavior was observed for models with 225mm of spacing, considering W460x74 and W530x72 sections. Also was verified that the lower the interaction degree, the greater the mid-span vertical displacement, which may exceed the limit of $L/200$.

7. Regarding the verification of strength with the calculation procedure, some models considering full interaction proved to be against safety ($M_{FE} \leq M_{Rk}$). On the other hand, all observations considering partial interaction proved to be safe ($M_{FE} > M_{Rk}$).

8. The numerical models with a 265mm hollow core unit models presented greater resistance than the 150mm hollow core unit models, considering the W360x51 section. However, for W460x74 and W530x72 sections, there were no significant differences. The basic difference between the models compared is 115mm of precast concrete. Therefore, for the numerical models evaluated, using a smaller amount of precast concrete volume provided a better efficiency of the structural system. The use of a lower volume of concrete in structural projects provides a reduction in the structure's own weight, and in terms of sustainability, a lower amount of CO2 emissions.

ACKNOWLEDGMENTS

The authors would like to thank Construção Metálica – Gerdau Aços Brasil for making available the data related to COPPETEC, PEC-18541. This work was supported by the São Paulo Research Foundation (FAPESP) [grant number #2018/22803-1]

REFERENCES

[1] Cabeza LF, Boquera L, Chàfer M, Vérez D. Embodied energy and embodied carbon of structural building materials: Worldwide progress and barriers through literature map analysis. Energy Build 2021;231:110612. https://doi.org/10.1016/j.enbuild.2020.110612.

[2] Whitworth AH, Tsavdaridis KD. Genetic Algorithm for Embodied Energy Optimisation of Steel-Concrete Composite Beams. Sustainability 2020;12:3102. https://doi.org/10.3390/su12083102.

[3] Whitworth AH, Tsavdaridis KD. Embodied Energy Optimization of Steel-Concrete Composite Beams using a Genetic Algorithm. Procedia Manuf 2020;44:417–24. https://doi.org/10.1016/j.promfg.2020.02.275.

[4] European committee for standardization. EN 1994-1-1: Eurocode 4 – Design of composite steel and concrete structures – Part 1-1: General rules for buildings. 2004.

[5] Ibrahim IS, Elliott KS, Abdullah R, Kueh ABH, Sarbini NN. Experimental study on the shear behaviour of precast concrete hollow core slabs with concrete topping. Eng Struct 2016;125:80–90. https://doi.org/10.1016/j.engstruct.2016.06.005.

[6] Baran E. Effects of cast-in-place concrete topping on flexural response of precast concrete hollow-core slabs. Eng Struct 2015;98:109–17. https://doi.org/10.1016/j.engstruct.2015.04.017.

[7] Girhammar UA, Pajari M. Tests and analysis on shear strength of composite slabs of hollow core units and concrete topping. Constr Build Mater 2008;22:1708–22. https://doi.org/10.1016/j.conbuildmat.2007.05.013.

[8] Araújo D de L, Sales MWR, Silva RPM, Antunes C de FM, Ferreira M de A. Shear strength of prestressed 160 mm deep hollow core slabs. Eng Struct 2020;218:110723. https://doi.org/10.1016/j.engstruct.2020.110723.

[9] Albero V, Saura H, Hospitaler A, Montalvà JM, Romero ML. Optimal design of prestressed concrete hollow core slabs taking into account its fire resistance. Adv Eng Softw 2018;122:81–92. https://doi.org/10.1016/j.advengsoft.2018.05.001.

[10] De Nardin S, Debs A El. State of the art of steel–concrete composite structures in Brazil. Proc Inst Civ Eng - Civ Eng 2013;166:20–7. https://doi.org/10.1680/cien.2013.166.6.20.

[11] Lam D. Capacities of headed stud shear connectors in composite steel beams with precast hollowcore slabs. J Constr Steel Res 2007;63:1160–74. https://doi.org/10.1016/j.jcsr.2006.11.012.

[12] Tawadrous R, Morcous G. Shear Strength of Deep Hollow-Core Slabs. ACI Struct J 2018;115. https://doi.org/10.14359/51701298.

[13] Ahmed K. El-Sayed and Abdulrahman M. Alhozaimy AIA-N. Web Shear Resistance of Prestressed Precast Deep Hollow Core Slabs. ACI Struct J n.d.;116. https://doi.org/10.14359/51706919.

[14] Souza PT de, Kataoka MN, El Debs ALHC. Experimental and numerical analysis of the push-out test on shear studs in hollow core slabs. Eng Struct 2017;147:398–409. https://doi.org/10.1016/j.engstruct.2017.05.068.

[15] Ahmed IM, Tsavdaridis KD. Life cycle assessment (LCA) and cost (LCC) studies of lightweight composite flooring systems. J Build Eng 2018;20:624–33. https://doi.org/10.1016/j.jobe.2018.09.013.

[16] Dong YH, Jaillon L, Chu P, Poon CS. Comparing carbon emissions of precast and cast-in-situ construction methods – A case study of high-rise private building. Constr Build Mater 2015;99:39–53. https://doi.org/10.1016/j.conbuildmat.2015.08.145.

[17] Lam D. Composite steel beams using precast concrete hollow core floor slabs. 1998. Ph.D. thesis. University of Nottingham, 1998.

[18] Batista EM, Landesmann A. Análise experimental de vigas mistas de aço e concreto compostas por lajes alveolares e perfis laminados. COPPETEC, PEC-18541 2016.

[19] Gouchman GH. Design of composite beams using precast concrete slabs in accordance with EUROCODE 4. SCI P401. The Steel Construction Institute; 2014.

[20] Araújo DL, Sales MWR, Paulo SM, El Debs ALHC. Headed steel stud connectors for composite steel beams with precast hollow-core slabs with structural topping. Eng Struct 2016;107:135–50. https://doi.org/10.1016/j.engstruct.2015.10.050.

[21] Lam D, Elliott KS, Nethercot DA. Experiments on composite steel beams with precast concrete hollow core floor slabs. Proc Inst Civ Eng - Struct Build 2000;140:127–38. https://doi.org/10.1680/stbu.2000.140.2.127.

[22] Lam D, Elliott KS, Nethercot DA. Parametric study on composite steel beams with precast concrete hollow core floor slabs. J Constr Steel Res 2000;54:283–304. https://doi.org/10.1016/S0143-974X(99)00049-8.

[23] Ellobody E, Lam D. Modelling of headed stud in steel-precast composite beams. Steel Compos Struct 2002;2:355–78. https://doi.org/10.12989/scs.2002.2.5.355.

[24] Hicks SJ, Lawson RM. Design of composite beams using precast concrete slabs. SCI P287. The Steel Construction Institute; 2003.

[25] Ferreira FPV, Martins CH, De Nardin S. A parametric study of steel-concrete composite beams with hollow core slabs and concrete topping. Structures 2020;28:276–96. https://doi.org/10.1016/j.istruc.2020.08.045.

[26] Ferreira FPV, Martins CH, De Nardin S. Advances in composite beams with web openings and composite cellular beams. J Constr Steel Res 2020;172:106182. https://doi.org/10.1016/j.jcsr.2020.106182.

[27] Walraven JC, Mercx WPM. The bearing capacity of prestressed hollow core slabs. Heron 1983;28:1–46.

[28] Nguyen TNH, Tan KH, Kanda T. Investigations on web-shear behavior of deep precast, prestressed concrete hollow core slabs. Eng Struct 2019;183:579–93. https://doi.org/10.1016/j.engstruct.2018.12.052.

[29] Joo H-E, Han S-J, Park M-K, Kim KS. Shear Tests of Deep Hollow Core Slabs Strengthened by Core-Filling. Appl Sci 2020;10:1709. https://doi.org/10.3390/app10051709.

[30] Michelini E, Bernardi P, Cerioni R, Belletti B. Experimental and Numerical Assessment of Flexural and Shear Behavior of Precast Prestressed Deep Hollow-Core Slabs. Int J Concr Struct Mater 2020;14:31. https://doi.org/10.1186/s40069-020-00407-y.

[31] Brunesi E, Bolognini D, Nascimbene R. Evaluation of the shear capacity of precast-prestressed hollow core slabs: numerical and experimental comparisons. Mater Struct 2015;48:1503–21. https://doi.org/10.1617/s11527-014-0250-6.

[32] Palmer KD, Schultz AE. Experimental investigation of the web-shear strength of deep hollow-core units. PCI J 2011;Fall:83–104.

[33] Dassault Systèmes Simulia. Abaqus 6.18 2016.

[34] Ferreira FPV, Rossi A, Martins CH. Lateral-torsional buckling of cellular beams according to the possible updating of EC3. J Constr Steel Res 2019;153:222–42. https://doi.org/10.1016/j.jcsr.2018.10.011.

[35] Ferreira FPV, Martins CH. LRFD for Lateral-Torsional Buckling Resistance of Cellular Beams. Int J Civ Eng 2020;18:303–23. https://doi.org/10.1007/s40999-019-00474-7.

[36] Rossi A, Ferreira FPV, Martins CH, Mesacasa Júnior EC. Assessment of lateral distortional buckling resistance in welded I-beams. J Constr Steel Res 2020;166:105924. https://doi.org/10.1016/j.jcsr.2019.105924.

[37] Ferreira FPV, Martins CH, De Nardin S. Assessment of web post buckling resistance in steel-concrete composite cellular beams. Thin-Walled Struct 2021;158:106969. https://doi.org/10.1016/j.tws.2020.106969.

[38] Ferreira FPV, Martins CH, De Nardin S. Sensitivity Analysis of Composite Cellular Beams to Constitutive Material Models and Concrete Fracture. Int J Struct Stab Dyn 2021;21:2150008. https://doi.org/10.1142/S0219455421500085.

[39] Ferreira FPV, Tsavdaridis KD, Martins CH, De Nardin S. Buckling and post-buckling analyses of composite cellular beams. Compos Struct 2021;262. https://doi.org/10.1016/j.compstruct.2021.113616.

[40] Ferreira FPV, Tsavdaridis KD, Martins CH, De Nardin S. Ultimate strength prediction of steel–concrete composite cellular beams with PCHCS. Eng Struct 2021;236:112082. https://doi.org/10.1016/j.engstruct.2021.112082.

[41] Chen S, Jia Y. Numerical investigation of inelastic buckling of steel–concrete composite beams prestressed with external tendons. Thin-Walled Struct 2010;48:233–42. https://doi.org/10.1016/j.tws.2009.10.009.

[42] Zhou W-B, Yan W-J. Refined nonlinear finite element modelling towards ultimate bending moment calculation for concrete composite beams under negative moment. Thin-Walled Struct 2017;116:201–11. https://doi.org/10.1016/j.tws.2017.02.011.

[43] El-Lobody E, Lam D. Finite Element Analysis of Steel-Concrete Composite Girders. Adv Struct Eng 2003;6:267–81. https://doi.org/10.1260/136943303322771655.

[44] Hillerborg A, Modéer M, Petersson P-E. Analysis of crack formation and crack growth in concrete by means of fracture mechanics and finite elements. Cem Concr Res 1976;6:773–81. https://doi.org/10.1016/0008-8846(76)90007-7.

[45] Lubliner J, Oliver J, Oller S, Oñate E. A plastic-damage model for concrete. Int J Solids Struct 1989;25:299–326. https://doi.org/10.1016/0020-7683(89)90050-4.

[46] Lee J, Fenves GL. Plastic-Damage Model for Cyclic Loading of Concrete Structures. J Eng Mech 1998;124:892–900. https://doi.org/10.1061/(ASCE)0733-9399(1998)124:8(892).

[47] Genikomsou AS, Polak MA. Finite element analysis of punching shear of concrete slabs using damaged plasticity model in ABAQUS. Eng Struct 2015;98:38–48. https://doi.org/10.1016/j.engstruct.2015.04.016.

[48] Duvaut G, Lions JL. Inequalities in Mechanics and Physics. vol. 219. Berlin, Heidelberg: Springer Berlin Heidelberg; 1976. https://doi.org/10.1007/978-3-642-66165-5.

[49] Carreira DJ, Chu KH. Stress-Strain Relationship for Plain Concrete in Compression. ACI J Proc 1985;82:797–804. https://doi.org/10.14359/10390.

[50] Carreira DJ, Chu KH. Stress-Strain Relatonship for Reinforced Concrete in Tension. J Am Concr Inst 1986;83:21–8.

[51] Behnam H, Kuang JS, Samali B. Parametric finite element analysis of RC wide beam-column connections. Comput Struct 2018;205:28–44. https://doi.org/10.1016/j.compstruc.2018.04.004.

[52] Wijesiri Pathirana S, Uy B, Mirza O, Zhu X. Flexural behaviour of composite steel–concrete beams utilising blind bolt shear connectors. Eng Struct 2016;114:181–94. https://doi.org/10.1016/j.engstruct.2016.01.057.

[53] Liu X, Bradford MA, Chen Q-J, Ban H. Finite element modelling of steel–concrete composite beams with high-strength friction-grip bolt shear connectors. Finite Elem Anal Des 2016;108:54–65. https://doi.org/10.1016/j.finel.2015.09.004.

[54] Sjaarda M, Porter T, West JS, Walbridge S. Fatigue Behavior of Welded Shear Studs in Precast Composite Beams. J Bridg Eng 2017;22:04017089. https://doi.org/10.1061/(ASCE)BE.1943-5592.0001134.

[55] Guezouli S, Lachal A. Numerical analysis of frictional contact effects in push-out tests. Eng Struct 2012;40:39–50. https://doi.org/10.1016/j.engstruct.2012.02.025.

[56] Crisfield MA. A fast incremental/iterative solution procedure that handles “snap-through.” Comput Struct 1981;13:55–62.

https://doi.org/10.1016/0045-7949(81)90108-5.

[57] Crisfield MA. Snap-through and snap-back response in concrete structures and the dangers of under-integration. Int J Numer Methods Eng 1986;22:751–67. https://doi.org/10.1002/nme.1620220314.

[58] Maewal A, Nachbar W. Stable Postbuckling Equilibria of Axially Compressed, Elastic Circular Cylindrical Shells: A Finite-Element Analysis and Comparison With Experiments. J Appl Mech 1977;44:475–81. https://doi.org/10.1115/1.3424103.

Ultimate strength prediction of steel-concrete composite cellular beams with PCHCS

Felipe Piana Vendramell Ferreira*[a], Konstantinos Daniel Tsavdaridis[b], Carlos Humberto Martins[c], Silvana De Nardin[a]

[a]Department of Civil Engineering, Federal University of São Carlos, Rod. Washington Luiz, km 235, São Carlos, São Paulo, Brazil.

[b]School of Civil Engineering, Faculty of Engineering and Physical Sciences, University of Leeds, Woodhouse Lane, LS2 9JT Leeds, UK.

[c]Department of Civil Engineering, State University of Maringá, Av. Colombo nº 5790, Maringá, Paraná, Brazil.

*Corresponding author

E-mail address: fpiana@live.com (F. P. V. Ferreira), K.Tsavdaridis@leeds.ac.uk (K. D. Tsavdaridis), chmartins@uem.br (C. H. Martins), snardin@ufscar.br (S. De Nardin)

Abstract

This paper aims to predict the ultimate behavior of steel-concrete composite cellular beams with precast hollow core slabs. A finite element model is developed by geometrical non-linear analysis. A parametric study is carried out, considering symmetric and asymmetric sections with precast hollow core slabs. The key parameters such as the web-post width and the opening diameter are varied, as well as the presence of the concrete topping. A total of 120 analyses were performed. The results are compared with composite slab models. For symmetrical sections, considering the hollow core slabs, although some observations occurred with the formation of the plastic mechanism, the predominant failure mode was the web post buckling. For asymmetric sections, the predominant failure mode was the combination of the plastic mechanism with the web post buckling, which were accompanied by the shear connector rupture. In both cases, considering symmetrical and asymmetrical sections, excessive cracking was observed in the upper part of the hollow core slab. In cases where the end post was greater than the web post, there was damage at the upper region of the hollow core slab/concrete topping, close to the support. The numerical models of composite cellular beams with hollow core slabs, when compared with the models of composite cellular beams with composite slabs, showed greater efficiency in structural behavior. The differences observed between the shear strengths of the analyzed models, considering hollow core slab and composite slab, hollow core slab with concrete topping and composite slab, and hollow core slab with concrete topping and hollow core slab were 33kN, 121kN and 92kN, respectively, considering symmetric sections. For the asymmetric sections, such differences were 81kN, 103kN and 76kN, considering hollow core slab and composite slab, hollow core slab with concrete topping and composite slab, and hollow core slab with concrete topping and hollow core slab, respectively. These results imply that the strength of the composite cellular beams was not limited only by the strength of the steel cellular beam, but also, of the slab, due to the resistance to shear stress.

Keywords: Cellular beams; Precast hollow core slabs; Concrete topping; Geometrical nonlinear analyses.

NOTATION

The following symbols are used in this paper:

HCU	Hollow core unit
PCHCS	Precast hollow core slab
PCHCSCT	Precast hollow core slab with concrete topping
b	the width of the concrete slab
b_f	the width of the flange
b_w	the width of the web post
b_{we}	the width of the end post
C_i	the axial force in concrete of a composite section
C_1	the dimensionless constant in Eq. (26)
C_2	the dimensionless constant in Eq. (27)
C_3	the dimensionless constant in Eq. (28)
D_o	the opening diameter
d	the depth of parent section;
d_{eff}	the effective depth of composite cellular beam
d_g	the depth of cellular beam
f_c	the compressive cylinder strength of concrete
$f_{c,PCHCS}$	the compressive cylinder strength of precast hollow core slab
f_s	the yield strength of transversal reinforcement
f_t	the concrete tension resistance
f_u	the ultimate strength of cellular beam
f_y	the yield strength of cellular beam
K_c	the ratio of the second stress invariant on the tensile meridian to that on the compressive meridian, $0.5 \leq K_c \leq 1.0$
L_b	the unrestrained length of composite cellular beam
L_p	the distance between support and load
l_{eff}	effective length of web-post
p	the length between the opening diameter centers
M_i	moment at i opening
M_{vh}	moment generated by horizontal shear force
$M_{W,e}$	elastic bending moment of web post
$M_{W,Rk}$	flexural strength of Ward's model;
t_f	the thickness of the flange
t_w	the thickness of the web
V	the global shear force
V_h	the horizontal shear force
y_o	the distance from the geometric center of the tee to bottom edge
$y_{o,inf}$	the distance from the geometric center of the bottom tee to bottom edge
β_c	the dimensionless constant in Eqs. (3-4)
ε	strain
ε_c	the compressive strain
ε_t	the tensile strain
$\overline{\lambda}$	reduced slenderness factor
λ_w	web slenderness ratio
μ	the viscosity parameter that represents the relaxation time
ξ	the eccentricity (defines the rate at which the function approaches the asymptote, the default value is 0.1)
σ	stress
σ_{b0}	the initial equibiaxial compressive yield stress
σ_{c0}	the initial uniaxial compressive yield stress
φ	the diameter of transversal reinforcement
χ	reduction factor
Ψ	dilation angle

1. INTRODUCTION

Steel-concrete composite beams associated with the cast in-situ concrete slabs, i.e. solid or composite slabs, possess some disadvantages such as the high operational cost of welding the shear connectors and the curing time of wet concrete in cold climates. To reduce such limitations, the use of precast concrete hollow core slabs (PCHCS) can be an alternative [1]. These elements are produced in specific environments with monitoring and strict technological control. The use of PCHCS offers advantages such as the possibility of overcoming large spans, speed, and reduced construction costs [2–4]. One of the common uses of PCHCS is in flooring systems. Generally, a concrete topping is made to provide resistance to actions and a smooth and uniform finish [5,6].

With the development of automated cutting and welding from the 1990s, cellular beams started to be manufactured at low costs, thus expanding the product in the civil construction market. Cellular steel beams are produced by means of two thermal cut lines, in the shape of semi-circles, along the entire longitudinal web length. Subsequently to the thermal cutting step, the parts are separated and then welding (**Fig. 1**). These beams are ideal for structures with open space requirements such as parking garages, industries and warehouses, factories, office buildings, schools and hospitals. In addition, cellular beams are a good solution to overcome large spans and reduce the structure's own weight.

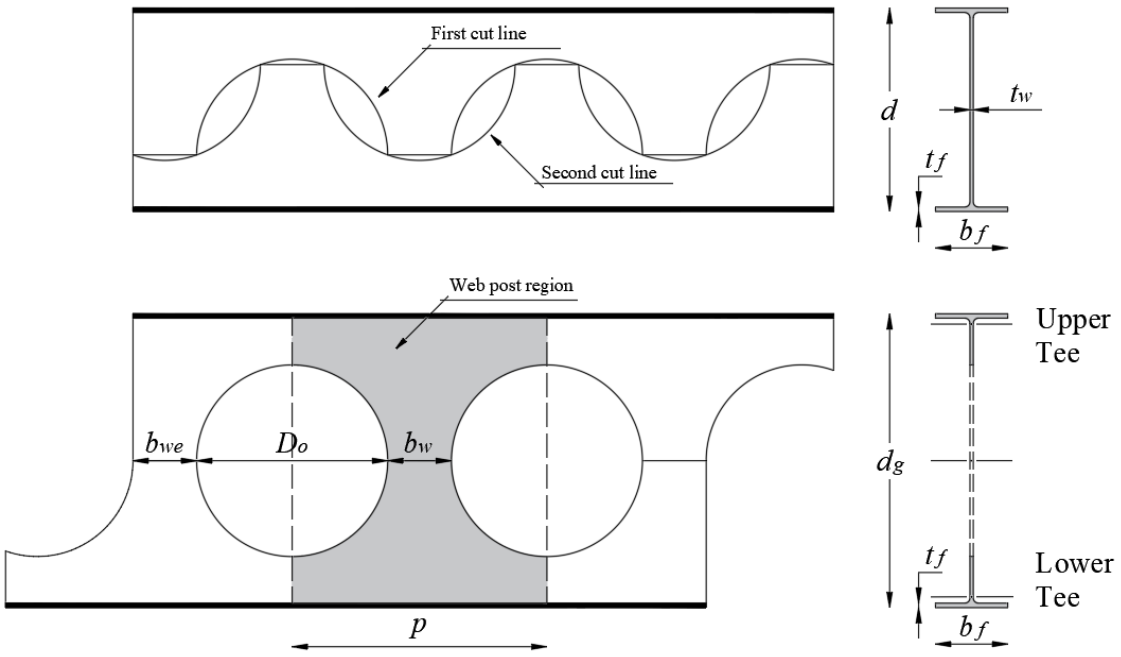

Fig. 1: Cellular beams manufacturing process [7]

Regarding their structural behavior, the strength of the composite cellular beams is associated with the failure mechanisms of the slab, i.e. cracking or crushing, combined with those of the cellular beams, such as the web post buckling (WPB) and the Vierendeel mechanism (VM). The WPB phenomenon becomes critical when the web post width is reduced [8–11]. As shown in **Fig. 2** [12], a horizontal shear force (V_h) acts along the welded joints, where y_0 is the distance from the geometric center of the tee section to the weld, and V is the global shear force. In the exemplified case, the AB edge is requested by tensile stresses, while the CD edge is requested by compressive stresses. As a result, the flexural behavior will arise in web post. This phenomenon is characterized by a double curvature (in the shape of "S"). On the other hand, the VM is dependent on the presence of high magnitude

shear force, and it is a phenomenon characterized by the distortion and formation of plastic hinges in regions close to the opening [13,14]. Physically, VM occurs when the ends of the tees reach the yield strength due to the combination of normal and tangential stresses. The main parameters that affect this structural behavior are the web thickness, the effective opening diameter and the number of shear connectors allocated above the opening (composite action) [12,15–19].

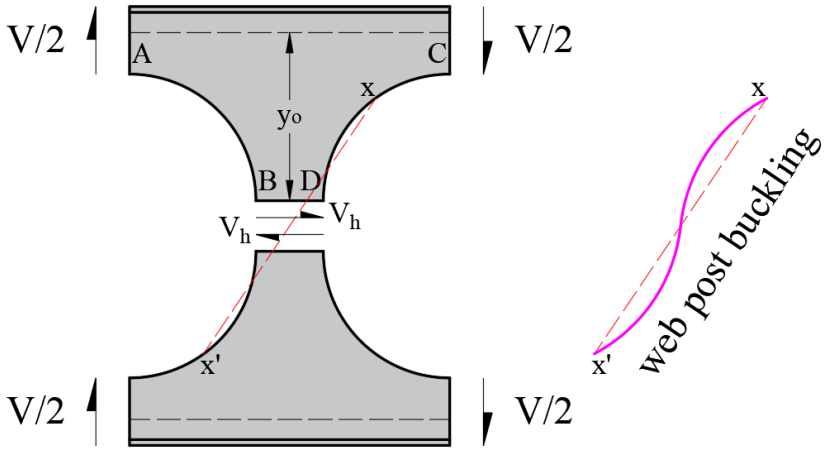

Fig. 2: Web post buckling (WPB), adapted from [12]

From the design point of view, desirable characteristics of the steel-concrete composite beams are still unquestionable. It is a structural system with widespread use worldwide and with very consolidated calculation procedures. Thus, if steel-concrete composite beams, PCHCS and steel profiles are structural elements with very interesting aspects for use in multi-storey buildings, the cellular section combination working together with the PCHCS is interesting and promising. However, it is not an association that has been investigated by the scientific community, and although the SCI-P355 [19] and Steel Design Guide 31[20] recommendations are directed at the behavior of composite beams with web openings, such recommendations are limited in the use of composite slabs [21]. The present study aims to predict the ultimate behavior of steel-concrete composite cellular beams with precast hollow core slabs. Three types of slabs are studied; PCHCS (LP15) with and without concrete topping, and a composite slab with the Holorib 51/150 steel sheets geometry. Due to limitations of the steel sheets, 150mm spacing between connectors is considered. A finite element model is developed by geometrical nonlinear analyses. The numerical model is calibrated, considering tests. A parametric study is carried out. The steel-concrete composite beams are simply supported, with a span of 6m. Symmetric (IPE 400) and asymmetric (IPE 400/HEB 340) sections are considered. For each section, the influence of the slab type is studied, and the key parameters such as the web-post width and the opening diameter are varied. The results are discussed, according to the parameters presented.

2. BACKGROUND

In this section, research studies are presented considering steel-concrete composite beams with PCHCS and composite cellular beams. In late 90's, Lam [22] studied the steel-concrete composite beams with PCHCS, considering pushout tests, as well as the flexural behavior. Subsequently, several studies were published. [3,23–26]. In Lam et al. [24] results of flexural tests were presented. The ductile behavior was observed, which can be controlled by the appropriate use of transverse reinforcement and in

situ concrete strength. Lam et al. [25] complemented the previous study, using the finite element method to develop a parametric analyses. In this study, it was reported that increasing the transverse reinforcement rate, significantly increases the flexural strength, but reduces the ductility leading to the fragile rupture of the concrete slab; the higher the slab depth, the greater the resistant moment, although the slab may fail due to excessive cracking. In 2003, Steel Construction Institute published SCI-P287 [27], which is a manual containing design criteria for composite beams with PCHCS. Subsequently, the SCI-P401 [28] was published, which is an update of the previous document. In this publication, recommendations are presented, considering the minimum dimensions, arrangement of headed stud connectors, transverse reinforcement rate, ultimate, and service limit states in the construction phase for the cases of full and partial interaction. Such publication is based on EC4 [29]. Batista and Landesmann [30] tested composite beams with PCHCS and concrete topping. The tests showed similar collapse modes, with the development of cracks initiated on the underside of the HCU and in the central region between the load application points. According to the authors, these cracks propagated along the width of the PCHCS, extending from the side face of the slab to the region of connection with the steel profile, a factor that reduced the stiffness of the composite beam. In Ferreira et al. [31] a parametric study of composite beams with PCHCS and concrete topping was presented. In this study, as observed in [5,6], the concrete topping increased the initial stiffness of the composite beams, as well as its ultimate strength.

On the other hand, considering composite cellular beams, the studies dated back to the early 2000s. In the literature there are studies considering composite beams with only a rectangular web opening with solid [32–39] or composite slabs [13,37-48], and composite plug systems with perforated beams [52–56]. In the latter case, one of the benefits is that WPB and VM cannot be achieved as the thin-walled perforated section with large closely spaced web opening is partially encased by concrete (one opening every other metal deck rib) which also acts as a shear connector with the concrete passing through. The present study focuses on cellular beams, which are those with periodical circular web openings, according to the manufacturing process shown in **Fig. 1**. In this scenario, several studies have investigated the behavior of composite cellular beams with asymmetric section [7,57–60]. Sheehan et al. [60] described that the asymmetric composite beams has been widely used in construction. The main advantage of using these elements is that the lower tee is formed by a more rigid section than the upper tee, to increase the resistance to bending and shearing. In Müller et al. [58] tests of two models were presented: composite symmetric and asymmetric cellular beams. Both specimens were designed in such a way that at one end it was possible to investigate the composite action, and at the other end, only the cellular section. The ultimate behavior of the tests was similar. According to the authors, the VM was observed for low loading values at the end corresponding to the composite action. Oppositely, at the end where there was only the cellular steel profile, the ultimate strength was reached by WPB. To explore a larger number of observations, the authors performed a parametric study to investigate the influence of the resistance of steel and concrete materials on the strength of the physical models. According to the authors, the resistance of the cellular profile is preponderant in the ultimate strength of composite cellular beams, since the it was reached by the WPB. Also, Nadjai et al. [59,61] examined composite symmetric and asymmetric cellular beams. Both models had the ultimate strength governed by WPB. Sheehan et al. [60] tested long spanning asymmetric composite cellular beams. The

interaction degree considered was lower than that recommended in EC4 [29]. The composite asymmetric cellular beams were subjected to uniformly distributed loads and concentrated loads, which were applied to 5/16 and 7/16 of the span length. The slip in the steel-concrete interface, the vertical displacements, the stress distribution, and the effect of the unscored construction were evaluated in the study. The authors observed that the composite cellular beams submitted to uniformly distributed loading resisted 3.4 times the estimated design load, despite the interaction degree considerably less than the minimum required by EC4 [29]. The composite cellular beam that was subjected to concentrated load had its strength 45% greater than that resisted by the cellular profile. This suggests the need for modifications in the prediction of resistance to the VM. In Ferreira et al. [7] the resistance of steel-concrete composite cellular beams was investigated by geometric nonlinear analyses. The key parameters such as the opening diameter and the web post width were varied. The authors concluded that the end post and the concrete slab contributed significantly to the shear strength of composite cellular beams. Thus, it is possible to state that, to date, there are no studies of composite cellular beams with PCHCS.

3. FINITE ELEMENT MODEL: VALIDATION STUDY

For the validation study, seven steel-concrete composite beams are modeled, considering symmetry (**Fig. 3**).Geometrical nonlinear analyses are processed using the ABAQUS® [62] software. The analyses are divided into two groups:

- Steel-concrete composite beams with hollow core slabs are processed in one step, considering the *Static Riks* analysis [31]. In this analyses, initial geometric imperfections are not considered, since the ultimate behavior of such systems is governed only by plastification of the steel profile, or crushing and cracking of the concrete slab. At the beginning of the analysis, it is necessary to implement the initial arc length, which refers to an initial percentage of the external load. Thus, in the next increments, the software, automatically during the analysis, adjusts the load increments so that the problem converges [62]. This type of analysis was also used in the literature [22,31,63,64].
- Steel-concrete composite cellular beams are processed in two steps: Buckling and Static Riks analysis [7,65–68]. Buckling analysis is used to estimate critical buckling loads in structures by obtaining eigenvalues and their eigenvectors. It is important to note that in this type of analysis, no imperfections, physical and geometric, are considered in the structure. In the second step, the Static Riks analysis is performed considering non-linear geometrical and material analysis. In the case of cellular beams, the initial geometric imperfection is imposed. The implementation of geometric imperfection is performed using the command *INITIAL CONDITIONS. It is important to note that residual stresses were not considered. This is due to the fact that these stresses do not influence the composite beams subjected to positive bending moment. Otherwise, when the composite beams are subjected to a negative bending moment, residual stresses are harmful, and the structure can reach the ultimate behavior by distortional buckling [69,70]. As described in [8], in cellular beams the initial imperfections are inevitable due to the manufacturing process, and therefore, it is a difficult task to be determined. In this way, the initial geometric imperfection factor was applied by a scale factor equal to dg/1000, according to sensitivity analyses performed by Ferreira et al. [7].

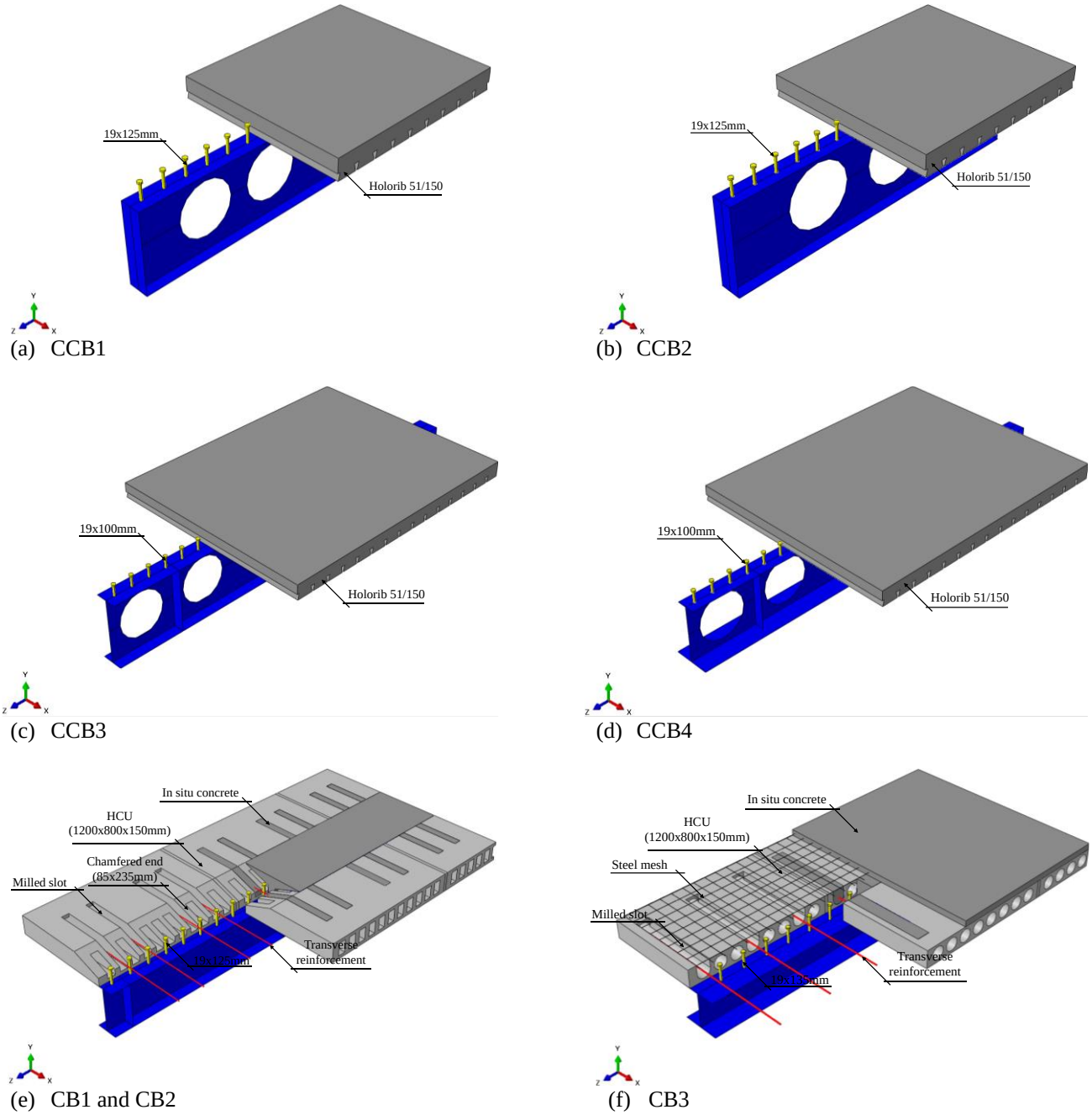

Fig. 3: Steel-concrete composite beams for the validation study, considering symmetry

3.1. TESTS

With regard to composite cellular beams, the tests results of models 1A (CCB1), 1B (CCB2), RWTH-1A (CCB3) and RWTH-1A (CCB4) were considered for the validation study [57–59,61]. It is worth mentioning that, although the steel sheets were not modeled, the Holorib HR 51/150 geometry was used to represent the concrete slab ribs. The headed stud connectors dimensions are 19x120mm (CCB1 and CCB2) and 19x100mm (CCB3 and CCB4), spaced at 150mm. For the composite beams with PCHCS, the numerical model validation was based on tests results of Lam [22], and Batista Landesmann [30]. In the models CB1 and CB2 [22], the HCU dimension were 1200x800x150mm, with a chamfer. The 19x125mm headed stud connectors were spaced in 150mm. On the other hand, in the CB3 model [30], the HCU dimension were 1200x800x150mm with a 50mm thick concrete topping, reinforced with Q138 steel mesh (4.2x100x100). The 19x135mm shear connectors were spaced in 200mm. In **Table 1**, the details of the models are presented.

Table 1: Models (in mm, MPa and GPa)

Model	Ref	d or d_g	D_o	p	Upper tee					Lower tee					E	Slab		Reinforcement		b	L_b	L_p
					b_f	t_f	t_w	f_y (flange/web)	f_u (flange/web)	b_f	t_f	t_w	f_y (flange/web)	f_u (flange/web)		f_c	$f_{c,PCHCS}$	φ	f_s			
CCB1	[59]	575	375	500	141.8	8.6	6.4	312	438.5	141.8	8.6	6.4	312	438.5	200	28.6	-	-	-	1200	4500	1750
CCB2	[59]	630	450	630	141.8	8.6	6.4	312	438.5	152.4	10.9	7.6	312	438.5	200	28.6	-	-	-	1200	4500	2250
CCB3	[58]	555	380	570	180	13.5	8.6	451/489	541/587	180	13.5	8.6	451/489	541/587	195	33.6	-	-	-	1800	6840*	1140/2850
CCB4	[58]	485	380	570	150	10.7	7.1	407/467	524/588	300	21.5	12	453/488	519/582	195	24.0	-	-	-	1800	6840*	1140/2850
CB1	[64]	355	-	-	171.5	11.5	7.4	310/355	$1.3f_y$	171.5	11.5	7.4	310/355	$1.3f_y$	205	25.6	40	16	585	1665	5700	1500
CB2	[64]	355	-	-	171.5	11.5	7.4	310/355	$1.3f_y$	171.5	11.5	7.4	310/355	$1.3f_y$	205	20.8	40	8	473	1665	5700	1500
CB3	[30]	299	-	-	306	11	11	345	450	306	11	11	345	450	200	30.0	45	12.5	500	1756	5830	1915

*Slab cut back by 285 mm at end of cellular beam

3.2. MATERIALS MODELS

In this section, the materials constitutive models used in numerical modeling are presented.

3.2.1 Concrete

The Concrete Damage Plasticity (CDP) [71–73] is adopted. The model takes into account hypotheses based on the theory of plasticity [74], and the stress-strain relationship is governed by a damaged elastic variable. The damage variables can take values from '0' (undamaged material) to '1' (total loss of strength). The **Eq. (1)** and **Eq. (2**) represents the damage variable, considering the concrete in compression and tension, respectively.

$$d_c = 1 - \left(\sigma / f_c\right) \tag{1}$$

$$d_t = 1 - \left(\sigma / f_t\right) \tag{2}$$

The CDP makes use of the resistance function of Lubliner et al. [72], with the modifications proposed by Lee and Fenves [73] to explain the different evolution of resistance under tension and compression. This function defines the direction of the deformations, when the material reaches the state of plastic behavior. The input parameters to characterize the plasticity are: dilation angle (ψ), eccentricity (ξ), the ratio of initial equibiaxial compressive yield stress to initial uniaxial compressive yield stress (σ_{b0}/σ_{c0}), the ratio of the second stress invariant on the tensile meridian to that on the compressive meridian (K_c), and the viscosity parameter that represents the relaxation (μ). **Table 2** presents the input parameters for defining the plastic behavior.

Table 2: CDP input parameters

Parameter	Value
Ψ (°)	40
ξ	0.1 (default)
σ_{b0}/σ_{c0}	1.16 (default)
K_c	2/3 (default)
μ (s^{-1})	0.001

The Carreira and Chu [75,76] models were adopted to represent the behavior of concrete in compression and tension, according to **Eqs. (3-5).**

$$\frac{\sigma}{f_c} = \frac{\beta_c\left(\varepsilon / \varepsilon_c\right)}{\beta_c - 1 + \left(\varepsilon / \varepsilon_c\right)^{\beta_c}} \tag{3}$$

$$\frac{\sigma}{f_t} = \frac{\beta_c\left(\varepsilon / \varepsilon_t\right)}{\beta_c - 1 + \left(\varepsilon / \varepsilon_t\right)^{\beta_c}} \tag{4}$$

$$\beta_c = \left(\frac{f_c}{32.4}\right)^3 + 1.55 \ \ (MPa) \tag{5}$$

3.2.2 Steel

For the transverse reinforcement and steel mesh, the elastic-perfectly plastic model was adopted (**Fig. 4a**). Regarding the headed stud connectors, the bilinear model was used [77] (**Fig. 4b**), i.e., the yield stress and the ultimate stress were 460 MPa and 559 MPa, respectively. The elongation at rupture was 18.8%. For the structural steel profiles, the quadrilinear model of Yun and

Gardner was used [78] (**Fig. 4c**). According to the authors, the quadrilinear diagrams are more accurate and they are in accordance with the experimental stress-strain curves across the tensile stress range. The model parameters are calculated, according to the **Eqs. (4-8)**. The implementation of the stress- strain relationship must be done with the real values, according to the **Eqs. (6-12).**

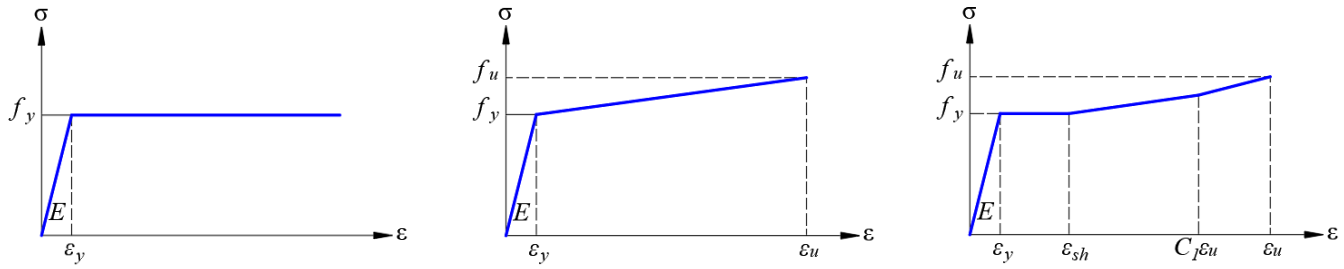

(a) Elastic-perfectly plastic (b) Bilinear (c) Quadrilinear [78]

Fig. 4: Stress-strain relationship for steel

$$f(\varepsilon)=\begin{cases} E\varepsilon, \varepsilon \le \varepsilon_y \\ f_y, \varepsilon_y < \varepsilon \le \varepsilon_{sh} \\ f_y + E_{sh}(\varepsilon - \varepsilon_{sh}), \varepsilon_{sh} < \varepsilon \le C_1\varepsilon_u \\ f_{C_1\varepsilon_u} + \left(\dfrac{f_u + f_{C_1\varepsilon_u}}{\varepsilon_u - C_1\varepsilon_u}\right), C_1\varepsilon_u < \varepsilon \le \varepsilon_u \end{cases} \quad (6)$$

$$\varepsilon_u = 0.6\left(1-\frac{f_y}{f_u}\right), \varepsilon_u \ge 0.06 \quad (7)$$

$$\varepsilon_{sh} = 0.1\frac{f_y}{f_u} - 0.055, 0.015 < \varepsilon_{sh} \le 0.03 \quad (8)$$

$$C_1 = \frac{\varepsilon_{sh} + 0.25(\varepsilon_u - \varepsilon_{sh})}{\varepsilon_u} \quad (9)$$

$$E_{sh} = \frac{f_u - f_y}{0.4(\varepsilon_u - \varepsilon_{sh})} \quad (10)$$

$$\sigma^{true} = \sigma^{nom}\left(1+\varepsilon^{nom}\right) \quad (11)$$

$$\varepsilon^{true} = \ln\left(1+\varepsilon^{nom}\right) \quad (12)$$

3.3. INTERACTION

Three types of interaction were considered [62]:

i. *Tie constraint (surface-to-surface):* this modeling technique allows to simulate the perfect bond between the contact surfaces. In this case, each node on the slave surface will have the same values for its degrees of freedom as the point on the master surface;

ii. *Embedded*: this type of interaction is used to specify that an element is embedded in another element;

iii. *Normal/tangential behavior (surface-to-surface)*: allows displacement in the normal and tangential direction to the contact surface plane.

The tie constraint was applied to the surface between on the bottom surfaces of the shear connectors and the upper flange, and between the precast and in-situ infill concrete [31]. The contact between the concrete and the transverse reinforcement, as well as the concrete and steel mesh, were made through the embedded region. The shear connectors were represented in the modeling and allocated in the concrete volume of the slab. In this methodology, the same volume of the shear connector is cut from the slab [79,80]. The purpose of this volume removal is such that the interaction between the contact surfaces of the slab and the shear connector occurs. The tangential behavior is based on the Coulomb friction model. According to the literature, the coefficient of friction between the steel and concrete surfaces varies between 0.2 to 0.83 [63,81–83]. Guezouli and Lachal [82] performed sensitivity analyses, via finite element method to investigate the mechanical behavior at the steel-concrete interface, considering pushout tests. In this study, the friction coefficients were varied by 0.1, 0.2, 0.3, 0.4 and 0.5, both for the interface between the connectors and the concrete slab, and for the interface between the concrete slab and the steel profile. The results of the parametric study were compared with tests. The authors recommended the use of the values of the friction coefficients equal to 0.2 and 0.3 for the interfaces between the connector-slab and slab-profile, respectively. Therefore, for the validation of the numerical model of the present work, the recommendation of Guezouli and Lachal [82], that is, for CCB1, CCB2, CCB3, CCB4, CB1, CB2 and CB3 models, the friction coefficients were taken equal to 0.2 and 0.3, for headed stud and slab interface, and slab and steel profile interface, respectively.

3.4. BOUNDARY CONDITIONS

The boundary conditions were applied considering the symmetry at the longitudinal axis [7,31]. Vertical displacement (Uy=0) in the support, and lateral displacement (Ux=0) at the ends of the slab were restrained. Longitudinal symmetry was applied at mid-span by restrictions to longitudinal displacement, rotation around the x and y axis (Uz=URx=URy=0). **Fig. 5** shows the boundary conditions that was applied in all models.

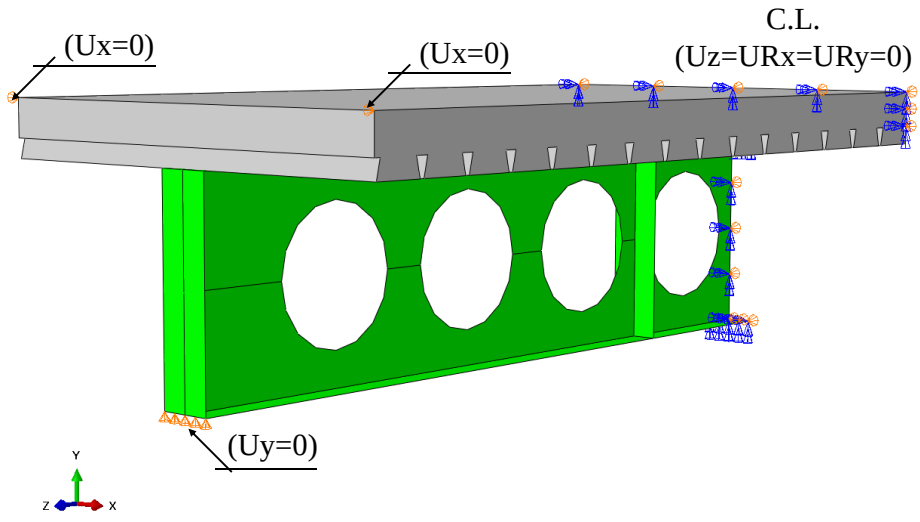

Fig. 5: Boundary conditions

3.5. DISCRETIZATION

Fig. 6 illustrates the discretization of the models. The dimension of the elements was taken according to previous studies [63,81,84] respecting the master and slave surfaces. The assignment of master and slave roles can have a significant effect on performance with surface-to-surface contact if the two surfaces have dissimilar mesh refinement; the solution can become quite expensive if the slave surface is much coarser than the master surface [62]. The steel profiles were discretized with shell-type finite elements. The S4R element is a quadrilateral element with four nodes and reduced integration. The headed stud connectors, the concrete slab, as well as the in-situ elements, were discretized by the solid element C3D8R, which has eight nodes, reduced integration, supports plastic analysis with large deformations, and allows the visualization of the crack in the CDP model. Both elements have six degrees of freedom per node - three rotations and three translations. The transverse reinforcement and the steel mesh were discretized by T3D2 truss elements, with two nodes and linear displacement.

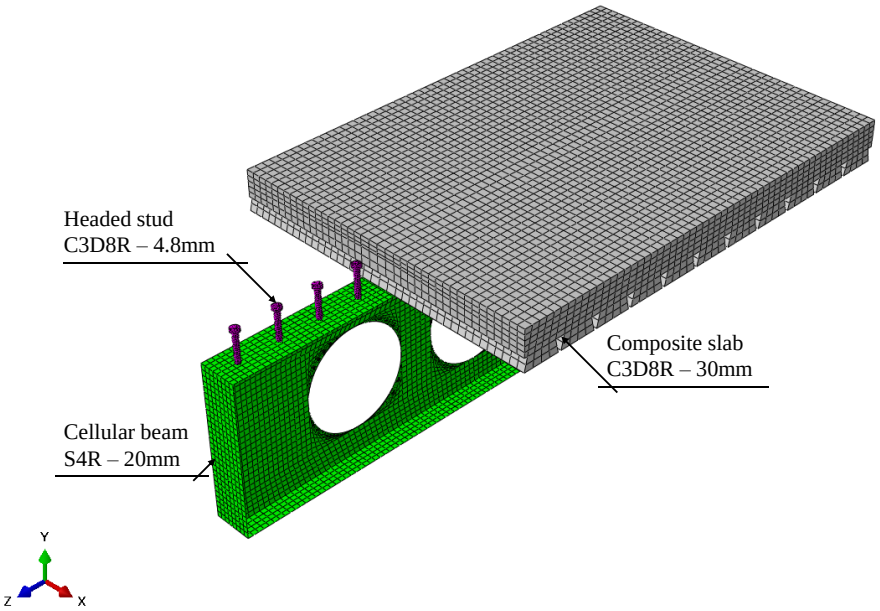

(a) CCB1, CCB2, CCB3 and CCB4 models

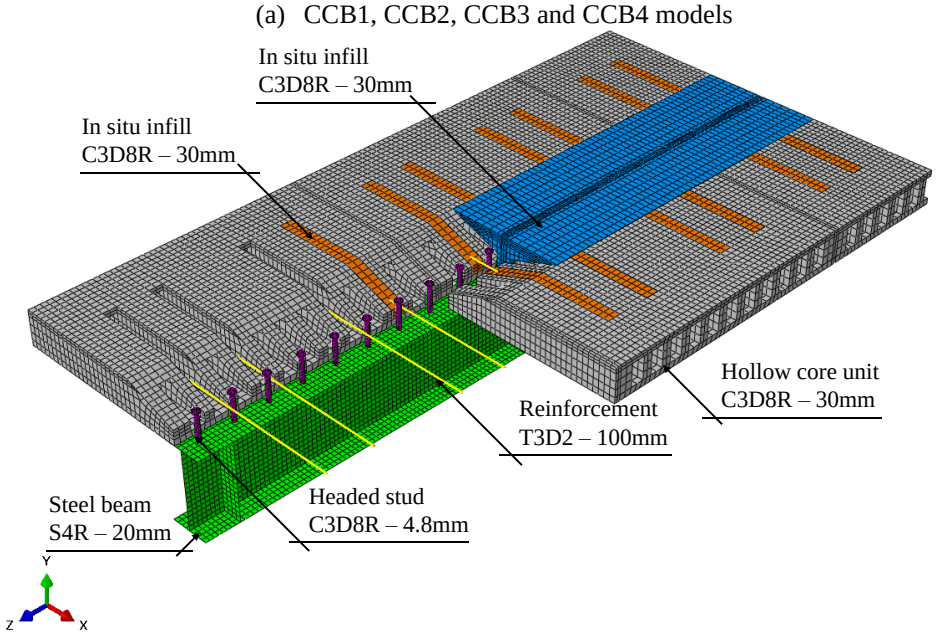

(b) CB1 and CB2 models

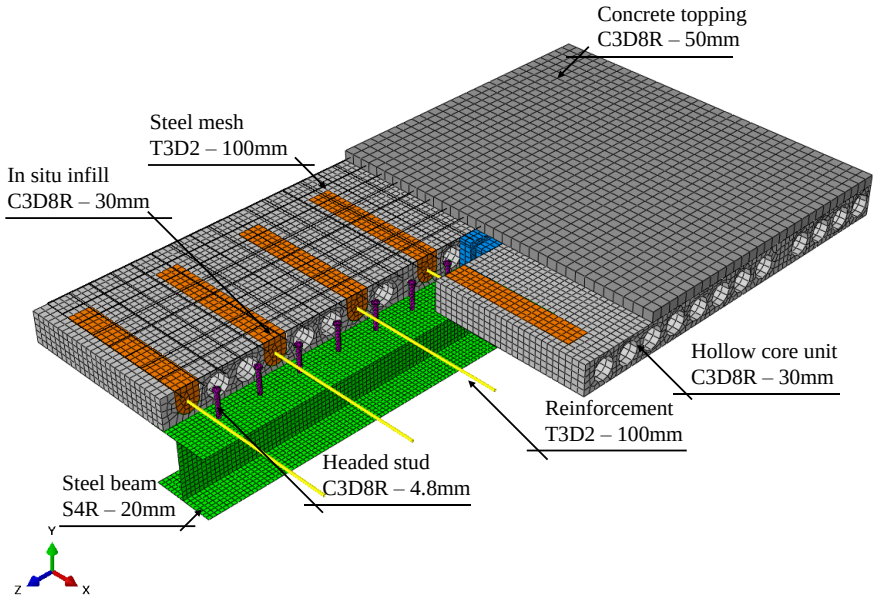

(c) CB3 model

Fig. 6: Discretization

3.6. VALIDATION RESULTS

In this section, the results of the numerical validation with the tests are discussed. Considering the models CCB1 and CCB2, both had the ultimate behavior defined by WPB, as shown in Nadjai [59] and Nadjai et al. [61]. **Fig. 7a-d** shows the comparison of the deformation of the numerical models with the tests. **Fig. 9a-b** shows the results of load per displacement, of models CCB1 and CCB2, respectively. Considering the CCB3 and CCB4 models, the failure modes were similar to that described by Hechler et al. [57] and Müller et al. [58]. According to the authors, the yield strength reached for low levels of loading in the openings, and the ultimate behavior was governed by WPB. **Fig. 7e** shows the deformation of CCB3 and CCB4 models. The ultimate behavior of models CB1, CB2 and CB3 are also shown. The failure modes of the CB1 and CB2 models were similar (**Fig. 8a**). As described by Lam [22], in the CB1 and CB2 models it was possible to observe the plastification of the lower flange and the excess of cracking in the lower part of the hollow core slab. On the other hand, the CB3 model (**Fig. 8b**) showed excessive cracking, mainly at the load application point, at the bottom of the hollow core slab. Such cracks extended to the sides of the slab, as described by Batista and Landesmann [30]. **Fig. 9** illustrates the response of the numerical models developed in comparison to the tests. **Table 3** shows the results. For models CCB1, CCB2, CCB3 and CCB4, the post buckling analysis ended when the structures reached WPB. For the CB1, CB2 and CB3 models, there was an iterative solution technique failure as a convergence problem. In this case, the CB1, CB2 and CB3 models, this behavior reached by excessive cracking (material failure).

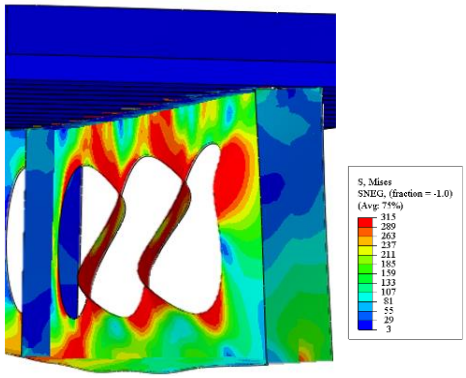

(a) WPB for CCB1 model

(b) Test CCB1 [59]

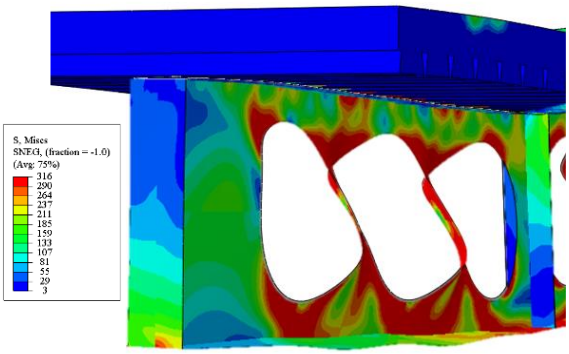

(c) WPB for CCB2 model

(d) Test CCB2 [59]

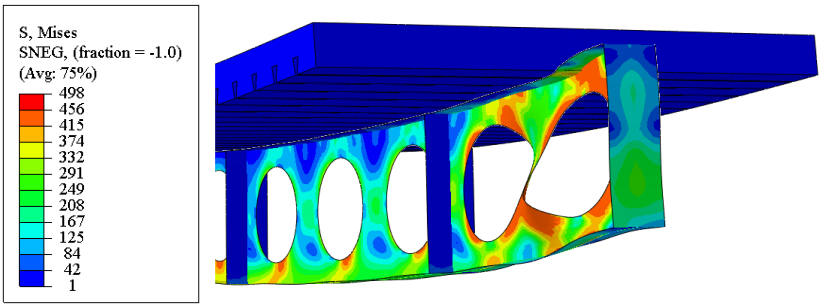

(e) WPB for CCB3 and CCB4 models

Fig. 7: Ultimate behavior of CCB1, CCB2, CCB3 and CCB4 models

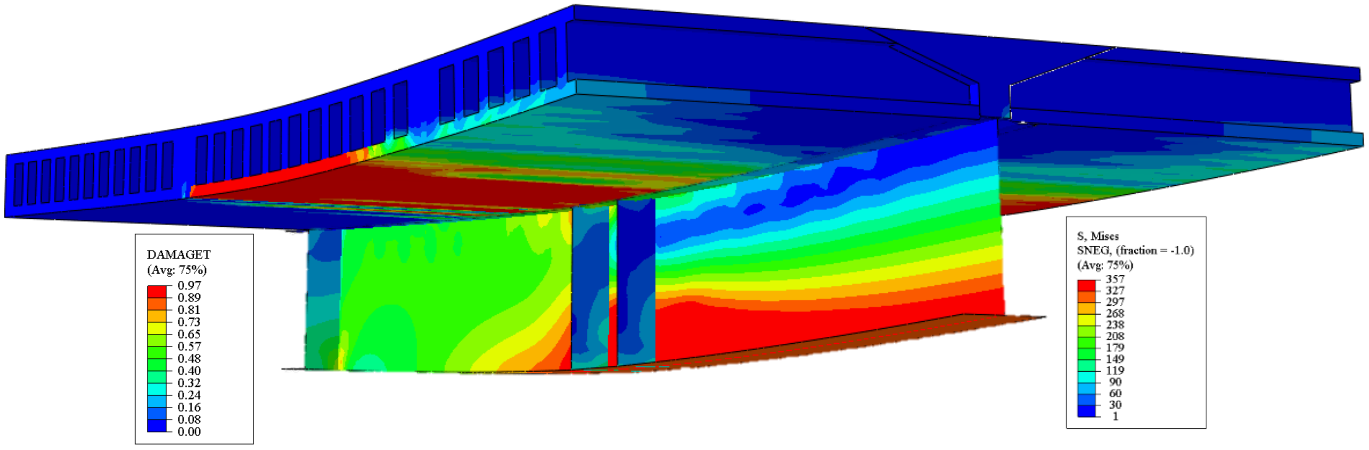

(a) CB1 and CB2 models

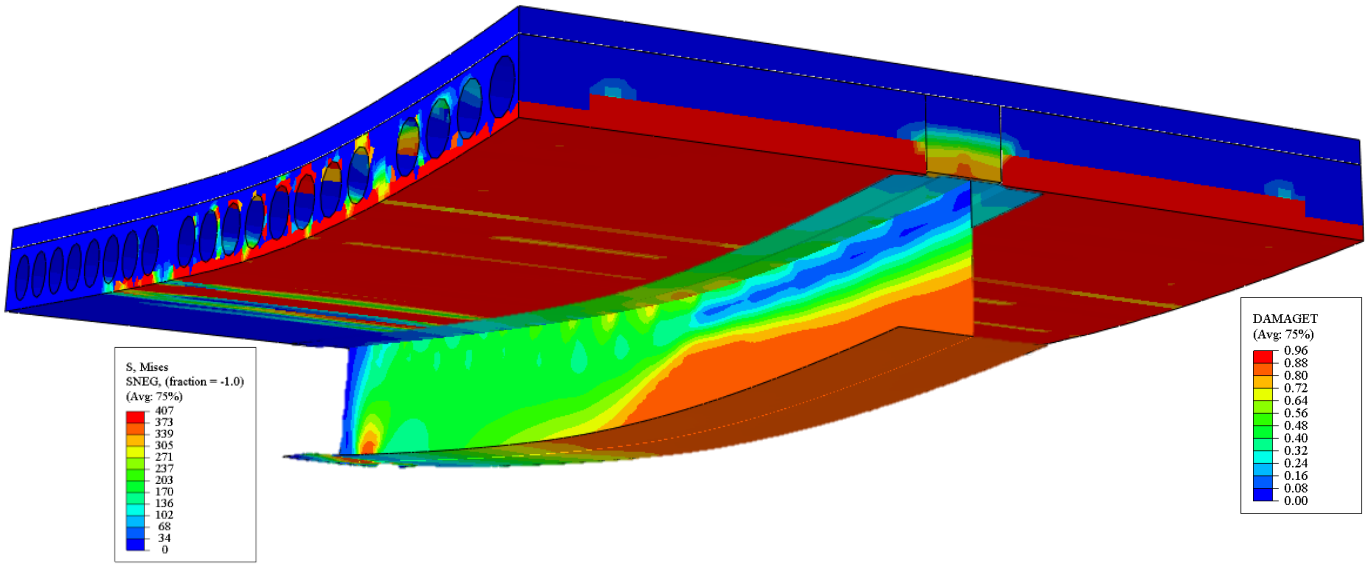

(b) CB3 model

Fig. 8: Ultimate behavior of CB1, CB2 and CB3 models

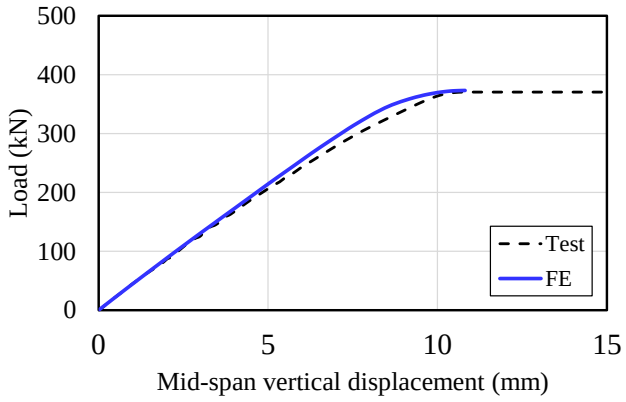

(a) CCB1

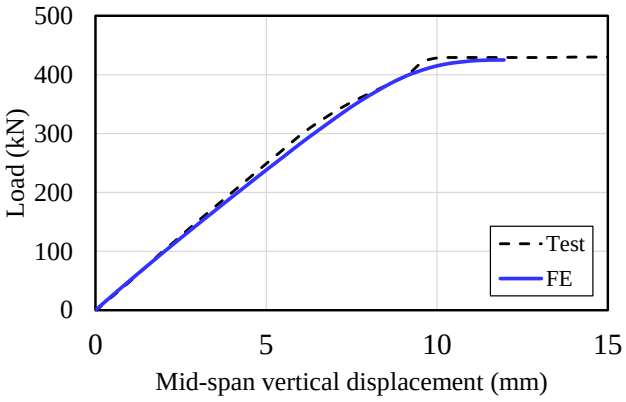

(b) CCB2

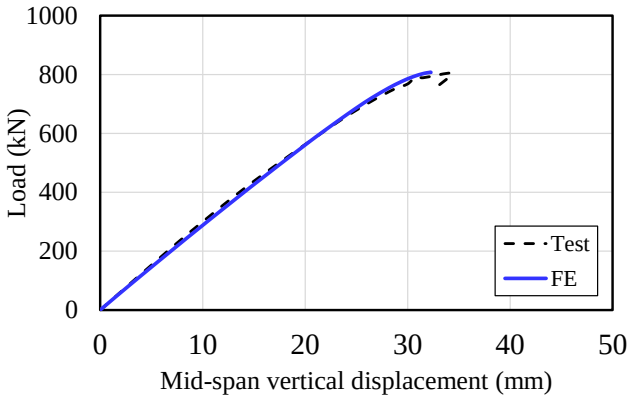

(c) CCB3

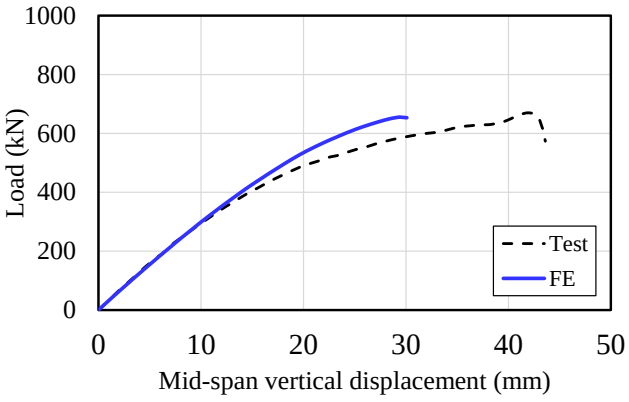

(d) CCB4

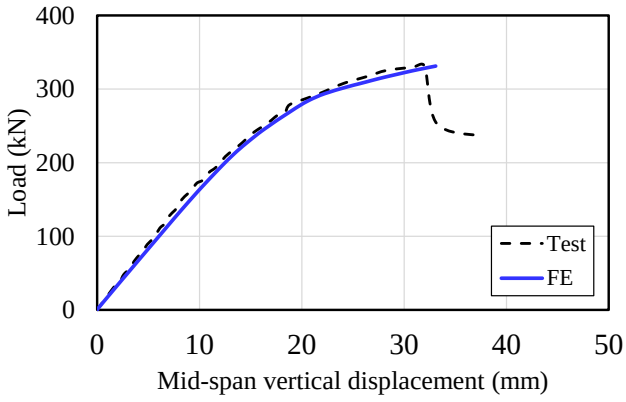

(e) CB1

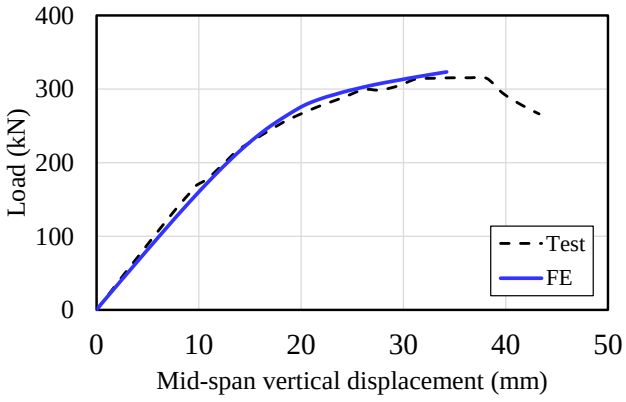

(f) CB2

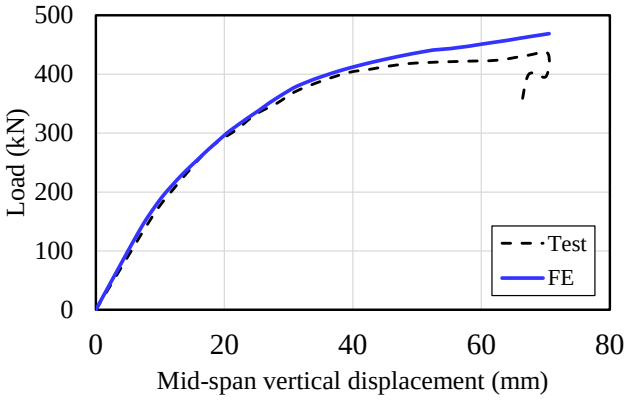

(g) CB3

Fig. 9: Validation results

Table 3: Summary of results

Model	P_{Test} (kN)	P_{FE} (kN)	P_{FE}/P_{Test}
CCB1	370	373	1.01
CCB2	430	425	0.99
CCB3	806	808	1.00
CCB4	658	655	1.00
CB1	331	331	1.00
CB2	316	323	1.02
CB3	442	469	1.06
		Average	1.01
		S.D	2.17%
		COV	0.05%

4. FINITE ELEMENT MODEL: PARAMETRIC STUDY

In view of the results obtained, it is possible to state that the numerical model is calibrated. Thus, as the composite cellular beams with PCHCS are similar structures to the models used in the validation study, it is possible to develop a numerical model to predict the ultimate behavior of these composite beams (**Fig. 10**).

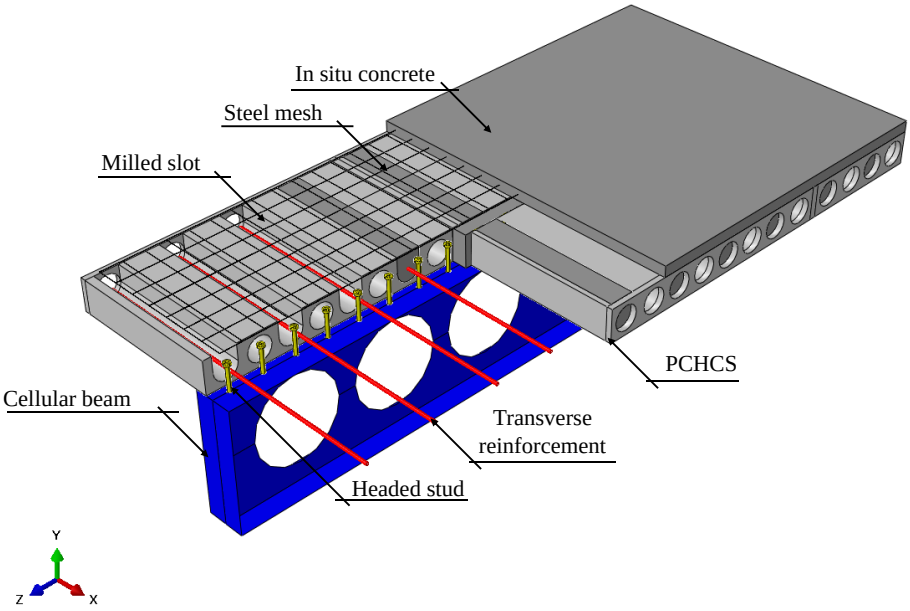

Fig. 10: Finite element model of composite cellular beam with precast hollow core slab and concrete topping

The following are the general considerations for the development of the parametric study:

i. Steel-concrete composite cellular beams are processed in two steps: Buckling and Static Riks analyses. The initial geometric imperfection factor was applied by a scale factor equal to *dg*/1000 [7];

ii. The material models are applied according to section 3.2;

iii. The interaction between parts is applied according to section 3.3;

iv. Two sections are considered, according **Table 4**;

v. For each section, three types of slabs are studied: composite beams with Holorib 51/150 geometry, and PCHCS (LP15 units) (**Fig 11**) with and without concrete topping;

vi. For the cellular profile, ASTM Gr.50 steel is considered, whose yield strength and ultimate strength are 345 MPa and 450 MPa, respectively. The modulus of elasticity and the Poisson's ratio are equal to 200 GPa and 0.3, respectively;

vii. The infill in situ concrete resistance is 30 MPa, and the PCHCS resistance is 40 MPa;

viii. For PCHCS, the filling of the 1st, 3rd, 5th and 7th core was considered, and a transversal reinforcement with 16mm of diameter is placed;

ix. For PCHCS, 70mm of gap is considered;

x. The thickness of concrete topping is 50mm, and a steel mesh is 4.2mm spaced at 100mm;

xi. The dimension of the headed studs is 19x120mm, spaced in 150mm;

xii. The composite beams are simply supported, according to boundary conditions presented in section 3.4 (**Fig. 5**), with a span of 6 m;

xiii. The width of the slab is equal to ¼ of the span;

xiv. Four-point bending is considered, and the loads are applied at 2m from the supports. Stiffeners were provided at the points of loads and supports (**Fig. 12**).

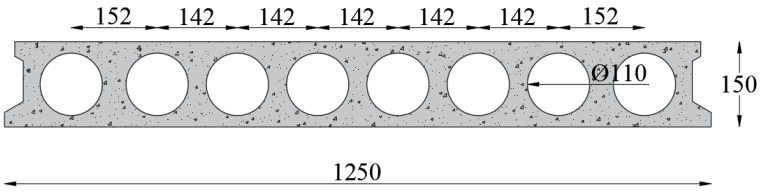

Fig. 11: LP 15

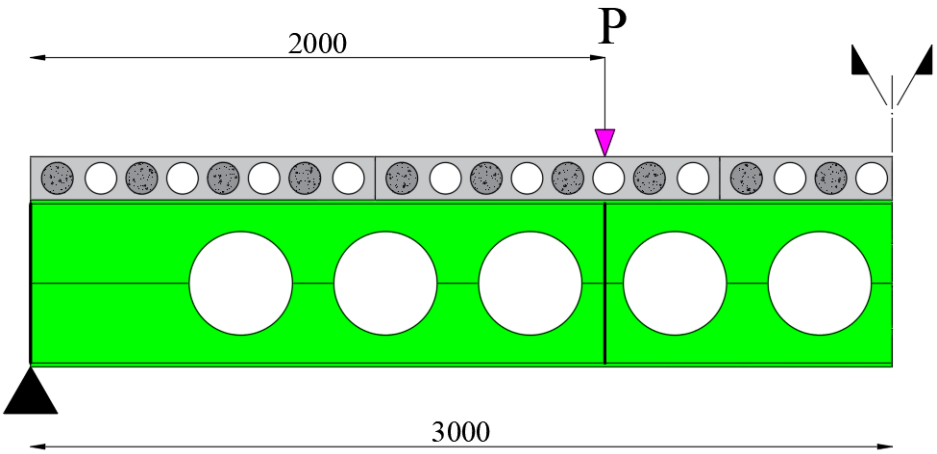

Fig. 12: Four-point bending for parametric study

Table 4: Cellular sections

Sections (Upper/Lower)	d_g	D_o/d	p/D_o	D_o	p	$i/2$
IPE 400 and IPE 400/HEB 340	580	0.8	1.2	320	384	7
		0.8	1.3	320	416	7
		0.8	1.4	320	448	6
		0.8	1.5	320	480	6
		0.9	1.2	360	432	6
		0.9	1.3	360	468	6
		0.9	1.4	360	504	5
		0.9	1.5	360	540	5
		1.0	1.2	400	480	6
		1.0	1.3	400	520	5
		1.0	1.4	400	560	5
		1.0	1.5	400	600	4
		1.1	1.2	440	528	5
		1.1	1.3	440	572	5
		1.1	1.4	440	616	4
		1.1	1.5	440	660	4
		1.2	1.2	480	576	5
		1.2	1.3	480	624	4
		1.2	1.4	480	672	4
		1.2	1.5	480	720	4

5. RESULTS AND DISCUSSION

A total of 120 analyses were carried out. Four failure modes were observed: web post buckling (WPB), web post buckling combined with plastic mechanism (WPB+PM), plastic mechanism (PM), and Vierendeel mechanism (VM). Except for WPB, for other failure modes, shear connector rupture was also observed. The results are discussed with emphasis on the composite cellular beam with PCHCS. At the end of the discussion, a comparative analysis is carried out to assess the ultimate strength depending on the type of slab.

5.1. SYMMETRIC SECTION

Regarding composite cellular beams with composite slabs, the predominant failure mode was WPB, although the WPB+PM and VM, with or without rupture of the shear connectors were also observed. To describe the behavior of these beams step by step, three points of displacement were monitored, considering the mid-span vertical displacement at 10mm, 20mm and the ultimate. In this scenario, the ultimate mid-span vertical displacement showed an average value of approximately 30mm.

The WPB was observed at models D_o/d=0.8-1.1, considering p/D_o=1.2-1.5. In this scenario, considering the mid-span vertical displacement at 10mm, the magnitude of the global shear force was 183.1±27.6 kN. The shear connectors had already reached the yield strength, with the value of von Mises stresses at 500±16.8 MPa. The lower tee was also reached the yield strength, with von Mises stress values at 345±2.7 MPa. The upper tee, on the other hand, although it was reached the yield strength (D_o/d=0.8; p/D_o=1.2-1.4, D_o/d=0.9; p/D_o=1.2-1.3, D_o/d=1.0; p/D_o=1.2-1.4, D_o/d=1.1; p/D_o=1.2-1.3, and D_o/d=1.2; p/D_o=1.2-1.5), the maximum

value of von Mises stresses were 335±18.4 MPa. The openings close to the support, as well as the web posts were in yielding. In this context, considering the composite slab, the lower part of the ribs, which were in the shear region, were damaged by tension. This means that the stresses had already reached the tensile strength of the concrete, as shown in **Eq. (2)**. The upper part of the composite slab, close to the support, was damaged. The concrete compression stresses were 8.1±0.9 MPa. With the progression of loading, for the mid-span vertical displacement prescribed at 20mm, there was a considerable increase in the magnitude of the global shear force (295.3±59.5 kN) in relation to the previous prescribed displacement (10mm). Also, there was an increase in plastic deformations, both in the shear connectors and in the upper and lower tees. The maximum von Mises stresses were equal to 489±6 MPa and 353±8 MPa, for the shear connectors and the tees, respectively. Note that in this step, the stress level was lower than the previous situation. This is due to the shear flow between the shear connectors. The damage extended to the side edges of the slab. At this stage, the compressive stresses in the concrete were 13.9±2.4 MPa. At last, considering the ultimate behavior, the global shear force reached 322.1±61.1 kN. The von Mises stresses for the shear connectors, upper and lower tees were equal to 520±38.2 MPa, 387±32.6 MPa and 389±32.4 MPa, respectively, and the compressive stresses in the concrete were 16.7±2.4 MPa. For models D_o/d=1.0; p/D_o=1.5 and D_o=1.1; p/D_o=1.4-1.5, the combination of WPB+PM was observed. During analysis, the behavior of the composite cellular beam was similar to that previously described. However, there was the formation of the plastic mechanism at the upper part of the opening, close to the support. For the series D_o/d=1.2, the failure modes observed were WPB (p/D_o=1.2), WPB+PM (p/D_o=1.3) and VM, with (p/D_o=1.4) or without rupture (p/D_o=1.5) of the shear connector. The VM, with or without rupture of the shear connector, depending on the longer width of the web post, providing greater resistance to the horizontal shearing force, which causes the Vierendeel moment. Another observation was that with the variation of the web post width, the shear connector rupture was observed. This means that it is not only the axial strengths of the slab and the lower tee that dictate the degree of interaction, but also the spacing between the openings. Next, in **Fig. 13**, the shear resistance values of the models are shown as a function of the key parameters, for the composite cellular beams with composite slab. It can be seen in the illustration that the lower the D_o/d ratio, the greater the shear resistance. On the other hand, there was no pattern with the variation of the p/D_o ratio, since the end post width was variable and influenced the resistance of composite cellular beams [7].

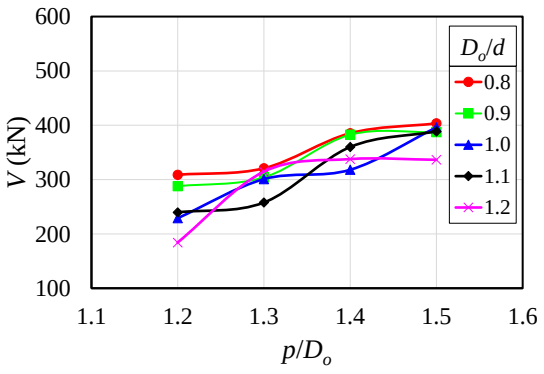

Fig. 13: Global shear force vs. key parameters for symmetric composite cellular beams with composite slab

Considering the composite cellular beam with hollow core slabs, the failure modes were similar to the models discussed previously. The failure modes observed were WPB (**Fig. 14**), the WPB+PM (**Fig. 15**) and the VM (**Fig. 16**). In the models, no shear connector rupture was observed.

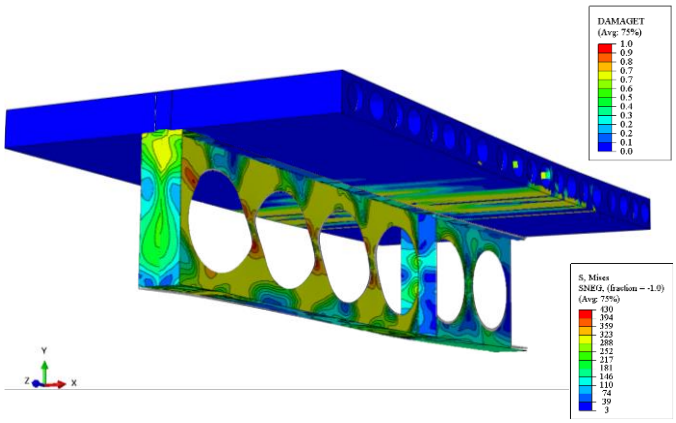

Fig. 14: Web post buckling for D_o/d=1.0; p/D_o=1.2 model, considering PCHCS and symmetrical section

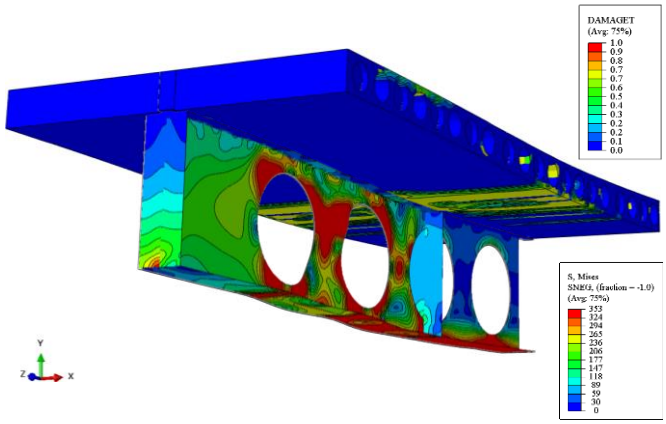

Fig. 15: Web post buckling combined with plastic mechanism for D_o/d=1.1; p/D_o=1.4 model, considering PCHCS and symmetrical section

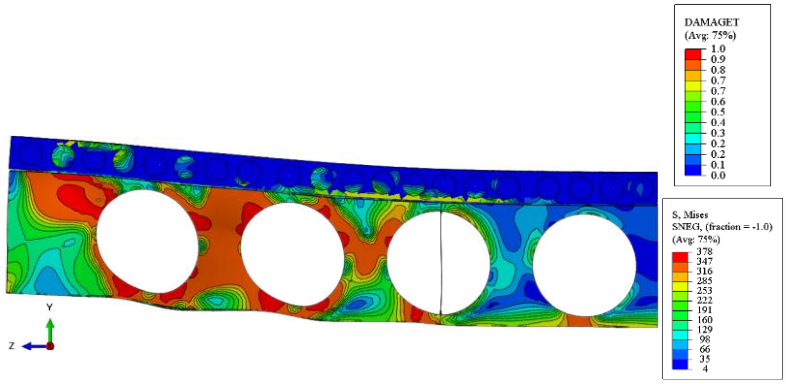

Fig. 16: Vierendeel mechanism without shear connector rupture for D_o/d=1.1; p/D_o=1.4 model, considering PCHCS and symmetrical section

For models D_o/d=0.8-1.1, considering p/D_o=1.2-1.5, the ultimate behavior was governed by WPB. In this scenario, considering the mid-span vertical displacement at 10mm, the magnitude of global shear load was 186.5±25.9 kN. The shear connectors had already reached the yield strength. The maximum von Mises stresses in the shear connectors, upper and lower tees

were 472±10.8 MPa, 325±21.4 MPa and 344±5.9 MPa, respectively. The openings near the support, as well as the web posts were also reached the yield strength. In this context, considering the PCHCS, the bottom edge, the gap and the unfilled core close to the region of the loading application point were damaged by tension. This means that the stresses had already reached the tensile strength. The upper part of the PCHCS was also damaged. At this stage, the concrete compressive stress was 10.2±0.9 MPa. With the progression of loading, considering the mid-span vertical displacement at 20mm, the global shear load presented values at 312.4±54.2 kN. There was an increase in plastic deformations, both in the shear connectors and in the upper and lower tees. The maximum von Mises stresses were 494±11.8 MPa, 352±6.4 MPa and 494±11.82 MPa, for the shear connectors, upper and lower tees, respectively. In relation to the PCHCS, with the progression of loading, the damage extended to the ends of the slab, increasing the damaged region. The concrete compressive stresses were 18.7±2.9 MPa. Regarding the ultimate behavior, the values of global shear force reached 337.0±59.4 kN. The von Mises stresses for the shear connectors, upper and lower tees were 518±14.5 MPa, 376±26.4 MPa and 381±29.8 MPa, respectively. In the ultimate strength, the damage by tension spread over the entire slab, and the concrete compressive stresses reached 23.0±4.7 MPa, and low slip values (almost null) were found at the steel-concrete interface. On the other hand, for the series D_o/d=1.2 with p/D_o=1.3;1.5, WPB+PM was verified (**Fig. 10**), and for the model p/D_o=1.4, the VM was observed (**Fig. 16**). The analysis was processed in a similar way to that previously described. Next, in **Fig. 17**, the global shear resistance values of the models are shown as a function of the key parameters, considering composite cellular beams with PCHCS.

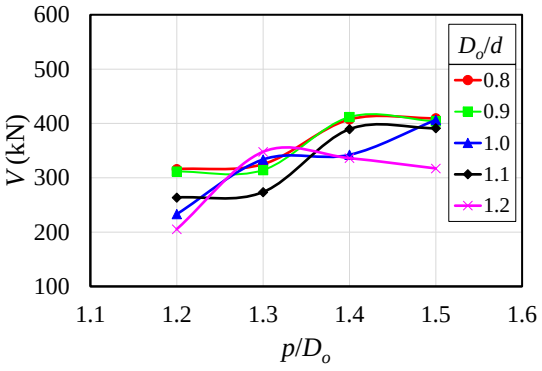

Fig. 17: Global shear force vs. key parameters for symmetric composite cellular beams, considering PCHCS and symmetrical section

In relation to the composite cellular beams with PCHCS and concrete topping, WPB (**Fig. 18**) was observed for most models. The WPB+PM (**Fig. 19**), PM, i.e., plastification of the lower flange or around the opening (**Fig. 20**), and VM (**Fig. 21**), also occurred.

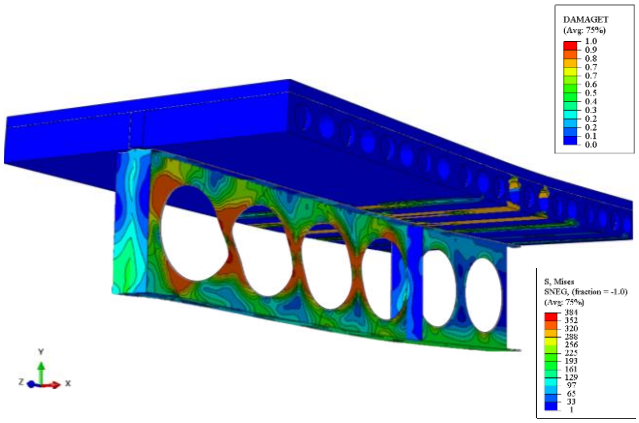

Fig. 18: Web post buckling for D_o/d=1.0; p/D_o=1.2 model, considering PCHCS with concrete topping and symmetrical section

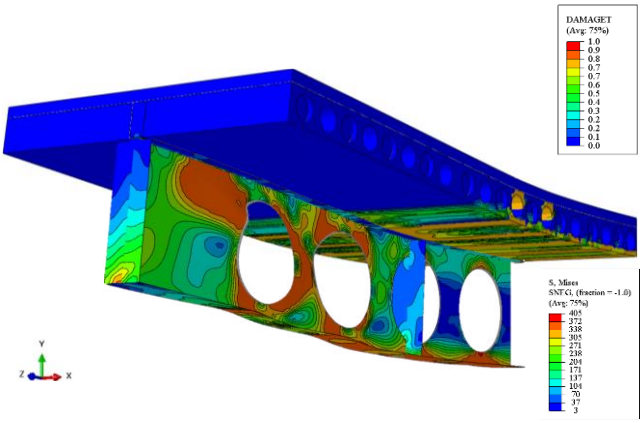

Fig. 19: Web post buckling combined with plastic mechanism for D_o/d=1.1; p/D_o=1.4 model, considering PCHCS with concrete topping and symmetrical section

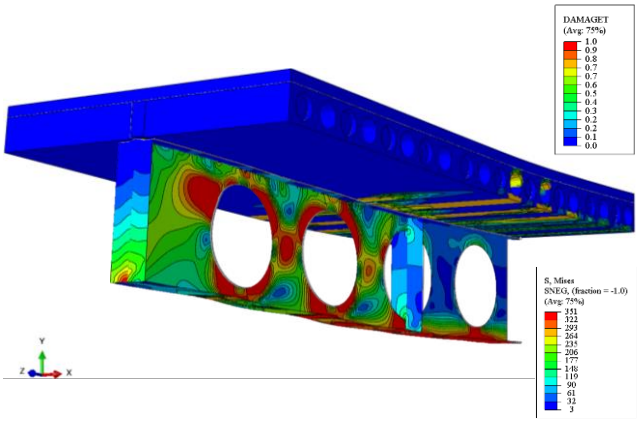

Fig. 20: Mechanism plastic for D_o/d=1.1; p/D_o=1.5 model, considering PCHCS with concrete topping and symmetrical section

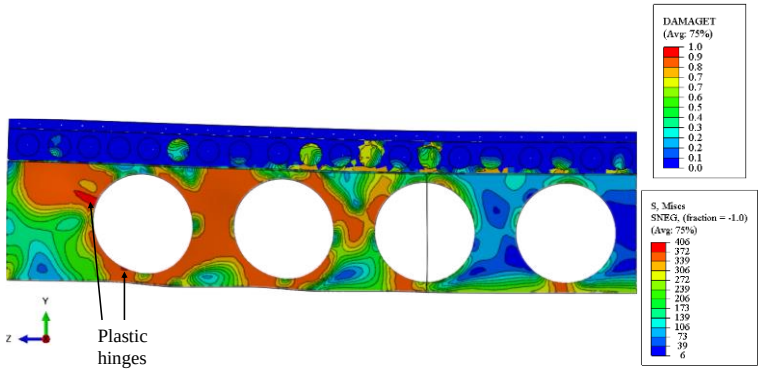

Fig. 21: Vierendeel mechanism for D_o/d=1.1; p/D_o=1.4 model, considering PCHCS with concrete topping and symmetrical section

For D_o/d=0.8; p/D_o=1.2-1.5, D_o/d=0.9; p/D_o=1.2-1.5, D_o/d=1.0; p/D_o=1.2-1.4, D_o/d=1.1; p/D_o=1.2-1.3 and D_o/d=1.2; p/D_o=1.2 models, the ultimate behavior was governed by WPB. Regarding the processing of the models, considering the mid-span vertical displacement at 10mm, the magnitude of global shear force was 231.5±28.8 kN. The shear connectors had already reached the yield strength, with the maximum von Mises stresses of 401±4.3 MPa. In this scenario, the von Mises stresses in the upper and lower tees were 334±14.5 MPa and 346±6.4 MPa, respectively. The openings and web posts, in the region of pure shear, were already in plastification. In this context of prescribed displacement, the elements of the PCHCS, such as the lower edge, the gap, the core without filling, were damaged. For situations in which the end post width is much greater than the web post width, damage was also verified in the upper part of the concrete topping, close to the support, where the shear is maximum. In this scenario, the concrete compressive stresses were 8.7±2.8 MPa. With the progression of loading, for the mid-span vertical displacement prescribed at 20mm, the global shear force presented values at 368.8±55.9 kN. There was an increase in plastic deformations, both in the shear connectors and in the upper and lower tees. In this context, the maximum von Mises stresses for the shear and tees connectors were 522±15.3 MPa and 354±9 MPa, respectively. In the PCHCS with concrete topping, there was an increase in the damaged region. The concrete compressive stresses were 16.8±5.3 MPa. In the ultimate strength, the magnitude of global shear force reached 383.1±65.3 kN. The von Mises stresses for the shear connectors, upper and lower tees were 557±33 MPa, 371±23.1 MPa and 378±30 MPa, respectively. In this scenario, considering the PCHCS, there was an increase in the damaged region, that is, excessive cracking, and the concrete compressive stresses reached 17.8±4.6 MPa. Also, low slip values were verified at the steel-concrete interface. An important observation was the contribution of the concrete topping, which it maintained as compression stresses below, in comparison with the PCHCS models. For the situations that occurred WPB+PM (D_o/d=1.0; p/D_o=1.5 and D_o/d=1.5; p/D_o=1.0), PM (D_o/d=1.1; p/D_o=1.4-1.5 and D_o/d=1.2; p/D_o=1.3) and VM (D_o/d=1.2; p/D_o=1.4), a higher loading was observed, as well as plastic deformations. This occurred due to the end and web posts widths. **Fig. 22** illustrates the shear resistance values of the models as a function of the key parameters, considering composite cellular beams with PCHCS and concrete topping.

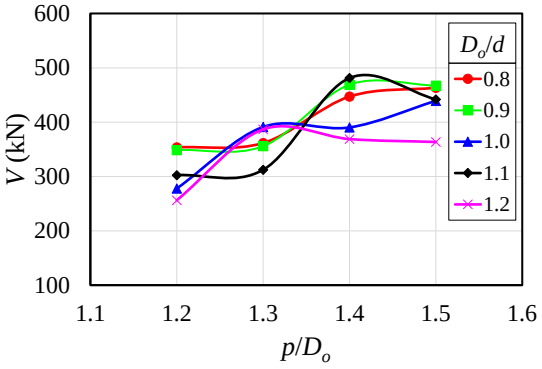

Fig. 22: Global shear force vs. key parameters for symmetric composite cellular beams, considering PCHCS with concrete topping and symmetrical section

5.2. ASYMMETRIC SECTION

Regarding the structural behavior of asymmetric composite cellular beams with composite slabs, the failure modes were WPB+PM, PM and VM, with or without shear connector rupture. Also, three points of mid-span vertical displacement were monitored to describe the structural behavior. The monitored points were 10mm, 20mm and 41.4±14mm.

The failure mode WPB+PM was observed for D_o/d=0.8; p/D_o=1.2-1.3 and 1.5, D_o/d=0.9; p/D_o=1.2-1.5, D_o/d=1.0; p/D_o=1.2-1.5, D_o/d=1.1; p/D_o=1.2-1.5 and D_o/d=1.2; p/D_o=1.2-1.3. In this scenario, the shear connector rupture was observed for D_o/d=0.8; p/D_o=1.2, D_o/d=0.9; p/D_o=1.2, D_o/d=1.0; p/D_o=1.2, and D_o/d=1.2; p/D_o=1.2. Regarding the structural behavior during the analysis, and considering the mid-span vertical displacement at 10mm, the global shear force presented values at 265.4±49.2 kN. The shear connectors had already reached the yield strength. The von Mises stresses in the shear connectors were 490±11.1 MPa. The upper and lower tees were also already in plastic regime, with von Mises stresses of 347±0.7 MPa, for both the lower and upper tees. The openings close to the support (shear region), as well as the web posts were also in a plastic regime. On the behavior of the composite slab, with the mid-span vertical displacement prescribed at 10mm, the lower part of the ribs that were in the shear region were damaged. For situations where the end-post was much larger than the web post, the upper part of the slab, which was close to the support, was damaged. At this stage, the concrete compressive stresses were 11.2±1.6 MPa. With the progression of loading, in which the global shear force was 373.9±75.6 kN and the mid-span vertical displacement at 20mm, there was an increase in plastic deformations, both in the shear connectors, and in the upper and lower tees. In this context, maximum von Mises stresses were 509±23 MPa and 361±9.9 MPa, for shear connectors and tees, respectively. In relation to the composite slab, there was an increase in the damaged region, and the concrete compressive stresses were 18.0±3.1 MPa. In the ultimate behavior, the global shear force reached 440.3±77.4 kN. The von Mises stresses for the shear connectors, upper and lower tees were 625±40.2 MPa, 435±46.6 MPa and 407±42.4 MPa, respectively. In this scenario, in the composite slab there was an increase in the damaged region, that was, the cracks extended from the lower part of the rib to the mid-height of the slab, and the compressive stresses of the concrete were measured in 24.5±3.0 MPa. In addition, there were low slip values at the steel-concrete interface. Oppositely, for D_o/d=0.8; p/D_o=1.4 and D_o/d=1.2; p/D_o=1.4-1.5, the formation of the plastic mechanism and the Vierendeel mechanism were observed, respectively. **Fig. 23** illustrates the resistance values, considering the global shear in function of the key parameters.

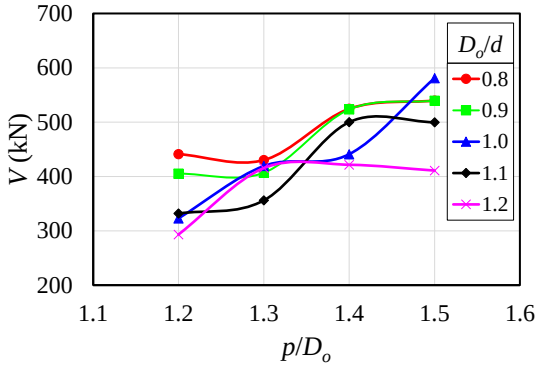

Fig. 23: Global shear force vs. key parameters for asymmetric composite cellular beams with composite slab

With regard to asymmetric composite cellular beams with PCHCS, the predominant failure modes were WPB+PM (**Fig. 24**). Only the D_o/d=1.2; p/D_o=1.5 model presented the plastic mechanism (**Fig. 25**), without buckling. For D_o/d=0.8; p/D_o=1.2-1.3 and 1.5, D_o/d=0.9-1.1; p/D_o=1.2, the shear connector rupture was observed. Considering the structural behavior of asymmetric composite cellular beams with PCHCS, for the mid-span vertical displacement prescribed at 10mm, the global shear force presented was 272±44.9 kN. The shear connectors had already reached the yield strength. The maximum stresses of von Mises were 482±7.4 MPa. In this scenario, the von Mises stresses in the tees were 346±0.7 MPa. The openings and web posts, which were close to the support, had already reached the yield strength. For the mid-span vertical displacement prescribed at 10mm, the bottom edge of the PCHCS, the gap and the unfilled core, close to the region of the loading application point, were damaged. The upper part of the PCHCS was also damaged. In this scenario, the concrete compressive stresses were 14.6±1.8 MPa. With the progression of loading, for the mid-span vertical displacement prescribed at 20mm, the global shear force was 391.5±72.7 kN. There was an increase in plastic deformations, both in the shear connectors and in the tees. In this context, the maximum von Mises stresses were 516±17.3 MPa and 357±6.1 MPa, for the shear connectors and the tees, respectively. In this scenario, the damage extended to the sides of the PCHCS. At this stage the compressive stresses were 25.2±4.5 MPa. In the ultimate behavior, for mid-span vertical displacement prescribed at 49.7±21.8 mm, the global shear load and the concrete compressive stresses reached 469.7±71.1 kN and 30.3±6.0 MPa, respectively. The von Mises stresses for the shear connectors, upper and lower tees were 617±44.1 MPa, 434±36.9 MPa and 420±52.1 MPa, respectively. In addition, low slip values (null) were also found at the steel-concrete interface. **Fig. 26** illustrates the shear resistance values of the models as a function of the key parameters, considering asymmetric composite cellular beams with PCHCS.

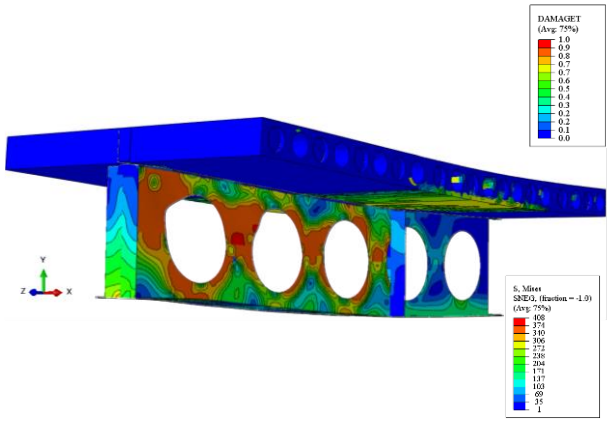

Fig. 24: Web post buckling combined with plastic mechanism for D_o/d=1.0; p/D_o=1.4 model, considering PCHCS and asymmetrical section

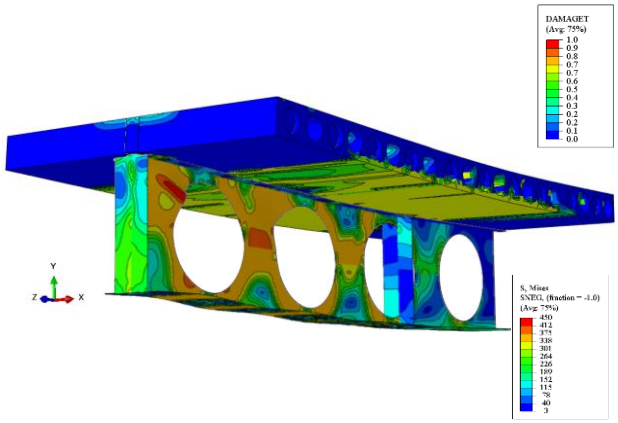

Fig. 25: Plastic mechanism for D_o/d=1.2; p/D_o=1.5 model, considering and asymmetrical section

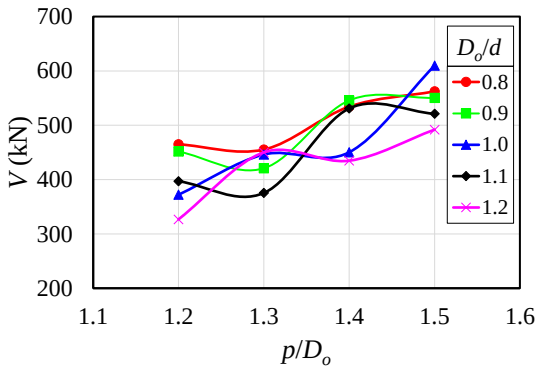

Fig. 26: Global shear force vs. key parameters for asymmetric composite cellular beams, considering PCHCS

With regard to the asymmetrical composite cellular beams with PCHCS and concrete topping, the failure modes observed were WPB+PM (**Fig. 27**), for D_o/d=0.8; p/D_o=1.1, D_o/d=0.9; p/D_o=1.2-1.3, D_o/d=1.0; p/D_o=1.2-1.4, D_o/d=1.1; p/D_o=1.2-1.3 and D_o/d=1.2; p/D_o=1.2-1.3, and PM (**Fig. 28**), for D_o/d=0.8; p/D_o=1.3-1.5, D_o/d=0.9; p/D_o=1.4-1.5, D_o/d=1.0; p/D_o=1.5, D_o/d=1.1; p/D_o=1.4-1.5 and D_o/d=1.2; p/D_o=1.4-1.5. In this scenario, there was no shear connector rupture for only D_o/d=1.1-1.2; p/D_o=1.3 models. Regarding the structural behavior analyzed, considering the mid-span vertical displacement prescribed at 10 mm, the global shear force was 331.4±50.6 kN. The shear connectors and the tees had already reached the yield strength, with von Mises stresses

of 488±8.1 MPa and 347±0.9 MPa, respectively. At this stage, the bottom edge of the PCHCS, the gap and the unfilled core near the region of the loading application point were damaged. The upper part of the concrete topping, next to the support, was also damaged. The concrete compressive stresses were 12.3±3.7 MPa. This was also verified for the previous situations, in which the end post width was greater than the web post width. With the progression of loading, for the mid-span vertical displacement at 20mm, the global shear load was 448.3±82.7 kN. There was an increase in plastic deformations in the shear and tees connectors. In this context, the maximum von Mises stresses were 557±28.3 MPa and 362±9.2 MPa, for the shear connectors and the tees, respectively. Considering the PCHCS with concrete topping, the damage extended to the side edges. The concrete compressive stresses were 20.4±6.5 MPa. In the ultimate behavior, for the mid-span vertical displacement at 37.3±8.6 mm, and the magnitude of global shear reached 513.3±71.2 kN. The von Mises stresses for the shear connectors, upper and lower tees were 659±11.9 MPa, 437±16.9 MPa and 414±29.4 MPa. The concrete compressive stresses were 20.0±4.6 MPa and, in most models, the shear connector rupture was observed. In addition, there were low slip values at the steel-concrete interface. **Fig. 29** illustrates the shear resistance values of the models as a function of the key parameters, considering asymmetric composite cellular beams with PCHCS and concrete topping.

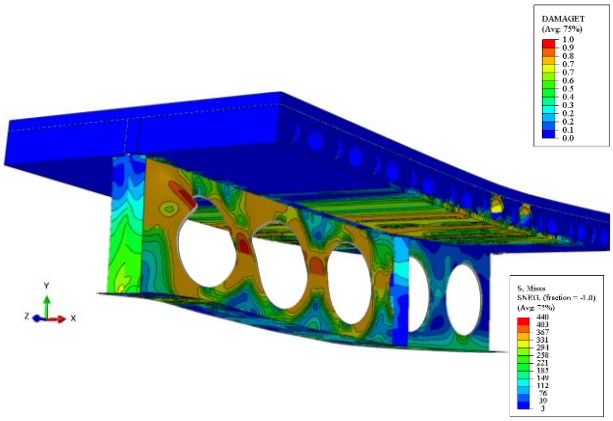

Fig. 27: Web post buckling combined with plastic mechanism for D_o/d=1.0; p/D_o=1.4 model, considering PCHCS with concrete topping and asymmetrical section

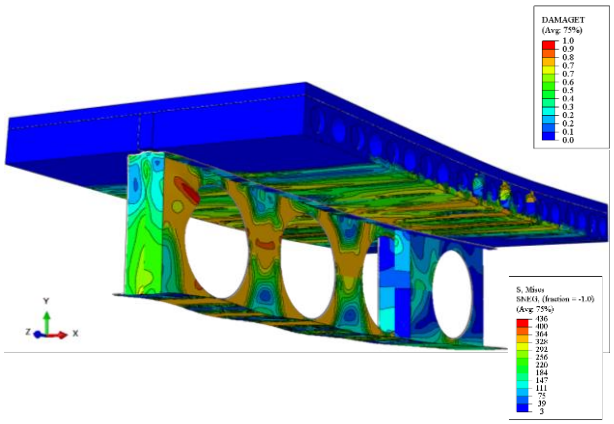

Fig. 28: Plastic mechanism for D_o/d=1.2; p/D_o=1.5 model, considering PCHCS with concrete topping and asymmetrical section

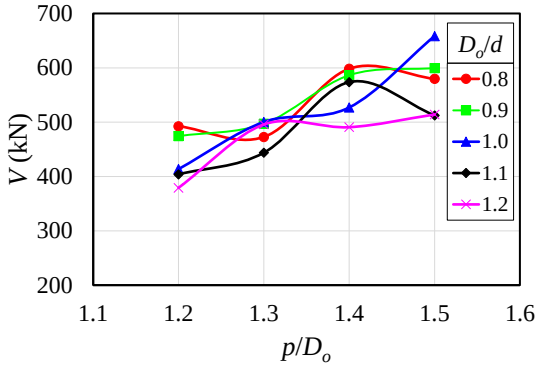

Fig. 29: Global shear force vs. key parameters for asymmetric composite cellular beams, considering PCHCS with concrete topping and asymmetrical section

5.3. COMPARATIVE ANALYSIS BETWEEN MODELS

In the previous sections, the behavior of composite cellular beams, considering composite slabs, PCHCS, and PCHCS with concrete topping were discussed. In this section, the shear resistance is discussed through comparative analyses. In **Fig. 30**, the results are illustrated considering the symmetric section. As shown in **Fig. 30a**, considering D_o/d=0.8, a situation in which the highest depth of the tee sections was found, the maximum differences between the PCHCS and the composite slab models (V_{PCHCS}-V_{CS}), PCHCS with concrete topping and composite slab models ($V_{PCHCSCT}$-V_{CS}), and PCHCS with concrete topping and PCHCS ($V_{PCHCSCT}$-V_{PCHCS}) were 22kN, 62 kN and 54 kN, respectively. These values were measured for p/D_o=1.4-1.5 and b_{we}/b_w=1.3-2.9. In these cases, it was observed that the PCHCS models obtained greater resistance when compared to the composite slab, for situations in which the ultimate strength was reached by WPB. This means that the slab contributed significantly to the strength of the composite cellular beams. For D_o/d=0.9 (**Fig. 30b**), the maximum differences between the resistance values were V_{PCHCS}-V_{CS}=29kN (p/D_o=1.4 and b_{we}/b_w=3.8), $V_{PCHCSCT}$-V_{CS}=86kN (p/D_o=1.4 and b_{we}/b_w=3.8), and $V_{PCHCSCT}$-V_{PCHCS}=64 kN (p/D_o=1.5 and b_{we}/b_w=2.2). Although in the present situation the depth of the tee sections decreased with increasing diameter, with increasing diameter the web post width was increased. Thus, when compared to the previous situation, the differences between the types of slab increased, showing the influence of the web posts width on the shear resistance. Considering D_o/d=1.0 (**Fig. 30c**), the maximum differences were measured for p/D_o=1.3. The values obtained were V_{PCHCS}-V_{CS}=33kN, $V_{PCHCSCT}$-V_{CS}=90kN and $V_{PCHCSCT}$-V_{PCHCS}=57kN. For these situations, WPB was observed. For D_o/d=1.1 (**Fig. 30d**), the maximum differences between the PCHCS and composite slab (V_{PCHCS}-V_{CS}), PCHCS with concrete topping and composite slab ($V_{PCHCSCT}$-V_{CS}), and PCHCS with concrete topping and PCHCS ($V_{PCHCSCT}$-V_{PCHCS}) were 29kN, 121 kN and 92 kN, respectively. These values were measured for p/D_o=1.4 and b_{we}/b_w=3.5. In this case, it was observed that as the opening diameter was increased, the difference between the PCHCS and composite slab was decreased. However, the differences between these two types of slab, when compared to the PCHCS with concrete topping, tend to increase. Finally, considering D_o/d=1.2, (**Fig. 30e**), for the situation that WPB occurred (p/D_o=1.2), the differences were V_{PCHCS}-V_{CS}=21kN, $V_{PCHCSCT}$-V_{CS}=72kN e $V_{PCHCSCT}$-V_{PCHCS}=51kN. For the other situations in which some plastic behavior was observed, such as the VM, the values of the differences decreased, since this ultimate behavior was governed by the yield strength of the tees. In **Fig. 31**, some examples of these differences are illustrated through the equilibrium trajectory, considering WPB.

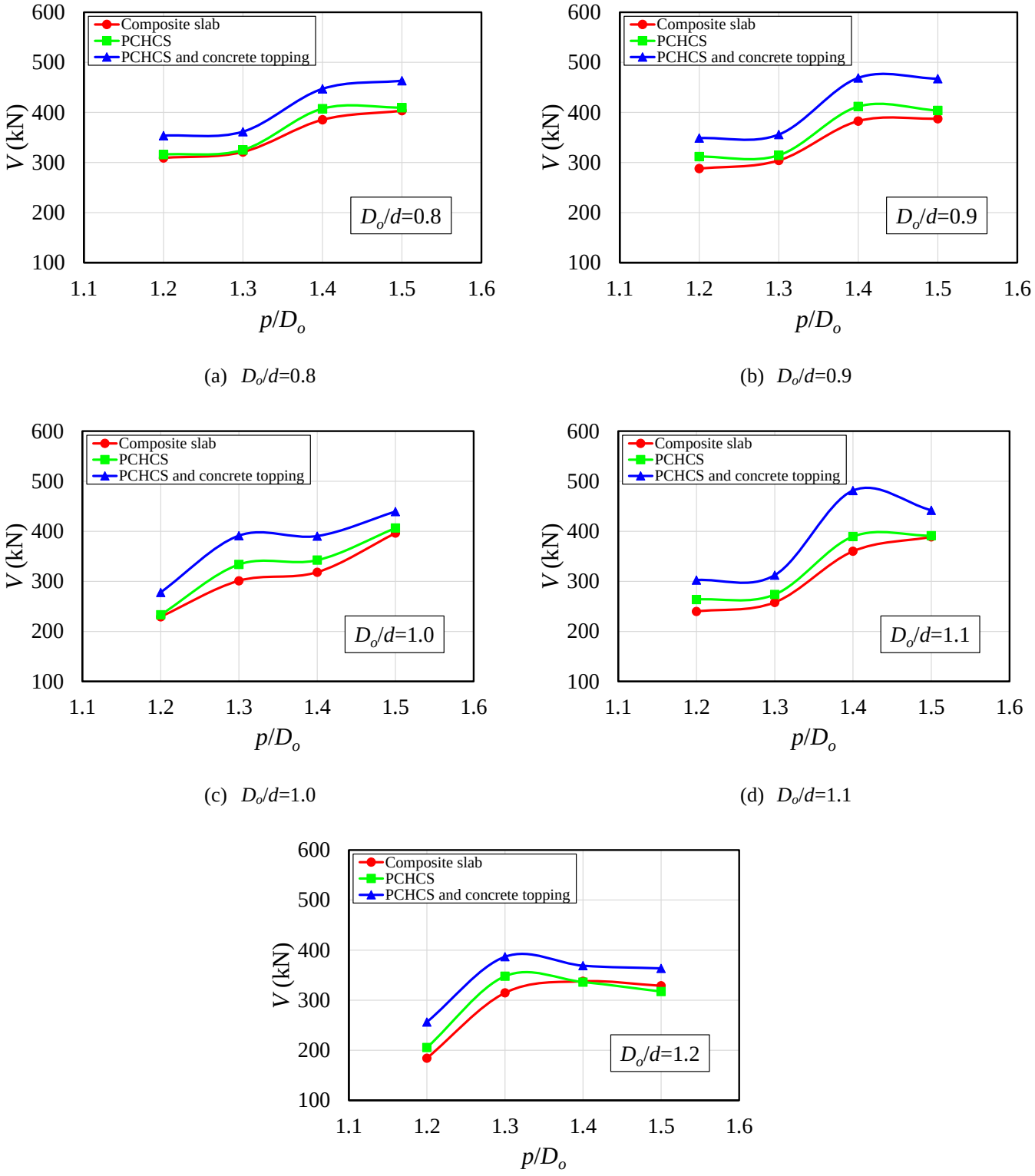

(a) D_o/d=0.8

(b) D_o/d=0.9

(c) D_o/d=1.0

(d) D_o/d=1.1

(e) D_o/d=1.2

531 **Fig. 30: Comparative analyses for symmetric composite cellular beams**

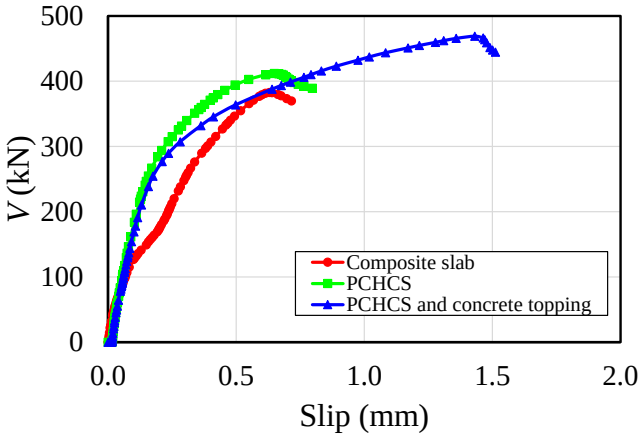

(a) Shear-slip relationship for D_o/d=0.9 and p/D_o=1.4

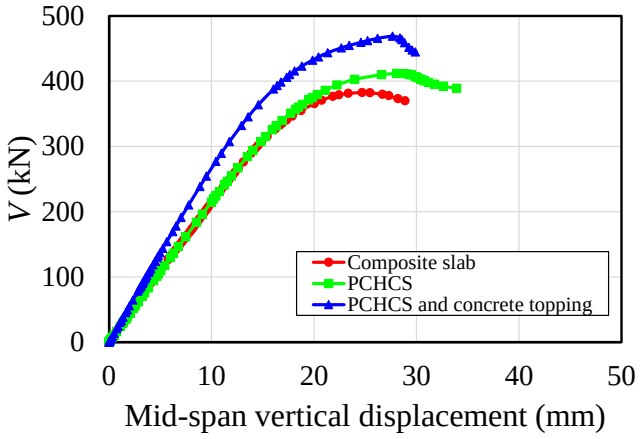

(b) Shear-deflection relationship for D_o/d=0.9 and p/D_o=1.4

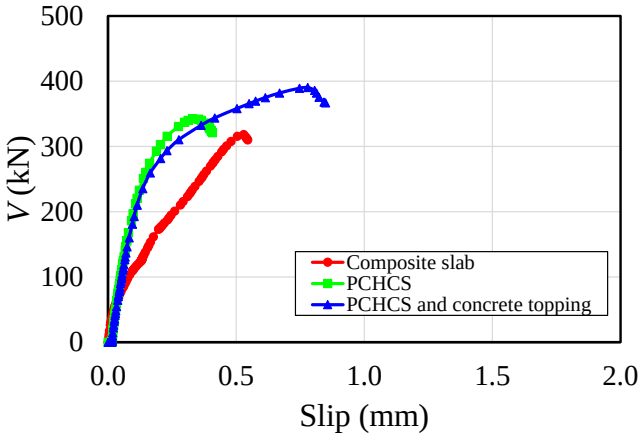

(c) Shear-slip relationship for D_o/d=1.0 and p/D_o=1.4

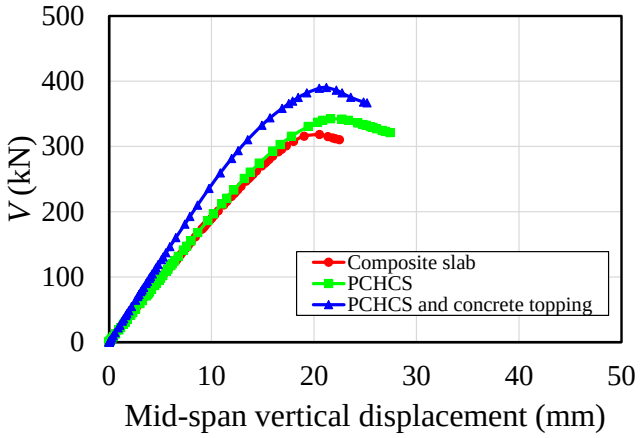

(d) Shear-deflection relationship for D_o/d=1.0 and p/D_o=1.4

Fig. 31: Differences in the behavior of composite cellular beams with slab variation, considering symmetrical section

On the other hand, **Fig. 32** illustrates the results for asymmetric section. Considering D_o/d=0.8 (**Fig. 32a**), the maximum differences were V_{PCHCS}-V_{CS}=25kN, $V_{PCHCSCT}$-V_{CS}=74kN and $V_{PCHCSCT}$-V_{PCHCS}=64kN. These values were measured for p/D_o=1.3-1.4 and b_{we}/b_w=1.3-2.9. For D_o/d=0.9 (**Fig. 32b**), the maximum differences between the resistance values were V_{PCHCS}-V_{CS}=46kN (p/D_o=1.2 and b_{we}/b_w=6.2), $V_{PCHCSCT}$-V_{CS}=90kN (p/D_o=1.3 and b_{we}/b_w=2.3), and $V_{PCHCSCT}$-V_{PCHCS}=76 kN (p/D_o=1.3 and b_{we}/b_w=2.3). Considering D_o/d=1.0 (**Fig. 32c**), the maximum differences were measured for p/D_o=1.2;1.4. The values obtained were V_{PCHCS}-V_{CS}=49kN (p/D_o=1.2), $V_{PCHCSCT}$-V_{CS}=91kN (p/D_o=1.4) and $V_{PCHCSCT}$-V_{PCHCS}=77kN (p/D_o=1.4). For these situations, WPB+PM with shear connector rupture was observed. For D_o/d=1.1 (**Fig. 32d**), the maximum differences were V_{PCHCS}-V_{CS}=65kN, $V_{PCHCSCT}$-V_{CS}=88kN and $V_{PCHCSCT}$-V_{PCHCS}=68kN. These values were measured for p/D_o=1.2-1.3 and b_{we}/b_w=1.6-4.6. Finally, considering D_o/d=1.2, (**Fig. 32e**), the differences were V_{PCHCS}-V_{CS}=81kN (p/D_o=1.5), $V_{PCHCSCT}$-V_{CS}=103kN (p/D_o=1.5) and $V_{PCHCSCT}$-V_{PCHCS}=56kN (p/D_o=1.4). In **Fig. 33**, some examples of these differences are illustrated through the equilibrium trajectory.

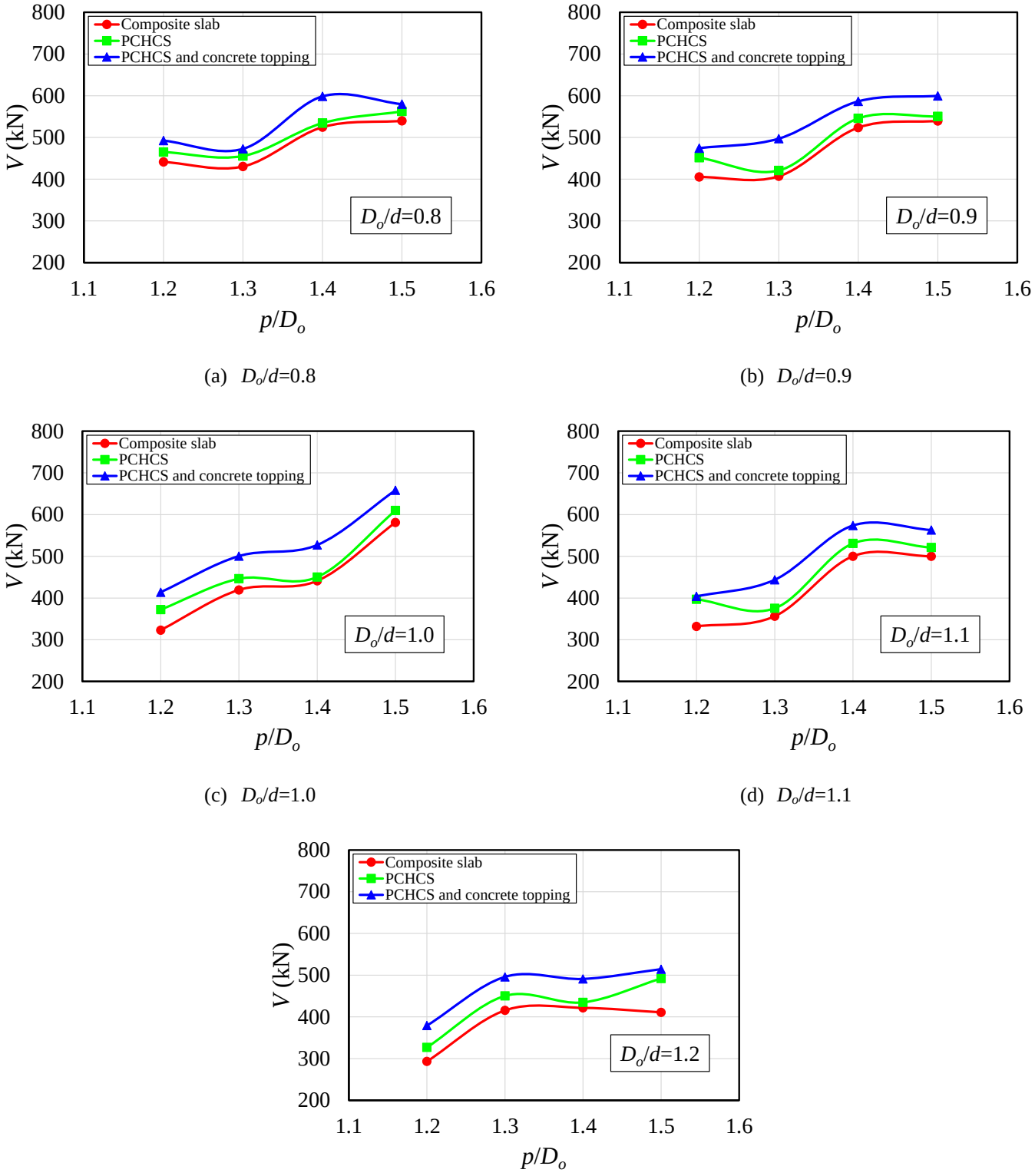

(a) D_o/d=0.8

(b) D_o/d=0.9

(c) D_o/d=1.0

(d) D_o/d=1.1

(e) D_o/d=1.2

Fig. 32: Comparative analyses for asymmetric composite cellular beams

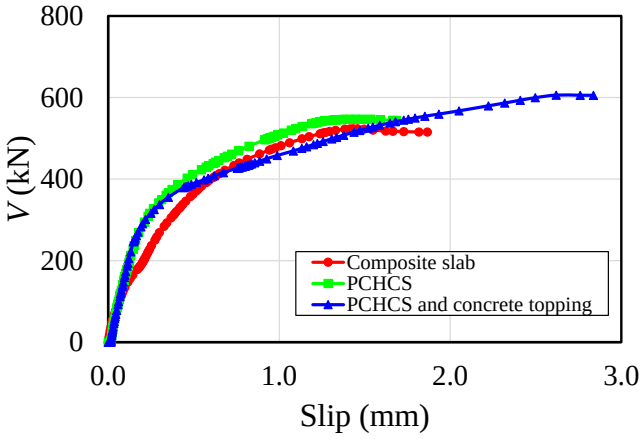

(a) Shear-slip relationship for D_o/d=0.9 and p/D_o=1.4

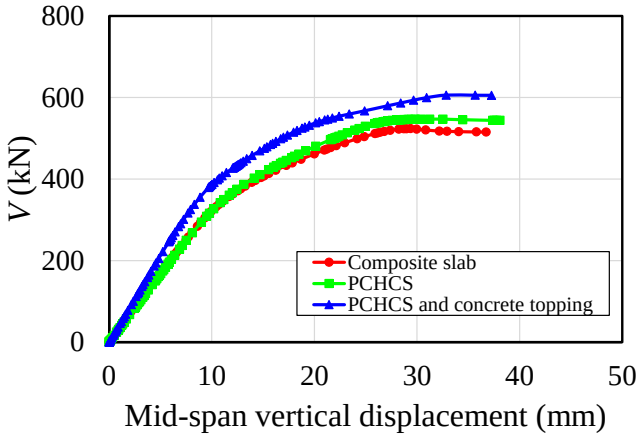

(b) Shear-deflection relationship for D_o/d=0.9 and p/D_o=1.4

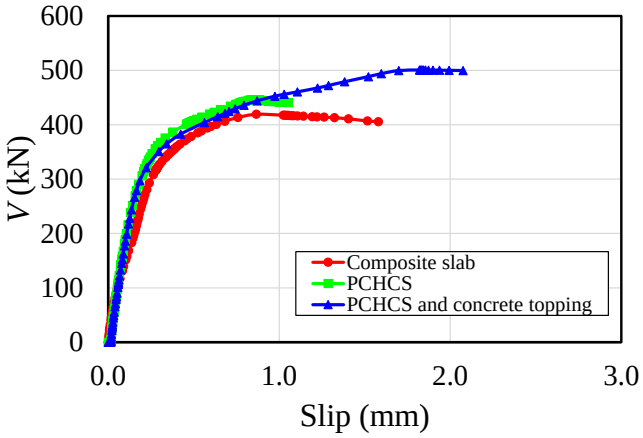

(c) Shear-slip relationship for D_o/d=1.0 and p/D_o=1.3

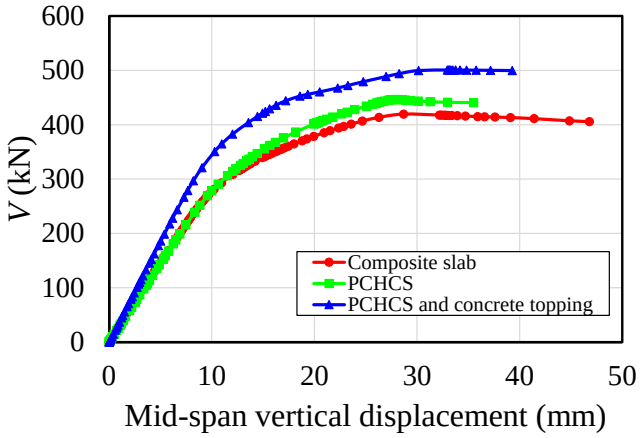

(d) Shear-deflection relationship for D_o/d=1.0 and p/D_o=1.3

Fig. 33: Differences in the behavior of composite cellular beams with slab variation, considering asymmetrical section

In general, for composite cellular beams with composite slab and PCHCS, the asymmetric section showed greater efficiency in terms of shear resistance. On the other hand, considering PCHCS with concrete topping, the symmetrical sections showed greater resistance. This was due to the ultimate behavior being governed by shear connector rupture. **Table 5** shows all the results obtained.

559 **Table 5: Summary of numerical results**

D_o/d	p/D_o	b_{we}/b_w	Symmetric section						Asymmetric section					
			Composite slab		PCHCS		PCHCS and concrete topping		Composite slab		PCHCS		PCHCS and concrete topping	
			V (kN)	Failure	V (kN)	Failure	V (kN)	Failure	V (kN)	Failure	V (kN)	Failure	V (kN)	Failure
0.8	1.2	5.4	309	WPB	316	WPB	354	WPB	441	WPB+PM*	465	WPB+PM*	493	WPB+PM*
	1.3	1.4	321	WPB	325	WPB	362	WPB	430	WPB+PM	455	WPB+PM*	473	PM*
	1.4	2.9	385	WPB	407	WPB	447	WPB	525	PM*	534	WPB+PM	599	PM*
	1.5	1.3	404	WPB	410	WPB	463	WPB	540	WPB+PM	562	WPB+PM*	580	PM*
0.9	1.2	6.2	288	WPB	312	WPB	349	WPB	405	WPB+PM*	452	WPB+PM*	474	WPB+PM*
	1.3	2.3	304	WPB	314	WPB	356	WPB	407	WPB+PM	421	WPB+PM	497	WPB+PM*
	1.4	3.8	383	WPB	412	WPB	469	WPB	524	WPB+PM	546	WPB+PM	586	PM*
	1.5	2.2	387	WPB	404	WPB	467	WPB	540	WPB+PM	550	WPB+PM	600	PM*
1.0	1.2	2.0	229	WPB	233	WPB	278	WPB	323	WPB+PM*	372	WPB+PM*	414	WPB+PM*
	1.3	3.8	301	WPB	334	WPB	391	WPB	419	WPB+PM	446	WPB+PM	501	WPB+PM*
	1.4	1.8	318	WPB	342	WPB	390	WPB	441	WPB+PM	450	WPB+PM	527	WPB+PM*
	1.5	3.5	396	WPB+PM	407	WPB+PM	439	WPB+PM	581	WPB+PM	610	WPB+PM	658	PM*
1.1	1.2	4.6	240	WPB	264	WPB	303	WPB	332	WPB+PM	397	WPB+PM*	404	WPB+PM*
	1.3	1.6	258	WPB	274	WPB	312	WPB	356	WPB+PM	376	WPB+PM	444	WPB+PM
	1.4	3.5	360	WPB+PM	390	WPB+PM	481	PM	500	WPB+PM	531	WPB+PM	574	PM*
	1.5	2.1	389	WPB+PM	391	WPB+PM	442	PM	500	WPB+PM	521	WPB+PM	563	PM*
1.2	1.2	1.8	184	WPB	205	WPB	256	WPB	293	WPB+PM*	327	WPB+PM*	379	WPB+PM*
	1.3	4.0	315	WPB+PM	348	WPB+PM	387	PM	416	WPB+PM	450	WPB+PM	496	WPB+PM
	1.4	2.1	338	VM	336	VM	369	VM	422	VM*	435	WPB+PM	491	PM*
	1.5	1.0	329	VM*	317	WPB+PM	364	WPB+PM	411	VM*	492	PM	514	PM*

560 *Shear connector rupture was observed

5.4. ULTIMATE STRENGTH OF COMPOSITE CELLULAR BEAMS WITH PCHCS VS. DESIGN RECOMENDATIONS

In this section, the numerical results are compared with the existing analytical procedures. Only the results of composite cellular beams with PCHCS and PCHCSCT are considered, since the WPB resistance of composite cellular beams with composite slab has been investigated in Ferreira et al. [7]. It is worth mentioning that, in the authors' conclusion, it was verified that the existing models underestimate the resistance of composite cellular beams, since the calculation models do not take into account the contribution of the concrete slab in the resistance to WPB.

As presented in section 5.3, the WPB was the predominant failure mode. Although WPB+PM has occurred in some situations, WPB is only considered the most critical situation, as presented by Lawson et al. [18]. For this, two calculation recommendations are used; SCI P355 [19] and Steel Design Guide 31 [85] are based on EC4 [29]and ANSI / AISC 360-16 [86]. For the calculation of the WPB resistance, SCI P355 [19] addresses the compressed bar theory (**Eqs. 13-19**):

$$\sigma_{Rk} = \chi f_y \tag{13}$$

$$\chi = \frac{1}{\phi + \sqrt{\phi^2 - \bar{\lambda}^2}} \leq 1.0 \tag{14}$$

$$\phi = 0.5\left[1 + 0.49\left(\bar{\lambda} - 0.2\right) + \bar{\lambda}^2\right] \tag{15}$$

$$\bar{\lambda} = \sqrt{\frac{f_y}{f_{cr,w}}} \tag{16}$$

$$f_{cr,w} = \frac{\pi^2 E}{\lambda_w^2} \tag{17}$$

$$\lambda_w = \frac{l_{eff}\sqrt{12}}{t_w} \quad l_{eff}\sqrt{12}/t_w \tag{18}$$

$$V_{Rk} = \sigma_{Rk} t_w b_w \tag{19}$$

On the other hand, Steel Design Guide 31 [85] is based on the horizontal shear force that acts on the web post, as shown previously in **Fig. 2**. For this, it will be necessary to extract the horizontal shear force from the numerical model (**Eqs 20-21**). This methodology is analogous to that presented in Ferreira et al. [7], as shown in **Fig 34**.

$$V_{h,FE} = \left| \frac{M_{FE(i+1)} - M_{FE(i)}}{d_{eff}} \right| \tag{20}$$

$$d_{ef,comp} = d_g - y_{o,\inf} + 0.5 t_c \tag{21}$$

For the case of four-point bending, a situation in which the global shear is constant, **Eq. (20)** can be replaced by **Eq. (22)**. Thus, the horizontal shear force of the numerical response is compared with the resistant horizontal shear force **(Eqs. 23-29)**.

$$V_{h,FE} = \frac{pV_{FE}}{d_{eff}} \tag{22}$$

$$M_{vh} = 0.9\left(\frac{D_o}{2}\right)V_h \tag{23}$$

$$M_{W,\mathrm{Rk}} = M_{W,e}\left[C1\left(\frac{p}{D_o}\right) - C2\left(\frac{p}{D_o}\right)^2 - C3\right] \tag{24}$$

$$M_{W,e} = \frac{t_w\left(p - D_o + 0.564D_o\right)^2}{6} f_y \tag{25}$$

$$C1 = 5.097 + 0.1464\left(\frac{D_o}{t_w}\right) - 0.00174\left(\frac{D_o}{t_w}\right)^2 \tag{26}$$

$$C2 = 1.441 + 0.0625\left(\frac{D_o}{t_w}\right) - 0.000683\left(\frac{D_o}{t_w}\right)^2 \tag{27}$$

$$C3 = 3.645 + 0.0853\left(\frac{D_o}{t_w}\right) - 0.00108\left(\frac{D_o}{t_w}\right)^2 \tag{28}$$

$$V_{h,\mathrm{Rk}} = \frac{M_{W,e}}{0.45D_o}\left[C1\left(\frac{p}{D_o}\right) - C2\left(\frac{p}{D_o}\right)^2 - C3\right] \tag{29}$$

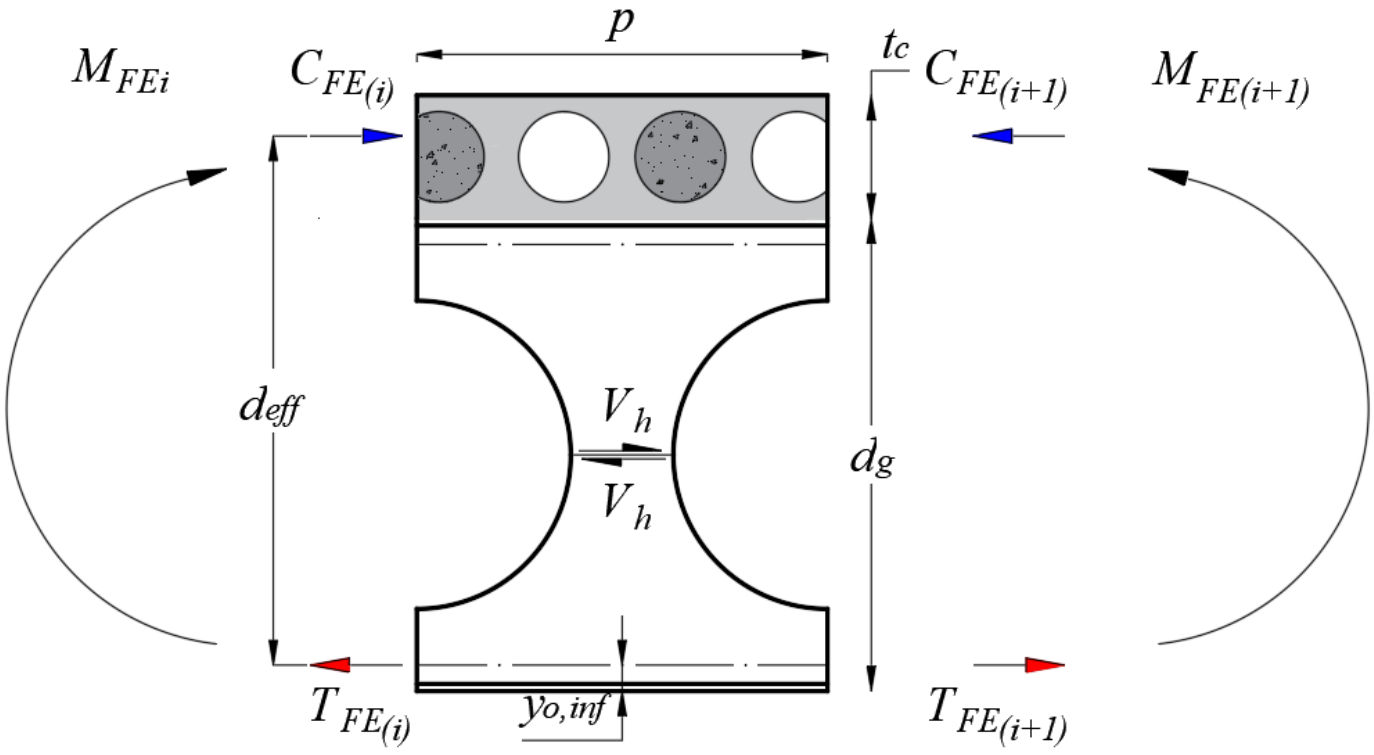

Fig. 34: Scheme for the extraction of the horizontal shear force

Next in **Fig. 35**, the results between the numerical and the calculation models are presented. As expected, both calculation models underestimate the resistance to WPB in composite cellular beams with PCHCS and PCHCSCT. It is worth mentioning that this has been verified previously in Ferreira et al [7], considering composite slabs, and since the strength of composite cellular beams with PCHCS and PCHCSCT presented greater resistance than the resistance of composite cellular beams with composite slabs, as shown in **Fig. 30** and **Fig. 32**, the ratio between the analytical and numerical models tends to be smaller. **Fig. 36** shows the normal distribution of comparisons between analytical and numerical responses.

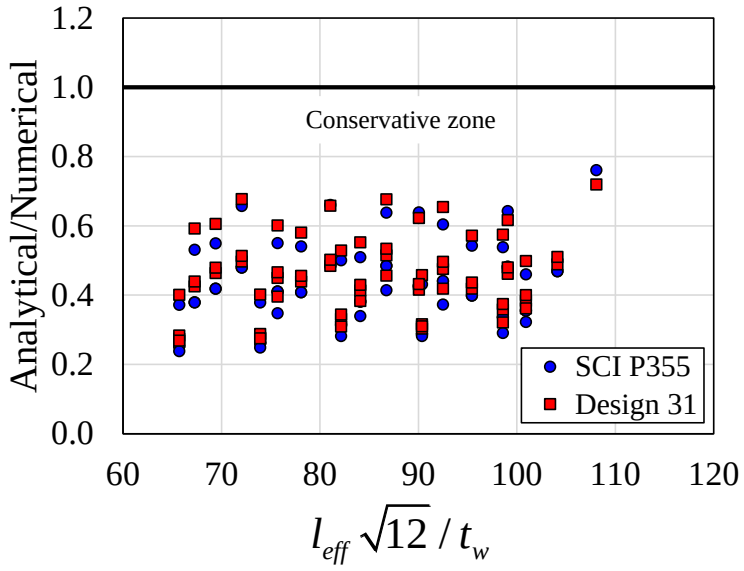

Fig. 35: Analytical vs. numerical response

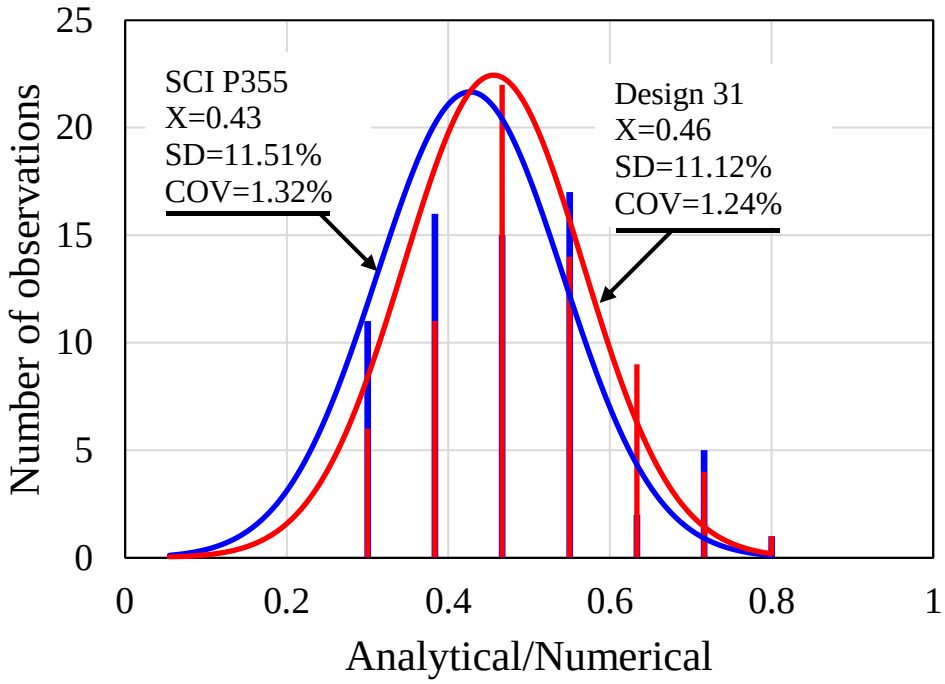

Fig. 36: Statistical analyses

CONCLUSIONS

The present work developed a numerical model capable of predicting the resistance of composite cellular beams with precast hollow core slabs with and without a concrete topping. A parametric study was carried out, considering symmetric, asymmetric sections, as well as key parameters, such as the web-post width and the opening diameter. The models developed were compared with models of composite cellular beams with composite slabs. The failure modes observed were web post buckling (WPB), web post buckling combined with plastic mechanism (WPB+PM), plastic mechanism (PM) and Vierendeel mechanism (VM). In some situations, the shear connector rupture was also observed. This showed that the web post width contributed to the change in the degree of interaction of composite cellular beams. The results showed that the resistance of composite cellular beams is not limited only by the steel cellular profile. In most of the observations, the resistance of composite cellular beams with precast hollow core slabs showed shear resistance equal or greater than the models of composite cellular beams, considering composite slabs. This means that existing calculation models, such as SCI-P355 and Steel Design Guide 31, can be used to design such structural systems. However, the models of composite cellular beams with precast hollow core slabs and concrete topping showed a significant and superior difference when compared with the models of cellular beams associated with composite slabs. Therefore, in this situation, the use of current calculation models can underestimate the strength of composite cellular beams with precast hollow core slabs and concrete topping. This is due to the fact that the hollow core slab with concrete topping presented greater resistance to shear stress.

ACKNOWLEDGMENTS

The authors would like to thank Construção Metálica – Gerdau Aços Brasil for making available the data related to COPPETEC, PEC-18541. This work was supported by the São Paulo Research Foundation (FAPESP) [grant number #2018/22803-1].

REFERENCES

[1] I.M. Ahmed, K.D. Tsavdaridis, The evolution of composite flooring systems: applications, testing, modelling and eurocode design approaches, J. Constr. Steel Res. 155 (2019) 286–300. https://doi.org/10.1016/j.jcsr.2019.01.007.

[2] S. De Nardin, A. El Debs, State of the art of steel–concrete composite structures in Brazil, Proc. Inst. Civ. Eng. - Civ. Eng. 166 (2013) 20–27. https://doi.org/10.1680/cien.2013.166.6.20.

[3] D. Lam, Capacities of headed stud shear connectors in composite steel beams with precast hollowcore slabs, J. Constr. Steel Res. 63 (2007) 1160–1174. https://doi.org/10.1016/j.jcsr.2006.11.012.

[4] F.D. Queiroz, P.C.G.S. Vellasco, D.A. Nethercot, Finite element modelling of composite beams with full and partial shear connection, J. Constr. Steel Res. 63 (2007) 505–521. https://doi.org/10.1016/j.jcsr.2006.06.003.

[5] I.S. Ibrahim, K.S. Elliott, R. Abdullah, A.B.H. Kueh, N.N. Sarbini, Experimental study on the shear behaviour of precast concrete hollow core slabs with concrete topping, Eng. Struct. 125 (2016) 80–90. https://doi.org/10.1016/j.engstruct.2016.06.005.

[6] E. Baran, Effects of cast-in-place concrete topping on flexural response of precast concrete hollow-core slabs, Eng. Struct. 98 (2015) 109–117. https://doi.org/10.1016/j.engstruct.2015.04.017.

[7] F.P.V. Ferreira, C.H. Martins, S. De Nardin, Assessment of web post buckling resistance in steel-concrete composite cellular beams, Thin-Walled Struct. 158 (2021) 106969. https://doi.org/10.1016/j.tws.2020.106969.

[8] P. Panedpojaman, T. Thepchatri, S. Limkatanyu, Novel design equations for shear strength of local web-post buckling in

cellular beams, Thin-Walled Struct. 76 (2014) 92–104. https://doi.org/10.1016/j.tws.2013.11.007.

[9] K.D. Tsavdaridis, C. D'Mello, Web buckling study of the behaviour and strength of perforated steel beams with different novel web opening shapes, J. Constr. Steel Res. 67 (2011) 1605–1620. https://doi.org/10.1016/j.jcsr.2011.04.004.

[10] F. Erdal, M.P. Saka, Ultimate load carrying capacity of optimally designed steel cellular beams, J. Constr. Steel Res. 80 (2013) 355–368. https://doi.org/10.1016/j.jcsr.2012.10.007.

[11] L.F. Grilo, R.H. Fakury, A.L.R. de Castro e Silva, G. de S. Veríssimo, Design procedure for the web-post buckling of steel cellular beams, J. Constr. Steel Res. 148 (2018) 525–541. https://doi.org/10.1016/j.jcsr.2018.06.020.

[12] D. Kerdal, D.A. Nethercot, Failure modes for castellated beams, J. Constr. Steel Res. 4 (1984) 295–315. https://doi.org/10.1016/0143-974X(84)90004-X.

[13] K.F. Chung, T.C.H. Liu, A.C.H. Ko, Investigation on vierendeel mechanism in steel beams with circular web openings, J. Constr. Steel Res. 57 (2001) 467–490. https://doi.org/10.1016/S0143-974X(00)00035-3.

[14] P. Panedpojaman, T. Rongram, Design Equations for Vierendeel Bending of Steel Beams with Circular Web Openings, World Congr. Eng. 2014. II (2014) 0–5.

[15] R. Redwood, S.H. Cho, Design of steel and composite beams with web openings, J. Constr. Steel Res. 25 (1993) 23–41. https://doi.org/10.1016/0143-974X(93)90050-3.

[16] K.D. Tsavdaridis, C. D'Mello, Vierendeel Bending Study of Perforated Steel Beams with Various Novel Web Opening Shapes through Nonlinear Finite-Element Analyses, J. Struct. Eng. 138 (2012) 1214–1230. https://doi.org/10.1061/(asce)st.1943-541x.0000562.

[17] R.M. Lawson, J.B.P. Lim, S.O. Popo-Ola, Pull-out forces in shear connectors in composite beams with large web openings, J. Constr. Steel Res. 87 (2013) 48–59. https://doi.org/10.1016/j.jcsr.2013.03.025.

[18] R.M.M. Lawson, J. Lim, S.J.J. Hicks, W.I.I. Simms, Design of composite asymmetric cellular beams and beams with large web openings, J. Constr. Steel Res. 62 (2006) 614–629. https://doi.org/10.1016/j.jcsr.2005.09.012.

[19] R.M. Lawson, S.J. Hicks, Design of composite beams with large web openings, The Steel Construction Institute, 2011.

[20] S.S. Fares, J. Coulson, D.W. Dinehart, AISC Steel Design Guide 31: Castellated and Cellular Beam Design, American Institute of Steel Construction, 2016.

[21] F.P.V. Ferreira, C.H. Martins, S. De Nardin, Advances in composite beams with web openings and composite cellular beams, J. Constr. Steel Res. 172 (2020) 106182. https://doi.org/10.1016/j.jcsr.2020.106182.

[22] D. Lam, Composite steel beams using precast concrete hollow core floor slabs, 1998. Ph.D. thesis. University of Nottingham, 1998.

[23] E. Ellobody, D. Lam, Modelling of headed stud in steel-precast composite beams, Steel Compos. Struct. 2 (2002) 355–378. https://doi.org/10.12989/scs.2002.2.5.355.

[24] D. Lam, K.S. Elliott, D.A. Nethercot, Experiments on composite steel beams with precast concrete hollow core floor slabs, Proc. Inst. Civ. Eng. - Struct. Build. 140 (2000) 127–138. https://doi.org/10.1680/stbu.2000.140.2.127.

[25] D. Lam, K.S. Elliott, D.A. Nethercot, Parametric study on composite steel beams with precast concrete hollow core floor slabs, J. Constr. Steel Res. 54 (2000) 283–304. https://doi.org/10.1016/S0143-974X(99)00049-8.

[26] D. Lam, Designing composite beams with precast hollowcore slabs to Eurocode 4, Adv. Steel Constr. 3 (2007) 594–606. https://doi.org/10.18057/IJASC.2007.3.2.

[27] S.J. Hicks, R.M. Lawson, Design of composite beams using precast concrete slabs., The Steel Construction Institute, 2003.

[28] G.H. Gouchman, Design of composite beams using precast concrete slabs in accordance with EUROCODE 4, The Steel Construction Institute, 2014.

[29] EUROPEAN COMMITTEE FOR STANDARDIZATION, EN 1994-1-1: Eurocode 4 – Design of composite steel and concrete structures – Part 1-1: General rules for buildings., (2004).

[30] E.M. Batista, A. Landesmann, Análise experimental de vigas mistas de aço e concreto compostas por lajes alveolares e perfis laminados. COPPETEC, PEC-18541, (2016).

[31] F.P.V. Ferreira, C.H. Martins, S. De Nardin, A parametric study of steel-concrete composite beams with hollow core slabs and concrete topping, Structures. 28 (2020) 276–296. https://doi.org/10.1016/j.istruc.2020.08.045.

[32] C.J. Granade, An investigation of composite beams having large rectangular openings in their webs, 1968. Partial M.Sc. thesis. University of Alabama, 1968.

[33] W.C. Clawson, D. Darwin, Composite beams with web openings, ASCE J. Struct. Div. 108 (1982) 145–162.

[34] W.C. Clawson, D. Darwin, Strength of composite beams at web openings, ASCE J. Struct. Div. 108 (1982) 623–641.

[35] S.H. Cho, An investigation on the strength of composite beams with web openings, 1982. M.Sc. thesis. Hanyang University, 1982.

[36] R. Narayanan, R.I.M. Al-Amery, T.M. Roberts, Shear strength of composite plate girders with rectangular web cut-outs, J. Constr. Steel Res. 12 (1989) 151–166. https://doi.org/10.1016/0143-974X(89)90030-8.

[37] T.M. Roberts, R.I.M. Al-Amery, Shear strength of composite plate girders with web cutouts, J. Struct. Eng. 117 (1991) 1897–1910. https://doi.org/10.1061/(ASCE)0733-9445(1991)117:7(1897).

[38] D.M. Todd, P.B. Cooper, Strength of composite beams with web openings, ASCE J. Struct. Div. 106 (1980) 431–444.

[39] C.M. DONOGHUE, Strength of composite beams with web openings, ASCE J. Struct. Div. 108 (1982) 2652–2667.

[40] R.G. Redwood, P.K. Wong, Web holes in composite beams with steel deck, in: Can. Struct. Eng. Conf. -1982, Canadian Steel Construction Council, Ontario, Toronto, 1982: pp. 1–41.

[41] E.H. Fahmy, Analysis of composite beams with rectangular web openings, J. Constr. Steel Res. 37 (1996) 47–62. https://doi.org/10.1016/0143-974X(95)00022-N.

[42] M.A. Benitez, D. Darwin, R.C. Donahey, Deflections of composite beams with web openings, J. Struct. Eng. 124 (1998) 1139–1147. https://doi.org/10.1061/(ASCE)0733-9445(1998)124:10(1139).

[43] K.. Chung, R.. Lawson, Simplified design of composite beams with large web openings to Eurocode 4, J. Constr. Steel Res. 57 (2001) 135–164. https://doi.org/10.1016/S0143-974X(00)00011-0.

[44] R.G. Redwood, G. Poumbouras, Tests of composite beams with web holes, Can. J. Civ. Eng. 10 (1983) 713–721. https://doi.org/10.1139/l83-100.

[45] R.C. Donahey, D. Darwin, Web openings in composite beams with ribbed slabs, J. Struct. Eng. 114 (1988) 518–534. https://doi.org/10.1061/(ASCE)0733-9445(1988)114:3(518).

[46] R.M. Lawson, K.F. Chung, A.M. Price, Tests on composite beams with large web openings to justify existing design methods, Struct. Enginee. 70 (1992) 1–7.

[47] S.H. Cho, R.G. Redwood, Slab behavior in composite beams at openings. II: tests and verification, J. Struct. Eng. 118 (1992) 2304–2322. https://doi.org/10.1061/(ASCE)0733-9445(1992)118:9(2304).

[48] J.W. Park, C.H. Kim, S.C. Yang, Ultimate Strength of Ribbed Slab Composite Beams with Web Openings, J. Struct. Eng. 129 (2003) 810–817. https://doi.org/10.1061/(asce)0733-9445(2003)129:6(810).

[49] R.G. Redwood, G. Poumbouras, Analysis of composite beams with web openings, J. Struct. Eng. 110 (1984) 1949–1958. https://doi.org/10.1061/(ASCE)0733-9445(1984)110:9(1949).

[50] D. Darwin, R.C. Donahey, LRFD for composite beams with unreinforced web openings, J. Struct. Eng. 114 (1988) 535–552. https://doi.org/10.1061/(ASCE)0733-9445(1988)114:3(535).

[51] S.H. Cho, R.G. Redwood, Slab behavior in composite beams at openings. I: analysis, J. Struct. Eng. 118 (1992) 2287–2303. https://doi.org/10.1061/(ASCE)0733-9445(1992)118:9(2287).

[52] K.D. Tsavdaridis, C. D'Mello, M. Hawes, Experimental study of ultra shallow floor beams (USFB) with perforated steel sections, in: 11th Nord. Steel Constr. Conf. 2009 (NSCC 2009), Malmö, Sweden, 2009: pp. 312–319.

[53] C. Maraveas, Z. Fasoulakis, K.D. Tsavdaridis, Fire Resistance of Axially Restrained and Partially Unprotected Ultra Shallow Floor Beams (USFB) and DELTABEAM Composite Beams, in: Appl. Fire Eng. - Proc. Int. Conf. Appl. Struct. Fire Eng. Conf., Manchester, U.K, 2017: pp. 7–8.

[54] R. Kansinally, K.. Tsavdaridis, Vibration Response of USFB Composite Floors, in: 13th Nord. Steel Constr. Conf. (NSCC

2015), Tampere, Finland, 2015: pp. 187–188.

[55] K.D. Tsavdaridis, C. D'Mello, B.Y. Huo, Experimental and computational study of the vertical shear behaviour of partially encased perforated steel beams, Eng. Struct. 56 (2013) 805–822. https://doi.org/10.1016/j.engstruct.2013.04.025.

[56] C. Maraveas, K.D. Tsavdaridis, A. Nadjai, Fire Resistance of Unprotected Ultra Shallow Floor Beams (USFB): A Numerical Investigation, Fire Technol. 53 (2017) 609–627. https://doi.org/10.1007/s10694-016-0583-5.

[57] O. Hechler, C. Müller, G. Sedlacek, Investigations on Beams with Multiple Regular Web Openings, in: Compos. Constr. Steel Concr. V, American Society of Civil Engineers, Reston, VA, 2006: pp. 270–281. https://doi.org/10.1061/40826(186)26.

[58] C. MÜLLER, O. HECHLER, A. BUREAU, D. BITAR, D. JOYEUX, L.G. CAJOT, T. DEMARCO, R.M. LAWSON, S. HICKS, P. DEVINE, O. LAGERQVIST, E. HEDMAN-PÉTURSSON, E. UNOSSON, M. FELDMANN, Large web openings for service integration in composite floors. Technical Steel Research. European Comission, Contract No 7210-PR/315. Final report, (2006).

[59] A. Nadjai, Performance of cellular composite floor beams at ambient temperature, 2005.

[60] T. Sheehan, X. Dai, D. Lam, E. Aggelopoulos, M. Lawson, R. Obiala, Experimental study on long spanning composite cellular beam under flexure and shear, J. Constr. Steel Res. 116 (2016) 40–54. https://doi.org/10.1016/j.jcsr.2015.08.047.

[61] A. Nadjai, O. Vassart, F. Ali, D. Talamona, A. Allam, M. Hawes, Performance of cellular composite floor beams at elevated temperatures, Fire Saf. J. 42 (2007) 489–497. https://doi.org/10.1016/j.firesaf.2007.05.001.

[62] Dassault Systèmes Simulia, Abaqus 6.18, (2016).

[63] M. Sjaarda, T. Porter, J.S. West, S. Walbridge, Fatigue Behavior of Welded Shear Studs in Precast Composite Beams, J. Bridg. Eng. 22 (2017) 04017089. https://doi.org/10.1061/(ASCE)BE.1943-5592.0001134.

[64] E. El-Lobody, D. Lam, Finite Element Analysis of Steel-Concrete Composite Girders, Adv. Struct. Eng. 6 (2003) 267–281. https://doi.org/10.1260/136943303322771655.

[65] F.P.V. Ferreira, A. Rossi, C.H. Martins, Lateral-torsional buckling of cellular beams according to the possible updating of EC3, J. Constr. Steel Res. 153 (2019) 222–242. https://doi.org/10.1016/j.jcsr.2018.10.011.

[66] F.P.V. Ferreira, C.H. Martins, LRFD for Lateral-Torsional Buckling Resistance of Cellular Beams, Int. J. Civ. Eng. 18 (2020) 303–323. https://doi.org/10.1007/s40999-019-00474-7.

[67] A. Rossi, F.P.V. Ferreira, C.H. Martins, E.C. Mesacasa Júnior, Assessment of lateral distortional buckling resistance in welded I-beams, J. Constr. Steel Res. 166 (2020) 105924. https://doi.org/10.1016/j.jcsr.2019.105924.

[68] F.P.V. Ferreira, C.H. Martins, S. De Nardin, Sensitivity Analysis of Composite Cellular Beams to Constitutive Material Models and Concrete Fracture, Int. J. Struct. Stab. Dyn. (2020) 2150008. https://doi.org/10.1142/S0219455421500085.

[69] S. Chen, Y. Jia, Numerical investigation of inelastic buckling of steel–concrete composite beams prestressed with external tendons, Thin-Walled Struct. 48 (2010) 233–242. https://doi.org/10.1016/j.tws.2009.10.009.

[70] W.-B. Zhou, W.-J. Yan, Refined nonlinear finite element modelling towards ultimate bending moment calculation for concrete composite beams under negative moment, Thin-Walled Struct. 116 (2017) 201–211. https://doi.org/10.1016/j.tws.2017.02.011.

[71] A. Hillerborg, M. Modéer, P.-E. Petersson, Analysis of crack formation and crack growth in concrete by means of fracture mechanics and finite elements, Cem. Concr. Res. 6 (1976) 773–781. https://doi.org/10.1016/0008-8846(76)90007-7.

[72] J. Lubliner, J. Oliver, S. Oller, E. Oñate, A plastic-damage model for concrete, Int. J. Solids Struct. 25 (1989) 299–326. https://doi.org/10.1016/0020-7683(89)90050-4.

[73] J. Lee, G.L. Fenves, Plastic-Damage Model for Cyclic Loading of Concrete Structures, J. Eng. Mech. 124 (1998) 892–900. https://doi.org/10.1061/(ASCE)0733-9399(1998)124:8(892).

[74] T. Yu, J.G. Teng, Y.L. Wong, S.L. Dong, Finite element modeling of confined concrete-I: Drucker–Prager type plasticity model, Eng. Struct. 32 (2010) 665–679. https://doi.org/10.1016/j.engstruct.2009.11.014.

[75] D.J. CARREIRA, K.H. CHU, Stress-Strain Relationship for Plain Concrete in Compression, ACI J. Proc. 82 (1985) 797–804. https://doi.org/10.14359/10390.

[76] D.J. Carreira, K.H. Chu, Stress-Strain Relatonship for Reinforced Concrete in Tension., J. Am. Concr. Inst. 83 (1986) 21–28.

[77] D.L. Araújo, M.W.R. Sales, S.M. Paulo, A.L.H.C. El Debs, Headed steel stud connectors for composite steel beams with precast hollow-core slabs with structural topping, Eng. Struct. 107 (2016) 135–150. https://doi.org/10.1016/j.engstruct.2015.10.050.

[78] X. Yun, L. Gardner, Stress-strain curves for hot-rolled steels, J. Constr. Steel Res. 133 (2017) 36–46. https://doi.org/10.1016/j.jcsr.2017.01.024.

[79] S. Wijesiri Pathirana, B. Uy, O. Mirza, X. Zhu, Flexural behaviour of composite steel–concrete beams utilising blind bolt shear connectors, Eng. Struct. 114 (2016) 181–194. https://doi.org/10.1016/j.engstruct.2016.01.057.

[80] U. Katwal, Z. Tao, M.K. Hassan, B. Uy, D. Lam, Load sharing mechanism between shear studs and profiled steel sheeting in push tests, J. Constr. Steel Res. 174 (2020) 106279. https://doi.org/10.1016/j.jcsr.2020.106279.

[81] X. Liu, M.A. Bradford, Q.-J. Chen, H. Ban, Finite element modelling of steel–concrete composite beams with high-strength friction-grip bolt shear connectors, Finite Elem. Anal. Des. 108 (2016) 54–65. https://doi.org/10.1016/j.finel.2015.09.004.

[82] S. Guezouli, A. Lachal, Numerical analysis of frictional contact effects in push-out tests, Eng. Struct. 40 (2012) 39–50. https://doi.org/10.1016/j.engstruct.2012.02.025.

[83] Y. Chen, Innovative shear connections for the accelerated construction of composite bridges, 2013. Ph.D. thesis. University of Waterloo, 2013.

[84] T.N.H. Nguyen, K.H. Tan, T. Kanda, Investigations on web-shear behavior of deep precast, prestressed concrete hollow core slabs, Eng. Struct. 183 (2019) 579–593. https://doi.org/10.1016/j.engstruct.2018.12.052.

[85] Sameer S. Fares, J. Coulson, David W. Dinehart, Castellated and Cellular Beam Design 31, Am. Inst. Steel Constr. (2016).

[86] American Institute of Steel Construction, ANSI/AISC 360-16 - Specification for structural steel buildings., (2016).

Composite action on web post buckling shear resistance of composite cellular beams with PCHCS and PCHCSCT

Felipe Piana Vendramell Ferreira*[a], Konstantinos Daniel Tsavdaridis[b], Carlos Humberto Martins[c], Silvana De Nardin[a]

[a]Department of Civil Engineering, Federal University of São Carlos, Rod. Washington Luiz, km 235, São Carlos, São Paulo, Brazil.

[b]School of Civil Engineering, Faculty of Engineering and Physical Sciences, University of Leeds, Woodhouse Lane, LS2 9JT Leeds, UK.

[c]Department of Civil Engineering, State University of Maringá, Av. Colombo nº 5790, Maringá, Paraná, Brazil.

*Corresponding author

E-mail address: fpiana@live.com (F. P. V. Ferreira), K.Tsavdaridis@leeds.ac.uk (K. D. Tsavdaridis), chmartins@uem.br (C. H. Martins), snardin@ufscar.br (S. De Nardin)

Abstract

This paper aims to study the composite action on web post buckling (WPB) resistance of composite cellular beams with precast hollow core slab (PCHCS) units and with precast hollow core slab units with concrete topping (PCHCSCT). Geometrical and material non-linear analyses are performed. A parametric study is developed, varying the opening diameter, the web post width and the shear studs spacing, with single and double row. It was found that the models with double row of shear studs showed global shear resistance greater than or equal to the models with only one row. For models with PCHCS, in some analyses there was a reduction in global shear resistance due to the absence of shear studs in the second opening, close to the support. For PCHCSCT models, there was an increase in the global shear resistance, in comparison with PCHCS models. However, in most of these models, the shear stud rupture occurred. Finally, the WPB models were compared with a simplified equation that take into account the global shear resistance due to buckling, composite action and Vierendeel bending. The average, standard deviation and variation value of the ratio between the analytical and numerical models were 0.833, 12.47% and 1.55%, respectively.

Keywords: Shear studs; Cellular beams; Precast hollow core slabs; Global shear force; Geometrical nonlinear analyses.

NOTATION

The following symbols are used in this paper:

CT Concrete Topping

PCHCS Precast hollow core slab

PCHCSCT Precast hollow core slab with concrete topping

VM Vierendeel mechanism

*VM** Vierendeel mechanism combined with shear stud rupture

WPB+PM Web post buckling combined with plastic mechanism

*WPB+PM** Web post buckling combined with plastic mechanism and shear stud rupture

A_T the area of the tee

A_{wT} the web area of the tee

b_f the width of the flange

b_w the width of the web post

b_{we} the width of the end post

C the axial compressive resistance of slab;

D_o the opening diameter

d the depth of parent section;

d_{sc} the diameter of shear stud;

d_g the depth of cellular beam

f_c the concrete compressive cylinder strength

$f_{cr,w}$ the buckling stress acting across the web-post

f_t the concrete tension strength

f_u the ultimate strength of cellular beam

f_y the yield strength of cellular beam

g gap (transverse distance between slab panels)

h_c the depth of concrete above decking profile

h_{eff} the effective depth of cellular section between centroids of the tees

h_s the total depth of slab

K_c the ratio of the second stress invariant on the tensile meridian to that on the compressive meridian, $0.5 \le K_c \le 1.0$

k the number of shear stud rows

L the length of composite cellular beam

L_e the distance between points of zero bending

l_o the opening length

l_{eff} the effective length of web-post

n the number of shear studs for $L/2$

n_f the number of shear studs for full shear connection

P_{sc} the resistance of shear stud

p the length between the opening diameter centers

s the shear stud spacing

t_f the thickness of the flange

t_w the thickness of the web

V the global shear force

$V_{pl,T}$ the plastic shear resistance of tee

V_{VC} the shear resistance due to composite action

V_{WPB} the web post buckling shear resistance

z_{pl} the depth of the plastic neutral axis of tee from outer face of flange

y_t the depth of the geometric axis of tee from outer face of flange

β_c the dimensionless constant in Eqs. (1-2)

ε strain

ε_c the compressive strain

ε_t the tensile strain

η $2n/n_f$

λ_0 the reduced slenderness factor

λ_w the web slenderness ratio

μ the viscosity parameter that represents the relaxation time

ξ the eccentricity (defines the rate at which the function approaches the asymptote, the default value is 0.1)

σ stress

σ_{b0} the initial equibiaxial compressive yield stress

σ_{c0} the initial uniaxial compressive yield stress

χ the reduction factor

Ψ the dilation angle

1. INTRODUCTION

Cellular beams are manufactured from a parent section that goes through the processes of thermal cutting, expansion and welding (**Fig. 1**). The result of manufacture is a beam with expanded section and periodical circular web openings. The cross-section expansion provides greater flexural stiffness, and the presence of openings favors air flow in closed environments as well as the passage of ducts for the integration of services. The composite cellular beams are able to span between 12m and 20m [1,2]. Solid or composite slabs have disadvantages, such as the high operational cost of welding the shear studs, and the curing time. Thus, to reduce some of these limitations, the use of PCHCS is an alternative [3]. Generally, in the construction buildings with PCHCS, a concrete topping (CT) is made to provide a smooth and uniform finish. The CT is 40 to 100 mm thick, of strength between 25 and 40 MPa, and a small amount of reinforcement to control the shrinkage [4,5].

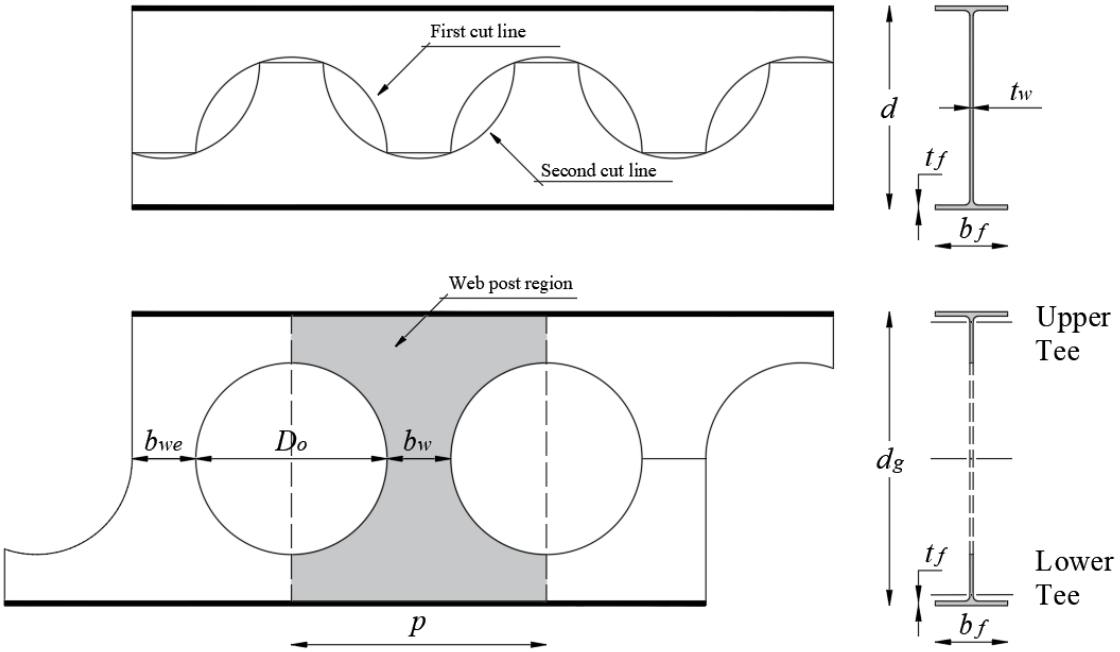

Fig. 1: Cellular beams manufacturing process [6]

The resistance of composite cellular beams is governed by slab failure modes, such as cracking or crushing, with cellular beam failure modes, such as web post buckling (WPB) and Vierendeel mechanism (VM) [6]. The WPB becomes critical when the web post width is reduced [7]. This phenomenon is characterized by a lateral displacement with torsion at the web post. The WPB resistance depends on geometric characteristics of the cellular beam, such as the opening diameter, the web post width and the web thickness [7–11]. The VM occurs when the tees reach the yield strength due to the combination of normal and tangential stresses. It is a phenomenon characterized by the distortion and formation of plastic hinges in regions close to the opening [11–13]. In the case of composite cellular beams, the main parameters that affect this structural behavior are the web thickness, the opening diameter, and the number of shear studs above the critical opening length (l_o) (**Fig. 2**), which is known as local composite action between the upper tee and slab [1,11,14]. For cellular beams, the critical opening length is equal $0.45D_o$ [1,15]. The shear studs are the mechanical devices most commonly used in construction. This is due to its flexible behavior, which allows slipping between the concrete slab and the steel profile before reaching the failure [16].

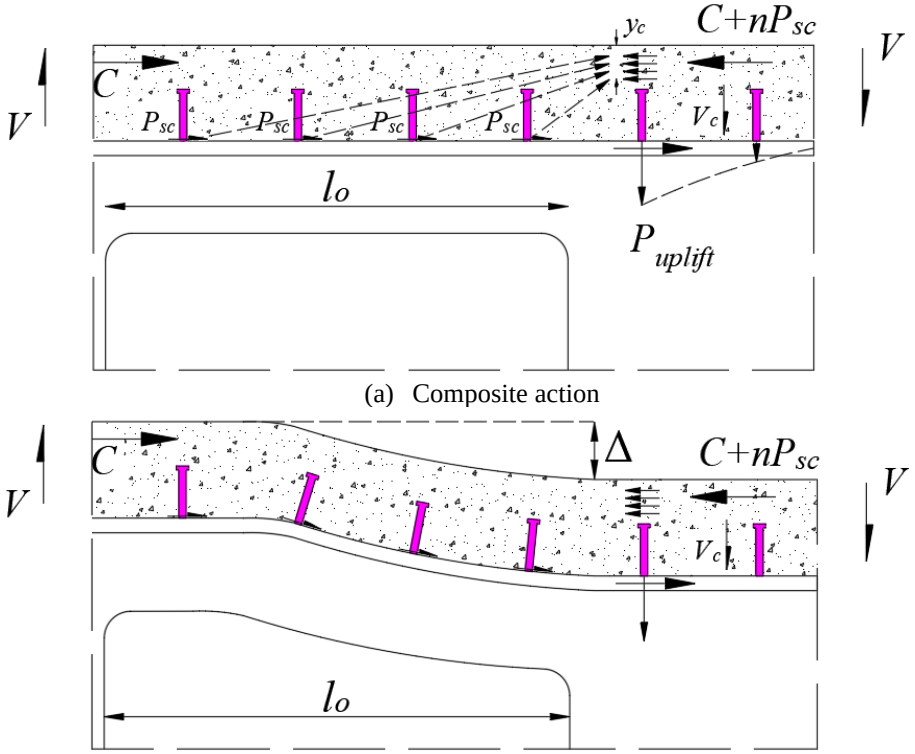

(a) Composite action

(b) Effects of flexibility at a long opening.

Fig. 2: Composite action of upper tee and slab, adapted from [1]

On the calculation and design of composite cellular beams, there are currently two recommendations: SCI P355 [15] and Steel Design Guide 31 [17], which are based on EC4 [18] and ANSI/AISC 360-16 [19], respectively. Both publications are aimed in composite cellular beams with steel-concrete composite slabs, condition in which the shear stud positions are limited by the position of the rib. The SCI P355 [15] recommendations considers the influence of shear studs in checking the bending (full or partial interaction), and in the VM resistance, as shown in **Fig. 2**. On the other hand, the Steel Design Guide 31 [17] considers the shear studs in checking the bending. Another project recommendations on cellular beams was presented by the Centre Technique Industriel de la Construction Métallique (CTICM) [20–22], and it is based on EC3 [23]. These calculation procedures were introduced in the ACB+ software for ArcelorMittal [24]. Verweij [21] described that the method is the most advanced[1], however, the coefficients for calculating the critical forces in the web-post are not available because they are property of ArcelorMittal.

There are studies in the literature that investigated the influence of the shear studs allocated above the opening length in composite beams with web openings [25–29]. However, such studies focused on composite beams with a single rectangular web opening, which is a different structural system from that with periodical web openings, as is the case with composite cellular beams (**Fig. 1**). In addition, the previous studies addressed only steel-concrete composite slabs. Ferreira et al. [30] developed a finite element model of composite cellular beams with PCHCS and PCHCSCT. However, the influence of composite action on resistance has not been investigated. This paper aims to study the shear studs spacing on global shear resistance of composite cellular beams with PCHCS and PCHCSCT. A numerical model is developed using the finite element method. A parametric study is carried out, varying the key parameters of the cellular beams, such as the web-post width and the opening diameter, as well as the spacing

[1] The method was based on a series of tests and numerical modeling.

between the shear studs in 150mm, 300mm and 450mm, with a single and double row. 240 geometrical and material non-linear analyses are performed. The composite action is studied, and the global shear force that causes the WPB is investigated as a function of spacing and the number of shear studs. The results are discussed, according to the parameters studied.

2. BACKGROUND

The studies of the flexural behavior of composite beams with PCHCS started with Lam [31]. Later, several studies were published by the author [32–36]. Lam et al. [35] presented four-point bending results of composite beams with PCHCS. The authors observed the ductile failure, which can be controlled by the appropriate use of transverse reinforcement. Lam et al. [36] complemented the previous study with parametric finite element analyses. The numerical modeling results allowed the determination of the effective width of the PCHCS. Until then, no results had been published on the influence of the shear studs, the infill concrete and the gap (g), which is the distance between the slab panels, on the flexural behavior. Ellobody and Lam [32] investigated such parameters with pushout tests. The authors observed that the resistance of the shear stud increased with the increase of the gap, for the transverse reinforcement diameter less than 16 mm. However, this increase was observed for gap widths of up to 80 mm. Lam [33] presented pushout tests, in order to investigate the influence of the slab cutting angle (chamfered or squared), the transverse reinforcement rate and the shear stud diameter. Transverse reinforcements were the dominant factor affecting the force-slip relationship. In 2003, the Steel Construction Institute (SCI) published the SCI P287 [37], which was a manual containing design recommendations for composite beams with PCHCS. Subsequently, the SCI P401 [38], an update of the previous document, was published. The updated document collects recommendations of minimum dimensions, considering the ultimate and service limit states in the construction phase for cases of full and partial interaction.

In view of the concrete topping influence, Baran [4] investigated the flexural behavior of PCHCSCT. The results showed improvements in the cracking moment, and in the initial stiffness of the PCHCS. Ibrahim et al. [5] conducted an experimental study of the shear-bending resistance of PCHCSCT. The authors observed that the ideal condition for the interface between the PCHCS and CT, aiming greater stiffness and resistance to shear, was the rough and wet. Araújo et al. [16] investigated the behavior of shear studs in composite beams with PCHCSCT by pushout tests. According to the authors, there were some changes in the resistance of each connector due to the presence of the CT. Batista and Landesmann [39] tested composite beams with PCHCSCT by four-point bending. The results showed similar collapse mode, i.e. the cracks propagated along the width of the PCHCSCT, extending from the side face of the slab to the region of connection with the steel profile; a factor that caused the stiffness of the composite beam to be reduced. Ferreira et al. [40] conducted a parametric study in composite beams with PCHCS and PCHCSCT. The authors concluded that the CT increased the initial stiffness of the composite beams, as well as its resistance, according to [4,5]. From the background exposed so far, it appears that studies of composite beams with PCHCS and PCHCSCT are quite recent.

The initial studies involving composite beams with web openings examined beams with a single rectangular opening formed by solid [41–48] or composite slabs [25–29,49–55]. Several studies have investigated the behavior of the steel-concrete interface as a function of the shear studs. Regarding the composite beams with rectangular web opening and solid slab, Todd and

Cooper [46] presented a calculation methodology to estimate the resistance of composite beams considering full interaction between steel-concrete interface. The authors' model underestimated the resistance of composite beams with rectangular web opening, when compared with Granade's tests results [41]. In Narayanan et al. [44], the shear resistance of composite girders with web rectangular openings was investigated. The results showed that if there is an adequate connection at the steel-concrete interface, the shear resistance of the composite girders with rectangular web openings would considerably increase the resistance of the composite action.

In the matter of the composite beams with rectangular web openings and composite slabs (with trapezoidal steel formwork), Redwood and Poumbouras [25] studied the need for shear studs, in the steel-concrete interface, allocated in the opening length. It was found that the absence of shear studs in the opening length significantly reduced the resistance of the composite beam with rectangular web openings. Subsequently, Redwood and Poumbouras [26] presented a model for the calculation of the resistance, considering the increase in compression stresses due to the slip caused by the deformation of the shear studs. Such methodology was shown to be conservative when compared to previous experimental results [25]. Donahey and Darwin [27] investigated the effects of the moment-shear ratio, quantity and position of the shear studs, orientation and position of the steel formwork. The results showed that when the number of connectors was increased above the opening, the resistance of the composite action was also increased. Cho and Redwood [28] presented a methodology capable of estimating the resistance of composite beams with rectangular web openings, considering the shear studs above the opening region as tensioned elements. This methodology was based on the truss concept. According to the authors, the basic concept of this analogy was that after cracking, the concrete carried a set of compression stresses in diagonals and the reinforcement tensile stresses. This approach related the shear resistance to the location of the shear studs. Subsequently, Cho and Redwood [29] found through tests that the shear studs positioned in the opening length were responsible for the contribution of the concrete slab in the shear resistance. It has been observed so far, that the studies which addressed the position of the shear studs considered only the composite beams with rectangular web openings. More information about these previous studies can be found in Ferreira et al. [56].

Regarding studies of composite cellular beams with periodical circular openings web openings (**Fig. 1**), Müller et al. [57] presented tests and parametric studies. According to the authors, the resistance of the cellular beam was preponderant, since the failure was achieved by the WPB. The models presented by Nadjai [58] and Nadjai et al. [59] had the ultimate resistance governed by the WPB; a conclusion similar to the models of Müller et al. [57]. Sheehan et al. [60] tested composite cellular beams with long spans. The authors observed that the composite cellular beams resisted 3.4 times the estimated design load, despite the interaction degree is considerably less than the minimum required by EC4 [18]. EC4 makes [18] recommendations on the minimum interaction degree for composite beams with spans less than 25m, considering symmetrical (**Eq. 1**) and asymmetric (**Eq. 2**) steel sections:

$$\eta \geq 1 - \left(\frac{355}{f_y}\right)\left(0.75 - 0.03L_e\right), \quad \eta \geq 0.4 \tag{1}$$

$$\eta \geq 1-\left(\frac{355}{f_y}\right)\left(0.3-0.015L_e\right), \quad \eta \geq 0.4 \tag{2}$$

Ferreira et al. [6] investigated the WPB resistance of composite cellular beams and verified the influence of the composite slab and the end-post width (b_{we}) on the resistance. The authors concluded that the existing procedures underestimate the WPB resistance. Ferreira et al. [61] complemented the previous study, considering buckling and post-buckling analyses. The authors verified the modes of deformation of the composite cellular beams, and concluded that for asymmetric sections, the web post buckling can be characterized by the formation of a C-shaped buckling curvature. Ferreira et al. [30] presented a finite element model which is capable of predicting the resistance of composite cellular beams with PCHCS and PCHCSCT. In this study, the resistance of composite cellular beams with PCHCS and PCHCSCT was compared with the resistance of composite cellular beams with composite slabs. According to the authors, the models with PCHCS and PCHCST showed greater resistance. Consequently, there are no yet studies that have investigated the influence of the shear studs positioning on the shear resistance of composite cellular beams with PCHCS and PCHCSCT.

3. FINITE ELEMENT MODEL: VALIDATION STUDY

In the present study is used the same numerical model that was developed and validated by Ferreira et al. [30]. Therefore, in this section the validation results are presented briefly. More information regarding the validation study can be found in [30]. The experimental studies and the validation results are presented in **Table 1** and **Fig. 3**, respectively.

Table 1: Models (in mm, MPa and GPa) [30]

Model	Ref	d or d_g	D_o	p	Upper tee					Lower tee				
					b_f	t_f	t_w	f_y (flange/web)	f_u (flange/web)	b_f	t_f	t_w	f_y (flange/web)	f_u (flange/web)
CCB1	[58]	575	375	500	141.8	8.6	6.4	312	438.5	141.8	8.6	6.4	312	438.5
CCB2	[58]	630	450	630	141.8	8.6	6.4	312	438.5	152.4	10.9	7.6	312	438.5
CCB3	[57]	555	380	570	180	13.5	8.6	451/489	541/587	180	13.5	8.6	451/489	541/587
CCB4	[57]	485	380	570	150	10.7	7.1	407/467	524/588	300	21.5	12	453/488	519/582
CB1	[62]	355	-	-	171.5	11.5	7.4	310/355	$1.3f_y$	171.5	11.5	7.4	310/355	$1.3f_y$
CB2	[62]	355	-	-	171.5	11.5	7.4	310/355	$1.3f_y$	171.5	11.5	7.4	310/355	$1.3f_y$
CB3	[39]	299	-	-	306	11	11	345	450	306	11	11	345	450

Model	Ref	Slab		Reinforcement		b	L	L_p
		f_c	$f_{c,PCHCS}$	φ	f_s			
CCB1	[58]	28.6	-	-	-	1200	4500	1750
CCB2	[58]	28.6	-	-	-	1200	4500	2250
CCB3	[57]	33.6	-	-	-	1800	6840*	1140/2850
CCB4	[57]	24.0	-	-	-	1800	6840*	1140/2850
CB1	[62]	25.6	40	16	585	1665	5700	1500
CB2	[62]	20.8	40	8	473	1665	5700	1500
CB3	[39]	30.0	45	12.5	500	1756	5830	1915

*Slab cut back by 285 mm at end of cellular beam

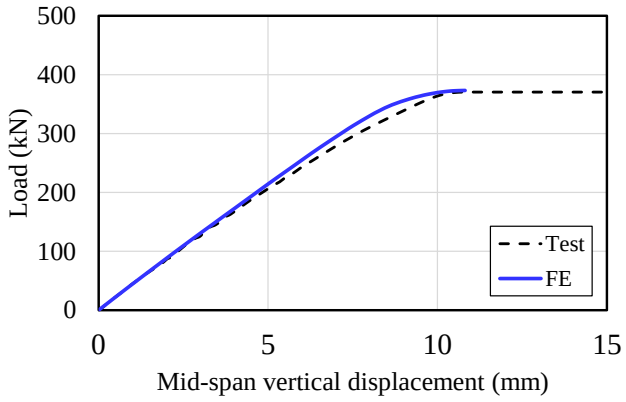

(a) CCB1

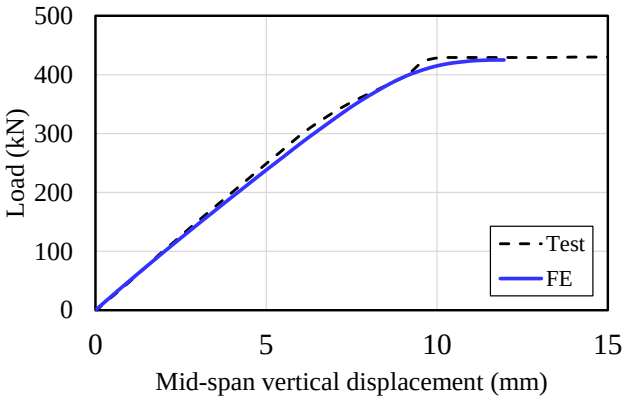

(b) CCB2

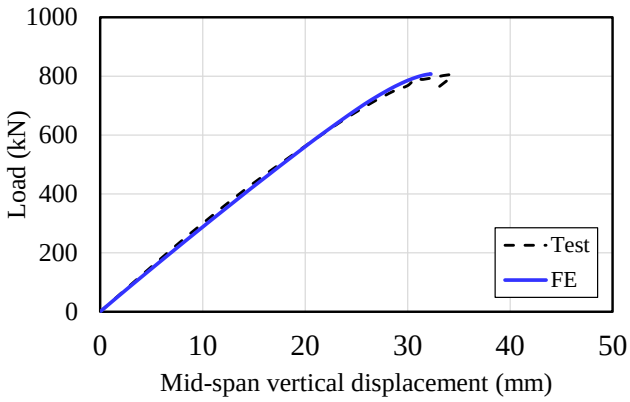

(c) CCB3

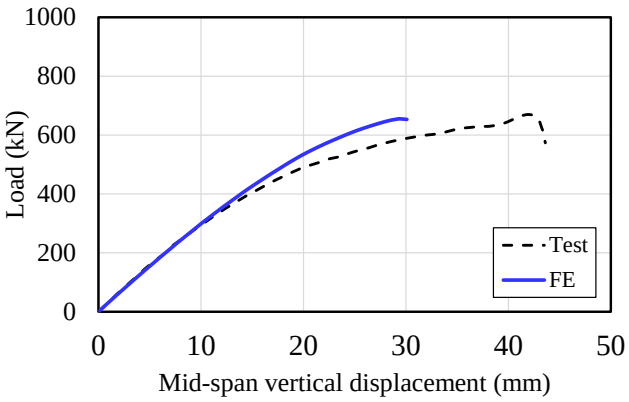

(d) CCB4

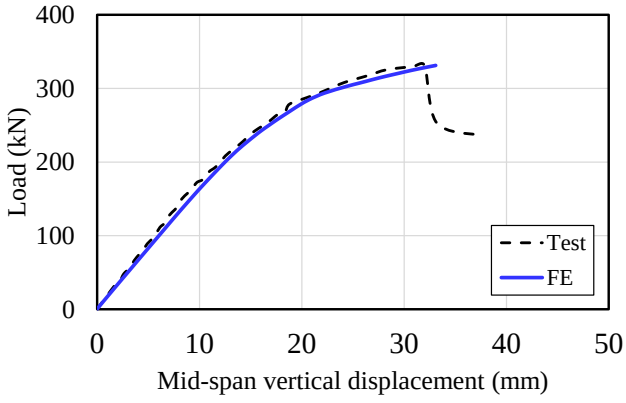

(e) CB1

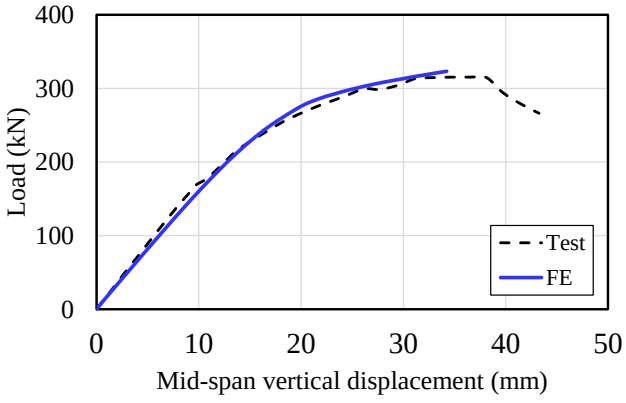

(f) CB2

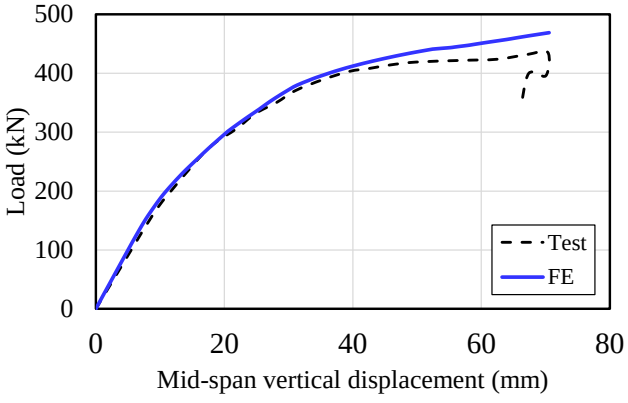

(g) CB3

153 **Fig. 3: Validation results** [30]

4. FINITE ELEMENT MODEL: PARAMETRIC STUDY

The general considerations of the parametric study are presented in this section, as well as the type of analyses, the constitutive materials models, the interaction between the contact surfaces, the boundary conditions and discretization. The following are the general considerations for the parametric study:

1. The yield stress and the ultimate stress of the shear stud are 460 MPa and 559 MPa, respectively. The elongation at rupture is 18.8%;
2. The W360x91 profile is considered as parent section. The total height of the cellular section (d_g) is 530mm;
3. The ASTM A572 Grade 50 steel is adopted (f_y=345 MPa and f_u=450 MPa). The Young's modulus is 200 GPa;
4. The ratio p/D_o is varied in 1.2, 1.3, 1.4 and 1.5, and the ratio D_o/d is varied in 0.8, 0.9, 1.0, 1.1 and 1.2;
5. For PCHCS LP15 units (**Fig 4**) is considered. The filling of the 1st, 3rd, 5th and 7th core is considered, and a transversal reinforcement with 16mm of diameter is placed;

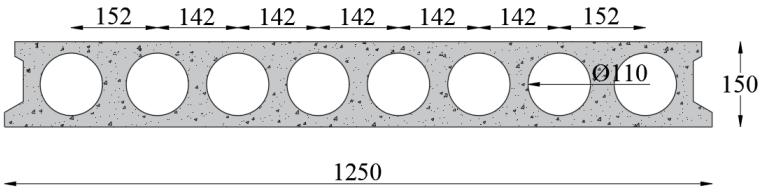

Fig. 4: LP 15

6. For PCHCS, 130mm of gap is considered;
7. The thickness of CT is 50mm, and a steel mesh is 4.2mm spaced at 100mm;
8. The shear stud dimension is 19x125mm. One and two rows of shear studs are considered, varying the longitudinal spacing in 150mm, 300mm and 450mm (**Fig.5**). The transversal spacing is $4d_{sc}$.

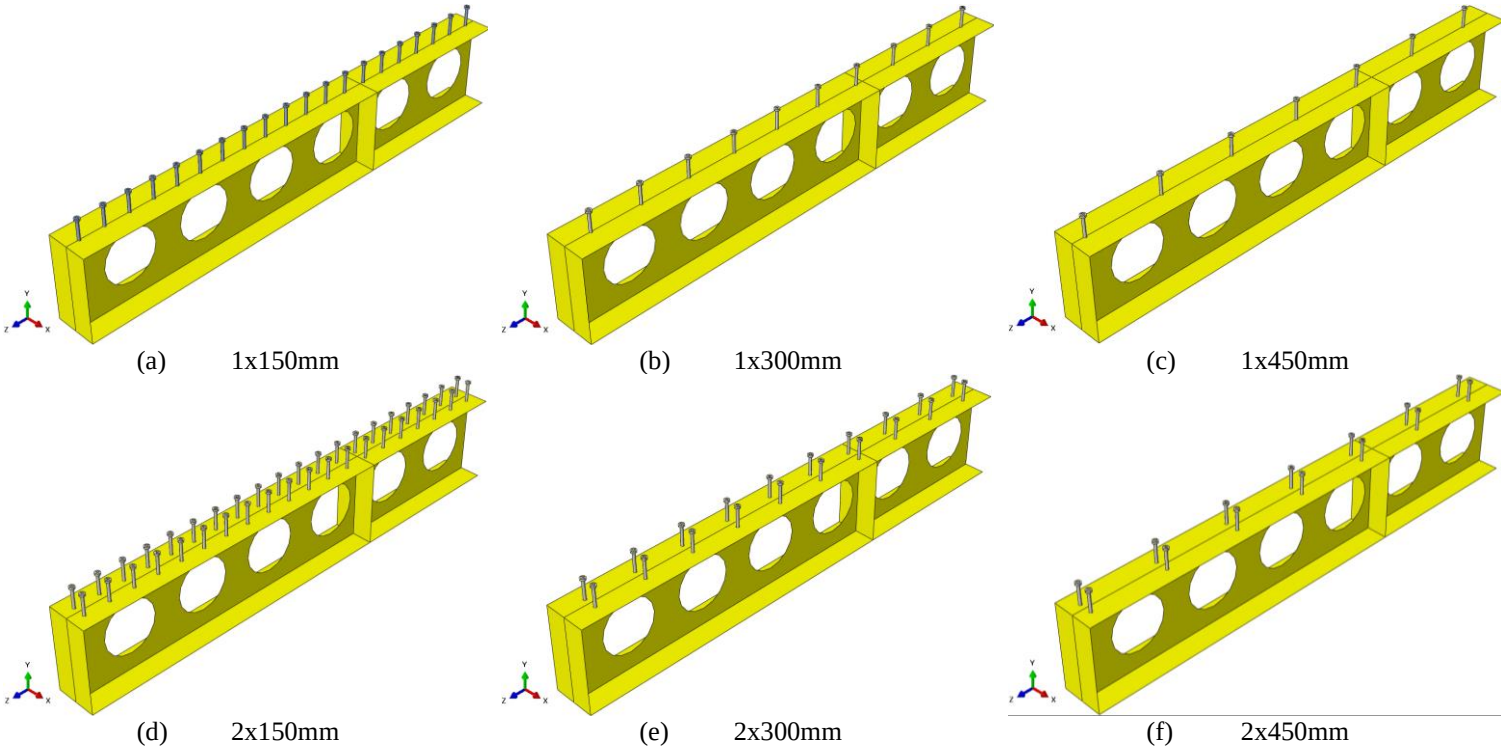

(a) 1x150mm (b) 1x300mm (c) 1x450mm

(d) 2x150mm (e) 2x300mm (f) 2x450mm

Fig. 5: Shear studs spacing for parametric study, considering symmetry at mid-span

9. The infill concrete average strength is 30 MPa, and the PCHCS average strength is 40 MPa; The modulus of elasticity is calculated according to EN 1992-1-1 [63];
10. The length of the composite cellular beam is equal 6m, and the slab width is $L/4$;
11. The composite cellular beams are simply supported and subjected to two-point loads, spaced symmetrically in 2m from supports. Stiffeners were provided at the point of load and support.
12. According to the specifications of EC4 [18] and SCI P355 [15], **Table 2** presents the minimum and maximum values of the interaction degrees (n/n_f) for each series analyzed, in which n is the number of shear studs provided between the points of zero and maximum moment. This value was taken as the number of connectors allocated in the length between the support and the mid-span. The design resistance values of the shear studs were performed according to the constitutive model described in section 4.2. In the case of concrete crushing, the value was reduced by a factor k=0.9. This factor takes account the influence of the confinement of the shear connectors due to the transverse reinforcement, and the geometry of the connectors relative to the hollow core units [38]. The number of shear studs required for full interaction degree (n_f) was taken as the lowest value between the concrete slab compressive resistance and the cellular section tensile resistance.

Table 2 – Interaction degree of models

Model	1x150mm	2x150mm	1x300mm	2x300mm	1x450mm	2x450mm
n	20	40	10	20	7	14
n/n_f	0.40-0.47	0.81-0.93	0.20-0.23	0.40-0.47	0.14-0.16	0.28-0.33
η_{min}[a]	0.41	0.41	0.41	0.41	0.41	0.41

[a]Calculated according to **Eq. (1)**.

4.1. BUCKLING AND POST-BUCKLING ANALYSIS

Buckling and post buckling analyses are widely used in buckling problems [6,61,64–68], such as WPB, that was previously described in the introduction section. The analyses are developed in two stages in ABAQUS® [69], considering the buckling and post-buckling analyses. In the buckling analysis, no material or geometrical imperfections are considered. The deformation mode response in the buckling analysis is used as an initial condition for post buckling analysis, that is, for the application of an initial geometric imperfection. In the post-buckling analysis, the initial geometric imperfection as well as the material and geometric nonlinearity are considered. The initial geometric imperfection is applied with a $d_g/1000$ amplitude, according to the sensitivity analyses carried out by Ferreira et al [6]. The implementation of the initial geometric imperfection is performed using *INITIAL CONDITIONS. Residual stresses are not considered. In the case of composite beams, residual stresses are harmful to study cases in which the composite beams are subjected to a negative bending moment [70,71]. To solve the post-buckling problem, the modified Riks algorithm is used (*Static Riks*). It is necessary to implement the initial arc length, which refers to an initial percentage of the external load. To solve the non-linearity equilibrium equations, the software uses the Newton-Raphson method.

4.2. MATERIALS MODELS

This section presents the constitutive material models used in numerical modeling.

4.2.1 Concrete

The Concrete Damage Plasticity (CDP) [72–74] is used, which is based on the theory of plasticity [75]. The input parameters (**Table 3**) to characterize the plasticity are: dilation angle (ψ), eccentricity (ξ), the ratio of initial equibiaxial compressive yield stress to initial uniaxial compressive yield stress (σ_{b0}/σ_{c0}), the ratio of the second stress invariant on the tensile meridian to that on the compressive meridian (K_c), and the viscosity parameter that represents the relaxation (μ). Carreira and Chu [76,77] stress-strain relationships models are used to represent the behavior of concrete in compression and tension (**Eqs. 3-5**).

Table 3: CDP input parameters

Parameter	Value	References
Ψ (º) (Infill)	40	[30,40,78–81]
Ψ (º) (HCU)	28	[82]
ξ	0.1 (default)	[69,78,79,82]
σ_{b0}/σ_{c0}	1.16 (default)	[69,78,79,82]
K_c	2/3 (default)	[69,78,79,82]
μ (s^{-1})	0.001	[78,79]

$$\frac{\sigma}{f_c} = \frac{\beta_c\left(\varepsilon/\varepsilon_c\right)}{\beta_c - 1 + \left(\varepsilon/\varepsilon_c\right)^{\beta_c}} \tag{3}$$

$$\frac{\sigma}{f_t} = \frac{\beta_c\left(\varepsilon/\varepsilon_t\right)}{\beta_c - 1 + \left(\varepsilon/\varepsilon_t\right)^{\beta_c}} \tag{4}$$

$$\beta_c = \left(\frac{f_c}{32.4}\right)^3 + 1.55 \ \ (MPa) \tag{5}$$

4.2.2 Steel

The transverse reinforcement and steel mesh are modeled with elastic-perfectly plastic model (**Fig. 6a**). For the shear studs, the bilinear model (**Fig. 6b**) is used. For cellular beams, the quadrilinear model of Yun and Gardner (**Eqs. 6-10**) [83] is adopted (**Fig. 6c**). The implementation of the stress- strain relationship must be done with the real values, according to the **Eqs. (11-12).**

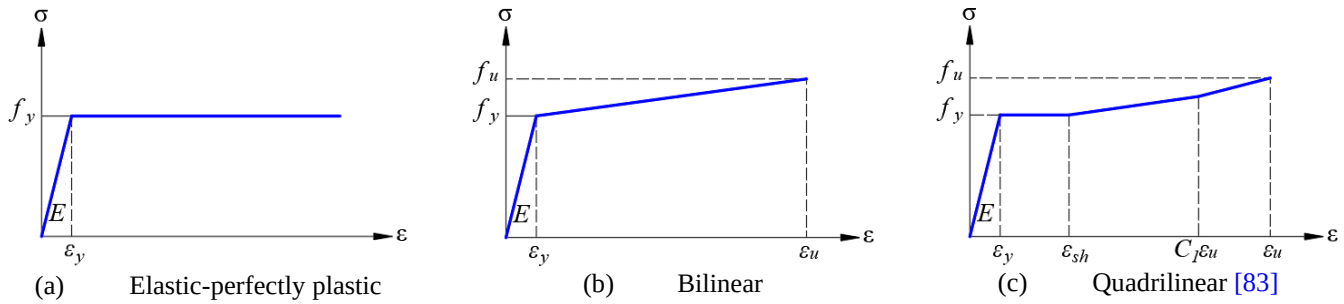

(a) Elastic-perfectly plastic (b) Bilinear (c) Quadrilinear [83]

Fig. 6: Stress-strain relationship for steel [30]

$$f(\varepsilon)=\begin{cases} E\varepsilon, \varepsilon \le \varepsilon_y \\ f_y, \varepsilon_y < \varepsilon \le \varepsilon_{sh} \\ f_y + E_{sh}(\varepsilon - \varepsilon_{sh}), \varepsilon_{sh} < \varepsilon \le C_1\varepsilon_u \\ f_{C_1\varepsilon_u} + \left(\dfrac{f_u + f_{C_1\varepsilon_u}}{\varepsilon_u - C_1\varepsilon_u}\right), C_1\varepsilon_u < \varepsilon \le \varepsilon_u \end{cases} \quad (6)$$

$$\varepsilon_u = 0.6\left(1-\frac{f_y}{f_u}\right), \varepsilon_u \ge 0.06 \quad (7)$$

$$\varepsilon_{sh} = 0.1\frac{f_y}{f_u} - 0.055, 0.015 < \varepsilon_{sh} \le 0.03 \quad (8)$$

$$C_1 = \frac{\varepsilon_{sh} + 0.25(\varepsilon_u - \varepsilon_{sh})}{\varepsilon_u} \quad (9)$$

$$E_{sh} = \frac{f_u - f_y}{0.4(\varepsilon_u - \varepsilon_{sh})} \quad (10)$$

$$\sigma^{true} = \sigma^{nom}\left(1+\varepsilon^{nom}\right) \quad (11)$$

$$\varepsilon^{true} = \ln\left(1+\varepsilon^{nom}\right) \quad (12)$$

4.3. INTERACTION

The modeling of hollow core slabs is complex. As an example, it can be cited the studies carried out by the references [82,84,85]. In Nguyen et al. [82] a three-dimensional numerical model of hollow core slabs was developed to investigate web-shear behavior. The steel strands were discretized with truss elements with a linear stress distribution. The authors consider the perfect bond between the steel strands and the precast concrete. The results of the numerical models presented an error of a maximum of 15% in comparison with the results of the experimental models. Subsequently, Nguyen and Tan [85] used the same modeling technique, however, considering hollow core slabs subjected to fire. This same technique was shown to be coherent when compared with the experimental results. In Elharouney et al. [84] the numerical model of hollow core slabs was developed in two steps. The first step consisted of applying the prestressing forces to the strands. In the second step, the boundary conditions were applied, as well as the external loading by displacement control.

The previous studies aimed to investigate the ultimate resistance of hollow core slabs. In the present work, PCHCS and PCHCSCT are disposed transversely in relation to the cellular profile, considering for this only an effective width. In this context, the effect of prestressing forces can be neglected. This modeling technique was previously used by references [30,31,36,62], which proved to be adequate for the representation of physical models in numerical models. Thus, three types of interaction between the contact surfaces are used. The tie constraint, which allows to simulate the perfect bond between the contact surfaces, it is applied to the surface between on the bottom surfaces of the shear studs and the upper flange, and between the precast and in-situ infill concrete [40]. The *Embedded region* is used to specify that an element is embedded in another element. This type of interaction is applied between the concrete and the transverse reinforcement, as well as the concrete and steel mesh. *Normal/tangential behavior* allows

displacement in the normal and tangential direction to the contact surface plane. It is applied between the gap- shear studs, and the slab-cellular beam surfaces. This technique has already been used by references [86,87]. The tangential behavior is based on the Coulomb friction model. The friction coefficients are taken equal to 0.2 and 0.3, for gap-shear studs, and slab-cellular beam interfaces, respectively [6,40,61,80,88].

4.4. BOUNDARY CONDITIONS AND DISCRETIZATION

The boundary conditions are applied according to references [6,40,61,62], considering symmetry at mid-span. For this, the vertical displacement (Uy=0) in the support, the lateral displacement (Ux=0) at the ends of the slab, and the mid-span (Uz=URx=URy=0) are restrained. Regarding the discretization, the dimensions of elements are taken according to others studies [6,61,80,82,89,90]. The cellular beams are discretized with S4R element, which is a quadrilateral element with four nodes and reduced integration. The shear studs, the PCHCS and the in-situ elements, were discretized by the solid element C3D8R, which has eight nodes and reduced integration. The transverse reinforcement as well as steel mesh are discretized with truss elements (T3D2), with two nodes and linear displacement. **Fig. 7a** shows the boundary conditions and discretization of composite cellular beams with PCHCS or PCHCS. **Fig. 7b** illustrates the discretization of the shear studs and gap.

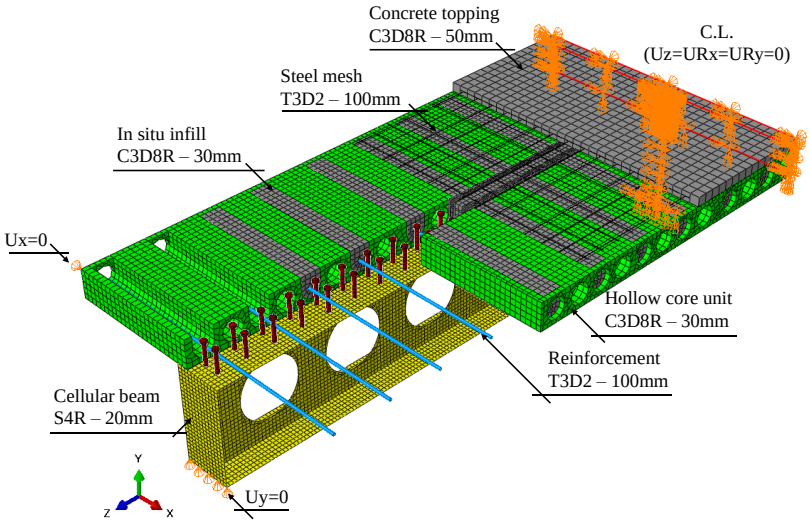

(a) Composite cellular beam with PCHCS(CT)

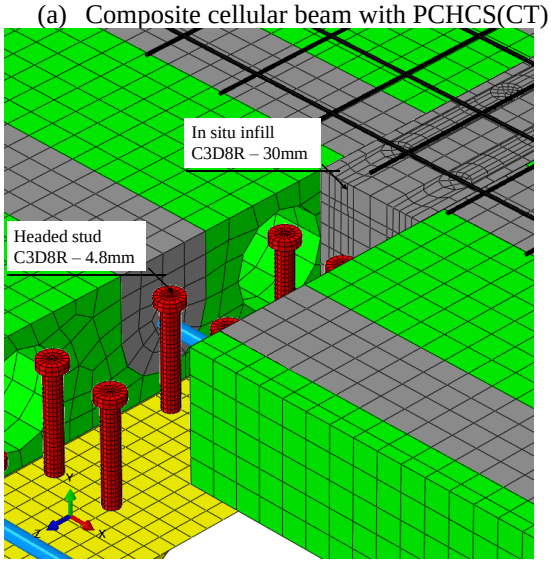

(b) Shear studs and gaps illustration

Fig. 7: Boundary conditions and discretization

5. RESULTS AND DISCUSSION

In total, 240 numerical models were developed for this parametric study. Some examples of the failure modes are illustrated in **Fig. 8.** Although the predominant failure mode observed was web post buckling combined with the plastic mechanism (WPB+PM) (**Fig. 8a)** and the formation of the Vierendeel mechanism (VM) (**Fig. 8b)**, these failure modes have been observed in combination with the shear stud rupture (WPB+PM* and VM*) (**Fig. 8c)**. The results are discussed, considering 150mm, 300mm and 450mm of spacing. At the end of the results and discussion section, a general analysis is made with the presentation of the results.

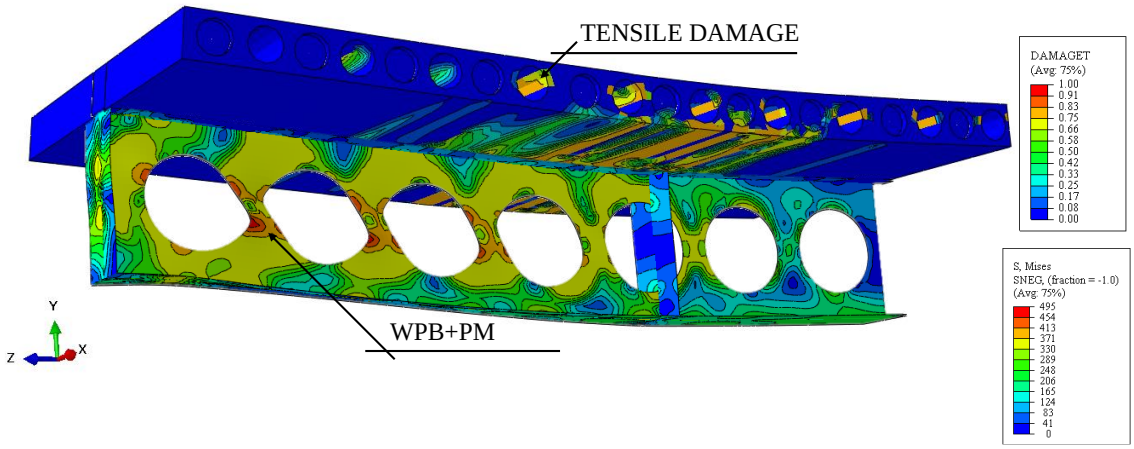

(a) WPB+PM: D_o/d=0.9 and p/D_o=1.3 with PCHCS and 2x150mm of spacing

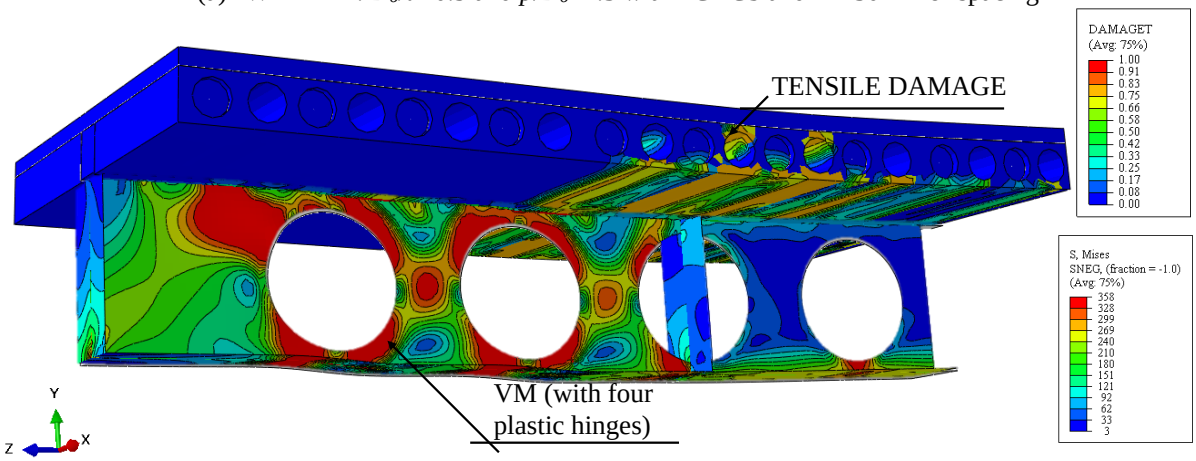

(b) VM: D_o/d=1.5 and p/D_o=1.5 with PCHCSCT and 1x300mm of spacing

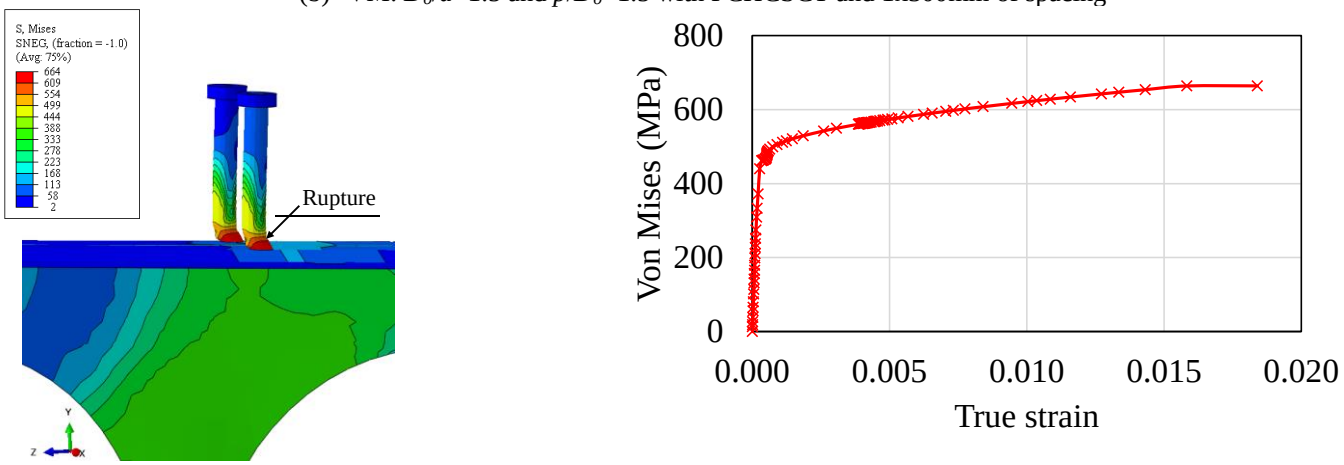

(c) Shear stud rupture

Fig. 8: Failure modes

5.1. 150MM OF SPACING

The total number of shear studs (n), from the support to the mid-span, is 20 and 40 for 1x150mm and 2x150mm, respectively. For the D_o/d=0.8-1.0, D_o/d=1.1; p/D_o=1.2-1.3 and D_o/d=1.2; p/D_o=1.4-1.5 models, the total number of shear studs above the opening (n_h) is 2 and 4 for 1x150mm and 2x150mm, respectively. For the D_o/d=1.1; p/D_o=1.4-1.5 and D_o/d=1.2; p/D_o=1.2-1.3 models, n_h is 3 and 6 for 1x150mm and 2x150mm, respectively. Notably, the larger the opening diameter, the greater n_h.

Regarding the development of the analyses, for the mid-span vertical displacement at 15.2±0.3mm (1x150mm) and 15.0±0.3mm (2x150mm), both the tees and the shear studs had already reached the yield strength. The global shear force values were 291.7±46.9kN and 304.5±51.1kN, for 1x150mm and 2x150mm, respectively. For the tees, the von Mises stresses were 347.7±1.1MPa and 347.7±1.2MPa, for 1x150mm and 2x150mm, respectively. Considering the shear studs, these stresses were 480.8±4.6MPa and 470.1±10.4MPa, for 1x150mm and 2x150mm, respectively. On the PCHCS, the upper regions close to the support, the lower part close to the loading application point, and the cores without filled were already damaged. The relative slip between the PCHCS and the cellular beam was 0.2±0.1mm and null, for 1x150mm and 2x150mm, respectively. With increasing loading, for the mid-span vertical displacement at 30.3±0.8mm (1x150mm), the measured values of the global shear force were 393.2±76.8kN (1x150mm) and 428.9±82.8kN (2x150mm). Notably, there was an increase in von Mises stresses. For the tees, the von Mises stresses were 379.4±22.2MPa (1x150mm) and 383.9±23.0MPa (2x150mm), and for the shear studs were 547.7±29.7MPa (1x150mm) and 485.2±5.3MPa (2x150mm). Regarding the PCHCS, there was an increase in the damaged region, and the relative slip between the PCHCS and the cellular beam was 0.9±0.3mm and 0.1±0.1mm, for 1x150mm and 2x150mm, respectively. Finally, in the ultimate resistance, the mid-span vertical displacements measured were 40.2±7.4mm (1x150mm) and 38.9±9.5mm (2x150mm). In these models, the stopping criterion adopted was verified when the peak load was reached. Thereafter, as the displacement increases, the load decreases. The global shear force was 419.3±85.7kN and 454.1±92kN, for 1x150mm and 2x150mm, respectively. For the tees, the von Mises stresses were 419.1±27.3MPa (1x150mm) and 417.2±30.8MPa (2x150mm). For the shear studs, the von Mises stresses were 590.0±30.5MPa (1x150mm) and 496.8±17.8MPa (2x150mm). It was observed in this circumstance, for 2x150mm, the stresses were lower than in relation to 1x150mm models. This can be explained as the shear studs have the capacity to absorb the shear flow at the steel-concrete interface. In this context, the relative slip between the PCHCS and the cellular beam was 1.4±0.4mm and 0.1±0.1mm, for 1x150mm and 2x150mm, respectively. An increase in damage was observed in the upper part of the slab on the ultimate resistance (**Fig. 9)**, especially in models where the end post width (b_{we}) was greater than the width of the others web posts (b_w).

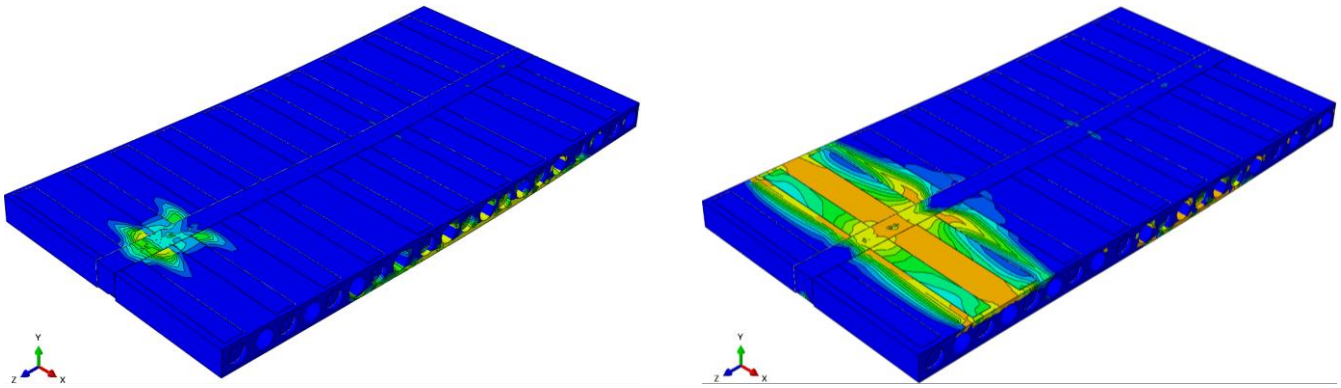

(a) D_o/d=0.8; p/D_o=1.3 and b_{we}/b_w=1.5 (b) D_o/d=0.8; p/D_o=1.5 and b_{we}/b_w=3.9

Fig. 9: Tensile damage above the supports, considering PCHCS models

Concerning the composite cellular beams with PCHCSCT, there was an increase in the axial resistance of the PCHCS due to the presence of the CT. In this context, the relative difference between the axial resistance of the PCHCSCT and the connection (nP_{sc}) increased. Regarding the analyses, the behavior was similar to composite cellular beams with PCHCS models. For the mid-span vertical displacement at 15.3±0.4mm (1x150mm) and 15.1±0.4mm (2x150mm), the global shear force, the von Mises stresses of tees and shear studs, and the relative slips were 352.3±51.8kN; 347.9±1.2MPa; 496.8±10.9MPa; 0.6±0.2mm and 389.3±65.3kN; 348.1±1.0MPa; 481.0±5.9MPa; 0.1±0.1mm, for 1x150mm and 2x150mm models, respectively. With the mid-span vertical displacements at 30.3±0.7mm (1x150mm) and 30.2±0.5mm (2x150mm), the global shear force, the von Mises stresses of tees and shear studs, and the relative slips were 446.1±86.0kN; 390.1±23.1MPa; 601.4±15.9MPa; 1.7±0.3mm and 485.5±102.4kN; 409.3±22.9MPa; 494.2±11.7MPa; 0.3±0.2mm, for 1x150mm and 2x150mm models, respectively. In the ultimate resistance, for the mid-span vertical displacements at 43.2±9.2mm (1x150mm) and 32.8±4.5mm (2x150mm), the global shear force, the von Mises stresses of tees and shear studs, and the relative slips were 474.8±77.2kN; 439.6±39.9MPa; 644.0±24.8MPa; 2.6±0.4mm and 508.2±90.9kN; 421.5±33.8MPa; 502.4±13.6MPa; 0.4±0.3mm, for 1x150mm and 2x150mm models, respectively.

Fig. 10 shows the influence of the concrete topping, considering the global shear force differences between the PCHCSCT and PCHCS models ($V_{PCHCSCT}$-V_{PCHCS}). According to the illustrations (**Fig. 10a-e**), for the models analyzed, the models with concrete topping obtained greater resistance in the structural system ($V_{PCHCSCT}$-V_{PCHCS} >0). Such observation was previously reported by Ferreira et al. [30]. The variations in the differences tend to be smaller when the failure modes were defined by the WPB+PM. In the other models, the variations of the differences tend to increase, mainly for the analyses in which the VM was observed. The maximum difference with a value equal to 113kN was observed for the model D_o/d=1.0 and p/D_o=1.2 with 1x150mm, which was observed WPB+PM. The minimum difference was analyzed for the D_o/d=0.8 and p/D_o=1.3 models with 2x150mm, which obtained VM for PCHCSCT model, and WPB+PM for PCHCS model. Such analyses demonstrate that the concrete topping influenced the change in the failure mode of the composite cellular beams.

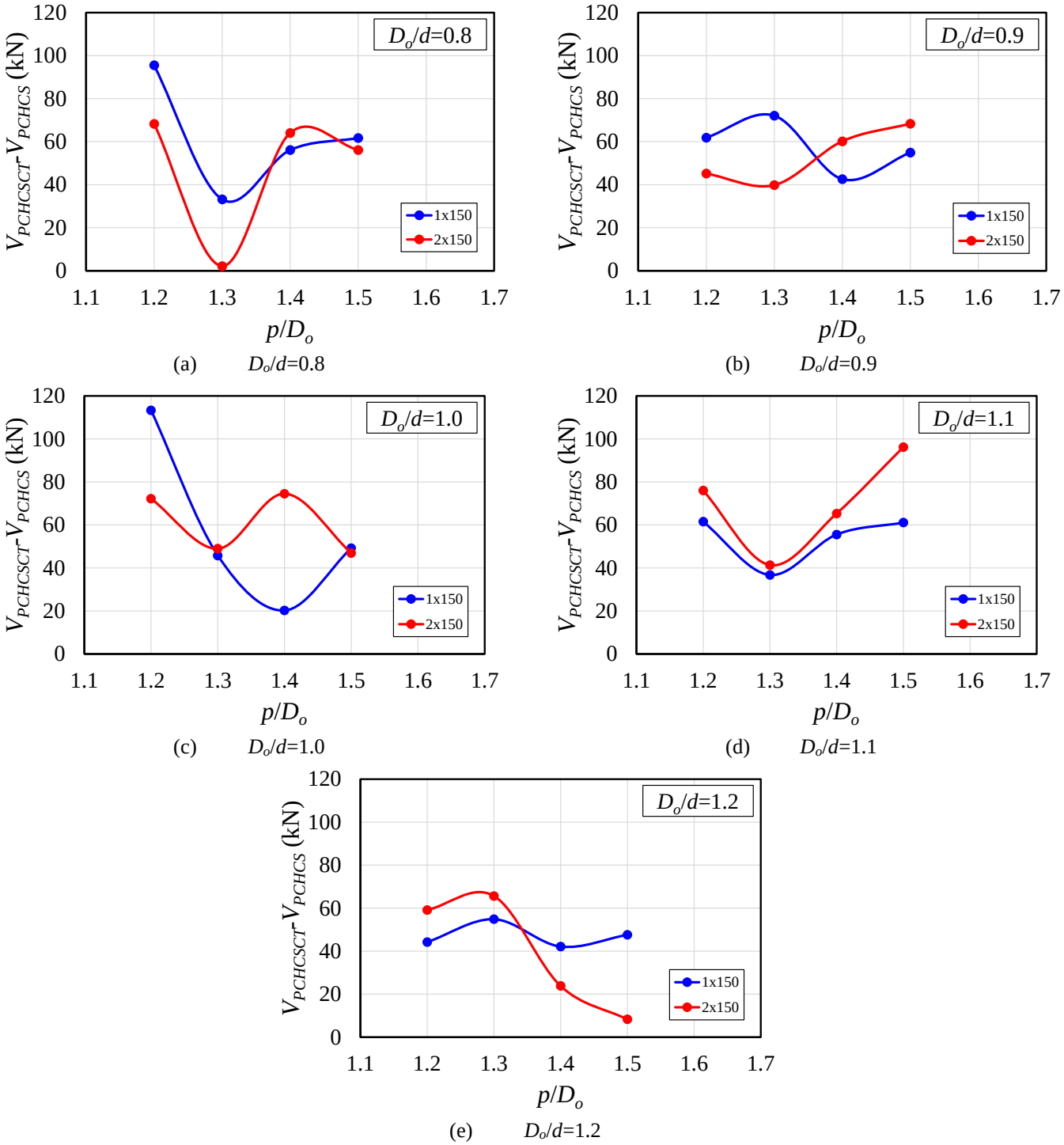

Fig. 10: The influence of concrete topping for models with 150mm of shear studs spacing

Fig. 11 illustrates the shear resistance of the models analyzed as a function of key parameters, such as the D_o/d and p/D_o. As shown in the illustration, for most of the cases, the 2x150mm models presented greater or equal shear resistance compared to 1x150mm models. This shows that the WPB resistance is also influenced by the composite action, that is directly relevant to the number of connectors above the opening. In addition, as shown in the illustration, a drop in resistance is observed for the models D_o/d=1.0 and p/D_o=1.2 (**Fig. 11c**), and D_o/d=1.2 and p/D_o=1.2(**Fig. 11e**) in compared to the models p/D_o=1.4. This was due to the fact that the end-post width of the models p/D_o=1.4 are longer than the end-post width of the models p/D_o=1.5. This was reported in Ferreira et al. [6]. The failure modes analyzed are presented (**Table 4**).

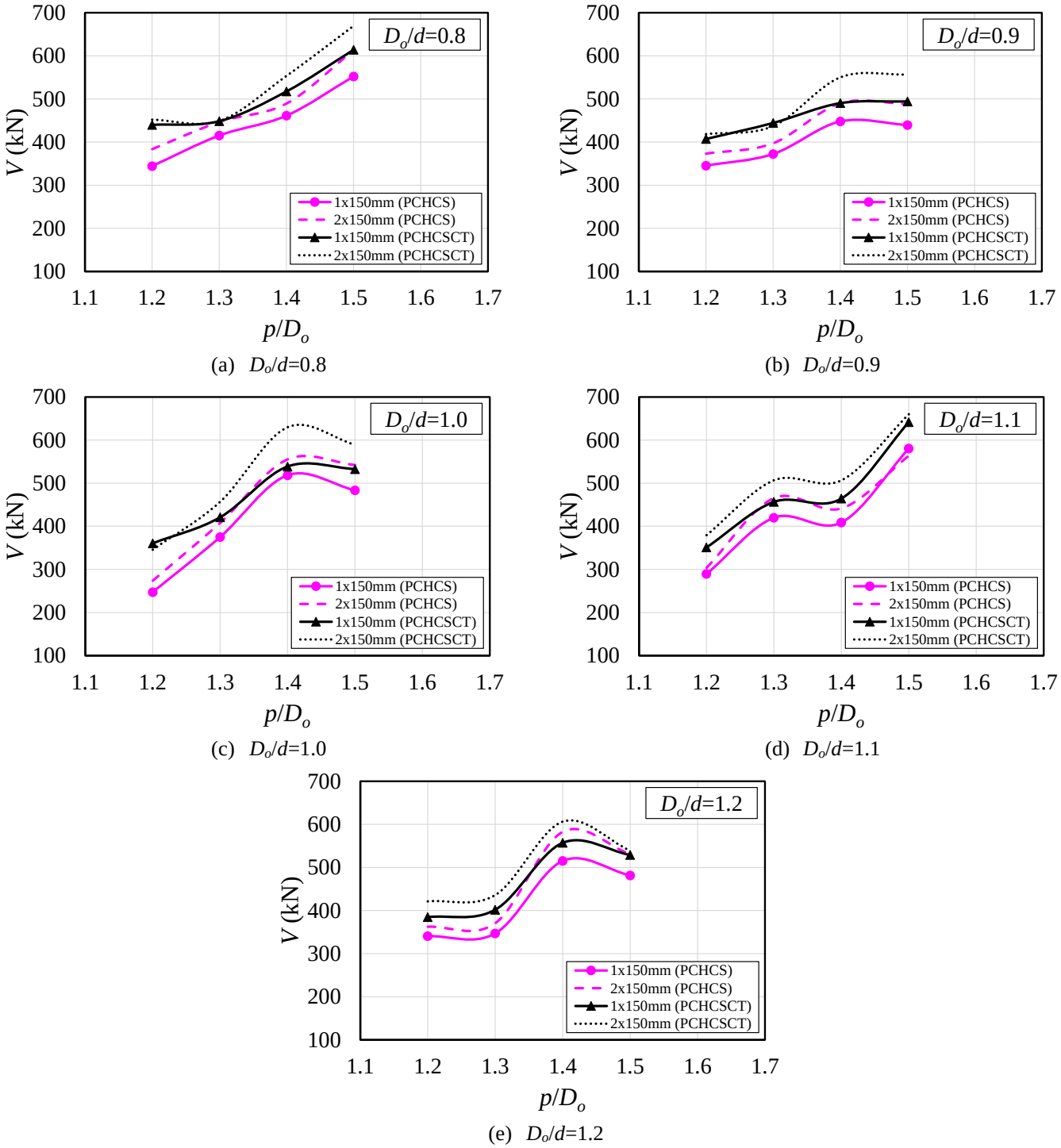

(a) D_o/d=0.8

(b) D_o/d=0.9

(c) D_o/d=1.0

(d) D_o/d=1.1

(e) D_o/d=1.2

Fig. 11: Results for models with 150mm of shear studs spacing, considering PCHCS and PCHCSCT

Table 4 – Failure modes for 1x150mm and 2x150mm models

D_o/d	p/D_o	1x150mm		2x150mm	
		PCHCSCT	PCHCS	PCHCSCT	PCHCS
0.8	1.2	WPB+PM*	VM	WPB+PM	VM
	1.3	WPB+PM*	WPB+PM	VM	WPB+PM
	1.4	WPB+PM	WPB+PM	WPB+PM	WPB+PM
	1.5	WPB+PM*	WPB+PM	WPB+PM	WPB+PM
0.9	1.2	WPB+PM*	WPB+PM	WPB+PM	WPB+PM
	1.3	WPB+PM*	WPB+PM	WPB+PM	WPB+PM
	1.4	WPB+PM	WPB+PM	WPB+PM	WPB+PM
	1.5	WPB+PM	WPB+PM	WPB+PM	WPB+PM
1.0	1.2	WPB+PM*	WPB+PM	WPB+PM	WPB+PM
	1.3	WPB+PM*	WPB+PM	WPB+PM	WPB+PM
	1.4	WPB+PM	WPB+PM	VM	WPB+PM
	1.5	WPB+PM	WPB+PM	VM	WPB+PM
1.1	1.2	WPB+PM*	WPB+PM	WPB+PM	WPB+PM
	1.3	WPB+PM	WPB+PM	WPB+PM	WPB+PM
	1.4	VM	WPB+PM	WPB+PM	WPB+PM
	1.5	VM*	WPB+PM	VM	VM
1.2	1.2	WPB+PM*	VM	WPB+PM	VM
	1.3	VM	VM	VM	VM
	1.4	VM*	VM	VM	VM
	1.5	VM*	VM	VM	VM

*The shear stud rupture occurred.

5.2. 300MM OF SPACING

In these analyses, n is 10 and 20 for 1x300mm and 2x300mm, respectively. For the D_o/d=0.8;1.0-1.1 and p/D_o=1.2-1.5, D_o/d=0.9 and p/D_o=1.2;1.4-1.5, D_o/d=1.2 and p/D_o=1.2-1.3;1.5 models, n_h is 1 and 2 for 1x300mm and 2x300mm, respectively. For the D_o/d=0.9; p/D_o=1.3 and D_o/d=1.2; p/D_o=1,4, n_h is 2 and 4 for 1x300mm and 2x300mm, respectively.

The structural behaviors of the composite cellular beams with PCHCS, considering 1x300mm and 2x300mm, were similar to the previous models described in section 5.1. For the mid-span vertical displacement at 15.3±0.4mm (1x300mm) and 15.2±0.3mm (2x300mm), the global shear force, the von Mises stresses of tees and shear studs, and the relative slips were 258.1±39.2kN; 347.3±1.2MPa; 520.6±22.2MPa; 0.9±0.2mm and 289.6±48.6kN; 347.8±1.3MPa; 479.7±4.2MPa; 0.3±0.1mm for 1x300mm and 2x300mm models, respectively. With the mid-span vertical displacements at 30.1±0.5mm (1x300mm) and 30.2±0.3mm (2x300mm), the global shear force, the von Mises stresses of tees and shear studs, and the relative slips were 342.7±71.3kN; 370.1±18.7MPa; 598.2±22.5MPa; 2.1±0.4mm and 397.3±74.1kN; 377.9±21.6MPa; 533.7±21.3MPa; 0.9±0.3mm for 1x300mm and 2x300mm models, respectively. In the ultimate resistance, for the mid-span vertical displacements at 39.0±5.3mm (1x300mm) and 40.5±8.4mm (2x300mm), the global shear force, the von Mises stresses of tees and shear studs, and the relative slips were 365.0±77.8kN; 411.9±27.7MPa; 640.5±23.6MPa; 2.7±0.6mm and 414.9±84.7kN; 420.2±32.9MPa; 571.9±36.9MPa; 1.4±0.5mm for 1x300mm and 2x300mm models, respectively. An important observation in the ultimate resistance was in relation to the decrease

in global shear resistance that the present discussion obtained in relation to the previous one (**Table 5**). **Fig. 12** shows an example, considering the D_o/d=0.9 and p/D_o=1.5 model.

Table 5 – Global shear force comparative analyses between the present and previous models, considering PCHCS (in kN)

$V_{(1x150)}$	$V_{(1x300)}$	$V_{(1x300)}/V_{(1x150)}$	$V_{(2x150)}$	$V_{(2x300)}$	$V_{(2x300)}/V_{(2x150)}$
419.3±85.7	365.0±77.8	0.87	454.1±92kN	414.9±84.7	0.91

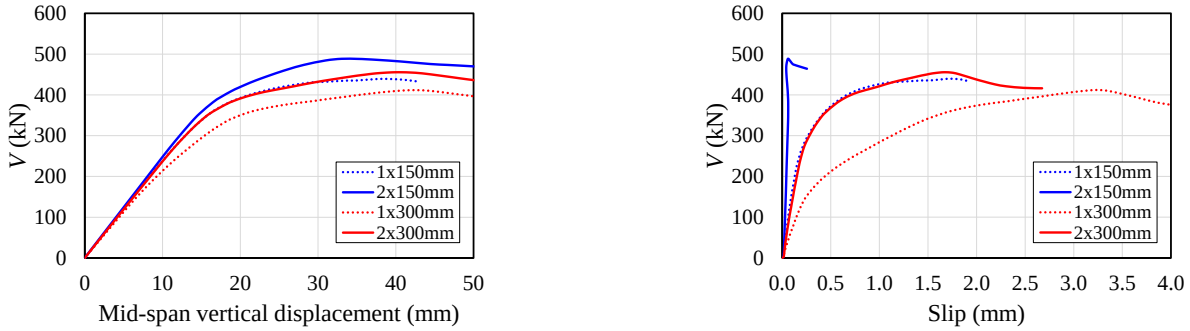

(a) Global shear force vs. mid-span vertical displacement (b) Global shear force vs. slip

Fig. 12: D_o/d=0.9 and p/D_o=1.5 models with PCHCS. Failure mode: WPB+PM

In view of the analyses carried out on the composite cellular beams with PCHCSCT, considering 1x300mm and 2x300mm, the structural behaviors were similar to described in section 5.1. For the mid-span vertical displacement at 15.3±0.4mm (1x300mm) and 15.5±0.3mm (2x300mm), the global shear force, the von Mises stresses of tees and shear studs, and the relative slips were 290.1±42.2kN; 347.3±1.2MPa; 554.0±22.6MPa; 1.4±0.2mm and 348.6±50.7kN; 348.1±1.6MPa; 494.9±11.8MPa; 0.6±0.2mm for 1x300mm and 2x300mm models, respectively. With the mid-span vertical displacements at 30.2±0.7mm (1x300mm and 2x300mm), the global shear force, the von Mises stresses of tees and shear studs, and the relative slips were 349.4±59.2kN; 376.9±20.0MPa; 636.7±26.2MPa; 2.8±0.3mm and 436.5±82.2kN; 395.5±21.6MPa; 581.5±25.1MPa; 1.7±0.4mm for 1x300mm and 2x300mm models, respectively. In the ultimate resistance, for the mid-span vertical displacements at 34.1±4.8mm (1x300mm) and 46.8±11.2mm (2x300mm), the global shear force, the von Mises stresses of tees and shear studs, and the relative slips were 395.9±62.0kN; 387.5±32.7MPa; 663.6±1.7MPa; 3.3±0.1mm and 483.7±70.7kN; 444.6±44.3MPa; 641.5±25.5MPa; 2.7±0.5mm for 1x300mm and 2x300mm models, respectively. **Table 6** and **Fig. 13** shows an example of comparations of the ultimate global shear force between the present and previous analyses.

Table 6 – Global shear force comparative analyses between the present and previous models with PCHCSCT (in kN)

$V_{(1x150)}$	$V_{(1x300)}$	$V_{(1x300)}/V_{(1x150)}$	$V_{(2x150)}$	$V_{(2x300)}$	$V_{(2x300)}/V_{(2x150)}$
474.8±77.2	395.9±62.0	0.83	508.2±90.9	483.7±70.7	0.95

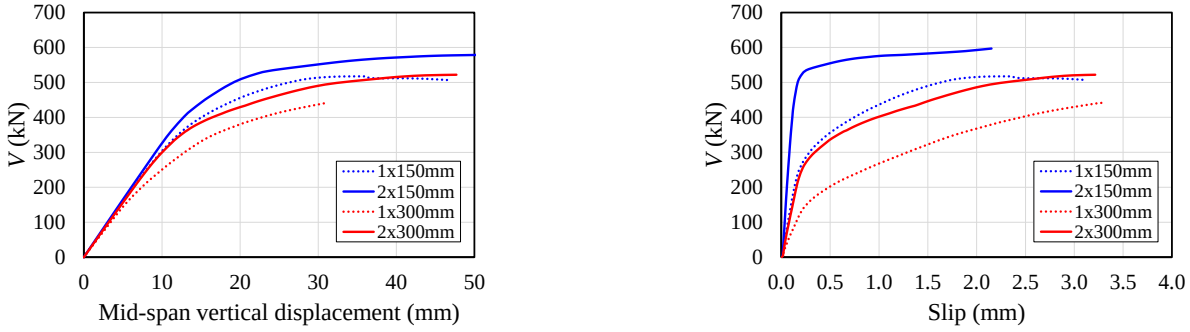

(a) Global shear force vs. mid-span vertical displacement (b) Global shear force vs. slip

Fig. 13: D_o/d=0.8 and p/D_o=1.4 models with PCHCSCT. Failure modes: WPB+PM (150mm) and WPB+PM* (300mm)

Fig. 14 illustrates the influence of the concrete topping ($V_{PCHCSCT}$-V_{PCHCS}). As shown in the figures (**Fig. 14a, Fig. 14c and Fig. 14d**), in some models the difference between the PCHCSCT and PCHCS models was negative ($V_{PCHCSCT}$-V_{PCHCS}<0). This was verified specifically for models p/D_o=1.5; D_o/d=0.8; 1.0 and 1.1 with 1x300mm, in which their failures modes were: VM (p/D_o=1.5; D_o/d=0.8;) and VM* (p/D_o=1.5; D_o/d=1.0-1.1) for PCHCSCT models, and WPB+PM* (p/D_o=1.5; D_o/d=0.8;1.1) and WPB+PM (p/D_o=1.5; D_o/d=1.0) for PCHCS models. It has been observed so far that, although the concrete topping has increased the resistance in previous analyses (**Fig. 10**), in the present models, the presence of the concrete topping and the reduced number of shear studs, contributed to the failure mode occurring in the connection, a factor that reduced the resistance of the global shear force. The maximum difference with a value equal to 126kN was observed for the model D_o/d=1.0 and p/D_o=1.2 with 2x300mm, which was verified WPB+PM for PCHCS model and WPB+PM* for PCHCSCT model. The minimum difference, which was of 22kN, occurred for the D_o/d=1.1 and p/D_o=1.5 model with 1x300mm. In these models, the failure modes analyzed were VM, and WPB+PM* for PCHCSCT and PCHCS models, respectively.

Fig. 15 illustrates the shear resistance of the models analyzed as a function of key parameters, such as the D_o/d and p/D_o. As shown in the illustration, it is observed that the models with 2x300mm presented greater resistance to global shear force than the models with 1x300mm. Also, similarly to what was presented and discussed in **Fig. 11c** and **Fig. 11e**, there was a drop in resistance as a function of the end-post width (**Fig 15c** and **Fig. 15e**). The failure modes analyzed are presented (**Table 7**).

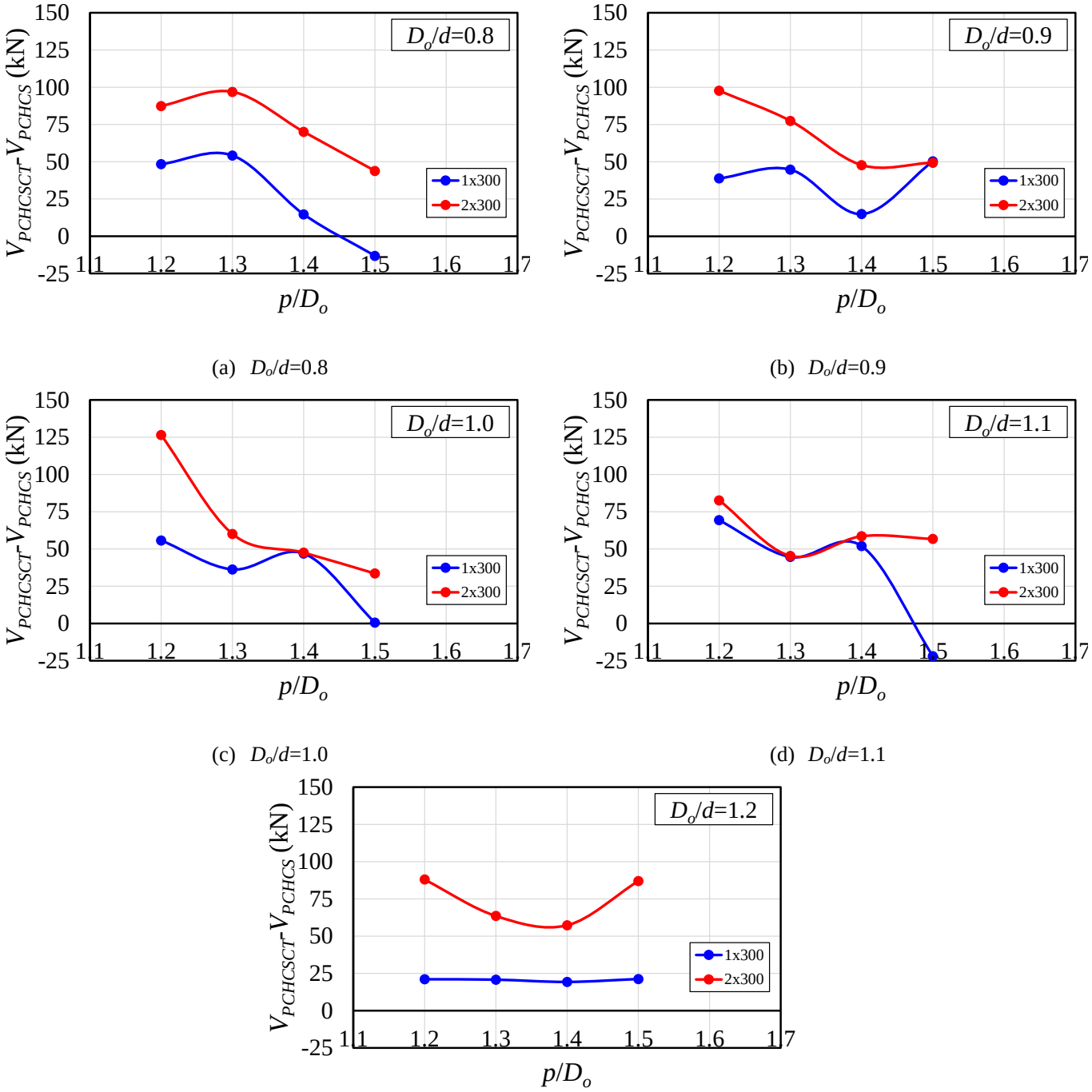

(a) D_o/d=0.8

(b) D_o/d=0.9

(c) D_o/d=1.0

(d) D_o/d=1.1

(e) D_o/d=1.2

Fig. 14: The influence of concrete topping for models with 300mm of shear studs spacing

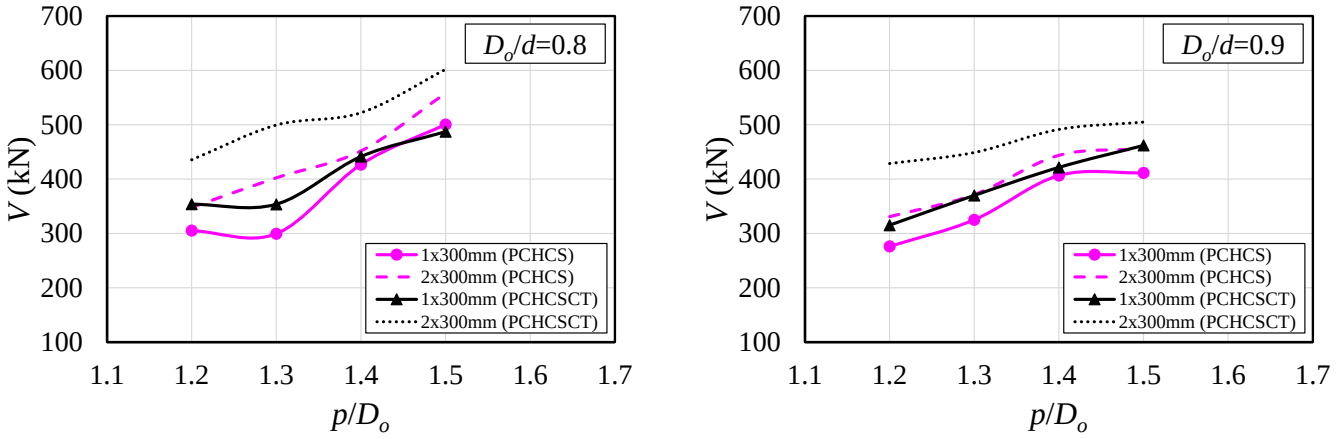

(a) D_o/d=0.8

(b) D_o/d=0.9

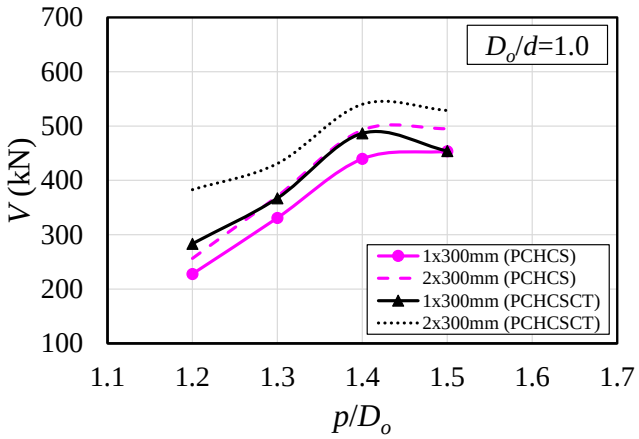

(c) D_o/d=1.0

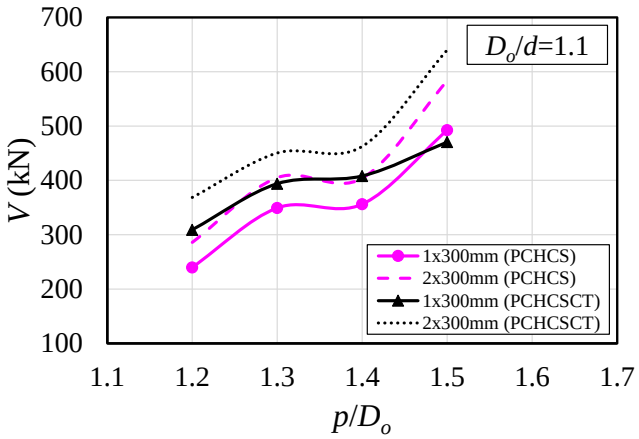

(d) D_o/d=1.1

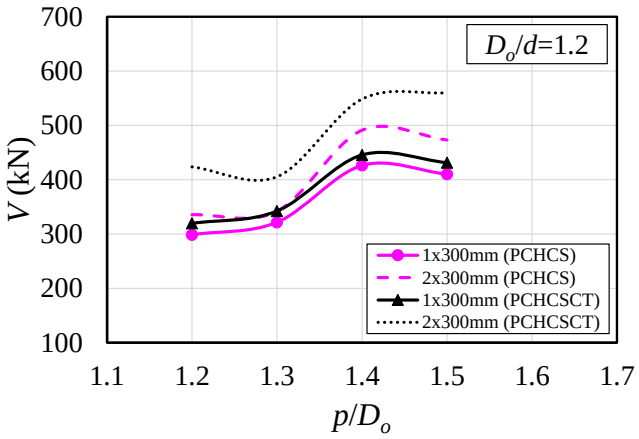

(e) D_o/d=1.2

Fig. 15: Results for models with 300mm of shear studs spacing, considering PCHCS and PCHCSCT

Table 7 – Failure modes for 1x300mm and 2x300mm models

D_o/d	p/D_o	1x300mm		2x300mm	
		PCHCSCT	PCHCS	PCHCSCT	PCHCS
0.8	1.2	VM*	VM	WPB+PM*	VM
	1.3	VM*	VM*	WPB+PM*	WPB+PM
	1.4	WPB+PM*	WPB+PM	WPB+PM*	WPB+PM
	1.5	VM	WPB+PM*	WPB+PM	WPB+PM
0.9	1.2	VM*	VM	WPB+PM*	VM
	1.3	WPB+PM*	WPB+PM	WPB+PM*	WPB+PM
	1.4	VM*	WPB+PM	WPB+PM	WPB+PM
	1.5	VM*	WPB+PM	WPB+PM	WPB+PM
1.0	1.2	WPB+PM*	WPB+PM	WPB+PM*	WPB+PM
	1.3	WPB+PM*	WPB+PM	WPB+PM	WPB+PM
	1.4	VM*	WPB+PM	VM	WPB+PM
	1.5	VM*	WPB+PM	VM	WPB+PM
1.1	1.2	VM*	WPB+PM	WPB+PM*	WPB+PM
	1.3	VM*	WPB+PM	WPB+PM	WPB+PM
	1.4	VM*	WPB+PM	VM	WPB+PM
	1.5	VM*	WPB+PM*	VM*	WPB+PM
1.2	1.2	VM*	VM	WPB+PM*	WPB+PM
	1.3	VM*	VM	VM	VM
	1.4	VM*	VM*	VM	VM
	1.5	VM*	VM*	VM*	VM

*The shear stud rupture occurred.

5.3. 450MM OF SPACING

In these analyses, n is 7 and 14, for 1x450mm and 2x450mm, respectively. For the D_o/d=0.8 and p/D_o=1.3 and 1.5; D_o/d=0.9 and p/D_o=1.3 and 1.5; D_o/d=1.0 and p/D_o=1.2 and 1.4; D_o/d=1.1 and p/D_o=1.3; D_o/d=1.2 and p/D_o=1.5, there are no shear studs above the opening closest to the support (n_h=0). For the other models, n_h is 1 and 2, considering 1x450mm and 2x450mm, respectively.

Regarding the analyses, for the mid-span vertical displacement at 15.5±0.4mm (1x450mm) and 15.3±0.5mm (2x450mm), the global shear force, the von Mises stresses of tees and shear studs, and the relative slips were 244.1±35.7kN; 347.2±1.1MPa; 533.0±16.4MPa; 1.1±0.2mm and 275.0±43.2kN; 347.5±1.1MPa; 484.5±6.9MPa; 0.5±0.2mm for 1x450mm and 2x450mm models, respectively. For mid-span vertical displacements at 30.3±0.8mm (1x450mm) and 30.3±0.5mm (2x450mm), the global shear force, the von Mises stresses of tees and shear studs, and the relative slips were 337.8±61.5kN; 365.7±15.2MPa; 611.1±21.0MPa; 2.4±0.4mm and 366.9±72.0kN; 372.6±19.7MPa; 558.1±25.0MPa; 1.4±0.3mm for 1x450mm and 2x450mm models, respectively. In the ultimate resistance, with the mid-span vertical displacements at 40.7±5.5mm (1x450mm) and 39.8±4.6mm (2x450mm), the global shear force, the von Mises stresses of tees and shear studs, and the relative slips were 358.2±71.0kN; 412.1±34.3MPa; 660.4±8.0MPa; 3.2±0.5mm and 398.1±82.7kN; 415.0±24.5MPa; 614.6±43.1MPa; 1.9±0.5mm for 1x450mm and 2x450mm models, respectively. **Table 8** and **Fig. 16** shows an example of comparations of the ultimate global shear force between the present (1x450mm and 2x450mm) and previous analyses (1x300mm and 2x300mm), considering composite cellular beams with PCHCS.

Table 8 – Global shear force comparative analyses between the present and previous models, considering PCHCS (in kN)

$V_{(1x300)}$	$V_{(1x450)}$	$V_{(1x450)}/V_{(1x300)}$	$V_{(2x300)}$	$V_{(2x450)}$	$V_{(2x450)}/V_{(2x300)}$
365.0±77.8	358.2±71.0	0.98	414.9±84.7	398.1±82.7	0.96

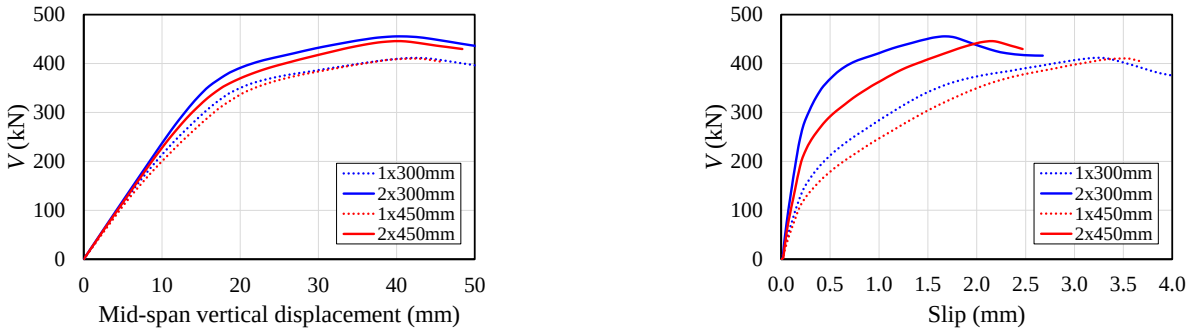

(a) Global shear force vs. mid-span vertical displacement (b) Global shear force vs. slip

Fig. 16: D_o/d=0.9 and p/D_o=1.5 models with PCHCS. Failure mode: WPB+PM

The differences between the average values of the global shear force tend to decrease, due to the failure mode being accompanied by the shear stud rupture. Another important observation was related to the ductile behavior at the interface between the PCHCS and the cellular beam. It was observed that the average slip value was 3.2±0.5mm, for the model in which there was a smaller number of connectors (1x450mm). According to EC4 [18], in order to characterize the ductile behavior at the interface, there must be a minimum 6mm of relative slip. Therefore, in all models of composite cellular beams with PCHCS analyzed so far, the behaviors at the interface were characterized as fragile.

Regarding the analyses performed on composite cellular beams with PCHCSCT, for 1x450 models, in all observations the shear stud rupture was observed. On the development of analyses, for the mid-span vertical displacement at 15.4±0.3mm (1x450mm) and 15.2±0.4mm (2x450mm), the global shear force, the von Mises stresses of tees and shear studs, and the relative slips were 269.4±35.3kN; 347.1±0.9MPa; 561.8±18.9MPa; 1.6±0.2mm and 318.3±42.9kN; 347.7±1.2MPa; 515.1.5±14.1MPa; 0.9±0.2mm for 1x450mm and 2x450mm models, respectively. With the mid-span vertical displacements at 30.1±0.5mm (1x450mm) and 30.1±1.3mm (2x450mm), the global shear force, the von Mises stresses of tees and shear studs, and the relative slips were 328.7±55.2kN; 371.8±18.5MPa; 640.7±16.6MPa; 3.0±0.3mm and 421.2±76.2kN; 380.4±24.2MPa; 603.2±21.8MPa; 2.2±0.4mm for 1x450mm and 2x450mm models, respectively. In the ultimate resistance, for the mid-span vertical displacements at 32.3±4.2mm (1x450mm) and 44.0±10.7mm (2x450mm), the global shear force, the von Mises stresses of tees and shear studs, and the relative slips were 371.1±58.6kN; 375.6±29.7MPa; 664 MPa; 3.5±0.2mm and 449.9±68.7kN; 435.7±46.5MPa; 659.1±11.4MPa; 3.1±0.4mm for 1x450mm and 2x450mm models, respectively. An example of comparations of the ultimate global shear force between the present (1x450mm and 2x450mm) and previous analyses (1x300mm and 2x300mm), considering composite cellular beams with PCHCSCT, is presented at in **Table 9** and **Fig. 17**.

Table 9 – Global shear force comparative analyses between the present and previous models with PCHCSCT (in kN)

$V_{(1x300)}$	$V_{(1x450)}$	$V_{(1x450)}/V_{(1x300)}$	$V_{(2x300)}$	$V_{(2x450)}$	$V_{(2x450)}/V_{(2x300)}$
395.9±62.0	371.1±58.6	0.94	483.7±70.7	449.9±68.7	0.93

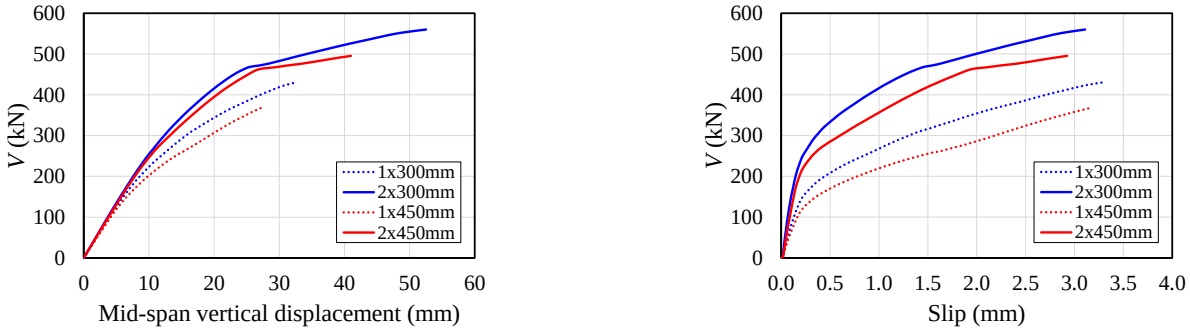

(a) Global shear force vs. mid-span vertical displacement (b) Global shear force vs. slip

Fig. 17: D_o/d=1.2 and p/D_o=1.5 models with PCHCSCT. Failure mode: VM*

Fig. 18 show the influence of the concrete topping ($V_{PCHCSCT}$-V_{PCHCS}). An important observation in p/D_o=1.5 (**Fig. 18a**) is the negative difference ($V_{PCHCSCT}$-V_{PCHCS}<0) for both 1x450mm and 2x450mm models. In the 1x450mm models the VM* was observed for both PCHCS and PCHCSCT models. For the PCHCS and PCHCSCT with 2x450mm models, the failure mode was WPB+PM* and VM*, respectively. The negative difference implies that the models with PCHCS obtained a greater global shear force compared to the models with PCHCSCT. This occurred due to the position of the neutral plastic axis. Although in the composite section with partial interaction there are two neutral plastic axes (one in cellular profile and one in the slab), in models with PCHCS, the neutral plastic axis was closer to the cellular profile. In this context, the slab will absorb a greater amount of compression stresses. On the other hand, with the presence of the concrete topping, the neutral plastic axis is closer to the compressed edge of the slab, a factor that intensifies the tensile stresses. The distance between the neutral plastic axis and the extreme fiber of the concrete slab in compression can be calculated as $nP_{sc}/0.85f_cb_{eff}$. Another observation is illustrated in **Fig. 18e**. In this illustration, for the models p/D_o=1.5 and 1x450mm, the failure modes were VM* and WPB+PM* for the models with PCHCS and PCHCSCT, respectively. In this scenario, the negative difference occurred due to the model with PCHCSCT having the resistance governed by the cellular profile. The maximum difference with a value equal to 85N was observed for the model D_o/d=0.9 and p/D_o=1.5 with 2x450mm (**Fig. 18b**). The minimum difference, which was -78kN, it was analyzed for the D_o/d=0.8 and p/D_o=1.5 model with 2x450mm (**Fig. 18a**).

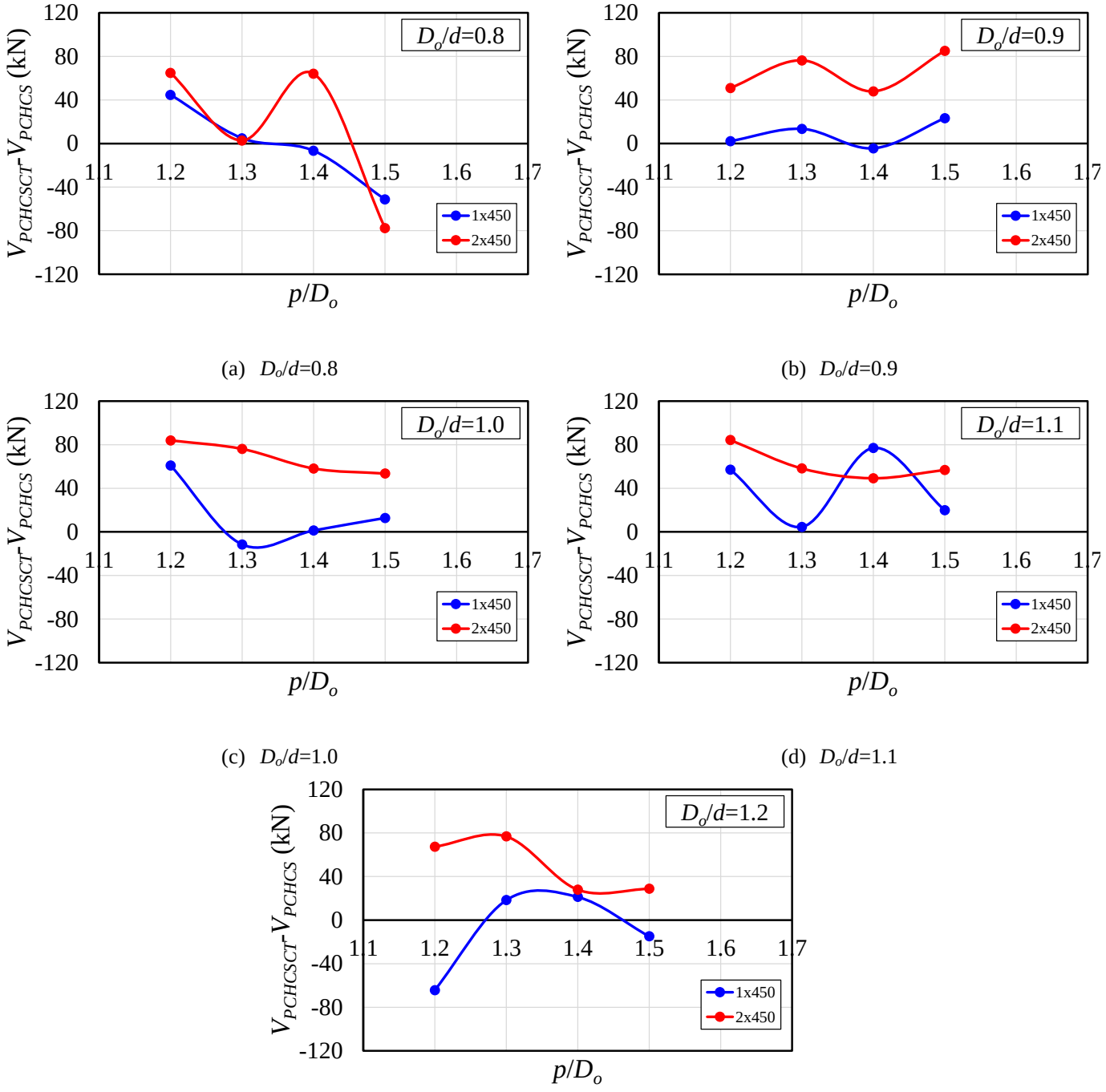

(a) D_o/d=0.8

(b) D_o/d=0.9

(c) D_o/d=1.0

(d) D_o/d=1.1

(e) D_o/d=1.2

Fig. 18: The influence of concrete topping for models with 450mm of shear studs spacing

Fig. 19 shows the shear resistance of the models analyzed as a function of key parameters, such as the D_o/d and p/D_o. It is observed that the models with 2x450mm presented greater resistance to global shear force than the models with 1x450mm. In addition, there is a drop in the resistance of the models D_o/d=1.0 and p/D_o=1.2 (**Fig 19c**), and D_o/d=1.2 and p/D_o=1.2 (**Fig 19e**), as previously presented (**Fig. 11c**, **Fig. 11e**, **Fig. 15c** and **Fig. 15e)**. Therefore, so far, it is possible to state that for all the models analyzed, double shear studs provided greater resistance than one line of shear studs. The failure modes analyzed are presented (**Table 10**).

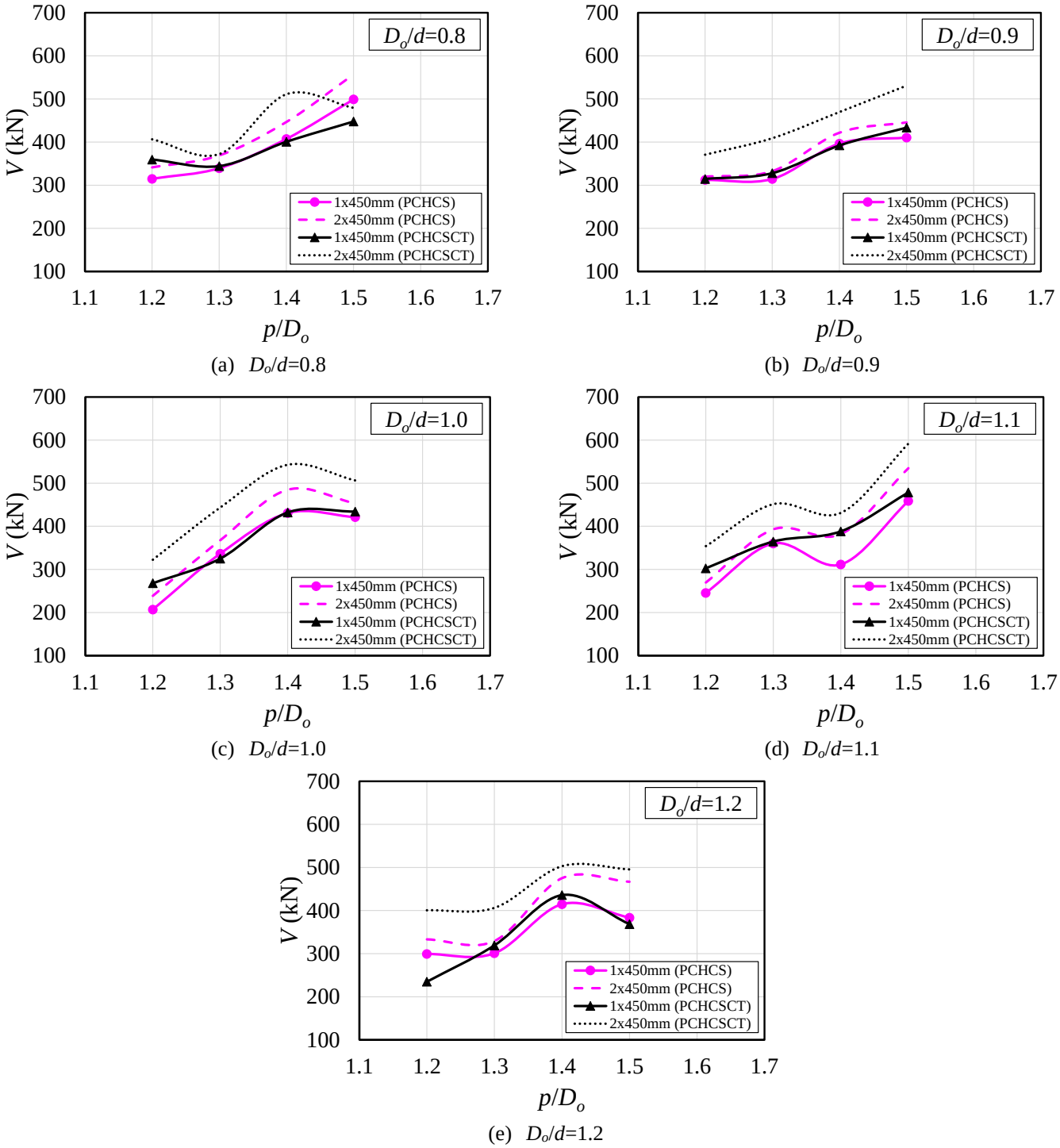

(a) D_o/d=0.8 (b) D_o/d=0.9

(c) D_o/d=1.0 (d) D_o/d=1.1

(e) D_o/d=1.2

Fig. 19: Results for models with 450mm of shear studs spacing, considering PCHCS and PCHCSCT

Table 10 – Failure modes for 1x450mm and 2x450mm models

D_o/d	p/D_o	1x450mm		2x450mm	
		PCHCSCT	PCHCS	PCHCSCT	PCHCS
0.8	1.2	VM*	VM*	WPB+PM*	VM*
	1.3	VM*	WPB+PM*	VM*	WPB+PM*
	1.4	VM*	WPB+PM*	WPB+PM*	WPB+PM
	1.5	VM*	PM*	VM*	WPB+PM
0.9	1.2	VM*	WPB+PM*	WPB+PM*	VM
	1.3	WPB+PM*	WPB+PM*	WPB+PM*	WPB+PM*
	1.4	VM*	WPB+PM*	WPB+PM*	WPB+PM*
	1.5	VM*	WPB+PM	WPB+PM*	WPB+PM
1.0	1.2	WPB+PM*	VM*	WPB+PM*	VM
	1.3	VM*	WPB+PM	WPB+PM*	WPB+PM
	1.4	VM*	WPB+PM*	VM	WPB+PM
	1.5	VM*	WPB+PM*	VM	WPB+PM*
1.1	1.2	VM*	WPB+PM	WPB+PM*	WPB+PM
	1.3	VM *	WPB+PM*	WPB+PM	WPB+PM*
	1.4	VM *	PM*	VM	WPB+PM
	1.5	VM*	VM*	VM*	VM
1.2	1.2	VM*	WPB+PM*	WPB+PM*	WPB+PM
	1.3	VM*	VM	WPB+PM*	VM
	1.4	VM*	VM*	VM*	WPB+PM
	1.5	VM*	VM*	VM*	VM

*The shear stud rupture occurred.

5.4. SUMMARY OF RESULTS

In this section the results are presented by the shear resistance of the models analyzed as a function of key parameters (D_o/d and p/D_o), considering composite cellular beams with PCHCS (**Fig. 20**) and PCHCSCT (**Fig. 21**). The illustrations are accompanied by the lateral view of the models ($L/4$ from support) to observe the shear stud position at most critical opening, which is the one that is closest to the support. It was observed in most models, that the greater the number of connectors, the greater the global shear resistance. In contrast, the smaller the number of connectors, the lower the global shear resistance. These resistance values tend to converge, since the failure mode is limited by the shear stud rupture. Another important factor regarding the number of shear studs is the equivalent resistance. For example, the resistance of the 1x150mm models was similar to the resistance of the 2x300 models. In both models, the number of shear studs is the same. Such observation was evaluated for the models with PCHCS and PCHCSCT. This statement is also valid for the 1x300mm and 2x450mm models. However, in this context, there was a small difference between the shear resistances, due to the difference between the number of shear studs, since the 1x300mm and 2x450 models have 10 and 14 shear studs (from support to mid-span), respectively. Regarding **Fig. 20a**, for the series D_o/d=0.8; p/D_o=1.3, there was a drop in resistance in the 1x300mm models compared to the 1x450mm models. This drop was also observed in **Fig. 20b** for the series D_o/d=0.9; p/D_o=1.2. This is attributed to the fact that the 1x300mm models do not have shear studs in the length of the second opening from the support, which may have caused the drop in resistance. An interesting observation presented in **Fig. 21a**, considering the series D_o/d=0.8; p/D_o=1.2-1.5 and 2x450mm, is the change in the ultimate resistance due to shear stud positioning.

For D_o/d=0.8; p/D_o=1.2;1.4, the WPB+PM* was observed, while for models D_o/d=0.8; p/Do=1.3;1.5, the VM* was observed. This is explained by the fact that the D_o/d=0.8; p/D_o=1.2;1.4 models included shear studs allocated above the first opening, unlike the D_o/d=0.8; p/Do=1.3;1.5 models, where shear studs were not allocated above the first opening. Finally, the results presented in **Fig. 20c**, **Fig. 20e**, **Fig. 21c** and **Fig. 21e** shows the pattern in the drop of resistance of the models p/Do=1.4 for the models p/Do=1.5, due to the end-post width, according to the previous discussion.

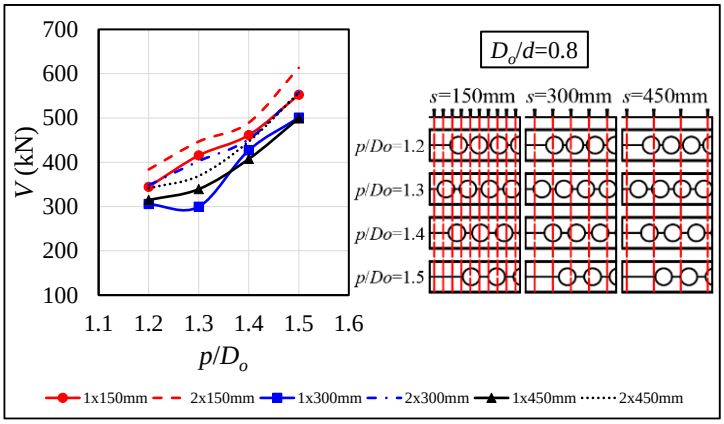

(a)D_o/d=0.8

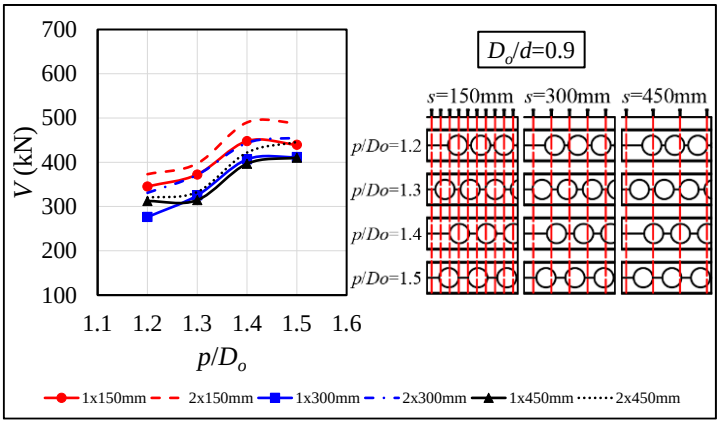

(b)D_o/d=0.9

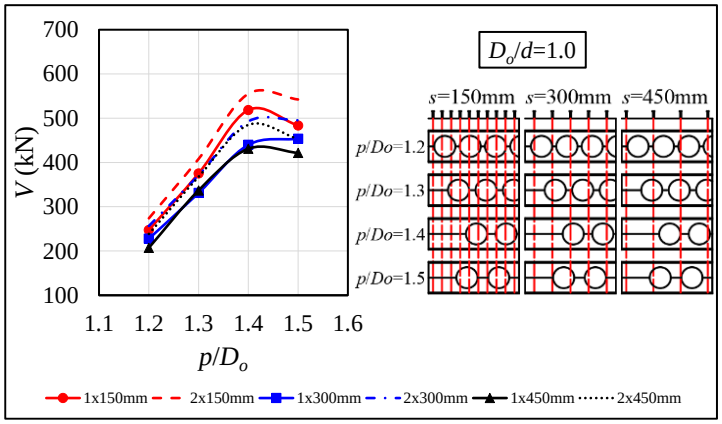

(a) D_o/d=1.0

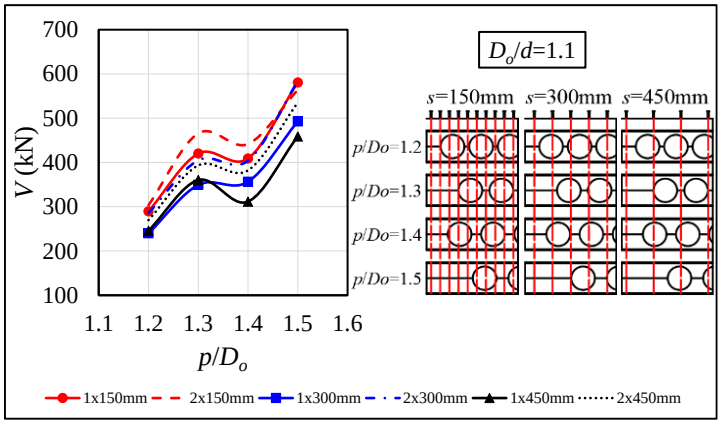

(b) D_o/d=1.1

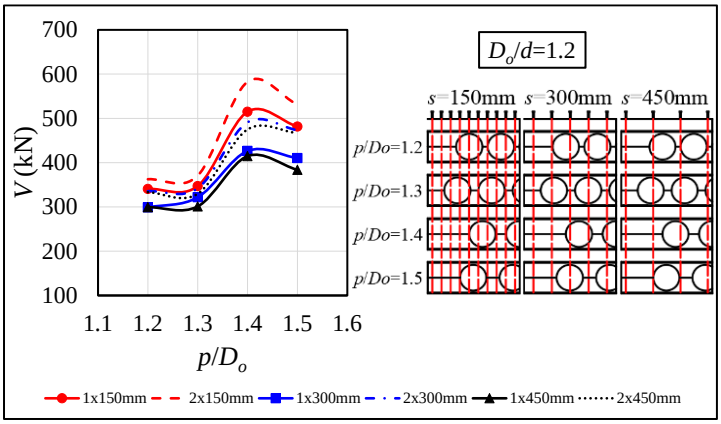

(c) D_o/d=1.2

Fig. 20: Summary of results for composite cellular beams with PCHCS

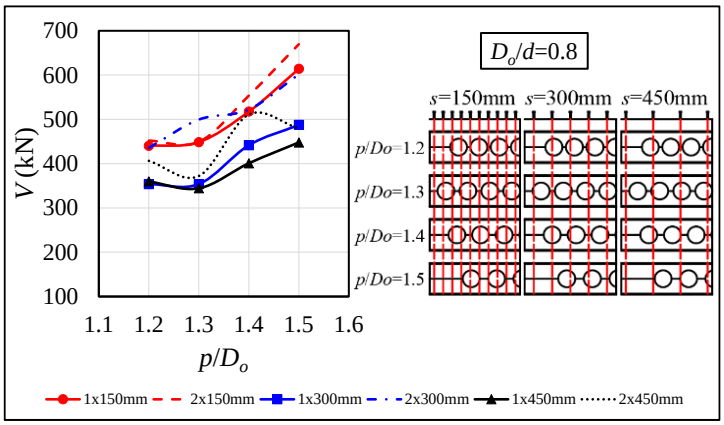

(a)D_o/d=0.8

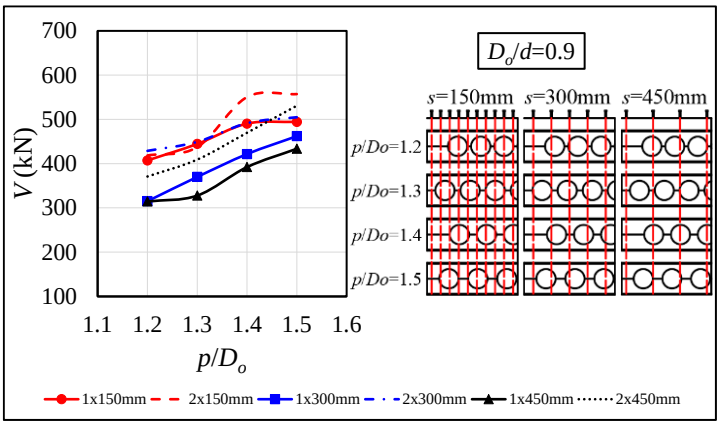

(b)D_o/d=0.9

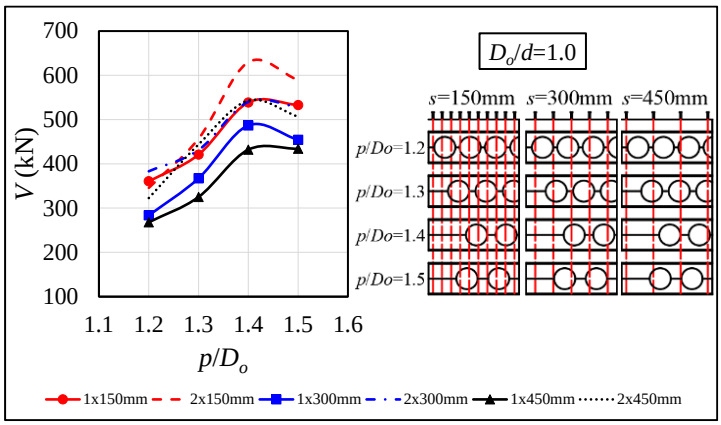

(c) D_o/d=1.0

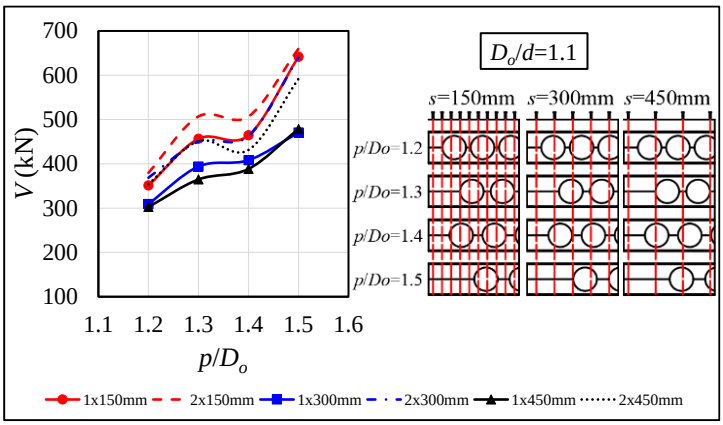

(d) D_o/d=1.1

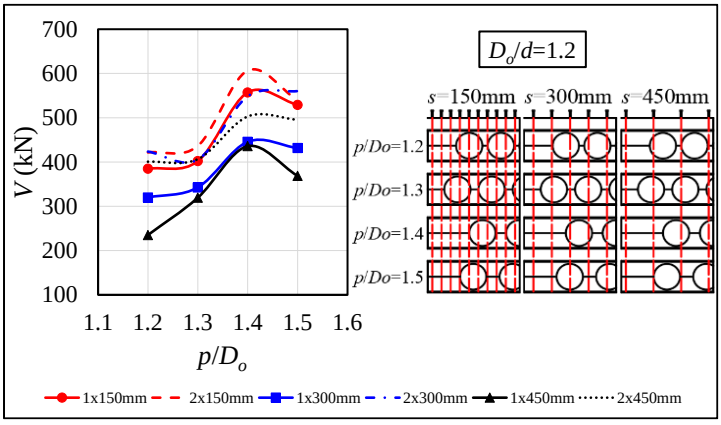

(e) D_o/d=1.2

Fig. 21: Summary of results for composite cellular beams with PCHCSCT

5.5. CALCULATION RECOMMENDATION

In this section, a calculation recommendation for WPB resistance of composite cellular beams with PCHCS or PCHCSCT is described. SCI P355 [15] presents equations for the limiting values of global shear force, considering partial (**Eq. 13**) and full interaction (**Eq. 14**). However, these equations were performed for composite beams with steel-concrete composite slabs.

$$V_{Rd} = \frac{V_{WPB}\left(D_o / p\right) + \left(4M_{bT,NV,Rd} / 0.45D_o\right)}{1 + h_{o,eff} / h_{eff}} + \frac{\Delta N_{sc,Rd}}{p}\left(y_t + h_s - 0.5h_c\right) \tag{13}$$

$$V_{Rd} = \left[V_{WPB}\left(D_o / p\right) + \left(4M_{bT,NV,Rd} / 0.45D_o\right)\right]\frac{\left(h_{eff} + h_s - 0.5h_c\right)}{h_{eff} + D_o} \tag{14}$$

The buckling resistance (V_{WPB}) is calculated according to **Eqs. (15-21)**, $M_{bT,NV,Rd}$ is the plastic resistance of the lower tee reduced due to axial tension multiplying by the approximate factor $\left[1-\left(N / N_{pl}\right)^2\right]$, and $\Delta N_{sc,Rd}$ is defined as the product of the number of connectors ($n_{sc,wp}$) in the web post width (p) by the shear studs resistance (P_{sc}).

$$\chi = \frac{1}{\phi + \sqrt{\phi^2 - \lambda_0{}^2}} \le 1.0 \tag{15}$$

$$\phi = 0.5\left[1 + \alpha\left(\lambda_0 - 0.2\right) + \lambda_0{}^2\right] \tag{16}$$

$$\lambda_0 = \sqrt{\frac{f_y}{f_{cr,w}}} \tag{17}$$

$$f_{cr,w} = \frac{\pi^2 E}{\lambda_w^2} \tag{18}$$

$$l_{eff} = 0.5\sqrt{b_w^2 + D_o^2} \le 0.7D_o \tag{19}$$

$$\lambda_w = \frac{l_{eff}\sqrt{12}}{t_w} \tag{20}$$

$$V_{WPB} = \chi f_y t_w b_w \tag{21}$$

Table 11: Imperfection factors for buckling curves according EC3

Buckling curve	*a*	*b*	*c*	*d*
Imperfection factor (α)	0.21	0.34	0.49	0.76

The SCI P355 [15] recommends using the buckling curve *c* (**Table 11**). The limits, for the use of the buckling curve *c*, are sections that have d/b_f>1.2 with 40mm<t_f≤100mm, and d/b_f≤1.2 with t_f≤100mm. However, the interaction degree of composite cellular beams is not clearly defined, according to the SCI P355 [15] specifications, since this recommendation suggests choosing the lowest calculated value, between the **Eqs. (13-14)**, for the resistance prediction. Similarly, from the study by Sheehan et al. [60]

- presented in section 2, the spacing between the shear studs significantly influenced the WPB resistance. This shows that the number of shear studs must be taken into account in the resistance calculation. In addition, the combination of WPB the formation of the Vierendeel plastic hinges were verified in all models especially at the web depth of the tees.

In this context, the present study proposes a simplified way of calculating the resistant global shear force, considering composite cellular beams with PCHCS or PCHCSCT (**Eq. 22**). V_{WPB} is calculated according **Eqs. (15-21)**. $V_{pl,T}$ is the plastic shear resistance due to both tees (**Eq. 23**), taking into account two factors: (A_{wt}/A_t) and (D_o/d). This is because stating that both tees are completely plasticized can lead to overestimated results. Finally, the shear resistance due to composite action can be taken according to **Eq. (24)**:

$$V_{Rd} = V_{WPB} + V_{pl,T} + V_{VC} \tag{22}$$

$$V_{pl,T} = 4\left[\frac{A_{wT} f_y \left(0.5h_{w,T} + t_f - z_{pl}\right) + A_{fT} f_y \left(0.5t_f - z_{pl} + z_{pl}{}^2 / t_f\right)}{0.45D_o}\right]\left(\frac{A_{wT}}{A_T}\right)\left(\frac{Do}{d}\right) \tag{23}$$

$$V_{VC} = k\frac{P_{sc}}{s}\left(y_t + 0.5h_c\right) \tag{24}$$

It is not obvious which buckling curve to use, as shown in **Eq. (14)** and **Table 6**. Following, the numerical results are compared with the buckling curves *c* (**Fig. 22a**), *b* (**Fig. 22b**) and *a* (**Fig. 22c**). As it is depicted, it was observed that when only buckling resistance is considered (V_{Rd}=V_{WPB}), the resistant values tend to underestimate the shear resistance of the composite cellular beams with PCHCS and PCHCSCT. In this context, it was verified that the average values of the ratio between the analytical and numerical models (V_{FE}) are less than 65%, i.e. V_{WPB}/V_{FE}<0.65. These values tend to decrease as the imperfection factor (α) was increased. On the other hand, when **Eq. (20)** was considered, the average values of the ratio between the analytical and numerical models are greater than 82% (V_{Rd}/V_{FE}>0.83). These values tend to increase, as the imperfection factor was reduced, and this ratio can reach 93% (V_{WPB}/V_{FE}>0.93) with the buckling curve *a*. In total, 142 numerical models were characterized by WPB. Considering the buckling curve *c*, only 10 observations overestimated the resistance of the models. In this context, the maximum value found for the ratio between **Eq. (20)** and the numerical model was 1.06. For buckling curves *b* and *a*, these values were increased. For the buckling curve *b*, 30observations were overestimated, with the maximum value of the ratio at 1.14. For the buckling curve *a*, 55 observations were overestimated, with the maximum value of the ratio at 1.23. Therefore, the buckling curve *c*, as recommended by SCI P355 [15] is a good option.

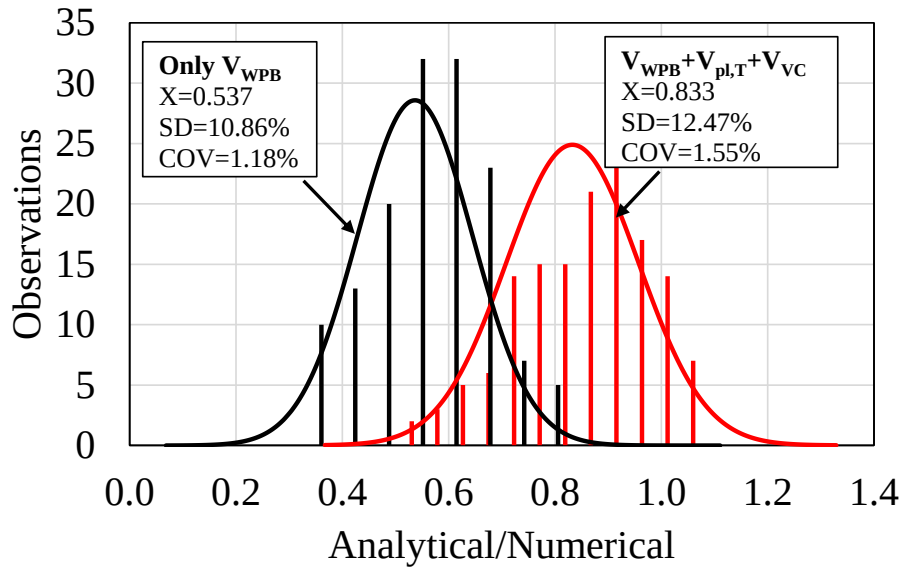

(a) V_{WPB} vs. $V_{WPB}+V_{pl,T}+V_{VC}$, considering bucking curve *c*

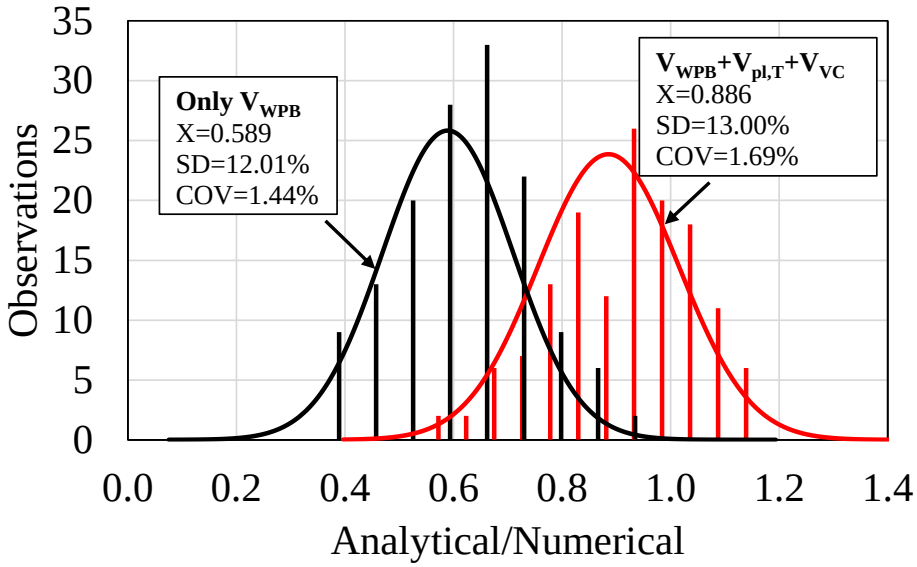

(b) V_{WPB} vs. $V_{WPB}+V_{pl,T}+V_{VC}$, considering bucking curve *b*

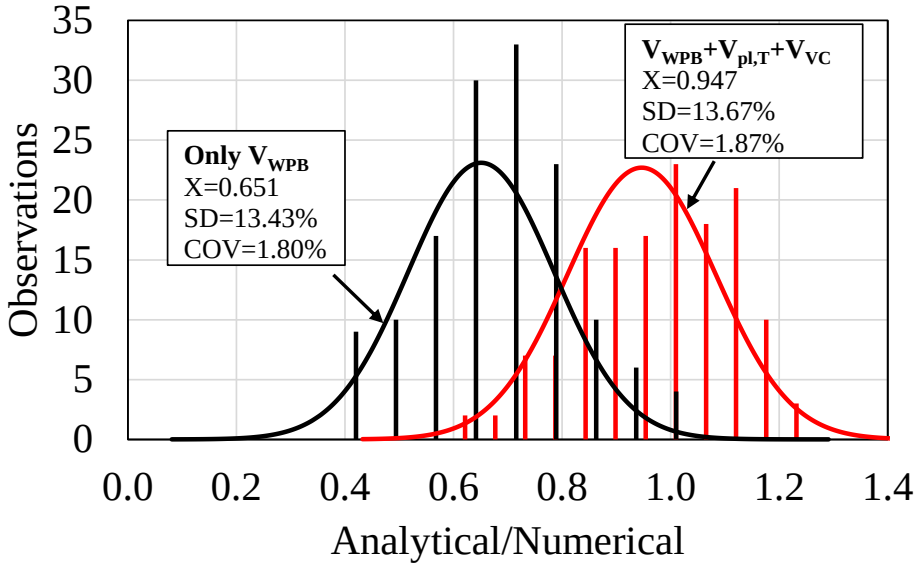

(c) V_{WPB} vs. $V_{WPB}+V_{pl,T}+V_{VC}$, considering bucking curve *a*

542 **Fig. 22: Statistical analyses**

CONCLUDING REMARKS

This paper developed a parametric study to investigate the composite action on the web post buckling resistance of composite cellular beams with PCHSC and PCHSCT. In this study, the opening diameter, the web post width and the shear studs spacing, with single and double row, were the parameters evaluated. The results of 240 models were presented and discussed. A proposed global shear resistance calculation approach of composite cellular beams with PCHCS and PCHCSCT was compared with the numerical results. It was concluded that:

1. The predominant failure mode was the combination of web post buckling with plastic mechanism. As the spacing between the shear studs was increased, that is, the number of connectors was reduced, this combination was accompanied by the shear stud rupture.
2. The shear stud rupture was observed, mainly for the analyses with PCHCSCT. In these models, the CT provided an increase in the axial resistance of the PCHCS, a factor that limited the resistance of the composite cellular beams to the resistance of the connection.
3. PCHCSCT models showed greater (or similar) global shear resistance than the PCHCS models. The CT contributed to the increase in global shear resistance. However, as the number of shear studs decreased, the resistance was similar due to the shear stud rupture. This showed that the resistance of the structural system was limited to the resistance of the connection, as the condition of partial interaction.
4. The models with two rows of shear stud presented greater global shear resistance than the models with a single row. This is due to the fact that the greater the number of connectors, the greater the resistance of the composite action. The global shear resistance was similar for the models that the shear stud rupture occurred;
5. Equivalent resistance of composite cellular beams has been verified. The models that presented the same number of shear studs, regardless of the spacing, obtained similar global shear resistance. As presented in the results summary section, the resistance of the 1x150mm models was similar to the resistance of the 2x300 models, and it is also valid for the 1x300mm and 2x450mm models. In both models that were compared, the number of shear studs is the same. This implies that the number of connectors influenced the behavior of the ultimate resistance. Therefore, the number of connectors is an important factor to be considered when calculating resistance.
6. There was a drop in global shear resistance due to the absence of shear studs in the openings close to the support. This was due to the absence of composite action. It is recommended to place shear studs above the openings next to the support, regardless of the spacing between the shear studs.
7. Ductile behavior at the connection interface was not observed in any model. This is because the relative slips greater than or equal to 6mm were not verified in any model. Therefore, even if it further reduces the number of connectors for ductile behavior to occur, it is likely that the connection will fail before reaching the acceptable slip value, which defines ductile behavior.

8. The composite action resistance is an important factor to be considered in the web post buckling resistance calculation. This means that the greater the number of shear studs, the greater the web post buckling resistance;

ACKNOWLEDGMENTS

The authors would like to thank Construção Metálica – Gerdau Aços Brasil for making available the data related to COPPETEC, PEC-18541. This work was supported by the São Paulo Research Foundation (FAPESP) [grant number #2018/22803-1].

REFERENCES

[1] Lawson RMM, Lim J, Hicks SJJ, Simms WII. Design of composite asymmetric cellular beams and beams with large web openings. J Constr Steel Res 2006;62:614–29. https://doi.org/10.1016/j.jcsr.2005.09.012.

[2] Lawson RM, Saverirajan AHA. Simplified elasto-plastic analysis of composite beams and cellular beams to Eurocode 4. J Constr Steel Res 2011;67:1426–34. https://doi.org/10.1016/j.jcsr.2011.03.016.

[3] Ahmed IM, Tsavdaridis KD. The evolution of composite flooring systems: applications, testing, modelling and eurocode design approaches. J Constr Steel Res 2019;155:286–300. https://doi.org/10.1016/j.jcsr.2019.01.007.

[4] Baran E. Effects of cast-in-place concrete topping on flexural response of precast concrete hollow-core slabs. Eng Struct 2015;98:109–17. https://doi.org/10.1016/j.engstruct.2015.04.017.

[5] Ibrahim IS, Elliott KS, Abdullah R, Kueh ABH, Sarbini NN. Experimental study on the shear behaviour of precast concrete hollow core slabs with concrete topping. Eng Struct 2016;125:80–90. https://doi.org/10.1016/j.engstruct.2016.06.005.

[6] Ferreira FPV, Martins CH, De Nardin S. Assessment of web post buckling resistance in steel-concrete composite cellular beams. Thin-Walled Struct 2021;158:106969. https://doi.org/10.1016/j.tws.2020.106969.

[7] Panedpojaman P, Thepchatri T, Limkatanyu S. Novel simplified equations for Vierendeel design of beams with (elongated) circular openings. J Constr Steel Res 2015;112:10–21. https://doi.org/10.1016/j.jcsr.2015.04.007.

[8] Tsavdaridis KD, D'Mello C. Web buckling study of the behaviour and strength of perforated steel beams with different novel web opening shapes. J Constr Steel Res 2011;67:1605–20. https://doi.org/10.1016/j.jcsr.2011.04.004.

[9] Erdal F, Saka MP. Ultimate load carrying capacity of optimally designed steel cellular beams. J Constr Steel Res 2013;80:355–68. https://doi.org/10.1016/j.jcsr.2012.10.007.

[10] Grilo LF, Fakury RH, Castro e Silva ALR de, Veríssimo G de S. Design procedure for the web-post buckling of steel cellular beams. J Constr Steel Res 2018;148:525–41. https://doi.org/10.1016/j.jcsr.2018.06.020.

[11] Kerdal D, Nethercot DA. Failure modes for castellated beams. J Constr Steel Res 1984;4:295–315. https://doi.org/10.1016/0143-974X(84)90004-X.

[12] Tsavdaridis KD, D'Mello C. Vierendeel Bending Study of Perforated Steel Beams with Various Novel Web Opening Shapes through Nonlinear Finite-Element Analyses. J Struct Eng 2012;138:1214–30. https://doi.org/10.1061/(asce)st.1943-541x.0000562.

[13] Chung KF, Liu TCH, Ko ACH. Investigation on vierendeel mechanism in steel beams with circular web openings. J Constr Steel Res 2001;57:467–90. https://doi.org/10.1016/S0143-974X(00)00035-3.

[14] Redwood R, Cho SH. Design of steel and composite beams with web openings. J Constr Steel Res 1993;25:23–41. https://doi.org/10.1016/0143-974X(93)90050-3.

[15] Lawson RM, Hicks SJ. Design of composite beams with large web openings. SCI P355. The Steel Construction Institute; 2011.

[16] Araújo DL, Sales MWR, Paulo SM, El Debs ALHC. Headed steel stud connectors for composite steel beams with precast hollow-core slabs with structural topping. Eng Struct 2016;107:135–50. https://doi.org/10.1016/j.engstruct.2015.10.050.

[17] Fares SS, Coulson J, Dinehart DW. AISC Steel Design Guide 31: Castellated and Cellular Beam Design. American Institute of Steel Construction; 2016.

[18] European committee for standardization. EN 1994-1-1: Eurocode 4 – Design of composite steel and concrete structures – Part 1-1: General rules for buildings. 2004.

[19] American Institute of Steel Construction. ANSI/AISC 360-16 - Specification for structural steel buildings. 2016.

[20] Vassart O, Hawer M, Simms I, Zhao B, Franssen JM, Nadjai A. European Commission. EUR 25122 Fire resistance of long span cellular beam made of rolled profiles. Luxemb Publ Off Eur Union 2012. https://doi.org/10.2777/38158.

[21] Verweij JG. Cellular beam-columns in portal frame structures. 2010. M.Sc. thesis. Delft University of Technology Civil Engineering, 2010.

[22] Bitar D, Demarco T, Martin P-O. Steel and composite cellular beams - Novel approach for design based on experimental studies and numerical investigations. 4th; Eur. Conf. Steel Compos. Struct. Eurosteel 2005, vol. b, Maastricht, Netherlands: Druck und Veragshaus,; ; n.d., p. 1.10-1.

[23] European committee for standardization. Eurocode 3: Design of steel structures—Part 1-1: General rules and rules for buildings 2005.

[24] ArcelorMittal. ACB® and Angelina® beams - A New Generation of Cellular Beams 2018.

[25] Redwood RG, Poumbouras G. Tests of composite beams with web holes. Can J Civ Eng 1983;10:713–21. https://doi.org/10.1139/l83-100.

[26] Redwood RG, Poumbouras G. Analysis of composite beams with web openings. J Struct Eng 1984;110:1949–58. https://doi.org/10.1061/(ASCE)0733-9445(1984)110:9(1949).

[27] Donahey RC, Darwin D. Web openings in composite beams with ribbed slabs. J Struct Eng 1988;114:518–34. https://doi.org/10.1061/(ASCE)0733-9445(1988)114:3(518).

[28] Cho SH, Redwood RG. Slab behavior in composite beams at openings. I: analysis. J Struct Eng 1992;118:2287–303. https://doi.org/10.1061/(ASCE)0733-9445(1992)118:9(2287).

[29] Cho SH, Redwood RG. Slab behavior in composite beams at openings. II: tests and verification. J Struct Eng 1992;118:2304–22. https://doi.org/10.1061/(ASCE)0733-9445(1992)118:9(2304).

[30] Ferreira FPV, Tsavdaridis KD, Martins CH, De Nardin S. Ultimate strength prediction of steel–concrete composite cellular beams with PCHCS. Eng Struct 2021;236:112082. https://doi.org/10.1016/j.engstruct.2021.112082.

[31] Lam D. Composite steel beams using precast concrete hollow core floor slabs. 1998. Ph.D. thesis. University of Nottingham, 1998.

[32] Ellobody E, Lam D. Modelling of headed stud in steel-precast composite beams. Steel Compos Struct 2002;2:355–78. https://doi.org/10.12989/scs.2002.2.5.355.

[33] Lam D. Capacities of headed stud shear connectors in composite steel beams with precast hollowcore slabs. J Constr Steel Res 2007;63:1160–74. https://doi.org/10.1016/j.jcsr.2006.11.012.

[34] Lam D. Designing composite beams with precast hollowcore slabs to Eurocode 4. Adv Steel Constr 2007;3:594–606. https://doi.org/10.18057/IJASC.2007.3.2.

[35] Lam D, Elliott KS, Nethercot DA. Experiments on composite steel beams with precast concrete hollow core floor slabs. Proc Inst Civ Eng - Struct Build 2000;140:127–38. https://doi.org/10.1680/stbu.2000.140.2.127.

[36] Lam D, Elliott KS, Nethercot DA. Parametric study on composite steel beams with precast concrete hollow core floor slabs. J Constr Steel Res 2000;54:283–304. https://doi.org/10.1016/S0143-974X(99)00049-8.

[37] Hicks SJ, Lawson RM. Design of composite beams using precast concrete slabs. SCI P287. The Steel Construction Institute; 2003.

[38] Gouchman GH. Design of composite beams using precast concrete slabs in accordance with EUROCODE 4. SCI P401. The Steel Construction Institute; 2014.

[39] Batista EM, Landesmann A. Análise experimental de vigas mistas de aço e concreto compostas por lajes alveolares e perfis laminados. COPPETEC, PEC-18541 2016.

[40] Ferreira FPV, Martins CH, De Nardin S. A parametric study of steel-concrete composite beams with hollow core slabs and concrete topping. Structures 2020;28:276–96. https://doi.org/10.1016/j.istruc.2020.08.045.

[41] Granade CJ. An investigation of composite beams having large rectangular openings in their webs. 1968. Partial M.Sc. thesis. University of Alabama, 1968.

[42] Clawson WC, Darwin D. Composite beams with web openings. ASCE J Struct Div 1982;108:145–62.

[43] Cho SH. An investigation on the strength of composite beams with web openings. 1982. M.Sc. thesis. Hanyang University, 1982.

[44] Narayanan R, Al-Amery RIM, Roberts TM. Shear strength of composite plate girders with rectangular web cut-outs. J Constr Steel Res 1989;12:151–66. https://doi.org/10.1016/0143-974X(89)90030-8.

[45] Roberts TM, Al-Amery RIM. Shear strength of composite plate girders with web cutouts. J Struct Eng 1991;117:1897–910. https://doi.org/10.1061/(ASCE)0733-9445(1991)117:7(1897).

[46] Todd DM, Cooper PB. Strength of composite beams with web openings. ASCE J Struct Div 1980;106:431–44.

[47] Donoghue CM. Strength of composite beams with web openings. ASCE J Struct Div 1982;108:2652–67.

[48] Clawson WC, Darwin D. Strength of composite beams at web openings. ASCE J Struct Div 1982;108:623–41.

[49] Benitez MA, Darwin D, Donahey RC. Deflections of composite beams with web openings. J Struct Eng 1998;124:1139–47. https://doi.org/10.1061/(ASCE)0733-9445(1998)124:10(1139).

[50] Chung K., Lawson R. Simplified design of composite beams with large web openings to Eurocode 4. J Constr Steel Res 2001;57:135–64. https://doi.org/10.1016/S0143-974X(00)00011-0.

[51] Redwood RG, Wong PK. Web holes in composite beams with steel deck. Can. Struct. Eng. Conf. -1982, Ontario, Toronto: Canadian Steel Construction Council; 1982, p. 1–41.

[52] Lawson RM, Chung KF, Price AM. Tests on composite beams with large web openings to justify existing design methods. Struct Enginee 1992;70:1–7.

[53] Park JW, Kim CH, Yang SC. Ultimate Strength of Ribbed Slab Composite Beams with Web Openings. J Struct Eng 2003;129:810–7. https://doi.org/10.1061/(asce)0733-9445(2003)129:6(810).

[54] Darwin D, Donahey RC. LRFD for composite beams with unreinforced web openings. J Struct Eng 1988;114:535–52. https://doi.org/10.1061/(ASCE)0733-9445(1988)114:3(535).

[55] Fahmy EH. Analysis of composite beams with rectangular web openings. J Constr Steel Res 1996;37:47–62. https://doi.org/10.1016/0143-974X(95)00022-N.

[56] Ferreira FPV, Martins CH, De Nardin S. Advances in composite beams with web openings and composite cellular beams. J Constr Steel Res 2020;172:106182. https://doi.org/10.1016/j.jcsr.2020.106182.

[57] Müller C, Hechler O, Bureau A, Bitar D, Joyeux D, Cajot LG, et al. Large web openings for service integration in composite floors. Technical Steel Research. European Comission, Contract No 7210-PR/315. Final report 2006.

[58] Nadjai A. Performance of cellular composite floor beams at ambient temperature. 2005.

[59] Nadjai A, Vassart O, Ali F, Talamona D, Allam A, Hawes M. Performance of cellular composite floor beams at elevated temperatures. Fire Saf J 2007;42:489–97. https://doi.org/10.1016/j.firesaf.2007.05.001.

[60] Sheehan T, Dai X, Lam D, Aggelopoulos E, Lawson M, Obiala R. Experimental study on long spanning composite cellular beam under flexure and shear. J Constr Steel Res 2016;116:40–54. https://doi.org/10.1016/j.jcsr.2015.08.047.

[61] Ferreira FPV, Tsavdaridis KD, Martins CH, De Nardin S. Buckling and post-buckling analyses of composite cellular beams. Compos Struct 2021;262:113616. https://doi.org/10.1016/j.compstruct.2021.113616.

[62] El-Lobody E, Lam D. Finite Element Analysis of Steel-Concrete Composite Girders. Adv Struct Eng 2003;6:267–81. https://doi.org/10.1260/136943303322771655.

[63] European committee for standardization. Eurocode 2: Design of concrete structures - Part 1-1 : General rules and rules for buildings 2004.

[64] Ferreira FPV, Rossi A, Martins CH. Lateral-torsional buckling of cellular beams according to the possible updating of EC3. J Constr Steel Res 2019;153:222–42. https://doi.org/10.1016/j.jcsr.2018.10.011.

[65] Ferreira FPV, Martins CH. LRFD for Lateral-Torsional Buckling Resistance of Cellular Beams. Int J Civ Eng 2020;18:303–23. https://doi.org/10.1007/s40999-019-00474-7.

[66] Rossi A, Ferreira FPV, Martins CH, Mesacasa Júnior EC. Assessment of lateral distortional buckling resistance in welded I-beams. J Constr Steel Res 2020;166:105924. https://doi.org/10.1016/j.jcsr.2019.105924.

[67] Rajana K, Tsavdaridis KD, Koltsakis E. Elastic and inelastic buckling of steel cellular beams under strong-axis bending. Thin-Walled Struct 2020;156:106955. https://doi.org/10.1016/j.tws.2020.106955.

[68] Ellobody E. Nonlinear analysis of cellular steel beams under combined buckling modes. Thin-Walled Struct 2012;52:66–79. https://doi.org/10.1016/j.tws.2011.12.009.

[69] Dassault Systèmes Simulia. Abaqus 6.18 2016.

[70] Chen S, Jia Y. Numerical investigation of inelastic buckling of steel–concrete composite beams prestressed with external tendons. Thin-Walled Struct 2010;48:233–42. https://doi.org/10.1016/j.tws.2009.10.009.

[71] Zhou W-B, Yan W-J. Refined nonlinear finite element modelling towards ultimate bending moment calculation for concrete composite beams under negative moment. Thin-Walled Struct 2017;116:201–11. https://doi.org/10.1016/j.tws.2017.02.011.

[72] Hillerborg A, Modéer M, Petersson P-E. Analysis of crack formation and crack growth in concrete by means of fracture mechanics and finite elements. Cem Concr Res 1976;6:773–81. https://doi.org/10.1016/0008-8846(76)90007-7.

[73] Lubliner J, Oliver J, Oller S, Oñate E. A plastic-damage model for concrete. Int J Solids Struct 1989;25:299–326. https://doi.org/10.1016/0020-7683(89)90050-4.

[74] Lee J, Fenves GL. Plastic-Damage Model for Cyclic Loading of Concrete Structures. J Eng Mech 1998;124:892–900. https://doi.org/10.1061/(ASCE)0733-9399(1998)124:8(892).

[75] Yu T, Teng JG, Wong YL, Dong SL. Finite element modeling of confined concrete-I: Drucker–Prager type plasticity model. Eng Struct 2010;32:665–79. https://doi.org/10.1016/j.engstruct.2009.11.014.

[76] Carreira DJ, Chu KH. Stress-Strain Relationship for Plain Concrete in Compression. ACI J Proc 1985;82:797–804. https://doi.org/10.14359/10390.

[77] Carreira DJ, Chu KH. Stress-Strain Relatonship for Reinforced Concrete in Tension. J Am Concr Inst 1986;83:21–8.

[78] Behnam H, Kuang JS, Samali B. Parametric finite element analysis of RC wide beam-column connections. Comput Struct 2018;205:28–44. https://doi.org/10.1016/j.compstruc.2018.04.004.

[79] Genikomsou AS, Polak MA. Finite element analysis of punching shear of concrete slabs using damaged plasticity model in ABAQUS. Eng Struct 2015;98:38–48. https://doi.org/10.1016/j.engstruct.2015.04.016.

[80] Ferreira FPV, Martins CH, De Nardin S. Sensitivity Analysis of Composite Cellular Beams to Constitutive Material Models and Concrete Fracture. Int J Struct Stab Dyn 2021;21:2150008. https://doi.org/10.1142/S0219455421500085.

[81] Ferreira FPV, Tsavdaridis KD, Martins CH, De Nardin S. Steel–Concrete-Composite Beams with Precast Hollow-Core Slabs: A Sustainable Solution. Sustainability 2021;13:4230. https://doi.org/10.3390/su13084230.

[82] Nguyen TNH, Tan KH, Kanda T. Investigations on web-shear behavior of deep precast, prestressed concrete hollow core slabs. Eng Struct 2019;183:579–93. https://doi.org/10.1016/j.engstruct.2018.12.052.

[83] Yun X, Gardner L. Stress-strain curves for hot-rolled steels. J Constr Steel Res 2017;133:36–46. https://doi.org/10.1016/j.jcsr.2017.01.024.

[84] Elharouney O, Elkateb M, Khalil A. Behaviour of prestressed hollow core slabs strengthened with NSM CFRP strips around openings: A finite element investigation. Eng Struct 2021;238:112262. https://doi.org/10.1016/j.engstruct.2021.112262.

[85] Nguyen HTN, Tan K-H. Shear response of deep precast/prestressed concrete hollow core slabs subjected to fire. Eng Struct 2021;227:111398. https://doi.org/10.1016/j.engstruct.2020.111398.

[86] Wijesiri Pathirana S, Uy B, Mirza O, Zhu X. Flexural behaviour of composite steel–concrete beams utilising blind bolt shear connectors. Eng Struct 2016;114:181–94. https://doi.org/10.1016/j.engstruct.2016.01.057.

[87] Katwal U, Tao Z, Hassan MK, Uy B, Lam D. Load sharing mechanism between shear studs and profiled steel sheeting in push tests. J Constr Steel Res 2020;174:106279. https://doi.org/10.1016/j.jcsr.2020.106279.

[88] Guezouli S, Lachal A. Numerical analysis of frictional contact effects in push-out tests. Eng Struct 2012;40:39–50. https://doi.org/10.1016/j.engstruct.2012.02.025.

[89] Sjaarda M, Porter T, West JS, Walbridge S. Fatigue Behavior of Welded Shear Studs in Precast Composite Beams. J Bridg Eng 2017;22:04017089. https://doi.org/10.1061/(ASCE)BE.1943-5592.0001134.

[90] Liu X, Bradford MA, Chen Q-J, Ban H. Finite element modelling of steel–concrete composite beams with high-strength friction-grip bolt shear connectors. Finite Elem Anal Des 2016;108:54–65. https://doi.org/10.1016/j.finel.2015.09.004.